The genus *Pheggomisetes* Knirsch, 1923 (Coleoptera: Carabidae: Trechinae) in Serbia: taxonomy, morphology and molecular phylogeny

MAJA VRBICA[1], ANDJELJKO PETROVIĆ[1], DEJAN PANTELIĆ[2], ALEKSANDAR J. KRMPOT[2], MIHAILO D. RABASOVIĆ[2], DANICA PAVLOVIĆ[2], SVETLANA JOVANIĆ[2], BORISLAV GUÉORGUIEV[3], STOYAN GORANOV[3], NIKOLA VESOVIĆ[1], DRAGAN ANTIĆ[1], ĐORĐE MARKOVIĆ[1], MATIJA PETKOVIĆ[1], LJUBIŠA STANISAVLJEVIĆ[1] and SREĆKO ĆURČIĆ[1*]

[1]*Institute of Zoology, University of Belgrade – Faculty of Biology, Studentski Trg 16, 11000 Belgrade, Serbia*
[2]*Institute of Physics, University of Belgrade, Pregrevica 118, 11080 Belgrade, Serbia*
[3]*National Museum of Natural History – Bulgarian Academy of Sciences, 1 Tsar Osvoboditel Blvd., 1000 Sofia, Bulgaria*

The genus *Pheggomisetes* Knirsch, 1923 consists of stenoendemic troglobitic ground beetles restricted to underground habitats in both Western Bulgaria and Southeast Serbia. A review of the genus in Serbia is given in this article. The following new taxa are described from three caves and pits on slopes of the Stara Planina Mountains in Southeast Serbia: ***Pheggomisetes serbicus* sp. nov.**, ***P. serbicus belensis* subsp. nov.** and ***P. globiceps ciniglavcensis* subsp. nov**. Also, *Pheggomisetes ninae* S. Ćurčić, Schönmann, Brajković, B. Ćurčić & Tomić, 2004, originally described as an independent species, is downgraded to a subspecies of *P. globiceps* Buresch, 1925 – ***P. globiceps ninae* S. Ćurčić, Schönmann, Brajković, B. Ćurčić & Tomić, 2004 comb. & stat. nov**. All the important morphological features of the taxa are listed in the article. The diagnoses of taxa are based on the characters ascertained by bright-field microscopy and nonlinear microscopy (NLM). The use of NLM in investigating *Pheggomisetes* anatomy is explained, and it is shown to be superior to classical microscopy in observing minute details of different structures (e.g. genitalia) on cross and longitudinal sections. A key to the species of *Pheggomisetes* (including the Serbian taxa) is given. In addition, we have included morphometric and molecular analyses of all Serbian *Pheggomisetes* taxa.

ADDITIONAL KEYWORDS: ground beetles – molecular systematics – morphometrics – new species – new subspecies – Trechini – troglobites.

INTRODUCTION

The genus *Pheggomisetes* Knirsch, 1923 includes four species and 12 subspecies of supposedly archaic troglobitic ground beetles, which have been highly modified during their evolution (Beron, 1994; Moravec, Uéno & Belousov, 2003; Ćurčić *et al.*, 2004). The genus occupies an isolated position in the tribe Trechini, alone forming a distinct phyletic series (Jeannel, 1928; Casale & Laneyrie, 1982; Casale, Vigna Tagli—anti & Juberthie, 1998). It is considered to be related to the Caucasian aphaenopsoid genus *Taniatrechus* Belousov & Dolzhansky, 1994 based on the supernumerary supraorbital and submentum setae, two widened male protarsomeres and male genital structure (Belousov & Dolzhansky, 1994; Belousov & Koval, 2009). All representatives of *Pheggomisetes* are stenoendemics and restricted to certain caves and pits in Western Bulgaria and Southeast Serbia. The currently known species of the genus are *Pheggomisetes buresi* (Knirsch, 1923); *Pheggomisetes globiceps* Buresch, 1925; *Pheggomisetes*

347

radevi Knirsch, 1924; and *Pheggomisetes ninae* S. Ćurčić, Schönmann, Brajković, B. Ćurčić & Tomić, 2004 (Casale & Laneyrie, 1982; Moravec *et al.*, 2003; Ćurčić *et al.*, 2004). One species (*P. ninae*) and one subspecies (*P. globiceps ilandjievi* V. Guéorguiev, 1964 according to Pretner, 1970) have been recorded in Serbia so far (Guéorguiev, 1964; Ćurčić *et al.*, 2004; Ćurčić, Brajković & Ćurčić, 2007; Nešić *et al.*, 2010).

The morphology and anatomy of *Pheggomisetes* taxa have been investigated by several authors (Jeannel, 1928; Decou & Botosaneanu, 1964; Juberthie & Decu, 1968). Jeannel (1928) was the first to investigate features of the mouthparts, the dorsal habitus and male genital structures. Other aspects of the nervous, digestive, genital and pygidial gland systems were analysed in *P. buresi* (Decou & Botosaneanu, 1964; Juberthie & Decu, 1968). Most recently, thanks to two-photon excitation autofluorescence (auto-TPEF) of the chitin, certain features of the mouthparts and male genitalia were presented for *P. ninae* (Rabasović *et al.*, 2015).

Troglobitic insects are depigmented or transparent, with a thin cuticle consisting mostly of homogeneous chitin (Christiansen, 2012). The use of TPEF microscopy seems to be a highly promising way to study troglobitic taxa like *Pheggomisetes* since it enables the investigator to avoid the fluorescence of pigments and other cuticle components. The fluorescent signal of chitin is dominant here, in contrast to the situation with strongly coloured insects.

Troglobitic beetles, including trechine ground beetles, are regarded as good models for deliberations about both biogeography and evolution since the reduced dispersal out of subterranean environments produces phylogenetic patterns of area distribution that largely match the geological history of mountain ranges and underground habitats (Ribera *et al.*, 2010; Faille *et al.*, 2014). The molecular phylogeny of trechine ground beetles (especially the troglobites) is largely unknown in spite of the fact that these are among the best-studied and widespread groups of beetles (Faille *et al.*, 2013). Within the Trechinae, the molecular phylogeny of *Trechus* species from Spain and subterranean Pyrenean taxa (Faille, Casale & Ribera, 2010a; Faille *et al.*, 2010b) and that of Alpine taxa (Faille *et al.*, 2013) have been more or less thoroughly treated in recently published articles (Contreras-Díaz *et al.*, 2007; Faille, Bourdeau & Fresneda, 2012; Faille *et al.*, 2014). Among other groups of ground beetles, representatives of the Carabinae and Harpalinae have been somewhat better studied with respect to molecular biology (Ober, 2002; Osawa, Su & Imura, 2004; Ober & Maddison, 2008; Ruiz, Jordal & Serrano, 2009; Ober & Heider, 2010; Andújar *et al.*, 2012; Deuve *et al.*, 2012; Šerić Jelaska *et al.*, 2014). Phylogenetic relationships of the highly diverse trechine fauna of the Balkan Peninsula are almost

unknown. One study only concluded that the genera *Neotrechus* Müller, 1913 and *Adriaphaenops* Noesske, 1928 are related to certain Alpine or Pyrenean taxa (Faille *et al.*, 2013). Sparse molecular data on the genus *Pheggomisetes* are mentioned solely by Faille *et al.* (2013).

Organized by the Institute of Zoology, University of Belgrade – Faculty of Biology, several field trips were carried out in Southeast Serbia from 2012 until 2014. They resulted in the discovery of one new species and two new subspecies of *Pheggomisetes*. The aims of this article were as follows: (1) to describe and diagnose the new trechine taxa; (2) to review the taxonomic status of *Pheggomisetes* taxa from Serbia; (3) to show the benefits of nonlinear microscopy (NLM) in investigating morphology of the beetles' internal chitinous structures (genitalia and some sclerites); (4) to conduct a morphometric study of all the investigated *Pheggomisetes* taxa; and (5) to perform a phylogenetic analysis of all the Serbian taxa using molecular data.

MATERIAL AND METHODS

SAMPLING INFORMATION

Ground beetle specimens were collected by hand or by pitfall trapping (the traps contained salt-saturated water/alcoholic vinegar and rotten meat as bait) (Faille *et al.*, 2012) in a number of underground habitats from Southeast Serbia and Western Bulgaria belonging to the Stara Planina (Balkan) Mountain system. The traps were placed on both the floor and walls in dark parts of the explored caves and pits, where the level of humidity was high. All the analysed *Pheggomisetes* taxa are troglobitic and live in underground habitats (caves and pits) in the Stara Planina (Balkan) Mountains of Southeast Serbia and Western Bulgaria. Collected specimens were transferred to 70% ethanol at room temperature, except in the case of specimens designated for molecular analysis, which were transferred to 96% ethanol at –20 °C. They were analysed in laboratories of the Institute of Zoology, University of Belgrade – Faculty of Biology, Belgrade, Serbia; the Department of Crop Science, University of Belgrade – Faculty of Agriculture, Belgrade, Serbia; and the Photonics Centre, Institute of Physics, University of Belgrade, Belgrade, Serbia.

MEASUREMENTS

AL – maximum length of antennae including the scape
AL/TL – ratio of maximum length of antennae including the scape to total body length (from the anterior margin of the clypeus to the elytral apex)
BW/PW – ratio of the elytral base width to maximum pronotum width as the greatest transverse distance

EL – elytral length (as the linear distance along the suture from the elytral base to the apex)

EL/EW – ratio of elytral length (as the linear distance along the suture from the elytral base to the apex) to maximum elytral width

EL/TL – ratio of elytral length (as the linear distance along the suture from the elytral base to the apex) to total body length (from the anterior margin of the clypeus to the elytral apex)

EW – maximum elytral width

EWP – position of maximum elytral width (percentage of length)

FL – length of frontal furrows

FL/HL – ratio of frontal furrow length to head length

HL – head length

HL/AL – ratio of head length to maximum length of antennae including the scape

HL/HW – ratio of head length to maximum head width

HL/PL – ratio of head length to pronotum length (along the median line)

HL/TL – ratio of head length to total body length (from the anterior margin of the clypeus to the elytral apex)

HW – maximum head width

HW/EW – ratio of maximum head width to maximum elytral width

HW/NW – ratio of maximum head width to maximum neck width

HW/PW – ratio of maximum head width to maximum pronotum width as the greatest transverse distance

HWP – position of maximum head width (percentage of length)

M – mean value for certain measurements

NW – maximum neck width

PaW – width of pronotal apex between tips of the anterior angles

PaW/PbW – ratio of pronotal apex width between tips of the anterior angles to pronotal base width between tips of the posterior angles

PaW/PW – ratio of pronotal apex width between tips of the anterior angles to maximum pronotum width as the greatest transverse distance

PbW – pronotal base width between tips of the posterior angles

PbW/PW – ratio of pronotal base width between tips of the posterior angles to maximum pronotum width as the greatest transverse distance

PL – pronotum length (along the median line)

PL/PW – ratio of pronotum length (along the median line) to maximum pronotum width as the greatest transverse distance

PL/TL – ratio of pronotum length (along the median line) to total body length (from the anterior margin of the clypeus to the elytral apex)

PW – maximum pronotum width as the greatest transverse distance

PW/EW – ratio of maximum pronotum width as the greatest transverse distance to maximum elytral width

PWP – position of maximum pronotum width (percentage of length)

R – range of total measurements performed

TL – total body length (from the anterior margin of the clypeus to the elytral apex)

COLLECTIONS

HT – holotype

IZFB – collection of the Institute of Zoology, University of Belgrade – Faculty of Biology, Belgrade, Serbia

NMNH – collection of the National Museum of Natural History, Sofia, Bulgaria

OTHER EXAMINED TAXA

Pheggomisetes buresi (Knirsch, 1923): one topotype male, Bulgaria, Balkan Mts., Ledenika Cave, 830 m a.s.l., near Vratsa, 19.VII.1963, leg. E. Pretner (IZFB).

Pheggomisetes globiceps globiceps Buresch, 1925: syntype male, Bulgaria, West Balkan range, Mt. Ponor Planina, Sofia district, a cave near Iskrets (= Dushnika Cave), village of Iskrets, 580 m a.s.l., 10.XII.1924, leg. D. Iltchev (NMNH); two topotype females, *idem*, 08.VII.1925, leg. N. Radev (NMNH); one topotype female, *idem*, 17.IX.1943, collector unknown (NMNH); one topotype male, *idem*, 15.II.1992, leg. I. Pandurski (NMNH); two topotype males and one topotype female, *idem*, 16.X–04.XI.2016, from pitfall traps, leg. B. Guéorguiev & S. Goranov (IZFB); one female, Bulgaria, West Balkan range, Mt. Ponor Planina, Sofia district, Otechestvo Cave, village of Iskrets, 720 m a.s.l., 24.V.1959, leg. A. Popov (NMNH); two males, *idem*, 16.X.2016, leg. B. Guéorguiev & S. Goranov (NMNH).

Pheggomisetes globiceps ilandjievi V. Guéorguiev, 1964: two topotype males and three topotype females, Bulgaria, Balkan Mts., Golyama Balabanova Dupka Cave, 1100 m a.s.l., village of Komshtitsa, near Godech, 12.X.1995, leg. B. Guéorguiev & V. Beshkov (IZFB); two topotype males and three topotype females, *idem*, 30.V.2015, leg. S. Goranov (IZFB).

TAXONOMIC AND MORPHOLOGICAL ANALYSES

The traditional method of studying insect morphology by bright-field microscopy was mainly used in the study. Apart from this, 3D images and clips obtained by NLM provided additional details that were used for descriptions of the genital structures and diagnoses of the studied taxa.

Bright-field microscopy

The genitalia were removed from the bodies, preserved in clove oil for a few days and subsequently fixed on microscope slides in Canada balsam. The beetles were then glued onto rectangular paper labels and analysed as dry specimens. Stemi 2000 and Stereo Discovery.V8 binocular stereomicroscopes (Carl Zeiss, Jena, Germany) with AxioCam MRc and Axio Cam ICc 1 digital cameras (Carl Zeiss, Jena, Germany) attached were used to photograph whole specimens, while a DMLS light microscope (Leica, Wetzlar, Germany) with a DC 300 camera (Leica, Wetzlar, Germany) attached was used to photograph the genitalia.

Nonlinear microscopy

Bright-field microscopy is most often used to study insect morphology, but recently a few articles have appeared treating the use of confocal fluorescence microscopy to observe certain structures of insects and crustaceans (Klaus, Kulasekera & Schawaroch, 2003; Michels, 2007; de Campos Vidal, 2011). NLM has also been introduced as a method offering unique insight into a variety of biological structures. This technique is similar to confocal microscopy (in employing localized laser excitation and scanning), but is characterized by higher penetration depth, reduced photodamage and photobleaching, and no need for specimen staining in most cases (Denk, Strickler & Webb, 1990; Williams, Zipfel & Webb, 2001; Mertz, 2004; Masters & So, 2008). Tissues and individual cells can be observed with high resolution of volume details. Up until now, NLM has been used extensively in biomedical research, but only marginally in entomology (Lin *et al.*, 2008; Chien *et al.*, 2011). It was recently confirmed that NLM can be used for deep imaging of chitinous structures (both chemically purified chitin and chitin originating from insect integument) (Rabasović *et al.*, 2015; Reinhardt, Breunig & König, 2017). On the basis of the autofluorescence properties of chitin, the TPEF modality of NLM was mainly used in the latter study. In addition, even a second harmonic generation signal originating from chitinous structures was detected, but this signal is unsuitable for imaging since it is weak and hindered by the much stronger auto-TPEF.

Before analysis, specimens were stored in 70% ethanol at room temperature. The genitalia were removed from the bodies and preserved in clove oil for 2 weeks. Genital structures were placed on double-sided adhesive tape on microscope slides in glycerin as the medium, with or without a cover slip, depending on the microscope objective used.

All variables that entered the statistical analysis were tested for normality using the Shapiro-Wilk test. A multivariate test of significance (one-way MANOVA) of normally distributed data, followed by a univariate test of significance (one-way ANOVA) for each variable, was used to identify which data sets (between groups) differ significantly. Non-normally distributed variables were compared between taxon samples using the Mann–Whitney U test ($P \leq 0.05$). MANOVA allows comparison of population means of all variables of interest at the same time (multivariate response) rather than considering multiple responses as a suite of univariate responses (Zar, 1999). The statistical test most often used in biology, Wilks' lambda, was applied (Zar, 1999). One-way MANOVA was used to examine the differences in morphological variation among Serbian *Pheggomisetes* taxa (species and subspecies). To describe and interpret effects from MANOVA, multivariate discriminant analysis (DA) was used only on normally distributed variables to determine the relative importance of characters as discriminators between a priori groups and the relative positions of centroids of the groups (Manly, 1986).

The distance matrix for subspecies was calculated based on the squared Mahalanobis distance between subspecies centroids, and a dendrogram was generated using UPGMA (unweighted pair group method with arithmetic mean) clustering. This was used to evaluate the phenetic relationships between subspecies. Statistical analyses were conducted using the Statistica 6 software package (StatSoft, Inc., 2001).

MOLECULAR ANALYSIS

DNA extraction, PCR amplification and sequencing

We used nine *Pheggomisetes* specimens (belonging to all Serbian taxa) for molecular analyses (Table 1). DNA was extracted from one hind leg of each specimen using the KAPA Express Extract Kit (Kapa Biosystems Inc., Boston, MA, USA) and following the manufacturer's instructions. The primers used to amplify the barcoding region of cytochrome *c* oxidase subunit I (*COI*) gene were Jerry [(CI-J-2183)5′-CAACATTTATTTTGATTTTTTGG-3′] and Pat [(TL2-N-3014)5′-TCCAAAGCACTAATCTGCCATATTA-3′] (Simon *et al.*, 1994). Each PCR was carried out in a volume of 25 µL containing 1 µL of extracted DNA, 9 µL of H_2O, 1.25 µL of each primer and 12.5 µL of KAPA2G^tm HotStart ReadyMix. All PCRs were conducted in an Eppendorf Mastercycler (Hamburg, Germany) using the following thermal

Table 1. Trechine specimens used for molecular analyses with GenBank accession numbers

Code	Locality	Taxon	Accession number
S3	Hodžina Dupka Pit	**Pheggomisetes globiceps ninae comb. & stat. nov.**	KY351544
S12	Tmna Dupka Cave	**P. globiceps ninae comb. & stat. nov.**	KY351545
S28	Petrlaška Pećina Cave	**P. globiceps ninae comb. & stat. nov.**	KY351546
S19	Propas Pit	**P. globiceps ciniglavcensis subsp. nov.**	KY351547
S21	Pež Dupka Cave	**P. serbicus serbicus subsp. nov.**	KY351548
S26	Suva Dupka Cave	**P. serbicus belensis subsp. nov.**	KY351549
S27	A cave in the vicinity of the Suva Dupka Cave	**P. serbicus belensis subsp. nov.**	KY351542
S41	Golyama Balabanova Dupka Cave	*P. globiceps ilandjievi*	KY351543
S66	Otechestvo Cave	*P. globiceps globiceps*	KY351550
S1	Zlotska (= Lazareva) Pećina Cave	*Duvalius (Paraduvalius) stankovitchi georgevitchi****	KY351551

*Outgroup.

profile: initial denaturation (95 °C for 5 min); amplification (35 cycles consisting of 60 s at 95 °C, 60 s at 51 °C and 120 s at 72 °C); and final extension (72 °C for 7 min).

The PCR products were purified using the QIAquick Purification Kit (QIAGEN Inc., Valencia, CA, USA) according to the manufacturer's instructions.

DNA sequencing was performed using automated equipment (Macrogen Inc., Seoul, South Korea).

Sequences were manually edited in FinchTV (Geospiza Inc., Seattle, WA, USA) and aligned using the ClustalW program integrated in MEGA5 (Tamura *et al.*, 2011).

Genetic divergence was estimated using Kimura's two-parameter (K2P) method of base substitution (Kimura, 1980).

Phylogenetic reconstruction was performed using maximum parsimony (MP), maximum likelihood (ML) and neighbor-joining (NJ) incorporated in the MEGA5 software package. One thousand bootstrap replicates were performed in every analysis to assess robustness of the trees. Tamura's three-parameter model (T92 + G) was identified as the best-fitting model of sequence evolution based on the Bayesian information criterion and corrected Akaike information criterion (Nei & Kumar, 2000) for the ML method of phylogenetic reconstruction. The subspecies *Duvalius* (*Paraduvalius*) *stankovitchi georgevitchi* (Jeannel, 1924) was used as an outgroup. The nucleotide sequence data were deposited in the GenBank database under accession numbers KY351542–KY351551 (Table 1). K2P model was used to estimate genetic divergence of the analysed taxa.

RESULTS AND DISCUSSION

TAXONOMY

FAMILY CARABIDAE LATREILLE, 1802

SUBFAMILY TRECHINAE BONELLI, 1810

TRIBE TRECHINI BONELLI, 1810

GENUS *PHEGGOMISETES* KNIRSCH, 1923

***PHEGGOMISETES SERBICUS* ĆURČIĆ, VRBICA & B. GUÉORGUIEV SP. NOV.**

(FIGS 1 AND 2A–H)

Material examined: Holotype male labelled as follows: 'Southeast Serbia, Stara Planina Mts., Pež Dupka Cave, 43°13′17.77″N 22°47′17.08″E, village of Dojkinci, 869 m a.s.l., near Pirot, 11.VII–10.X.2013, from pitfall traps, leg. D. Antić & M. Petković' (white label, printed)/'Holotypus *Pheggomisetes serbicus* sp. nov. Ćurčić, Vrbica & Guéorguiev det. 2016' (red label, printed) (IZFB). Paratypes: six males and eight females, same data as for holotype (IZFB); three males and four females labelled as follows: 'Southeast Serbia, Stara Planina Mts., Pež Dupka Cave, village of Dojkinci, 869 m a.s.l., near Pirot, 11.VII.2013, leg. D. Antić & M. Petković' (IZFB). All paratypes are labelled with white printed locality labels and with red printed labels 'Paratypus *Pheggomisetes serbicus* sp. nov. Ćurčić, Vrbica & Guéorguiev det. 2016'.

Description: TL R 5.55–6.675 mm (M 6.11 mm) (HT 6.30 mm). Head oval, HL/HW R 1.18–1.34 (M 1.26) (HT 1.27), widest somewhat before its middle, scarcely wider than pronotum (Fig. 1). Frontal furrows long, slightly exceeding mid head level, deeply impressed

Figure 1. *Pheggomisetes serbicus* **sp. nov.** from the Než Dupka Cave, village of Dojkinci (near Pirot), Stara Planina Mts., Southeast Serbia. Holotype male, habitus (dorsal view). Scale = 5.0 mm.

anteriorly and sigmoidally curved. Neck narrow, HW/NW R 1.97–2.75 (M 2.50) (HT 2.19). Antennae long, around the same length as TL in males, while shorter than TL in females.

Pronotum widest somewhat after the anterior third, almost as long as wide (Fig. 1). Anterior pronotal margin concave, shorter than pronotal base. Lateral pronotal margins rounded anteriorly and slightly concave posteriorly. Pronotal base somewhat concave in the middle. Fore pronotal angles obtuse, rounded. Hind pronotal angles acute, almost right.

Elytra relatively long, oval, convex, with the lateral sides rounded anteriorly, widest slightly after the mid level, EL/EW R 1.61–1.83 (M 1.725) (HT 1.81). Elytral base slightly narrower than pronotum (Fig. 1). Humeral angles obtuse, rounded and quite elevated. Elytral apex rounded.

Legs and claws long and thin (Fig. 1).

Median lobe of the aedeagus in lateral view curved, with a rounded somewhat elevated apex (Fig. 2A, E). Basal bulb small, rounded. Parameres with three apical setae each. Median lobe in dorsal view straight, with a rounded apex, narrowing towards basal bulb (Fig. 1B). Gutter-shaped copulatory piece covered with numerous spines (Fig. 2B, F), wide at its basal three fifths and markedly narrowed at its apical two fifths.

Male abdominal sternite IX (urite) subtriangular, slightly elongate, slightly longer than aedeagus (Fig. 2C, G). Apophysis narrow, constricted proximally.

Both gonocoxites IX and gonosubcoxites IX as presented in Figure 2D, H. Gonocoxites IX of moderate length, slightly curved, apically rounded, basally completely jointed with massive gonosubcoxites IX (Fig. 2D, H).

Chaetotaxy. Frons with six to seven (HT – 7) setae on each side. Pronotum with normal chaetotaxy (two pairs of setae). Five to seven setae on third interstria (HT – 7) on each elytron (Fig. 1).

Elytral umbilicate series: First three humeral setae close to marginal gutter, fourth being somewhat farther from the gutter, distance between umbilicate pores 2 and 3 shortest, while between pores 3 and 4 longest; median series at around the middle of the elytra, two setae being somewhat distanced from marginal gutter, distance between pores 5 and 6 about as long as distance between pores 2 and 3; apical series: setae 7 and 8 being somewhat distanced from marginal gutter, distance between pores 7 and 8 longer than distance between pores 3 and 4 (Fig. 1).

Differential diagnosis: The new species is compared here with the other known *Pheggomisetes* species (Casale & Laneyrie, 1982; Moravec *et al.*, 2003). A comparison of the new species with *P. ninae* is not provided here since the latter taxon is regarded as a subspecies of *P. globiceps* (see below).

The new species differs from *P. globiceps* in having a smaller value of TL M (6.11 vs. ≥ 6.295 mm), a smaller value of HL M (1.39 vs. ≥ 1.40 mm), smaller values of AL M (5.91, males 6.01, females 5.70 vs. ≥ 6.525 mm, males ≥ 6.56 mm, females ≥ 6.30 mm), smaller values of AL/TL M (0.97, males 0.99, females 0.92 vs. ≥ 1.01, males ≥ 1.05, females ≥ 0.97), a greater value of HL/AL M (0.235 vs. ≤ 0.225), a greater value of FL M (0.75 vs. ≤ 0.68 mm), a greater value of FL/HL M (0.54 vs. ≤ 0.48), different shape of the humeral angles (more rounded, quite elevated vs. more obtuse, less elevated), a greater value of EL/TL M (0.55 vs. ≤ 0.54) and different shape of the copulatory piece in dorsal aspect (more markedly narrowed apically vs. gradually narrowed apically) (Tables 2 and 3; Figs 1–13; Supporting Information, Table S1) (Jeannel, 1928; Guéorguiev, 1964; this study). Even though the differences
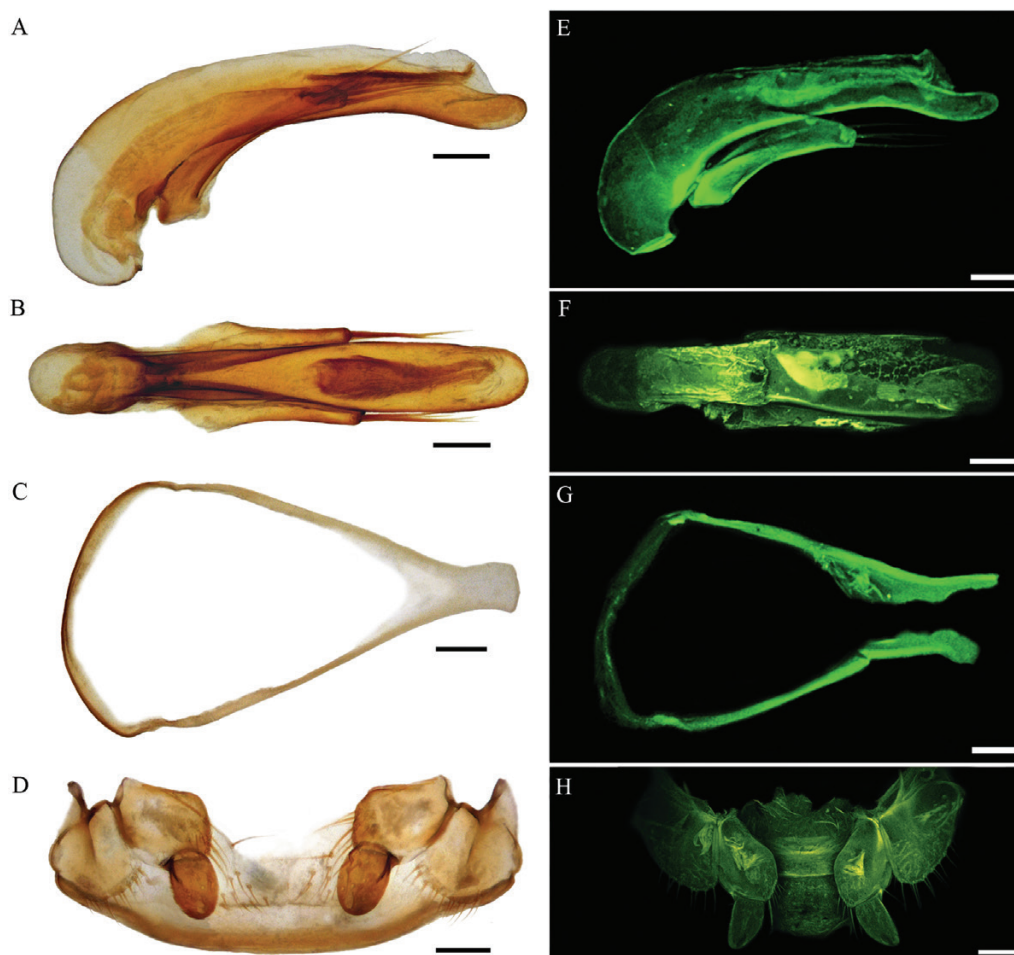
Figure 2. *Pheggomisetes serbicus* **sp. nov.** from the Pež Dupka Cave, village of Dojkinci (near Pirot), Stara Planina Mts., Southeast Serbia. Bright-field (A–D) and TPEF (E–H) microscopy images. A, E, holotype male, aedeagus (lateral view). B, F, holotype male, aedeagus (dorsal view). C, G, holotype male, abdominal sternite IX (urite). D, H, paratype female, gonocoxites IX and gonosubcoxites IX. Scales = 0.1 mm.

obtained between the mean values of certain measurements (HL) and ratios (HL/AL, EL/TL) are very small (Supporting Information, Table S1), the distributions of ranges in the two species show statistically significant differences (Table 3).

The new species differs from *P. radevi* in having a smaller value of TL R (5.55–6.675 vs. 7–8 mm), a greater value of HL/HW M (1.26 vs. 1.00), different shape of the head (widest slightly before its mid part, posteriorly somewhat convex vs. widest around its mid part, posteriorly very convex), a smaller value of HW/NW M (2.50 vs. *c.* 3.00), different shape of the pronotum (weakly narrowed basally, strongly rounded anteriorly, well sinuate in back vs. strongly narrowed basally, weakly rounded anteriorly, strongly sinuate in back), a different value of PaW/PbW (pronotal apex between tips of the anterior angles narrower than pronotal base between tips of the posterior angles vs. pronotal apex

between tips of the anterior angles wider than pronotal base between tips of the posterior angles), different shape of the hind pronotal angles (almost right, not prominent vs. acute, protruding backwards and outwards), different form of the elytra (less elongate, with more prominent shoulders vs. more elongate, with less prominent shoulders), different shape of the median lobe (less bent vs. more bent) and different shape of the basal bulb (relatively small, rounded vs. medium-sized, relatively elongate) (Jeannel, 1928; Guéorguiev, 1964; this study).

The new species differs from *P. buresi* in having a smaller value of TL R (5.55–6.675 vs. 7.20–9.00 mm), different shape of the head (less elongate, posteriorly more convex, abruptly narrowing towards the neck vs. more elongate, posteriorly less convex, gradually narrowing towards the neck), a different position of maximum head width (slightly in front of the

Table 2. Results of ANOVA for each variable between *P. serbicus* sp. nov. and *P. globiceps* (exact significance level $P \leq 0.05$, marked in bold)

Variable	F	P-value
HL	**4.760**	**0.033**
HW	0.273	0.603
FL	**11.519**	**0.001**
HL/HW	1.346	0.251
HL/AL	**54.485**	**< 0.001**
HL/PL	0.559	0.458
HL/TL	**22.596**	**< 0.001**
HW/NW	1.875	0.176
HW/PW	0.040	0.843
AL/TL	**17.269**	**< 0.001**
PW	1.092	0.300
PL/PW	3.788	0.056
PaW	**5.207**	**0.026**
PbW	0.287	0.594
PaW/PW	3.582	0.063
PbW/PW	0.047	0.829
PaW/PbW	3.744	0.058
EW	**11.428**	**0.001**
EWP	0.673	0.415
BW/PW	0.643	0.426

Table 3. Results of Mann–Whitney *U* test between *P. serbicus* sp. nov. ($n = 24$) and *P. globiceps* ($n = 44$) (exact significance level $P \leq 0.05$, marked in bold)

Variable	U	P-value
TL	**116.5**	**< 0.001**
HWP	447.5	0.305
AL	**1.5**	**< 0.001**
FL/HL	**250.0**	**< 0.001**
HW/EW	**320.0**	**0.014**
PL	**345.5**	**0.026**
PWP	**233.5**	**< 0.001**
PL/TL	**224.5**	**< 0.001**
PW/EW	**245.0**	**0.001**
EL	431.0	0.325
EL/EW	**351.5**	**0.042**
EL/TL	**206.0**	**< 0.001**

middle vs. anteriorly), a greater value of HW/NW M (2.50 vs. *c*. 2.00), different form of the lateral pronotal margins (a little rounded anteriorly, slightly sinuate posteriorly vs. somewhat arcuate), different shape of the hind pronotal angles (almost right, not prominent vs. acute, protruding backwards and outwards), different shape of the elytra (less elongate, with more pronounced shoulders vs. more elongate, with less pronounced shoulders), different shape of

the median lobe (less elongate, less bent vs. more elongate, more bent) and different shape of the basal bulb (relatively small, rounded vs. relatively massive, elongate) (Jeannel, 1928; Guéorguiev, 1964; this study).

Among the three known species of the genus, *P. globiceps* is the smallest one and the only species that has right hind angles of the pronotum (Jeannel, 1928; Guéorguiev, 1964). It has a pronotum that is weakly narrowed basally, with lateral margins moderately rounded anteriorly and weakly sinuate posteriorly, in addition to a relatively narrow elytral base (Jeannel, 1928; Guéorguiev, 1964). Thus, it is quite clear that *P. serbicus* sp. nov. shares the same character states and is closely related to it. In addition, *P. buresi* differs from all other congeners in having a rather thick neck. No significant differences within the genus are evident in the male genitalia (especially in regard to shape of the median lobe), even at the species level (Jeannel, 1928; Guéorguiev, 1964; this article).

Variability: The number of setae on both frons (six to seven on each side) and elytra can vary (five to seven on each side).

Etymology: The new species is named after Serbia, its *terra typica*.

Distribution: The type locality is the Pež Dupka Cave in the village of Dojkinci (near Pirot) in the Stara Planina Mountains of Southeast Serbia. The new species inhabits a few caves in the villages of Dojkinci and Bela in the Stara Planina Mountains of Southeast Serbia; *P. buresi* and *P. radevi* live in caves near the town of Vratsa and villages of Chiren, Eliseyna, Chelopek, Druzhevo and Milanovo in the West Stara Planina Mountains of Western Bulgaria; and *P. globiceps* inhabits numerous caves in the West Stara Planina Mountains and Pre-Balkan region of Western Bulgaria, as well as a few caves in the villages of Petrlaš and Činiglavci in the Stara Planina Mountains of Southeast Serbia (Guéorguiev & Guéorguiev, 1995; this study).

PHEGGOMISETES SERBICUS BELENSIS ĆURČIĆ, VRBICA & B. GUÉORGUIEV **SUBSP. NOV.**

(FIGS 4 AND 5A–H)

Material examined: Holotype male labelled as follows: 'Southeast Serbia, Stara Planina Mts., Suva Dupka Cave, 43°14′40.9″N 22°44′16.5″E, village of Bela, 801 m a.s.l., near Pirot, 25.V.2014, leg. S. Ćurčić, D. Antić & I. Petrović' (white label, printed)/'Holotypus *Pheggomisetes serbicus belensis* subsp. nov. Ćurčić, Vrbica & Guéorguiev det. 2016' (red label, printed) (IZFB). Paratypes: three males

and two females, same data as for holotype (IZFB); four males and eight females labelled as follows: 'Southeast Serbia, Stara Planina Mts., Suva Dupka Cave, village of Bela, 801 m a.s.l., near Pirot, 25.V-05.VII.2014, from pitfall traps, leg. D. Antić' (IZFB); one female labelled as follows: 'Southeast Serbia, Stara Planina Mts., a cave in the vicinity of the Suva Dupka Cave, 43°14′30.84″N 22°44′9.40″E, village of Bela, 793 m a.s.l., near Pirot, 25.V-05.VII.2014, from pitfall traps, leg. D. Antić' (IZFB). All paratypes are labelled with white printed locality labels and with red printed labels 'Paratypus *Pheggomisetes serbicus belensis* subsp. nov. Ćurčić, Vrbica & Guéorguiev det. 2016'.

Description: TL R 5.70–6.60 mm (M 6.045 mm) (HT 5.925 mm). HL/HW R 1.23–1.33 (M 1.27) (HT 1.24) (Fig. 4). Frontal furrows reaching mid head level. HW/NW R 2.09–2.50 (M 2.24) (HT 2.25).

Anterior pronotal margin clearly (in males) or slightly (in females) concave, shorter than pronotal base (Fig. 3). Lateral pronotal margins very slightly concave posteriorly.

Elytra with lateral sides almost straight in the anterior half, EL/EW R 1.62–1.92 (M 1.77) (HT 1.71) (Fig. 4).

Median lobe of the aedeagus in lateral view slightly convex dorsally at around the level of two fifths, having an almost straight apex (Fig. 5A, E). Median lobe
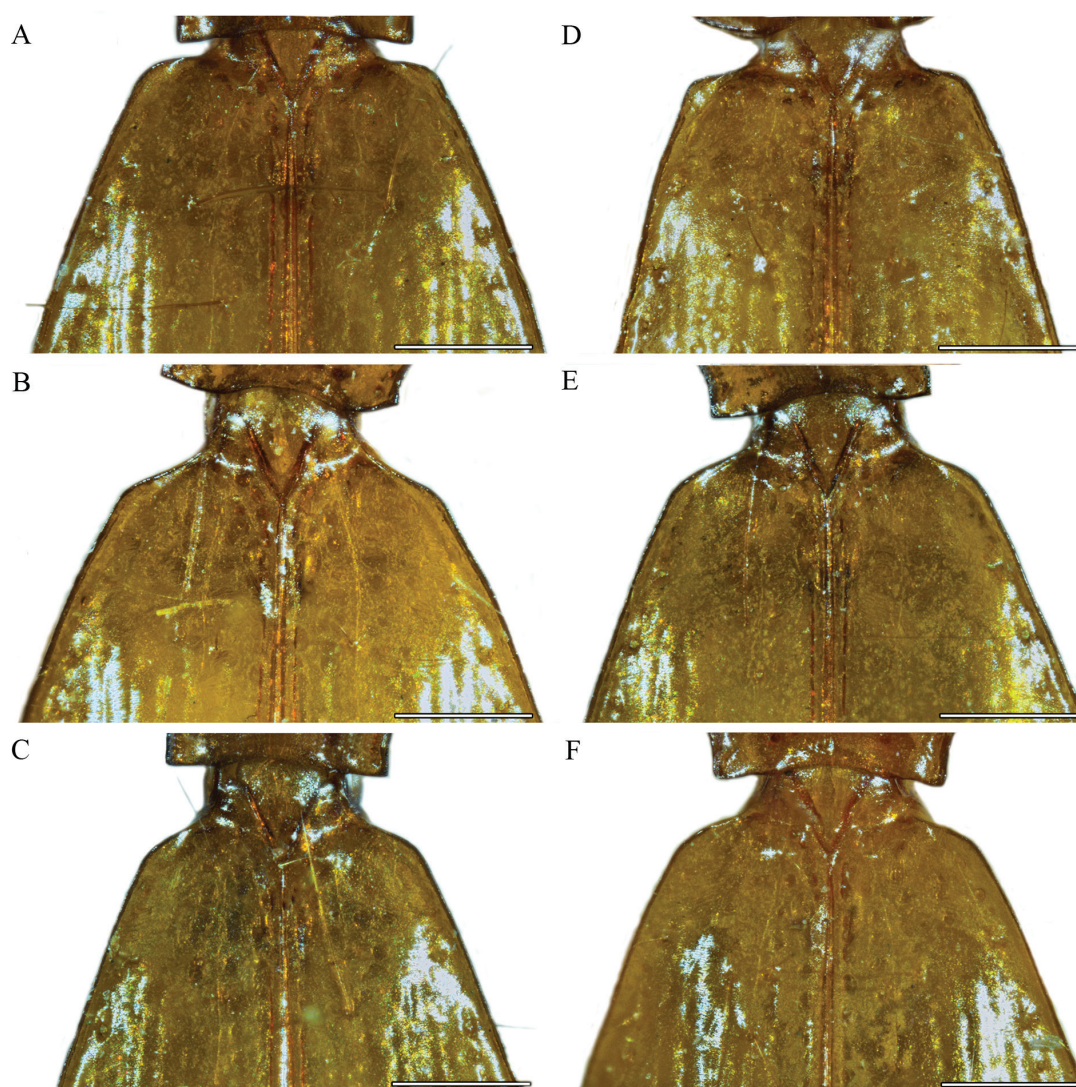
Figure 3. Shape of the shoulders in the *Pheggomisetes* subspecies analysed. A, **P. serbicus serbicus subsp. nov**. B, **P. globiceps ciniglavcensis subsp. nov**. C, **P. globiceps ilandjievi**. D, **P. serbicus belensis subsp. nov**. E, **P. globiceps ninae comb. & stat. nov**. F, *P. globiceps globiceps*. Scales = 0.5 mm.

Figure 4. *Pheggomisetes serbicus belensis* **subsp. nov.** from the Suva Dupka Cave, village of Bela (near Pirot), Stara Planina Mts., Southeast Serbia. Holotype male, habitus (dorsal view). Scale = 5.0 mm.

in dorsal view as presented in Figure 5B, F and inner sac as presented in Figure 5A, B, E, F.

Male abdominal sternite IX (urite) as presented in Figure 5C, G, subtriangular, slightly elongate, slightly longer than aedeagus. Apophysis narrow, constricted proximally.

Both gonocoxites IX and gonosubcoxites IX as presented in Figure 5D, H.

Chaetotaxy. Frons with six to eight (HT – 6) setae on each side. Pronotum with normal chaetotaxy (two pairs of setae). Five to seven setae on third interstria (HT – 6–7) on each elytron (Fig. 4).

Elytral umbilicate series: First three humeral setae close to marginal gutter, fourth being somewhat farther from the gutter, distance between umbilicate pores 2 and 3 shortest, distance between pores 1 and 2 approximately the same as between pores 3 and 4; median series at around the middle of the elytra, two setae being somewhat distanced from the gutter, distance between pores 5 and 6 somewhat shorter than distance between pores 2 and 3; apical series: setae 7 and 8 being somewhat distanced from marginal gutter, distance between pores 7 and 8 longer than distance between pores 3 and 4 (Fig. 4).

Differential diagnosis: The new subspecies is compared with the nominal subspecies, *P. serbicus serbicus* subsp. nov.

The new subspecies clearly differs from *P. serbicus serbicus* subsp. nov. in having a smaller value of TL M (6.045 vs. 6.11 mm), a different value of FL/HL M (frontal furrows reaching mid head level vs. frontal furrows somewhat exceeding mid head level), a smaller value of HW/NW M (2.24 vs. 2.50), a smaller value of FL M (0.68 vs. 0.75 mm), a greater value of AL M (5.99 vs. 5.91 mm), different shape of the anterior pronotal margin in females (less concave vs. more concave), different shape of the pronotal base in the middle (less concave vs. more concave), different shape of the lateral margins of the elytra anteriorly (more straight vs. rounded), a greater value of PaW/PbW M (0.78 vs. 0.74), a greater value of EL/EW M (1.77 vs. 1.725), a different position of certain humeral and median setae (distance between pores 2 and 3 shortest, distance between pores 1 and 2 approximately the same as between pores 3 and 4, distance between pores 5 and 6 somewhat shorter than distance between pores 2 and 3 vs. distance between pores 2 and 3 shortest, distance between pores 3 and 4 longest, distance between pores 5 and 6 about as long as distance between pores 2 and 3) belonging to the elytral umbilicate series, different shape of the median lobe apex in lateral aspect (almost straight vs. somewhat elevated) and different shape of the median lobe's basal bulb in lateral aspect (more curved vs. less curved) (Supporting Information, Table S1) (this study).

Variability: The number of setae on both frons (six to eight on each side) and elytra can vary (five to seven on each side).

Etymology: The new subspecies is named after the village of Bela, in which the type locality is situated.

Distribution: It inhabits two caves in the village of Bela (near Pirot) in the Stara Planina Mountains of Southeast Serbia – the Suva Dupka Cave and a cave in its vicinity.
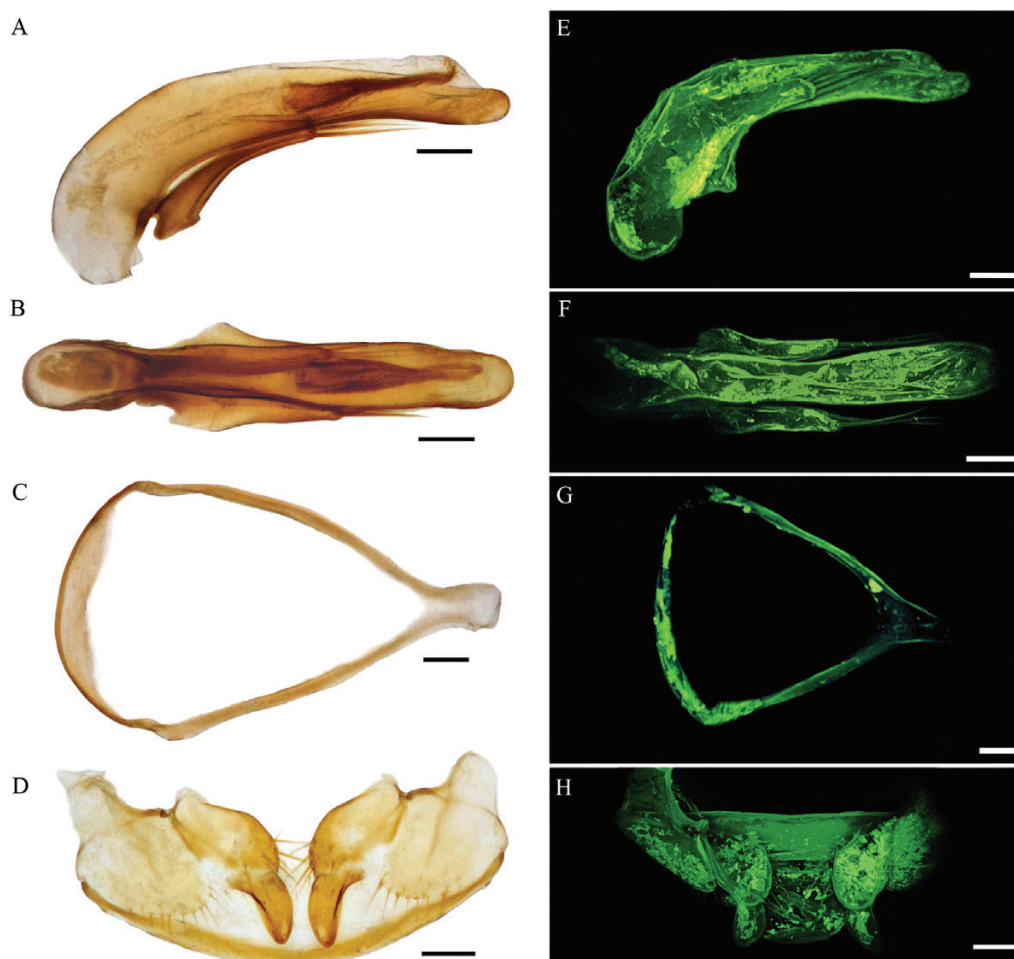
Figure 5. *Pheggomisetes serbicus belensis* **subsp. nov.** from the Suva Dupka Cave, village of Bela (near Pirot), Stara Planina Mts., Southeast Serbia. Bright-field (A–D) and TPEF (E–H) microscopy images. A, E, holotype male, aedeagus (lateral view). B, F, holotype male, aedeagus (dorsal view). C, G, holotype male, abdominal sternite IX (urite). D, H, paratype female, gonocoxites IX and gonosubcoxites IX. Scales = 0.1 mm.

PHEGGOMISETES GLOBICEPS BURESCH, 1925

PHEGGOMISETES GLOBICEPS CINIGLAVCENSIS
ĆURČIĆ & VRBICA, **SUBSP. NOV.**

(FIGS 6 AND 7A–H)

Pheggomisetes globiceps ilandjievi: Gajović *et al.* (2011: 80).

Material examined: Holotype male labelled as follows: 'Southeast Serbia, Stara Planina Mts., Propas Pit, 43°04′05.7″N 22°44′18.5″E, village of Činiglavci, 714 m a.s.l., near Pirot, 29.V-08.VII.2013, from pitfall traps, leg. Đ. Marković & M. Petković' (white label, printed)/'Holotypus *Pheggomisetes globiceps ciniglavcensis* subsp. nov. Ćurčić, Vrbica & Guéorguiev det. 2016' (red label, printed) (IZFB). Paratypes: 29 males and 20 females, same data as for holotype (IZFB). All paratypes are labelled with white printed locality labels and with red printed labels 'Paratypus

Pheggomisetes globiceps ciniglavcensis subsp. nov. Ćurčić, Vrbica & Guéorguiev det. 2016'.

Description: TL R 6.15–6.825 mm (M 6.46 mm) (HT 6.525 mm). Head oval, HL/HW R 1.19–1.355 (M 1.275) (HT 1.19), widest somewhat before its mid part, scarcely wider than pronotum (Fig. 6). Frontal furrows almost reaching mid head level, deeply impressed anteriorly and sigmoidally curved. Neck narrow, HW/NW R 2.17–2.61 (M 2.405) (HT 2.50). Antennae long, longer (in males) or slightly shorter (in females) than TL.

Pronotum widest somewhat after the anterior third, almost as long as wide (Fig. 6). Anterior pronotal margin slightly concave, shorter than pronotal base. Lateral pronotal margins rounded anteriorly and slightly concave posteriorly. Pronotal base very slightly concave in the middle. Fore pronotal angles obtuse, rounded. Hind pronotal angles acute, almost right.

Figure 6. *Pheggomisetes globiceps ciniglavcensis* **subsp. nov.** from the Propas Pit, village of Činiglavci (near Pirot), Stara Planina Mts., Southeast Serbia. Holotype male, habitus (dorsal view). Scale = 5.0 mm.

Elytra relatively long, oval, convex, widest somewhat after the mid level, EL/EW R 1.53–1.73 (M 1.64) (HT 1.68). Elytral base slightly wider than pronotum (BW/PW R 0.85–1.10, M 1.03, HT 1.00) (Fig. 6). Humeral angles obtuse, rounded and relatively elevated. Elytral apex rounded.

Legs and claws long and thin (Fig. 6).

Median lobe of the aedeagus curved, slightly convex dorsally around the basal fourth, with a rounded apex (Fig. 7A, B, E, F). Basal bulb small, rounded. Parameres with three setae each, of which two are apically positioned. Triangular gutter-shaped copulatory piece covered with numerous thorns (Fig. 7B, F), gradually narrowed apically in dorsal aspect.

Male abdominal sternite IX (urite) subtriangular, slightly elongate, somewhat longer than aedeagus (Fig. 7C, G). Apophysis narrow, gradually narrowing distally.

Both gonocoxites IX and gonosubcoxites IX as presented in Figure 7D, H. Gonocoxites IX slightly elongate, somewhat curved, apically rounded, basally completely jointed with massive gonosubcoxites IX (Fig. 7D, H).

Chaetotaxy. Frons with five to seven setae (HT – 6–7) on each side. Pronotum with normal chaetotaxy (two pairs of setae). Six to eight setae on third interstria (HT – 6–7) on each elytron (Fig. 6).

Elytral umbilicate series: First three humeral setae close to marginal gutter, fourth being somewhat farther from the gutter, distance between umbilicate pores 2 and 3 shortest, distance between pores 1 and 2 is approximately the same as between pores 3 and 4; median series at around the middle of the elytra, two setae being somewhat distanced from marginal gutter, distance between pores 5 and 6 about as long as distance between pores 2 and 3; apical series: setae 7 and 8 being somewhat distanced from marginal gutter, distance between pores 7 and 8 longer than distance between pores 3 and 4 (Fig. 6).

Differential diagnosis: The known subspecies of *P. globiceps* differ in shape of the head, length and depth of the frontal furrows, shape of the hind pronotal angles, lateral margins of the head and pronotum, the HL/PL and shape of the humeral angles (Guéorguiev, 1964). Some new characters should also be taken into account in separating *Pheggomisetes* taxa (e.g. TL, HL, HL/HW, HL/AL, HL/TL, HW/NW, HW/PW, HW/EW, AL, AL/TL, PL, PL/PW, PL/TL, PaW, PbW, PW, PW/EW, PWP, EW, EL/EW, BW/PW, elytral umbilicate series position, and aedeagus and copulatory piece shapes) (Tables 2 and 3; Supporting Information, Table S1). The new subspecies is compared here with the morphologically and geographically closest subspecies of *P. globiceps* and the nominotypical subspecies. The former are *P. globiceps ilandjievi* (Figs 10, 11A–D) and *P. globiceps ninae* comb. & stat. nov. (with the head elongately ovoid, lateral margins of the head moderately rounded, head slightly rounded both anteriorly and posteriorly as well, acute/right posterior pronotal angles, pronotum basally constricted, head slightly broader than pronotum and humeral angles slightly elevated) (Guéorguiev, 1964; Ćurčić *et al.*, 2004; this article).

Pheggomisetes globiceps ciniglavcensis subsp. nov. differs from *P. globiceps ilandjievi* in having a smaller value of TL M (6.46 vs. 6.60 mm), different shape of the head (widest at 2/5 of its length vs. widest slightly before the middle), a smaller value of HL/HW M (1.275
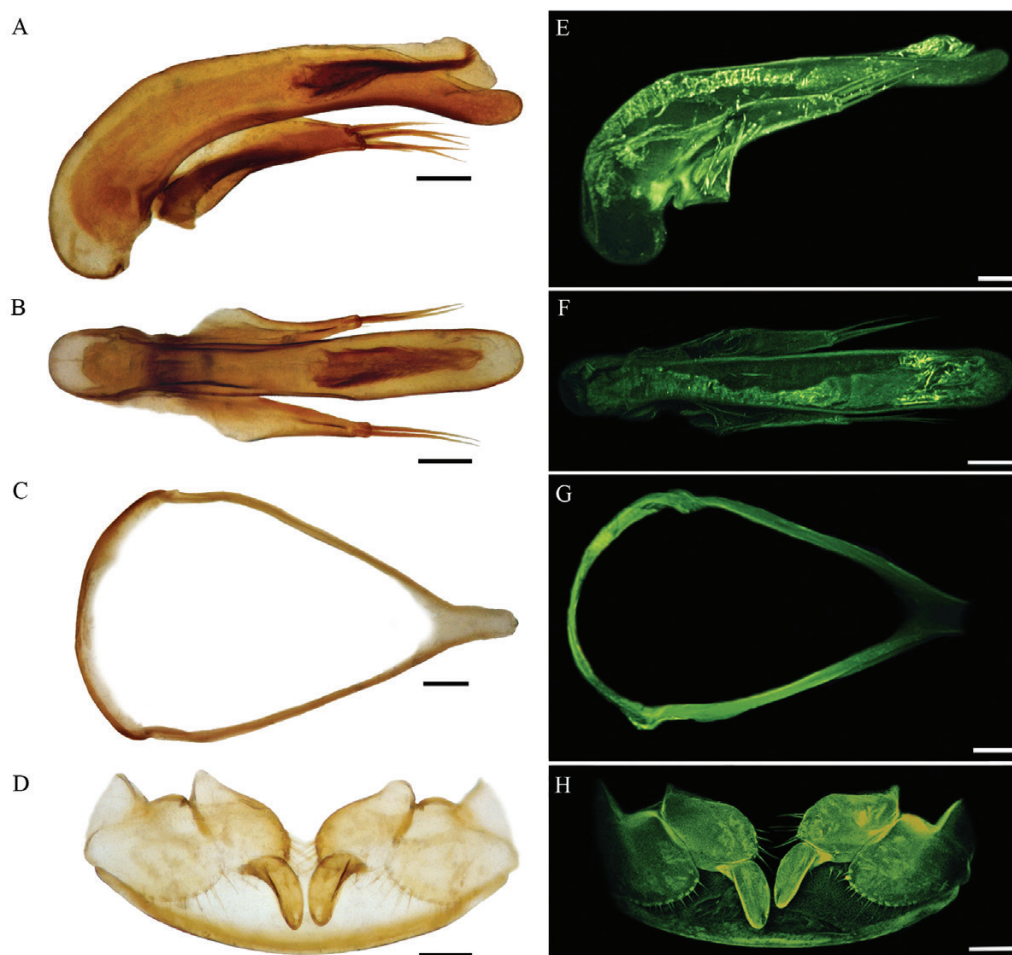
Figure 7. ***Pheggomisetes globiceps ciniglavcensis* subsp. nov.** from the Propas Pit, village of Činiglavci (near Pirot), Stara Planina Mts., Southeast Serbia. Bright-field (A–D) and TPEF (E–H) microscopy images. A, E, holotype male, aedeagus (lateral view). B, F, holotype male, aedeagus (dorsal view). C, G, holotype male, abdominal sternite IX (urite). D, H, paratype female, gonocoxites IX and gonosubcoxites IX. Scales = 0.1 mm.

vs. 1.32), a greater value of AL M (6.775 vs. 6.64 mm), a greater value of AL/TL M (1.05 vs. 1.01), different shape of the lateral pronotal margins (less rounded anteriorly, more concave posteriorly vs. more rounded anteriorly, less concave posteriorly), greater values of PaW (R 0.63–0.68, M 0.66 vs. R 0.53–0.595 mm, M 0.57 mm), a greater value of PbW M (0.83 vs. 0.75 mm), a greater value of PaW/PW M (0.64 vs. 0.57), different shape of the humeral angles (less rounded and less elevated vs. more rounded and more elevated), a smaller value of EL/EW M (1.64 vs. 1.83), a greater value of BW/PW M (1.03 vs. 0.95), different shape of the median lobe (slightly convex dorsally around the basal fourth, with a narrower apex in dorsal view vs. not convex dorsally around the basal fourth, with a wider apex in dorsal view) and different size of the basal bulb (smaller vs. bigger) (Supporting Information, Table S1) (Guéorguiev, 1964; this study).

Pheggomisetes globiceps ciniglavcensis subsp. nov. differs from *P. globiceps ninae* comb. & stat. nov. in having a greater value of TL M (6.46 vs. 6.295 mm), a smaller value of HL/HW M (1.275 vs. 1.30), a greater value of FL M (0.68 vs. 0.63 mm), greater values of AL M (6.775, males 6.84, females 6.50 vs. 6.525 mm, males 6.56 mm, females 6.30 mm), a greater value of HW/NW M (2.405 vs. 2.26), a greater value of EL M (3.50 vs. 3.36 mm), a greater value of EW M (2.135 vs. 1.99 mm), a smaller value of EL/EW M (1.64 vs. 1.69), a greater value of BW/PW M (1.03 vs. 0.91), different shape of the median lobe (narrower, somewhat more curved basally, then regularly curved, slightly convex dorsally around the basal fourth, with a narrow anterior part in dorsal view vs. thicker, regularly curved, somewhat convex dorsally in the middle, with a wide anterior part in dorsal view) and a different number of parameral

setae (three, two of them apical vs. five, three of them apical) (Supporting Information, Table S1) (Ćurčić *et al.*, 2004; this study).

Pheggomisetes globiceps ciniglavcensis subsp. nov. differs from *P. globiceps globiceps* (Figs 12, 13A–D) in having different shape of the head (widest at the anterior 2/5 of its length vs. widest somewhat after the middle), a greater value of HW/NW M (2.405 vs. 2.24), greater values of AL M (6.775, males 6.84, females 6.50 vs. 6.585 mm, males 6.775 mm, females 6.30 mm), a smaller value of HL/PL M (1.51 vs. 1.63), a greater value of PL/PW M (0.91 vs. 0.88), a greater value of EW M (2.135 vs. 2.02 mm), a smaller value of EL/EW M (1.64 vs. 1.725), a greater value of BW/PW M (1.03 vs. 0.885), different shape of the median lobe (narrower, elongate, with more elongate basal bulb vs. wider, stout, especially basally, with a short stout basal bulb) and different shape of the copulatory piece in dorsal aspect (gradually narrowing towards the apex vs. wide at the basal 3/5 and markedly narrowed at the apical 2/5) (Supporting Information, Table S1) (Guéorguiev, 1964; this study).

Variability: The number of setae on both frons (five to seven on each side) and elytra can vary (six to eight on each side).

Etymology: The subspecies is named after the village of Činiglavci, in which the type locality is situated.

Distribution: It lives solely in the Propas Pit in the village of Činiglavci (near Pirot) in the Stara Planina Mountains of Southeast Serbia.

Remarks: The new subspecies was originally treated as *P. globiceps ilandjievi* by Gajović *et al.* (2011), who collected a sample several years ago.

PHEGGOMISETES GLOBICEPS NINAE S. ĆURČIĆ, SCHÖNMANN, BRAJKOVIĆ, B. ĆURČIĆ & TOMIĆ, 2004 COMB. & STAT. NOV.

(FIGS 8 AND 9A–H)

Material examined: Sixty topotype males and 75 topotype females, Southeast Serbia, Stara Planina Mts., Hodžina Dupka Pit, 43°04′27.9″N 22°47′48.5″E, 692 m a.s.l., village of Petrlaš, near Dimitrovgrad, 26.VI-24.IX.2012, from pitfall traps, leg. Đ. Marković & D. Dragulović (IZFB); nine males and 25 females, Southeast Serbia, Mt. Stara Planina Mts., Petrlaška (= Velika) Pećina Cave, 43°04′27.81″N 22°47′46.50″E, 701 m a.s.l., village of Petrlaš, near Dimitrovgrad, 26.VI-24.IX.2012, both collected by hand and from pitfall traps, leg. D. Antić & S. Ćurčić (IZFB); one male and one female, *idem*, 03.XII.2012, leg. D. Antić &

Figure 8. *Pheggomisetes globiceps ninae* **comb. & stat. nov.** from the Hodžina Dupka Pit, village of Petrlaš (near Dimitrovgrad), Stara Planina Mts., Southeast Serbia. Topotype male, habitus (dorsal view). Scale = 5.0 mm.

S. Ćurčić (IZFB); one female, *idem*, 19.IX.2013, leg. P. Beron (IZFB); two females, Southeast Serbia, Stara Planina Mts., Džemanska Propast Pit, 43°07′44.2″N 22°79′15.9″E, 738 m a.s.l., village of Petrlaš, near Dimitrovgrad, 24.IX.2012, leg. M. Petković & D. Dragulović (IZFB); one male, Southeast Serbia, Stara Planina Mts., Tmna Dupka Cave, 43°04′42.0″N 22°47′24.5″E, 720 m a.s.l., village of Petrlaš, near
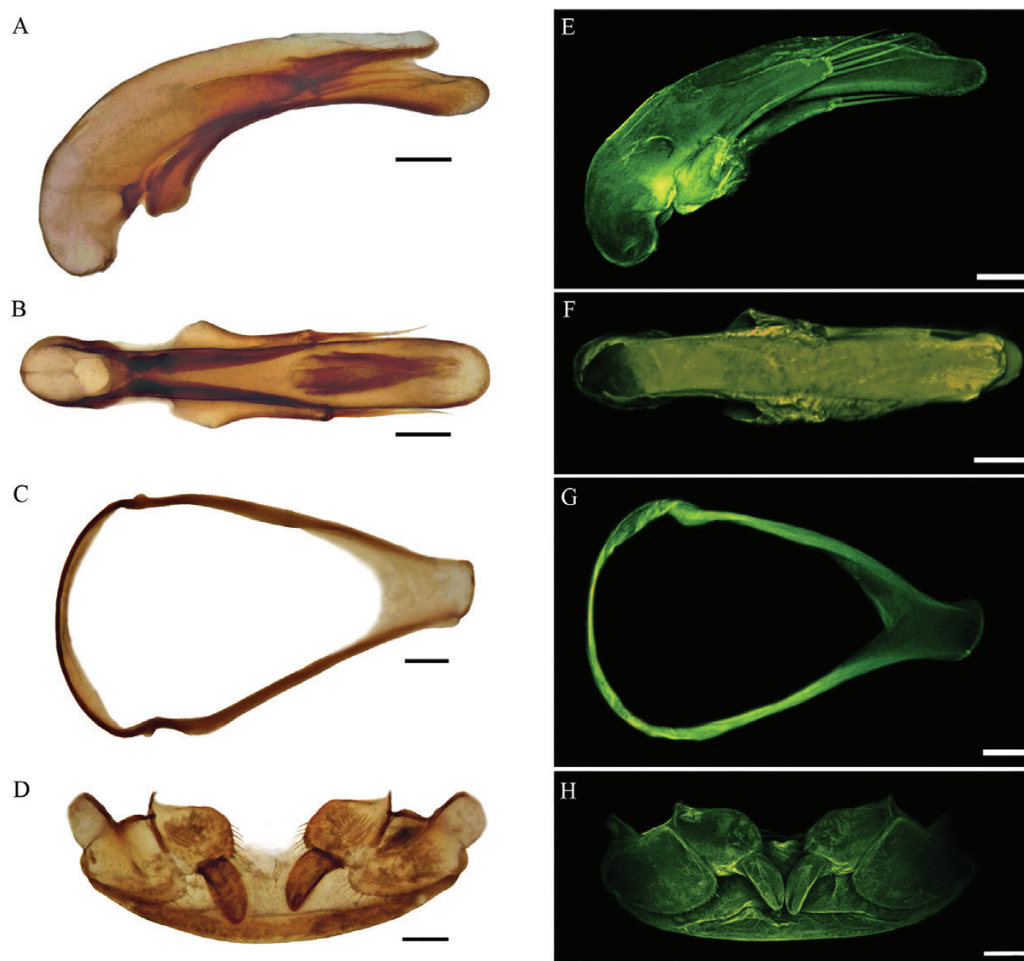
Figure 9. *Pheggomisetes globiceps ninae* comb. & stat. nov. from the Hodžina Dupka Pit, village of Petrlaš (near Dimitrovgrad), Stara Planina Mts., Southeast Serbia. Bright-field (A–D) and TPEF (E–H) microscopy images. A, E, topotype male, aedeagus (lateral view). B, F, topotype male, aedeagus (dorsal view). C, G, topotype male, abdominal sternite IX (urite). D, H, topotype female, gonocoxites IX and gonosubcoxites IX. Scales = 0.1 mm.

Dimitrovgrad, 24.IX.2012, leg. S. Ćurčić (IZFB); two males and ten females, *idem*, 24.IX-03.XII.2012, from pitfall traps, leg. D. Antić & S. Ćurčić (IZFB).

Description: The description has been already presented by Ćurčić *et al.* (2004).

Elytral umbilicate series: First three humeral setae close to marginal gutter, fourth being somewhat farther from the gutter, distance between umbilicate pores 2 and 3 shortest, distance between pores 3 and 4 longest; median series at around the middle of the elytra, two setae being somewhat distanced from marginal gutter, distance between pores 5 and 6 somewhat shorter than distance between pores 2 and 3; apical series: setae 7 and 8 being somewhat distanced from marginal gutter, distance between pores 7 and 8 shorter than distance between pores 3 and 4 (Fig. 8).

Differential diagnosis: The subspecies is compared here with both the morphologically and geographically closest subspecies of *P. globiceps* and the nominotypical subspecies. The former are *P. globiceps ilandjievi* and *P. globiceps ciniglavcensis* subsp. nov. (Guéorguiev, 1964; this study).

Pheggomisetes globiceps ninae comb. & stat. nov. differs clearly from *P. globiceps ilandjievi* in having a smaller value of TL M (6.295 vs. 6.60 mm), smaller values of AL M (6.525, males 6.56, females 6.30 vs. 6.64 mm, males 6.675 mm, females 6.60 mm), a smaller value of HW/NW M (2.26 vs. 2.35), a greater value of PaW M (0.61 vs. 0.57 mm), a greater value of PbW M (0.79 vs. 0.75 mm), different shape of the pronotal base in males (straight vs. concave), different shape of the hind pronotal angles (almost right vs. acute, rarely right), a smaller value of EL M (3.36 vs. 3.555 mm), a
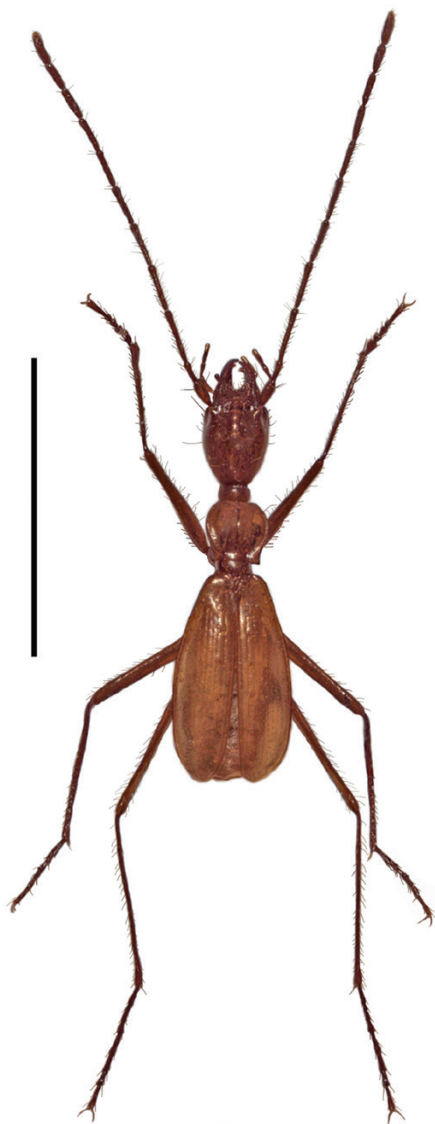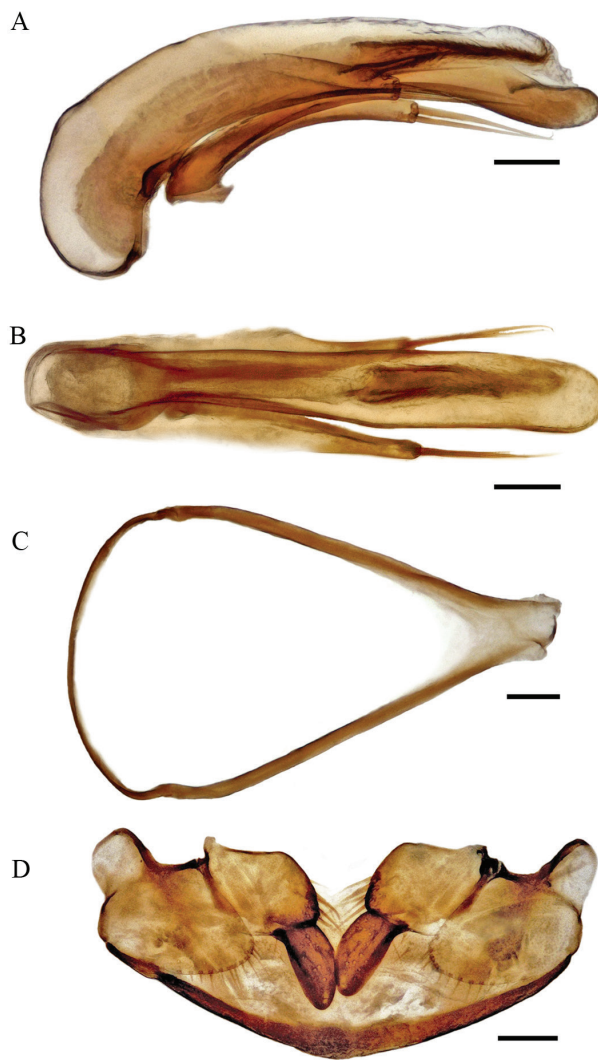
Figure 10. *Pheggomisetes globiceps ilandjievi* from the Golyama Balabanova Dupka Cave, village of Komshtitsa (near Sofia), Stara Planina Mts., Western Bulgaria. Topotype male, habitus (dorsal view). Scale = 5.0 mm.

Figure 11. *Pheggomisetes globiceps ilandjievi* from the Golyama Balabanova Dupka Cave, village of Komshtitsa (near Sofia), Stara Planina Mts., Western Bulgaria. A, topotype male, aedeagus (lateral view). B, topotype male, aedeagus (dorsal view). C, topotype male, abdominal sternite IX (urite). D, topotype female, gonocoxites IX and gonosubcoxites IX. Scales = 0.1 mm.

greater value of EW M (1.99 vs. 1.905 mm), a smaller value of EL/EW M (1.69 vs. 1.83), different shape of the median lobe (thicker, with a wider anterior part in dorsal view vs. more elongate, with a narrower anterior part in dorsal view) and a different number of parameral setae (five vs. three to four) (Supporting Information, Table S1) (Guéorguiev, 1964; Ćurčić *et al.*, 2004; this study).

All morphological differences between *P. globiceps ninae* comb. & stat. nov. and *P. globiceps ciniglavcensis* subsp. nov. are mentioned above (see the Differential diagnosis of *P. globiceps ciniglavcensis*

subsp. nov.) (Figs 6, 7A–H, 8, 9A–H; Supporting Information, Table S1) (Ćurčić *et al.*, 2004; this study).

P. globiceps ninae comb. & stat. nov. can be easily distinguished from *P. globiceps globiceps* on the basis of having a smaller value of TL M (6.295 vs. 6.405 mm), a smaller value of HL M (1.40 vs. 1.47 mm), a smaller value of HW M (1.08 vs. 1.17 mm), a greater value of HL/HW M (1.30 vs. 1.26), different shape of the head (widest at around the anterior 2/5 of its length vs. widest somewhat after the middle), a smaller value of HL/PL M (1.52 vs. 1.63), a smaller value of
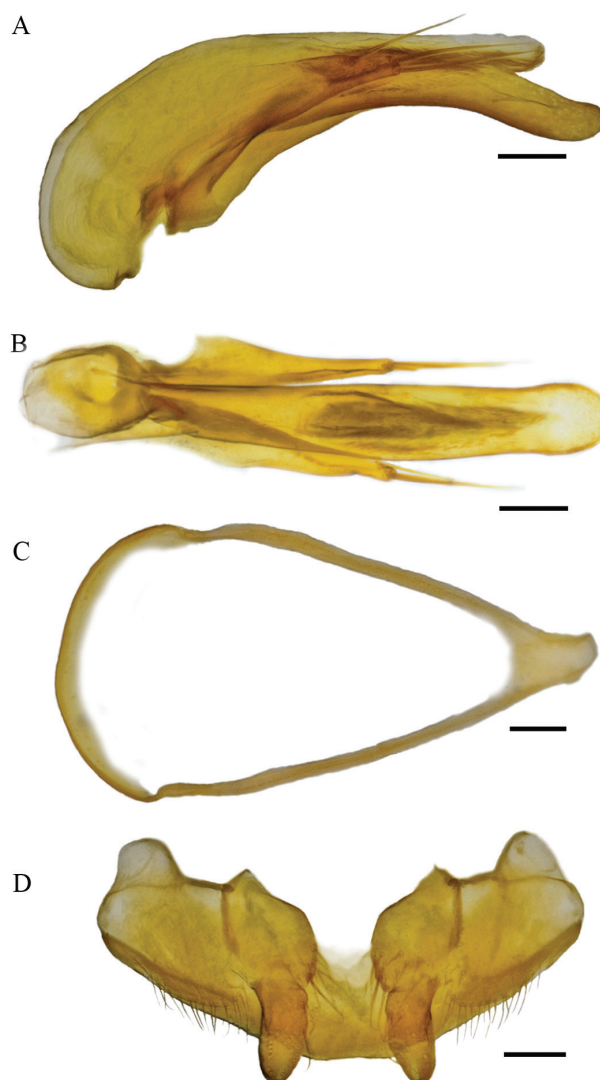
Figure 12. *Pheggomisetes globiceps globiceps* from the Dushnika Cave, village of Iskrets (near Sofia), Mt. Ponor Planina, Western Bulgaria. Topotype male, habitus (dorsal view). Scale = 5.0 mm.

HW/PW M (1.07 vs. 1.14), a greater value of PL/PW M (0.92 vs. 0.88), a smaller value of EL M (3.36 vs. 3.47 mm), a different number of parameral setae (five vs. three to four) and different shape of the median lobe (somewhat convex dorsally around the middle, with a somewhat elongate basal bulb vs. somewhat convex dorsally around the basal third, with a stout, relatively small basal bulb) (Supporting Information, Table S1) (Guéorguiev, 1964; Ćurčić *et al.*, 2004; this study).

Distribution: It lives in a few caves and pits on the western border of the Odorovačko Polje (692–738 m a.s.l.) in the village of Petrlaš (near Dimitrovgrad) in the Stara Planina Mountains of Southeast Serbia.

Figure 13. *Pheggomisetes globiceps globiceps* from the Dushnika Cave, village of Iskrets (near Sofia), Mt. Ponor Planina, Western Bulgaria. A, topotype male, aedeagus (lateral view). B, topotype male, aedeagus (dorsal view). C, topotype male, abdominal sternite IX (urite). D, topotype female, gonocoxites IX and gonosubcoxites IX. Scales = 0.1 mm.

Remarks: Interestingly, the taxon was originally treated as *P. globiceps ilandjievi* by Pretner (1970), who collected the first specimens from the Hodžina Dupka Pit with P. R. Deeleman. A similar opinion was expressed by Nešić *et al.* (2010) in a recent contribution. After the performed morphological and molecular analyses, we found that there is no difference between *Pheggomisetes* specimens from the Hodžina Dupka Pit, the Petrlaška (= Velika) Pećina Cave, the Džemanska Propast Pit and the Tmna Dupka Cave, all situated in the village of Petrlaš near Dimitrovgrad in the Stara Planina Mountains
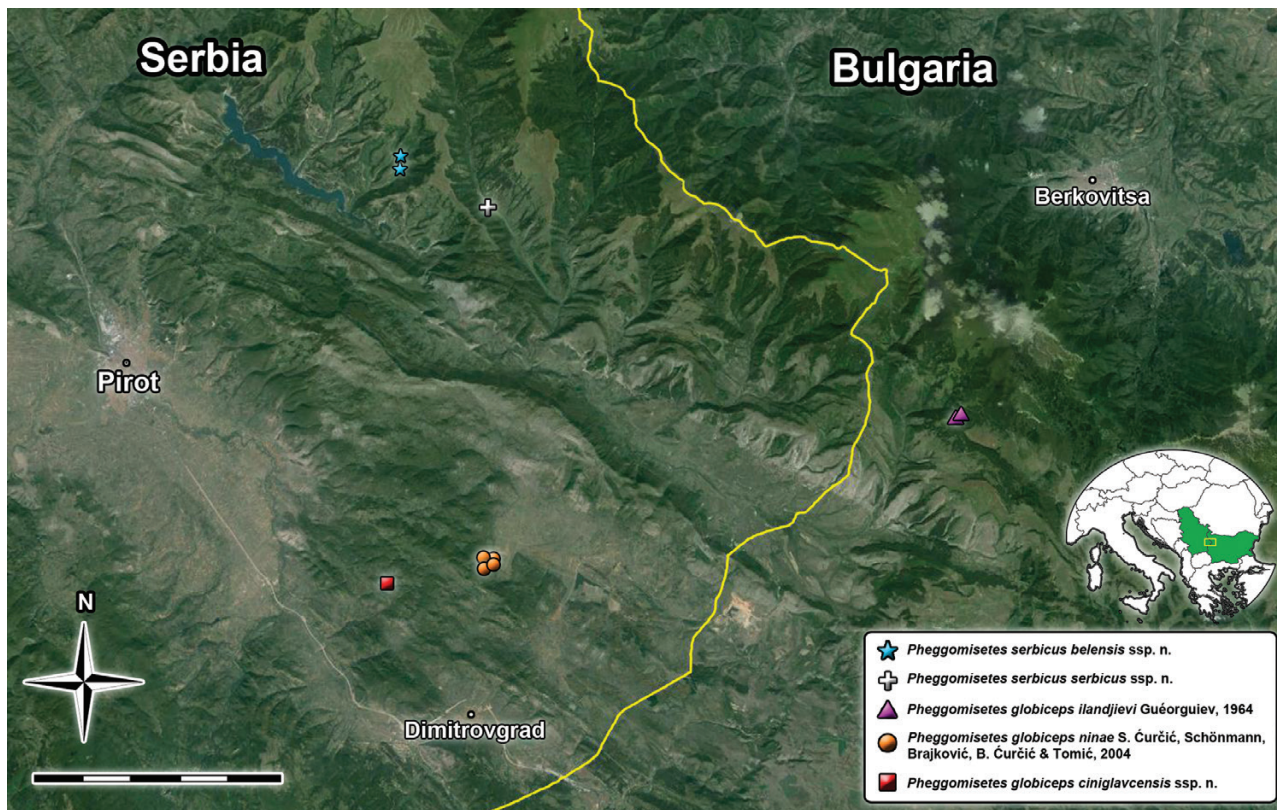
Figure 14. Distribution of *Pheggomisetes* taxa in Serbia and the immediate surroundings. Scale = 10 km.
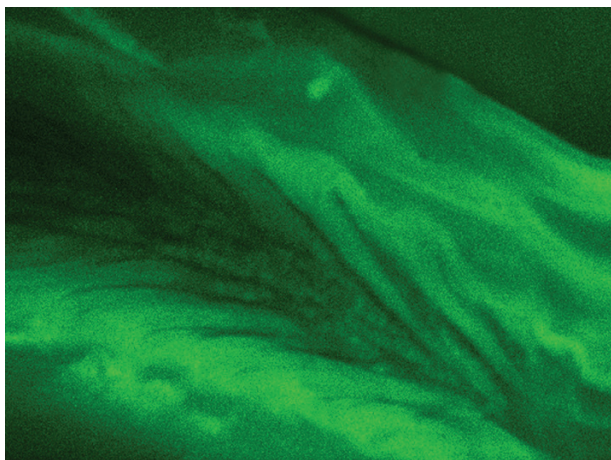
Figure 15. TPEF microscopy image of part of the tooth-like copulatory piece of ***P. globiceps ninae* comb. & stat. nov.**, showing fine details of the structure.

of Southeast Serbia. They all belong to the same taxon, which was previously described under the name *P. ninae*.

After a thorough morphological analysis supported by molecular data, we established that the existing differences between *P. ninae* and other *Pheggomisetes* species are not great enough to treat it as a distinct species. The taxon in question deserves a subspecies rank within *P. globiceps* since certain smaller differences (both morphological and phylogenetical) were proved to exist between it and the geographically nearest subspecies of *P. globiceps*, but these were not significant enough to convince us of the need to separate it as a species. To be specific, certain morphological differences were observed in regard to TL, AL, HW/NW, FL, FL/HL, PaW, PbW, PaW/PW, shape of the lateral pronotal margins, pronotal base shape, EL, EW, EL/EW, BW/PW, shape of the humeral angles and position of the elytral umbilicate series (Supporting Information, Table S1), but shapes of the aedeagi and copulatory pieces are quite similar, indicating that the above-mentioned differences are in reality interpopulational, not interspecific (an assertion supported by small genetic differences recorded between the given taxon and its closest relatives, 0.5 and 1.3%, respectively). We therefore suggest that the taxonomic status of *P. ninae* be changed to *P. globiceps ninae* comb. & stat. nov.

<div style="border:1px solid">

KEY TO SPECIES OF THE GENUS *PHEGGOMISETES* KNIRSCH, 1923 (FIG. 14)

1 Neck constriction very broad and not abrupt in dorsal view, while flat in lateral view. Head elliptical, cheeks less rounded (Northwest Bulgaria) ………………….………......……………….…..……… *P. buresi* (Knirsch, 1923)

– Neck constriction narrow and abrupt in dorsal view, while deeper in lateral view. Head circular or ovoid, cheeks more rounded ……………………………………………………………………….……………….......... 2

2 Pronotum clearly narrowed in front of base. Head very broad in posterior third, with frontal furrows very deep (Northwest Bulgaria) …………………………………….………….…………………*P. radevi* Knirsch, 1924

– Pronotum not narrowed in front of base, sometimes with lateral margins more or less sinuate in posterior third. Head narrower in posterior third, with frontal furrows less deep ....……………………………………… 3

3 Longer TL M ($\geq$ 6.295 mm), antennae longer (M $\geq$ 6.525 mm), longer than body, frontal furrows not reaching middle of the head, humeral angles more obtuse, less elevated, copulatory piece gradually narrowed apically (Western Bulgaria and Southeast Serbia) [*P. globiceps* Buresch, 1925] 4

– Smaller TL M ($\leq$ 6.11 mm), antennae shorter (M $\leq$ 5.99 mm), slightly shorter than body, frontal furrows exceeding/reaching middle of the head, humeral angles more rounded, quite elevated, copulatory piece more markedly narrowed apically (Southeast Serbia) [*P. serbicus* Ćurčić, Vrbica & B. Guéorguiev, sp. nov.] 5

4 TL M 6.295 mm, antennae shorter (M 6.525 mm), humeral angles more elevated, HW/NW M 2.26, EL M 3.36 mm, EW M 1.99 mm, elytra at the base narrower than pronotum, median lobe thicker, regularly curved, somewhat convex dorsally in the middle, with a wide anterior part in dorsal view (Southeast Serbia) …………….. *P. globiceps ninae* S. Ćurčić, Schönmann, Brajković, B. Ćurčić & Tomić, 2004 comb. & stat. nov.

–   TL M 6.46 mm, antennae longer (M 6.775 mm), humeral angles less elevated, HW/NW M 2.405, EL M 3.50 mm, EW M 2.135 mm, elytra at the base slightly wider than pronotum, median lobe narrower, somewhat more curved basally, then regularly curved, slightly convex dorsally around the basal fourth, with a narrow anterior part in dorsal view (Southeast Serbia) …………….…………………………………………………… …………….……………………………..........……. *P. globiceps ciniglavcensis* Ćurčić & Vrbica, subsp. nov.

5 TL M 6.11 mm, frontal furrows somewhat exceeding mid head level, HW/NW M 2.50, FL M 0.75 mm, AL M 5.91 mm, anterior pronotal margin more concave in females, pronotal base more concave in the middle, PaW/PbW M 0.74, EL/EW M 1.725, lateral margins of elytra rounded anteriorly, median lobe apex somewhat elevated, basal bulb and basal part of median lobe narrower (Southeast Serbia) ……………. …………….……………………..……………......…… *P. serbicus serbicus* Ćurčić, Vrbica & B. Guéorguiev, subsp. nov.

– TL M 6.045 mm, frontal furrows reaching mid head level, HW/NW M 2.24, FL M 0.68 mm, AL M 5.99 mm, anterior pronotal margin less concave in females, pronotal base less concave in the middle, PaW/PbW M 0.78, EL/EW M 1.77, lateral margins of elytra more straight anteriorly, median lobe apex almost straight, basal bulb and basal part of median lobe wider (Southeast Serbia) ………..………………..……………………… …………………………………………………….……… *P. serbicus belensis* Ćurčić, Vrbica & B. Guéorguiev, subsp. nov.

</div>

TPEF MICROSCOPY OF THE INTERNAL STRUCTURES OF *PHEGGOMISETES*

Certain well-chitinized internal morphological structures of *Pheggomisetes* ssp. were observed by two-photon excited autofluorescence microscopy. The samples were not fluorescently labelled, so autofluorescence was detected and used for imaging. For the study, we used a 25× numerical aperture 0.8 water/glycerin immersion objective and 930-nm excitation wavelength. This somewhat longer wavelength was utilized to avoid the autofluorescence of residual tissues remaining after beetle dissection. In addition, it was possible to penetrate deeper (up to 200 µm for the studied sample) through the chitinous cuticle due to the reduced two-photon absorption of chitin (Rabasović *et al.*, 2015).

We present TPEF 3D images of the male (aedeagus) and female (gonocoxites IX and gonosubcoxites IX) genitalia and the male abdominal sternite IX (urite) of all *Pheggomisetes* taxa from Serbia. The images revealed morphological details similar to those observed using classical bright-field microscopy (Figs 2E–H, 5E–H, 7E–H, 9E–H). In addition, selected 3D video clips of the three morphological structures are included, showing them in rotation around the longitudinal, lateral and vertical axes (Supporting Information, Appendices S1–S6). This makes it possible for the structures to be observed in every direction, which provides better insight into the shape and spatial relations of internal structures.

The aedeagus is observed both laterally and dorsally (Figs 2E, F, 5E, F, 7E, F, 9E, F). The structure of both the surface (the fine relief) and the inner part (the copulatory piece composed of numerous tooth-like structures and the inner sac) of the median lobe (Fig. 15) is clearly distinguished. Both strongly (e.g. the copulatory piece) and weakly (e.g. the inner sac) chitinized parts of the aedeagus are visible (Figs 2E, F, 5E, F, 7E, F, 9E, F). All parts of the aedeagus (median
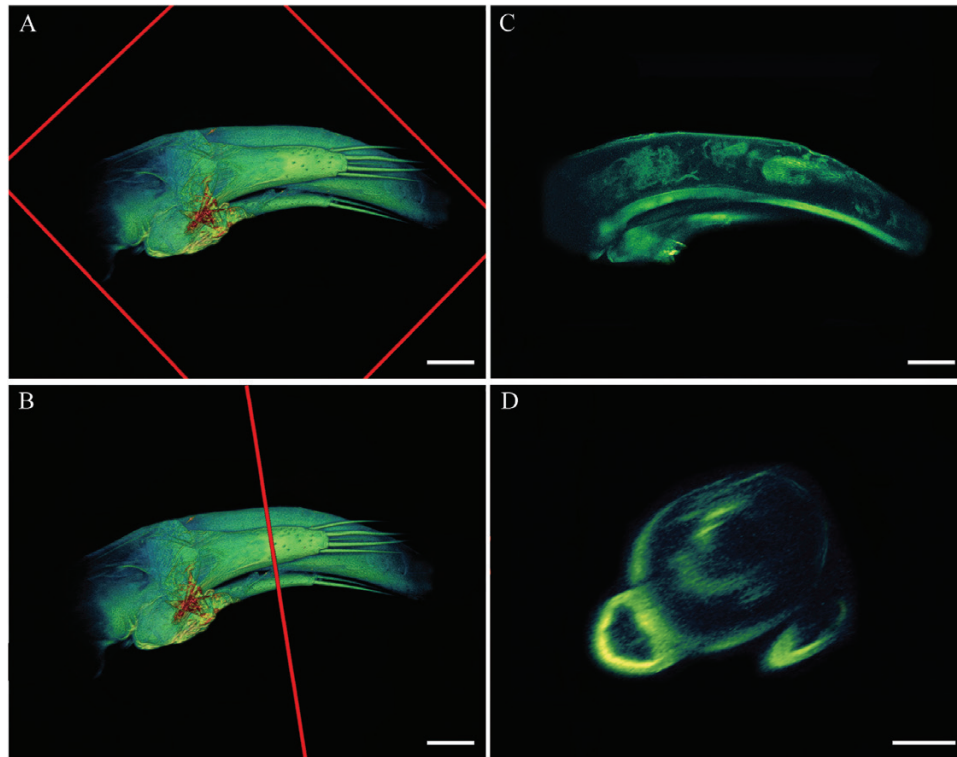
Figure 16. TPEF microscopy images of the aedeagus of *P. globiceps ninae* **comb. & stat. nov.** A, lateral view with longitudinal section plane (red square). B, lateral view with cross-sectional plane (red line). C, a corresponding longitudinal section. D, a corresponding cross section. Scales = 0.10 mm (A–C) and 0.05 mm (D).

lobe, basal bulb, parameres and their setae, copulatory piece and inner sac) are sharply delimited from each other (Figs 2E, F, 5E, F, 7E, F, 9E, F), as in the case of the images recorded earlier by bright-field microscopy (Figs 2A, B, 5A, B, 7A, B, 9A, B).

One of the male internal sclerites, abdominal sternite IX (urite), is clearly visible and can be imaged by TPEF microscopy since it is well chitinized (Figs 2G, 5G, 7G, 9G). The shape and thickness of the structure are as visible as in the photographs obtained by bright-field microscopy (Figs 2C, 5C, 7C, 9C).

Similarly, the parts of the female genitalia, which are highly sclerotized (gonocoxites IX and gonosubcoxites IX), were also observed. Sharply delimited parts of the aforementioned female genital structures are visible. The setation and fine relief are distinctly discernible on the surface, while the internal structure can also be observed (Figs 2H, 5H, 7H, 9H).

The images of both cross and longitudinal sections of *Pheggomisetes* male genitalia (Fig. 16C, D) show the clear advantage of NLM vs. traditional classical microscopy in investigating anatomical features. To be specific, all features of the internal structures (e.g. shape and position of copulatory piece) are discernible on any section of the genitalia using this method (Fig. 16A–D). Apart from internal characteristics of the structures, their thickness can be ascertained and measured as well. One more benefit of using TPEF is that it provides additional data on the shapes of certain structures (e.g. median lobe, parameres, parameral setae) on cross sections (any level) (Fig. 16D), which cannot be detected by classical light microscopy. The images can be further used to calculate data on the structure's surface, shape and volume. The female genitalia can be observed in a similar manner as well.

STATISTICAL MORPHOMETRIC ANALYSIS

Only 20 variables (eight commonly used morphological trait measurements and 12 ratio variables) passed the Shapiro-Wilk normality test (HL, HW, FL, PW, PaW, PbW, EW, EWP, HL/HW, HL/AL, HL/PL, HL/TL, HW/NW, HW/PW, AL/TL, PL/PW, PaW/PW, PbW/PW, PaW/PbW and BW/PW) and were further used for parametric analyses. Normality tests were also performed on log-transformed data, but they resulted in the same 20 variables.

Descriptive statistics of the quantitative traits and ratio variables of *P. globiceps* and *P. serbicus* sp.

nov. subspecies from Serbia are given in Supporting Information, Table S1.

One-way MANOVA of samples of the two *Pheggomisetes* species revealed significant differences between the species [Wilks' Λ = 0.095, F (20, 40) = 19, $P < 0.001$]. Post hoc pairwise comparison using Scheffe's test indicated that seven variables are statistically significant (Table 2). The HL/AL and HL/TL variables have the most distinct discriminative power. AL/TL, FL, EW, PaW and HL are statistically less important for distinguishing the two species.

Table 3 presents the results of non-parametric comparisons between samples of the two species (for non-normally distributed variables) using the Mann–Whitney U test. Ten variables are recognized as statistically significant, but AL and TL are most important, while EL/TL and PL/TL are somewhat less important, followed by PWP, PW/EW, FL/HL, HW/EW, PL and EL/EW.

One-way MANOVA of *Pheggomisetes* taxa (populations belonging to two species and six subspecies)

revealed significant differences in the variation of eight commonly used morphological trait measurements and 12 ratios [Wilks' Λ = 0.095, F (20, 40) = 18.941, $P < 0.001$ and Wilks' Λ = 0.003, F (90, 222) = 5.890, $P < 0.001$, respectively].

The results of linear DA of 20 variables showed that the total correct percentage of the classification matrix of all six *Pheggomisetes* subspecies was very high (95.59%). Only one specimen from the *P. serbicus belensis* group is classified into the *P. serbicus serbicus* group, and one specimen from the *P. globiceps ciniglavcensis* group is classified into the *P. globiceps ninae* group.

All pairwise squared Mahalanobis distances between the taxa were significant at a level of 99%. UPGMA cluster analysis of the squared Mahalanobis distances clustered both *P. serbicus* sp. nov. subspecies in the same branch and all the analysed subspecies of *P. globiceps* together in another branch, indicating that the two species are clearly separate (Fig. 17).

On the basis of morphometric study, it can be asserted that the phenetically closest subspecies
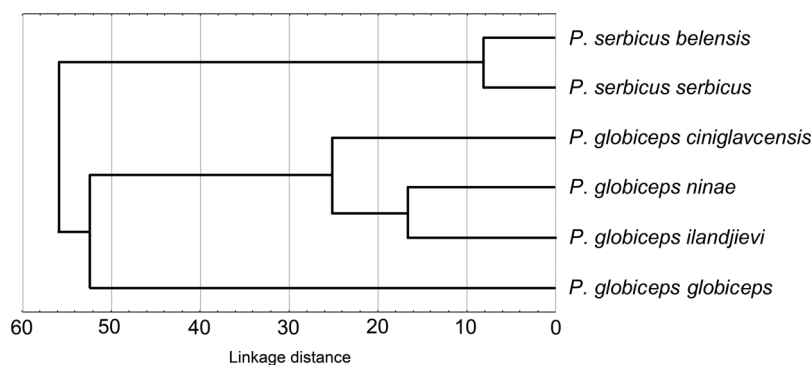
Figure 17. UPGMA tree diagram of two *Pheggomisetes* species and six subspecies based on squared Mahalanobis distances (scale shown) obtained from eight analysed morphological trait measurements and 12 ratio variables.
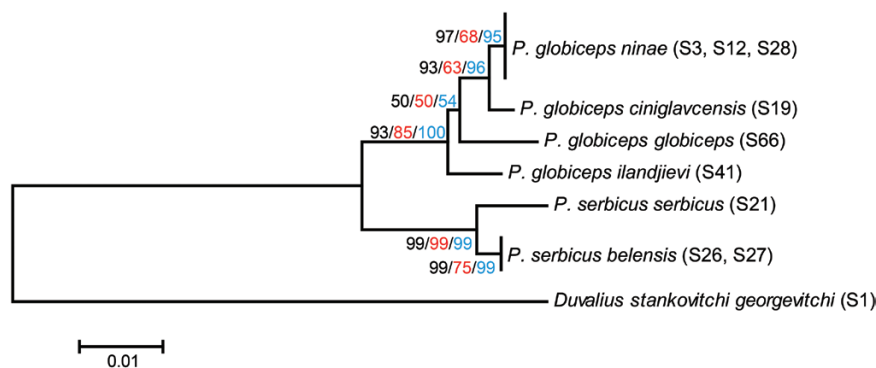
Figure 18. Phylogenetic tree of *Pheggomisetes* taxa based on *COI* sequences obtained using the neighbor-joining (NJ), maximum parsimony (MP) and maximum likelihood (ML) methods. Bootstrap values are indicated above/below branches in the following order: NJ (black)/MP (red)/ML (blue). *Duvalius stankovitchi georgevitchi* was used as the outgroup taxon. Specimen codes are listed in parentheses.

© 2017 The Linnean Society of London, *Zoological Journal of the Linnean Society*, 2018, **183**, 347–371

within *P. globiceps* are *P. globiceps ninae* comb. & stat. nov., *P. globiceps ilandjievi* and *P. globiceps ciniglavcensis* subsp. nov., while *P. globiceps globiceps* is morphologically somewhat separate (Fig. 17).

Unquestionably, there is a need for a comprehensive morphometric analysis within the genus, including all currently existing taxa and more numerous samples of specimens, to obtain the most precise results possible.

MOLECULAR AND PHYLOGENETIC ANALYSES

Since the taxonomy of *Pheggomisetes* is not well settled (Guéorguiev, 1964; Ćurčić *et al.*, 2004), a substantial molecular analysis performed on the taxa could help us to solve some taxonomic problems. An appreciable interspecific, intraspecific and individual variability of characters (number of supraorbital, elytral and parameral setae; dorsal outlines of the head, pronotum and elytra) is evident (Guéorguiev, 1964; Nešić *et al.*, 2010) within this morphologically isolated genus (Jeannel, 1928; Guéorguiev, 1977). For these reasons, we performed a molecular analysis of the Serbian taxa and their closest Bulgarian relatives that were available to us.

Phylogenetic reconstruction of *Pheggomisetes* taxa was performed using three different methods, and all of them resulted in trees with the same topology (Fig. 18). Specimens were grouped into two distinct, well-supported clades. The mean genetic distance between clades was 3.6%.

The taxa grouped within the first clade belong to *P. globiceps*. Four recognized subspecies are clustered separately with high bootstrap support. *Pheggomisetes globiceps globiceps* and *P. globiceps ilandjievi* are separate from the subclade consisting of *P. globiceps ciniglavcensis* subsp. nov. and *P. globiceps ninae* comb. & stat. nov. The genetic distances between subspecies range from 0.5% between *P. globiceps ciniglavcensis* subsp. nov. and *P. globiceps ninae* comb. & stat. nov. up to 1.8% between *P. globiceps globiceps* and *P. globiceps ilandjievi*. The distance between *P. globiceps ilandjievi* and *P. globiceps ciniglavcensis* subsp. nov. was 1.5%, while distance between *P. globiceps ilandjievi* and *P. globiceps ninae* comb. & stat. nov. was 1.3%. Conversely, the distance between *P. globiceps globiceps* and *P. globiceps ciniglavcensis* subsp. nov. was 1.5%, while distance between *P. globiceps globiceps* and *P. globiceps ninae* comb. & stat. nov. was 1.3%.

The taxa grouped within the second clade belong to the newly described *P. serbicus* sp. nov., which clearly differentiates into two subspecies, viz., *P. serbicus serbicus* subsp. nov. and *P. serbicus belensis* subsp. nov., with a mean genetic distance of 1.1% between them.

The obtained levels of sequence divergence between the species (> 3.5%) and subspecies (0.5–1.8%) are significant at species/subspecies levels (Hebert, Ratnasingham & de Waard, 2003), as was recently shown for the trechine genus *Paraphaenops* Jeannel, 1916 (Ortuño *et al.*, 2016), as well as for other animal models (Hebert *et al.*, 2003).

The recorded molecular data are in agreement with the results achieved by classical taxonomic analysis (based on morphological characters and their variations) of Serbian *Pheggomisetes* taxa, thus confirming the correctness of erecting three taxa new to science (a species and two subspecies) and assigning a new status (subspecific within *P. globiceps*) to a taxon previously treated as a species.

On the basis of two analysed *Pheggomisetes* taxa (*P. globiceps globiceps* Buresch, 1925 and *P. globiceps ninae* comb. & stat. nov., the latter being treated as *P. globiceps ilandjievi*), Faille *et al.* (2013) hypothesized that the genus is most likely an adelphotaxon of a clade containing isotopic species of the largely paraphyletic *Duvalius* Delarouzée, 1859 and five other subterranean genera. More genera inhabiting both Dinaric and Balkan mountain ranges need to be included in a comprehensive phylogenetic analysis to establish the true relationships of subterranean trechines in the region and disclose the origin and paths of colonization of different lineages on the Balkan Peninsula (Faille *et al.*, 2013).

CONCLUSIONS

On the basis of the results of taxonomic, morphological and molecular analyses, we were able to identify one new trechine ground beetle species (*P. serbicus* sp. nov.) and two new subspecies (*P. serbicus belensis* subsp. nov. and *P. globiceps ciniglavcensis* subsp. nov.), in addition to which we propose a change in the status of one taxon (*P. globiceps ninae* comb. & stat. nov.). The new trechine taxa belong to an isolated and probably ancient phyletic lineage that most likely originated in the Oligocene (Guéorguiev, 1977; Ćurčić *et al.*, 2004; Faille *et al.*, 2013). The aforementioned new taxa are all relicts whose current distribution is limited to confined underground localities in Southeast Serbia.

The use of TPEF microscopy in this study has provided better knowledge and additional information about the morphology and anatomy of *Pheggomisetes* taxa. It is one more tool that taxonomists can use to define more easily the taxonomic status of lower taxa, especially ones whose morphology is difficult to examine using classical light microscopy. NLM images and 3D models enable investigators to achieve deeper penetration into chitinized tissues, thereby revealing in-volume details that represent additional information useful in the determination of taxa.

In analysing partial sequences of the *COI* gene, we confirmed our taxonomic findings. In this study, we show that the *COI* gene can be used for molecular identification of *Pheggomisetes* taxa.

It would be of importance in the future to arrange a comprehensive morphological and molecular analysis of *Pheggomisetes* specimens from all known sites in both Bulgaria and Serbia to find out whether they belong to the taxa and species groups already known or whether a new classification would be more appropriate. In addition, a detailed molecular study of all *Pheggomisetes* subspecies (especially those subordinate to *P. globiceps*) with analysis of various morphological characteristics is needed to define their true taxonomic position.

ACKNOWLEDGEMENTS

REFERENCES

Andújar C, Gómez-Zurita J, Rasplus JY, Serrano J. 2012. Molecular systematic and evolution of the subgenus *Mesocarabus* Thomson, 1875 (Coleoptera: Carabidae: *Carabus*), based on mitochondrial and nuclear DNA. *Zoological Journal of the Linnean Society* **166:** 787–804.

Belousov IA, Dolzhansky VY. 1994. A new aphaenopsoid genus of the tribe Trechini from the Caucasus. *Mitteilungen der Münchner Entomologischen Gesellschaft* **84:** 59–63.

Belousov IA, Koval AG. 2009. To the knowledge on the aphaenopsoid trechine beetles (Coleoptera: Carabidae: Trechini) of the Caucasus. *Caucasian Entomological Bulletin* **5:** 163–173.

Beron P. 1994. Résultats des recherches biospéléologiques en Bulgarie de 1971 à 1994 et liste des animaux cavernicoles Bulgares. *Tranteeva* **1:** 1–137.

Casale A, Laneyrie R. 1982. Trechodinae et Trechinae du Mónde. Tableau dés sous-familles, tribus, séries phylétiques, genres, et catalogue général des espèces. *Mémoires de Biospéologie* **9:** 1–226.

Casale A, Vigna Taglianti A, Juberthie C. 1998. Coleoptera Carabidae. In: Juberthie C, Decu V, eds. *Encyclopaedia biospeologica. Tome II*. Moulis-Bucharest: Société de Biospéologie & Académie Roumaine, 1047–1081.

Chien CH, Chen WW, Wu JT, Chang TC. 2011. Label-free imaging of *Drosophila* in vivo by coherent anti-Stokes Raman scattering and two-photon excitation autofluorescence microscopy. *Journal of Biomedical Optics* **16:** 016012.

Christiansen K. 2012. Morphological adaptations. In: White WB, Culver DC, eds. *Encyclopedia of caves, 2nd edn*. Amsterdam: Elsevier, 517–528.

Contreras-Díaz HG, Moya O, Oromí P, Juan C. 2007. Evolution and diversification of the forest and hypogean ground-beetle genus *Trechus* in the Canary Islands. *Molecular Phylogenetics and Evolution* **42:** 687–699.

Ćurčić SB, Brajković MM, Ćurčić BPM. 2007. *The carabids of Serbia*. Belgrade–Vienna: Institute of Zoology, Faculty of Biology, University of Belgrade, Committee for Karst and Speleology, Serbian Academy of Sciences and Arts, Department of Conservation Biology, Vegetation- and Landscape Ecology, Faculty of Life Sciences, University of Vienna & UNESCO MAB Committee of Serbia.

Ćurčić SB, Schönmann H, Brajković MM, Ćurčić BPM, Tomić VT. 2004. On a new cave-dwelling beetle (Trechinae, Carabidae) from Serbia. *Archives of Biological Sciences, Belgrade* **56:** 109–113.

de Campos Vidal B. 2011. Butterfly scale form birefringence related to photonics. *Micron* **42:** 801–807.

Decou V, Botosaneanu L. 1964. Quelques données relatives a l'anatomie de *Pheggomisetes bureschi* Knirsch (Coleoptera, Trechinae). *Annales de Spéléologie* **19:** 759–768.

Denk W, Strickler JH, Webb WW. 1990. Two-photon laser scanning fluorescence microscopy. *Science* **248:** 73–76.

Deuve T, Cruaud A, Genson G, Rasplus JY. 2012. Molecular systematics and evolutionary history of the genus *Carabus* (Col. Carabidae). *Molecular Phylogenetics and Evolution* **65:** 259–275.

Faille A, Andújar C, Fadrique F, Ribera I. 2014. Late Miocene origin of a Ibero-Maghrebian clade of ground beetles with multiple colonisations of the subterranean environment. *Journal of Biogeography* **41:** 1979–1990.

Faille A, Bourdeau C, Fresneda J. 2012. Molecular phylogeny of the *Trechus brucki* group, with description of two new species from the Pyreneo-Cantabrian area (France, Spain) (Coleoptera, Carabidae, Trechinae). *ZooKeys* **217:** 11–51.

Faille A, Casale A, Balke M, Ribera I. 2013. A molecular phylogeny of Alpine subterranean Trechini (Coleoptera: Carabidae). *BMC Evolutionary Biology* **13:** 248.

Faille A, Casale A, Ribera I. 2010a. Phylogenetic relationships of Western Mediterranean subterranean Trechini groundbeetles (Coleoptera: Carabidae). *Zoologica Scripta* **40:** 282–295.

Faille A, Ribera I, Deharveng L, Bourdeau C, Garnery L, Quéinnec E, Deuve T. 2010b. A molecular phylogeny shows the single origin of the Pyrenean subterranean Trechini ground beetles (Coleoptera: Carabidae). *Molecular Phylogenetics and Evolution* **54:** 97–106.

Gajović V, Mandić M, Njunjić I, Pavićević D. 2011. Kompleksna speleološka istraživanja jame Propas' u Činiglavcima. In: Ćalić

J, ed. *Conference Proceedings of the 7th Symposium on Karst Protection*, 21–22 May 2011, Bela Palanka, Serbia. Belgrade: Academic Speleological Alpinistic Club, 71–81.

Guéorguiev VB. 1964. Révision du genre *Pheggomisetes* Knirsch (Coleoptera, Carabidae). *Časopis Československé Společnosti Entomologické* **61:** 265–278.

Guéorguiev VB. 1977. *La faune troglobie terrestre de la péninsule Balkanique. Origine, formation et zoogéographie, special edn*. Sofia: Bulgarian Academy of Sciences.

Guéorguiev VB, Guéorguiev BV. 1995. *Catalogue of the ground-beetles of Bulgaria (Coleoptera: Carabidae)*. Sofia-Moscow: Pensoft Publishers.

Hebert PDN, Ratnasingham S, de Waard JR. 2003. Barcoding animal life: cytochrome *c* oxidase subunit 1 divergences among closely related species. *Proceedings of the Royal Society of London B: Biological Sciences* **270:** 596–599.

Jeannel R. 1928. Monographie des Trechinae. Morphologie comparée et distribution géographique d'un groupe de Coléoptères (Troisième Livraison). Les Trechini cavernicoles. *L'Abeille* **35:** 1–808.

Juberthie C, Decu V. 1968. Les glandes pygidiales de quelques Trechitae cavernicoles. *Annales de Spéléologie* **23:** 195–210.

Kimura M. 1980. A simple method for estimating evolutionary rates of base substitutions through comparative studies of nucleotide sequences. *Journal of Molecular Evolution* **16:** 111–120.

Klaus AV, Kulasekera VL, Schawaroch V. 2003. Three-dimensional visualization of insect morphology using confocal laser scanning microscopy. *Journal of Microscopy* **212:** 107–121.

Lin CY, Hovhannisyan V, Wu JT, Lin CW, Chen JH, Lin SJ, Dong CY. 2008. Label-free imaging of *Drosophila* larva by multiphoton autofluorescence and second harmonic generation microscopy. *Journal of Biomedical Optics* **13:** 050502.

Manly FJB. 1986. *Multivariate statistical methods – a primer*. New York: Chapman and Hall.

Masters BR, So PTC. 2008. *Handbook of biomedical nonlinear optical microscopy*. Oxford: Oxford University Press.

Mertz J. 2004. Nonlinear microscopy: new techniques and applications. *Current Opinion in Neurobiology* **14:** 610–616.

Michels J. 2007. Confocal laser scanning microscopy: using cuticular autofluorescence for high resolution morphological imaging in small crustaceans. *Journal of Microscopy* **227:** 1–7.

Moravec P, Uéno S-I, Belousov IA. 2003. Tribe Trechini. In: Löbl I, Smetana A, eds. *Catalogue of Palaearctic Coleoptera. Vol. 1. Archostemata – Myxophaga – Adephaga*. Stenstrup: Apollo Books, 288–346.

Nei M, Kumar S. 2000. *Molecular evolution and phylogenetics*. Oxford: Oxford University Press.

Nešić D, Kličković M, Pavićević D, Mijatović M, Ognjenović S. 2010. Rezultati novijih istraživanja Petrlaških pećina. *Zaštita prirode* **61:** 117–142.

Ober KA. 2002. Phylogenetic relationships of the carabid subfamily Harpalinae (Coleoptera) based on molecular sequence data. *Molecular Phylogenetics and Evolution* **24:** 228–248.

Ober KA, Heider TN. 2010. Phylogenetic diversification patterns and divergence times in ground beetles (Coleoptera: Carabidae: Harpalinae). *BMC Evolutionary Biology* **10:** 262.

Ober KA, Maddison DR. 2008. Phylogenetic relationships of tribes within Harpalinae (Coleoptera: Carabidae) as inferred from 28S ribosomal DNA and the *wingless* gene. *Journal of Insect Science* **8:** 63.

Ortuño VM, Sendra A, Reboleira ASPS, Fadrique F, Faille A. 2016. The Iberian genus *Paraphaenops* Jeannel, 1916 (Coleoptera: Carabidae: Trechini): morphology, phylogeny and geographical distribution. *Zoologischer Anzeiger* **266:** 71–88.

Osawa S, Su Z-H, Imura Y. 2004. *Molecular phylogeny and evolution of carabid ground beetles*. Tokyo: Springer Verlag.

Pretner E. 1970. *Antrosedes longicollis* sp. n. iz Bosne, razprostranjenost vrste *Blattodromus herculeus* Reitter in rod *Pheggomisetes* v Srbiji (Coleoptera: Bathysciinae in Trechinae). *Razprave IV razreda SAZU* **13:** 153–164.

Rabasović MD, Pantelić DV, Jelenković BM, Ćurčić SB, Rabasović MS, Vrbica MD, Lazović VM, Ćurčić BPM, Krmpot AJ. 2015. Nonlinear microscopy of chitin and chitinous structures: a case study of two cave-dwelling insects. *Journal of Biomedical Optics* **20:** 016010.

Reinhardt K, Breunig HG, König K. 2017. Autofluorescence lifetime variation in the cuticle of the bedbug *Cimex lectularius*. *Arthropod Structure & Development* **46:** 56–62.

Ribera I, Fresneda J, Bucur R, Izquierdo A, Vogler AP, Salgado JM, Cieslak A. 2010. Ancient origin of a Western Mediterranean radiation of subterranean beetles. *BMC Evolutionary Biology* **10:** 29.

Ruiz C, Jordal B, Serrano J. 2009. Molecular phylogeny of the tribe Sphodrini (Coleoptera: Carabidae) based on mitochondrial and nuclear markers. *Molecular Phylogenetics and Evolution* **50:** 44–58.

Simon C, Frati F, Beckenbach A, Crespi B, Liu H, Flook P. 1994. Evolution, weighting and phylogenetic utility of mitochondrial gene sequences and a compilation of conserved polymerase chain reaction primers. *Annals of the Entomological Society of America* **87:** 651–701.

StatSoft, Inc. 2001. *STATISTICA (data analysis software system), version 6*. Available at: www.statsoft.com

Šerić Jelaska L, Jambrošić Vladić Ž, Radovanović H, Franjević D. 2014. Comparison of molecular and morphological systematics of *Carabus* species (Coleoptera: Carabidae) with special emphasis on species from Dinaric karst. *Periodicum Biologorum* **116:** 249–257.

Tamura K, Peterson D, Peterson N, Stecher G, Nei M, Kumar S. 2011. MEGA5: molecular evolutionary genetics analysis using maximum likelihood, evolutionary distance, and maximum parsimony methods. *Molecular Biology and Evolution* **28:** 2731–2739.

Williams RM, Zipfel WR, Webb WW. 2001. Multiphoton microscopy in biological research. *Current Opinion in Chemical Biology* **5:** 603–608.

Zar J. 1999. *Biostatistical analysis, 4th edn*. New Jersey: Prentice Hall.

SUPPORTING INFORMATION

Additional Supporting Information can be found in the online version of this article at the publisher's web-site:

Table S1. Measurements, morphometric ratios, and qualitative characteristics of *Pheggomisetes* taxa analysed in the current paper. Numerical unbolded values out of parentheses represent mean values, the bold ones are standard deviations (SD), while the ones in parentheses are ranges. The most important characters for distinction of taxa are underlined (* - values in mm).

Appendix S1. TPEF microscopy video clip showing rotation of the aedeagus of ***P. globiceps ninae* comb. & stat. nov.** around the vertical axis.

Appendix S2. TPEF microscopy video clip showing rotation of the aedeagus of ***P. globiceps ninae* comb. & stat. nov.** around the lateral axis.

Appendix S3. TPEF microscopy video clip showing rotation of the male abdominal sternite IX (urite) of ***P. globiceps ninae* comb. & stat. nov.** around the longitudinal axis.

Appendix S4. TPEF microscopy video clip showing rotation of the male abdominal sternite IX (urite) of ***P. globiceps ninae* comb. & stat. nov.** around the lateral axis.

Appendix S5. TPEF microscopy video clip showing rotation of gonocoxites IX and gonosubcoxites IX of ***P. globiceps ciniglavcensis* subsp. nov.** around the longitudinal axis.

Appendix S6. TPEF microscopy video clip showing rotation of gonocoxites IX and gonosubcoxites IX of ***P. globiceps ciniglavcensis* subsp. nov.** around the lateral axis.

Full length article

Micromechanical imaging of dentin with Brillouin microscopy

Tijana Lainović [a], Jérémie Margueritat [b], Quentin Martinet [b], Xavier Dagany [b], Larisa Blažić [a,c], Dejan Pantelić [d], Mihailo D. Rabasović [d], Aleksandar J. Krmpot [d], Thomas Dehoux [b,*]

[a] *Faculty of Medicine, School of Dental Medicine, University of Novi Sad, Hajduk Veljkova 3, 21000 Novi Sad, Serbia*
[b] *Univ Lyon, Univ Claude Bernard Lyon 1, CNRS, Institut Lumière Matière, F-69622, Villeurbanne, France*
[c] *Dental Clinic of Vojvodina, Hajduk Veljkova 12, 21000 Novi Sad, Serbia*
[d] *Institute of Physics Belgrade, University of Belgrade, Pregrevica 118, 11080 Belgrade, Serbia*

A B S T R A C T

The structure of teeth can be altered by diet, age or diseases such as caries and sclerosis. It is very important to characterize their mechanical properties to predict and understand tooth decay, design restorative dental procedures, and investigate their tribological behavior. However, existing imaging techniques are not well suited to investigating the micromechanics of teeth, in particular at tissue interfaces. Here, we describe a microscope based on Brillouin light scattering (BLS) developed to probe the spectrum of the light scattered from tooth tissues, from which the mechanical properties (sound velocity, viscosity) can be inferred with *a priori* knowledge of the refractive index. BLS is an inelastic process that uses the scattering of light by acoustic waves in the GHz range. Our microscope thus reveals the mechanical properties at the micrometer scale without contact with the sample. BLS signals show significant differences between sound tissues and pathological lesions, and can be used to precisely delineate carious dentin. We also show maps of the sagittal and transversal planes of sound tubular dentin that reveal its anisotropic microstructure at 1 μm resolution. Our observations indicate that the collagen-based matrix of dentine is the main load-bearing structure, which can be considered as a fiber-reinforced composite. In the vicinity of polymeric tooth-filling materials, we observed the infiltration of the adhesive complex into the opened tubules of sound dentine. The ability to probe the quality of this interfacial layer could lead to innovative designs of biomaterials used for dental restorations in contemporary adhesive dentistry, with possible direct repercussions on decision-making during clinical work.

Statement of Significance

Mechanical properties of teeth can be altered by diet, age or diseases. Yet existing imaging modalities cannot reveal the micromechanics of the tooth. Here we developed a new type of microscope that uses the scattering of a laser light by naturally-occurring acoustic waves to probe mechanical changes in tooth tissues at a sub-micrometer scale without contact to the sample. We observe significant mechanical differences between healthy tissues and pathological lesions. The contrast in mechanical properties also reveals the microstructure of the polymer-dentin interfaces. We believe that this new development of laser spectroscopy is very important because it should lead to innovative designs of biomaterials used for dental restoration, and allow delineating precisely destructed dentin for minimally-invasive strategies.

© 2020 Acta Materialia Inc. Published by Elsevier Ltd. All rights reserved.

1. Introduction

Human dentin is an organized, hard, mineralized tissue of the tooth, composed of 70 wt% calcified tissue (hydroxyapatite), 20 wt% organic phase (mostly composed of collagen type I as well as other fibrils), and 10 wt% water [1]. It is perfused with microtubules that allow sensory communication with the underlying pulp and nerves [2]. This fiber-composite-like structure provides an anisotropic distribution of mechanical properties that support masticatory stress concentrated in the surrounding enamel [3],[45–47]. Tooth mechanical strength can be altered by diet, age or diseases such as caries or sclerosis [44]. It is essential to characterize the mechanical properties of teeth to predict and understand tooth decay, design restorative dental procedures, and investigate their tribological behavior.

Most of the methods used for characterization have been inherited from material science, and involve destructive testing such as

compression tests [57], or nanoindentation with AFM tips or normalized indenters [3,47]. These techniques have notably allowed demonstrating the loss of hardness in caries-affected dentin [58]. Using dynamic mechanical analysis, the storage and loss moduli of intertubular and peritubular dentin have been obtained with frequencies up to 100 Hz [59]. Fatigue tests can also be deployed to analyze the fracture behavior of teeth [60]. Recently, recording the deformation of dentin in the vicinity of holes milled by a focused ion beam has revealed the existence of residual stresses [61]. In restorative dentistry, shear bond tests and 3-points bend tests have allowed assessing the efficacy and durability of bonding procedures [62,63]. Due to the variety of techniques and the complexity of the dentin microstructure, there is a lack of quantified consensus regarding the mechanical properties of dentin [38]. Moreover, such approaches are clearly difficult to implement *in vivo*. Dentinal pathological changes can be detected by visuotactile and radiographic methods to help clinicians establish relevant diagnostics, and propose adequate therapies [4]. However, such approaches cannot give precise information on the microstructure, nor precisely delineate caries margins [5], and are highly dependent on the clinician [6].

Acoustic techniques have long been used to probe the mechanics of dentin, initially analyzing the reflection or transmission of ultrasonic pulses emitted from a piezoelectric transducer in the MHz range [39]. Later implementations in tooth tissues in various sound and pathological states used resonant ultrasonic spectroscopy, Kinney et al. [38] acoustic microscopy, Maev et al. [7,9] surface waves [10] and laser ultrasonics [11,12]. The implementation of surface acoustic waves in acoustic microscopy has allowed probing dentin at frequencies up to 1 GHz [8]. In these procedures, however, the acoustic lens has to be defocused, resulting in measurements averaged over a 1 mm-diameter area. Thus, they are not suited to investigating the micromechanics of the tooth, in particular at tissue interfaces. Acoustic microscopy has also been used to measure the reflection of bulk waves and produce images of the acoustic impedance in dentin at a resolution of 23 μm [8]. With this technique, images at 1.2 GHz have also been obtained in bone at a resolution of 1 μm, suggesting potential for micro-imaging in dentin [55].

State-of-the-art microscopies, such as multiphotonic and nonlinear technologies [41] can offer optical resolution but cannot provide any information on the mechanics of the sample. Laser spectroscopies have recently come into vogue, offering quantitative imaging of the chemical structure of tooth tissues and restorative materials [13–16]. In this paper we propose a new approach to probe acoustic waves in the GHz range by laser spectroscopy, thus offering quantitative microscopy with a contrast based on the mechanical properties of tooth tissues.

We have developed a microscope based on Brillouin light scattering (BLS) to probe mechanical changes in tooth tissues, by measuring the characteristics of the scattered light. BLS is an inelastic process similar to Raman scattering. Raman-based techniques rely on the scattering of light by optical phonons, and operate at THz frequencies. They provide information on the molecular structure of the sample. By contrast, Brillouin scattering uses the scattering of light by acoustic phonons [18]. Since acoustic phonons have lower energies than optical phonons, Brillouin scattering produces frequency shifts in the GHz range that reveal the mechanical properties of the sample. Developed in the 1960s for solid-state physics, BLS has only recently emerged as a key technology in life sciences due to its ability to produce non-contact, label-free microscopic images of the mechanical properties of cells and tissues [19]. It has notably been applied for the analysis of biological fibers, connective tissues and muscles [17,20,21], eye tissues [22,23], bone [24,26] and tumors [35].

We prepared thick slices of teeth extracted in accordance with the ethical requirements for ex-vivo studies. We obtained maps of Brillouin frequency shift and linewidth that can be interpreted as maps of sound velocity and viscosity. In order to illustrate the potential of our approach in different areas of dentistry, we analyzed carious lesions, the mechanical anisotropy of sound dentin, and the structure of the dentin-resin interface. Our results first show significant changes between sound tissues and pathological lesions. Such results allow precisely delineating deteriorated dentin, paving the way for minimally invasive strategies. We also provide maps of the sagittal and transversal planes of sound tubular dentin that reveal its anisotropic microstructure with a 1 μm resolution, several orders of magnitude below previous reports [38]. Our observations indicate that the collagen-based matrix of dentin is the main load-bearing structure, which can be considered as a fiber-reinforced composite. In the vicinity of polymeric tooth-filling materials, we observed the infiltration of the adhesive complex into the opened tubules of sound dentin. We confirmed our observations with two-photon excitation fluorescence (2PEF) and second harmonic generation (SHG) microscopies that reveal teeth microstructure due to two-photon excited autofluorescence and collagen-specific second-order nonlinear optical susceptibility [27]. The ability to probe the quality of this interfacial layer could lead to innovative designs of biomaterials used for dental restorations in contemporary adhesive dentistry, with possible direct repercussions on decision-making during clinical work.

2. Materials and methods

2.1. Sample preparation and staining

Teeth were collected at the Faculty of Medicine, School of Dental Medicine, at the Department of Oral Surgery of the Dental Clinic of Vojvodina, Serbia. They were extracted for medical reasons and donated voluntarily by patients after they read and signed the informed written consent. This study was approved by the Ethical Board of the Dental Clinic of Vojvodina, Serbia. All types of permanent teeth were analyzed, including incisors, canines, premolars, and molars. Since extracted human teeth are difficult to collect, different groups of teeth were included in the study. Having previously confirmed that there were no statistically significant differences in variances for the dentinal tissue among the various tooth groups, we pooled together different groups in order to increase the significance of statistical tests. The teeth were classified in the following groups: sound teeth with intact hard tissues (two subgroups – teeth cut perpendicularly to their longitudinal axis, teeth cut longitudinally), teeth with carious lesions in dentin [score 5 on the International Caries Detection and Assessment System (ICDAS) scale; distinct cavity with visible dentin], restored teeth with composite resin.

Freshly extracted teeth were kept in 0.5% chloramine solution until cutting. They were then sectioned across the sagittal and transversal tooth axes in 0.5+/−0.05 mm thick slices by a water-cooled, low-speed diamond saw using a hard tissue microtome. Samples were wet-polished with abrasive sandpaper sheets of silicone-carbide of increasing grit numbers (400–2000). This was followed by polishing with a diamond paste on a soft fabric, in order to eliminate surface corrugations. The smear layer produced by polishing was removed by 10% polyacrylic acid used for 5 s, after which the samples were rinsed, slightly dry-aired and disinfected in a 0.5% chloramine solution. After preparation, each slice was kept in a plastic bag with 100 mL distilled water. In these conditions, the samples kept their natural moisture until examination. However, during the measurements, the samples were tested in dry conditions in air.
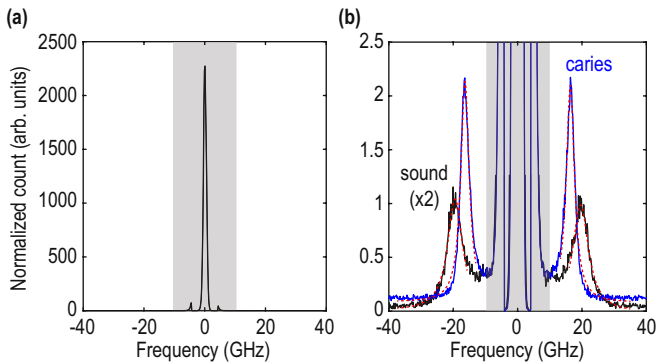
Fig. 1. Typical spectrum. (a) Raw spectrum where the contribution of Rayleigh scattering is indicated by the gray box. (b) Zoom on the Stokes (negative frequencies) and anti-Stokes (positive frequencies) peaks for sound tissue (black, intensity multiplied by 2 for clarity) and a caries lesion (blue line). Fits by Lorentzian functions are superimposed (red dashed lines). (For interpretation of the references to colour in this figure legend, the reader is referred to the web version of this article.)

Teeth restored with composite used for the imaging of the dentin-adhesive interface were prepared according to the standard dental adhesive placement procedure, after the etching procedure by using 37% ortho-phosphoric acid for 15 s, rinsing, and placing a single bond universal adhesive (3 M Deutschland GmbH, LOT 663414), before restoration with the Filtek Ultimate Body composite. For 2PEF imaging of the dentin-adhesive interface, a water solution containing 0.5% eosin-Y was added in small quantities into the adhesive in order to distinguish the adhesive from the surrounding dentinal tissue.

2.2. Nonlinear laser scanning microscopy

Teeth specimens were observed by a nonlinear optical microscopy setup at the Institute of Physics in Belgrade. The homemade nonlinear laser-scanning microscope used in this study has been described in detail elsewhere [42,43]. Briefly, a Ti:Sapphire femtosecond laser (Coherent, Mira 900-F) tunable in the 700–1000 nm range and a Yb:KGW (Time-Bandwidth Products AG, Yb GLX) femtosecond laser at 1040 nm were used as laser light sources. The samples were imaged using a Carl Zeiss, EC Plan-NEOFLUAR, 40 × 1.3 oil immersion objective or a Plan-APOCHROMAT 20x/0.8 air objective for laser focusing and signal collection. A visible interference filter (415 nm–685 nm) positioned in front of the detector was used to remove scattered laser light in the fluorescence images. Thus, the whole visible range was detected in two-photon fluorescence images. Tooth auto-fluorescence was excited by the Ti: Sapphire laser at 730 nm. Eosin-Y fluorescence was excited by the Ti:Sapphire laser at 820 nm. Narrowband interference filters (10 nm FWHM) were used for second-harmonic generation imaging. The SHG filter central wavelength was 520 nm (FB520-10, Thorlabs) for the Yb:KGW laser. The SHG filter central wavelength was 420 nm (FB420-10, Thorlabs) for the Ti:Sapphire laser when tuned at 840 nm. The SHG excitation wavelength and filter were selected so that fluorescence leakage to the SHG channel was minimal.

2.3. Brillouin spectroscopy

BLS uses the scattering of light by phonons. Thermal phonons (incoherent vibrations) produce a broad peak at low frequencies due to Rayleigh scattering, while acoustic phonons (coherent vibration) with wavenumbers that fulfill the Bragg condition produce well-defined peaks (Fig. 1). Using a monochromatic light beam of wavelength λ in a normal incidence backscattering geometry, forward propagating phonons produce a positive shift at a frequency $f = 2nV/\lambda$ (anti-Stokes peak) with a width $\Gamma = \omega f \nu/V^2$, where

V is the sound velocity, ν is the kinematic viscosity and n is the refractive index. Backward propagating phonons create a negative Stokes peak at $-f$.

For comparison with the literature, it can be useful to express the loss and storage moduli. Assuming that the sample is homogeneous over the scattering volume, the BLS spectra can be interpreted as the response of a damped harmonic oscillator with frequency position f and full width at half maximum Γ. In this approximation, the storage modulus is $' = \rho(f\lambda/2n)^2$, where ρ is the mass density. The linewidth Γ is ascribed to the loss modulus $M'' = \rho\Gamma f(\lambda/2n)^2$. It is however not mandatory to evaluate M' and M'', and the mechanical properties can be assessed using only V and ν.

From these equations it is clear that BLS probes the sound velocity and viscosity of the sample, but f and Γ both depend linearly on n. The mechanical properties V and ν and the refractive index n both contribute to the frequency shift and linewidth, but with our measurement alone, we cannot distinguish their respective influences. Interestingly, we can also determine the loss tangent [59] $\tan\varphi = \frac{M''}{M'} = \frac{\Gamma}{f}$ that does not depend on the refractive index. More importantly, in situations where Γ (resp. f) does not vary, i.e. both n and ν are constant as in Fig. 3, variations of f can be attributed to changes in the sound velocity (resp. viscosity). Note that at the high magnifications we used, Γ can increase artificially due to the finite solid angle of collection of the backscattered light.

The size of the laser spot, estimated using the Rayleigh criterion, corresponds to an ellipsoid of ~1 μm in the lateral direction and ~10 μm in the axial direction. Although this is an overestimation, since the penetration inside the tooth at 647.1 nm is not known, we consider that the volume of the laser spot defines a scattering volume of ~40 μm^3.

2.4. Brillouin microscope

The Brillouin spectrometer is based on a tandem Fabry-Pérot interferometer (JRS Scientific Instruments) [35]. In order to reduce phototoxicity, we used a $\lambda = 647.1$ nm continuous-wave laser as a light source (instead of classical designs based on a frequency-doubled YAG laser at 532 nm) which gives a $\frac{\lambda}{2n} \approx 200$ nm acoustic resolution, where $n = 1.6$ is the typical refractive index of dentin. The spectrometer offers a 40 GHz free spectral range sampled with a 30 MHz sampling rate. Appropriate signal analysis allows obtaining an accuracy of 6 MHz at a -10 dB noise level. It is equipped with two sets of mirrors with 95% reflectivity, and an avalanche photodiode (Count$^®$ Blue, Laser Components) with a dark count lower than 10 counts/s (typically 2 counts/s) and a quantum efficiency of 65% at this wavelength. The spectrometer is coupled with an inverted life science microscope (Eclipse Ti-U, Nikon) equipped with a micro-positioning stage (Mad City Labs). The collimated linearly-polarized laser light is focused onto the sample using a 100 × objective (NA 0.9), providing a resolution of ~1 μm. The typical power used at the focus was 5 mW, resulting in a power density over the scattering volume a hundred times smaller than that previously reported in tissues and cells, again to ensure low phototoxicity. The backscattered light is collected by the same objective lens and collected outside the microscope using a telescope. Particular attention was paid to comply with the f-number (f/18) of the spectrometer to maximize photon collection on the photodiode. Spectra were acquired by averaging over ~100 acquisitions.

2.5. Dentinal positions examined

The middle crown sections were probed by the BLS microscope. In this area, the tubules form an "S" curve and diverge in the tooth

crown. We selected intertubular regions manually for BLS measurements. Note that these regions might also contain the signature of the peritubular wall, but not that of the tubular lumen which does not produce any BLS signal.

For the study of caries, the tooth was cut longitudinally to show the dentinal carious zones, including caries-infected and caries-affected dentin. The data were collected in the sagittal plane in the middle-dentinal crown portion. The BLS scanning passed from the sound dentin over the histopathological carious layers to the carious decay.

The dentin-adhesive interfaces were tested, passing over the composite restoration, the adhesive layer, the hybrid layer, the etched dentin, and to the completely untreated dentinal core.

2.6. Data analysis

Raw spectra sampled at 30 MHz were recorded by the proprietary software of the spectrometer (Ghost software, Table Stable Ltd., Switzerland). When only one peak was observed on each side of the Rayleigh line (see Fig. 1b for instance), we fitted the anti-Stokes and Stokes peaks separately to a Lorentzian function using Matlab and extracted amplitude A, frequency shift f and linewidth Γ. We chose the Lorentzian function since it is that best suited for analyzing solid samples [50]. Values for each peak were then averaged. When two closely-spaced peaks were observed, we sequentially windowed around each peak and fitted the windows individually with a single Lorentzian function. This procedure may slightly underestimate the true spacing between the two peaks, but it reduces the error of the fit and hence allows automating the fitting procedure to analyze large images.

In Figs. 3,6 and 7, we plot point distributions where jitter has been added to the data points to avoid overlap. This type of plot, called plot spread plot, allows visualizing the distribution of points within a distribution, and identify possible outliers. The data collected from the different groups of samples were statistically analyzed using Matlab software (version R2017a). The level of significance (*p*-value) was evaluated according to an unpaired two-tailed *t*-test.

3. Results

3.1. Mechanical signature of carious lesions

Brillouin spectra were recorded for sound tissues ($n = 34$ in 5 different teeth) and carious lesions ($n = 39$ in 5 different teeth). These data were acquired in the sagittal plane in the middle-dentinal crown portion (see Material and Methods). By way of illustration, we plot a typical spectrum in Fig. 1. Fig. 1a shows that the raw spectrum is dominated by Rayleigh scattering (grey box). Fig. 1b shows a zoom on the Stokes (negative frequencies) and anti-Stokes (positive frequencies) peaks for the sound tissue and caries lesion. We fit these peaks with Lorentzian functions (dashed lines) to extract the frequency shift f and linewidth Γ (**Methods**). The distributions of frequency and linewidth values are plotted in Fig. 2a and b, respectively. Note that the spreading of the data is larger in the case of caries because BLS features depend on the position within the highly heterogeneous lesion, as discussed below. The frequency shift is clearly different between sound and carious conditions. We do not, however, observe any significant variation in the linewidth. This observation suggests that BLS features could be used to delineate lesions.

To investigate this, we scanned the laser along a line across the frontier between sound tissue and a caries lesion. Fig. 3 shows the frequency shift f and linewidth Γ measured from the sound region (left) to the core of the lesion (right). We can see that Γ does not
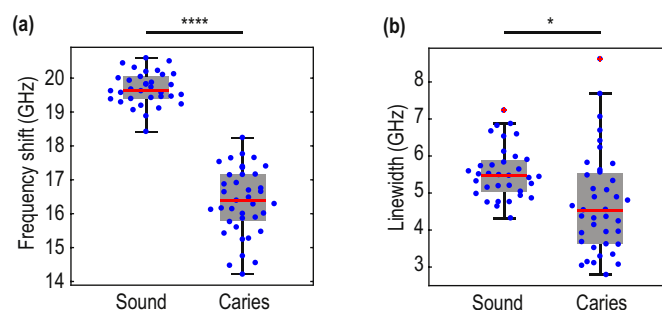
Fig. 2. Comparison between sound tissues ($n = 34$) and carious lesions ($n = 39$). Distributions of (a) frequency shift and (b) linewidth (****$p<0.0001$, *$p<0.05$, unpaired two-tailed *t*-test). The bottom and top edges of each gray box indicate the 25th and 75th percentiles, respectively. The red central line indicates the median. The whiskers extend to the most extreme data points, not considering outliers ('+' symbol). (For interpretation of the references to colour in this figure legend, the reader is referred to the web version of this article.)
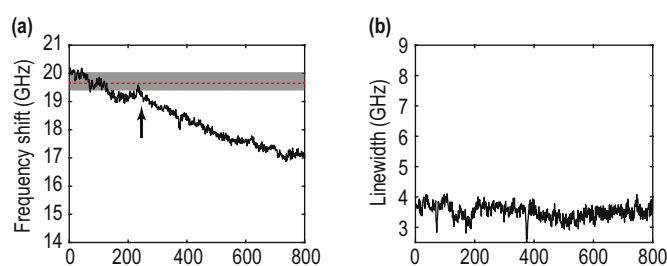

Fig. 3. Scan across a caries lesion. (a) frequency shift and (b) linewidth. The gray box and red dashed line indicate the 25th and 75th percentiles and median identified in Fig. 2a. The upward arrow indicates the position where the frequency shift falls below the 25th percentile. (For interpretation of the references to colour in this figure legend, the reader is referred to the web version of this article.)

vary, as already observed in Fig. 2b, meaning that the refractive index does not change across the probed region (see **Methods**). On the other hand, f decreases slowly. In this situation, we can ascertain that the sound velocity is the main contributor to the change observed in f.

The slow decrease in f makes the precise delineation difficult. As a reference, we indicate the median (red dashed line) and the 25th and 75th percentiles (grey box) measured in Fig. 2a. The upward arrow indicates where f falls below the 25th percentile. This criterion can be used to define the limit of the sound tissue. In this example, f decreases almost linearly by ~ 0.01 GHz/μm within the lesion. Given the spreading of the data for sound dentin measured in Fig. 2a, ~ 0.2 GHz between the mean and the 25th percentile, such a decrease would lead to a precision of 20 μm in the identification of the lesion margins.

3.2. Mechanical anisotropy of the dentin

Sound dentin is composed of a mineralized collagen matrix (intertubular dentin) perfused by microtubes called tubules surrounded by peritubular mineralized dentinal tissue (peritubular dentin). This structure leads to an anisotropic distribution of mechanical properties, largely documented in the literature on the macroscale [38]. To investigate the anisotropy of the sound tubular dentin on the microscopic scale, sound teeth were cut longitudinally and transversally (**Methods**). The microstructure of the sound dentin in the sagittal and transversal planes is clearly revealed by the combination of the 2PEF image obtained with the Ti:Sapphire tuned at 730 nm and the SHG image obtained with the Ti:Sapphire tuned at 840 nm (Figs. 4 and 5). The typical tubular structure of
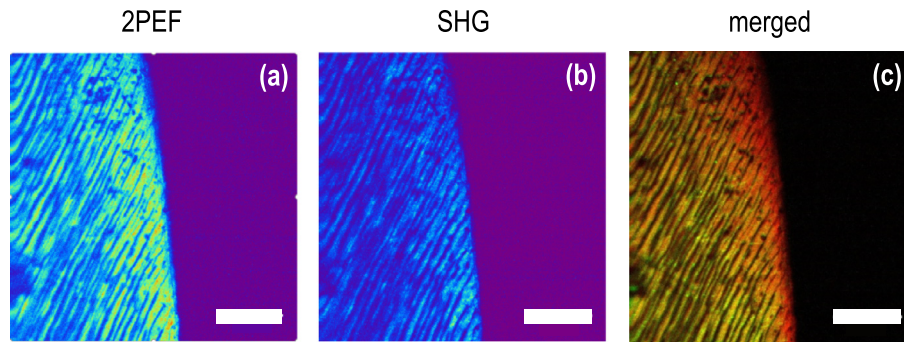
Fig. 4. 2PEF and SHG images of sound dentin in the sagittal plane. (a) The 2PEF image reveals the tubular structure of dentin; (b) the SHG image reveals the presence of collagen type I, (c) merged. Scale bars: 20 µm.
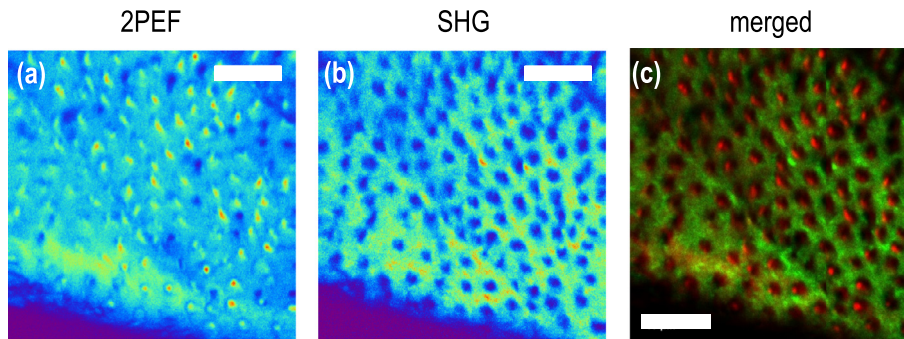

Fig. 5. 2PEF and SHG images of sound dentin in the transversal plane. (a) The 2PEF image reveals the tubular structure of dentin; (b) the SHG image reveals the presence of collagen type I, (c) merged. Scale bars: 20 µm.

dentin appears clearly on the 2PEF image. Collagen type I, a triple-helical molecule, the organic component on which the dentin is mostly built, is aligned in a non-centrosymmetric manner, and is responsible for the contrast in the SHG images. The SHG images of dentin thus reveal the intertubular dentin, which is less mineralized than the peritubular dentin [28].

The exposed surfaces in the sagittal and transversal planes were mapped with BLS. The laser was scanned in a raster pattern at a resolution of 1 µm and spectra were recorded at each pixel. The resulting images obtained in the sagittal (along the tubules) and transversal planes (perpendicular to the tubules) of the tooth are shown in Figs. 6 and 7, respectively. In the sagittal plane, the tubules are clearly visible on the optical image (Fig. 6a), and are characterized by a lower amplitude (Fig. 6b) and a lower f (Fig. 6c). We define an amplitude threshold of $A_{th} = 0.5A_m$, where A_m is the maximum amplitude that separates the tubular region (containing tubules and peritubular dentin) from the surrounding intertubular dentin. Pixels in the f and Γ images that correspond to an amplitude $A < A_{th}$ are ascribed to the tubular region, and the remaining pixels to the intertubular dentin. The distribution of pixels for f and Γ are shown in Figs. 6e and 6f. While the linewidth does not allow distinguishing the two components (as observed in Fig. 6d), f-values are slightly higher for the tubules.

In the transverse plane, the tubules appear as disks on the optical image (Fig. 7a). They are also clearly visible on the BLS images, characterized here too by a low amplitude (Fig. 7b). In this case, however, the low amplitude of the Brillouin peaks does not allow identifying f or Γ-values in the tubular regions, and only the peritubular and intertubular dentin appear in the f and Γ images, Figs. 7d and 7f. This is because the tubules cause a depression in the transverse plane that defocuses the laser beam. Considering pixels where $A < A_{th}$ therefore reveals only the distributions of values for the intertubular dentin, plotted in Figs. 7c and 7e, respectively. The f and Γ values differ significantly ($p < 0.0001$) in

the sagittal and transverse planes, suggesting that the matrix itself is anisotropic.

3.3. Characterization of the dentin-resin interface

In this section, we examine the adhesive interface between sound dentin and tooth-filling resin. Fig. 8a shows a typical sample with an adhesive interface indicated by the arrow. A merged 2PEF image obtained with the Ti:Sapphire tuned at 820 nm and an SHG image obtained with the Yb:KGW (Fig. 8b) reveals the typical structure of the interface between dentin (SHG, blue pseudocolor) and adhesive (labeled by eosin in 2PEF, red pseudocolor). This image reveals that the low-viscous monomer adhesive protrudes in-between the exposed dentinal collagen fibers of intertubular dentin, or in the tubules themselves, forming the so-called hybrid layer. Extensions of monomer entering a few individual dentinal tubules, i.e. resin tags, are also observable (a typical extension is indicated by a white arrow).

We probed the interface between sound dentin and resin with BLS. Fig. 9a shows a typical spectrum where we recognize the signature of sound dentin at around 20 GHz (blue area). In addition, we also observe a second peak at around 13 GHz (pink area), revealing the presence of the adhesive. This result demonstrates that BLS is able to detect the presence of the two components mixed in the hybrid layer. To investigate this, we recorded BLS images in a typical hybrid layer. The frequency shift (Fig. 9b) and linewidth (Fig. 9c) both allow us to observe the adhesive, hybrid layer and dentin. The adhesive is recessed in the vicinity of the hybrid layer (left part of Figs. 9b and 9c), causing the laser to defocus and the signal to fall below detectable levels. Such pixels with an amplitude lower than 0.1 are shown in white. These images clearly highlight the ability of BLS to quantify adhesive interfaces and reveal the infiltration of the adhesive in the hybrid layer.
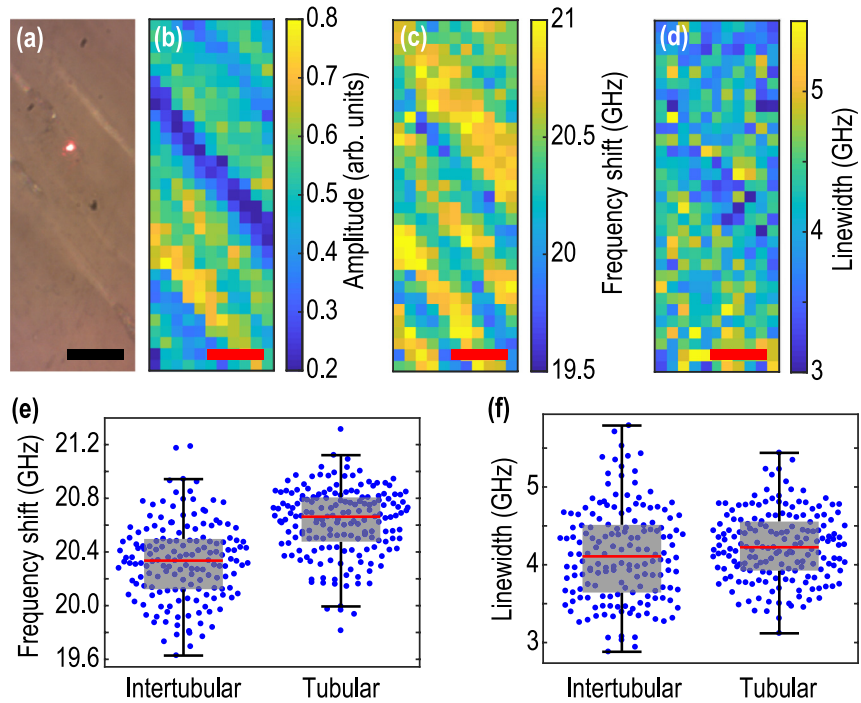
Fig. 6. Images of sound dentin in the sagittal plane. (a) Optical image, (b) amplitude of the Brillouin peaks, (c) frequency shift and (d) linewidth. Panels (e) and (f) show the distribution of f and Γ-values measured in panels (c) and (d), respectively. The tubular region is identified in panel (b) by amplitude values lower than 50% of the maximum amplitude, and the intertubular dentin corresponds to the remaining pixels. Scale bars: 5 µm.
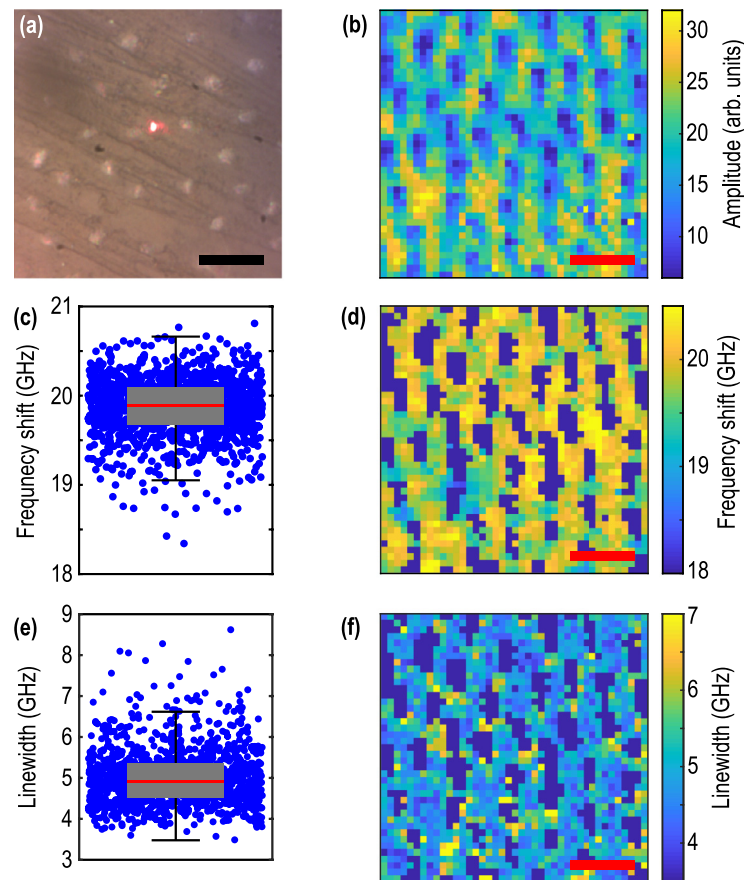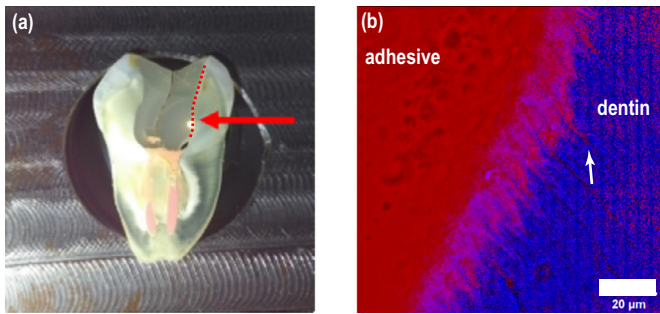

Fig. 7. Images of sound dentin in the transversal plane. (a) Optical image, (b) amplitude of the Brillouin peaks, (d) frequency shift, and (f) linewidth. Panels (c) and (e) show the distribution of f and Γ-values measured in panels (d) and (f), respectively. Scale bars: 10 µm.

Fig. 8. Structure of a typical dentin adhesive interface. (a) photograph of an dentin-resin adhesive interface shown by a dashed line and arrow. (b) Merged 2PEF and SHG images of a dentin-adhesive interface. A 2PEF micrograph reveals the adhesive colored by eosin Y (red pseudocolor) and a SHG micrograph reveals dentin (blue pseudocolor). The arrow points to a typical resin tag. Scale bar: 20 μm. (For interpretation of the references to colour in this figure legend, the reader is referred to the web version of this article.)

4. Discussion

We demonstrated the potential of BLS to examine non-destructively and with high resolution the mechanical properties of different sound, diseased and restored dental tissues. The BLS maps in the sagittal and transverse planes clearly reveal the tubular structure of dentin. We segmented the images to separate the tubular region from the surrounding intertubular dentin. With this approach the peritubular dentin might contribute to segmented intertubular dentin, depending on the threshold value. However, we found that the intertubular dentin was stiffer compared to the peritubular dentin, in line with previous publications [47]. This suggests peritubular dentin contributes marginally to the stiffness of segmented-intertubular dentin. Our results showed $f_s \sim 20.4$ GHz in the sagittal plane, and $f_t \sim 19.8$ GHz in the transverse plane for the matrix alone. These values correspond to sound velocities $V_s = \frac{f\lambda}{2n_s} \approx 4100$ m/s and $V_t = \frac{f\lambda}{2n_t} \approx 4300$ m/s, assuming refractive indices $n_s = 1.6$ and $n_t = 1.5$ in the sagittal and transverse planes, respectively [37]. These sound velocity values are comparable with the values measured by acoustic interferometry (from 3900 to 4100 m/s, see [40]) and acoustic microscopy (from 4100 to 4200 m/s, see [56]). Ref. [8] gives lower values (3800–3900 m/s) but it is important to note that these are surface wave velocities, not bulk waves as in the other works, and that the algorithm they use greatly depends on the assumed sym-

metry of the sample. For further comparisons, we can also estimate the storage moduli $M'_s = \rho V_s^2 \sim 36$ GPa and $M'_t = \rho V_t^2 \sim 38$ GPa, assuming a mass density $\rho \sim 2100$ kg/m^3 (see **Materials and Methods, "Brillouin spectroscopy"**) [36]. Our values, ~36–38 GPa, are comparable with previous results obtained by resonant ultrasound spectroscopy (36.5 GPa, see [48]) and with simulated values [45]. Variations between these different values can come from uncertainties in n, ρ, the assumed symmetry, the type of acoustic wave (bulk or surface wave) or the sample itself. In particular, water content can also play a role. Note that, while the samples were stored in a hydrated environment, the BLS measurements were performed in ambient conditions (see **Material and Methods, "Sample preparation and staining"**). Future studies should consider a possible hydration-dependent Brillouin frequency shift in dentin, since more anisotropic dentinal values have been observed in hydrated environments [48]. In addition, simultaneous measurements of the refractive indices should make it possible to perform a quantitative determination of the sound velocity.

The difference between the frequencies of sound dentin and those of carious lesions is very clear ($p < 0.0001$). The transition from sound dentin to caries allowed delineation at a precision of 20 μm for the samples we probed. The linewidth $\Gamma = 2\pi\eta(2n/\lambda)^2$ was constant across this region, meaning that both n and kinematic viscosity η are constant. The change in f can thus be ascribed to a reduction in the sound velocity of the tooth in the lesion. This observation demonstrates the high specificity of BLS, and its ability to produce quantitative indicators of tooth decay. In the future, it will be necessary to repeat such measurements on a larger population of samples to obtain a robust delineation threshold. In contemporary clinical practice, the visuotactile method is the dominant approach for caries delineation, but it is obviously less resolved than BLS, and operator-dependent. To avoid inter-examiner variations, visual examination can be aided by dyes, light-fluorescence based methods, and fiber-optic transillumination. In this context, BLS has unique potential for providing quantitative information at the microscale in a label-free, non-invasive, non-ionizing manner. Further comparison with histological sections of lesions with different scores should reveal the sensitivity of BLS, and grant new minimally invasive strategies in dentistry. As has been done for cancer therapy [35], ophthalmology [30] and orthopedic treatments [25], BLS could be used as a platform for the early diagnosis of tooth decay, micrometric precision caries detection during clinical work, and for monitoring the efficacy of therapeutic techniques [31,34].
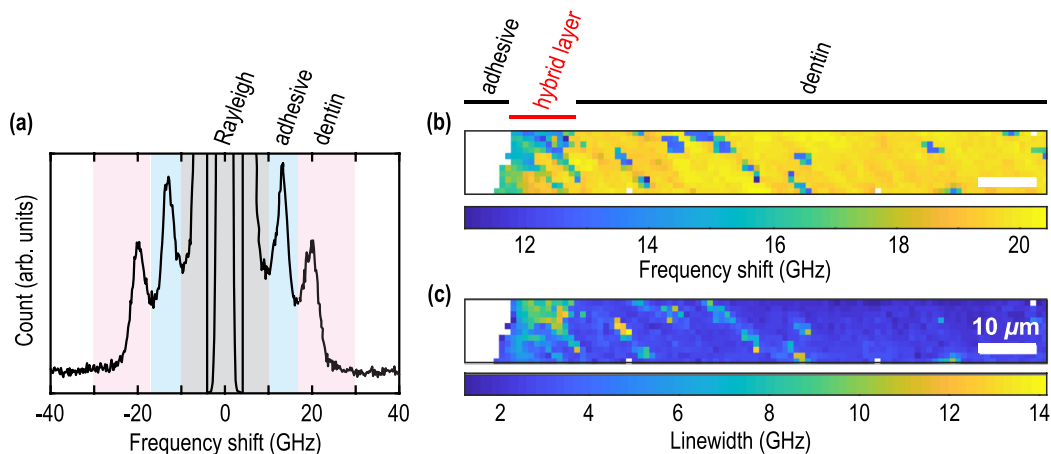

Fig. 9. Imaging the hybrid layer. (a) Typical spectrum at the dentin-adhesive interface. The peaks arising from dentin and adhesive are shown in blue and pink, respectively. (b) Frequency shift and (c) linewidth maps of the hybrid layer. Scale bars: 10 μm. (For interpretation of the references to colour in this figure legend, the reader is referred to the web version of this article.)

BLS images of the hybrid layer provide new information on the spatial distribution of mechanical properties at the adhesive junction. This interface is of great interest in modern adhesive dentistry [51] since it is suspected to be the main reason for restoration failure [52]. It has indeed been demonstrated that the effectiveness of hybrid layer remineralization processes (for instance after treatment with ion-releasing materials and therapeutic phosphoproteins [34], or after collagen cross-linking treatment [53]) is associated with increased stiffness [54]. In the future, in combination with fatigue tests and refractive index measurements, as well as other techniques such as acoustic microscopy [49] and Raman spectroscopy [13], BLS could be used to test the stiffness and viscosity of different types of adhesives under preclinical investigation and the weakening of the hybrid layer by enzyme-based degradation of collagen, adhesive, mineral-depleted dentin [31,32] and caries lesions [33]. Our results also show a reduction of the frequency shift near the interface. To explain this, it can be postulated that etching at the interface is responsible for reduced stiffness, as observed by SAM [49]. If such an effect could be detected by BLS, it would be another advantage for investigations in adhesive dentistry. To investigate this in the future we will compare dentin prepared by different total-etch and self-etch dental adhesive protocols, as well as specific treatments for hybrid layer reinforcement. Moreover, the hybrid layer is subjected to multiaxial stresses during functional use, and it has been predicted that stress concentration in the underlying hard dental tissues depends on the stiffness of this interface [29]. In the future, BLS could also help studying the impact of wear on this interface at the microscale.

Clinically, it should be possible to develop a BLS fiber-optic tool for dental applications. Similar developments are being implemented for other applications, such as cancer diagnostics. The development of a fiber optic probe would require the area of interest to be directly accessible from the surface (not buried under other tissues), in the depth of the laser light penetration. For example, exposed carious lesions could be probed with microscopic precision, and carious-sound dentin thresholds could be defined based on the features of the BLS spectra. The adhesive interface between dentin and adhesive is rarely directly exposed, though BLS could be used during preclinical investigations in adhesive dentistry. Moreover, BLS could be used to probe dentin-adhesive interfaces directly in non-carious cervical lesions in the case where the overlying enamel has worn away. Beyond dentistry, BLS could also provide new tools for investigating the link between microwear, stiffness, and diet, offering important information in the field of paleobiology.

Declaration of Competing Interest

We declare no conflict of interest.

Acknowledgements

References

[1] M. Goldberg, A.B. Kulkarni, M. Young, A. Boskey, Dentin: structure, composition and mineralization, Front. Biosci. (Elite Ed) 3 (2011) 711.

[2] S.R. Stock, A.C. Deymier-Black, A. Veis, A. Telser, E. Lux, Z. Cai, Bovine and equine peritubular and intertubular dentin, Acta Biomater. 10 (2014) 3969.

[3] J.H. Kinney, M. Balooch, S.J. Marshall, G.W. Marshall JR, T.P. Weihs, Hardness and Young's modulus of human peritubular and intertubular dentine, Arch. Oral Biol. 41 (I) (1996) 9–13.

[4] S.K. Makhijaa, M.E. Robinson, J.D. Bader, D.A. Shugars, M.S. Litaker, H.R. Im, D.B. Rindal, D.J. Pihlstrom, C. Meyerowitz, V.V. Gordan, M.H. Buckberg, G.H. Gilbert, Dentists' decision strategies for suspicious occlusal caries lesions in a national dental PBRN study, J. Dent. 69 (2018) 83.

[5] F. Schwendicke, S. Paris, Y.-.K. Tu, Effects of using different criteria for caries removal: a systematic review and network meta-analysis, J. Dent. 43 (1) (2015) 1–15.

[6] G.J. Joves, G. Inoue, A. Sadr, T. Nikaido, J. Tagami, Nanoindentation hardness of intertubular dentin in sound, demineralized and natural caries-affected dentin, J. Mech. Behav. Biomed. Mater. 32 (2014) 39–45.

[7] R. Maev, L. Denisova, E. Maeva, D. AA, New data on histology and physico-mechanical properties of human tooth tissue obtained with acoustic microscopy, Ultrasound Med. Biol., 28 (2002) 131–136.

[8] K. Raum, K. Kempf, H.J. Hein, J. Schubert, P. Maurer, Preservation of microelastic properties of dentin and tooth enamel in vitro—A scanning acoustic microscopy study, Dent. Mater. 2 (3) (2007) 1221–1228.

[9] A. Shelke, M. Blume, M. Mularczyk, C. Landes, R. Sader, J. Bereiter-Hahn, Visualisation of localized elastic properties in human tooth and jawbone as revealed by scanning acoustic microscopy, Ultrasound Med. Biol. 39 (5) (2013) 853–859.

[10] S. Toda, T. Fujita, H. Arakawa, K. Toda, Nondestructive testing in human teeth using a leaky Lamb wave device, Ultrasonics 44 (2006) e1151–e1155.

[11] K. Sun, L. Yuan, Z. Shen, Q. Zhu, J. Lu, X. Ni, Experimental and numerical studies for nondestructive evaluation of human enamel using laser ultrasonic technique, Appl. Opt. 52 (28) (2013) 6896–6905.

[12] H.-.C. Wang, S. Fleming, Y.-.C. Lee, M. Swain, S. Law, J. Xue, Laser ultrasonic evaluation of human dental enamel during remineralization treatment, Biomed. Opt. Express 2 (2) (2011) 345–355.

[13] H. Salehi, E. Terrer, I. Panayotov, B. Levallois, B. Jacquot, H. Tassery, F. Cuisinier, Functional mapping of human sound and carious enamel and dentin with Raman spectroscopy, J. Biophotonics 6 (2013) 765–774.

[14] R. Ramakrishnaiah, G. ur Rehman, S. Basavarajappa, A.A. Al Khuraif, B.H. Durgesh, A.S. Khan, I. ur Rehman, Applications of Raman spectroscopy in dentistry: analysis of tooth structure, Appl. Spectrosc. Rev. 50 (4) (2015) 332–350.

[15] C. de, C.A. Lopes, P.H.J.O. Limirio, V.R. Novais, P. Dechichi, Fourier transform infrared spectroscopy (FTIR) application chemical characterization of enamel, dentin and bone, Appl. Spectrosc. Rev. 53 (9) (2018) 747–769.

[16] Z.A. Steelman, D.S. Ho, K.K. Chu, A. Wax, Light-scattering methods for tissue diagnosis, Optica 6 (2019) 479–489.

[17] R. Harley, D. James, A. Miller, J.W. White, Phonons and the elastic moduli of collagen and muscle, Nature 267 (1977) 285–287.

[18] L. Brillouin, Diffusion de la lumière et des rayonnés X par un corps transparent homogène; influence de l'agitation thermique, Ann. Phys. 17 (1922) 88–122.

[19] F. Palombo, D. Fioretto, Brillouin light scattering: applications in biomedical sciences, Chem. Rev. 119 (2019) 7833–7847.

[20] J. Randall, J.M. Vaughan, S. Cusak, Brillouin scattering in systems of biological significance, Philos. Trans. R. Soc. A 293 (1979) 341–348.

[21] F. Palombo, C.P. Winlove, R.S. Edginton, E. Green, N. Stone, S. Caponi, M. Madami, D. Fioretto, Biomechanics of fibrous proteins of the extracellular matrix studied by Brillouin scattering, J. R. Soc. Interface 11 (2014) 20140739.

[22] J.M. Vaughan, J.T. Randall, Brillouin scattering, density and elastic properties of the lens and cornea of the eye, Nature 284 (5755) (1980) 489–491.

[23] G. Scarcelli, S.H. Yun, Confocal brillouin microscopy for three-dimensional mechanical imaging, Nat. Photonics 2 (1) (2008) 39.

[24] S. Lees, N.J. Tao, S.M. Lindsay, Studies of compact hard tissues and collagen by means of brillouin light scattering, Connect. Tissue Res. 24 (3–4) (1990) 187–205.

[25] R. Tsubota, K. Fukui, and M. Matsukawa, "Local ultrasonic wave velocities in trabeculae measured by micro-Brillouin scattering," J. Acoust. Soc. Am., vol. 2, pp. EL109–EL114, 135AD.

[26] V. Mathieu, K. Fukui, M. Matsukawa, M. Kawabe, E. Soffer, F. Anagnostou, G. Haiat, Micro-Brillouin scattering measurements in mature and newly formed bone tissue surrounding an implant, J. Biomech. Eng. 133 (February) (2011) 021006-1-021006-6.

[27] M. Oheim, D. Michael, M. Geisbauer, M. Dorte, R. Chow, Principles of two-photon excitation fluorescence microscopy and other nonlinear imaging approaches, Adv. Drug Deliv. Rev. 58 (2006) 788–808.

[28] R. Elbaum, E. Tal, A.I. Perets, D. Oron, D. Ziskind, Y. Silberberg, H.D. Wagner, Dentin micro-architecture using harmonic generation microscopy, J. Dent. 35 (2) (2007) 150–155.

[29] A. Misra, V. Singh, R. Parthasarathy, Material-tissue Interfacial phenomena: Challenges in Mathematical Modeling, Elsevier Ltd, 2016.

[30] S.H. Yun, D. Chernyak, Brillouin microscopy: assessing ocular tissue biomechanics, Curr. Opin. Ophthalmol. 29 (4) (2018) 299–305.

[31] S. Sauro, V.P. Feitosa, T.F. Watson, D.H. Pashley, Therapeutic bonding approaches to remineralize dentin-bonded interfaces, Dent. Mater. 32 (Supplement 1) (2016) e3–e4.

[32] M. Hashimoto, H. Ohno, H. Sano, M. Kaga, H. Oguchi, In vitro degradation of resin–dentin bonds analyzed by microtensile bond test, scanning and transmission electron microscopy, Biomaterials 24 (2003) 3795–3803.

[33] M. Oliveir, F. Chasqueira, S. Arantes-Oliveira, S. Pessanha, The use of micro-Raman spectroscopy for the analysis of caries-affected dentin adhesive interfaces, Int. J. Adhesion Adhesives 87 (2020) 216–222.

[34] S. Sauro, R. Osorio, T.F. Watson, M. Toledano, Influence of phosphoproteins ' biomimetic analogs on remineralization of mineral-depleted resin – dentin interfaces created with ion-releasing resin-based systems, Dent. Mater. 31 (7) (2015) 759–777.

[35] J. Margueritat, A. Virgone-Carlotta, S. Monnier, H. Delanoë-Ayari, H.C. Mertani, A. Berthelot, Q. Martinet, X. Dagany, C. Rivière, J.-P. Rieu, T. Dehoux, High-frequency mechanical properties of tumors measured by Brillouin light scattering, Phys. Rev. Lett. 122 (2019) 018101.

[36] Regine Gradl, Irene Zanette, Maite Ruiz-Yaniz, Martin Dierolf, Alexander Rack, Paul Zaslansky, Franz Pfeiffer, Mass density measurement of mineralized tissue with grating-based X-Ray phase tomography, PLoS One 11 (2016) e0167797.

[37] I. Hariri, A. Sadr, Y. Shimada, J. Tagami, Y. Sumi, Effects of structural orientation of enamel and dentine on light attenuation and local refractive index: an optical coherence tomography study, J. Dentistry 40 (2012).

[38] J.H. Kinney, S.J. Marshall, G.W. Marshall, The mechanical properties of human dentin: a critical review and re-evaluation of the dental literature, Crit. Rev. Oral. Biol. Med. 14 (2003) 13–29.

[39] G. Kossoff, C.J. Sharpe, Examination of the contents of the pulp cavity in teeth, Ultrasonics 4 (1966) 77–83.

[40] S. Lees, F.R. Rollins, Anisotropy in hard dental tissues, J. Biomech. 5 (1972) 557–566.

[41] T. Cloitre, I.V. Panayotov, H. Tassery, C. Gergely, B. Levallois, F.J. Cuisinier, Multiphoton imaging of the dentine-enamel junction, J. Biophotonics 6 (2013) 330–337.

[42] M. Rabasović, D. Pantelić, B. Jelenković, S. Ćurčić, M. Rabasović, M. Vrbica, et al., Nonlinear microscopy of chitin and chitinous structures: a case study of two cave-dwelling insects, J. Biomed. Opt. 20 (2015) 016010.

[43] K. Bukara, S.Z. Jovanić, I.T. Drvenica, A. Stančić, V. Ilić, M.D. Rabasović, D.V. Pantelić, B.M. Jelenković, B. Bugarski, A.J. Krmpot, Mapping of hemoglobin in erythrocytes and erythrocyte ghosts using two photon excitation fluorescence microscopy, J. Biomed. Opt. 22 (2017) 026003.

[44] D. Zaytsev, S. Grigoriev, P. Panfilov, Deformation behavior of root dentin under Sjogren's syndrome, Mater. Lett. 65 (2011) 2435–2438.

[45] Y. Yoon, Estimation of the elastic constants of dentin, Int. J. Precision Eng. Manufact. 14 (2013) 317–322.

[46] S. Seyedkavoosi, I. Sevostianov, Multiscale micromechanical modeling of the elastic properties of dentin, J. Mech. Behav. Biomed. Mater. 100 (2019) 103397.

[47] Y.-R. Zhang, W. Du, X.-D. Zhou, H.-Y. Yu, Review of research on the mechanical properties of the human tooth, Int. J. Oral Sci. 6 (2014) 61–69.

[48] J.H. Kinney, J.R. Gladden, G.W. Marshall, S.J. Marshall, J.H. So, J.D. Maynard, Resonant ultrasound spectroscopy measurements of the elastic constants of human dentin, J. Biomech. 37 (2004) 437–441.

[49] O. Marangos, A. Misra, P. Spencer, B. Bohaty, J.L. Katz, Physico-mechanical properties determination using microscale homotopic measurements: application to sound and caries-affected primary tooth dentin, Acta Biomater. 5 (2009) 1338–1348.

[50] C.J. Montrose, V.A. Solovyev, T.A. Litovitz, Brillouin scattering and relaxation in liquids, J. Acoust. Soc. Am. 43 (1968) 117.

[51] L. Breschi, T. Maravic, S.R. Cunhaa, A. Combaa, M. Cadenaro, L. Tjäderhanee, D.H. Pashley, F.R. Tay, A. Mazzoni, Dentin bonding systems: from dentin collagen structure to bond preservation and clinical applications, Dent. Mater. 34 (2018) 78–96.

[52] P. Spencer, Q. Ye, J. Park, E.M. Topp, A. Misra, Y. Wang, B.S. Bohaty, V. Singh, F. Sene, J. Eslick, J.L. Katz, Adhesive/dentin interface: the weak link in the composite restoration, Ann. Biomed. Eng. 38 (6) (2011) 1989–2003.

[53] T. Maravić, L. Breschi, A. Comba, S.R. Cunha, V. Angeloni, C. Nuccia, J. Hebling, D. Pashley, F. Tay, A. Mazzoni, Experimental use of an acrolein-based primer as collagen cross-linker for dentine bonding, J. Dent. 68 (2018) 85–90.

[54] Z. Zhang, M. Mutlay, A. Tezvergil-Mutlay, F.R. Tay, D.H. Pashley, D. Arola, Effects of EDC crosslinking on the stiffness of dentin hybrid layers evaluated by nanoDMA over time, Dent. Mater. 33 (2017) 904–914.

[55] K. Raum, Microelastic imaging of bone, IEEE Trans. Ultrason. Ferroelec. Freq. Control 55 (2008) 1418–1431.

[56] J. Kushibiki, K.L. Ha, H. Kato, N. Chubachi, F. Dunn, Application of acoustic microscopy to dental material characterization, in: Proceedings of the Ultrasonics Symposium, 1987.

[57] R. Wang, L. Niu, Q. Li, Q. Liu, H. Zuo, The peritubular reinforcement effect of porous dentine microstructure, PLoS One 12 (2017) 1–15.

[58] G.J. Joves, G. Inoue, A. Sadr, T. Nikaido, J. Tagami, Nanoindentation hardness of intertubular dentin in sound, demineralized and natural caries-affected dentin, J. Mech. Behav. Biomed. Mater. 32 (2014) 39–45.

[59] H. Ryou, E. Romberg, D.H. Pashley, F.R. Tay, D. Arola, Nanoscopic dynamic mechanical properties of intertubular and peritubular dentin, J. Mech. Behavior Biomed. Mater. 7 (2012) 3–16.

[60] M. Yahyazadehfar, D. Zhang, D. Arola, On the importance of aging to the crack growth resistance of human enamel, Acta Biomater. 32 (2016) 264–274.

[61] T. Sui, A.J.G. Lunt, N. Baimpas, M.A. Sandholzer, T. Li, K. Zeng, G. Landini, A.M. Korsunsky, Understanding nature's residual strain engineering at the human dentine–enamel junction interface, Acta Biomater. 32 (2016) 256–263.

[62] S. Liaqat, A. Aljabo, M. Khan, H. Ben Nuba, L. Bozec, P. Ashley, A. Young, Characterization of dentine to assess bond strength of dental composites, Materials 8 (2015) 2110–2126.

[63] M. Özcan, M. Jonasch, Effect of cyclic fatigue tests on aging and their translational implications for survival of all-ceramic tooth-borne single crowns and fixed dental prostheses, J. Prosthodont. 27 (2018) 364–375.

Effects of temperature and pressure on luminescent properties of Sr_2CeO_4:Eu^{3+} nanophosphor

A. Vlasic[a], D. Sevic[a,*], M.S. Rabasovic[a], J. Krizan[b], S. Savic-Sevic[a], M.D. Rabasovic[a], M. Mitric[c], B.P. Marinkovic[a], M.G. Nikolic[a]

[a] *Institute of Physics Belgrade, University of Belgrade, P.O. Box 68, Pregrevica 118, 11080 Belgrade, Serbia*
[b] *AMI, d. o. o, Ptuj, Slovenia*
[c] *Vinca Institute of Nuclear Science, University of Belgrade, P. O. Box 522, 11001 Belgrade, Serbia*

ARTICLE INFO

ABSTRACT

In this paper we describe the synthesis and characterization of the Sr_2CeO_4:Eu^{3+} nanopowder and possibilities of its application for temperature and high pressure sensing. The material was prepared using simple solution combustion synthesis. X-ray powder diffraction (XRD), scanning electron microscope (SEM) and photo-luminescence (PL) techniques have been used to confirm and characterize the prepared material. Time resolved analysis of emission spectra was achieved by using the streak camera system. Measured lifetime values of luminescence emission and the intensity ratios of spectral lines were used for determining the calibration curves for remote temperature sensing. We have analyzed sensitivity improvement of the intensity ratio method by using a temporal evolution of emission lines and simulation of delayed gating of one of them. Pressure effects on optical properties of Sr_2CeO_4:Eu^{3+} nanophosphor are also investigated.

1. Introduction

Thermographic phosphors are widely used in many applications [1–10]. They typically consist of a ceramic host and rare-earth dopant. These materials are structurally stable regarding various parameters, including temperature, pressure, magnetic field, electromagnetic radiation. The temperature dependency of their luminescence is used for remote temperature sensing. For obvious reasons, non contact measurements have many advantages. The luminescence lifetime is usually used for determining the temperature in a point; and the ratio of intensities of two spectral lines is often used for surface (2D) temperature measurements [3,5]. Mechanical influences on nanophosphor photoluminescence are also vastly investigated [9–13].

Strontium Cerium Oxide (Sr_2CeO_4) phosphors doped with europium ions (Eu^{3+}), Sr_2CeO_4:Eu^{3+} are thoroughly investigated and several applications have been found. As pointed out in [14], emission color change in a wide range of temperatures proves a great potential of Eu3 + :Sr2CeO4 nanocrystals for industrial applications, particularly in nanothermometric technology. Moreover, additional application possibilities for this material are provided by the fact that the samples with different grain sizes are characterized by various luminescence colors [14]. The possibility of application of this nanophosphor in single-color and two-color fluorescence thermometry techniques in temperature

range of 303–523 K has been proposed in [15]. In [16] it was shown that the Eu^{3+} doped Sr_2CeO_4 phosphors emitting white light (by combining blue, green and red emissions) has potential applications not only in the fields of lamps and display devices under 280 nm excitation, but also in the field of LEDs under near UV (350 nm) excitation. Recently, paper considering Sr_2CeO_4:Eu^{3+} as a source of anti-stokes white light generated under near infrared excitation was published [17]. Various methods of synthesis and studies of structural and luminescent characteristics of nanophosphors based on Sr_2CeO_4:Eu^{3+} or nondoped Sr_2CeO_4 are reported in [14–24], and references therein.

In this study, Sr_2CeO_4:Eu^{3+} nanopowders were efficiently prepared using a Solution Combustion Synthesis (SCS) method [25,26]. The main characteristics of this process are simplicity and low cost. Moreover, it is possible to tune the size and morphology of particles. The structure of prepared materials has been confirmed and characterized using X-ray powder diffraction (XRD), scanning electron microscope (SEM) and photoluminescence (PL) techniques. The excitation and emission spectra, luminescence lifetimes and rise time of synthesized nanopowders were analyzed by using the streak camera system. PL spectra were obtained at different excitation wavelengths using Optical Parametric Oscillator (OPO). Continuous excitation at 405 nm was achieved by a laser diode. The most of europium luminescence comes from slow decay transitions from the $^5D_0$ state. Lifetimes of the slow decay lines

---

are measured and reported in many publications. However, there are not many publications providing results regarding lifetimes of fast decay transitions, or rise times of slow decay transitions [27–31] of europium. In this study, we have estimated the lifetime and the rise time of europium transitions from the $^5D_1$ and $^5D_0$ states. Beside the lifetime, the luminescence rise time measurements [32] can be used for high temperature remote thermometry [2,28,30,31] as well. However, the uncertainty of these measurements is relatively high.

In our recent publication [33] we have shown that $Sr_2CeO_4:Eu^{3+}$ made by solution combustion synthesis could be used as a red phosphor. Now we study the possibility of using the synthesized $Sr_2CeO_4:Eu^{3+}$ for temperature measurements. We analyze the temperature effects on the intensity ratio of europium lines and their photoluminescence lifetime. We estimate a possible sensitivity improvement of the intensity ratio method by using the temporal evolution of emission lines, as proposed in [3]. Pressure effects on optical properties of $Sr_2CeO_4:Eu^{3+}$ nanophosphor are also investigated and, to the best of our knowledge, firstly presented in detail here. Our research followed the approach of simultaneous analysis of temperature dependencies and mechanical influences on nanophosphor photoluminescence [9,10].

2. Experimental procedure

2.1. The preparation of samples

Europium doped Sr_2CeO_4 nanopowders were prepared by solution combustion method, similarly as described in [25,26]. Stoichiometric quantities of starting chemicals $Sr(NO_3)_2$, $5CH_4N_2O$, $Ce(NO_3)_3*6H_2O$, and $Eu(NO_3)_3*6H_2O$ with the purity of 99.99% were chosen to obtain the Eu^{3+} concentration in Sr_2CeO_4 of 2.5 at% ($Sr_{2-0.05}Eu_{0.05}CeO_4$). The used chemicals were purchased from ABCR, and urea, $(NH_2)_2CO$, from Sigma-Aldrich. The dry mixture of 10.32 g (48.75 mmol) of $Sr(NO_3)_2$, 15.015 g (250 mmol) of CH_4N_2O, 10.86 g (25 mmol) of $Ce(NO_3)_3*6H_2O$ and 0.558 g (1.25 mmol) of $Eu(NO_3)_3*6H_2O$ was combined with the mixture of 4.8 g (60 mmol) of ammonium nitrate and 3.003 g (50 mmol) of urea which were used as organic fuels. The prepared starting reagents were combusted with the flame burner at approximately 500 °C, yielding a voluminous foamy pink powder in an intensive exothermic reaction. After the solution combustion synthesis, the nanopowder was annealed for 2 h, in air atmosphere, at 900 °C. The annealing of the material is needed to achieve optimal optical characteristis of synthesized material.

2.2. Experimental details

X-ray diffraction measurements were done at room temperature using a Philips PW 1050 instrument, with Ni filtered Cu $K_{\alpha1,2}$ radiation (λ = 0.15405 nm). The structure of nanopowders was also observed by a high resolution scanning electron microscope (SEM) equipped with a high brightness Schottky Field Emission gun (FEGSEM, TESCAN) operating at 4 kV. The samples were coated with gold/palladium to make them conductive for SEM analysis.

As an excitation source for photoluminescence measurements we used the output of the Optical Parametric Oscillator (Vibrant OPO), continuously tunable over a spectral range from 320 nm to 475 nm. Laser pulse duration is about 5 ns, at a repetition rate of 10 Hz. Time-resolved streak images of the luminescence response of $Sr_2CeO_4:Eu^{3+}$ nanopowder excited by the OPO system were acquired by Hamamatsu streak camera equipped with a spectrograph.

Excitation spectrum of $Sr_2CeO_4:Eu^{3+}$ was acquired using Fluorolog SPEX. For temperature and pressure dependent measurements we also used Ocean Optics USB2000 and AVANTES AvaSpec 2048TEC USB2 spectrometers and continuous laser diode excitation at 405 nm. The experimental setup for luminescence measurement as a function of temperature is described in [34].

High pressure was achieved using Membrane Diamond Anvil Cell (MDAC) manufactured by BETSA (France), with a 300 μm culet diameter (the culet is the tiny facet at the very bottom of faceted gemstones, added to protect the fragility of the pointed tip). Principle of operation of Diamond Anvil Cell (DAC) is based on the fact that very high pressures can be obtained by reasonable mechanical forces if tips of diamond anvils have small surface area, because obtained pressure equals the ratio of mechanical force versus surface area of culet. The measured sample is placed between the tips of opposite anvils, which are tightened by mechanical force. On earlier models, the necessary mechanical force pushing the anvils to each other was obtained by tightening screw. In the case of membrane DAC used here, the force on the piston pushing the upper anvil is generated by pressurized helium, which presses a circular membrane. This solution enables fine control and adjustment of the force applied to the anvils. In order to get the uniform distribution of pressure on the sample the transmitting fluid should be used. The metal gasket is often used to prevent the leakage of this fluid. The shape of gasket is formed by pressing it between two opposed anvils of the MDAC, first without the sample. Then, the gasket with the sample, pressure transmitting fluid and a small ruby sphere is compressed by the same anvils. The diamond anvils are optically transparent, so the optical measurements of pressurized sample are possible. We used the sample in the form of powder and a 4:1 mixture of methanol and ethanol as a pressure transmitting medium. The pressure was determined from the redshift of the ruby R1 line.

3. Results and discussion

3.1. Structure

XRD pattern of our of $Sr_2CeO_4:Eu^{3+}$ nanopowder sample is shown in Fig. 1. Observed peaks are in good agreement with the published results [14–24] and ICSD card 50-0115. The XRD pattern, shown in Fig. 1, proves the good crystallinity of our sample. The lack of any significant additional peaks confirms that doping the material with Eu^{3+} did not change the crystalline structure of Sr_2CeO_4. The X-ray Line Profile Fitting Program (XFIT) with a Fundamental Parameters convolution approach to generating line profiles [35] was used for the calculation of both the crystallite size and the microstrain parameter of the synthesized powder. Three most intense peaks were included in the fitting procedure, and the obtained values for crystallite size and microstrain are 114.0 nm and 0.14%, respectively.

The representative SEM image of our sample of $Sr_2CeO_4:Eu^{3+}$ material is presented in Fig. 2. The SEM image confirms the previously calculated average size of the prepared material. The image of the
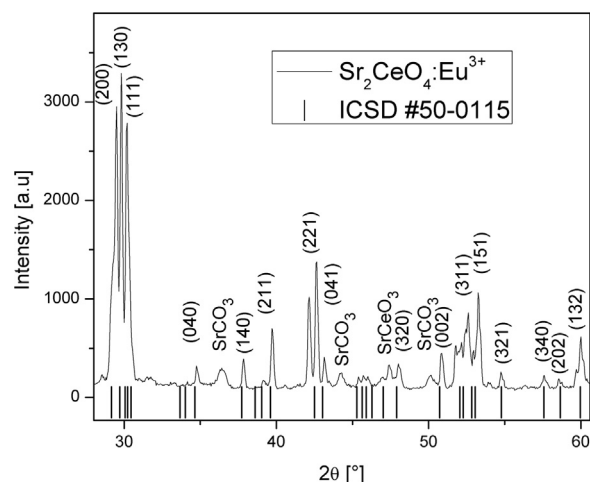

Fig. 1. XRD profile of $Sr_2CeO_4:Eu^{3+}$ nano phosphor prepared by solution combustion method, with respective Miler indices for prominent peaks.
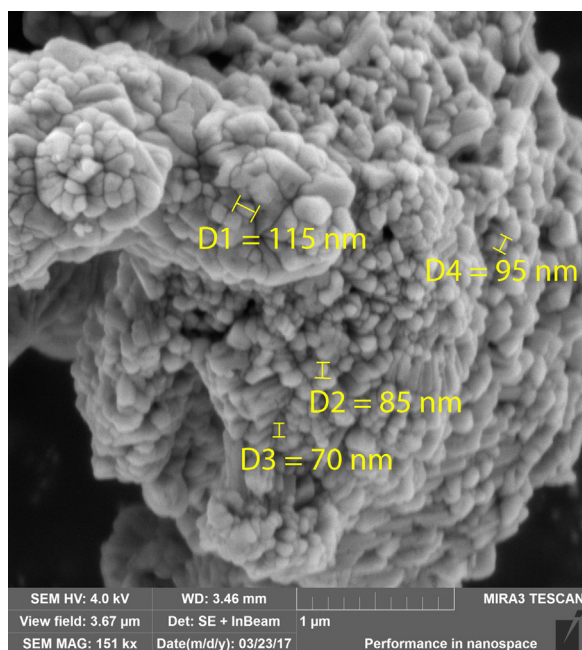
Fig. 2. SEM image of $Sr_2CeO_4:Eu^{3+}$ nano phosphor prepared by solution combustion method.

synthesized material shows the irregular crystallite size distribution. The agglomerated grains can be also noticed. The particles with dimensions from 67 nm to over 120 nm can be easily observed in Fig. 2. Effects of annealing temperatures on particle size and thus resulting overall influence on the luminescence of $Sr_2CeO_4:Eu^{3+}$ nanocrystals are studied in detail in [14,18]. It was observed that with increasing the annealing temperature the grain sizes also increase. The annealing temperature of 900 °C was chosen to obtain optimal luminescence response of synthesized material.

3.2. Optical properties

3.2.1. Luminescence excitation and emission spectra

The excitation spectrum of $Sr_2CeO_4:Eu^{3+}$ nano phosphor, corresponding to the 614 nm emission, is shown in Fig. 3. The wide band, up to about 400 nm, corresponds to a strong absorption of light by the Sr_2CeO_4 host and a charge transfer from host to Eu dopant [14–18,23]. Narrow peaks, at higher wavelengths, come from the direct excitation of europium. The peaks are denoted by corresponding europium transitions. The similar excitation spectra are presented in [14–19].
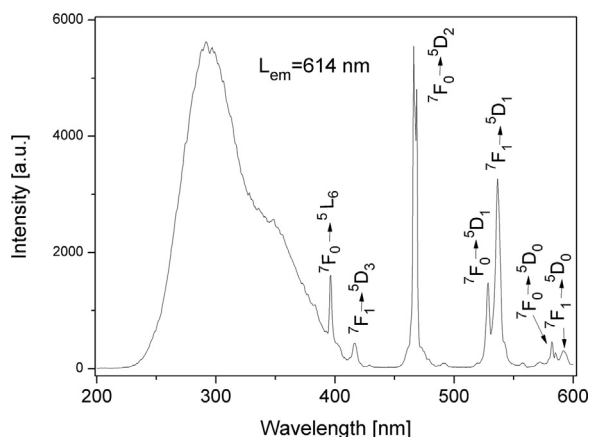
Fig. 3. Excitation spectrum of $Sr_2CeO_4:Eu^{3+}$ nano phosphor, corresponding to the 614 nm emission.
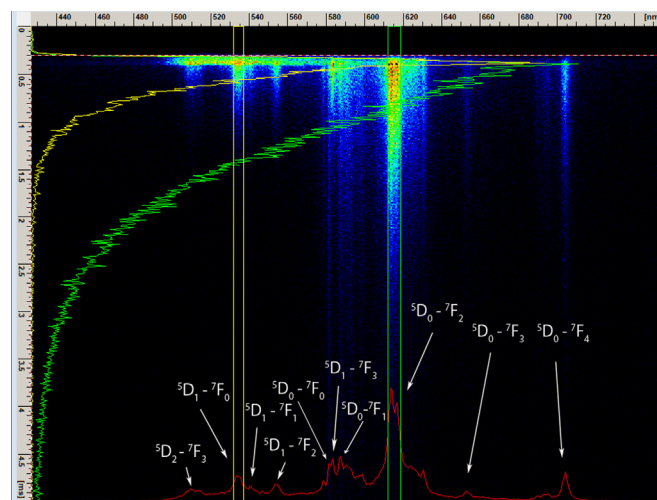
Fig. 4. Streak image of the photoluminescence spectrum of $Sr_2CeO_4:Eu^{3+}$ nanophosphor. (OPO excitation at 330 nm).

The streak image of the time resolved photoluminescence spectrum of the $Sr_2CeO_4:Eu^{3+}$ using the 330 nm excitation is presented in Fig. 4. Horizontal scale of streak image corresponds to wavelength, vertical scale shows development of spectra in time. Images are presented in pseudocolor, where different colors mean different optical intensities. The Eu transitions are denoted in Fig. 4, according to [27,36]. The slow decay transitions originating from $^5D_0$ state, are well explained in literature and their detailed description can be found in our previous work [25]. Positions of the different $^5D_0 - {}^7F_J$ transitions are located so that the distance between a J and the J+1 line increases with increasing J value. Transition $^5D_0–^7F_1$ is very close to the $^5D_0 - {}^7F_0$ transition [36]. The weak $^5D_0 - {}^7F_0$ transition, which is forbidden by both electric-and magnetic- dipole selection rules in the case of the free ion, occurs due to a weak J mixing by the crystalline field [37]. Magnetic dipole transition like $^5D_0–^7F_1$ are allowed by the Laporte selection rule, but their intensities are weak and comparable to those of the induced electric dipole transitions [36]. The fast decay transitions from $^5D_2$ and $^5D_1$ are also denoted in Fig. 4. The $^5D_1 - {}^7F_3$ transition (583 nm), located closely between the $^5D_0 - {}^7F_0$ (582 nm) and the $^5D_0 – {}^7F_1$ (587 nm) transitions is easy to identify on the time resolved image. Its time integrated peak has a comparable intensity to the intensities of peaks originating from nearby $^5D_0$ levels (see the line profile denoted by a red curve in Fig. 4). The luminescence spectra presented in publications usually do not have the time resolution, so it is hard to guess which transitions are short lived. Streak image presented in Fig. 4. shows clearly that the $^5D_1 - {}^7F_3$ transition has a much higher intensity and a much shorter lifetime than nearby transitions from $^5D_0$ state.

3.2.2. Lifetime and rise time analysis

We conducted the time resolved analysis for transitions which are identified in Fig. 4. The streak image of photoluminescence spectrum of $Sr_2CeO_4:Eu^{3+}$ nanophosphor with the time range of 200 µs is shown in Fig. 5. The time range in Fig. 5. was selected to get a clear visual impression of time development of luminescence signals at their beginning and to enable a rough estimate of rise time of all transitions shown in Fig. 4. To obtain the more precise values of rise time we had to use streak camera time range of 5 µs.

We obtained that the lifetime of the level $^5D_1$ is about 0.21 ms and the level $^5D_0$ lifetime is about 0.78 ms. For the fast decay the lifetime is much longer than reported for other hosts in [27,32], where transitions from $^5D_1$ level have a fast decay with the order of lifetime of about 10 µs. Other references [14,20,33] provide the values of slow decay time of $Sr_2CeO_4:Eu^{3+}$ nanophosphor more or less similar to our result. Decay curve of the most intensive $^5D_0 – {}^7F_2$ transition is usually used for

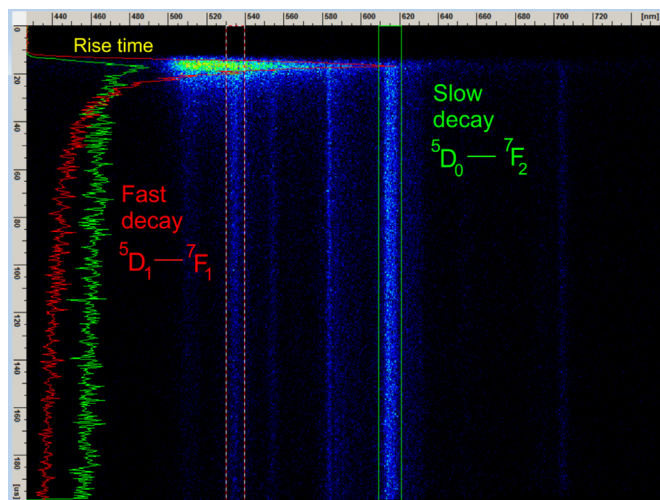**Fig. 5.** Streak image of photoluminescence spectrum of Sr_2CeO_4:Eu^{3+} nanophosphor with the time range of 200 μs tuned for analysis of rise time of all transitions. (OPO excitation at 330 nm.).

europium luminescence lifetime measurements [26].

In [32] we have proved that our experimental setup is capable of detecting fast rise times. We calculate the rise time according to Ranson equation [38,39]. YVO_4:Eu^{3+} nanoposphor has clearly detectable rise time of slow decay transitions [32], for the $^5D_0$ – $^7F_2$ line it is about 8.1 μs. This relatively long luminescence rise time is related to energy transfer mechanism in YVO_4:Eu^{3+} nanoposphor and it is useful for practical considerations. Our measurements of Sr_2CeO_4:Eu^{3+} nanophosphor show that the luminescence rise time of $^5D_0$ - $^7F_2$ line of 0.39 μs is too short to be of practical use if cost effective equipment is to be used. So, it seems to us that for temperature sensing based on photoluminescence rise time measurements the other europium doped hosts, for example Yttrium orthovanadate YVO_4:Eu^{3+}, would be more appropriate.

3.2.3. The temperature dependency of intensity ratio of spectral lines

The luminescence of samples was measured both using pulsed (OPO) and continuous excitation. The measured luminescence spectra of Eu^{3+} doped Sr_2CeO_4 at various temperatures are presented in Fig. 6.

The spectral line intensities from the $^5D_0$ and $^5D_1$ transitions depend on two physical processes. The first process is the thermalization of the $^5D_1$ level with rising temperature, where the energy difference to populate the $^5D_1$ level from the $^5D_0$ level is fully covered by phonons. The second process is nonradiative quenching of the $^5D_0$ and $^5D_1$ levels through the charge transfer state. Configuration coordinate model,
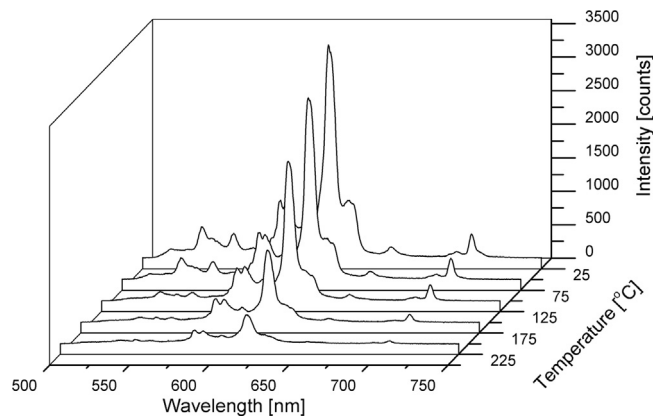
Fig. 6. Luminescence spectra of Eu^{3+} doped Sr_2CeO_4 at various temperatures. (Continuous laser diode excitation at 405 nm).
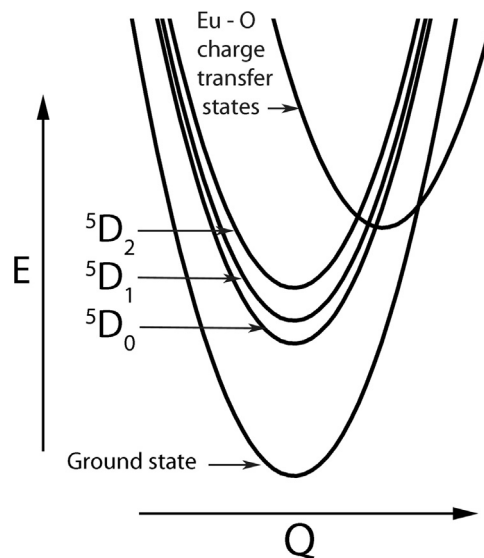
Fig. 7. Configuration coordinate model of Sr_2CeO_4:Eu^{3+} nanophosphor relevant for understanding the temperature dependency of intensity ratio of spectral lines.

based on the same line of thought as presented in [15], is shown in Fig. 7. The Eu^{3+} - O_2 charge transfer state intersects not only with the europium ground state but also with three excited states, $^5D_2$, $^5D_1$ and $^5D_0$. By increasing the sample temperature the electrons in the $^5D_0$ state are thermally pushed to the crossover point and nonradiatively go to the ground state via the charge transfer state. Regarding the $^5D_1$ state, part of electrons go the same path as described for $^5D_0$ state. However, part of them go only to the $^5D_0$ level via charge transfer state. This explains why is $^5D_1$ state more rapidly quenched by temperature than $^5D_0$ state. So, the thermalization and quenching through charge transfer both have significant influence on the fluorescence intensity ratio (FIR). This means that the measured results cannot be simply fitted to the Boltzmann distribution. However, in order to apply the intensity ratio method in thermometry, it is required to calculate and fit a calibration function of analyzed potential thermophosphor. Based on considerations in [34,40], we decided to use the simple empirical equation for fitting the calculated intensity ratios of experimental data: $IR(T) = A + C \cdot e^{-T/\alpha}$, [34,40], where T is temperature in K, and empirical A, C and α are constants obtained through fitting of measured data.

The absolute thermal sensitivity Sa of the intensity ratio method is defined as the rate at which IR changes with the temperature:

$$Sa = \left| \frac{dIR}{dT} \right| \qquad (1)$$

The relative thermal sensitivity of the intensity ratio method Sr is determined using formula:

$$Sr = \left| \frac{1}{IR} \frac{dIR}{dT} \right| \qquad (2)$$

The temperature sensing calibration curve, shown in Fig. 8, was determined by calculating intensity ratio of photoluminescence spectral peaks at 614 nm and 537 nm. The calculation was repeated for all spectra, measured at different temperatures, first for increasing, then for decreasing temperatures. This kind of temperature sensing is useful up to 400 K, where the calculated intensity ratio values stop increasing and curve flattens beyond reasonable fitting.

3.2.4. Improved sensitivity of intensity ratio method based on temporal analysis

As proposed in [3], it is possible to improve the sensitivity of the intensity ratio method by using the temporal evolution of emission
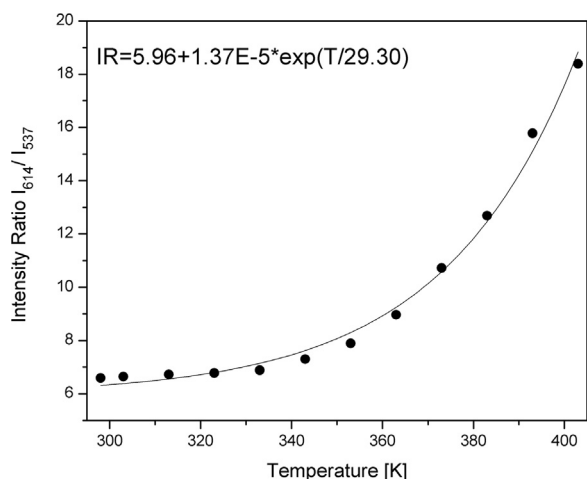
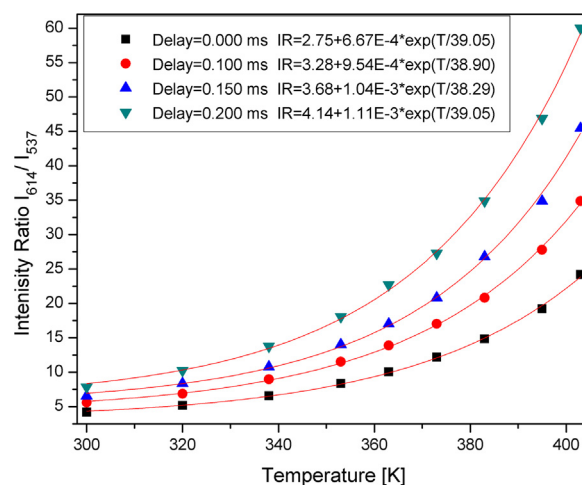**Fig. 8.** Temperature sensing calibration curve of $Sr_2CeO_4:Eu^{3+}$ nanophosphor. (Continuous laser diode excitation at 405 nm).

Fig. 10. Temperature sensing calibration curves of $Sr_2CeO_4:Eu^{3+}$ nanophosphor, for various delays of gating the signal at 537 nm. (Pulsed laser excitation at 330 nm).

lines. If integrated-in-time intensity of one of the signals is recorded with delayed gate, the additional temperature dependence is introduced in intensity ratio calculation. Namely, at low temperatures where emission lifetime is long the small gate delay of one of the signals will have relatively small effect on intensity ratio. However, at higher temperatures where the lifetime is short, the delayed gate will give rise to an increased signal difference. Moreover, this method of recording the signal with gated delay offers an efficient solution for minimizing or eliminating the effects of host luminescence, overlapping of emission from thermally coupled levels, and stray light originating from other intense transitions or from the laser excitation.

The method is illustrated in Fig. 9. The use of streak camera proves the concept, real application will be based on gated CCD cameras and appropriate bandwidth filters for selecting the emission lines. For calculation of intensity ratio the line at 614 nm is used integrated in time from its beginning, and line at 537 nm is integrated in time with various delays.

Temperature sensing calibration curves of $Sr_2CeO_4:Eu^{3+}$ nanophosphor for various delays of gating the signal at 537 nm are shown in Fig. 10.

It could be seen in Fig. 10 that intensity ratio between lines at 614 nm and 537 nm increases with increasing the gate delay of signal at 537 nm. However, increasing the delay decreases the integrated signal

intensity, so we didn't use delays larger than 200 μs. The host luminescence and other emission not belonging to europium lines at 537 nm and 614 nm spoil the temperature sensitivity. However, they last up to 100 μs, so their influence is eliminated for delays higher than 100 μs. Absolute and relative temperature sensitivities of $Sr_2CeO_4:Eu^{3+}$ nanophosphor are shown in Fig. 11. Increased sensitivity obtained by delayed gate of 537 nm emission is obvious from Fig. 11. It should be pointed out that continuous laser excitation at 405 nm pumps mainly the europium directly, resulting with much better elimination of host emission. However, the emission is generally weaker when europium is excited directly.

We have shown that continuous laser excitation provides satisfactory results. Increased sensitivity could be obtained by much more complex measurements technique presented here.

3.2.5. Luminescence lifetime temperature dependency

The temperature sensing calibration curve, shown in Fig. 12, was determined by calculating lifetime of spectral line at 614 nm. When the temperature was increased higher than 200 °C the intensity of measured spectra become too low to achieve reliable calculation of luminescence lifetime. Analysis presented in [41] shows that the temperature dependence of intensity ratio and luminescence lifetime, for the ideal
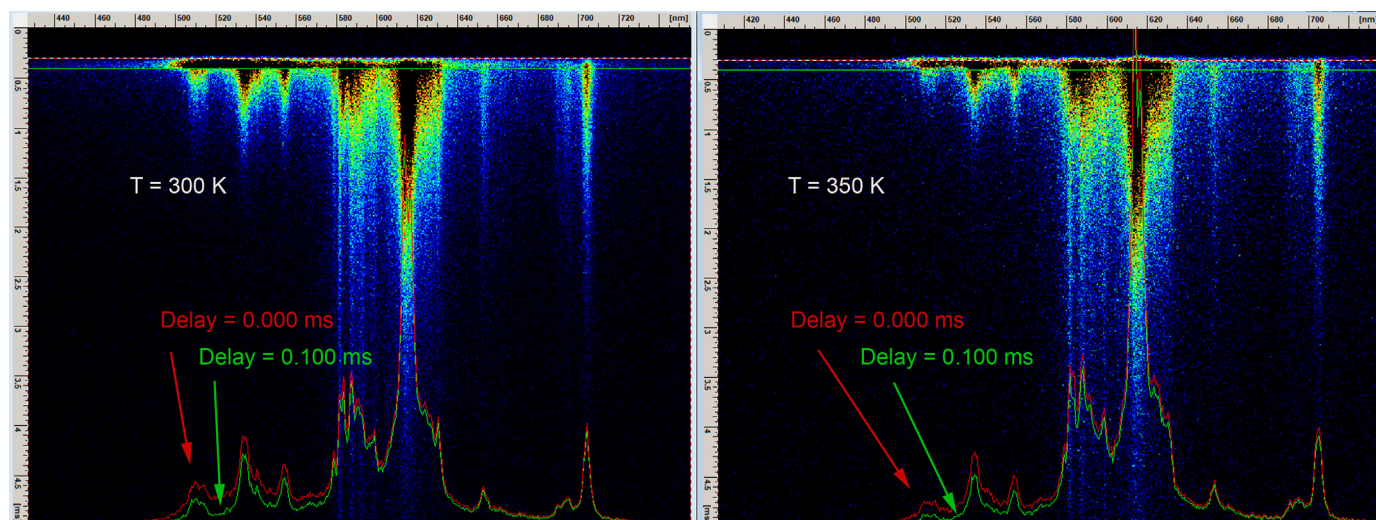

Fig. 9. Streak images of optical emission of $Sr_2CeO_4:Eu^{3+}$ at room temperature (left) and at 80 °C (right). Pulsed laser excitation is at 330 nm. The red profile corresponds to time integration of the whole signal, the green one to integration gated after 100 μs delay.
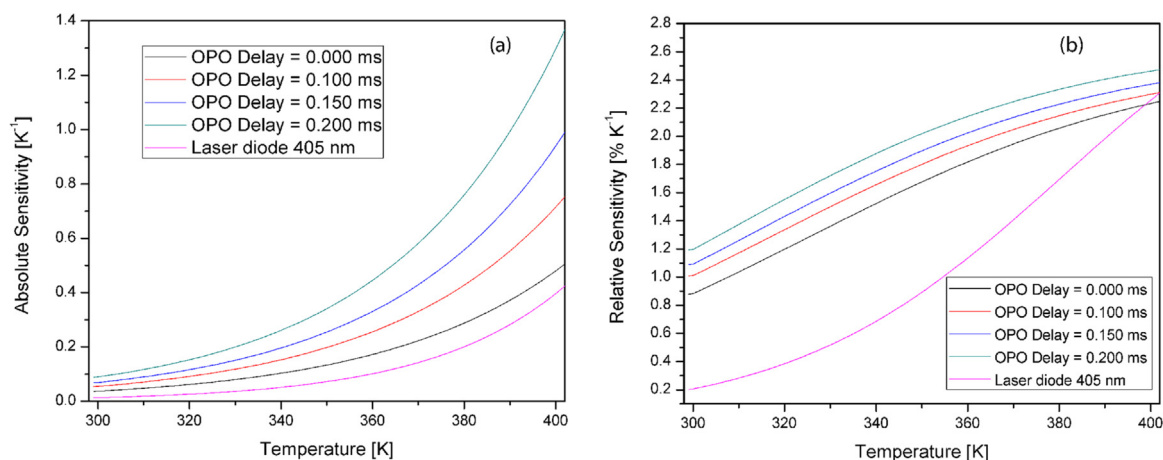
Fig. 11. (a) Absolute and (b) relative sensitivity of $Sr_2CeO_4:Eu^{3+}$ nanophosphor as a function of temperature.

case, differ only in magnitude by a certain factor. So, we will use the same form of empirical equation for fitting the lifetime experimental data as we used for fitting the intensity ratio, namely: $F(T) = A + C \cdot e^{-T/\alpha}$, [34,40], where T is temperature in K, and A, C and α empirical constants obtained through fitting of measured data.

In [42] europium hosted in PMMA matrix was used for lifetime based temperature sensing, in a range between 0 and 70 °C, with reported lifetimes between 0.28 ms and 0.4 ms. Temperature sensitive europium probes, excited at 405 nm, are described in [43], where reported lifetimes are in the range between 0.15 ms and 0.7 ms, corresponding to the same temperature sensing range as in [42], between 0 and 70 °C. In [44] the sensed temperature range is between 10 and 50 °C, measured lifetimes are between 0.12 ms and 0.35 ms. It seems that europium, hosted in another medium like PMMA, provides lesser sensing range with better sensitivity. Compared to our results of intensity ratio method, the luminescence lifetime method offers increased sensing range, because only the most intensive europium line at 614 nm is used for temperature sensing calibration curve determination. The intensity ratio calculations become unreliable when the intensity of the line at 537 nm turned out to be too small due to temperature increasing. Our measurements show that sensor based on $Sr_2CeO_4:Eu^{3+}$ nano phosphor covers not only the physiological temperature range but also the higher temperatures that are of interest when monitoring the thermal behaviour of electronic devices. Compared to other hosts doped with europium, TiO_2 [41], Gd_2O_3 [45], $YNbO_4$, [46] and Lu_2O_3 [47], including references therein, it is easy to notice that there is usual trade-off between the sensitivity and sensing range, so the optimal host could be selected based on desired sensing range.
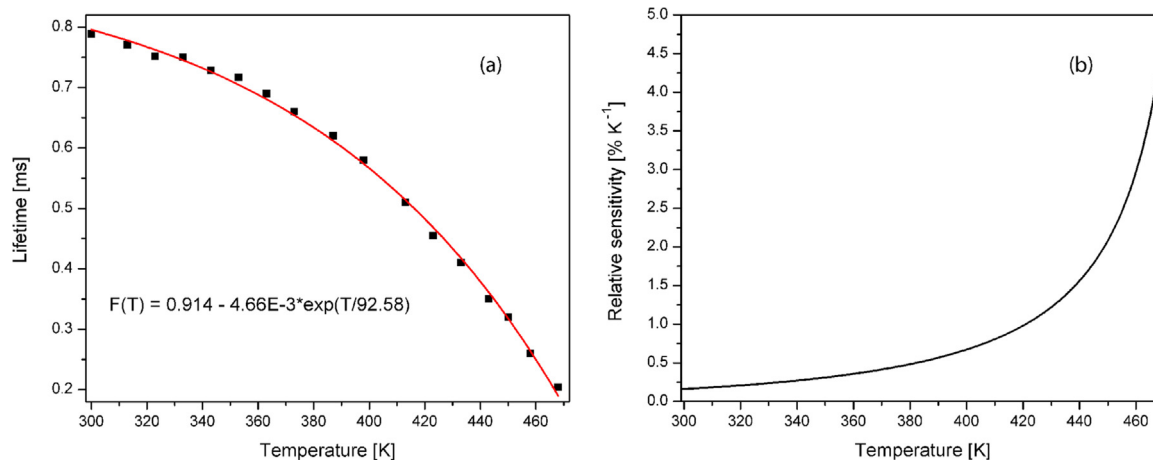
Methods for temperature sensing based on fluorescence intensity ratio and lifetime are not sensitive, regarding errors, to fluctuations in excitation intensity and light collection efficiency [3]. Moreover, if the lifetime of the used nanophosphor (measured here between 0.2 ms and 0.78 ms) is much longer than the laser pulse (5 ns), evaluation error could be neglected [3]. So, we conclude that measurement errors mostly originate from the fitting procedures and least-square errors in extracting the temperatures from the calibration curve [3]. For all presented methods, the relative errors are smaller than 3% in the whole measuring range and bellow 1% for temperatures above 350 K.

3.2.6. The high pressure effects on $Sr_2CeO_4:Eu^{3+}$ photoluminescence

The spectral responses were measured at various pressures in order to analyze the high pressure effects on photoluminescence emission of $Sr_2CeO_4:Eu^{3+}$ nanophosphor. Luminescence spectra of Eu^{3+} doped Sr_2CeO_4 at various pressures are shown in Fig. 13. To check the existence of hysteresis, the spectral measurements were performed successively, first for increasing and then for decreasing pressure.

It is well known that rare earth ions are highly sensitive to local symmetry. Any change in the symmetry is observable in their luminescence spectra [48]. In the paper by Zhang et al. [49] dependencies between the phase transitions of the crystal structure induced by pressure and the changes in the luminescence spectrum of the Eu^{3+} ion are explained. It was shown in [49] that the red shift rate and relative intensity ratio of emissions vary along with increasing pressure. Namely, the red shift of emissions can be ascribed to the expansion of the f orbit of the Eu^{3+}; and the relative intensity ratio variation of emissions is attributed to the change of crystal field due to the phase
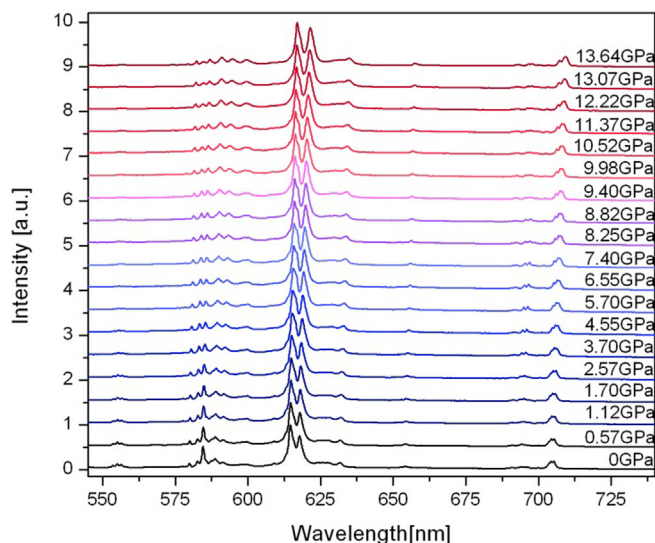

Fig. 12. Luminescence lifetime temperature dependence of $Sr_2CeO_4:Eu^{3+}$ nano phosphor and its relative sensitivity.

Fig. 13. Luminescence spectra of Eu^{3+} doped Sr_2CeO_4 at various pressures. (Continuous laser diode excitation at 405 nm).

transition.

Changes and deformations of luminescence spectrum which imply phase transitions are easily identified in Fig. 3 in [49]. Fig. 13. shows that, in presented pressure range, there are no such deformations of
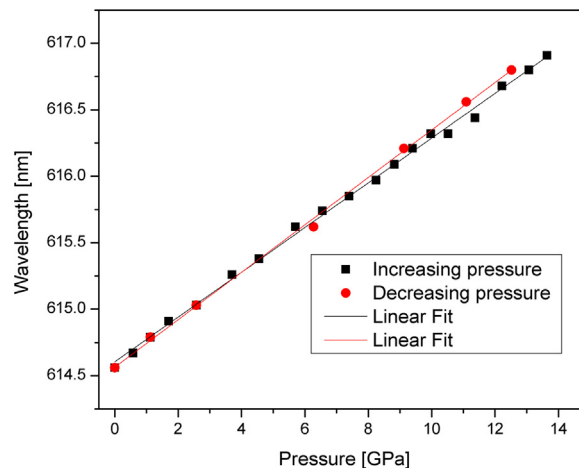

Fig. 15. Pressure induced shift in wavelength of the highest intensity peak, at 614.56 nm at atmospheric pressure.

$Sr_2CeO_4:Eu^{3+}$ luminescence spectrum. This means that our sample didn't undergo the phase transition.

Our measurements show that after decompression the luminescence spectrum of $Sr_2CeO_4:Eu^{3+}$ is completely restored. Other publications show similar results for different host matrixes [13,50].

Pressure induced change in the crystal lattice parameters also disturb the position of energy levels [11–13,49–51]. The variation of
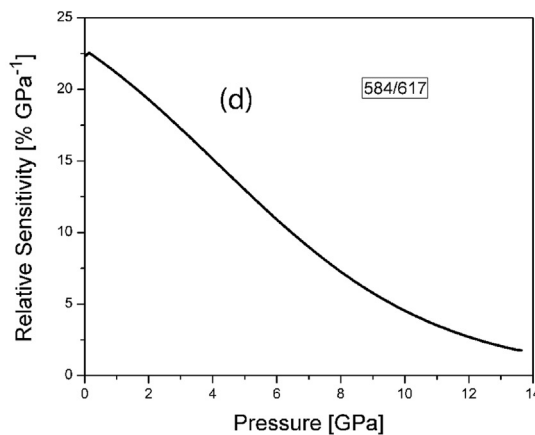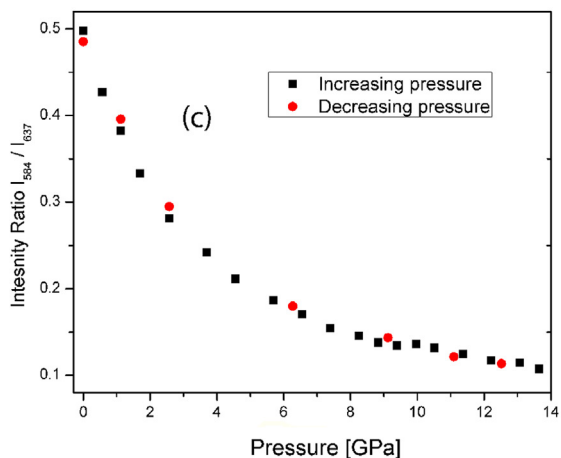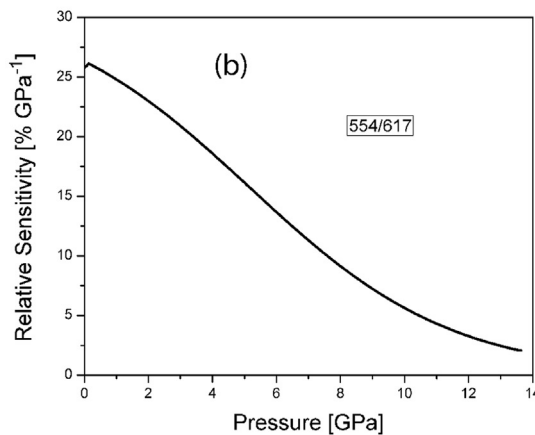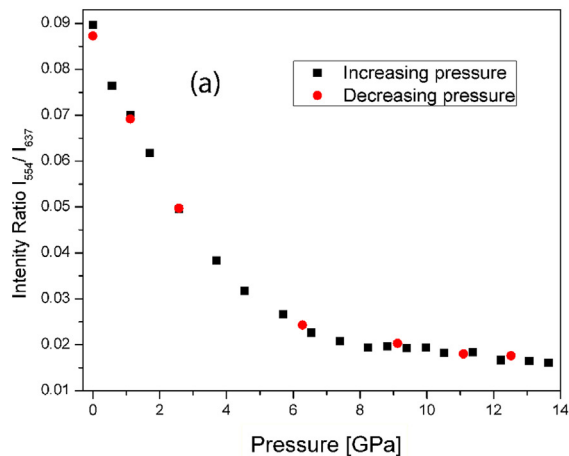
Fig. 14. High pressure sensing calibration curves of $Sr_2CeO_4:Eu^{3+}$ nanophosphor. (a) Intensity ratio I_{554}/I_{614}. (b) Its relative sensitivity. (c) Intensity ratio I_{584}/I_{614}. (d) Its relative sensitivity. (Continuous laser diode excitation at 405 nm.).

energy of $^5D_1$ and $^5D_0$ levels and change of charge transfer region position leads to a rise in probability for non-radiative transitions. The applied pressure predominantly affects $^5D_1$ level, as can be seen in Fig. 13. A slight variation in the intensity of the most prominent $^5D_0 \rightarrow ^7F_2$ transition lines can also be observed in Fig. 13. The intensity ratios of intensities of emission lines from $^5D_1$ and $^5D_0$ states are shown in Fig. 14. Exact positions of luminescence peaks used for calculating the intensity ratios are at 554.2 nm, 584.52 nm and 617 nm at atmospheric pressure. The observed decrease of intensity ratio with rising pressure is also due to greater dependence of non-radiative transitions from $^5D_1$ state. The values for both compression and decompression of sample are displayed in the Fig. 14. The hysteresis is negligible, which means the repeatability is good. For intensity ratio of lines at 584 nm and 637 nm, the reliable part of curve is from 0 GPa up to 10 GPa (for intensity ratio of lines at 554 nm and 637 nm the reliable part of curve is up to 8 GPa), which opens the possibility for using the material as a pressure sensor.

Another method of sensing pressure is based on measuring the pressure induced red shift in wavelength of appropriately selected, usually highest intensity peak. Pressure induced shift in wavelength of the highest intensity peak of Sr_2CeO_4:Eu^{3+} luminescence (614.56 nm at atmospheric pressure) is shown in Fig. 15. The proposed method is very usable, with almost linear curve, for high pressures up to 14 GPa. Red-shift rate was estimated to be about $0.17 \text{ nm} \times \text{GPa}^{-1}$. The rate is the same for other emission lines from $^5D_0$ state, and for $^5D_0 \rightarrow ^7F_1$ it is about $0.096 \text{ nm} \times \text{GPa}^{-1}$.

To the best of our knowledge, there are no published results regarding using of Sr_2CeO_4:Eu^{3+} nanophosphor for pressure sensing. Compared to the other materials doped with the Eu^{3+} ions, Sr_2CeO_4 provides similar pressure sensing range in terms of unambiguousness as $ZrGeO_4$ [11], $LaPO_4$ [12], $GdVO_4$ [13] and TiO_2 [50]. Y_2O_3 host offers much wider unambiguous pressure sensing range [49]. Under unambiguous we mean the fact that one luminescence intensity ratio corresponds to only one pressure. So, it seems that Sr_2CeO_4 is quite promising for making devices for remote pressure sensing.

To estimate errors of pressure sensing in our study the similar line of thought holds as for temperature sensing methods. For intensity ratio method relative errors are smaller than 8% in pressure range up to 10 GPa. For method of sensing pressure based on measuring the pressure induced red shift in wavelength of highest intensity peak the relative error is below 2% for the whole measured range (up to 14 GPa).

4. Conclusion

In this paper we described the synthesis and characterization of the Sr_2CeO_4:Eu^{3+} nanopowder. Beside luminescence kinetics of slow decay transitions we also estimated their rise time and lifetime of fast decay transitions. Measured values of lifetime of luminescence emission of lines originating from transitions from $^5D_0$ level and intensity ratios of two spectral lines were used for determining the calibration curves for remote temperature sensing. We have showed that, for analyzed Sr_2CeO_4:Eu^{3+} material, the temperature sensing based on ratio of intensities of two lines is useful up to 400 K, while sensing based on lifetime of spectral line at 614 nm could be used up to 460 K. We have obtained sensitivity improvement of the intensity ratio method by simulating the delayed gating of acquiring the intensity of one of spectral lines. The using of streak camera proved the proposed concept. The real application will be based on gated cameras and appropriate bandwidth filters for selecting the emission lines. Also, we have analyzed the effects of pressure on photoluminescence response of synthesized material. To the best of our knowledge, this analysis is first presented here. Results of all our analyses prove that Sr_2CeO_4:Eu^{3+} nanopowder prepared by a simple and low cost solution combustion synthesis method is appropriate material for remote temperature and pressure sensing and for various other optoelectronic devices.

References

[1] D. Jaque, F. Vetrone, Nanoscale 4 (2012) 4301–4326.
[2] C.D.S. Brites, P.P. Lima, N.J.O. Silva, A. Millan, V.S. Amaral, F. Palacio, L.D. Carlos, Nanoscale 4 (2012) 4799–4829.
[3] M. Aldén, A. Omrane, M. Richter, G. Särner, Prog. Energy Combust. Sci. 37 (2011) 422–461.
[4] S.W. Allison, G.T. Gillies, Rev. Sci. Instrum. 68 (1997) 2615–2650.
[5] L.P. Goss LP, A.A. Smith, M.E. Post ME, Rev. Sci. Instrum. 60 (1989) 3702–3706.
[6] A.L. Heyes, J. Lumin. 129 (2009) 2004–2009.
[7] M.M. Gentleman, D.R. Clarke, Surf. Coat. Technol. 188–189 (2004) 93–100.
[8] A.H. Khalid, K. Kontis, Sensors 8 (2008) 5673–5744.
[9] S.A. Wade, S.F. Collins, G.W. Baxter, J. Appl. Phys. 94 (2003) 4743–4756.
[10] S.A. Wade, D.I. Forsyth, K.T.V. Grattan, Rev. Sci. Instrum. 72 (2001) 3186–3190.
[11] R. Rao, T. Sakuntala, S.N. Achary, A.K. Tyagi, J. Appl. Phys. 106 (2009) (123517-1-5).
[12] Z. Zhi, Z. Jian, D. Zejun, J. Rare Earths 28 (2010) 254–257.
[13] C.C. Zhang, Z.M. Zhang, R.C. Dai, Z.P. Wang, J.W. Zhang, Z.J. Ding, J. Phys. Chem. C 114 (2010) 18279–18282.
[14] M. Stefanski, L. Marciniak, D. Hreniak, W. Strek, Mater. Res. Bull. 76 (2016) 133–139.
[15] L. Shi, H. Zhang, C. Li, Q. Su, RSC Adv. 1 (2011) 298–304.
[16] K. Suresh, N.V. Poornachandra Rao, K.V.R. Murthy, Bull. Mater. Sci. 37 (2014) 1191–1195.
[17] M. Stefanski, M. Lukaszewicz, D. Hreniak, W. Strek, J. Chem. Phys. 146 (2017) (104705-1-7).
[18] M. Stefanski, L. Marciniak, D. Hreniak, W. Strek, J. Chem. Phys. 142 (2015) (184701-1-7).
[19] X. Yang, Z. Shao, H. Ru, J Mater. Sci. Technol. 32 (2016) 1066–1070.
[20] T. Grzyb, A. Szczeszak, J. Rozowska, J. Legendziewicz, S. Lis, J. Phys. Chem. C 116 (2012) 3219–3226.
[21] C.A. Rao, P. Rao, V. Nannapaneni, K.V.R. Murthy, Adv. Mater. Lett. 4 (2013) 207–212.
[22] B.W.R. Kumar, K.V.R. Murthy, B.S. Rao, M. Shaik, Int. J. Sci. Innov. Discov. 1 (2011) 145–150.
[23] C.A. Rao, P.R.V. Nannapaneni, K.V.R. Murthy, J. Sci. Res. 5 (2013) 1–11.
[24] J. Gomes, A.M. Pires, O.A. Serra, Quim. Nova 27 (2004) 706–708.
[25] M.S. Rabasovic, D. Sevic, J. Krizan, M. Terzic, J. Mozina, B.P. Marinkovic, S. Savic Sevic, M. Mitric, M.D. Rabasovic, N. Romcevic, J. Alloy. Compd. 622 (2015) 292–295.
[26] J. Krizan, M. Mazaj, V. Kaucic, I. Bajsic, J. Mozina, Acta Chim. Slov. 61 (2014) 608–614.
[27] M.D. Chambers, P.A. Rousseve, D.R. Clarke, J. Lumin. 129 (2009) 263–269.
[28] S.W. Allison, S.M. Goedeke, M.R. Cates, W.A. Hollerman, J.I. Eldridge, T.J. Bencic, Oak Ridge National Laboratory Report No 123055, 2005. (Published through SciTech Connect, 03/24/2005).
[29] X. Li, X. Wei, Y. Qin, Y. Chen, C. Duan, M. Yin, J. Alloy. Compd. 657 (2016) 353–357.
[30] J.R. Darwent, C.D. Flint, P.J. O'Grady, Chem. Phys. Lett. 127 (1986) 547–550.
[31] A.H. Khalid, K. Kontis, Meas. Sci. Technol. 20 (2009) (025305-1-9).
[32] D. Sevic, M.S. Rabasovic, J. Krizan, S. Savic-Sevic, M. Mitric, M. Gilic, B. Hadzic, N. Romcevic, Mater. Res. Bull. 88 (2017) 121–126.
[33] M.S. Rabasovic, J. Krizan, P. Gregorcic, M.D. Rabasovic, N. Romcevic, D. Sevic, Opt. Quantum Electron. 48 (2016) 163.
[34] M.D. Rabasovic, B.D. Muric, V. Celebonovic, M. Mitric, B.M. Jelenkovic, M.G. Nikolic, J. Phys. D: Appl. Phys. 49 (2016) (485104-1-6).
[35] R.W. Cheary, A. Coelho, A fundamental parameters approach to X-ray line-profile fitting, J. Appl. Crystallogr. 25 (1992) 109–121.
[36] K. Binnemans, Coord. Chem. Rev. 295 (2015) 1–45.
[37] Y. Dwivedi, S.C. Zilio, Opt. Express 21 (2013) 4717–4727.
[38] S.W. Allison, S.M. Goedeke, M.R. Cates, W.A. Hollerman, J.I. Eldridge, T.J. Bencic, Oak Ridge National Laboratory Report No 123055, 2005. (Published through SciTech Connect, 03/24/2005).
[39] R.M. Ranson, E. Evangelou, C.B. Thomas, Appl. Phys. Lett. 72 (1998) 2663–2664.
[40] D. Ananias, C.D.S. Brites, L.D. Carlos, J. Rocha, Eur. J. Inorg. Chem. 2016 (2016) 1967–1971.
[41] M.G. Nikolic, Z. Antic, S. Culubrk, J.M. Nedeljkovic, M.D. Dramicanin, Sens. Actuators B 201 (2014) 46–50.
[42] J. Yu, L. Sun, H. Peng, M.I.J. Stich, J. Mater. Chem. 20 (2010) 6975–6981.
[43] S.M. Borisov, O.S. Wolfbeis, Anal. Chem. 78 (2006) 5094–5101.
[44] H.S. Peng, M.I.J. Stich, J.B. Yu, L.N. Sun, L.H. Fischer, O.S. Wolfbeis, Adv. Mater. 22 (2010) 716–719.
[45] M.G. Nikolic, A.Z. Al-Juboori, V. Đordjevic, M.D. Dramicanin, Phys. Scr. T157 (2013) (014056-1-5).
[46] Lj.R. Đačanin, M.D. Dramicanin, S.R. Lukic-Petrovic, D.M. Petrovic, M.G. Nikolic, Radiat. Meas. 56 (2013) 143–146.
[47] V. Lojpur, Z. Antic, R. Krsmanovic, M. Medic, M.G. Nikolic, M.D. Dramicanin, J. Serb. Chem. Soc. 77 (2012) 1735–1746.
[48] G. Blasse, B.C. Grabmaier, Luminescent Materials, Springer Verlag, Berlin, 1994.
[49] J. Zhang, H. Cui, P. Zhu, C. Ma, X. Wu, H. Zhu, Y. Ma, Q. Cui, J. Appl. Phys. 115 (2014) 023502.
[50] Z. Zhao, Q.G. Zeng, Z.M. Zhang, Z.J. Ding, J. Lumin. 122–123 (2007) 862–865.
[51] S. Surendra Babu, P. Babu, C.K. Jayasankar, Th Troster, W. Sievers, G. Wortmann, J. Phys.: Condens. Matter 18 (2006) 1927–1938.
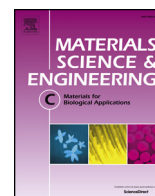
NIR photo-driven upconversion in NaYF$_4$:Yb,Er/PLGA particles for *in vitro* bioimaging of cancer cells

Lidija Mancic[a,*], Aleksandra Djukic-Vukovic[b], Ivana Dinic[c], Marko G. Nikolic[d], Mihailo D. Rabasovic[d], Aleksandar J. Krmpot[d], Antonio M.L.M. Costa[e], Dijana Trisic[f], Milos Lazarevic[g], Ljiljana Mojovic[b], Olivera Milosevic[a]

[a] *Institute of Technical Sciences of the Serbian Academy of Sciences and Arts, Belgrade, Serbia*
[b] *Department of Biochemical Engineering and Biotechnology, Faculty of Technology and Metallurgy, University of Belgrade, Serbia*
[c] *Innovation Center of the Faculty of Chemistry, University of Belgrade, Serbia*
[d] *Photonic Center, Institute of Physics Belgrade, University of Belgrade, Zemun, Belgrade, Serbia*
[e] *Department of Chemical and Materials Engineering, Pontifical Catholic University of Rio de Janeiro, Rio de Janeiro, Brazil*
[f] *Clinic for Pediatric and Preventive Dentistry, School of Dental Medicine, University of Belgrade, Serbia*
[g] *Institute of Human Genetics, School of Dental Medicine, University of Belgrade, Serbia*

ABSTRACT

Lanthanide-doped fluoride up-converting nanoparticles (UCNPs) represent the new class of imaging contrast agents which hold great potential for overcoming existing problems associated with traditionally used dyes, proteins and quantum dots. In this study, a new kind of hybrid NaYF$_4$:Yb,Er/PLGA nanoparticles for efficient biolabeling were prepared through one-pot solvothermal synthesis route. Morphological and structural characteristics of the as-designed particles were obtained using X-ray powder diffraction (XRPD), scanning and transmission electron microscopy (SEM/TEM), energy dispersive spectroscopy (EDS), Fourier transform infrared (FTIR) and photoluminescence (PL) spectroscopy, while their cytotoxicity as well as up-conversion (UC) labeling capability were tested *in vitro* toward human gingival cells (HGC) and oral squamous cell carcinoma (OSCC). The results revealed coexistence of the cubic (*Fm*-3*m*) and hexagonal (*P*6$_3$/*m*) phase in spherical and irregularly shaped nanoparticles, respectively. PLGA [Poly(lactic-*co*-glycolic acid)] ligands attached at the surface of UCNPs particles provide their enhanced cellular uptake and enable high-quality cells imaging through a near-infrared (NIR) laser scanning microscopy (λ_{ex} = 980 nm). Moreover, the fact that NaYF4:Yb,Er/PLGA UCNPs show low cytotoxicity against HGC over the whole concentration range (10–50 μg/mL) while a dose dependent viability of OSCC is obtained indicates that these might be a promising candidates for targeted cancer cell therapy.

1. Introduction

Head and neck cancers represent the sixth most common cancer worldwide, with the highest incidence rates in Melanesia, South-Central Asia and Central and Eastern Europe [1]. Among them, oral squamous cell carcinoma (OSCC) is the most common malignant epithelial neoplasm affecting the oral cavity. The incidence of oral cavity cancer appearance is higher in males and as the major risk factors are considered smoking, alcohol use, smokeless tobacco use and human papillomavirus (HPV). Early stages of disease are asymptomatic and very similar to other mucosal diseases and if diagnosed at advanced stages result with a 5-year survival rate of around 50%. Fatal outcomes are mostly caused by local recurrence and neck lymph node metastasis [2]. Therefore, advancements in both, early diagnosis and therapy, are necessary and most likely will come from innovative non-invasive selective optical techniques [3]. Among the various optical diagnostic methods, fluorescence imaging is of immense importance since that provides accurate visualization of the molecular and functional processes in the human body [4].

Moreover, with the current progress in designing of the new hybrid multifunctional lanthanide-doped up-conversion nanoparticles (UCNPs) whose excitation/emission falls into the biological tissue transparency window, superior optical diagnostic and targeted drug delivery is expectable in the near future [5, 6]. Due to efficient two-phonon excitation and the large anti-Stokes shift UCNPs are able to emit visible or UV photons under excitation by near-infrared (NIR) light, to achieve deeper tissue penetration, and to exhibit higher photochemical stability in comparison with a traditionally used fluorophores [7]. The

---

effectiveness of these materials is principally dependent on the crystal structure and phonon energy of a host matrix, as well as, on the choice and concentration of lanthanide dopants. Efficient lanthanide pairs which can easily upconvert low energy photons into higher ones comprise ytterbium (Yb^{3+}) as a sensitizer and erbium (Er^{3+}), thulium (Tm^{3+}) or holmium (Ho^{3+}) as activator. The rich energy levels and long-lived intermediate excited states of activators provide various energy transfer pathways for UC emissions in visible spectra. Following initial Yb^{3+} excitation by 980 nm laser, energy transfer upconversion (ETU), excited state absorption (ESA), photon avalanche (PA), cooperative energy transfer (CET) and cross-relaxation (CR) processes take place determining resulting fluorescence efficiency of UCNPs [8]. Among many compounds, fluoride based cubic or hexagonal crystal lattices of $NaYF_4$ phase have been extensively studied as the most efficient hosts because of their low phonon energy (*i.e.*, 350 cm^{-1}), which minimize harmful non-radiative relaxations, and high optical transparence necessary for migration of NIR photons. In particular, hexagonal phase exhibits approximately one order of magnitude higher UC emission in comparison to cubic counterpart since it possess a higher degree of asymmetry, multisite occupation with lanthanide dopant ions and shorter distance among them. Since that particle size also affects the luminescence efficiency (higher energy transfer loss is attributed to the higher density of the surface defects) different synthesis strategies were developed to highlight tailored performances of specially designed core-shell, hybrid and composite UCNPs for cell imaging and tracking, drug delivery, photodynamic therapy and target recognition of biospecies [9, 10]. Although showing remarkable characteristics during both *in vitro* and *in vivo* investigations studied structures were usually obtain through complex multi-steps procedure which involves decomposition of organometallic compounds in oleic acid and subsequent ligand exchange (or oxidation, coating, intercalation, *etc.*). Usage of toxic and hazardous substances during synthesis raised deep concerns regarding potential toxicity of synthesized UCNPs [11–13]. Recently, it was shown that such obtained UCNPs could regain their cytotoxicity upon interaction with cells if weakly coordinated surface groups are used to render them biocompatible after synthesis [14]. Thus, the safe biological application of UCNPs implies establishing of facile and reliable procedure which would minimize the usage of toxic solvents and provide hydrophilic reactive surface *in situ* toward enhanced conjugation of proteins and drugs. One-pot polymer assisted hydrothermal approach, originally reported by Wang et al. [15] is a simple procedure which enables direct synthesis of water-dispersible UCNPs. To date, it was used for *in situ* functionalization of UCNPs surface with a wide range of biocompatible capping ligands, including carboxylic and amine/imine groups of polymers, such as: polyethylenimine (PEI), polyacrylic acid (PAA), polyvinylpyrrolidone (PVP) and polyethylene glycol (PEG) [16–18]. Among others, we have also shown that PVP-, PEG- and EDTA-assisted hydro/solvothermal route, performed in a controlled manner, led to the generation of hydrophilic/biocompatible upconverting particles with a different shape (spherical, rod, prisms, octahedron and desert-rose) [19, 20]. Here, we reported for the first time usages of poly(lactic-*co*-glycolic acid) (PLGA) *during* solvothermal synthesis of $NaYF_4$:Yb/Er nanoparticles. PLGA, approved by the United States Food and Drug Administration and European Medicine Agency for pharmaceutical application and human use, is one of the most widely utilized biodegradable polymer with a minimal toxicity associated with its use as scaffolds for tissue engineering or for delivery of macromolecular therapeutics [21–23]. For example, PLGA nanoparticles have been proposed as a delivery medium of an amphiphilic Gd^{3+} complex developed for the need of high sensitive magnetic resonance imaging (MRI) and imaging guided drug delivery applications [24]. Similarly, it was shown that pH-responsive PLGA(UCNPs/doxorubicin hydrochloride) nanocapsules obtained through self-assembly strategy could act as T1-weighted contrast agents MRI, cell imaging label and effective chemotherapy drug delivery system [25]. Due to fact that PLGA comprises both, hydrophilic and hydrophobic moiety, it was

usually used in combination with PEG in the form of amphiphilic block-copolymer for posterior UCNPs coating *via* flash nanoprecipitation. PEG-PLGA layer formed in such way provides excellent UCNPs colloidal stability in deionized water, buffers and serum media, but in the case of a thicker layer formation decrease of the upconversion luminescence was observed [26]. Recently, fabrication of a multifunctional nanovector for simultaneous gene delivery and real-time intracellular tracking based on UCNPs modified by positively charged amphiphilic polymer and PEG–PLGA copolymer was reported [27]. In accordance to the literature, PLGA solely was used, up to date, only for coating of the bare UCNPs through intercalation process, but obtained biocompatible particles sized around 250 nm exhibited negligible cellular uptake and mild cytotoxicity (cellular viability of about 80%) when applied at concentration of 62.5 μg/mL to the human keratinocyte and fibroblast cells [28].

In this study, a new kind of hybrid NaYF4:Yb,Er/PLGA nanoparticles for efficient cell labeling was prepared through one-pot solvothermal synthesis using non-toxic reagents. Hence, PLGA functional groups attached *in situ* to the UCNPs surface ensure excellent biocompatibility without compromising upconverting process. Furthermore, NaYF4:Yb,Er/PLGA UCNPs demonstrated dose-dependent cytotoxicity against oral squamous cell carcinoma (OSCC) without damaging healthy non-cancerous human gingival cells (HGC), so could be considered as promising and reasonably safe candidate for theranostic.

2. Materials and methods

2.1. Synthesis and characterization of NaYF₄:Yb,Er/PLGA UCNPs

All of the chemicals used for PLGA mediated solvothermal synthesis of $NaY_{0.8}Yb_{0.17}Er_{0.03}F_4$ were purchased from Sigma-Aldrich. Deionized water was used throughout. Defined stoichiometric amounts of rare earth nitrates (5 mmol in total) were dissolved in 15 ml of deionized water and then mixed with 5 ml of NaF solution (1.75-fold excess) and 0.1 g of PLGA (lactide:glycolide, 75:25; Mr. 66,000–107,000) dissolved in 40 ml of acetone. Obtained mixture was stirred for 15 min, transferred to 100 ml Teflon lined autoclave and sealed. Since that PLGA is thermally stable until 250 °C under atmospheric pressure [29] synthesis was carried out at twice lower temperature of 120 °C with a continual stirring (100 rpm) for 24 h. After cooling, the as-prepared NaYF₄:Yb,Er/ PLGA UCNPs were washed with acetone by centrifuging (8000 rpm, 10 min) and dried at 80 °C for 3 h.

The NaYF₄:Yb,Er/PLGA UCNPs were characterized by the X-ray powder diffraction (XRPD) using Bruker D8 Discovery equipped with a Cu-Kα source (λ = 1.5406 Å). The pattern was recorded with a step scan of 0.02° and accounting time of 5 s per step. Powders microstructural data were acquired through combined La Bail and Rietveld refinement in Topas 4.2 software. For cubic α- and hexagonal β-NaYF₄ phase refinements were carried out in *Fm*-3*m* (No. 225) and *P*63/*m* (No. 176) space groups, respectively. The morphological features of the as-prepared particles were investigated by means of both, scanning and transmission electron microscopy (JEOL JSM-6701F SEM and JEOL JEM 2010 TEM operating at 200 kV at phase contrast and selected area electron diffraction (SAED) modes) coupled with energy dispersive spectroscopy (EDS). For the aforementioned analyses the particles were suspended in isopropyl alcohol and dropped directly on the stub (for SEM) or on lacey carbon film supported on a Cu grid after 20 min sonication (for TEM). The SemAfore 5.21 JEOL software was used to construct particle size distribution diagrams, while Fourier processing of high resolution TEM images was performed with Digital Micrograph 3.7.4 Gatan Inc. software. Detection of the PLGA ligands on the particles surface was done by Fourier transform infrared spectroscopy (FTIR) using Thermo Scientific Nicolet 6700 spectrophotometer (Thermo Fisher Scientific) with a Smart iTR Diamond Attenuated Total Reflectance accessory. Spectra were recorded using typically 128 scans at the resolution of 4 cm^{-1}. Dynamic light scattering measurements of

the UCNPs hydrodynamic radius (R_H) were performed on a Malvern Zetasizer Nano ZS in the de-ionized water and medium used for testing of the cell viability and imaging. For that purpose, $NaYF_4$:Yb,Er/PLGA UCNPs were dispersed at the concentration of 1 mg/ml and passed through a 0.45 μm cellulose syringe filter before DLS measurements. Photoluminescence emission measurement was performed at room temperature using Spex Fluorolog with C31034 cooled photomultiplier under diode laser excitation at 980 nm. From obtained spectrum the chromaticity coordinate calculation was done.

2.2. OSCC and HGC cultures

Human tumor and healthy gingival tissues were obtained from the patients at the Clinic of Maxillofacial Surgery of School of Dental Medicine, University of Belgrade immediately after the surgery, with signed informed consent approval from each patient prior to study participation. The planning experiments were approved by the Ethical Committee of the School of Dental Medicine (36/31), University of Belgrade.

Tumor tissues were oral squamous cell carcinoma (OSCC) of a tongue. Preparation of the cell cultures was performed using slightly modified procedure of Pozzi et al. [30]. Dulbecco's Modified Eagle Medium (DMEM) supplemented with 20% fetal bovine serum (FBS) and 100 U/ml penicillin-streptomycin (Sigma-Aldrich, St. Louis, USA) was used to transport the tissue sample. The tissue samples were minced with blades into small pieces. The cells were grown in DMEM supplemented with 10% FBS and 100 U/ml penicillin-streptomycin seeded onto T25 cell culture flasks. The cells were maintained at 37 °C in humidified atmosphere containing 5% CO_2. The medium was changed every 2–3 days and the cells were passaged prior to reaching 80% confluence. To avoid fibroblast contamination in cultures, brief exposure to TrypLE Express (Thermo Fisher Scientific, Waltham, USA) was used. OSCC used for the present study were obtained after the third passage.

Human gingival tissues were obtained from three different, healthy patients, aged 19–25 years, during extraction of the impacted third molar. The gingival tissue was transported in Gibco Dulbecco's modified Eagle's F12 medium (D-MEM/F12; Thermo Fisher Scientific), supplemented with 20% FBS and 1% antibiotic/antimycotic (ABAM; Thermo Fisher Scientific) solution. The gingival tissue was rinsed in phosphate-buffered saline (PBS) from Sigma-Aldrich (St. Louis, USA) and subjected to outgrowth isolation method. Tissue was minced into approximately 1 mm^2 fragments, and placed in 25-cm^2 culture flasks with DMEM/F12 supplemented with 10% FBS and 1% ABAM, and incubated at 37 °C in 5% CO_2. The cells were allowed to reach 80% confluence prior to passage. The culture medium was changed every 2–3 days. HGC after the second passage were used in this study.

2.3. MTT assay

For assessment of cytotoxicity, $NaYF_4$:Yb,Er/PLGA UCNPs suspensions with three different concentrations (10, 25 and 50 μg/ml) were prepared. For each concentration, adequate mass of $NaYF_4$:Yb,Er/PLGA UCNPs was aseptically weighted and suspended in sterile water, shaken vigorously and sonicated for 3 min. OSCC and HGC were seeded in a 96-well plate (10,000 cells per well) and incubated at 37 °C in humidified 5% CO_2 atmosphere. After 24 h hours 100 μl of the $NaYF_4$:Yb,Er/PLGA UCNPs were added (10, 25 or 50 μg/ml) in each plate. Incubation with the cell cultures was stopped after 24 h by discarding of spent media, and medium containing 3-(4,5-dimethylthiazol-2-yl)-2,5 diphenyltetrazolium bromide (MTT, 0.5 mg/ml) (Sigma-Aldrich, St. Louis, USA) was added to each well and than incubated for additional 4 h, as previous described by Castiglioni et al. [31]. The supernatant was discarded and formazan crystals were dissolved in 100 μl dimethyl sulfoxide (DMSO) (Sigma-Aldrich, St. Louis, USA) by shaking in duration of 20 min at 37 °C. Optical density was measured at 540 nm using ELISA
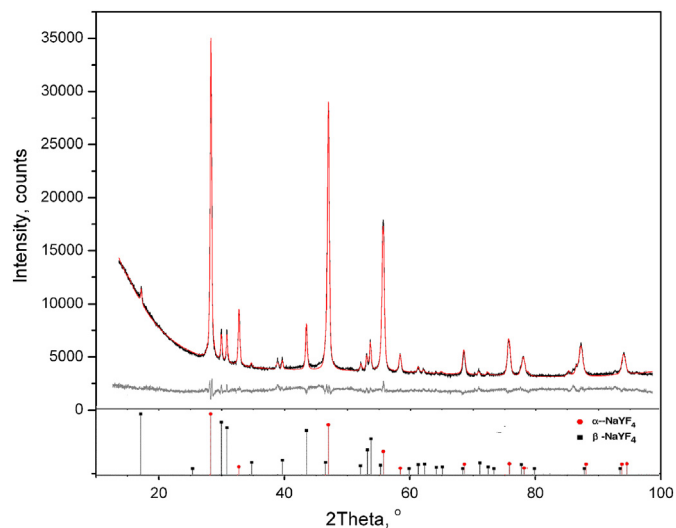

Fig. 1. XRPD pattern of $NaYF_4$:Yb,Er/PLGA UCNPs (black), refined structure (red) and difference curve (gray); Standard patterns of cubic (PDF 01-077-2042) and hexagonal (PDF 01-016-0334) $NaYF_4$ phase are given as bottom bar line diagram. (For interpretation of the references to color in this figure legend, the reader is referred to the web version of this article.)

microplate reader (Enzyme-linked immunosorbent assay) RT-2100c, Rayto, China). Three wells without $NaYF_4$:Yb,Er/PLGA UCNPs were used as a control group.

2.4. Statistical analysis

According to the cytotoxicity test procedure, the experiments were performed in triplicate and repeated three times in the independent experiments. Cells viability, expressed by the ratio of absorbance of the cells incubated with UCNPs to that of the cells incubated with culture medium only, were given in diagram as the mean ± standard deviation (SD).

2.5. Cells imaging by laser scanning microscopy

For the visualization of $NaYF_4$:Yb,Er/PLGA UCNPs uptake, the lowest concentration of $NaYF_4$:Yb,Er/PLGA UCNPs suspension (10 μg/ml) was filtered through 0.45 μm syringe filter to separate large agglomerates and to avoid saturation during visualization. Filtered solution was used further for incubation with cells and preparation of samples for laser scanning microscopy. Sterilized 22 mm × 22 mm glass coverslips were placed in 6-well plates, and 10,000 of OSCC and HGC were seeded per coverslip and incubated at 37 °C in humidified atmosphere containing 5% CO_2. The next day cells were exposed to $NaYF_4$:Yb,Er/PLGA UCNPs solution and incubated for another 24 h. Coverslips with adherent cells were gently rinsed with PBS twice and fixated with 4% paraformaldehyde (PFA) (Sigma-Aldrich, St. Louis, USA) for 20 min. Residuals of PFA were washed by PBS (3 × 3 min), coverslips were dried, 10 μl of Mowiol (Sigma-Aldrich, St. Louis, USA) was placed on fixated cells, and coverslips were placed on microscopic slides with cells positioned in between. Samples were stored in a dark until they were observed under confocal microscopy.

The homemade nonlinear laser scanning microscope used in this study was described in detail elsewhere [32]. Ti:Sapphire laser (Coherent, Mira 900-F) was used as a laser light source. It operates in two regimes. The first regime generates femto-second (FS) pulses at 730 nm convenient for unlabeled cell imaging since that enables two photon excitation of auto-fluorescence in cells. Note that two photon excitation here is considered as excitation of the molecule with no intermediate levels between ground and excited state and it is not related to
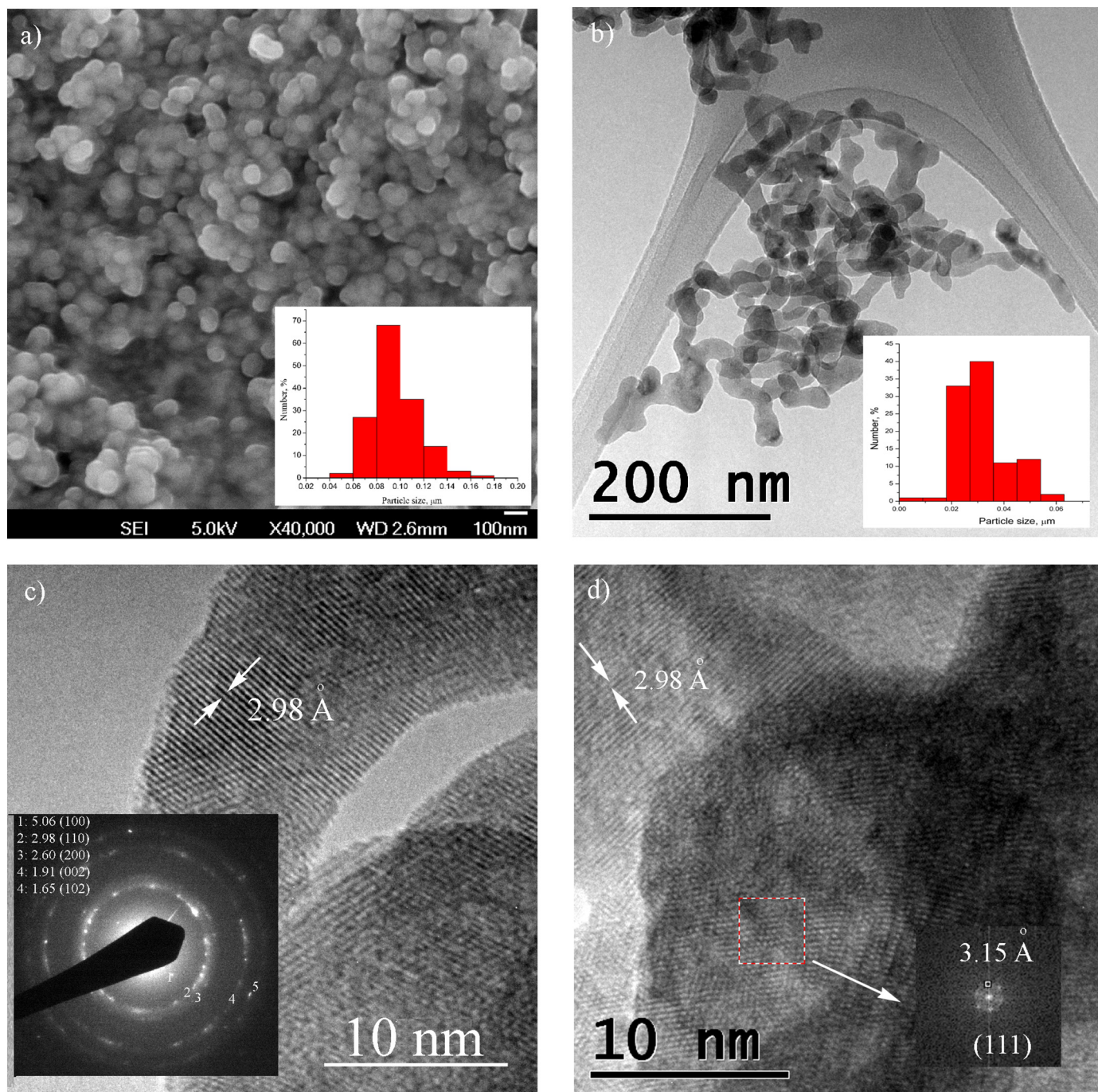
Fig. 2. SEM (a) and TEM (b–d) images of NaYF$_4$:Yb,Er/PLGA UCNPs. Corresponding particle size distribution histograms are given as insets in a and b; SAED inset in c represents d values of the interplanar spacing of hexagonally crystallized elongated nanoparticles, while FFT (inset in d) confirms cubic crystal cell arrangements in a spherical ones.

upconversion process. The second regime comprises generation of continuous wave (CW) radiation at 980 nm and was used for the excitation of NaYF$_4$:Yb,Er/PLGA UCNPs in cells. Due to the long UCNPs lifetime, the scanning rate was reduced during imaging in order to extend pixel dwell time. Hence the pixel dwell time was several times longer than fluorescence lifetime. Each fixed cell culture was imaged using Carl Zeiss, EC Plan-NEOFLUAR, 40 × 1.3 oil immersion objective for laser focusing and collection of the fluorescence. A visible interference filter (415 nm–685 nm) positioned in front of detector is used to remove scattered laser light. Thus, the whole visible range has been detected either for auto-fluorescence from cells or up-conversion from NaYF$_4$:Yb,Er/PLGA UCNPs in cells.

3. Results and discussion

3.1. Structural and morphological properties of NaYF$_4$:Yb,Er/PLGA UCNPs

To confirm the composition and the crystallinity of the synthesized NaYF$_4$:Yb,Er/PLGA UCNPs XRPD analysis was performed. Pattern presented in Fig. 1. reflects that obtained sample is a mixture of well crystallized cubic (*Fm-3m*) and hexagonal (*P63/m*) phase since all of the reflections, *i.e.* their positions and intensities, are in a good agreement with the reported 01-077-2042 and 01-016-0334 ICDD data, presented as bottom bar line diagram in the same figure. In general, NaYF$_4$ material has three different polymorphs: low temperature cubic, hexagonal
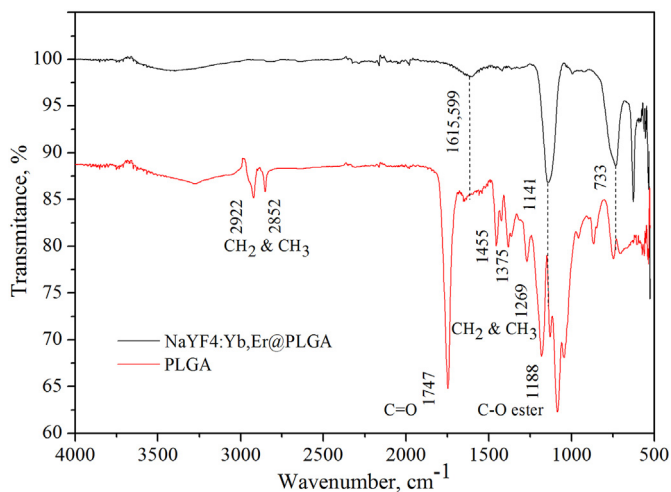
Fig. 3. FTIR of pure PLGA and NaYF$_4$:Yb,Er/PLGA UCNPs.

Fig. 5. MTT assay comparing viability of OSCC and HGC incubated with NaYF$_4$:Yb,Er/PLGA UCNPs for 24 h.

and high-temperature cubic – whose structure lacks detailed characterization [33]. In a low- temperature cubic phase (Fm-3m) there is only one site coordinated by eight fluoride anions over which Na$^+$ and RE^{3+} ions are randomly distributed in the cationic sub-lattice, whereas in the hexagonal ($P63/m$) there are two types of low-symmetry sites at which dopants could be arranged. As it is indicated recently, high-temperature cubic phase could be described with the same space group as a low-temperature one, but with the well-ordered distribution of sodium and RE cations [34]. The unit cell parameters of low-temperature cubic phase and hexagonal one crystallized in the NaYF$_4$:Yb,Er/ PLGA sample were determined from XRPD data to be (Å): a = 5.4764(1); and a = 5.9785(3), c = 3.5088(4); respectively. Since cubic phase prevails in the sample (~85 wt%), refinement of this phase was performed starting from the ICSD 6025 card data. Decreased occupation of the cation site by Na$^+$ and Y^{3+} of 0.98(1) and 0.76(1) corresponds well with a nominal compound stoichiometry, while R$_{Bragg}$ value of 1.79 reflects good compliance with the structural model used during refinement. The average crystallite size of 33(1) nm was calculated using volume weighted mean column height broadening
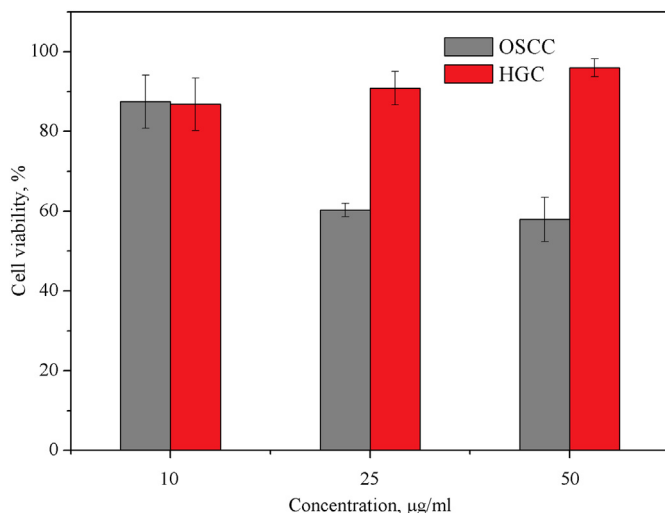
modeled by a Voigt function while Gaussian microstrain distribution was determined to be 0.113(4).

The morphological characteristic of the NaYF$_4$:Yb,Er/PLGA UCNPs were evaluated based on SEM and TEM analysis, Fig. 2. As presented in Fig. 2a, sample is composed of uniform and well defined spherical particles with average size around 100 nm. Backscattered electron images and EDS chemical analysis (not presented) implied compositional homogeneity and high particles purity. As it is notable from SEM, particles are stick together due to the PLGA presence. TEM analysis revealed existence of smaller nanoparticles with elongated shape and length up to 60 nm, Fig. 2b. The high resolution TEM image presented at Fig. 2c, exposes their good crystallinity, clear lattice fringes and the interplanar spacing of 2.98 Å which might be associated with a (110) plane of hexagonal phase. Furthermore, diffraction pattern *via* SAED mode presented as inset at the same figure pointed out that all of determined *d* values are consistent with the interplanar spacings of the hexagonal NaYF$_4$ phase (PDF 01-016-0334) confirming results derived
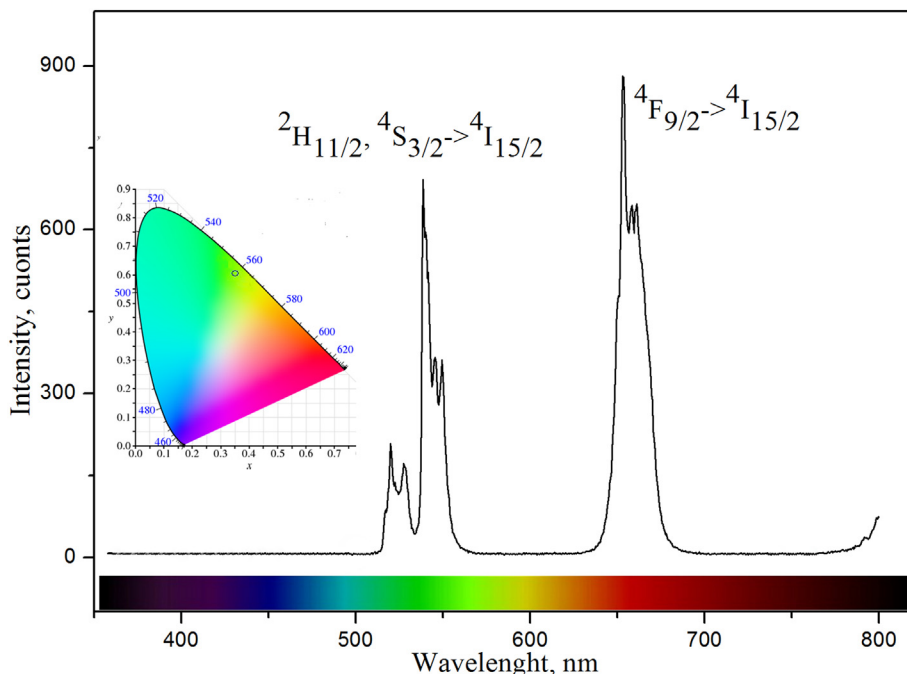

Fig. 4. Up-converted spectrum of NaYF$_4$:Yb,Er/PLGA UCNPs excited at 980 nm and corresponding CIE diagram (given as inset).
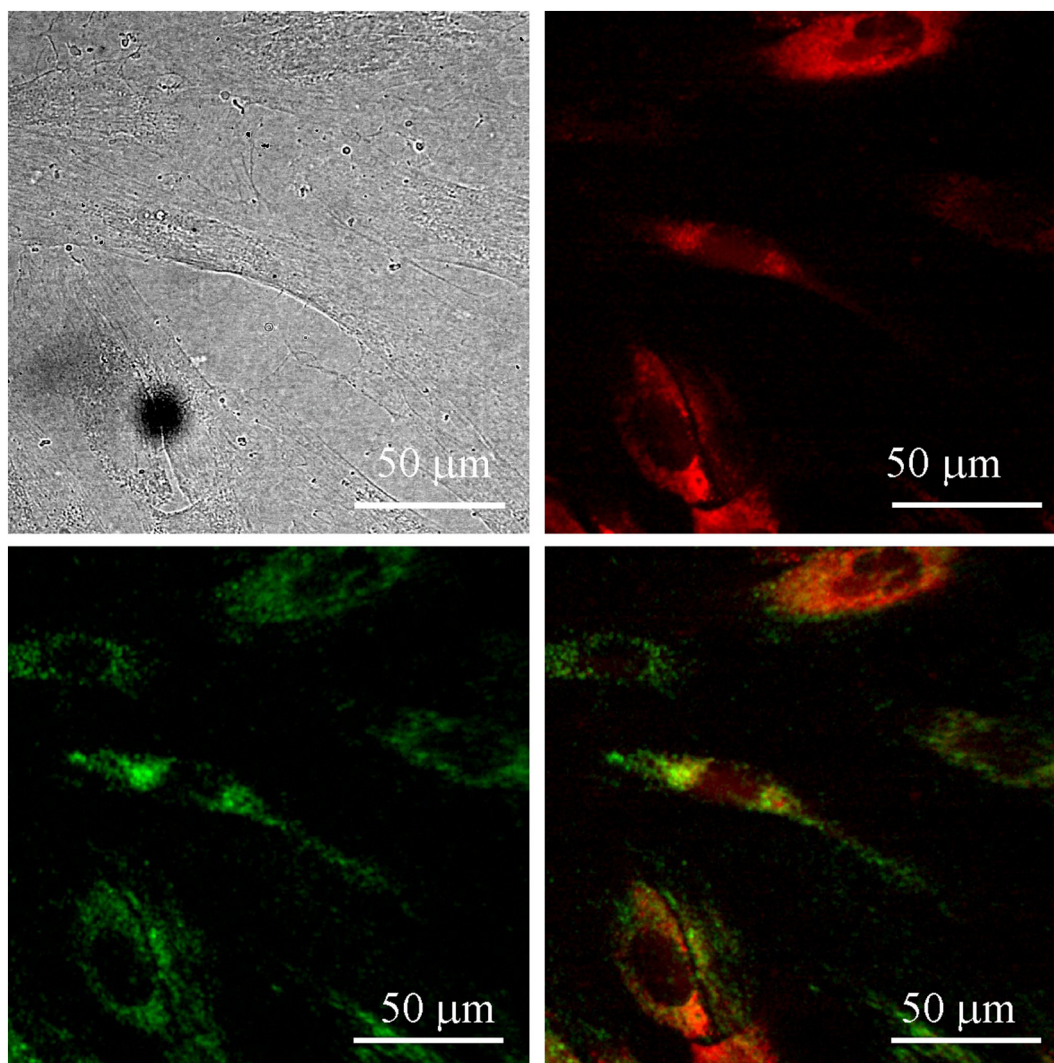
Fig. 6. Images of OSCC following 24 h incubation with 10 µg/ml of NaYF$_4$:Yb,Er/PLGA: bright field (top-left) and cells auto-fluorescence upon femto-second excitation at 730 nm (top-right), pseudo color image of the NaYF$_4$:Yb,Er/PLGA UCNPs upon CW excitation at 980 nm (bottom-left) and their positioning in cells, revealed through co-localization of the cell auto-fluorescence and the UCNPs emission (bottom-right). (For interpretation of the references to color in this figure legend, the reader is referred to the web version of this article.)

from XRPD. Cubic NaYF$_4$ phase was detected in somewhat smaller nanoparticles with a spherical shape, as it is shown in Fig. 2d. Confined growth of NaYF$_4$ nanocrystals was presumably caused by the interaction between the lanthanide ions and the carboxyl end groups of PLGA, which presence is verified further by FTIR analysis.

Colloidal size, polydispersity index (PDI) and stability of the NaYF$_4$:Yb,Er/PLGA UCNPs solutions were estimated from dynamic light scattering measurements, Fig. S1. While a monomodal size distribution was obtained in water (due instant agglomeration of the nanoparticles sized below 20 nm), the bimodal one was preserved in a medium over time (24 h). As a result, slightly higher average hydrodynamic diameter (R_{Hav}) of the NaYF$_4$:Yb,Er/PLGA UCNPs was detected in water (177 nm, PDI 0.32) than in medium (127 nm, PDI 0.31). Minimal changes distinguished after 1 h, confirms good stability of both colloids (195 nm, PDI 0.32; and 127 nm, PDI 0.31; in water and medium, respectively). With prolongation of time, after 24 h, magnitude of the NaYF$_4$:Yb,Er/PLGA UCNPs R_{Hav} in water increased to 488 nm (PDI 0.3), while stayed unchanged in medium which is further used for cells bioimaging (122 nm, PDI 0.34).

Infrared absorption spectra of pure PLGA and NaYF$_4$:Yb,Er/PLGA UCNPs were recorded and presented at Fig. 3. Pure PLGA exhibited characteristic absorption bands which are classified in accordance to

the literature [35] as follows: CH$_3$ and CH$_2$ asymmetric stretching at 2850 and 2920 cm^{-1} respectively; C=O stretching around 1750 cm^{-1}, CH$_3$ and CH$_2$ symmetric angular deformation in the 1500–1250 cm^{-1} region and C−O ester stretching in the 1300–1150 cm^{-1} region. FTIR analysis of NaYF$_4$:Yb,Er/PLGA UCNPs revealed a decreased PLGA absorption due to side-chain vibrations as well as low-frequency shifting of its most intense band associated to the C=O stretching, which might be due to the carboxylic acid salts formation, O=C−ONa, as it was suggested in the literature [36]. This evident that applied synthesis method preserves the highly reactive carboxylic acid groups on UCNPs surface which is very important for their conjugation with biomolecules containing −NH$_2$ group, like antibodies, streptavidin and DNA, creating in that way carriers with high binding potential for targeted imaging and therapy [13].

3.2. Optical properties of NaYF$_4$:Yb,Er/PLGA UCNPs

The upconversion spectrum of NaYF$_4$:Yb,Er/PLGA UCNPs is presented in Fig. 4. Following excitation with 980 nm into the $^2F_{5/2}$ state of Yb^{3+} and subsequent energy transfer from Yb^{3+} to Er^{3+} ions (and *vice versa*), three distinct Er^{3+} emission bands centered at 520, 539 and 653 nm are clearly observed in the visible part of spectrum. The double
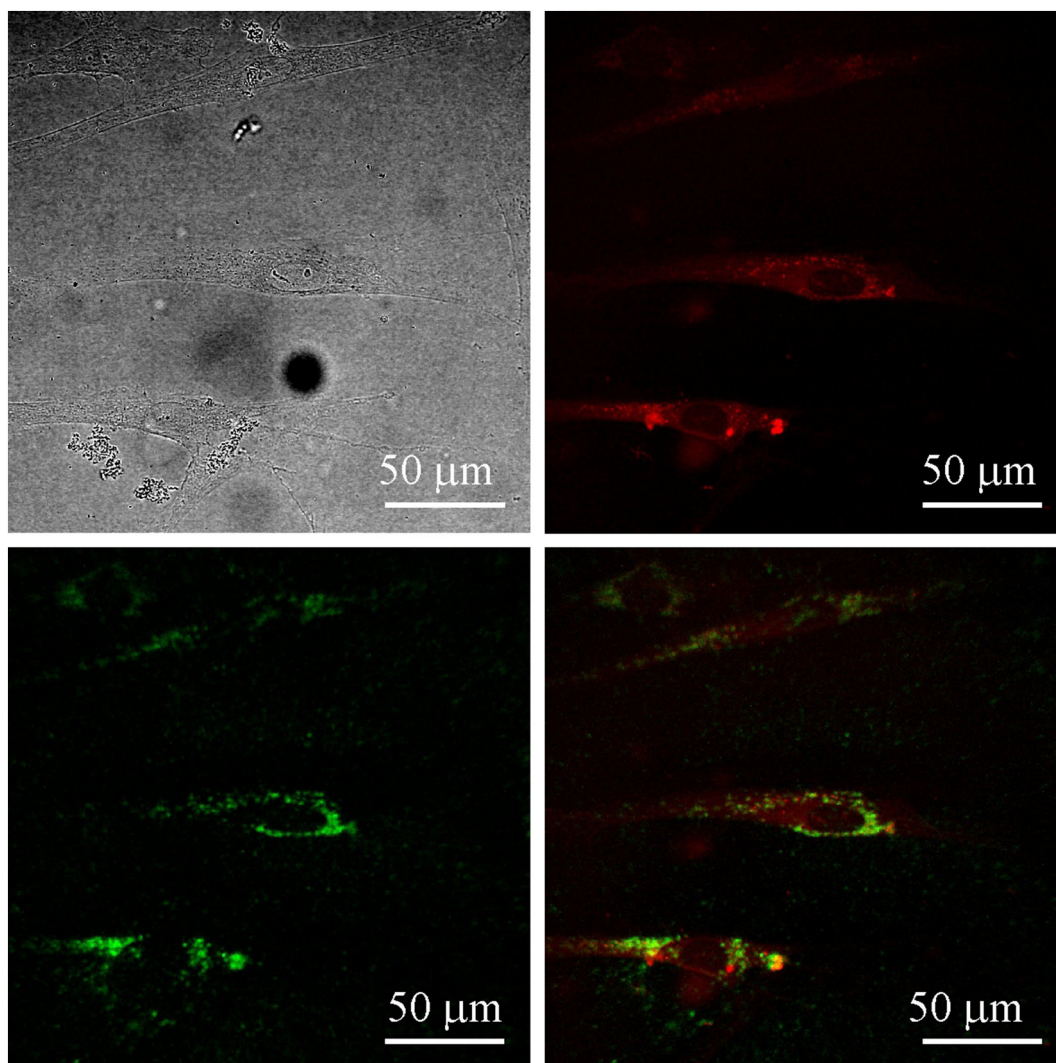
Fig. 7. Images of HGC following 24 h incubation with 10 μg/ml of NaYF$_4$:Yb,Er/PLGA: bright field (top-left) and cells auto-fluorescence upon femto-second excitation at 730 nm (top-right), pseudo color image of the NaYF$_4$:Yb,Er/PLGA UCNPs upon CW excitation at 980 nm (bottom-left) and their positioning in cells, revealed through co-localization of the cell auto-fluorescence and the UCNPs emission (bottom-right). (For interpretation of the references to color in this figure legend, the reader is referred to the web version of this article.)

green emissions between 512 and 533 nm and between 533 and 560 nm are attributed to the ^{2}H$_{11/2} \rightarrow ^4$I$_{15/2}$ and ^{4}S$_{3/2} \rightarrow ^4$I$_{15/2}$ transitions respectively, while a red emission observed between 630 and 690 nm is due to the ^{4}F$_{9/2} \rightarrow ^4$I$_{15/2}$ transition. Green band emission at 539 nm, characterized by several narrow lines associated with a splitting of the ^{4}S$_{3/2}$ energy level by the matrix electric field, reflects the homogeneous distribution of Er^{3+} in the NaYF$_4$ phase [20]. On the other hand, the red emission appears due to a direct population of ^{4}F$_{9/2}$ level from ^{4}I$_{13/2}$ level (following the non-radiative decay from ^{4}I$_{11/2}$ level which is intensified in nanocrystals) and a non-radiative relaxation from ^{4}F$_{7/2}$ through the ^{2}H$_{11/2}$ and ^{4}S$_{3/2}$ levels. As a result, the integrated green to red emission ratios of 0.62 and CIE of (0.37, 0.61) determines the final color output of NaYF$_4$:Yb,Er/PLGA UCNPs, Fig. 4. Photostability of the NaYF$_4$:Yb,Er/PLGA UCNPs emission was also traced during 1 h, Fig. S2. As one could see, exceptionally stable UC luminescence signal was recorded.

3.3. Cytotoxicity of NaYF$_4$:Yb,Er/PLGA UCNPs

The viability of HSCC and HGC after 24 h exposure to NaYF$_4$:Yb,Er/PLGA UCNPs at concentrations of 10, 25 and 50 μg/ml, expressed in terms of percentages compared to the surviving cells in the control group is presented at Fig. 5. As it is notable from Fig. 5, the viability of HGC was highly preserved after 24 h exposure, being above 88% for all examined concentrations of NaYF$_4$:Yb,Er/PLGA UCNPs. At the same time, the tolerance of OSCC was found variable with the increase of NaYF$_4$:Yb,Er/PLGA UCNPs concentration. Only in the case of the lowest concentration viability of OSCC implied non-significant cytotoxicity of 89%, while higher NaYF$_4$:Yb,Er/PLGA concentrations exerted in them certain level of cytotoxicity, *i.e.* cell viability of only 60% was detected. This is quite surprising since cancer cells are usually highly resistant to therapeutics. Obtained data regarding preserved viability of HGC corroborated well by recent conclusions about cytotoxicity of bare and PLGA coated NaYF4:Yb:Er UCNPs tested on human skin cells [28]. Guller et al. [28] used the solvent evaporation technique for posterior formation of PLGA shell over the NaYF$_4$:Yb/Er nanoparticles that have been synthesized through decomposition of rare earth trifluoroacetates in oleic acid/octadecene mixture. Although the authors reported much lower internalization capacity, higher sensitivity of keratinocytes than of fibroblasts has been achieved, emphasizing the importance of studying normal cells. As it will be shown latter, maintaining of the high HGC viability in this study is not a consequence of the lower internalization of NaYF$_4$:Yb,Er/PLGA UCNPs in them, so evaluated differences in OSCC viability indicates that synthesized UCNPs could be

useful in therapeutic treatments of cancer cells.

3.4. In vitro laser scanning microscopy imaging of OSCC and HGC

For the evaluation of the NaYF$_4$:Yb,Er/PLGA UCNPs capability to be internalized in OSCC and HGC, the lowest NaYF$_4$:Yb,Er/PLGA UCNPs concentration of 10 μg/mL has been used. For this concentration, no significant cytotoxicity has been observed in both OSCC and HGC (Section 3.3) and therefore, it could be considered as the most promising concentration for diagnostic purpose.

Visualization of the OSCC and HGC labeled with the NaYF$_4$:Yb,Er/PLGA UCNPs was done using of a safe 980 nm laser intensity of 6 and 7.5 mW, respectively. The size of the imaged region was approximately 200 × 200 μm^2. Images of the OSCC are shown in Fig. 6. The top row, left panel shows bright field image of the sample. A pseudo color image of the cells auto-fluorescence upon femto-second excitation at 730 nm is shown in top-right panel. Bottom row - left panel shows the pseudo color image of the NaYF$_4$:Yb,Er/PLGA UCNPs upon CW excitation at 980 nm. Overlapping of the latter two images clearly implicates that observed fluorescence spots are related to the non-specific uptake of UCPNs through cell membrane and their positioning in a cytoplasmic area around cells nuclei. Size of the fluorescence spots indicates UCNPs aggregation in cells.

The consistent finding of the UCNPs internalization in the HGC has been drawn from Fig. 7, which presents HGCs labeled in the same way as OSCC. The fact that UCNPs are mainly localized in the vicinity of the cells nuclei, without visible entering in, designates that UCNPs didn't provoke gene disruption. In order to show comparable level of the NaYF$_4$:Yb,Er/PLGA UCNPs internalization in OSCC and HGC, quantification of the UCNPs signal from the Figs. 6 and 7, as well as additional one which show labeling of a single OSCC were done, and results obtained are presented in Supplement File (Figs. S3 and S4). Significant cellular internalization of NaYF$_4$:Yb,Er/PLGA UCNPs coupled with the preserved cells viability indicates that these could be useful theranostics for oral cavity cancers.

As it is pointed out before, the amount of literature showing cells viability and labeling with UCNPs is respectable and summarized in many reviews, but great majority is focused on cancer cells testing. At the same time, data about mucosal cytotoxicity and drug deliver capacity of UCNPs tested on primary cultures and normal cells are limited and inconsistent in achieved results due to the considerable disparity of the UCNPs characteristics and type of protective organic shell used [37–39]. Thus, it is not easy to compare these with data presented in this study but it is worth to note that realistic UCNP-assisted imaging depth nowadays is estimated to be up to 1 cm [28], which corresponds well with the depth of skin and mucosa, so successful OSCC and HGC labeling with NaYF$_4$:Yb,Er/PLGA UCNPs holds promise for these to be used as theranostic agents in the future.

4. Conclusion

In conclusion, we have demonstrated the successful fabrication of the new NaYF$_4$:Yb,Er/PLGA UCNPs that could be used as probes for NIR-excited fluorescence (*in vitro*) imaging of human mucosal cells. Comprehensive morphological and structural analyses implied crystallization of a low-temperature cubic phase in spherical nanoparticles (~100 nm), as well as, hexagonal one in elongated nanocrystals (~60 nm). As a consequence of the upconversion, green emission (between 512 and 533 nm and between 533 and 560 nm) and red emission (between 630 and 690 nm) are both prominent in spectra, yielding a final light green output (CIE 0.37, 0.61). PLGA functional groups present at NaYF$_4$:Yb,Er UCNPs surface make them accessible for further conjugation with biologically important molecules, while in the present form enable non-specific cellular uptake without compromising cells viability. Moreover, evidences about lower cytotoxicity under significant internalization of NaYF$_4$:Yb,Er/PLGA UCNPs in the vicinity of

the cell nucleus without gene disrupting, represent an important step toward application of UCNP-based particles for diagnosis or the treatment of cancer cells.

Appendix A. Supplementary data

Supplementary data to this article can be found online at https://doi.org/10.1016/j.msec.2018.05.081.

References

[1] N. Vigneswaran, M.D. Williams, Epidemiological trends in head and neck cancer and aids in diagnosis, Oral Maxillofac. Surg. Clin. North Am. 26 (2) (2014) 123–141.

[2] A.K. Markopoulos, Current aspects on oral squamous cell carcinoma, Open Dent. J. 6 (2012) 126–130.

[3] J.H. Wang, B. Wang, Q. Liu, Q. Li, H. Huang, L. Song, T.Y. Sun, H. Wang, X.F. Yu, C. Li, P.K. Chu, Bimodal optical diagnostics of oral cancer based on Rose Bengal conjugated gold nanorod platform, Biomaterials 34 (2013) 4274–4283.

[4] P. Padmanabhan, A. Kumar, S. Kumar, R.K. Chaudhary, B. Gulyás, Nanoparticles in practice for molecular-imaging applications: an overview, Acta Biomater. 41 (2016) 1–16.

[5] X. Huang, J. Lin, Active-core/active-shell nanostructured design: an effective strategy to enhance Nd^{3+}/Yb^{3+} cascade sensitized upconversion luminescence in lanthanide-doped nanoparticles, J. Mater. Chem. C 3 (2015) 7652–7657.

[6] K. Presley, J. Hwang, S. Cheong, R. Tilley, J. Collins, M. Viapiano, J. Lannutti, Nanoscale upconversion for oxygen sensing, Mater. Sci. Eng. C 70 (2017) 76–84.

[7] X. Zhu, Q. Su, W. Feng, F. Li, Anti-stokes shift luminescent materials for bio-applications, Chem. Soc. Rev. 46 (2017) 1025–1039.

[8] H. Dong, L.D. Sun, C.H. Yan, Energy transfer in lanthanide upconversion studies for extended optical applications, Chem. Soc. Rev. 44 (2015) 1608–1634.

[9] P. Zhao, W. Ji, S. Zhou, L. Qiu, L. Li, Z. Qian, X. Liu, H. Zhang, X. Cao, Upconverting and persistent luminescent nanocarriers for accurately imaging-guided photothermal therapy, Mater. Sci. Eng. C 79 (2017) 191–198.

[10] B. Hou, W. Yang, C. Dong, B. Zheng, Y. Zhang, J. Wu, H. Wang, J. Chang, Controlled co-release of doxorubicin and reactive oxygen species for synergistic therapy by NIR remote-triggered nanoimpellers, Mater. Sci. Eng. C 74 (2017) 94–102.

[11] S. Chen, C. Zhang, G. Jia, J. Duan, S. Wang, J. Zhang, Size-dependent cytotoxicity of europium doped NaYF4 nanoparticles in endothelial cells, Mater. Sci. Eng. C 43 (2014) 330–342.

[12] X. Wu, G. Chen, J. Shen, Z. Li, Y. Zhang, G. Han, Upconversion nanoparticles: a versatile solution to multiscale biological imaging, Bioconjug. Chem. 26 (2015) 166–175.

[13] J. Zhou, Z. Liu, F. Li, Upconversion nanophosphors for small-animal imaging, Chem. Soc. Rev. 41 (2012) 1323–1349.

[14] G.K. Das, D.T. Stark, I.M. Kennedy, Potential toxicity of up-converting nanoparticles encapsulated with a bilayer formed by ligand attraction, Langmuir 30 (2014) 8167–8176.

[15] F. Wang, D.K. Chatterjee, Z. Li, Y. Zhang, X. Fan, M. Wang, Synthesis of polyethylenimine/NaYF4 nanoparticles with upconversion fluorescence, Nanotechnology 17 (2006) 5786–5791.

[16] M. Wang, C.-C. Mi, J.-L. Liu, X.-L. Wu, Y.-X. Zhang, W. Hou, F. Li, S.-K. Xu, One-step synthesis and characterization of water-soluble NaYF4:Yb,Er/Polymer nanoparticles with efficient up-conversion fluorescence, J. Alloys Compd. 485 (2009) L24–L27.

[17] T. Cao, Y. Yang, Y. Gao, J. Zhou, Z. Li, F. Li, High-quality water-soluble and surface-functionalized upconversion nanocrystals as luminescent probes for bioimaging, Biomaterials 32 (2011) 2959–2968.

[18] A. Sedlmeier, H.H. Gorris, Surface modification and characterization of photon-upconverting nanoparticles for bioanalytical applications, Chem. Soc. Rev. 44 (2015) 1526–1560.

[19] I. Dinic, M.E. Rabanal, K. Yamamoto, Z. Tan, S. Ohara, L.T. Mancic, O.B. Milosevic, PEG and PVP assisted solvothermal synthesis of NaYF4:Yb^{3+}/Er^{3+} up-conversion nanoparticles, Adv. Powder Technol. 27 (2016) 845–853.

[20] I. Dinic, S. Ohara, T. Koji, M.E. Rabanal, A.M. Costa, B.A. Marinkovic, L. Mancic, O. Milosevic, Compositional and structural dependence of upconverting RE-fluorides obtained through EDTA assisted hydrothermal synthesis, Adv. Powder Technol. 28 (1) (2017) 73–82.

[21] H.M. Mansour, M. Sohn, A. Al-Ghananeem, P.P. Deluca, Materials for pharmaceutical dosage forms: molecular pharmaceutics and controlled release drug delivery aspects, Int. J. Mol. Sci. 11 (2010) 3298–3322.

[22] H.K. Makadia, S.J. Siegel, Poly lactic-co-glycolic acid (PLGA) as biodegradable controlled drug delivery carrier, Polymer 3 (3) (2011) 1377–1397.

[23] F. Danhier, E. Ansorena, J.M. Silva, R. Coco, A. Le Breton, V. Préat, PLGA-based

nano particles: an overview of biomedical applications, J. Control. Release 161 (2) (2012) 505–522.

[24] R.N. Mariano, D. Alberti, J.C. Cutrin, S.G. Crich, S. Aime, Design of PLGA based nanoparticles for imaging guided applications, Mol. Pharm. 11 (2014) 4100–4106.

[25] J. Zhao, H. Yang, J. Li, Y. Wang, X. Wang, Fabrication of pH-responsive PLGA(UCNPs/DOX) nanocapsules with upconversion luminescence for drug delivery, Sci. Rep. 7 (2017) (Article No. 18014).

[26] S.J. Budijono, J. Shan, N. Yao, Y. Miura, T. Hoye, R.H. Austin, Y. Ju, R.K. Prud'Homme, Synthesis of stable block-copolymer-protected NaYF$_4$:Yb^{3+}, Er^{3+} up-converting phosphor nanoparticles, Chem. Mater. 22 (2010) 311–318.

[27] X. Bai, S. Xu, J. Liu, L. Wang, Upconversion luminescence tracking of gene delivery via multifunctional nanocapsules, Talanta 150 (2016) 118–124.

[28] A.E. Guller, A.N. Generalova, E.V. Petersen, A.V. Nechaev, I.A. Trusova, N.N. Landyshev, A. Nadort, E.A. Grebenik, S.M. Deyev, A.B. Shekhter, A.V. Zvyagin, Cytotoxicity and non-specific cellular uptake of bare and surface-modified upconversion nanoparticles in human skin cells, Nano Res. 8 (5) (2015) 1546–1562.

[29] R.M. Mainardes, M.P.D. Gremião, R.C. Evangelista, Thermoanalytical study of praziquantel-loaded PLGA nanoparticles, Braz. J. Pharm. Sci. 42 (4) (2006) 523–530.

[30] V. Pozzi, D. Sartini, R. Rocchetti, A. Santarelli, C. Rubini, S. Morganti, R. Giuliante, S. Calabrese, G. Di Ruscio, F. Orlando, M. Provinciali, F. Saccucci, L. Lo Muzio, M. Emanuelli, Identification and characterization of cancer stem cells from head and neck squamous cell carcinoma cell lines, Cell. Physiol. Biochem. 36 (2015) 784–798.

[31] S. Castiglioni, C. Caspani, A. Cazzaniga, J.A. Maier, Short- and long-term effects of silver nanoparticles on human microvascular endothelial cells, World J. Biol. Chem. 5 (2014) 457–464.

[32] K. Bukara, S. Jovanic, I.T. Drvenica, A. Stancic, V. Ilic, M.D. Rabasovic, D. Pantelic, B. Jelenkovic, B. Bugarski, A.J. Krmpot, Mapping of hemoglobin in erythrocytes and erythrocyte ghosts using two photon excitation fluorescence microscopy, J. Biomed. Opt. 22 (2) (2017) 026003(8 pages).

[33] T. Laihinen, M. Lastusaari, L. Pihlgren, L.C.V. Rodrigues, J. Holsa, Thermal behaviour of the NaYF$_4$:Yb^{3+},R^{3+} materials, J. Therm. Anal. Calorim. 121 (2015) 37–43.

[34] L. Wang, X. Li, Z. Li, W. Chu, R. Li, K. Lin, H. Qian, Y. Wang, C. Wu, J. Li, D. Tu, Q. Zhang, L. Song, J. Jiang, X. Chen, Y. Luo, Y. Xie, Y. Xiong, A new cubic phase for α NaYF$_4$ host matrix offering high upconversion luminescence efficiency, Adv. Mater. 27 (2015) 5528–5533.

[35] A.T.C.R. Silva, B.C.O. Cardoso, M.E.S.R. Silva, R.F.S. Freitas, R.G. Sousa, Synthesis, characterization, and study of PLGA copolymer in vitro degradation, J. Biomater. Nanobiotechnol. 6 (2015) 8–19.

[36] J.B. Lee, Y.G. Ko, D. Cho, W.H. Park, B.N. Kim, B.C. Lee, I.K. Kang, O.H. Kwon, Modification of PLGA nanofibrous mats by electron beam irradiation for soft tissue regeneration, J. Nanomater. (2015) 10, http://dx.doi.org/10.1155/2015/295807 (Article ID 295807).

[37] U. Bazylińska, D. Wawrzyńczyk, J. Kulbacka, R. Frąckowiak, B. Cichy, A. Bednarkiewicz, M. Samoć, K.A. Wilk, Polymeric nanocapsules with upconverting nanocrystals cargo make ideal fluorescent bioprobes, Sci. Rep. 6 (2016) 29746.

[38] H.C. Guo, R.Z. Hao, H.S. Qian, S.Q. Sun, D.H. Sun, H. Yin, Z.X. Liu, X.T. Liu, Upconversion nanoparticles modified with aminosilanes as carriers of DNA vaccine for foot-and-mouth disease, Appl. Microbiol. Biotechnol. 95 (2012) 1253–1263.

[39] L. Zhao, A. Kutikov, J. Shen, C. Duan, J. Song, G. Han, Stem cell labeling using polyethylenimine conjugated (α-NaYbF$_4$:Tm^{3+})/CaF$_2$ upconversion nanoparticles, Theranostics 3 (4) (2013) 249–257.

Photon diagnostics at the FLASH THz beamline

Rui Pan, Ekaterina Zapolnova, Torsten Golz, Aleksandar J. Krmpot, Mihailo D. Rabasovic, Jovana Petrovic, Vivek Asgekar, Bart Faatz, Franz Tavella, Andrea Perucchi, Sergey Kovalev, Bertram Green, Gianluca Geloni, Takanori Tanikawa, Mikhail Yurkov, Evgeny Schneidmiller, Michael Gensch and Nikola Stojanovic

IUCr Journals
CRYSTALLOGRAPHY JOURNALS ONLINE

research papers

Photon diagnostics at the FLASH THz beamline[1]

Rui Pan,[a] Ekaterina Zapolnova,[a] Torsten Golz,[a] Aleksandar J. Krmpot,[b] Mihailo D. Rabasovic,[b] Jovana Petrovic,[c,d] Vivek Asgekar,[e] Bart Faatz,[a] Franz Tavella,[f] Andrea Perucchi,[g] Sergey Kovalev,[h] Bertram Green,[h] Gianluca Geloni,[i] Takanori Tanikawa,[i] Mikhail Yurkov,[a] Evgeny Schneidmiller,[a] Michael Gensch[j,k] and Nikola Stojanovic[a]*

[a]Deutsches Elektronen-Synchrotron (DESY), Notkestrasse 85, D-22607 Hamburg, Germany, [b]Institute of Physics Belgrade, Pregrevica 118, 11080 Belgrade, Serbia, [c]Vinca Institute of Nuclear Sciences, Belgrade, Serbia, [d]Center for Free-Electron Laser Science, Deutsches Elektronen-Synchrotron (DESY), Notkestrasse 85, D-22607 Hamburg, Germany, [e]Department of Physics, S. P. Pune University, Pune, India, [f]SLAC National Accelerator Laboratory, Menlo Park, California, USA, [g]Elettra – Sincrotrone Trieste SCpA, 34149 Basovizza, Trieste, Italy, [h]Helmholtz-Zentrum Dresden-Rossendorf (HZDR), Bautzner Landstraße 400, 01328 Dresden, Germany, [i]European XFEL, Holzkoppel 4, 22869 Schenefeld, Germany, [j]German Aerospace Center (DLR), Institute of Optical Sensor Systems, Rutherfordstraße 2, 12489 Berlin, Germany, and [k]Institute of Optics and Atomic Physics, Technical University of Berlin, Strasse des 17 Juni 135, 10623 Berlin, Germany. *Correspondence e-mail: nikola.stojanovic@desy.de

The THz beamline at FLASH, DESY, provides both tunable (1–300 THz) narrow-bandwidth (~10%) and broad-bandwidth intense (up to 150 uJ) THz pulses delivered in 1 MHz bursts and naturally synchronized with free-electron laser X-ray pulses. Combination of these pulses, along with the auxiliary NIR and VIS ultrashort lasers, supports a plethora of dynamic investigations in physics, material science and biology. The unique features of the FLASH THz pulses and the accelerator source, however, bring along a set of challenges in the diagnostics of their key parameters: pulse energy, spectral, temporal and spatial profiles. Here, these challenges are discussed and the pulse diagnostic tools developed at FLASH are presented. In particular, a radiometric power measurement is presented that enables the derivation of the average pulse energy within a pulse burst across the spectral range, jitter-corrected electro-optical sampling for the full spectro-temporal pulse characterization, spatial beam profiling along the beam transport line and at the sample, and a lamellar grating based Fourier transform infrared spectrometer for the on-line assessment of the average THz pulse spectra. Corresponding measurement results provide a comprehensive insight into the THz beamline capabilities.

1. Introduction

FLASH, the free-electron laser (FEL) in Hamburg at DESY, provides ultrafast XUV and soft X-ray radiation for users to perform pump–probe experiments. FLASH has two independent FEL undulator beamlines (Faatz *et al.*, 2016): FLASH1 and FLASH2. Each FEL branch ends with a dedicated experimental hall that has a number of beamlines.

FLASH1 has a unique feature, a dedicated THz undulator installed downstream of the XUV undulators. This feature allows the generation of intense THz pulses by the same electron bunch that generates XUV pulses (Stojanovic & Drescher, 2013), as shown in Fig. 1. As THz and XUV undulators are separated by empty drift space, XUV and THz pulses generated by the same electron bunch are naturally synchronized with no more than 5 fs timing jitter (Frühling *et al.*, 2009). Furthermore, THz pulses are carrier envelope phase (CEP) stable. Downstream of the THz undulator, the electron beam is deflected to ground by the so-called electron beam dump magnet (hereon referred to as the dump magnet). This
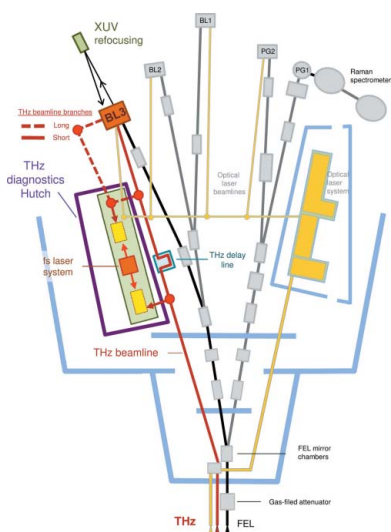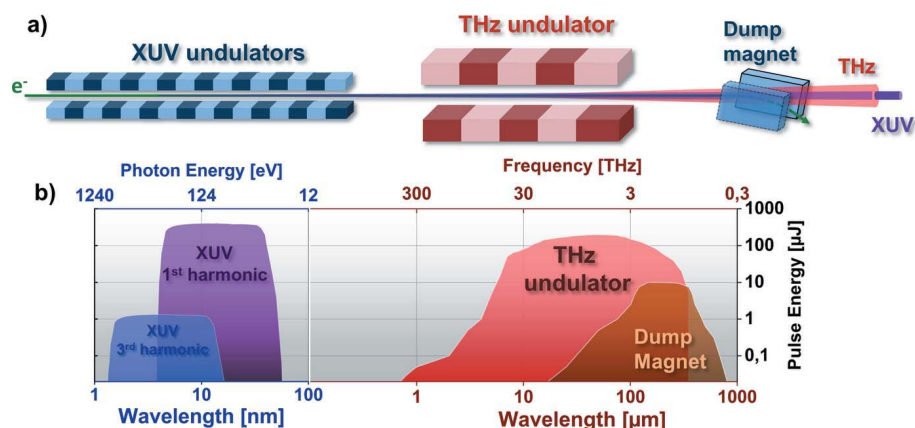
Figure 1
Scheme of the FLASH1 THz photon sources. (*a*) The THz undulator is located downstream of the XUV undulators, separated by free space. The electron beam dump magnet follows the THz undulator. (*b*) Representation of the pulse energies that can be obtained at FLASH1 from the XUV and THz sources over a wide spectral range.

stage separates the electron beam from the photon (THz and XUV) beams. The dump magnet on its own generates an intense THz transient, mainly by the edge and bending radiation process (Tavella *et al.*, 2011; Geloni *et al.*, 2009*a,b*). Only a fraction of the total bending radiation is collected in the THz beamline downstream (estimated to be 11.4%), as beamline design is optimized for the radiation in the forward direction, while bending radiation is created tangentially along the bend. THz and XUV beams are separated by a large flat mirror (210 mm × 140 mm) with a 10 mm aperture for the XUV beam (Gensch *et al.*, 2008). Transport of the THz beam into the experimental hall over ∼70 m requires multiple collimations and this is provided by all-reflective optics. By this unique photon generation scheme, the photon spectrum of FLASH1 is extended to the long-wavelength range. As shown in Fig. 1, FLASH1 covers the XUV range from 1.4 nm to 52 nm including harmonics (Tiedtke *et al.*, 2009), and the THz range from 1 μm to above 300 μm (300 THz to 1 THz). With an independent and synchronized near-infrared (NIR) laser (Redlin *et al.*, 2011) having a center wavelength of 800 nm, FLASH1 can provide XUV, THz and NIR laser beams for users at the same time to study photon–matter interactions.

Based on the scheme shown in Fig. 1, there are two types of intense THz sources. The first is a THz undulator (Grimm *et al.*, 2010) that generates tunable, linearly polarized (horizontally), narrow-bandwidth ($\Delta\lambda/\lambda = 10\%$) radiation. The wavelength is tunable from 1 μm to above 300 μm. The longest wavelength that can be reached depends on the electron beam energy for a given THz undulator period and peak field (see Fig. 2). Pulse energies delivered to the experiment can reach up to 150 μJ, depending on the FLASH accelerator parameters (mainly the electron bunch charge and its compression).

The second source of THz radiation is the dump magnet that generates edge and bending radiation. The edge radiation is generated by the longitudinal acceleration of the electron beam at the interface between the free space and the dump

magnet magnetic field (Tavella *et al.*, 2011; Geloni *et al.*, 2009*a,b*). This kind of radiation has a broad spectral bandwidth (quasi single-cycle temporal profile), is radially polarized and generated in the forward direction to the electron beam propagation. Electrons also generate the bending radiation along the bending arc of the dump magnet. The dump magnet vacuum chamber acceptance angle for the bending radiation is relatively small (2.4°) compared with 21° of the complete bend that the electrons experience. Thus only a fraction of the bending radiation radiated in the forward radiation is collected into the THz beamline. Also, the bending radiation has a broad bandwidth (quasi single-cycle temporal profile) and is linearly polarized. The bending radiation is collected by the THz beamline mostly from the bending plane and is thus polarized mainly in the vertical direction, orthogonal to the THz undulator pulse polarization. Combined edge and bending dump magnet radiation can reach a pulse energy of over 10 μJ. This radiation is generated parasitically and can be used independently from the undulator radiation.

The THz beamline delivers the beam to the end-station at the end of the BL3 XUV beamline in the FLASH1 experimental hall (see Fig. 3). The THz beam can be delivered to the experiment via two branches, a short one with ultra-high-vacuum transport (10^{-9} mbar) and a long one via THz diagnostics hutch with high-vacuum transport (10^{-7} mbar). Due to the difference in optical path, the THz pulse arrives later than the XUV pulse to the end-station, 12 ns for the short branch and 21 ns for the long branch. We use two approaches to achieve temporal overlap of the XUV and THz pulses in the experiment: the first is delaying the XUV pulse by refocusing via multilayer mirrors; the second is to generate two electron bunches at the FLASH electron gun timed to achieve temporal overlap of the respective THz and XUV pulses in the experiment (Zapolnova *et al.*, 2018).
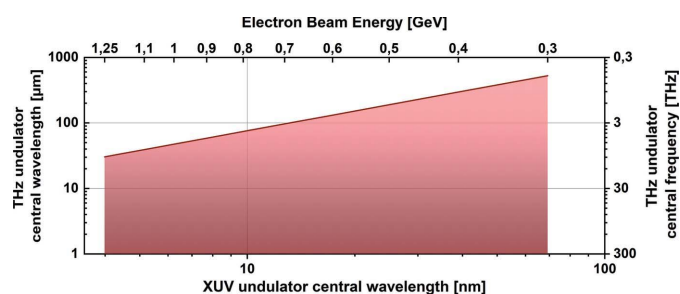

Figure 2
THz undulator spectral range. The shaded area represents the range where the fundamental frequency of the THz undulator radiation can be reached for FLASH1 as a function of the FEL XUV wavelength (lower horizontal axis) and the electron beam energy in the linac (upper horizontal axis).
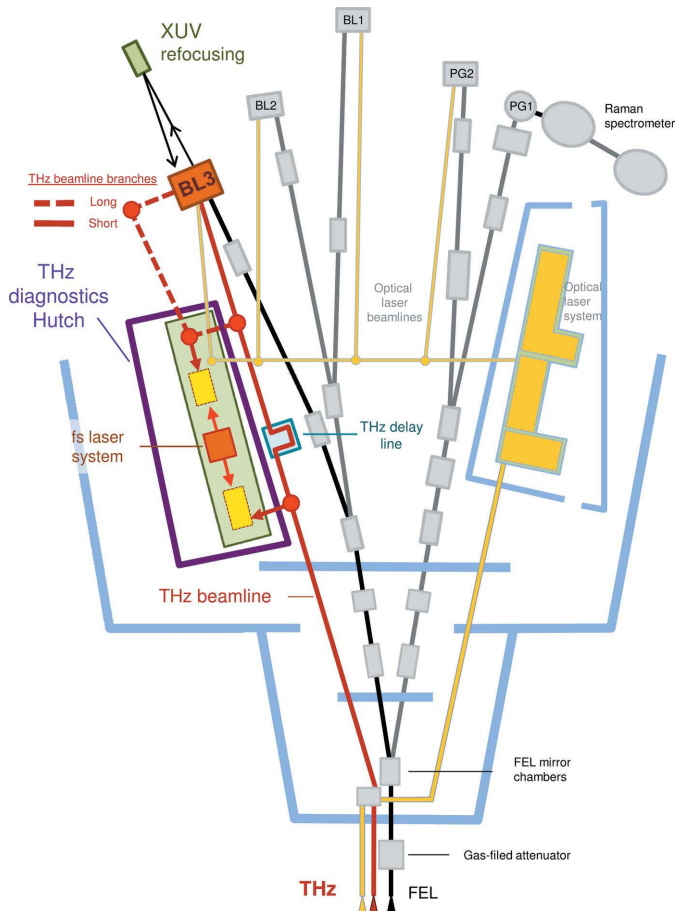
Figure 3
Scheme of the THz beamline in the FLASH1 experimental hall. THz beam is delivered to the end-station at the BL3 XUV beamline, via one of the two branches.

There are many unique applications for the CEP stable intrinsically synchronized THz pulses from the FLASH THz beamline. One important scientific area is in atomic and molecular physics. Here the THz field can act as a streak camera, allowing molecular reactions to be clocked and processes induced by the femtosecond-long XUV pulses from FLASH on a timescale of a few femtoseconds (Frühling *et al.*, 2009; Schütte *et al.*, 2012; Oelze *et al.*, 2017; Schmid *et al.*, 2019). An emerging new class of experiments at FLASH is the application of the strong THz fields for these tunable narrow-band pulses in selective excitation or selective THz control of matter [for a description of this field see, for example, Green *et al.* (2016), Buzzi *et al.* (2018), Kampfrath *et al.* (2013) and Kovalev *et al.* (2017)]. The first experiments performed at FLASH have focused on driving the magnetization dynamics in magnetic thin films by selective phonon excitation (Radu, 2019) and on the THz control of dynamic surface processes (Waltar *et al.*, 2018).

2. THz diagnostics

In a typical THz-pump/XUV-probe experiment at FLASH, determination of the properties of the driving THz pulse is of key importance. Based on the needs of the user experiments in

past years, we have developed diagnostics tools to fully characterize the THz beam at the experiment. Presently, all the tools are developed in the THz diagnostics hutch at FLASH1 experimental hall and will be transferred to the end-station at BL3 beamline (see Fig. 3). In this paper we present tools for the full spectral, temporal and spatial characterization of the THz pulses and the pulse-energy measurement. Thereby we discuss some of the major challenges for diagnostics, *i.e.* the extremely broad THz spectral range of FLASH sources, 1 MHz repetition rate in 10 Hz bursts and jitter to externally synchronized lasers (Azima *et al.*, 2009; Tavella *et al.*, 2011), that can be used for THz waveform characterization.

2.1. THz power measurement

We measure the THz pulse energies using a radiometer (RM3700, head RjP-735/RF, by Laser Probe). We have cross-referenced this detector to a PTB (The National Metrology Institute of Germany) traceable 3A-P-THz, by Ophir Optronics Solutions (Green *et al.*, 2016). The radiometer detector has a cavity pyroelectric probe and it has a time constant of 1 ms. Its temporal response prevents us from resolving individual pulses of the FLASH micro-pulses within a 1 MHz burst. However, the detector time constant is well matched to the maximal duration of the 1 MHz burst (with duration of 0.8 ms, containing up to 800 pulses) defined by the FLASH accelerator. Therefore, the integration is performed over all micro-bunches in a burst, which allows for determination of the average THz pulse energy with good accuracy.

Fig. 4 depicts the THz pulse energy as a function of central wavelength of the THz undulator. The total THz beamline transmission (from the source until the end of beamline) as a function of wavelength is depicted as well. We calculate the beamline transmission by modeling the THz source and the optical transport with the *Synchrotron Radia-*
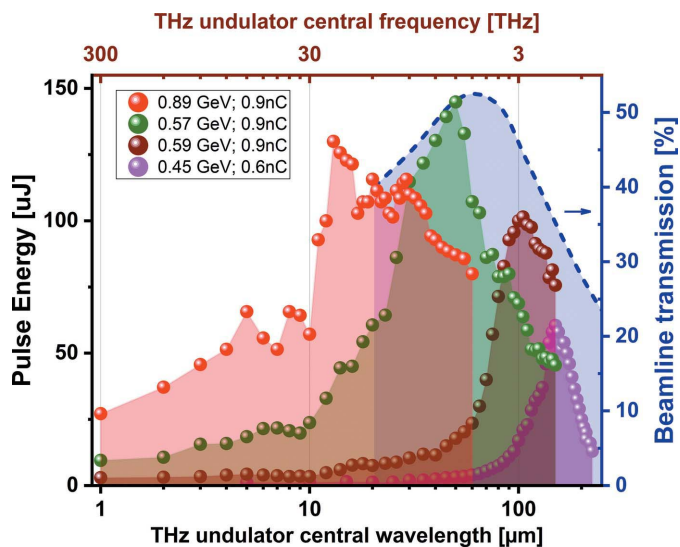

Figure 4
THz pulse energies measured at the beamline end-station for different conditions of the FLASH accelerator. The blue dashed line shows the beamline transmission, calculated using the *SRW* software package (Chubar & Elleaume, 1998).

tion Workshop (SRW) software package (Chubar & Elleaume, 1998). We also account for the Fresnel losses in the diamond window that separates the beamline from the accelerator vacuum (Gensch et al., 2008). We present examples of four measurements taken for different electron beam settings of the FLASH accelerator. Note that the abrupt end of the THz undulator tuning range at long wavelengths relates to the maximal wavelength that can be reached at a particular electron beam energy and is determined by the maximum field (1.2 T) inside the undulator (see also Fig. 2).

2.2. THz temporal profile measurements

The THz time domain spectroscopy (TDS) via electro-optic sampling (EOS) method is a well established technique for the full characterization of the THz pulse temporal structure (Wu & Zhang, 1995; Schmuttenmaer, 2004), in a broad spectral range. The electric field of the THz pulse changes the bire-fringence of the EOS crystal. This transient change is sampled by an ultrashort laser pulse. By scanning the laser pulse in time, the complete THz pulse shape can be reconstructed.

At an accelerator-based light source, such as FLASH, the laser system is synchronized to the master clock of the FLASH accelerator (Schulz et al., 2015). One of the main limiting factors for the use of an externally synchronized laser for EOS detection is the temporal jitter between the FEL and the laser pulses. Jitter limits the temporal resolution and subsequently the spectral bandwidth of EOS detection. We have measured the jitter of the probe laser (pulse duration 20 fs FWHM) in the THz hutch to the FLASH THz pulses to be around 100 fs RMS ($\sim$200 fs peak-to-peak). To solve this, we chose to detect the THz pulses' arrival time on a single-shot basis using spectral decoding electro-optic detection (EOSD) (Jiang & Zhang, 1998). This technique enables single-shot THz detection by imprinting the THz pulse electric field onto a stretched probe laser pulse, thus defining the arrival time of one with respect to the other. Spectral decoding is photon efficient (for a single-shot method) and enables the arrival time detection even with femtosecond oscillator pulses, which allows for a high-repetition-rate arrival time detection scheme that can be matched to the FLASH pulse pattern. Full EO detection of the THz pulses at FLASH then comprises two main components: arrival time monitoring by spectral decoding in combination with scanning electro-optic sampling (EOS). EOS data are sorted for their arrival time and the THz pulse shape is retrieved. The complete detection setup is installed in a high-vacuum chamber (10^{-7} mbar) to avoid measurement distortions by absorption in ambient air. We achieved a temporal resolution of the arrival time sorting of 9.7 fs RMS. Most importantly, the EOS sampling has a bandwidth of 37–3000 µm (0.1–8 THz) limited by the gallium phosphide (GaP) EOS crystal (100 µm thick). The setup has been developed in collaboration with the TELBE team at HZDR and details can be found in the literature (Kovalev et al., 2017; Golz, 2018).

Two typical examples of measured THz waveform profiles are shown in Figs. 5(a) and 5(b). The THz and the probing laser beam are overlapped and focused on the GaP EOS

crystal, with beam sizes of 350 µm FWHM and 70 µm FWHM, respectively. The THz undulator was set to nominal wave-lengths of 155 µm and 42 µm (corresponding to frequencies of 1.93 THz and 7.1 TH, respectively). For the long-wavelength example, unfiltered and spectrally filtered pulses are presented. The wire-grid THz bandpass filter used has been centered at 155 µm wavelength (1.93 THz) with 15% spectral bandwidth. For the unfiltered pulse, it is interesting to observe that the electric field and high-harmonic content increase along the pulse. This indicates the change of the electron bunch form factor (Nodvick & Saxon, 1954) inside the undulator. In the respective unfiltered THz pulse spectrum [see Fig. 5(c)] we clearly observe the first harmonic peaking at 169 µm (1.77 THz) and the third harmonic at 52 µm (5.68 THz), and the baseline includes the broadband spectrum from the dump magnet radiation. As expected, the measure-ment with the THz bandpass filter shows a strong peak around 160 µm (1.87 THz), with a small (few percent) leakage between 75 and 100 µm (3 and 4 THz). Similarly, in the spectrum of the short-wavelength pulse (tuned to 42 µm) we observe the first harmonic peaking at 43 µm (7 THz).
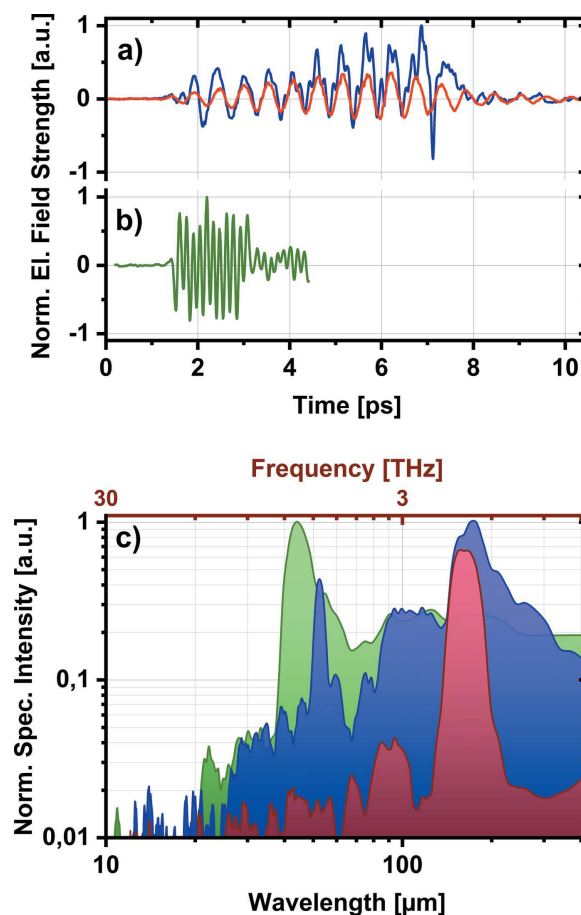

Figure 5
THz pulse waveforms measured by arrival-time-sorted time domain spectroscopy (TDS). (a) The THz pulse produced by the undulator set at the nominal wavelength of 155 µm (1.93 THz). The unfiltered temporal profile is shown by the blue line and the filtered by the red line, with 155 µm (1.93 THz) bandpass filter (15% bandwidth). (b) The unfiltered THz pulse at 43 µm (7 THz) (green line). (c) The corresponding THz pulse spectra.

It is worth noting that the EOSD scheme can be used as a THz arrival-time detection tool in other experiments. A recent application evaluated the timing jitter between two electron bunches with 21 ns delay timed for temporal overlap of THz and XUV pulses at the experimental end-station at BL3 (Zapolnova *et al.*, 2018).

2.3. THz beam profile

Knowledge of the transverse THz beam profile is important as it allows precise determination of the fluence (and the peak field) on the sample, as well as optimal optical design to maximize the beam transmission in the experiment. We model the THz source and the radiation transport using the *SRW* software package (Chubar & Elleaume, 1998) and observe the strong interference effects between undulator and dump magnet radiation (edge and bending radiation) at FLASH (Asgekar *et al.*, 2014).

An example of the measured THz beam profile from the dump magnet, with the THz undulator switched off, is shown in Fig. 6(*a*). An example of the THz undulator beam tuned to 88 μm (3.4 THz) is shown in Fig. 6(*b*). The beams have been imaged in the THz diagnostics hutch so that they image the plane approximately 10 m downstream of the radiation source. We perform 2D raster scanning of the beams. As a detector we employ an amplified pyroelectric detector (LME-501 from InfraTec). Both measurements have been performed with 30 μm long-pass THz spectral filter. The profiles have been reproduced by *SRW* calculation, whereby the integration of the output power was performed over the 30–300 μm

(1–10 THz) spectral range to account for the filtering, and the form factor of a 50 fs RMS long electron bunch was used.

For the dump magnet, both the measurement and calculation render a half-moon-like structure that can be explained by interference of the edge radiation with the bending radiation from the dump magnet. For the THz undulator beam we observe slight asymmetry in the horizontal plane which can be explained by interference of the undulator and the dump magnet radiation (Asgekar *et al.*, 2014).

We focus both beams with an off-axis parabolic mirror of focal length 150 mm and measure the beam profile with a Pyrocam III camera from Ophir Photonics for the dump magnet and with a microbolometer camera for the undulator beam. The results are shown in Figs. 6(*c*) and 6(*d*), respectively. We observe a beam size of 600 μm FWHM for the dump magnet and 350 μm FWHM for the undulator beam.

Moreover, we follow the THz undulator beam profile evolution, by wavefront propagation in *SRW*. The undulator radiation wavelength is set to 160 μm (1.87 THz). For an experimental confirmation, we measure the beam profile in the THz diagnostics hutch at five different positions along the beam path [see Fig. 7(*a*)], using the knife-edge technique. Zero
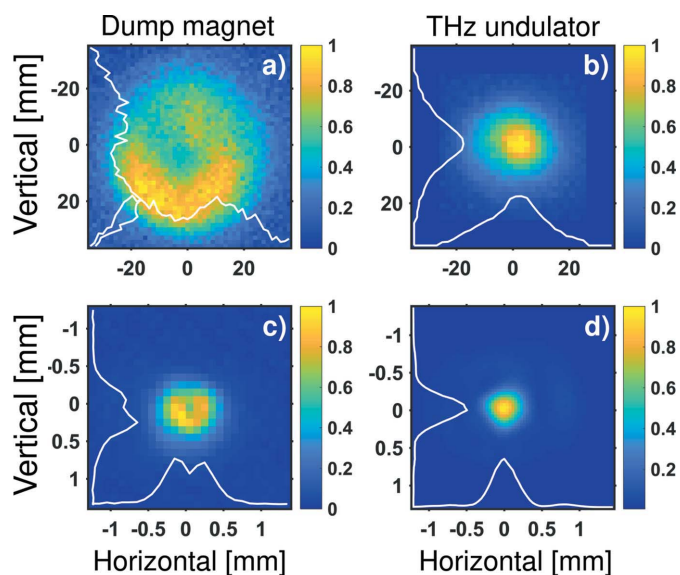
Figure 6
(Top) THz transverse beam profiles at FLASH. (*a*) Dump magnet (the THz undulator is off), and (*b*) THz undulator tuned to 88 μm (3.4 THz), unfocused beam profiles measured in the THz hutch; beam position imaged 10 m from the virtual source. Note that the undulator profile is padded with zeros to fill in the same image size. (Bottom) The same beams focused. (*c*) Dump magnet beam (600 μm FWHM), and (*d*) THz undulator beam (350 μm FWHM).
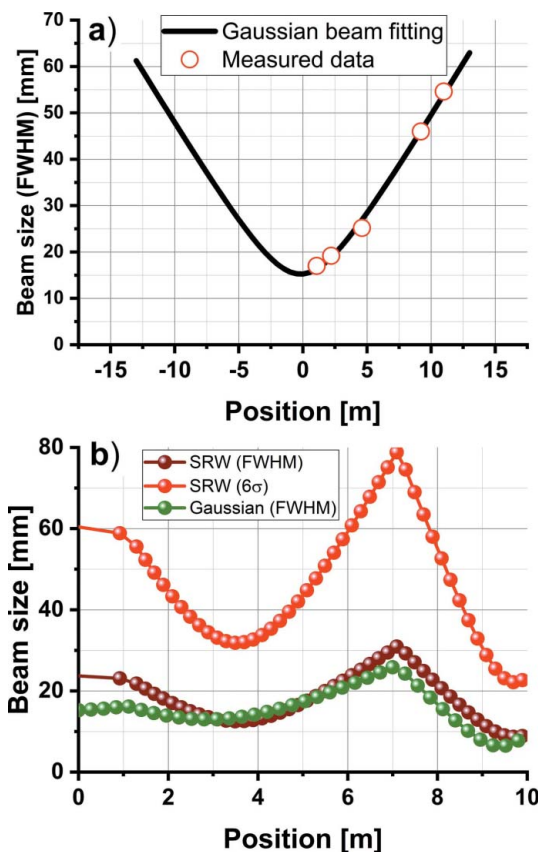
Figure 7
THz undulator beam size at 160 μm (1.87 THz) and its propagation. (*a*) Beam size measured at five different locations along the beam path (red circles) fitted by a Gaussian beam propagation. (*b*) THz beam propagation over the 10 m path, with the focusing mirrors inserted at the 1 m and 7 m position marks. The THz beam was approximated by fitted Gaussian beam (FWHM) (green curve) and calculated from the source by *SRW* (FWHM) (brown curve) and 6σ (red curve).

position denotes the THz beamline window at which the beam is extracted into the THz diagnostics station. We assume a Gaussian beam profile and obtain the beam parameters by fitting. The plot in Fig. 7(*b*) compares the beam size evolution (FWHM) calculated by *SRW* (brown curve) with the approximated Gaussian beam propagation (ABCD matrix formalism), fitted from the measured data (green curve), for the last 10 m of the THz beamline transport. Two toroidal mirrors with focal lengths of 3.8 m and 1.8 m are inserted at the 1 m and 7 m position marks, respectively. In this particular example, the goal was to couple the THz beam into an experimental chamber through a 25 mm aperture, located at the 10 m position mark, with highest possible transmission. The red curve depicts the THz beam size at the equivalent of 6σ (or 99.7% beam energy), and at the 10 m position mark we achieve the desired sub-25 mm beam size. We observe a reasonable agreement between these two numerical models, with the big advantage of the Gaussian beam propagation providing very fast and efficient evaluation of the beam sizes in the optical system.

2.4. THz spectrum measurement

For a quick THz spectral characterization, when temporal pulse structure is not necessary, we have developed the variation of the Fourier transform infrared (FTIR) spectrometer based on a reflective lamellar grating. Unlike the most commonly used Michelson interferometer (based on amplitude division), the reflective lamellar grating interferometer (Richards, 1964; Bell, 1972) divides the wavefront spatially. Because of this, the reflective lamellar grating design has a key advantage: a high (close to 100%) and smooth efficiency response (*e.g.* typical Fabry–Perot interferences that plague Michelson interferometers are absent). A comparison of the efficiency of the lamellar grating and the Michelson interferometer can be found in Fig. 3 of Richards (1964). As a side note, owing to a large spectral bandwidth, the lamellar gratings have found application in extreme ultraviolet (XUV) spectroscopy and metrology (Gebert *et al.*, 2014; Usenko *et al.*, 2017).

As shown in Fig. 8, the lamellar grating spectrometer consists of two interleaved gratings, manufactured from a 100 mm-diameter gold-coated copper mirror. One is fixed and the other is mounted on the motorized stage responsible for introducing the optical delay between the split beams. For detection a pyroelectric detector (LME-501 from InfraTec) with a 2 mm × 2 mm chip size was used.

The THz beam is collimated in a way that uniformly illuminates the gratings. The period of the grating (h = 2 mm) is chosen to match the spectral range of the THz sources at FLASH. The long-wavelength limit (Bell, 1972) for lamellar gratings is $\lambda_{max} < h/2$, which is 1 mm (corresponding to
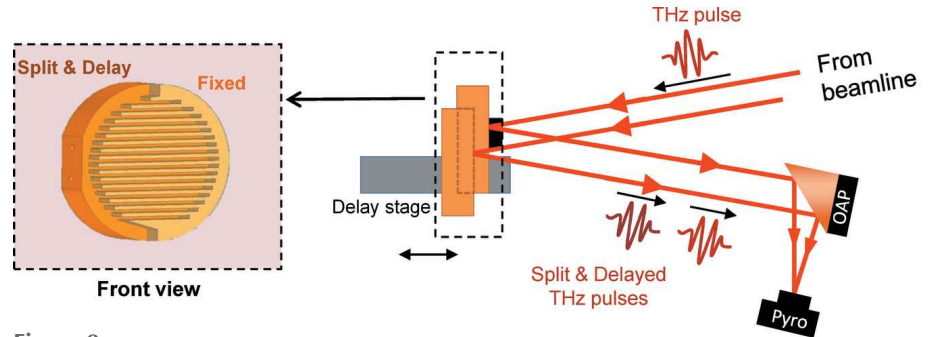

Figure 8
Scheme of the lamellar grating interferometer. OAP: off-axis parabolic mirror.

0.3 THz) in our case. For wavelengths longer than λ_{max}, a cavity effect starts decreasing the modulation depth of the THz waves, which are polarized parallel to the fringes. The high-frequency limit for this geometry is 30 µm (corresponding to 10 THz), which is determined by diffraction theory and depends on the geometry of the device (Strong & Vanasse, 1960; Naftaly *et al.*, 2008; Ferhanoglu *et al.*, 2009): $\lambda_{min} = hs/f$, where f = 130 mm is the focal length of the parabolic mirror and s = 2 mm is the width of the exit slit of the detector (defined by the detector effective aperture).

An example of the measured interferogram and the calculated spectrum is shown in Fig. 9. The THz pulse was generated by the edge radiation and filtered by a 215 µm (1.4 THz) bandpass filter. The fluctuations of the shot-to-shot THz pulse energy at FLASH can be as high as 20% RMS, depending on the FLASH accelerator settings. We split a small portion of the beam for a reference measurement that is then used to
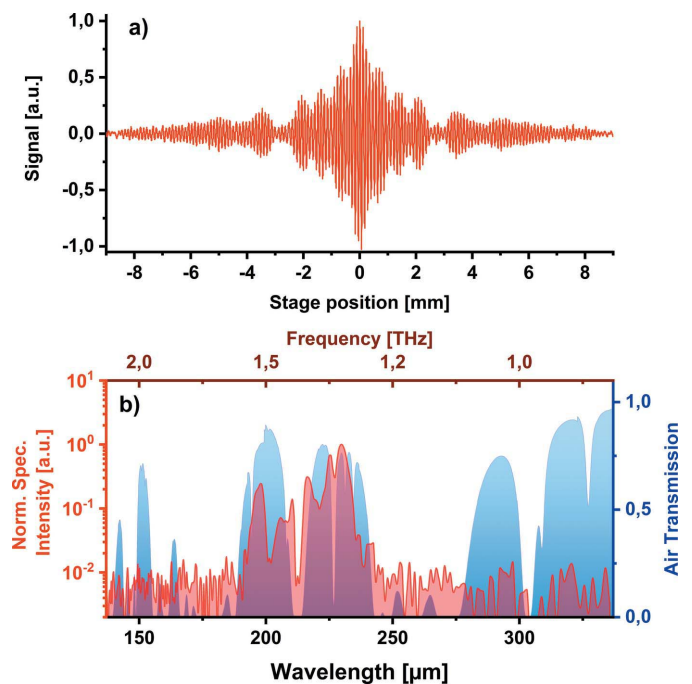

Figure 9
FTIR measurement for THz edge radiation with 215 µm (1.4 THz) THz bandpass filter. (*a*) Double-sided interferogram. (*b*) Respective spectrum (red curve) and air transmission with water vapor (in blue) show the strong absorption lines in this spectral range.

normalize the measured interferogram on a single-shot basis. The normalized interferogram in Fig. 9(a) was obtained during 20 min of scanning at 10 Hz repetition rate (12000 shots). Fig. 9(b) shows the normalized spectrum, obtained by taking a Fourier transform of the measured interferogram. We observe the spectral content as expected from the filter response with a signal-to-noise ratio exceeding 100.

Measurement has been performed in ambient air and we observe a strong modulation from the water vapor absorption lines. We are currently upgrading it to an all-in-vacuum spectrometer.

3. Conclusion

We have presented a range of THz diagnostic tools developed for THz/XUV pump–probe experiments at FLASH1, DESY. The THz pulse energy is an important parameter for optimization of the FLASH accelerator, and it reaches values from tens of µJ up to 150 µJ. The upgrade of a currently used radiometer to an online monitor is in progress. The THz temporal profile can be measured with 10 fs timing resolution and covers the spectral range from 37 to 3000 µm (0.1 to 8 THz). The ongoing development of this technique will explore the use of different EOS crystals to extend the measured bandwidth to shorter wavelengths, GaSe (Kübler et al., 2005) and SiC (Naftaly et al., 2016) being good candidates that should allow THz detection in the 10–40 THz and 0.1–15 THz spectral windows, respectively. To fully exploit the high THz pulse energies at FLASH, we are upgrading the single-shot EOSD THz detection technique to one via tilted laser pulse front (Teo et al., 2015). This technique is free from the spectral distortions that plague EOSD (Jamison et al., 2008) and allows for the full bandwidth of the pulse to be retrieved (limited only by the EOS crystal). The measurements of the transversal THz beam profile are used for the design of the beam transfer line and calibration of the peak field and intensity in the experiment. A broadband FTIR spectrometer, covering the spectral range 30–1000 µm (0.3–10 THz), based on a reflective lamellar grating is developed for spectral measurements. It will be permanently installed inside the THz beamline vacuum environment for distortion-free THz spectrum measurements, enabling quick and robust spectral studies [e.g. suitable for THz shaping by emerging THz meta-materials (Yen et al., 2004; Monticone & Alù, 2017; Stojanović et al., 2018; Polley et al., 2018)].

References

Asgekar, V., Geloni, G., Kocharyan, V., Stojanovic, N., Michel, P. & Gensch, M. (2014). *Infrared Phys. Technol.* **64**, 26–32.

Azima, A., Düsterer, S., Radcliffe, P., Redlin, H., Stojanovic, N., Li, W., Schlarb, H., Feldhaus, J., Cubaynes, D., Meyer, M., Dardis, J., Hayden, P., Hough, P., Richardson, V., Kennedy, E. T. & Costello, J. T. (2009). *Appl. Phys. Lett.* **94**, 144102.

Bell, R. J. (1972). *Introductory Fourier Transform Infrared Spectroscopy.* New York: Academic Press.

Buzzi, M., Först, M., Mankowsky, R. & Cavalleri, A. (2018). *Nat. Rev. Mater.* **3**, 299–311.

Chubar, O. & Elleaume, P. (1998). *Proceedings of the Sixth European Particle Accelerator Conference (EPAC'98)*, 22–26 June 1998, Stockholm, Sweden, pp. 1177–1179.

Faatz, B., Plönjes, E., Ackermann, S., Agababyan, A., Asgekar, V., Ayvazyan, V., Baark, S., Baboi, N., Balandin, V., Bargen, N., Bican, Y., Bilani, O., Bödewadt, J., Böhnert, M., Böspflug, R., Bonfigt, S., Bolz, H., Borges, F., Borkenhagen, O., Brachmanski, M., Braune, M., Brinkmann, A., Brovko, O., Bruns, T., Castro, P., Chen, J., Czwalinna, M. K., Damker, H., Decking, W., Degenhardt, M., Delfs, A., Delfs, T., Deng, H., Dressel, M., Duhme, H., Düsterer, S., Eckoldt, H., Eislage, A., Felber, M., Feldhaus, J., Gessler, P., Gibau, M., Golubeva, N., Golz, T., Gonschior, J., Grebentsov, A., Grecki, M., Grün, C., Grunewald, S., Hacker, K., Hänisch, L., Hage, A., Hans, T., Hass, E., Hauberg, A., Hensler, O., Hesse, M., Heuck, K., Hidvegi, A., Holz, M., Honkavaara, K., Höppner, H., Ignatenko, A., Jäger, J., Jastrow, U., Kammering, R., Karstensen, S., Kaukher, A., Kay, H., Keil, B., Klose, K., Kocharyan, V., Köpke, M., Körfer, M., Kook, W., Krause, B., Krebs, O., Kreis, S., Krivan, F., Kuhlmann, J., Kuhlmann, M., Kube, G., Laarmann, T., Lechner, C., Lederer, S., Leuschner, A., Liebertz, D., Liebing, J., Liedtke, A., Lilje, L., Limberg, T., Lipka, D., Liu, B., Lorbeer, B., Ludwig, K., Mahn, H., Marinkovic, G., Martens, C., Marutzky, F., Maslocv, M., Meissner, D., Mildner, N., Miltchev, V., Molnar, S., Mross, D., Müller, F., Neumann, R., Neumann, P., Nölle, D., Obier, F., Pelzer, M., Peters, H., Petersen, K., Petrosyan, A., Petrosyan, G., Petrosyan, L., Petrosyan, V., Petrov, A., Pfeiffer, S., Piotrowski, A., Pisarov, Z., Plath, T., Pototzki, P., Prandolini, M. J., Prenting, J., Priebe, G., Racky, B., Ramm, T., Rehlich, K., Riedel, R., Roggli, M., Röhling, M., Rönsch-Schulenburg, J., Rossbach, J., Rybnikov, V., Schäfer, J., Schaffran, J., Schlarb, H., Schlesselmann, G., Schlösser, M., Schmid, P., Schmidt, C., Schmidt-Föhre, F., Schmitz, M., Schneidmiller, E., Schöps, A., Scholz, M., Schreiber, S., Schütt, K., Schütz, U., Schulte-Schrepping, H., Schulz, M., Shabunov, A., Smirnov, P., Sombrowski, E., Sorokin, A., Sparr, B., Spengler, J., Staack, M., Stadler, M., Stechmann, C., Steffen, B., Stojanovic, N., Sychev, V., Syresin, E., Tanikawa, T., Tavella, F., Tesch, N., Tiedtke, K., Tischer, M., Treusch, R., Tripathi, S., Vagin, P., Vetrov, P., Vilcins, S., Vogt, M., Wagner, A. Z., Wamsat, T., Weddig, H., Weichert, G., Weigelt, H., Wentowski, N., Wiebers, C., Wilksen, T., Willner, A., Wittenburg, K., Wohlenberg, T., Wortmann, J., Wurth, W., Yurkov, M., Zagorodnov, I. & Zemella, J. (2016). *New J. Phys.* **18**, 062002.

Ferhanoglu, O., Seren, H. R., Lüttjohann, S. & Urey, H. (2009). *Opt. Express*, **17**, 21289–21301.

Frühling, U., Wieland, M., Gensch, M., Gebert, T., Schütte, B., Krikunova, M., Kalms, R., Budzyn, F., Grimm, O., Rossbach, L., Plönjes, E. & Drescher, M. (2009). *Nat. Photon.* **3**, 523.

Gebert, T., Rompotis, D., Wieland, M., Karimi, F., Azima, A. & Drescher, M. (2014). *New J. Phys.* **16**, 073047.

Geloni, G., Kocharyan, V., Saldin, E., Schneidmiller, E. & Yurkov, M. (2009a). *Nucl. Instrum. Methods Phys. Res. A*, **605**, 409–429.

Geloni, G., Kocharyan, V., Saldin, E., Schneidmiller, E. & Yurkov, M. (2009b). *Nucl. Instrum. Methods Phys. Res. A*, **607**, 470–487.

Gensch, M., Bittner, L., Chesnov, A., Delsim-Hashemi, H., Drescher, M., Faatz, B., Feldhaus, J., Fruehling, U., Geloni, G., Gerth, C., Grimm, O., Hahn, U., Hesse, M., Kapitzki, S., Kocharyan, V., Kozlov, O., Matyushevsky, E., Morozov, N., Petrov, D., Ploenjes, E., Roehling, M., Rossbach, J., Saldin, E. L., Schmidt, B., Schmueser, P., Schneidmiller, E. A., Syresin, E., Willner, A. & Yurkov, M. V. (2008). *Infrared Phys. Technol.* **51**, 423–425.

Golz, T. (2018). PhD thesis, Hamburg University, Germany.

Green, B., Kovalev, S., Asgekar, V., Geloni, G., Lehnert, U., Golz, T., Kuntzsch, M., Bauer, C., Hauser, J., Voigtlaender, J., Wustmann, B., Koesterke, I., Schwarz, M., Freitag, M., Arnold, A., Teichert, J., Justus, M., Seidel, W., Ilgner, C., Awari, N., Nicoletti, D., Kaiser, S., Laplace, Y., Rajasekaran, S., Zhang, L., Winnerl, S., Schneider, H., Schay, G., Lorincz, I., Rauscher, A. A., Radu, I., Mährlein, S., Kim, T. H., Lee, J. S., Kampfrath, T., Wall, S., Heberle, J., Malnasi-Csizmadia, A., Steiger, A., Müller, A. S., Helm, M., Schramm, U., Cowan, T., Michel, P., Cavalleri, A., Fisher, A. S., Stojanovic, N. & Gensch, M. (2016). *Sci. Rep.* **6**, 22256.

Grimm, O., Morozov, N., Chesnov, A., Holler, Y., Matushevsky, E., Petrov, D., Rossbach, J., Syresin, E. & Yurkov, M. (2010). *Nucl. Instrum. Methods Phys. Res. A*, **615**, 105–113.

Jamison, S., Gillespie, W. & Phillips, P. (2008). *Signal*, **1**, 2.

Jiang, Z. & Zhang, X.-C. (1998). *Appl. Phys. Lett.* **72**, 1945–1947.

Kampfrath, T., Tanaka, K. & Nelson, K. A. (2013). *Nat. Photon.* **7**, 680.

Kovalev, S., Green, B., Golz, T., Maehrlein, S., Stojanovic, N., Fisher, A. S., Kampfrath, T. & Gensch, M. (2017). *Struct. Dyn.* **4**, 024301.

Kübler, C., Huber, R. & Leitenstorfer, A. (2005). *Semicond. Sci. Technol.* **20**, S128–S133.

Monticone, F. & Alù, A. (2017). *Rep. Prog. Phys.* **80**, 036401.

Naftaly, M., Dean, P., Miles, R. E., Fletcher, J. R. & Malcoci, A. (2008). *Quantum Electron.* **14**, 443–448.

Naftaly, M., Molloy, J., Magnusson, B., Andreev, Y. & Lanskii, G. (2016). *Opt. Express*, **24**, 2590–2595.

Nodvick, J. S. & Saxon, D. S. (1954). *Phys. Rev.* **96**, 180–184.

Oelze, T., Schütte, B., Müller, M., Müller, J. P., Wieland, M., Frühling, U., Drescher, M., Al-Shemmary, A., Golz, T., Stojanovic, N. & Krikunova, M. (2017). *Sci. Rep.* **7**, 40736.

Polley, D., Hagström, N. Z., Schmising, C. K., Eisebitt, S. & Bonetti, S. (2018). *J. Phys. B At. Mol. Opt. Phys.* **51**, 224001.

Radu, I. (2019). In preparation.

Redlin, H., Al-Shemmary, A., Azima, A., Stojanovic, N., Tavella, F., Will, I. & Düsterer, S. (2011). *Nucl. Instrum. Methods Phys. Res. A*, **635**, S88–S93.

Richards, P. L. (1964). *J. Opt. Soc. Am.* **54**, 1474–1484.

Schmid, G., Schnorr, K., Augustin, S., Meister, S., Lindenblatt, H., Trost, F., Liu, Y., Stojanovic, N., Al-Shemmary, A., Golz, T., Treusch, R., Gensch, M., Kübel, M., Foucar, L., Rudenko, A., Ullrich, J., Schröter, C. D., Pfeifer, T. & Moshammer, R. (2019). *Phys. Rev. Lett.* **122**, 073001.

Schmuttenmaer, C. A. (2004). *Chem. Rev.* **104**, 1759–1779.

Schulz, S., Grguraš, I., Behrens, C., Bromberger, H., Costello, J., Czwalinna, M., Felber, M., Hoffmann, M., Ilchen, M., Liu, H., Mazza, T., Meyer, M., Pfeiffer, S., Prędki, P., Schefer, S., Schmidt, C., Wegner, U., Schlarb, H. & Cavalieri, A. L. (2015). *Nat. Commun.* **6**, 5938.

Schütte, B., Bauch, S., Frühling, U., Wieland, M., Gensch, M., Plönjes, E., Gaumnitz, T., Azima, A., Bonitz, M. & Drescher, M. (2012). *Phys. Rev. Lett.* **108**, 253003.

Stojanović, D. B., Beličev, P. P., Gligorić, G. & Hadžievski, L. (2018). *J. Phys. D Appl. Phys.* **51**, 045106.

Stojanovic, N. & Drescher, M. (2013). *J. Phys. B At. Mol. Opt. Phys.* **46**, 192001.

Strong, J. & Vanasse, G. A. (1960). *J. Opt. Soc. Am.* **50**, 113–118.

Tavella, F., Stojanovic, N., Geloni, G. & Gensch, M. (2011). *Nat. Photon.*, **5**, 162.

Teo, S. M., Ofori-Okai, B. K., Werley, C. A. & Nelson, K. A. (2015). *Rev. Sci. Instrum.* **86**, 051301.

Tiedtke, K., Azima, A., von Bargen, N., Bittner, L., Bonfigt, S., Düsterer, S., Faatz, B., Frühling, U., Gensch, M., Gerth, C., Guerassimova, N., Hahn, U., Hans, T., Hesse, M., Honkavaar, K., Jastrow, U., Juranic, P., Kapitzki, S., Keitel, B., Kracht, T., Kuhlmann, M., Li, W. B., Martins, M., Núñez, T., Plönjes, E., Redlin, H., Saldin, E. L., Schneidmiller, E. A., Schneider, J. R., Schreiber, S., Stojanovic, N., Tavella, F., Toleikis, S., Treusch, R., Weigelt, H., Wellhöfer, M., Wabnitz, H., Yurkov, M. V. & Feldhaus, J. (2009). *New J. Phys.* **11**, 023029.

Usenko, S., Przystawik, A., Jakob, M. A., Lazzarino, L. L., Brenner, G., Toleikis, S., Haunhorst, C., Kip, D. & Laarmann, T. (2017). *Nat. Commun.* **8**, 15626.

Waltar, K., Haase, J., Lucchini, M., van Bokhoven, J. A., Hengsberger, M., Osterwalder, J. & Castiglioni, L. (2018). *Opt. Express*, **26**, 8364–8374.

Wu, Q. & Zhang, X. (1995). *Appl. Phys. Lett.* **67**, 3523–3525.

Yen, T.-J., Padilla, W., Fang, N., Vier, D., Smith, D., Pendry, J., Basov, D. & Zhang, X. (2004). *Science*, **303**, 1494–1496.

Zapolnova, E., Golz, T., Pan, R., Klose, K., Schreiber, S. & Stojanovic, N. (2018). *J. Synchrotron Rad.* **25**, 39–43.

FULL ARTICLE

Naturally safe: Cellular noise for document security

Danica Pavlović[1] | Mihailo D. Rabasović[1] | Aleksandar J. Krmpot[1] | Vladimir Lazović[1] | Srećko Čurčić[2] | Dejan V. Stojanović[3] | Branislav Jelenković[1] | Wang Zhang[4] | Di Zhang[4] | Nenad Vukmirović[1] | Dimitrije Stepanenko[1] | Branko Kolarić[1,5] [ID] | Dejan V. Pantelić[1]*

[1]Institute of Physics, University of Belgrade, Belgrade, Serbia

[2]Institute of Zoology, University of Belgrade—Faculty of Biology, Belgrade, Serbia

[3]Institute of Lowland Forestry and Environment, University of Novi Sad, Novi Sad, Serbia

[4]State Key Lab of Metal Matrix Composite, Shanghai Jiao Tong University, Shanghai, China

[5]MNM Group, Department of Physics, UMONS, Mons, Belgium

Correspondence
Dejan V. Pantelić, Institute of Physics, University of Belgrade, Photonics Center, Pregrevica 118, 11080 Zemun, Belgrade, Serbia.
Email: pantelic@ipb.ac.rs

Abstract
Modern document protection relies on the simultaneous combination of many optical features with micron and submicron structures, whose complexity is the main obstacle for unauthorized copying. In that sense, documents are best protected by the diffractive optical elements generated lithographically and mass-produced by embossing. The problem is that the resulting security elements are identical, facilitating mass-production of both original and counterfeited documents. Here, we prove that each butterfly wing-scale is structurally and optically unique and can be used as an inimitable optical memory tag and applied for document security. Wing-scales, exhibiting angular variability of their color, were laser-cut and bleached to imprint cryptographic information of an authorized issuer. The resulting optical memory tag is extremely durable, as verified by several century-old insect specimens still retaining their coloration. The described technique is simple, amenable to mass-production, low cost and easy to integrate within the existing security infrastructure.

KEYWORDS
biophotonics, complexity, iridescence, optical document security, variability
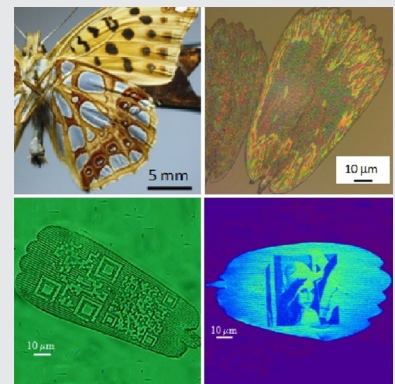
1 | INTRODUCTION

Insects have been used more than any other living creatures as a blueprint for design of novel devices. Butterflies and moths (order: Lepidoptera) are particularly inspiring, due to vast number of species (nearly 180 000) [1] and peculiar

optical properties of their wings covered with large number (500–1000/mm²) of tiny, overlapping scales [2] (see section 1 of Appendix S1 for a short description of their properties). Some of them are structurally colored [3] that is, produce colors by interference, diffraction and scattering, rather than pigments. This is due to complex, regular or

irregular, micro/nanostructures, which can be classified in several groups according to their morphology [4]. Most frequently, iridescence (characterized by directionally dependent coloration [3]) can be observed.

Back into the XVIII century, Benjamin Franklin came up with an idea to reproduce the complexity of natural structures for document protection. He printed venation patterns of plant leaves on dollar bills to prevent counterfeiting [5]. Nowadays, his method was superseded by artificial security components, such as optically variable devices (OVDs) [6]. Diffractive optical elements (DOEs) are commonly exploited for the purpose, due to their, inherently complex microstructures, recognizable optical pattern and capability for mass-production by embossing. There is a significant drawback: for the specific type of document, all embossed copies of DOEs are identical. If a fake DOE is manufactured, counterfeited document can be made in large quantities, too. For that reason, an important goal is to invent a device which will provide unique and individual protection for each document. Protective elements should be highly complex, unique, difficult to reverse engineer and imitate. In the relevant literature, such objects are called physical one-way functions and can be realized by embedding randomly dispersed plastic, micron-sized spheres in a transparent medium and observing mesoscopic light scattering [7]. As another example, we mention using a randomized pattern of scattering from paper-based substrates [8].

Imprints of naturally occurring structures were proposed as security elements by Hamm-Dubischar [9], Biermann and Rauhe [10], and Rauhe [11], who presented the idea of document protection using biomineralized shells of radiolarians and diatoms. The protection is based on the structural complexity of their shells. The main problem is that optical effects are not particularly conspicuous, and the complexity can be assessed only at the morphological level, using scanning electron microscopy (SEM). Another problem is that structural variations among individuals of the same species seem to be small.

Whichever security element is used, it must be integrated in a security system relying on three inspection lines [6]: the first line is overt and can be visually inspected by anyone; the second is semi-covert and uses machine inspection; while the third one is covert and relies on forensic inspection with highly specialized equipment.

Here, we analyze the structural complexity, randomness, variability and uniqueness of the optical pattern of iridescent butterfly wing scales. We aim to establish their usefulness as inimitable OVDs for individualized, covert and overt, optical document security. Additionally, we investigate wing-scales as a memory medium for inscription of additional cryptographic information.

2 | STRUCTURE AND IRIDESCENCE OF *ISSORIA LATHONIA* BUTTERFLY WING-SCALES

In this section, we analyze morphological and optical features of scales belonging to the underside silver wing-patches of the Queen of Spain Fritillary, *Issoria lathonia* (Linnaeus, 1758), (see Figure 1A and section 2 of Appendix S1 for a short description of the butterfly's life history). This particular species was studied for the characteristic coloration of individual wing-scales, consisting of red, green and bluish spots randomly dispersed along a grating-like structure (see reflection microscope image in Figure 1B,C). The resulting silver color is produced by the local, additive spectral mixing [12].

Field-emission gun scanning electron microscope (FEGSEM) images reveal detailed structure of the scale's upper lamina (UL in Figure 1D). It consists of lamellar longitudinal ridges (R) regularly separated by a distance of 1.5 μm. There is, also, a fish-bone-shaped sub-wavelength grating (SW) with period of 150 nm, radiating from ridges. The interior of the scale is hollow, filled only with nano-pillars, separating UL and lower lamina (LL).

Nonlinear optical microscopy was used to analyze three-dimensional (3D) structure of wing-scales using two-photon excited fluorescence (TPEF) of chitin. Nonlinear microscope was constructed in-house [13] (see Appendix S1 for details) and used to reveal that the wing scales have irregular, wavy shape (see Figure 1E). This significantly contributes to variability of the resulting optical pattern, together with variation of the thicknesses of upper and lower laminae and their mutual distance.

We have found that the individual wing scales are iridescent, that is, the color pattern strongly depends on illumination and observation directions. The pattern has maximum brightness and sharpness for orthogonal illumination, directly through the microscope objective (resulting in an image like in Figure 1C).

3 | VARIABILITY OF OPTICAL PATTERN AND UNIQUENESS OF BUTTERFLY WING-SCALES

In this section, we will establish a connection between the wing scale morphology and the resulting reflection spectrum. To do that, we have to make a numerical model, enabling us to calculate the reflection spectrum of a single wing scale, removed from the wing and attached to a transparent substrate (as in Figure 1C). For simplicity, each scale is represented by two, wavy thin plates, separated by the layer of air. To approximate waviness each scale is divided into a number of vertical sections with different positions
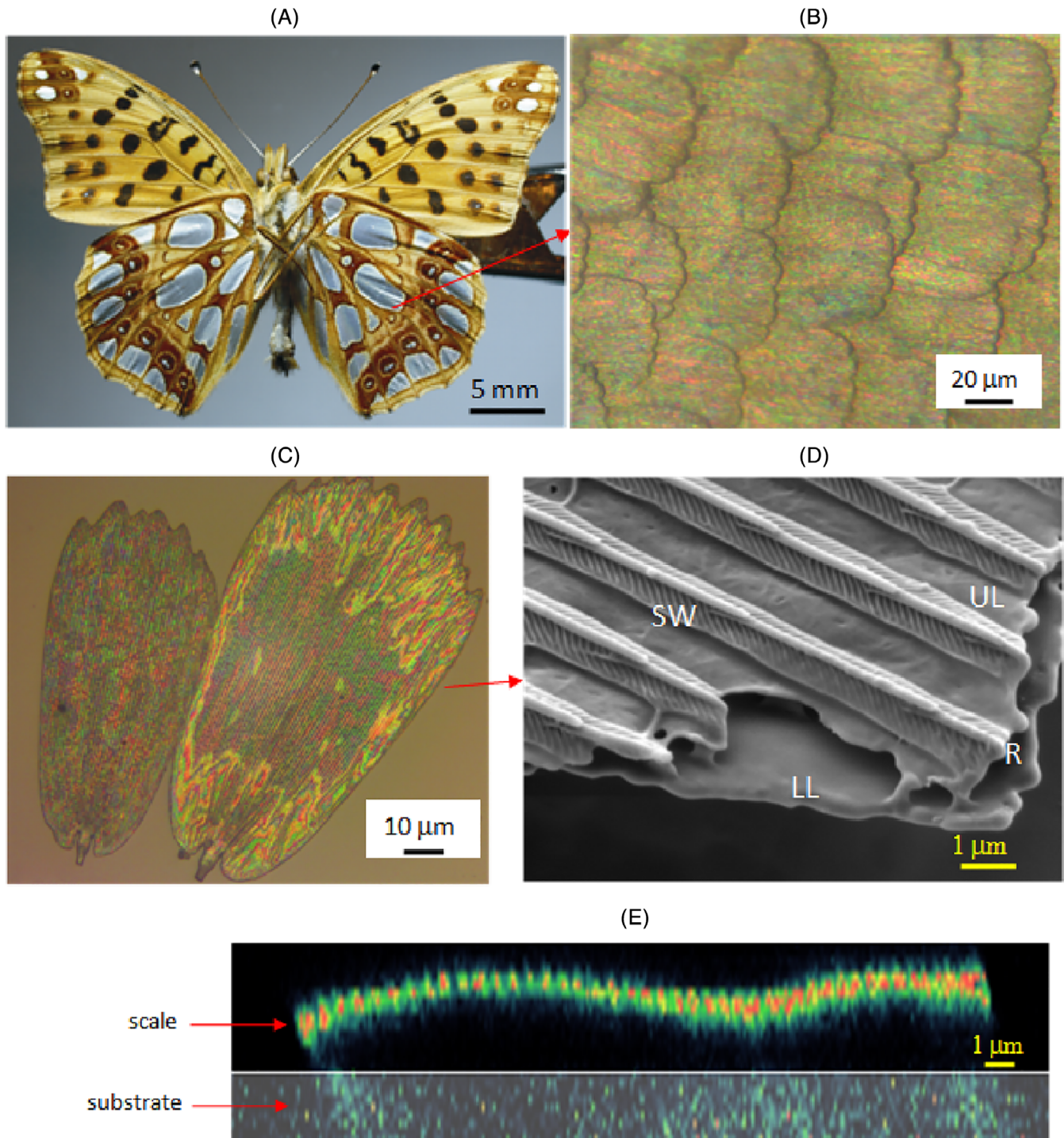
FIGURE 1 A, Ventral side of *Issoria lathonia* butterfly. B, Reflection microscope (10×, 0.25 NA) image of wing scales from the silver patch. C, Reflection microscope image (20×, 0.4 NA) image of two isolated wing-scales, removed from the wing of *I. lathonia*. D Scanning electron microscope image of the *I. lathonia* wing scale. LL and UL are lower and upper lamina, respectively, R is a ridge, while SW is a, fishbone-shaped, sub-wavelength grating. E, Wavy cross-section of butterfly wing scale (as recorded on a nonlinear optical scanning microscope)

and thicknesses of layers (Figure 2A). Each section contains two layers of chitin, the first of which was regarded as a sub-wavelength scattering surface, due to its irregularity and presence of the subwavelength grating (Figure 1D). Both layers are separated from the glass substrate by an additional air layer.

Reflection spectrum of each section was calculated using a transfer matrix method, modified to include the effects of
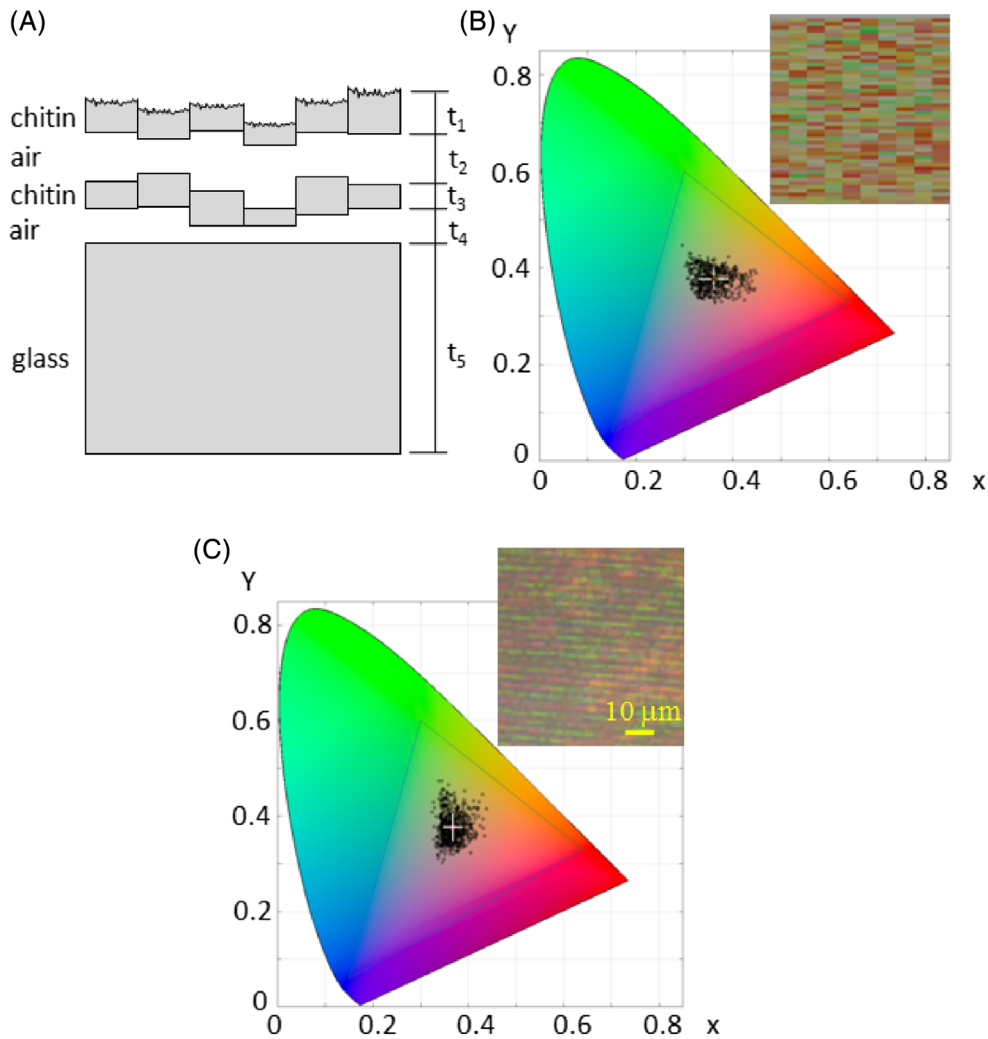
FIGURE 2 A, A theoretical model of a wing scale on the glass substrate. B, Color coordinates of a modeled pattern are presented in a CIE 1931 diagram, together with the color pattern in the inset. C, Color coordinates of *Issoria lathonia* pattern are presented in a CIE 1931 diagram. A section of a *I. lathonia* wing scale pattern, used to calculate color coordinates, is presented in the inset. Crosses in B and C represent average color value and their lengths indicate SDs in *x*- and *y*-directions

scattering [14]. Layer thicknesses (t_1, t_2, ..., t_5 in Figure 2A) and their corresponding refractive indices were the parameters of the model, as well as the root mean square roughness (RMS) of the surfaces.

To simulate the wing scale as a whole, the same calculation was performed for each section. The starting point of our simulation was the layer thicknesses estimated from Figures 1D,E) (~100 nm chitin, ~1000 nm air layer thickness—see section 3 of Appendix S1 for the complete list of parameter values). Layer thicknesses were stochastically varied (according to normal distribution) with pre-defined SD $\sigma = 15$ nm. Following the calculation of spectrum for each section, *xyY* color coordinates were calculated. They were presented in a CIE 1931 diagram (black dots in Figure 2B), which was designed to closely match human color perception (through three color-matching functions) [15]. It is, also, a useful tool to represent RGB values of color-camera images recorded through this research.

Calculated colors are, also, represented as a pattern of rectangular colored patches (see inset in Figure 2B). For

comparison, color coordinates of experimentally recorded pattern (inset in Figure 2C) were also computed and presented in CIE 1931 diagram (Figure 2C).

We were not able to obtain perfect match in CIE diagrams (Figures 2B,C), for the same reason which prevents a counterfeiter to forge a wing scale—complexity of the problem. However, we were able to match the position of the mean color coordinate (small white crosses in CIE diagrams) of theoretical and experimental image. The shape of the color scattering distribution is different, but the SDs are similar.

The most important result is that the variation of layer thicknesses by only ±15 nm leads to experimentally recorded variability of coloration. This means that one trying to copy the exact coloration pattern of the wing scale, has to maintain an extreme precision of manufacturing—at least one-tenth of the layer thickness variability (~1.5 nm). The task is well beyond practical limits of modern technology, and cellular noise precludes replication of identical wing-scales by natural means.

Wing-scales described above have a sufficient number of degrees of freedom (in terms of layer thicknesses and waviness) to enable significant variability. Here, we want to find how difficult would be to find two identical scales.

We first analyze the statistical properties of the wing-scales color patterns by decomposing an image into its RGB components and calculating two-dimensional (2D) autocorrelation function for each color channel separately—see details in section 4 of Appendix S1. It can be seen (Figure S1) that autocorrelation peak is asymmetrical, that is, its width along the wing-scale grating was estimated at 30 μm, while in the orthogonal direction it is 1.5 μm.

By taking into account that average dimensions of the scales are 50×100 μm, we can easily calculate that there are $[50/1.5] \times [100/30] = 33 \times 3 = 99$ (numbers were rounded to the nearest integer) statistically independent, colored patches. We can discriminate intensity of a single color channel in, at least, 10 discrete levels—easily achievable for any low-cost or mobile phone camera. In that case, we may estimate that there are, at least theoretically, 10^{99} wing-scales with different patterns per every channel. Thus, finding a scale exactly the same as another, previously chosen, one is impossible from any practical point of view.

Each wing-scale is a dead remnant of an individual cell and thus reflects intrinsic randomness of cellular development. This is a natural consequence of cellular noise [16], which is a well-established fact in biology, resulting in non-deterministic relation between genotype and phenotype. The important thing about butterfly wing scales is that they "freeze" the cellular noise, by leaving it in a state just before the cell died. Cellular noise cannot be switched-off and it is expected to be similar in all other butterfly species. In that sense, the similar level of randomness is expected on all wing-scales of all butterflies [17] including those of the *Issoria lathonia* species.

4 | OPTICAL DOCUMENT PROTECTION WITH WING SCALES

The main idea of this research is to use butterfly wing-scales as a natural, hologram-like, OVDs, permanently attached to a document (eg, a plastic credit card). In contrast to artificial OVDs, natural ones are unique (guaranteed by the cellular noise) and difficult to copy (due to their layered, micro- and nano-scale patterns).

We decided to use a near-field color pattern as a security feature of a document protection system and read it under the optical microscope. Practical inability to place a document at exactly the same position and orientation within the reading system requires shift- and rotation-invariant pattern recognition algorithm. We decided to use algorithm based

on Fourier-Mellin transform (FMT) [18] which fulfills the above requirements.

Nine *I. lathonia* wing-scales were attached to a glass substrate and their reflection microscope images were recorded at several positions and orientations (55 images in all). The recorded images were first decomposed into RGB components and the green one (G) was transformed using FMT. Correlations between corresponding FMT pairs were calculated and the corresponding statistical distribution is shown in Figure 3. The correlation coefficient, corresponding to the same wing-scale at displaced positions, had typical values around 0.4, while it never had values below 0.1. The most frequent values of correlation coefficient for two different wing-scales were around 0.02, and were never larger than 0.06. By placing validity threshold at 0.08, correct discrimination between wing scales is guaranteed.

To correct for accidental tilt or defocusing of the wing scale image, we have recorded images at 3 to 4, closely spaced, focal positions. Consequently, focus stacking algorithm was used (using Picolay free software) to extract well-focused parts in each recorded image and combine them in a single, sharp image.

In order to build a strong security system, malicious party has to be prevented from picking any butterfly wing-scale and attaching it to a document. This can be performed by making a document self-verifying by using a digital signature of the document issuer, within the public key infrastructure (PKI) system [19]. Here, we show that the necessary authentication information can be written on the wing-scale itself.

We used femtosecond laser-processing to additionally modify butterfly wing scales and exploit them as a write-
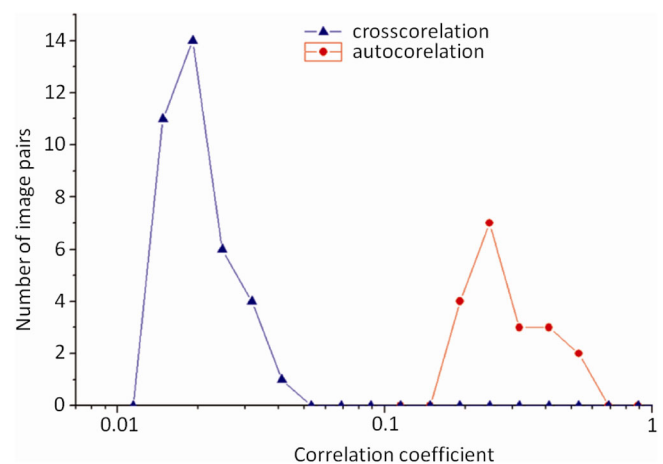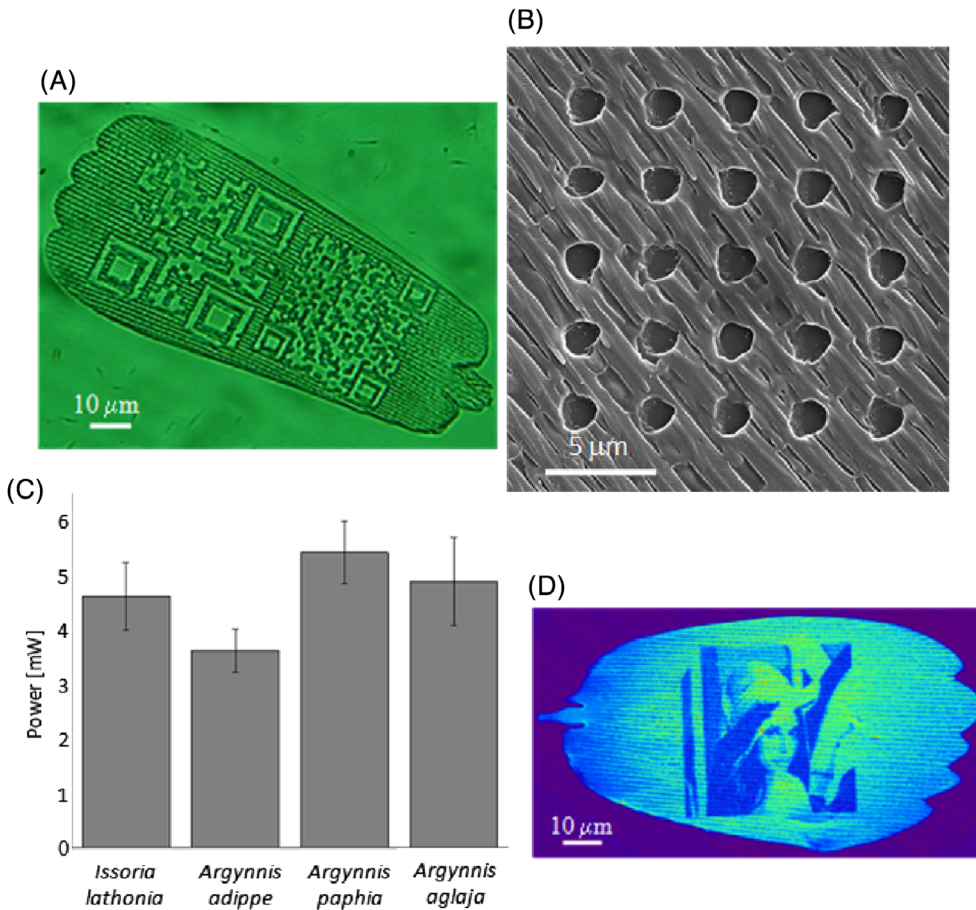

FIGURE 3 Cross- and auto-correlations of ensemble of 55 pairs of wing-scale images. Graph shows a number of image pairs vs the corresponding correlation coefficient. Maximum cross-correlation coefficient is at 0.02, while autocorrelation coefficient is always above 0.2

FIGURE 4
(A) Transmission microscope image of a femtosecond-laser-cut wing scale (QR-codes). (B) Array of holes on a *Issoria lathonia* wing-scale showing the minimum achievable diameter of a laser cut. (C) Thresholds for laser cutting of four butterfly species used throughout this research. (D) Selectively bleached wing scale with a Lena image observed by fluorescence modality of a nonlinear microscope

only memory. The software of a home-made nonlinear-microscope [13] was modified to enable vector and raster drawing of an arbitrary image (see section 5 of Appendix S1 for additional details). Depending on the average laser power, repetition rate and dwell time, wing scale can be cut (as in Figure 4A). Minimal diameter of a laser cut achieved throughout this research is 1.7 μm, as shown in Figure 4B. Damage threshold is 4.5 mW (using 40×1.3 NA microscope objective) and 8.0 mW (with 20×0.8 NA microscope objective). Three more butterfly species were analyzed in that respect, with similar damage thresholds (Figure 4C). In practice, we operated above threshold to enable reliable and repeatable laser-drawing. That is why we achieved the minimum cut width which is considerably above the lateral resolution of our femtosecond system [13]. Based on that and the average size of the wing-scale (~50×100 μm^2), we estimated the information capacity of a single scale at about 3000 bits, providing that the damaged spot is treated as binary 1, and undamaged as binary 0.

Here, we point out that each bit, written on the wing-scale, reduces the number of statistically independent patches. We will assume that one half of the wing-scale surface is laser processed (reducing the original wing-scale area of $50 \times 100 = 5000$ μm^2 to approximately $35 \times 70 = 2450$ μm^2). That leaves approximately $[35/1.5] \times [70/30] = 23 \times 2 = 46$ colored patches

(numbers are, again, rounded to the nearest integer). Thus, as in the previous section, we may estimate the number of different wing scales at 10^{46} (per every RGB channel), each one being protected by 1500 bits of additional information.

By reducing the laser power below the damage threshold, we were able to bleach the autofluorescence of the wing-scale and use it to inscribe covert information (Figures 4D) as a gray level image.

5 | DISCUSSION AND CONCLUSIONS

While speaking of document protection, an important question immediately comes to mind: how difficult it is to counterfeit wing-scale? Forgeries can be produced by either (a) imitating the structure or (b) imitating the corresponding optical effect with another, possibly simpler, structure. The first approach is based on "reverse-engineering" and manufacturing of identical protective element structure, while the second one is based on imitating the optical effect.

Reverse engineering of butterfly wing-scales implies analysis of the 3D morphology and material properties (refractive index and absorption) followed by some-kind of lithographic copying of both the morphology and material properties. Even with the most advanced technologies

(microtomography, electron or X-ray holography), this approach will be extremely limited in terms of available resolution of 3D analytic and lithographic methods (of the order of 10 nm), duration and cost [20].

Imitating the optical effect requires careful analysis of iridescence across the whole visible spectrum and angular range, followed by finding a method to faithfully reproduce the optical wavefront. This also poses a fundamental question: is it possible to have identical wave-fields generated by different structures? The question goes into scattering theory, with a plethora of papers dealing with the uniqueness of the direct and inverse problems. There is no general answer to the question, because it depends on the nature of the scatterer (penetrable or non-penetrable), boundary conditions (conductive, dielectric, amplifying), wavelength and angular range of probing radiation [21]. There are more or less exotic situations where uniqueness is not guaranteed, such as amplifying medium or medium with optical cloaks [22]. But, for the range of problems relevant to this work, the answer is no—there are no two different scatterers producing the same scattered field (far or near) [23].

The wing-scales are best protected by their uniqueness implying necessity to counterfeit every single document time and again. Another point is that, both the material composition and morphology are unique, producing a plethora of optical effects: overall shape, iridescence, absorption, polarization, fluorescence, moiré, defects, far and near-field diffraction pattern, local spectra, etc. In addition, scales possess different optical properties on their upper and under side, which may be used to produce security features which can be read from both sides in perfect alignment (so-called see-through register). Simultaneous use of all or some of the mentioned effects vastly increases the capabilities of wing scale as a protective element.

An important question is whether wing scales can be copied by some of holographic methods. Up to now, volume and surface relief holograms have been copied using contact [24], non-contact [25] or scanning [26] methods. However, these techniques are not useful for copying step-index, layered structure of wing scales, because of the sinusoidal nature of holographic gratings. Additionally, subwavelength gratings of wing-scales (S in Figure 3) cannot be copied, due to evanescent fields obtained by diffraction. These tiny structures are essential for the final coloration of the wing scale, because they produce uniformly scattered radiation in the blue part of the spectrum (see blue component of the wing scale pattern in Figure 8A).

It should be emphasized that Lepidoptera species are not equally suitable for document protection. As already mentioned, these structures must have complex nanometer to micron-size features, with significant variability and must be difficult to analyze and reverse engineer. We preferred

nymphalid species, possessing silver patches on their wings. Other Lepidoptera species, with structurally colored scales have been tested. However, the scales of these species were not so easy to process and manipulate, with the equipment at our disposal.

There is a number of ways how insect scales can be manipulated and attached to documents, as described in the following patent applications [27–29]. Generally speaking, they have to be, either embedded within the transparent medium with large refractive index difference (compared to that of the scale), or placed in a recess with a transparent, protective, covering. The procedure can be performed by micromanipulation or by standard printing techniques (silkscreen, flexo-printing).

Once embedded, scale contents have to be read by some means, which depends on the insect species, type of the scales and the optical effect sought for. In addition to iridescence pattern detection described above, there are other choices: overall shape of the scale, near field color pattern, far-field diffraction pattern, moiré pattern, or pattern of defects (looking like minutia in a fingerprint), with many variations (such as phase and amplitude) and combinations (by recording simultaneously several effects). Reading devices can be based on far- or near-field detection, holography or scanning techniques using CD/DVD readout heads. In the context of document protection, strong variability of patterns with angular position of illumination and observation, as well as the polarization sensitivity are very important. This is what prevents malicious attacks by simple color laser-printing.

The document protection described here is limited to machine reading level. It can be extended to the forensic level, by reading electron microscope image (Figure 1D)), with, for example, cross-rib distances serving as a random feature. If visual protection is desired, a large number of scales can be transferred to another substrate, so to cover large area, visible with the naked eye. One of the scales can be chosen for machine and forensic protection, as described in Reference [28].

Practical implications of the proposed document protection method are numerous. There are thousands of wing scales on a single butterfly specimen suitable for document protection (we have estimated 40 000 iridescent wing scales on *I. lathonia* silver spots). With appropriate choice of butterfly species (eg, Morpho spp.) this number can be much larger. If commercially available dry butterfly specimens are used, we have estimated the cost of a single wing scale at $85 \cdot 10^{-6}$ \$. Alternatively, butterfly species can be reared using well-established techniques of sericulture (silkworm raising). Wing-scales can be collected cheaply and applied using any of standard printing techniques (silk-screen, offset, ink-jet). Range of applications is huge: banknotes, credit-

cards, CD/DVDs, bonds, valuable goods. It is not even hard to imagine using wing-scales as a hardware lock for digital information security.

The base material of wing-scales is chitin, which is extremely and verifiably durable. Natural history museums have century-old butterfly specimens retaining their structural coloration and we have more than 30 years old specimens of *I. lathonia* with silver patches as shiny as in live insects. Even more, fossilized insects retain their iridescence after petrifaction and last for millions of years [30]. This should be compared to, recently described, five-dimensional optical memory [31], claiming "seemingly unlimited lifetime."

Wing scales may reversibly change their dimensions in response to temperature variation [32], humidity and vapors [33]. As a consequence, there is a slight spectral shift, but it is too small to affect application of wing scales in document security, under normal atmospheric conditions. Systematic changes during extended periods of time are not expected due to hydrophobicity, insolubility and biological inertness of wing-scales [34]. However, we have not measured the long-term stability of wing scale patterns, we plan to perform accelerated aging tests in the near future and reveal details regarding the effect of aging on pattern stability.

Anyway, the validity period of most documents is less than 10 years, a period during which wing scales are expected to remain unaffected. Furthermore, taking into account the chemical and physical stability of chitin and the fact that optical response of the insects a hundred and more centuries-old (from museum) and from fossil samples exhibit extraordinary similarity with visual response measured from "the fresh" samples, suggest that corresponding patterns are very stable and could have long-term cryptographic applications.

CONFLICT OF INTEREST

Institute of Physics Belgrade is the applicant and the owner of three pending patent applications given in a list of references [27–29] whose contents is partially described in this paper. Five authors (D.V.P., D.P., M.D.R., V.L. and A.J.K.) are also authors of abovementioned patent applications. Specific aspects of manuscript covered in patent applications are: laser cutting and bleaching of wing scales, as well as a partial list of butterfly species usable for this purpose.

AUTHOR CONTRIBUTIONS

D.V.P. conceived the idea; M.D.R., A.J.K. and D.V.P. have constructed the nonlinear microscope used in this research. D.P., A.J.K., M.D.R. and V.L. performed experiments and measurements. D.V.P. designed an optical model of wing-scales, while N.V. and D.S. performed the theoretical analysis of uniqueness of butterfly wing-scales. B.J. D. Z., W. Z. and B. K were included in data analysis and supervised the research. D.S., S.Ć and D.P. made adequate choice of appropriate butterfly species used in this research, while D.V.P., D.P. and M.D.R. prepared the manuscript, based on comments of other authors. This work is performed in partial fulfillment of the requirements for the PhD degree of Vladimir Lazović at the University of Belgrade, Faculty of Physics. All authors gave final approval for publication and agree to be held accountable for the work performed therein.

ETHICAL STANDARDS

Insects used in this research are NOT on the list of strictly protected and protected species defined in: By-law on proclamation and protection of strictly protected and protected wild species of plants, animals and fungi, Official gazette of the Republic of Serbia Nos. 5/2010 and 47/2011. All experiments were performed on dry specimens from the collection of Dejan Stojanović. The research did not include live insects.

ORCID

Branko Kolarić https://orcid.org/0000-0003-0203-7897

REFERENCES

[1] G. F. Robert, P. H. Adler, *Insect Biodiversity, Science and Society*, Chichester, UK: Willey-Blackwell, **2009**.

[2] X. Zhou, S. W. Applebaum, M. Coll, *Environ. Entomol.* **2000**, *29*, 1289.

[3] S. M. Doucet, M. G. Meadows, *J. R. Soc. Interface* **2009**, *6*, S115.

[4] W. Zhang, J. Gu, Q. Liu, H. Su, T. Fan, D. Zhang, *Phys. Chem. Chem. Phys.* **2014**, *16*, 19767.

[5] E. P. Newman, *Proc. Am. Philos. Soc.* **1971**, *115*, 341.

[6] R. L. Van Renesse, *Optical document security*, 3rd ed. Norwood, MA: Artech House, **2004**.

[7] R. Pappu, B. T. J. Recht, N. Gershenfeld, *Science* **2002**, *297*, 2026.

[8] J. D. R. Buchanan et al., *Science* **2005**, *436*, 475.

[9] Hamm-Dubischar, C. Patent No. WO 2007031077 (A1), Inorganic marking particles for characterizing products for proof of authenticity method for production and use thereof (**2007**).

[10] Biermann, N. & Rauhe, H., Method for Producing Security Markings. WO2004070667 A2 (**2004**).

[11] Rauhe, H., Verfahren zur Herstellung von informationstragenden mikropartikulären Gemischen. Patent DE10238506 A1 (**2004**).

[12] P. Vukusic, R. Kelly, I. Hooper, *J. Roy. Soc. Interface* **2009**, *6*, S193.

[13] D. M. Rabasović et al., *J. Biomed. Opt.* **2015**, *20*(016010), 1.

[14] D. Pantelić, S. Savić-Šević, D. V. Stojanović, S. Ćurčić, A. J. Krmpot, M. Rabasović, D. Pavlović, V. Lazović, V. Milošević, *Phys. Rev. E* **2017**, *95*, 032405.

[15] J. e. Schanda, *Colorimetry: Understanding the CIE System*. Hoboken, NJ: John Wiley & Sons, **2007**.

[16] I. G. Johnston et al., *PLoS Comput. Biol.* **2012**, *8*, e1002416:1.

[17] A. Dinwiddie, R. Null, M. Pizzano, L. Chuong, A. Leigh Krup, H. Ee Tan, N. H. Patel, *Dev. Biol.* **2014**, *392*, 404.

[18] J. Wood, *Pattern Recog.* **1996**, *29*, 1.

[19] L. O'Gorman, I. Rabinovich, *IEEE Trans. Pattern Anal. Mach. Intell.* **1998**, *20*, 1097.

[20] K. Watanabe, T. Hoshino, K. Kanda, Y. Haruyama, T. Kaito, S. Matsui, *J. Vac. Sci. Technol. B* **2005**, *23*, 570.

[21] D. Colton, R. Kress, *Inverse Acoustic and Electromagnetic Scattering Theory*, 2nd ed. New York, NY: Springer, **1998**.

[22] F. Monticone, A. Alu, *Phys. Rev. X* **2013**, *3*(041005), 1.

[23] G. Bao, P. Li, J. Lin, F. Triki, *Inverse Probl* **2015**, *31*, 093001.

[24] S. Toxqui-López, A. Olivares-Pérez, I. Fuentes-Tapia, A. Quintero-Romo, *Opt. Mater.* **2007**, *29*, 1604.

[25] B. D. Chrysler, R. K. Kostuk, *Appl. Optics* **2018**, *57*, 8887.

[26] M. Okui, K. Wakunami, R. Oi, Y. Ichihashi, B. J. Jackin, K. Yamamoto, *Appl. Optics* **2018**, *57*, 4117.

[27] Pantelic, D., Rabasovic, M., Krmpot, A., Lazovic, V. & Pavlovic, D., Security device individualized with biological particles. PCT/EP2015/081398 (**2015**).

[28] Pantelic, D., Rabasovic, M., Krmpot, A., Lazovic, V. & Pavlovic, D., Security tag containing a pattern of biological particles. PCT/EPO2015/081400 (**2015**).

[29] Pantelic, D., Rabasovic, M., Krmpot, A., Lazovic, V. & Pavlovic, D., Security tag with laser-cut particles of biological origin. PCT/EP2015/081407 (**2015**).

[30] M. E. McNamara et al., *PLoS Biol.* **2011**, *9*, e1001200:1.

[31] J. Zhang, M. Gecevičius, M. Beresna, P. G. Kazansky, *Phys. Rev. Lett.* **2014**, *112*, 033901.

[32] A. D. Pris, Y. Utturkar, C. Surman, W. G. Morris, A. Vert, S. Zalyubovskiy, T. Deng, H. T. Ghiradella, R. A. Potyrailo, *Nat Photon* **2012**, *6*, 195.

[33] R. A. Potyrailo, H. Ghiradella, A. Vertiatchikh, K. Dovidenko, J. R. Cournoyer, E. Olson, *Nat photonics* **2007**, *1*, 123.

[34] H.-M. Hu, J. A. Watson, B. W. Cribb, G. S. Watson, *Biofouling* **2011**, *27*, 1125.

SUPPORTING INFORMATION

Additional supporting information may be found online in the Supporting Information section at the end of this article.

Observation of second harmonic generation in doped polymeric carbon monoxide

Michael G. Pravica [a,*], Mihailo D. Rabasovic [b], Aleksandar J. Krmpot [b], Petrika Cifligu [a], Blake Harris [a], Egor Evlyukhin [a], Marko G. Nikolic [b]

[a] Department of Physics and Astronomy, University of Nevada Las Vegas (UNLV), Las Vegas, NV 89154-4002, USA
[b] Photonics Center, Institute of Physics Belgrade, University of Belgrade, Pregrevica 118, 11080 Belgrade, Serbia

A B S T R A C T

Second harmonic generation (SHG) experiments were conducted on samples of a novel material: doped polymeric CO (dp-CO) that were synthesized via synchrotron X-ray irradiation of SrC$_2$O$_4$ and high pressure. The goal of the study was to ascertain if the novel material is rugged enough to handle high levels of radiation to enable its possible use as future sensors or optoelectronic devices. Three samples were tested. Two of the smaller samples that were synthesized in a diamond anvil cell (DAC) and recovered at ambient conditions rapidly decomposed/degraded in the presence of the strong 3.6×10^9 mW/cm^2 intensity optical beam. The larger sample that was synthesized in a Paris-Edinburgh cell at 3 GPa after 1.5 h of hard X-ray white beam irradiation and also recovered to ambient conditions was not damaged by a 6.1×10^9 mW/cm^2 strength optical beam and exhibited second harmonic generation. This lends credence that this novel material (when synthesized under select conditions) may offer utility as a rugged radiation hardened and easy to manufacture nonlinear optical device.

© 2019 Elsevier B.V. All rights reserved.

1. Introduction

In the quest to synthesize novel and industrially-useful materials, highly ionizing and highly penetrating hard X-rays (>7keV) in conjunction with high pressure offer a unique and relatively unexplored means to create rugged and radiation-hardened materials that may not be synthesizable by conventional means. High energy X-rays (>7keV) can overcome large thermodynamic activation barriers to ionize atoms, forcing atomic and molecular fluidity, which, coupled with high pressure (to force these radicals and ions closer together to interact), may create unique compounds. We have been developing useful hard X-ray photochemistry for a variety of applications for chemical synthesis and decomposition [1]. From the initial observation of O$_2$ production from synchrotron X-ray irradiated chlorate salts [2,3]: (e.g. KClO$_4$ $\overset{h\nu}{\to}$ 2O$_2$ + KCl), we have been able to successfully release O$_2$ [2,3], Cl$_2$ [4], H$_2$ [5], N$_2$ [6], NO$_2$ [7], and F$_2$[8] inside a diamond anvil cell (DAC) or other sealed and/or pressurized chamber *in situ* to create unique metastable states of matter and observe molecular diffusion and reactions of these relatively mobile reactants (e.g. O$_2$ + 2F$_2$ $\overset{h\nu}{\to}$ 2OF$_2$) [5,9] at extreme conditions. By exploiting our methods to release fluorine

in situ inside a DAC, we have strong evidence of the synthesis of HgF$_4$ by irradiating a pressurized mixture of HgF$_2$ and XeF$_2$ (the latter compound releasing F$_2$ [1]). The fluorine then reacted with HgF$_2$ via: HgF$_2$ + F$_2$ $\overset{h\nu}{\to}$ HgF$_4$ as predicted [10]. We have also demonstrated that novel structures of known compounds (such as CsO$_2$) can be created using our irradiation methods [11].

One interesting compound that we have synthesized using our methods is a variant of polymeric CO (poly-CO) which is conventionally produced by pressurizing CO to >5 GPa [12,13] or >3 GPa with optical assistance [14]. By irradiating strontium oxalate powder at various pressures (including ambient), a novel yellowish-red amorphous compound was formed that was recoverable at ambient conditions [15,16]. Infrared spectroscopy of the recovered irradiated samples indicated the presence of trapped CO$_2$, SrCO$_3$, and characteristic spectral lines that were detected in poly-CO [16,17]. Based on this evidence and X-ray absorption studies [16], the following primary reactions were suspected [17]:

$$SrC_2O_4 \overset{h\nu}{\to} SrCO_3 + CO$$

$$n(CO) \to poly\text{-}CO$$
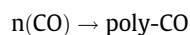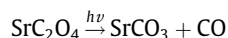
Conventional poly-CO is an unstable solid that decomposes into graphite and CO$_2$ in a matter of days and is very light sensitive [12–14]. Our synthesized material, however, is very stable (lasting for

periods of at least 3 years) and traps CO_2 inside it for at least as long as the compound lasts suggesting the possibility of a CO_2-storage medium [16,18]. We suspect that the presence of $SrCO_3$ as a dopant stabilizes the compound. There is a strong pressure dependence of the synthesis [17]. This novel compound exhibits wide bandgap semiconductor properties suggesting its potential use as a solar material or other optoelectronic device/sensor [18]. Due to the IR spectral similarity to conventionally synthesized poly-CO, we termed the compound doped solid [16] or doped polymeric [15] CO. We wish to emphasize, however, that this material is not the same as pure poly-CO as it traps CO_2, is produced via irradiation of an oxalate salt (as opposed to pressurization of CO), and has been found to be very stable, unlike conventionally-synthesized poly-CO. Rather, it is a novel material that has yet-to-be-uncovered properties.

Related to this discovery, a natural question arises when considering what kind of light fields this compound may sustain before being damaged. And, given the strongly coupled (even if amorphous) nature of this unique extended solid, could it possibly serve as an radiation-hardened optical mixer? After all, HMX, an organic explosive, has a strong second harmonic mixing coefficient [19]. Thus, we sought to determine the effect of high intensity laser fields on our synthesized samples with the aim of determining their survivability under these extreme conditions and, to ascertain if we could produce frequency doubled light.

2. Experimental

2.1. Sample preparation

Preparation and irradiation of our samples was performed at the High Pressure Collaborative Access Team's 16 BM-B beamline at the Advanced Photon Source. We used two different means to pressurize our samples: a Paris-Edinburgh Cell (PEC) for larger samples and diamond anvil cell (DAC) for smaller samples (<3 nl). For the PEC preparation, white strontium oxalate powder (SrC_2O_4 – Alfa Aesar 97% purity) was manually loaded into a prepared composite gasket chamber which surrounded a 1 mm diameter by 1 mm deep MgO cup. The sample was pressurized by applying mechanical load to two WC anvils, bringing them towards one another with the gasket squeezed in between via a high pressure oil hydraulic apparatus. The MgO cup also served as the pressure calibrant. This setup has been described elsewhere [20].

For samples loaded in the DAC, we employed a symmetric-style DAC with 300 μm culet-opposed diamonds. A 0.01" thick stainless steel gasket was preindented (by the opposed anvils) to a 70 μm initial thickness and then drilled in the center of the indentation via electric discharge machining to create a 120 μm diameter sample hole. Strontium oxalate powder was then manually loaded into the sample chamber along with a ~10 μm diameter ruby for pressure measurement.

After pressurization (as verified by the respective calibrants), each of the samples were irradiated with "white" X-rays for approximately 1.5 h. The beam was chosen to be typically defocused (PEC) or slightly defocused (DAC) to completely irradiate the samples. After irradiation, samples were recovered after depressurization to ambient conditions. For the PEC sample, the surrounding/confining composite gasket material was manually removed. For the DAC samples, the gaskets were removed from the DAC and the samples remained intact in the gasket hole.

2.2. Nonlinear optical measurements

Our optical studies were undertaken at the home made nonlinear optical facility located at the Institute of Physics in Belgrade, Serbia. For more detailed description of the experimental setup and scheme, please refer to ref. [21]. In this study the laser light from mode locked Ti:Sa laser (MIRA 900, Coherent Inc.) tuned to 840 nm was focused onto the sample by 20×0.8 air objective (Zeiss plan-Apochromat®). The second harmonic generation (SHG) signal passed through a narrow band filter of central wavelength 420 nm and bandwidth of 10 nm and was detected by photo multiplier tube (PMT). Due to the thickness of the samples, our measurements were performed in reflection.

3. Results

The samples under study were placed under the nonlinear microscope with a 20x objective (NA = 0.8) and a controllable translation stage. A video monitoring system was used to align
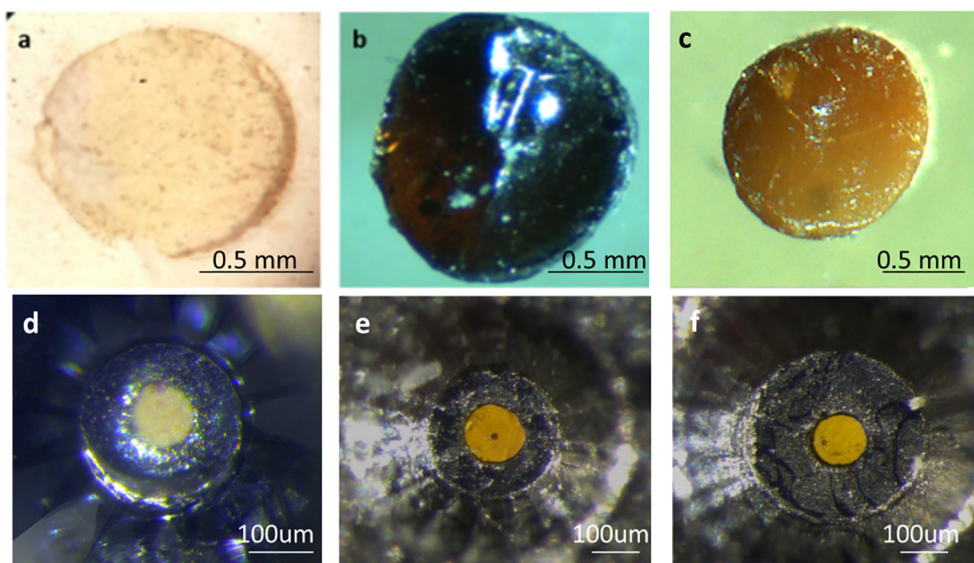

Fig. 1. Pictures of the recovered (to ambient conditions) products synthesized via X-ray irradiation at different pressure points in PEC cells (top photos) and DAC (bottom photos). a) PEC sample at ambient pressure. b) PEC sample produced at 4 GPa. c) PEC sample at 10 GPa. d) DAC sample at ambient. e) DAC sample produced at 4 GPa. f) DAC sample at 10 GPa. From reference [18].

the samples into the visual field of the microscope. The focused beam size was diffraction limited (diameter of approximately 0.5 μm). Three samples were studied. The first two were poly-CO samples that were created in a DAC (see e and f of Fig. 1). They had a yellowish waxlike consistency. The third sample was synthesized in a PEC at 3 GPa and had a similar look and consistency to reddish-brown beer bottle glass (see Fig. 1b).

When the samples produced inside a DAC were respectively irradiated with the high powered laser light (7mW), they rapidly decomposed in the beam (seconds to minutes) and no second harmonic light was generated. The third PEC-made sample, on the other hand (Fig. 1b), produced a second harmonic signal at 420 nm when placed in the path of the laser beam (see Fig. 2). The SHG signal appeared to be stable with time and no visual damage on this sample was immediately evident. For comparison purposes, a slide of virgin, unirradiated strontium oxalate powder was analyzed for SHG using the sample experimental conditions that were used in above-described measurements and no SHG light was observed (see Fig 3) demonstrating that irradiation of the oxalate salt is critical for SHG signal. Accurate determination of the SHG absolute efficiency is affected by a number of various experimental conditions (pulse duration, pulse energy, pulse-to-pulse stability, repetition rate etc) that are not easily and precisely controllable. It is a nontrivial task that is rarely performed in practice for this kind of experiment. Thus, we have compared efficiencies of the SHG in our samples and starch, since starch is the most common test sample in nonlinear microscopy. PEC generates second harmonic 30–100 times weaker than the starch grains.
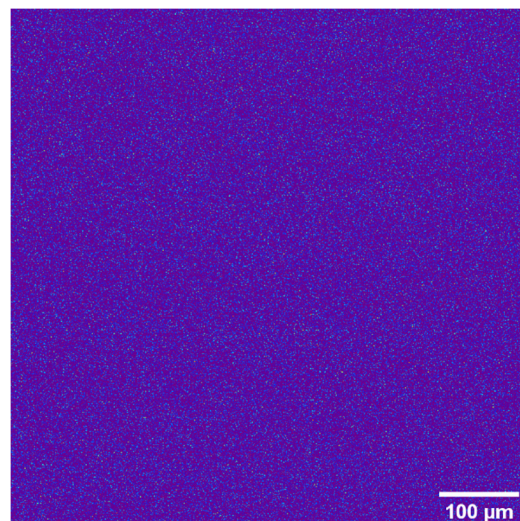
Fig. 3. Imaging scans of a slide consisting of virgin powdered SrC_2O_4 that had not been irradiated by X-rays demonstrating no SHG signal at a similar intensity level and thus that the SHG signal observed in Fig. 2 was due to the novel material (dp poly-CO).

4. Discussion

The samples made in a DAC did not survive the intense focused laser beam. Yet the PEC-made sample did. This may be due to to

Fig. 2. SHG in the third sample that was made in a PEC taken from two different regions of the sample.

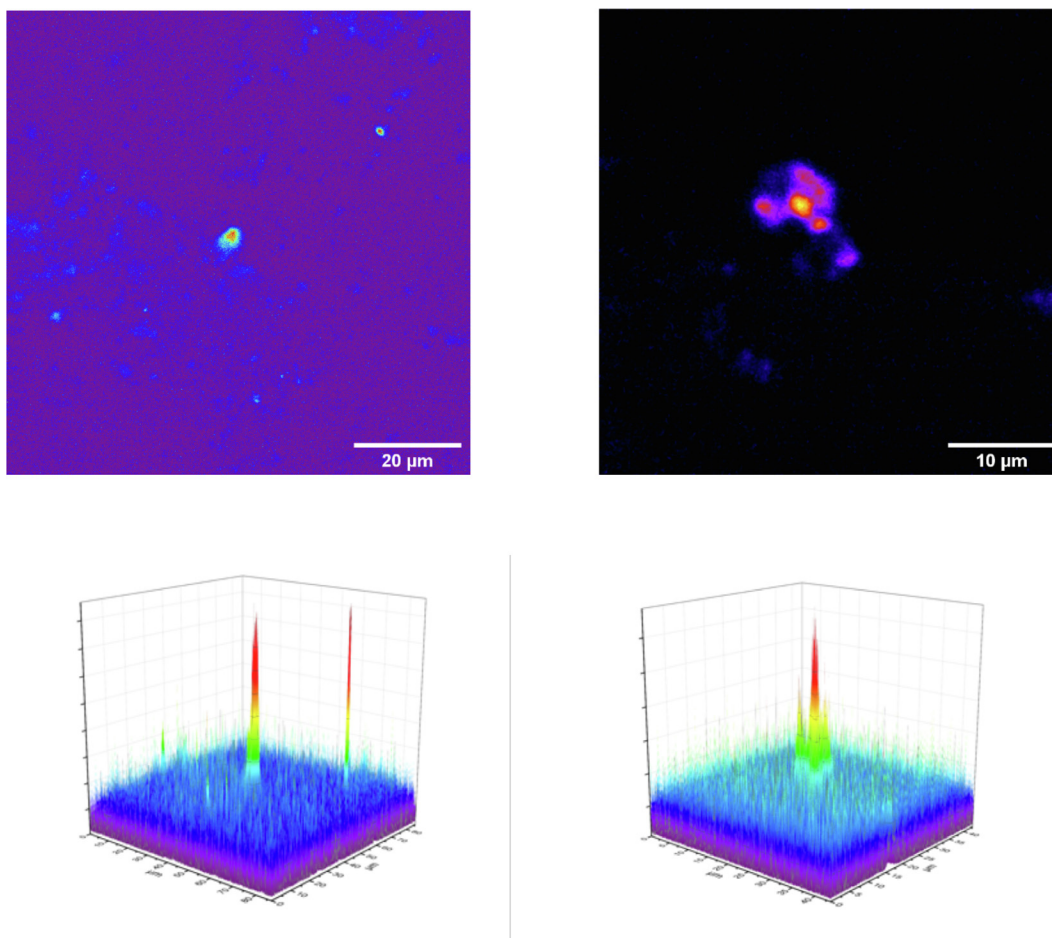differing flux density conditions of the X-ray beam when the different samples were irradiated leading to somewhat different synthetic or incomplete pathways. As the third sample was far larger, it may be able to handle more heat and not thermally decompose under any heating caused by the laser beams. Further studies are planned to ascertain why our DAC samples decomposed in the presence of the laser beam.

Every indication suggests that our synthesized samples (both those made in the DAC and PEC) are largely amorphous. The high SHG intensity spots that were observed in Fig. 2 suggest that there may submicron crystals present in our sample which cause large SHG when oriented properly relative to the incident laser polarization. This may also imply that the synthetic process is incomplete which may also have resulted in less resilient DAC-made samples. Conventionally produced poly-CO, on the other hand is a waxy, amorphous material which is unable to survive the intense laser fields required for SHG. Thus, though the mixing efficiency of light may be lower than when using an oriented single crystal, this novel material may have utility as a relatively easy to synthesize radiation-hardened sensor/nonlinear mixer that appears to be chemically stable (or at least metastable) and may also yield more insights on the synthetic process/crystallization of our samples with extended irradiation and/or pressure.

5. Conclusion

We have conducted further studies of a novel material that we call doped polymeric or solid CO to interrogate its ability to behave as a nonlinear mixer and withstand high radiation flux. We have found that one of our larger glass-like samples exhibited second harmonic generation and was not damaged by the laser beam. Further work will seek to better understand and optimize synthetic and crystallization parameters in the hopes of creating a useful sensor and/or optical mixer for use at extreme or ambient conditions.

Declaration of Competing Interest

The authors declare that they have no known competing financial interests or personal relationships that could have appeared to influence the work reported in this paper.

Acknowledgements

References

[1] M. Pravica, S. Schyck, B. Harris, P. Cifligu, B. Billinghurst, Pap. Phys. 11 (2019), 110001-1-6.
[2] M. Pravica, L. Bai, C. Park, Y. Liu, M. Galley, J. Robinson, N. Bhattacharya, Rev. Sci. Inst. 82 (2011), 106102-1-3.
[3] M. Pravica, B. Hulsey, L. Bai, D. Sneed, Q. Smith, G. Guardala, J. Phys.: Conf. Series 500 (2) (2014), 022009.
[4] M. Pravica, D. Sneed, Q. Smith, L. Bai, Chem. Phys. Lett. 530 (2013) 74–76.
[5] M. Pravica, D. Sneed, M. White, Y. Wang, J. Chem. Phys. 141 (2014) 091101.
[6] M. Pravica, Y. Liu, L. Bai, Chem. Phys. Lett. 555 (2013) 113–115.
[7] D. Goldberger, C. Park, E. Evlyukhin, P. Cifligu, M. Pravica, J. Phys. Chem. A 22 (44) (2018) 8722–8728.
[8] M. Pravica, D. Sneed, M. White, Y. Wang, R. Sci, Instr. 85 (2014), 086110.
[9] M. Pravica, M. White, Y. Wang, Y. Xiao, P. Chow, Chim. Oggi 36 (4) (2018) 50–52.
[10] M. Miao, J. Botana, M. Pravica, D. Sneed, C. Park, Jpn. J. Appl. Phys. 56 (2017), 05FA10.
[11] E. Evlyukhin, E. Kim, D. Goldberger, P. Cifligu, S. Schyck, P. Weck, M. Pravica, Phys. Chem. Chem. Phys. 20 (2018) 18949–18956.
[12] W.J. Evans, M. Lipp, C.-S. Yoo, H. Cynn, J.L. Herberg, R.S. Maxwell, M. Nicol, Chem. Materials 18 (2006) 2520.
[13] M. Lipp, W. Evans, B. Baer, C.-S. Yoo, Nat. Materials 4 (2005) 21.
[14] M. Ceppatelli, A. Serdyukov, R. Bini, H.J. Jodl, J. Phys. Chem. B 113 (2009) 6652.
[15] M. Pravica, D. Sneed, Q. Smith, B. Billinghurst, T. May, M. White, K. Dziubek, Cogent Phys. 3 (2016), 1169880:1-8.
[16] M. Pravica, E. Evlyukhin, P. Cifligu, B. Harris, N. Chen, Y. Wang, Chem. Phys. Lett. 686 (2017) 183–188.
[17] D. Goldberger, E. Evlyukhin, P. Cifligu, Y. Wang, M. Pravica, J. Phys. Chem. A 121 (2017) 7108–7113.
[18] E. Evlyukhin, E. Kim, P. Cifligu, D. Goldberger, S. Schyck, B. Harris, S. Torre, G. Rossman, M. Pravica, J. Mater. Chem. C 6 (2018) 12473–12478.
[19] B.F. Henson, B.W. Asay, R.K. Sander, S.F. Son, J.M. Robinson, P.M. Dickson, Phys. Rev. Lett. 82 (6) (1999) 1213–1216.
[20] Y. Kono, C. Park, C. Kenney-Benson, G. Shen, Y. Wang, Phys. Earth Planet. Inter. 228 (2014) 269–280.
[21] M.D. Rabasović, D.V. Pantelić, B.M. Jelenković, S.B. Ćurčić, M.S. Rabasović, M.D. Vrbica, V.M. Lazović, B.P.M. Ćurčić, A.J. Krmpot, J. Biomed. Opt. 20 (2015), 016010.

OPEN

Local redox conditions in cells imaged via non-fluorescent transient states of NAD(P)H

Johan Tornmalm [ID]1, Elin Sandberg1, Mihailo Rabasovic [ID]2 & Jerker Widengren [ID]1*

The autofluorescent coenzyme nicotinamide adenine dinucleotide (NADH) and its phosphorylated form (NADPH) are major determinants of cellular redox balance. Both their fluorescence intensities and lifetimes are extensively used as label-free readouts in cellular metabolic imaging studies. Here, we introduce fluorescence blinking of NAD(P)H, as an additional, orthogonal readout in such studies. Blinking of fluorophores and their underlying dark state transitions are specifically sensitive to redox conditions and oxygenation, parameters of particular relevance in cellular metabolic studies. We show that such dark state transitions in NAD(P)H can be quantified via the average fluorescence intensity recorded upon modulated one-photon excitation, so-called transient state (TRAST) monitoring. Thereby, transitions in NAD(P)H, previously only accessible from elaborate spectroscopic cuvette measurements, can be imaged at subcellular resolution in live cells. We then demonstrate that these transitions can be imaged with a standard laser-scanning confocal microscope and two-photon excitation, in parallel with regular fluorescence lifetime imaging (FLIM). TRAST imaging of NAD(P)H was found to provide additional, orthogonal information to FLIM and allows altered oxidative environments in cells treated with a mitochondrial un-coupler or cyanide to be clearly distinguished. We propose TRAST imaging as a straightforward and widely applicable modality, extending the range of information obtainable from cellular metabolic imaging of NAD(P)H fluorescence.

Cellular redox balance is central to the regulation of energy production and intermediary metabolism, as well as for cell survival, growth and proliferation. Alterations in this balance have been coupled to a broad range of pathological conditions, including neurodegenerative, infectious and inflammatory diseases, and cancer[1–3]. Two major determinants of cellular redox balance are the nicotinamide adenine dinucleotide ($NAD^+/NADH$) and nicotinamide adenine dinucleotide phosphate ($NADP^+/NADPH$) redox couples. The primary role of NAD^+ is to act as an electron acceptor in catabolic pathways, while NADPH acts as a central electron donor in anabolic pathways[4]. Both NADH and NADPH, hereinafter referred to as NAD(P)H, are fluorescent, while their oxidized forms, $NAD(P)^+$, are not.

NAD(P)H autofluorescence, typically studied by laser scanning microscopy (LSM) and two-photon excitation (TPE)[5], offers a versatile readout for label-free metabolic imaging of cells and tissues[6–8]. Several relations between metabolic cellular phenotypes and the recorded fluorescence properties of NAD(P)H can be exploited. By optical redox ratioing (ORR), comparing cellular fluorescence intensity of NAD(P)H with that of oxidized flavin adenine dinucleotide (FAD^+), it is possible to estimate the balance between oxidative phosphorylation and glycolysis for adenosine triphosphate (ATP) production in cells[9,10]. However, inhomogeneous intra-cellular concentrations of NAD(P)H and FAD^+, together with local variations in fluorescence quantum yield due to enzyme binding[11], makes plain intensity quantification of cellular metabolic states difficult. Fluorescence lifetime microscopy (FLIM) can account for these effects and determine the ratio of free to protein-bound NAD(P)H by the fraction of short (τ_{free}) and long (τ_{bound}) fluorescence lifetimes in the sample. This free-vs-bound ratio has been found to be a sensitive indicator of cellular energy metabolism[12,13], capable to identify metabolic phenotypes representing early pathological conditions in cells[7,14–17], mitochondria and other subcellular compartments[18]. Moreover, local variations in τ_{bound}, attributed to binding of NAD(P)H to different enzymes and conformational heterogeneities of those enzymes, have been reported to reflect different cellular metabolic states[19]. Still, despite numerous successful examples of the use of NAD(P)H fluorescence and TPE FLIM to non-invasively monitor

1Experimental Biomolecular Physics, Department of Applied Physics, Royal Institute of Technology (KTH), Albanova University Center, 106 91, Stockholm, Sweden. 2Institute of Physics, University of Belgrade, Pregrevica 118, Belgrade, 11080, Serbia. *email: jwideng@kth.se

cellular metabolism, identify metabolic cellular phenotypes, and the many potential clinical applications of such assessments [8,20], the biochemical basis for variations in ORR, free-vs-bound NAD(P)H, and τ_{bound} is not yet fully understood[11]. The assessments are influenced by artifacts and give only a relatively limited view of the metabolic states of the cells. NADH and NADPH show almost identical fluorescence properties in aqueous solution[21,22], and have been found difficult to separately detect inside cells[23]. The two co-enzymes take part in several, distinctly different metabolic pathways[4], and changes in the redox balance within cells may thus lead to different changes in the reduced, fluorescent fractions of each of these compounds, and in their protein-bound fractions. This complicates the interpretation of changes in the NAD(P)H fluorescence readouts in cells[11], and changes in NADH and NADPH fluorescence may even cancel each other out.

One way to overcome current limitations in label-free cellular metabolic imaging is to use additional, orthogonal information in the NAD(P)H fluorescence. Such information can be obtained from the fluorescence blinking of NAD(P)H, upon transitions to and from photo-induced dark states. Studies by fluorescence correlation spectroscopy (FCS) and other single-molecule techniques have shown that blinking properties of organic fluorophores, generated by transitions to and from dark triplet and photo-oxidized states, are highly sensitive to the immediate environment around the fluorophores[24,25]. Notably, these transitions are specifically sensitive to redox conditions and oxygenation, parameters of particular relevance in cellular metabolic studies. The photophysics underlying such blinking properties in NAD(P)H have been extensively studied, in particular by transient absorption and electron spin resonance (ESR) spectroscopy[26–29]. However, although these methods have proven useful for the photophysical characterization of NAD(P)H itself, they do not lend themselves to studies in live cells. FCS is compatible with live cell studies, but requires single-molecule detection conditions. The fluorescence brightness of individual NAD(P)H molecules is too weak for FCS studies, in any sample medium.

Here, we show that the major photophysical transitions of NAD(P)H can be determined by monitoring its fluorescence intensity in response to systematic modulation of a laser excitation source, by so-called transient state (TRAST) spectroscopy/imaging[30,31]. We first characterized dark-state transitions of NADH in aqueous solution, and demonstrate that, by this simple and widely applicable method, we can obtain the same data as from transient state absorption and ESR spectroscopy. We then show that these transitions can be imaged on a local, subcellular scale in live cells, providing information on redox environments and metabolic states not clearly reflected in traditional fluorescence parameters. The proposed procedure circumvents all major limitations of FCS and related single-molecule techniques to assess NAD(P)H dark state transitions in live cells and can be applied in parallel with standard TPE FLIM assessments.

Results

From TRAST measurements on NADH in aqueous solution using one-photon excitation (OPE) in the UV, a photophysical model for NADH was established, tested under different experimental conditions, and compared to literature[26–29]. Based on this model, we investigated the photophysical properties of NADH in aqueous solution upon TPE, with an IR laser systematically scanned with different speeds across the sample. Thereby, we could determine a slightly modified photophysical model for NADH under TPE conditions. Using a similar laser-scanning approach, we finally demonstrated TRAST imaging of NAD(P)H in live cells, and that orthogonal information about metabolic states of cells can be obtained, assessed in parallel with the full toolbox of TPE FLIM.

Solution measurements with one-photon excitation. TRAST measurements were performed on NADH in aqueous solution, using a confocal setup with a stationary 355 nm laser beam for OPE. The excitation laser was intensity-modulated, so that samples were subject to square-wave excitation pulse trains of varying duration, w (see Methods and Materials). We analysed the photophysics of NADH under different environmental and excitation conditions by so-called TRAST curves[30,32,33], showing the normalized time-averaged fluorescence of NADH, $\langle F_{exc}(w) \rangle_{norm}$, as a function of pulse duration, w. By varying the measurement conditions to specifically affect one or several of the major photo-induced states of NADH, and guided by previous photophysical studies of NADH by transient absorption and ESR spectroscopy[26–29], we could define a photophysical model for NADH relevant for our measurement conditions. This model was verified by global fitting of all the TRAST curves, whereby also the rate parameters for the photophysical transitions of NADH were determined. (Hereinafter, stated confidence intervals for determined rate parameter values and slopes are 95% confidence intervals).

Effects of excitation intensity and oxygen concentration. Figure 1A shows TRAST curves recorded from an air-saturated solution of NADH, under different excitation intensities. The curves are approximately flat in the time range of 500 ns to 10 μs, indicating little or no triplet state population present within the typical time scale for triplet state relaxation, as observed for organic fluorophores[24] and autofluorescent compounds[32,33]. For pulse durations, w, from 10 μs up to 1 ms, a prominent dark state build-up can be noted. The time-scale and multi-exponential behaviour of this decay, resulting in an almost linearly declining TRAST curve, is compatible with stepwise photo-oxidation of NADH to its non-fluorescent form NAD$^+$.

To support these interpretations, we repeated the measurements in atmospheres of pure oxygen and pure argon (Fig. 1B). Oxygen-saturated measurements revealed an increased decay in the TRAST curves on a time scale of around 100 μs. Given the minimal triplet state population already under air-saturated conditions (Fig. 1A), the triplet state can be neglected entirely in a pure atmosphere of oxygen, a potent triplet state quencher. The increased decay is instead attributed to an increased build-up of photo-oxidized NADH, promoted by the presence of more oxygen. Complete de-oxygenation by argon also resulted in a minor increase of the TRAST curve decay, but on a faster time-scale. This effect is compatible with the presence of a minor triplet state population, barely observable under air-saturated conditions.
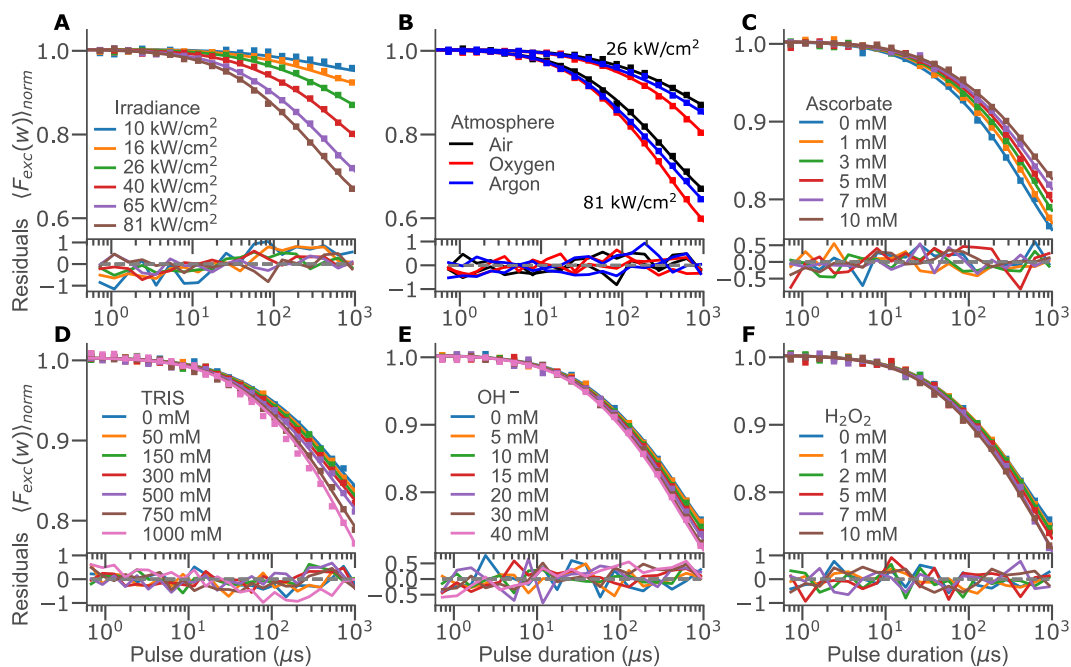
Figure 1. Experimental TRAST curves recorded from 1 μM NADH (50 mM TRIS, pH 7.4, if not stated otherwise) under OPE. (**A**) Irradiance (I_{exc}) dependence (10 to 81 kW/cm^2). (**B**) Influence of oxygen on the TRAST curves (only two irradiances shown for clarity). Titrations of (**C**) sodium ascorbate, (**D**) TRIS buffer at pH 7.4, (**E**) sodium hydroxide in aqueous solution without TRIS buffer and (**F**) H$_2$O$_2$ (measured at 50 kW/cm^2). All curves (A-F, solid lines) were fitted simultaneously (see Global parameter fitting to TRAST curves generated under OPE) and are shown with absolute residuals, multiplied by a factor of 100 for clarity.

Photophysical model for NADH. The observations in the TRAST curves, as shown in Fig. 1A,B, are well in line with previous photophysical studies of NADH. With optical detection of magnetic resonance (ODMR) and photoluminescence studies, no[34], or very minor[35] evidence of triplet state formation in NADH could be observed upon excitation at 313 nm or longer wavelengths. In contrast, transient state absorption[26,27,29] and ESR[28,36] studies show that radical cations of NADH are readily formed upon light excitation. Based on the effects of excitation intensity and oxygen concentration observed with TRAST (Fig. 1A,B), and taking these previous studies of NADH photophysics[26–29,34–36] into account, we constructed a photophysical model for NADH (Fig. 2). The purpose of the model is to include all dark state transitions captured in our TRAST measurements (but to leave out details of dark states, such as tautomerizations, two electron ejection, multiple protonation and dimerization states, which cannot be distinguished from each other by our TRAST measurements).

In the model of Fig. 2, the first step of NADH photo-oxidation is the ejection of a single electron, forming the radical cation ·NADH$^+$. Some controversy remains in literature whether this electron ejection has a one-photon[27] or a step-wise two-photon[26,29] excitation dependence, and under what conditions the two different electron ejection models would apply. To investigate which model is suitable for our TRAST measurements, we studied how the decay amplitudes, A_{TRAST}, of the TRAST curves were related to the applied excitation irradiance, I_{exc}. A_{TRAST} represents the total dark state build-up in NADH for long w. In absence of excitation saturation ($k_{01} \ll k_{10}$) and neglecting any triplet state formation, the effective photo-oxidation rate from ^{0}NADH to NAD$^+$ is $k'_{ox} \propto A_{TRAST}/(1 - A_{TRAST})$. A log-log plot of $A_{TRAST}/(1 - A_{TRAST})$ versus I_{exc} produces a straight line with a slope of 1.06 ± 0.1 (data not shown), suggesting a predominantly linear I_{exc}-dependence under our experimental conditions. A similar analysis of initial fluorescence intensity (i.e. the fluorescence intensity recorded for short w, with negligible dark state build-up) versus I_{exc} gives a slope of 0.97 ± 0.05 (data not shown), confirming that $k_{01} \ll k_{10}$ over the range of I_{exc} used.

Finally, we performed TRAST measurements (43 kW/cm^2) with additions of up to 10 mM potassium iodide (KI), known to affect both intersystem crossing and triplet state quenching in many fluorophores[37]. However, no changes in A_{TRAST} could be found under our experimental conditions. This suggests that triplet state formation in NADH is minor and that electron ejection from the triplet state can be neglected as a pathway for ·NADH$^+$ formation.

Redox, pH and buffer dependence. To confirm the model of Fig. 2, and to investigate the sensitivity of TRAST measurements to biological factors such as pH, redox balance and buffer strength, we performed TRAST experiments with sodium ascorbate (anti-oxidant, 0–10 mM), hydrogen peroxide (oxidant, 0–10 mM), sodium hydroxide (pH, 0–40 mM) or TRIS buffer (0–1 M) added into the NADH solution.

After formation of the radical cation ·NADH$^+$, fast deprotonation (by a concerted electron-H atom transfer from ·NADH$^+$) is known to follow, at first-order rates in the range of 10^6 s^{-1}[29]. ·NADH$^+$ is strongly acidic and
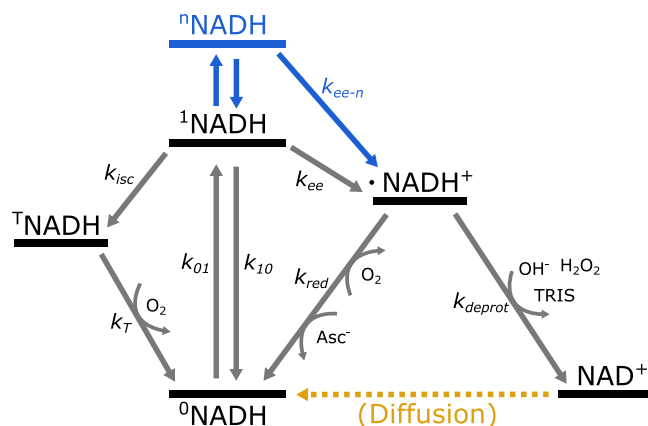
Figure 2. Photophysical model for NADH, adapted for TRAST analysis. Excitation takes place from the singlet ground state (^{0}NADH) to the first excited singlet state (^{1}NADH), or to a higher excited singlet state (^{n}NADH). Excitation can result in dark state formation, via intersystem crossing to a triplet state (^{T}NADH), or via electron-ejection into a radical cation ($\cdot$NADH$^+$). $\cdot$NADH$^+$ rapidly deprotonates into a neutral radical, $\cdot$NAD[40], followed by a second one-electron oxidation to form the stable oxidized form NAD$^+$. As a competing route, $\cdot$NADH$^+$ can also return to ^{0}NADH, by recombining with a free electron, or taking up an electron from an electron donor. The short-lived $\cdot$NAD radical was not explicitly included in the model, since although it can also dimerize, leading to a manifold of other reactions[57], the one dominating process under our experimental conditions is the further oxidation to NAD$^+$. Rate parameters: ground state excitation rate (k_{01}), combined fluorescence and non-radiative decay rate (k_{10}), intersystem crossing rate (k_{isc}), triplet relaxation rate (k_T), electron ejection rate from ^{1}NADH (k_{ee}), electron ejection rate from ^{n}NADH (k_{ee-n}), radical deprotonation rate (k_{deprot}), radical reduction rate (k_{red}). The blue part of the model refers to transitions which under our experimental conditions only took place with TPE, as discussed in the main text. The yellow part of the model represents diffusion mediated recovery of ^{0}NADH in the excitation volume of the experiment (see SI section 4).

the deprotonation from $\cdot$NADH$^+$ to NAD$^+$ is essentially irreversible under biologically relevant conditions[38,39]. However, the fact that reported values for the NADH electron ejection yields are higher than the corresponding photo-oxidation yields[27], suggests that $\cdot$NADH$^+$ can also recombine with a solvated electron, thereby returning to ^{0}NADH. We investigated this recombination by adding ascorbate (Asc$^-$) as an electron donor, which was found to decrease the decay amplitudes in the TRAST curves (Fig. 1C), consistent with promoted recombination of $\cdot$NADH$^+$ back to ^{0}NADH. However, the decrease was lower than for other auto-fluorescent compounds[32] or fluorophores[25]. This can be explained by the comparably short lifetime of $\cdot$NADH$^+$, and that reduction back to ^{0}NADH competes with rapid deprotonation and further oxidation to NAD$^+$.

In contrast to Asc$^-$, addition of hydrogen peroxide (H$_2$O$_2$), hydroxide ions (OH$^-$) or TRIS buffer slightly increased the decay amplitude of the recorded TRAST curves (Fig. 1D–F). This indicates an increased formation of NAD$^+$, with the compounds acting as acceptors of either protons (TRIS), or electron-H atom units[38,39]. The relatively weak effects seen in the TRAST curves upon addition of these compounds supports the view that they have a minor relative effect on the fast deprotonation rate of $\cdot$NADH$^+$[29].

We also investigated if NADPH shows different photo-oxidation dark state transitions compared to NADH. However, no significant differences could be observed under the experimental conditions applied for the NADH studies described above.

Global parameter fitting to TRAST curves generated under OPE. Based on the rate equations following from the photophysical model of NADH (Fig. 2), and by use of eq. (S3) with simplifications according to (S10) and (S12), rate parameters were numerically fitted (see Methods and Materials) to all the recorded TRAST curves described above. In the fit, the excitation rate ($k_{01} = \sigma \Phi_{exc}$) was set based on a reported excitation cross section, σ, of $2.0 \cdot 10^{-17}$ cm^2 (at 355 nm)[21] and a local photon flux calculated as $\Phi_{exc} = I_{exc} \lambda / (hc)$, where hc / λ is the photon energy. All other rates (k_{isc}, k_T, k_{ee} k_{red}, k_{deprot} and diffusion recovery parameters) were fitted globally (to same values for all 53 TRAST curves). Linear concentration dependencies were assumed for k_T (O$_2$), k_{red} (O$_2$ and Asc$^-$), and k_{deprot} (H$_2$O$_2$, OH$^-$ and TRIS buffer). A constraint was added on the combined ^{1}NADH decay rates ($k_{10} + k_{isc} + k_{ee} = 1/\tau_F$) to reproduce the experimental fluorescence lifetime $\tau_F = 0.4$ ns[21,27].

Fitted curves with residuals are shown in Fig. 1A–F, and the fitted parameter values in Table 1. The intersystem crossing rate, k_{isc}, was determined to $0.9 \cdot 10^6$ s^{-1}, which is comparable to k_{isc} rates of organic fluorophores with low triplet quantum yields, Φ_T[24]. However, since τ_F of NADH is approximately an order of magnitude shorter than for such fluorophores, its Φ_T is also lower (~0.0004), which explains the very minor triplet state build-up noticed in the TRAST curves, and reported difficulties to detect ^{T}NADH formation by e.g. flash photolysis[26]. The decay rate of ^{T}NADH, k_T, is largely due to diffusion-controlled quenching by molecular oxygen, and is comparable to k_T rates of organic fluorophores[24] and other autofluorescent compounds[32,33]. The photo-induced electron ejection rate, k_{ee}, was determined to $5.3 \cdot 10^6$ s^{-1}, orders of magnitude higher than photo-oxidation rates for organic fluorophores under similar conditions[25], but comparable to that of tryptophan[32]. On the other hand, the

4

Rate	Addition	Global fit	95% conf.	Unit
k_{isc}	–	0.93	±0.21	μs^{-1}
k_T	– O_2	0.021 1.6	±0.0044 ±0.29	μs^{-1} $mM^{-1}\mu s^{-1}$
k_{ee}	–	5.3	±0.49	μs^{-1}
k_{red}	– O_2 Asc^-	2.8 −1.6 0.25	±0.51 ±0.34 ±0.027	μs^{-1} $mM^{-1}\mu s^{-1}$ $mM^{-1}\mu s^{-1}$
k_{deprot}	– $TRIS$ H_2O_2 OH^-	3.9 0.012 0.4 0.16	±0.38 ±0.0033 ±0.23 ±0.055	μs^{-1} $mM^{-1}\mu s^{-1}$ $mM^{-1}\mu s^{-1}$ $mM^{-1}\mu s^{-1}$

Table 1. Rate parameter values for the NADH model in Fig. 2, as determined by global fitting of TRAST curves recorded in aqueous solution under OPE at 355 nm (Fig. 1). Confidence intervals reflect specifically the uncertainty in the global, non-linear least square fit of the TRAST curves.

resulting electron ejection quantum yield, $\Phi_{ee} \sim 0.002$, is much lower than those determined by flash photolysis[26,27], $\Phi_{ee} \sim 0.08 - 0.4$. This suggests that a large fraction of the ejected electrons recombine with ·NADH$^+$, thereby forming ^{0}NADH, before full dissociation from ·NADH$^+$. Flash photolysis studies show that this recombination takes place on a time scale of pico- to nanoseconds[26]. In our model, on the slower time scale reflected in the TRAST measurements, the combined electron ejection and recombination process is therefore contained in the overall decay rate, k_{10}, from ^{1}NADH to ^{0}NADH. ·NADH$^+$ molecules not directly recombining with their ejected electrons can either return to ^{0}NADH by taking up another electron from the solvent molecules (k_{red}), or undergo de-protonation by a concerted electron-H atom transfer[38] into NAD$^+$ (k_{deprot}). From the TRAST data, k_{deprot} was determined to $3.9 \cdot 10^6 \text{s}^{-1}$, which agrees well with literature data[29,40]. Given its nature, it is reasonable that k_{deprot} is increased upon addition of OH$^-$, TRIS and H$_2$O$_2$, as observed. Second order rate constants of k_{deprot} have only been reported for OH^{-}[40], and is in agreement with the value found in this study (see Table 1). For the solvent-mediated reduction rate of ·NADH$^+$, k_{red}, we determined a first order rate of $2.8 \cdot 10^6 \text{ s}^{-1}$, and second order rate constants, $k_{Q,red}$, of $2.5 \cdot 10^8 \text{ M}^{-1}\text{ s}^{-1}$ and $-1.6 \cdot 10^9 \text{ M}^{-1}\text{ s}^{-1}$ for Asc$^-$ and O$_2$, respectively. The value for $k_{Q,red}(\text{Asc}^-)$ is about an order of magnitude higher than that determined for tryptophan[32], but correspondingly lower than that for the organic dye rhodamine 6 G[25], under similar experimental conditions. The negative value of $k_{Q,red}(\text{O}_2)$ likely reflects the high electron affinity of molecular oxygen, which reduces the supply of electrons available to ·NADH$^+$, for recombination back to ^{0}NADH. This is in agreement with the finding that O$_2$ increases the overall photo-oxidation rate of NADH to NAD^{+}[41].

To exclude alternative photophysical models, we also evaluated 8 variations of the model in Fig. 2 and determined the most likely candidate based on the Akaike and Bayesian information criteria (AIC and BIC)[42–44]. Indeed, the AIC and BIC scores clearly favour the model of Fig. 2, with a one-photon excitation dependence of k_{ee}, which solely originates from ^{1}NADH, and not from ^{T}NADH, yet with ^{T}NADH included in the model (See SI section 8 for details regarding the evaluated models and the resulting relative likelihoods). The NAD$^+$ state in our model in reality represents several states, all non-fluorescent and long-lived. On the time-scale of the TRAST experiments the recovery rate from NAD$^+$ back to ^{0}NADH can thus be solely attributed to a diffusion-mediated net influx of fresh molecules, from the solution outside of the focused laser excitation beam. To account for this influx, we used two dark states with separate recovery rates in the model, representing the different influx rates along the elongated axial and shorter radial dimension of the laser-excited detection volume (see SI section 4 for details). This is also the diffusion model favoured by the AIC and BIC analysis. The effective diffusion recovery rates were kept constant throughout the global analysis and did not affect any relative changes seen in the TRAST curves.

Solution measurements with two-photon excitation.
With the photophysical model established for OPE TRAST measurements of NADH in aqueous solution, we next investigated how this model applies to TPE by a pulsed Ti:Sapphire laser beam, circularly scanned in the sample (see Methods and Materials). TRAST curves were generated by varying the scanning speed, as previously demonstrated for OPE[31], while recording the average fluorescence intensity for each effective excitation duration, w_{eff}.

Excitation power dependence and ascorbate titration effects. TRAST curves under TPE, with time-averaged I_{exc} varying from 2.6 to 5.2 MW/cm^2 are shown in Fig. 3C. The initial fluorescence intensity plotted against I_{exc} on a log-log scale yields a fitted slope of 2.0 ± 0.36 (Fig. 3A), in agreement with the expected TPE dependence. Plotting the effective photo-oxidation rates, $k'_{ox} \propto A_{TRAST}/(1 - A_{TRAST})$, in the same way (Fig. 3A), yields a slope of 2.8 ± 0.2. This compares well with the power-cubed dependence reported for photo-bleaching of several fluorophores, including NADH, under similar TPE conditions[45], but is not compatible with the linear electron ejection model used above for OPE. We therefore modified the NADH electronic state model by adding a second pathway for electron ejection, k_{ee-n}, taking place via OPE of ^{1}NADH to a higher electronic state, ^{n}NADH. Electron ejection from ^{n}NADH then takes place with a much higher yield compared to ^{1}NADH, see Fig. 2 (blue addition). Similar non-linear effects on photo-bleaching and photo-oxidation have also been observed in fluorophores upon OPE at I_{exc} levels at or beyond saturation[46,47]. A two-photon electron ejection dependence has also been reported from flash photolysis studies of NADH using 355 nm excitation[26,29]. In those studies, the average I_{exc}-levels within the laser excitation pulses were typically more than two orders of magnitude higher than the highest I_{exc} levels applied in our OPE TRAST measurements (Fig. 1A).
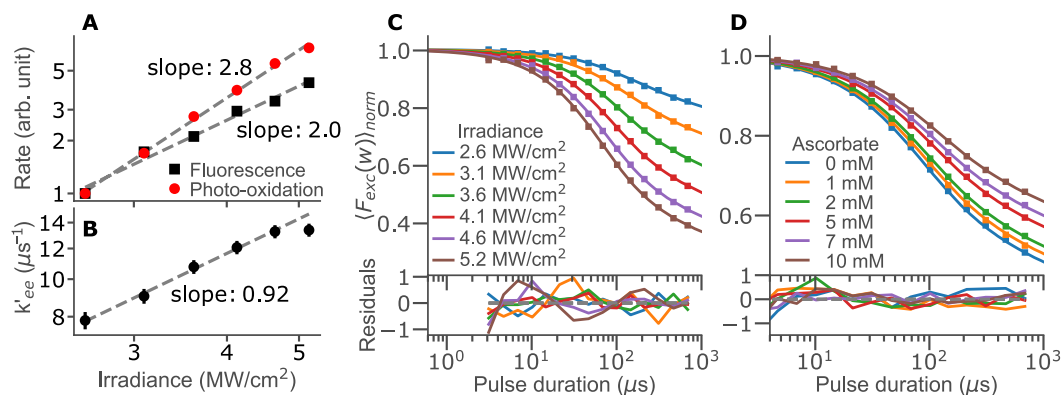
Figure 3. TPE TRAST measurements of 10 μM NADH in 50 mM TRIS buffer, pH 7.4. (**A**) Excitation irradiance dependence of the effective photo-oxidation (red circles) and fluorescence emission (black squares) rates, under TPE. The rates are displayed on a log-log scale, in arb. units, with slopes determined by a linear fit. (**B**) Excitation irradiance dependence of the fitted k_{ee} rates from the TRAST curves in (**C**), displayed on a log-log scale. The slope is determined by a linear fit, excluding the highest excitation intensity. (**C**) Experimental TRAST curves from NADH with different excitation irradiances applied. (**D**) Experimental TRAST curves from NADH (4.6 MW/cm²) with different concentrations of ascorbate added. TRAST curves in C and D were fitted as described in the main text, with absolute residuals multiplied by a factor of 100 for clarity.

In a similar way as with OPE (Fig. 1C), we recorded TRAST curves of NADH with TPE in the presence of Asc⁻. The recorded TRAST curves (Fig. 3D) also readily reflect the presence of a reducing agent, with decreasing decay amplitudes in the TRAST curves upon Asc⁻ titration, in agreement with an increased rate from $\cdot$NADH⁺ back to ⁰NADH.

Global parameter fitting to TRAST curves generated under TPE. TRAST curves recorded under TPE with different I_{exc} (Fig. 3C) and from samples with different concentrations of Asc⁻ (Fig. 3D) were subject to a global fit, based on a model including electron ejection from a higher excited state, ⁿNADH, as discussed above. The excitation rates were calculated from an NADH TPE cross section of 0.4 GM[48], and by taking pulse characteristics and spatial distribution of I_{exc} in the laser focus into account (see Methods and Materials and SI). Under the experimental conditions and range of w applied, k_{isc}, k_T, $k_{Q,T}(O_2)$ can be expected not to have any significant influence on the TRAST curves and were therefore fixed to the values determined under OPE. ⁿNADH has a very short lifetime ($\ll$ns) and cannot be resolved on the time-scale of the TRAST experiments. Similar to previous studies of organic fluorophores under saturating OPE[25], the photo-induced electron ejection can therefore be assumed to take place both via ¹NADH and ⁿNADH and can be fitted as one effective rate, k'_{ee}. Because of excitation of ¹NADH to ⁿNADH, k'_{ee} can also be expected to have an I_{exc} dependence. The k'_{ee} rate was therefore fitted individually to each of the TRAST curves in Fig. 3C. The remaining rate parameters, k_{red}, k_{deprot}, $k_{Q,red}(Asc^-)$, and the diffusion recovery parameter, were all fitted globally, as for the OPE TRAST curves discussed above. The global parameter values, as fitted to the curves in Fig. 3C,D, are $k_{red} = 2.9 \pm 1.4$ μs⁻¹, $k_{deprot} = 4.4 \pm 2.7$ μs⁻¹, and $k_{Q,red}(Asc^-) = 0.63 \pm 0.34$ μs⁻¹ mM⁻¹. The wider confidence intervals obtained from the TPE data reflect the smaller dataset used and that the maximum speed of the scanner is on the limit to allow analysis of the faster triplet state relaxation of NADH. Nonetheless, all rates are in reasonable agreement with those determined from the OPE TRAST data (Table 1), indicating that they are not influenced by the different mode of excitation (pulsed TPE) and excitation modulation (scanning). The individually fitted k'_{ee} values are shown in Fig. 3B. Plotted on a log-log scale, they display a slope of 0.9 ± 0.1, suggesting a one photon excitation to occur from ¹NADH to ⁿNADH, from where a more efficient photo-oxidation then can take place. The slope in Fig. 3B is well in agreement with the I_{exc}-dependence of the overall photo-oxidation rate, as shown in Fig. 3A.

As for the OPE data, we also evaluated alternative photophysical models for the data obtained under TPE, based on the AIC and BIC criteria. Thereby, both a model with an I_{exc}-independent k'_{ee} rate (two-photon model), and with a k'_{ee} rate proportional to the photon flux squared (four-photon model) could be clearly discarded (see SI section 8).

Two-photon NAD(P)H imaging of live cells. *TRAST imaging.* We then performed scanned TPE TRAST imaging of unlabelled mouse myoblast cells. Through repeated line-by-line scans over the same field-of-view, while applying different scan speeds, we could extract the same TRAST information as for circular scanning in solution (Fig. 3), but now in a spatially resolved manner (Fig. 4). The photo-damage of cells in TPE microscopy is confined to the focal excitation volume, but follows a non-linear excitation intensity dependence[49]. To minimize photo-toxic effects on the cells, we only used two different scan speeds, with effective durations of excitation faster ($w_f = 12$ μs) and slower ($w_s = 600$ μs) than the overall decay time of the TRAST curves, as determined above (Fig. 3). Thereby, the total excitation light dose never exceeded TPE dose levels where long-term (days) photo-toxic effects can start to occur (10 kJ/cm², determined at a peak excitation irradiance of 1.2 TW/cm²,
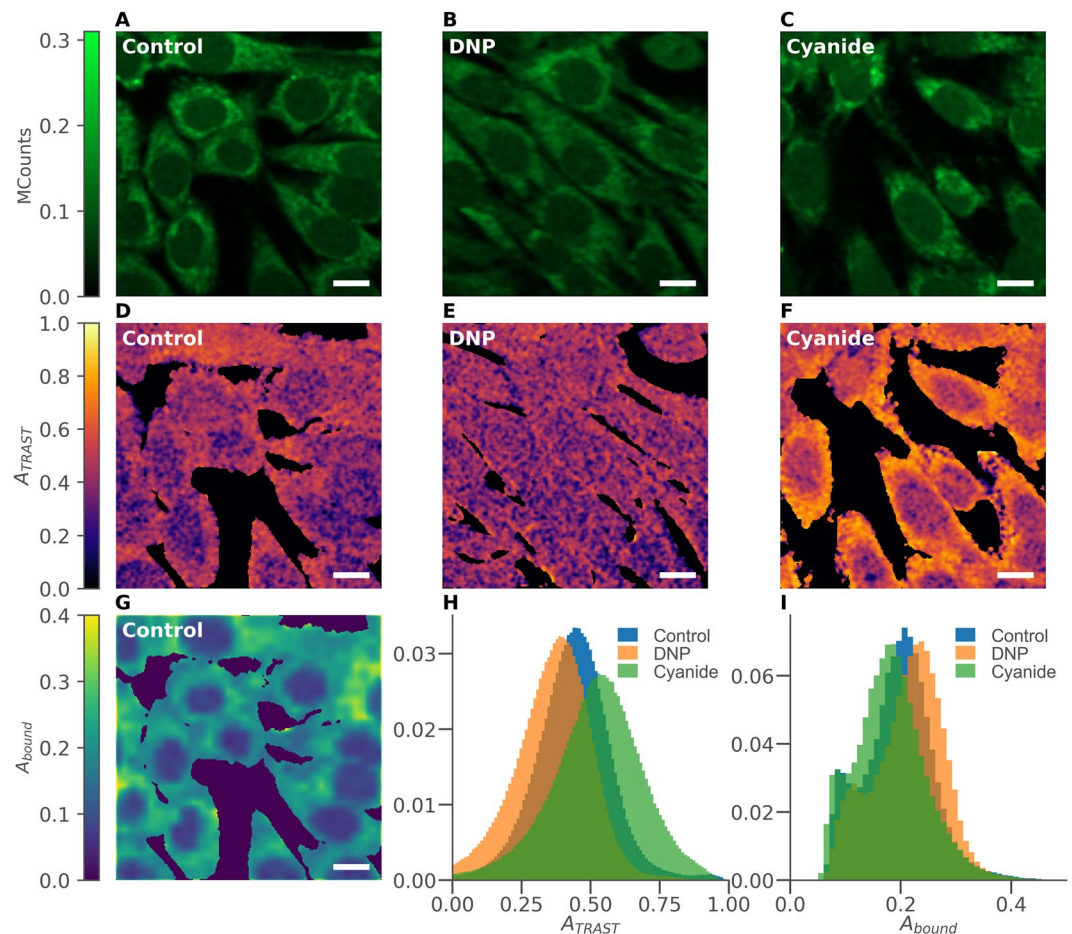
Figure 4. TPE images of cultured mouse myoblast cells in clear DMEM imaging medium (control), or with either $200\,\mu M$ DNP or $1\,mM$ cyanide added directly to the medium 30 minutes before measurements. Fluorescence intensity images (fast scan), $F(w_f)$, of (**A**) control cells, (**B**) DNP-exposed cells, and (**C**) cyanide-exposed cells. TRAST images showing the NAD(P)H dark state population, $A_{TRAST} = (F(w_f) - (F(w_s))/(F(w_f)$, for (**D**) control cells, (**E**) DNP-exposed cells, and (**F**) cyanide-exposed cells, corresponding to the above fluorescence intensity images in A, B, and C. (**G**) Image showing the fraction of bound NAD(P)H, A_{bound}, as determined by FLIM (corresponding to the images in A and D). (**H**) Normalized histograms of A_{TRAST} in pixels belonging to contol cells (blue), DNP-exposed cells (orange) and cyanide-exposed cells (green). (**I**) Corresponding distributions of A_{bound} in contol cells (blue), DNP-exposed cells (orange) and cyanide-exposed cells (green). Distributions shown in H and I are based on 131 control cells, 130 DNP-exposed cells, and 160 cyanide-exposed cells. In both histograms, the number of pixles included were: 932494 (control), 917523 (DNP), 1177003 (cyanide). (Scalebars: $10\,\mu m$).

twice the one used in this study)[50]. From the difference in average fluorescence intensity, recorded pixel-by-pixel upon fast and slow scanning ($F(w_f)$ and $F(w_s)$), we then imaged the local photo-induced dark state build-up of NADH in the cells as $A_{TRAST} = (F(w_f) - (F(w_s))/(F(w_f)$. With knowledge of the NADH electronic state model for TPE, this build-up could then be related to changes in the local environment experienced by NAD(P)H in the cells. In parallel with the TRAST imaging, we also recorded full TPE FLIM data from the NAD(P)H fluorescence using time-correlated single photon counting (TCSPC, see Methods and Materials).

Figure 4A shows a regular NAD(P)H fluorescence intensity image, $F(w_f)$, of unlabelled mouse myoblast cells in a clear DMEM imaging medium. The corresponding TRAST image is shown in Fig. 4D, displaying a lower NAD(P)H dark state population in the cell nuclei as opposed to the cytosol. Averaging A_{TRAST} over 131 cells confirmed this observation and resulted in an average dark state population of $\langle A_{TRAST}\rangle_{control} = 0.43 \pm 0.02$, with a clear separation between the nuclear, $\langle A_{TRAST}\rangle_{nucl} = 0.38 \pm 0.02$, and cytosolic, $\langle A_{TRAST}\rangle_{cyto} = 0.45 \pm 0.02$, regions.

To investigate how changes in the metabolic states of the cells can influence A_{TRAST} of NAD(P)H, we also imaged cells with either $1\,mM$ cyanide (n = 160 cells) or $200\,\mu M$ of the mitochondrial un-coupler dinitrophenol (DNP)[51] (n = 130) added to the culturing medium 30 minutes before acquiring the images (see Methods and Materials). While no particular differences can be identified in the fluorescence intensity images (Fig. 4A–C), the TRAST images revealed a significant increase in A_{TRAST} of NAD(P)H in cells exposed to cyanide (Fig. 4F), with $\langle A_{TRAST}\rangle_{cyanide} = 0.52 \pm 0.02$. In contrast, cells exposed to DNP showed a decreased dark state amplitude, $\langle A_{TRAST}\rangle_{DNP} = 0.36 \pm 0.02$, particularly in the cytosolic regions. The opposite effects of DNP and cyanide exposure

on A_{TRAST} likely reflect the opposite effects of these compounds on the electron transport chain (ETC) in the mitochondria of the cells. While DNP as an un-coupler induces an increased activity in the ETC, cyanide is an ETC inhibitor[11]. Histograms of A_{TRAST} values from these three different categories of cells (control, DNP-exposed, cyanide-exposed), recorded from individual pixels in the TRAST images, are shown in Fig. 4H. The spread in A_{TRAST} values largely reflects differences in the oxidative environment between nuclear and cytosolic regions of the cells, in particular for the cyanide exposed cells. Despite this spread however, the different categories of cells can be clearly distinguished based on these whole cell pixel histograms.

TPE scanned TRAST measurements of NADH in TRIS buffer showed no effect of either 1 mM cyanide or 200 μM DNP (data not shown), i.e. cyanide and DNP themselves did not directly influence A_{TRAST}.

TRAST imaging, combined with fluorescence lifetime data.   Next, we analysed how the TRAST images, as recorded above using TCSPC, relates to FLIM-analysis of the same data. The combined TCSPC data from all measured cells was fitted to a two-exponential fluorescence decay model (see Methods and Materials). The two lifetimes, representing the average lifetimes of free and bound NAD(P)H in the cells, were determined to τ_{free} = 0.4 ns and τ_{bound} = 2.4 ns. The τ_{free} value is well in agreement with what has been reported previously[12,52]. τ_{bound} depends on what proteins NAD(P)H is bound to, as well as on local viscosity. Our average τ_{bound} value lies well within the reported range of fluorescence lifetimes of protein-bound NAD(P)H (around 1 ns up to 3.5 ns), in solution or in different cells[3,12,17,52,53]. It also lies in between reported intracellular lifetimes of NADH (~1.5 ns) and NADPH (~4 ns)[54]. With τ_{free} and τ_{bound} fixed to 0.4 ns and 2.4 ns, respectively, the relative amplitudes of the two lifetime components were fitted pixel-wise in the cellular images, using a maximum likelihood estimator (MLE) (see Methods and Materials). Correcting for the difference in fluorescence brightness (by assuming that the fluorescence quantum yields of the free and bound fractions are proportional to τ_{free} and τ_{bound}, respectively) allows the bound fraction of NAD(P)H, A_{bound}, to be calculated in each pixel. Thereby, cellular images showing the fraction of bound NAD(P)H were generated (Fig. 4G), revealing a lower A_{bound} in the nuclear regions of the cells. The cytosol regions of the cells were found to contain sub-regions with enhanced levels of bound NAD(P)H, localized around the nuclei. Their locations corresponds to that expected for mitochondria, in which typically also a larger fraction of bound NAD(P)H is found[18,54]. However, when comparing A_{bound} between control cells and those exposed to cyanide or DNP, only minor differences could be observed (Fig. 4I), with $\langle A_{bound} \rangle_{control}$ = 0.20 ± 0.01, $\langle A_{bound} \rangle_{cyanide}$ = 0.18 ± 0.01, and $\langle A_{bound} \rangle_{DNP}$ = 0.21 ± 0.01. The effects observed in the FLIM data upon addition of DNP are minor, and not as evident as the differences we see in the dark state population by TRAST imaging (Fig. 4H). Similarly, the effects observed upon addition of cyanide are more prominent in the TRAST compared to the FLIM images. Like $\langle A_{TRAST} \rangle$, also $\langle A_{bound} \rangle$ shows opposite effects upon addition of DNP and cyanide, reflecting the different mechanisms of action of these compounds. The slight increase and decrease in A_{bound} found in cells exposed to DNP and cyanide, respectively, is in agreement with previous NAD(P)H FLIM studies of cells exposed to similar uncouplers and blockers, when added over comparable exposure times and doses[18,19,54].

Overall Fig. 4A–I thus indicate that the NAD(P)H dark state population, as imaged by TRAST, can reflect changes in the local environment upon addition of either cyanide or DNP. These changes are also reflected in the NAD(P)H bound fraction, as imaged by FLIM, although to a smaller degree. To investigate to what extent both TRAST and lifetime data can be used to identify cells based on such changes, we calculated the average bound fraction, $\langle A_{bound} \rangle$, and dark state amplitude, $\langle A_{TRAST} \rangle$, for each individual cell studied above, see Fig. 5A. We then used a standard machine learning algorithm (*random forest classifier, scikit-learn, python*, see Method and Materials) to perform a simple classification of all the 421 cells studied as belonging to either the control, DNP-exposed, or cyanide-exposed group. On an individual cell level, the average classification accuracy when using $\langle A_{TRAST} \rangle$ was 64%, while the corresponding analysis based on $\langle A_{bound} \rangle$ resulted in 52% of the cells being correctly identified. Using both $\langle A_{TRAST} \rangle$ and $\langle A_{bound} \rangle$ together resulted in a better classification accuracy of 75% for single cells, indicating that the two parameters represent at least partially independent information. All single cell classification probabilities are summarized in Supplementary Fig. S5. The predictive capacity can be considerably improved by sampling more than one cell from the same category. Figure 5B shows the extrapolated accuracies, based on the probabilities in Supplementary Fig. S5, to correctly classify a group of N cells. In this case each individual cell is evaluated separately, and the final category is assigned based on the most common result. In our case, a 99% accuracy would be obtained if both TRAST and lifetime data from 19 cells is used. The same accuracy using only TRAST data requires 129 cells, while using only lifetime data would require ≫200 cells.

As seen in Fig. 4D–F, additions of DNP or cyanide tend to affect A_{TRAST} differently in nuclear and cytosolic regions of the cells. With the stronger response generally seen in the cytosolic regions, the classification accuracy could potentially be increased if only pixels from the cytosol are included. In Fig. 5C,D, the corresponding single cell averages as in Fig. 5A are shown, but now only including pixels from the cytosolic and nuclear regions of the cells, respectively. In our case, only a minor benefit in the classification could be noted.

The general trend observed in Fig. 5A is that there is a negative correlation between $\langle A_{TRAST} \rangle$ and $\langle A_{bound} \rangle$ upon perturbation of the cells with either DNP or cyanide. This observation might seem counter-intuitive from a photodynamic point of view (Fig. 2), since an increase in $\langle A_{bound} \rangle$ also represents an increase in the average NAD(P)H fluorescence lifetime, $\langle \tau_F \rangle$. In a model where excitation to ^{1}NADH (or ^{n}NADH) leads to dark state formation with an average electron ejection quantum yield of $\langle \Phi_{ee} \rangle = k_{ee} \cdot \langle \tau_F \rangle$, an increased fluorescence lifetime is expected to result in a correspondingly higher photo-induced dark state formation. However, flash photolysis studies of NADH[27] indicate that electron ejection, observed via transient absorption of solvated electrons, is not directly coupled to the excitation (since the absorption is not observed within the time of the laser excitation pulse) or to the population of ^{1}NADH (since the transient absorption of solvated electrons appears at a much faster time-scale than the lifetime of ^{1}NADH). Electron ejection was instead suggested to take place from an "intermediate state", possibly an excited vibrational state of ^{1}NADH. If electron ejection does not take place from
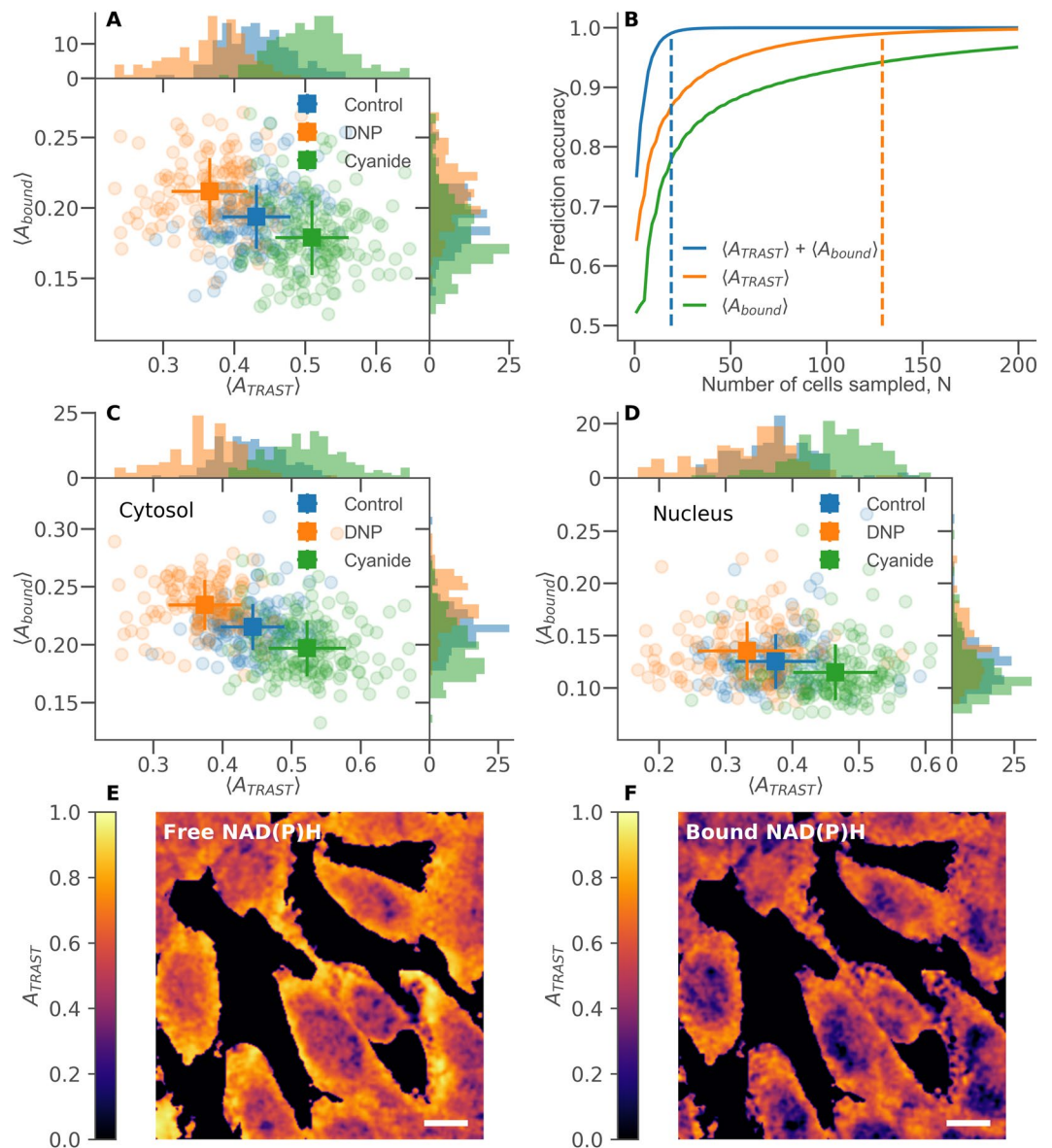
Figure 5. (**A**) Distributions of average dark state amplitudes, $\langle A_{TRAST}\rangle$, and bound fractions, $\langle A_{bound}\rangle$, of NAD(P)H, calculated as individual cell averages for control cells and cells exposed to either $200\,\mu M$ DNP or 1 mM cyanide. Square markers indicate sample average and standard deviation. (**B**) Average prediction accuracy as a function of number of cells sampled, N, when classifying cells as belonging to either the control, DNP-exposed or cyanide-exposed group. The classification was based on the machine learning procedure described in Methods and Materials. Utilizing both $\langle A_{TRAST}\rangle$ and $\langle A_{bound}\rangle$ together results in the highest accuracy. Dashed lines indicate the point of 99% accuracy (19 cells for A_{TRAST} combined with $\langle A_{bound}\rangle$, 129 cells for $\langle A_{TRAST}\rangle$ only, $\gg$200 for $\langle A_{bound}\rangle$ only). Manually selecting the cell nuclei in each image allows the separation of Fig. 5A into the distribution for the cytosolic (**C**) and nuclear regions (**D**). Utilizing the images of A_{bound} (e.g. Fig. 4G) for both fast and slow scanning allows TRAST images to be generated for free (**E**) and bound (**F**) NAD(P)H separately. Both these images are extracted from the image in Fig. 4F, showing cyanide-exposed cells. (Scalebars: $10\,\mu m$).

a vibrationally relaxed ^{1}NADH, then the electron ejection yield can be independent of τ_F. This can explain the observation that $\langle A_{TRAST}\rangle$ and $\langle A_{bound}\rangle$ are not directly coupled, and suggests that $\langle A_{TRAST}\rangle$ does indeed reflect a changed oxidative environment in the cell, as opposed to the variations in fluorescence lifetime (bound fraction) reported by FLIM. This implies that FLIM and TRAST imaging data do provide orthogonal information and that better identification of cellular metabolic states is possible when both modalities are used in parallel.

Given that TRAST and FLIM data is imaged in parallel, it is also possible to produce TRAST images based on subsets of the recorded photon counts. Using the fractions of bound NAD(P)H, determined by FLIM in both the fast and slow fluorescence images, it is possible to calculate A_{TRAST} for free and bound NAD(P)H separately. This is demonstrated in Fig. 5E,F, where a TRAST image of cyanide-exposed cells (Fig. 4F) has been separated into the contributions from free and bound NAD(P)H.

In conclusion, we show in this work that the dynamics of photo-induced dark states of NAD(P)H can be monitored by TRAST. The transient state data obtained by TRAST compares well with flash photolysis data but can be applied on a much broader range of samples and measurement conditions. We show that TRAST imaging of NAD(P)H can be applied on live cells, adds information about the local metabolic state of the cells, and allows classification of cells with higher accuracy than when based on FLIM alone. TRAST imaging is straight-forward and can be applied in parallel with FLIM for label-free cellular metabolic imaging. This will add additional independent parameters, increase specificity and sensitivity and thereby help overcome some of the limitations encountered in such measurements.

Methods and Materials

Theory of transient state (TRAST) spectroscopy.
TRAST spectroscopy determines fluorophore blinking kinetics by monitoring how systematic changes in the excitation pattern affect the time-averaged fluorescence signal returned[30–33,55,56]. In this work, we implemented TRAST in a confocal setting, first using on/off modulation of the stationary excitation laser, and later in a scanned configuration by systematically varying the scan speed whilst imaging.

Stationary TRAST. The emitted luminescence intensity from a sample can for most fluorophores, including NADH, be considered proportional to the population of the first excited singlet state. The time averaged fluorescence signal resulting from a rectangular excitation pulse of duration w is then

$$\langle F_{exc}(w)\rangle = cq_f q_D k_{10} \frac{1}{w} \int_{t=0}^{w} \left(\iiint {}^1NADH(\bar{r}, t)\, CEF(\bar{r})\, dV \right) dt \tag{1}$$

where $CEF(\bar{r})$ is the normalized collection efficiency function, c is the fluorophore concentration, q_f is the fluorescence quantum yield and q_D is the overall detection quantum yield of the instrument. The simulations of the excited singlet state population, ${}^1NADH(\bar{r}, t)$, are outlined in SI section 1, with further simplifications to Eq. (1) described in Data Analysis and in SI sections 4 and 5. By monitoring the change in $\langle F_{exc}(w)\rangle$ in response to varying pulse durations, the set of photophysical rate parameters that best match the experimental data can be determined (see Data Analysis).

In order to collect enough photons even for short w, pulse trains consisting of N identical excitation pulses, of pulse period T, are recorded onto a single exposure of the integrating detector. For each pulse train, a constant illumination time, $t_{ill} = N \cdot w$, is typically maintained. At the same time, the excitation duty cycle, $\eta = w/T$, is kept low to make sure the sample can relax back to the same initial condition before the onset of the next excitation pulse. Each value of w then completely defines an excitation pulse train, recorded in its entirety by the detector using an exposure time of $t_{exp} = t_{ill}/\eta$. A so-called TRAST curve is produced by measuring $\langle F_{exc}(w)\rangle$ from pulse trains over a range of excitation durations and normalizing at the shortest pulse duration used, w_0.

$$\langle F_{exc}(w)\rangle_{norm} = \left(\frac{1}{N}\sum_{i=1}^{N} \langle F_{exc}(w)\rangle_i \right) / \left(\frac{1}{N_0}\sum_{i=1}^{N_0} \langle F_{exc}(w_0)\rangle_i \right) \tag{2}$$

where $\langle F_{exc}(w)\rangle_i$ is the fluorescence response from the i:th pulse in the pulse train. If the duty cycle is low, $\langle F_{exc}(w)\rangle_i$ can be assumed identical for all i and the expression simplifies further. Note that the normalization step of Eq. (2) cancels out many experimental constants in the calculation of $\langle F_{exc}(w)\rangle_i$, e.g. fluorophore quantum yield, sample concentration and overall detection efficiency of the optical system.

Scanned TRAST with TPE. Excitation modulation can also be achieved by scanning a focused excitation beam across the sample, using the scan speed, v, to control the duration of excitation, w. For a homogeneous solution sample we get

$$\langle F_{exc}(v)\rangle = cq_f q_D k_{10} \iiint {}^1\text{NADH}(\bar{r}, v) \cdot CEF(\bar{r})\, dV \tag{3}$$

Here the coordinates are defined from the perspective of the laser, such that the normalized $CEF(\bar{r})$ remains time-independent. A TRAST curve is then produced by converting the scan speed to an effective fluorophore excitation duration, w_{eff} (see SI section 3), and then, analogous to Eq. (2), normalizing by the excitation duration corresponding to the fastest scan speed, $w_{eff,0}$

$$\left\langle F_{exc}(w_{eff})\right\rangle_{norm} = \left\langle F_{exc}(w_{eff})\right\rangle / \left\langle F_{exc}(w_{eff,0})\right\rangle \tag{4}$$

If TRAST imaging is to be performed, the fluorescence time trace is first binned to pixels before the TRAST ratio is taken for each pixel separately. This TRAST approach can be realized on any standard confocal scanning microscope, without the need for intensity modulation (see Fig. 6). Furthermore, measurement times can be significantly reduced compared to stationary TRAST, since photon collection does not have to be interrupted to allow the sample to recover. Suitable fluorophore recovery time between excitations is instead achieved by setting the length of the path to be scanned, while photon collection is continuously ongoing at other locations in the sample. Supplementary Fig. S3 shows an example of an intensity trace recorded using scanned TRAST in NADH solution.
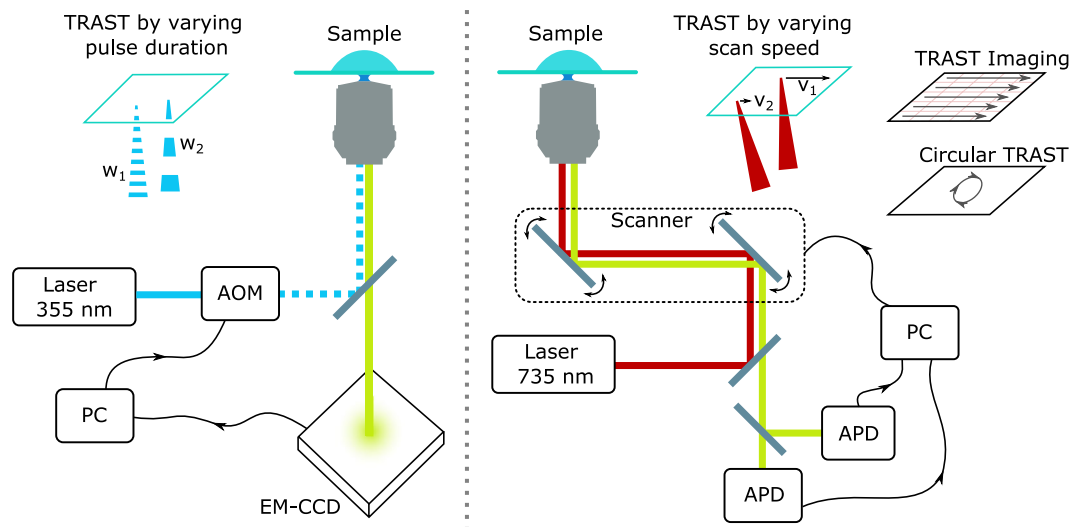
Figure 6. Schematic representation of stationary TRAST (**A**) and scanned TRAST (**B**). See Instrumentation for details.

Compared to stationary TRAST, simulating the speed dependent $^1NADH(\bar{r}, v)$ is much more computationally intensive. The excitation pulses in scanned TRAST are no longer rectangular in time since scanning with a Gaussian beam creates a continuous rise and fall of the excitation rate, $k_{01}(t)$, as the beam passes by. The TPE laser is also pulsed, adding a fs time dependence to the excitation pattern as well. In this work, we designed a simplified model with continuous rectangular excitation pulses of amplitudes and durations such as to generate equivalent effects on the NADH transient state build-up. The fs pulse micro-time averaging is described in SI section 2 and the macro-time variations due to scanner movement in SI section 3.

Instrumentation. *OPE TRAST measurements.* One-photon measurements were performed on a home built, epi-illuminated microscope using a 355 nm continuous wave (CW) solid state laser (Cobolt Zouk, 20 mW) for excitation. The laser beam was chopped to square pulses by an acousto-optical modulator (AOM; MQ110-A1-UV, AA Opto-Electronics, Orsay), and then focused into the sample by a water immersion objective (40×, NA 1.2, Zeiss, C-Apochromat). The $1/e^2$-radius of the laser beam in the focal plane was 863 nm. Fluorescence from the sample was collected through the same objective, separated from the excitation light by a dichroic beamsplitter (Di02-R405, Semrock) and a 364 nm long-pass filter (BL01–364R, Semrock), and then detected by a 658×496 pixel EM-CCD camera (Andor Luca). By only considering the signal focused on a few central pixels, an effective 100 μm pinhole was introduced. Control of the AOM modulation as well as synchronisation with the detection was handled by a digital I/O card (PCI-6602, National Instruments) and a custom Matlab script.

Excitation pulse durations, w, were set from 500 ns to 1 ms and were distributed logarithmically. For a given w, the number of identical pulse repetitions, N, was selected to maintain a constant total illumination time, $t_{ill-OPE} = w \cdot N = 50$ ms. The pulse train duty cycle was set to $\eta = 1\%$. Any bleaching of the sample was accounted for by inserting brightness reference measurements as every third pulse train. For these reference measurements, we used the shortest available pulse duration, w_0, to avoid any dark state build-up.

TPE TRAST measurements. The measurements were based on a commercial, epi-illuminated, confocal laser scanning microscope (Olympus FV1200) with a water immersion objective (60×, NA 1.2, Olympus, UPlanSApo) and the pinhole set to its maximum size (800 μm). The microscope was modified to allow external control of the galvo-scanning mirrors using a digital I/O card (DaqBoard/3001USB, Measurement Computing) controlled by custom software written in Matlab. The excitation source was a mode-locked Ti:Sapphire laser (Coherent, Mira) tuned to 735 nm, with a repetition rate of 76 MHz and a pulse width measured to 150 fs FWHM. The beam radius in the focal plane was measured to 327 nm ($1/e^2$) by scanning 24 nm fluorescent beads (FluoSpheres, Carboxylate-Modified Microspheres 505/515, #F8787, Invitrogen) deposited on a regular cover slide. Fluorescence light was separated from the excitation light by a 680 nm dichroic mirror (Chroma) and a 680 nm short-pass filter (ET680sp-2P8, Chroma), before focused onto two APD detectors (Perkin & Elmer, SPCM-AQR-14) connected to a TCSPC module (HydraHarp 400). An additional emission filter (HQ445/60, Chroma) was added for cell-imaging to separate the NAD(P)H emission from that of other autofluorescent species in the cells.

For solution measurements, a circular scanning pattern of 28.3 μm diameter was used, with the scan speed adjusted in 14 steps to yield effective excitation pulse durations between 2 μs and 690 μs (see SI section 3). Data was collected for 0.5 s at each fixed speed, and the whole measurement sequence was repeated 20 times for a total illumination time of $t_{ill-TPE} = 20 \cdot 0.5 s = 10 s$ per scan speed. Any sample bleaching or evaporation could

be tracked directly in the data, since each scan speed was repeated 20 times (see Supplementary Fig. S3 for an example of scanned TRAST data).

For live cell scanned TRAST imaging, traditional line-by-line scanning was performed in a $90 \times 90 \, \mu m$ field of view, binned to 128×128 pixels. The excitation intensity was measured to $2.6 \, MW/cm^2$. To minimize photo-toxicity, only two scan speeds (corresponding to $w_f = 12 \, \mu s$ and $w_s = 600 \, \mu s$ effective laser dwell times) were used. The faster scan was repeated 50 times in order to reach directly comparable photon counts, i.e. $50w_f = w_s$. These repeated frames also serve as bleaching reference points for each pixel. After image alignment (see Data Analysis), the pixel-by-pixel TRAST decay amplitude was extracted as the normalized difference between the two images, $A_{TRAST} = (F(w_f) - F(w_s))/(F(w_f))$.

Data analysis. *Solution measurements.* TRAST curves were analysed using custom software implemented in Matlab. Pre-processing included the subtraction of a static background component as well as corrections for any changes in sample concentration due to bleaching or evaporation. The background is due to ambient light and detector dark counts and typically amounted to 100 counts per second and pixel, corresponding to about 10% of the total signal in our measurements. The concentration correction was based on brightness references acquired throughout each measurement at regular intervals. The effect of bleaching turned out to be negligible, while concentration changes due to evaporation typically caused around 2% drift in brightness over the course of one measurement.

Stationary TRAST curves, recorded under OPE with a stationary laser beam, were simulated by use of eq. (S3), using the average excitation rate in eq. (S12) (see SI section 5) and the simplified diffusion model in eq. (S10) (see SI section 4). For a given photophysical model, the rate parameters that best described the experimental data were then found through non-linear least squares optimization.

For TRAST data acquired by laser scanning, we used a rectangular pulse shape approximation described in SI section 3 as well as the TPE pulse averaging in eq. (S6) (SI section 2) and spatial averaging in eq. (S13) in SI section 5. Thereby, scanned TRAST data could be fitted in the same way as stationary TRAST curves, with no modifications to the fitting algorithm.

Scanned TRAST Imaging. Scanned TRAST images were expressed as the pixel-by-pixel dark state amplitude, calculated by comparing the recorded average fluorescence intensity from fast and slow scanning, $A_{TRAST} = (F(w_f) - F(w_s))/(F(w_f))$.

When recording confocal laser scanning images, a scan-speed dependent offset of the images was observed. The difference between fast and slow scanning amounted to $0.63 \, \mu m$ or a fixed 0.9 pixel offset. This offset becomes crucial if ratio images are to be produced and an image alignment step was added to prevent edge effect near high contrast regions of the images. First, both images were oversampled (using scikit-image, v. 0.21.2, in Python) by a factor of 10 and translated to maximize the correlation between the two. The overlaid images were then returned to original resolution before calculating a TRAST image. This procedure is very similar to the treatment in[31].

FLIM and free/bound NADH ratios. The data acquired for scanned TRAST imaging, could also be used for FLIM analysis. To get the best possible photon statistics, the combined dataset of all measured cells was first fitted to two lifetime components, yielding $\tau_{free} = 0.4 \, ns$ and an average $\tau_{bound} = 2.4 \, ns$ (see Results). These lifetimes were then fixed, and only their relative amplitude was fitted for each pixel individually using maximum likelihood estimation (MLE). The MLE included deconvolution with the instrument response function (IRF) for each respective detection channel and the estimated amplitude was weighted by relative brightness to obtain the fraction of bound NAD(P)H in each pixel (Fig. 4G). With the large difference between τ_{free} and τ_{bound}, the MLE could reliably differentiate between the short and long lifetime components, even if some uncertainty in the local lifetime of bound NAD(P)H is assumed. The estimated bound fraction showed only minor variations when τ_{bound} was varied between 2 and 3 ns.

Cell classification using machine learning. The boundary of each cell (in total 131 control, 130 DNP-exposed, and 160 cyanide-exposed cells) was manually selected in the fluorescence intensity images (e.g. Fig. 4A). For each cell, the average A_{TRAST} and bound fraction of NAD(P)H was then calculated based on the corresponding TRAST (e.g. Fig. 4D) and lifetime (e.g. Fig. 4G) images. A standard python machine learning algorithm (*scikit-learn, v. 0.21.2 sklearn.ensemble.RandomForestClassifier*) was used with default parameters, except for *n_estimators* = 500 and *max_depth* = 4. Training was performed on a random subset consisting of 80% of the cells, while the remaining 20% were kept for evaluating the model's predictive capacity. Given the small sample set (421 cells) we report the average prediction accuracy based on 10^3 training/evaluation runs, each using a new random subset of cells for training. The resulting probability matrices for cell classification are shown in Supplementary Fig. S5. These matrices were then used to calculate the prediction accuracy when evaluating multiple cells of the same type, as seen in Fig. 5B. This combined predictive accuracy refers to the total probability of all possible combinations of individual cell classification which result in the correct category receiving more votes than either of the two incorrect alternatives. In the classification in Fig. 5B, groups of control, DNP-exposed and cyanide-exposed cells were assumed to be equally likely to occur.

Sample preparation. Stocks of β-nicotinamide adenine dinucleotide (NADH; reduced disodium salt, Sigma N0786), β-nicotinamide adenine dinucleotide 2′-phosphate (NADPH; reduced tetrasodium salt, Sigma N0411), as well as TRIS buffer, sodium ascorbate, hydrogen peroxide and sodium hydroxide were all purchased from Sigma. Aliquots of 1 mM NADH in 50 mM TRIS buffer (pH 7.4) were prepared and stored at −80 °C. A new vial was thawed on every measurement day and further diluted using the same TRIS buffer. NADPH was treated in the same way. Solutions of sodium ascorbate were prepared daily using the same TRIS buffer.

Experiments with 355 nm excitation used quartz cover slides (CFQ-2417, UQG Optics) to avoid the strong background seen from regular glass cover slips at this wavelength.

Experiments with modified atmospheres were performed in a lightly pressurized chamber (custom built, 14 ml cylindrical container, bottom made from a replaceable CFQ-2417 quartz cover slide) with a constant flow of either argon or oxygen. The gas first flowed through a bubble humidifier to reduce evaporation of the sample.

Cell culture. C_2C_{12} cells (mouse myoblasts, ATCC CRL-1772) were grown in Gibco DMEM/F-12 (1:1) + GlutaMAX medium (ThermoFisher, 31331–028) supplemented by 10% FBS (Biowest, VWR #S1810–500). 24 hours before measurements, cells were seeded in #1.5 glass bottom microscopy wells (Nunc Lab-Tek II 8-well Chambered Coverglass), using the same medium. 30 minutes before measurements, the medium was changed to clear Gibco FluoroBrite DMEM imaging medium (ThermoFisher, A18967–01). The imaging medium contained either no additions ("control cells"), 200 µM dinitrophenol (Sigma D198501) ("DNP-exposed cells") or 1 mM potassium cyanide (Sigma 60178) ("cyanide-exposed cells").

Data availability

The datasets generated during and/or analysed during the current study are available from the corresponding author on reasonable request.

References

1. Srivastava, S. Emerging therapeutic roles for NAD(+) metabolism in mitochondrial and age-related disorders. *Clinical and Translational Medicine* **5**, UNSP25 (2016).
2. Martinez-Outschoorn, U. E., Peiris-Pages, M., Pestell, R. G., Sotgia, F. & Lisanti, M. P. Cancer metabolism: a therapeutic perspective. *Nature Reviews Clinical Oncology* **14**(1), 11–31 (2017).
3. Chakraborty, S., Nian, F. S., Tsai, J. W., Karmenyan, A. & Chiou, A. Quantification of the Metabolic State in Cell-Model of Parkinson's Disease by Fluorescence Lifetime Imaging Microscopy. *Scientific Reports* **6**, 19145 (2016).
4. Ying, W. H. NAD(+)/ NADH and NADP(+)/NADPH in cellular functions and cell death: Regulation and biological consequences. *Antioxidants & Redox Signaling* **10**(2), 179–206 (2008).
5. Denk, W., Strickler, J. H. & Webb, W. W. 2-photon laser scanning fluorescence microscopy. *Science* **248**(4951), 73–76 (1990).
6. Huang, S. H., Heikal, A. A. & Webb, W. W. Two-photon fluorescence spectroscopy and microscopy of NAD(P)H and flavoprotein. *Biophysical Journal* **82**(5), 2811–2825 (2002).
7. Skala, M. C. *et al. In vivo* multiphoton microscopy of NADH and FAD redox states, fluorescence lifetimes, and cellular morphology in precancerous epithelia. *Proc. Natl. Acad. Sci. USA* **104**(49), 19494–19499 (2007).
8. Kolenc, O. I. & Quinn, K. P. Evaluating Cell Metabolism Through Autofluorescence Imaging of NAD(P)H and FAD. *Antioxidants & Redox Signaling* **30**(6), 875–889 (2019).
9. Chance, B., Schoener, B., Oshino, R., Itshak, F. & Nakase, Y. Oxidation-reduction ratio studies of mitochondria in freeze-trapped samples - NADH and flavoprotein fluorescence signals. *Journal of Biological Chemistry* **254**(11), 4764–4771 (1979).
10. Hou, J. *et al.* Correlating two-photon excited fluorescence imaging of breast cancer cellular redox state with seahorse flux analysis of normalized cellular oxygen consumption. *Journal of Biomedical Optics* **21**(6), 060503 (2016).
11. Blacker, T. S. & Duchen, M. R. Investigating mitochondrial redox state using NADH and NADPH autofluorescence. *Free Radical Biology and Medicine* **100**, 53–65 (2016).
12. Lakowicz, J. R., Szmacinski, H., Nowaczyk, K. & Johnson, M. L. Fluorescence lifetime imaging of free and protein-bound NADH. *Proc. Natl. Acad. Sci. USA* **89**(4), 1271–1275 (1992).
13. Chorvat, D. & Chorvatova, A. Multi-wavelength fluorescence lifetime spectroscopy: a new approach to the study of endogenous fluorescence in living cells and tissues. *Laser Physics Letters* **6**(3), 175–193 (2009).
14. Yu, Q. R. & Heikal, A. A. Two-photon autofluorescence dynamics imaging reveals sensitivity of intracellular NADH concentration and conformation to cell physiology at the single-cell level. *Journal of Photochemistry and Photobiology B-Biology* **95**(1), 46–57 (2009).
15. Skala, M. C. *et al. In vivo* multiphoton fluorescence lifetime imaging of protein-bound and free nicotinamide adenine dinucleotide in normal and precancerous epithelia. *Journal of Biomedical Optics* **12**(2), 024014 (2007).
16. Wang, H. W. *et al.* Differentiation of apoptosis from necrosis by dynamic changes of reduced nicotinamide adenine dinucleotide fluorescence lifetime in live cells. *Journal of Biomedical Optics* **13**(5), 054011 (2008).
17. Plotegher, N. *et al.* NADH fluorescence lifetime is an endogenous reporter of alpha-synuclein aggregation in live cells. *FASEB Journal* **29**(6), 2484–2494 (2015).
18. Li, D., Zheng, W. & Qu, J. Y. Time-resolved spectroscopic imaging reveals the fundamentals of cellular NADH fluorescence. *Optics Letters* **33**(20), 2365–2367 (2008).
19. Kalinina, S. *et al.* Correlative NAD(P)H-FLIM and oxygen sensing-PLIM for metabolic mapping. *Journal of Biophotonics* **9**(8), 800–811 (2016).
20. Dravid, U. A. & Mazumder, N. Types of advanced optical microscopy techniques for breast cancer research: a review. *Lasers in Medical Science* **33**(9), 1849–1858 (2018).
21. Scott, T. G., Spencer, R. D., Leonard, N. J. & Weber, G. Emission properties of NADH. Studeis of fluorescence lifetimes and quantum efficiencies of NADH, AcPyADH, and simplified synthetic models. *Journal of the American Chemical Society* **92**(3), 687–695 (1970).
22. Visser, A. & Vanhoek, A. The fluorescence decay of reduced nicotinamides in aqueous-solution after excitation with a UV-mode locked Ar ion laser. *Photochemistry and Photobiology* **33**(1), 35–40 (1981).
23. Drozdowicz-Tomsia, K. *et al.* Multiphoton fluorescence lifetime imaging microscopy reveals free-to-bound NADH ratio changes associated with metabolic inhibition. *Journal of Biomedical Optics* **19**(8), 086016 (2014).
24. Widengren, J., Mets, Ü. & Rigler, R. Fluorescence correlation spectroscopy of triplet-states in solution - a theoretical and experimental-study. *Journal of Physical Chemistry* **99**(36), 13368–13379 (1995).
25. Widengren, J., Chmyrov, A., Eggeling, C., Löfdahl, P. Å. & Seidel, C. A. M. Strategies to improve photostabilities in ultrasensitive fluorescence spectroscopy. *Journal of Physical Chemistry A* **111**(3), 429–440 (2007).
26. Lindqvist, L., Czochralska, B. & Grigorov, I. Determination of the mechanism of photo-ionization of NADH in aqueous-solution on laser excitation at 355 nm. *Chemical Physics Letters* **119**(6), 494–498 (1985).
27. Boldridge, D. W., Morton, T. H. & Scott, G. W. Formation kinetics and quantum yield of photon-induced electron ejection from NADH in aqueous-solution. *Chemical Physics Letters* **108**(5), 461–465 (1984).

28. Umrikhina, A. V., Luganskaya, A. N. & Krasnovsky, A. A. ESR signals of NADH and NADPH under illumination. *FEBS Letters* **260**(2), 294–296 (1990).

29. Czochralska, B. & Lindqvist, L. Biphotonic one-electron oxidation of NADH on laser excitation at 353 nm. *Chemical Physics Letters* **101**(3), 297–299 (1983).

30. Sandén, T., Persson, G., Thyberg, P., Blom, H. & Widengren, J. Monitoring kinetics of highly environment sensitive states of fluorescent molecules by modulated excitation and time-averaged fluorescence intensity recording. *Analytical Chemistry* **79**(9), 3330–3341 (2007).

31. Sandén, T., Persson, G. & Widengren, J. Transient State Imaging for Microenvironmental Monitoring by Laser Scanning Microscopy. *Analytical Chemistry* **80**(24), 9589–9596 (2008).

32. Hevekerl, H., Tornmalm, J. & Widengren, J. Fluorescence-based characterization of non-fluorescent transient states of tryptophan - prospects for protein conformation and interaction studies. *Scientific Reports* **6**, 35052 (2016).

33. Tornmalm, J. & Widengren, J. Label-free monitoring of ambient oxygenation and redox conditions using the photodynamics of flavin compounds and transient state (TRAST) spectroscopy. *Methods* **140**, 178–187 (2018).

34. Ross, J. B. A., Rousslang, K. W., Motten, A. G. & Kwiram, A. L. Base interactions in the triplet state of NAD+ and NADH. *Biochemistry* **18**(9), 1808–1813 (1979).

35. Nikandrov, V. V., Brin, G. P. & Krasnovskii, A. A. Light-induced activation of NADH and NADPH. *Biochemistry-Moscow* **43**(4), 507–514 (1978).

36. Fukuzumi, S., Inada, O. & Suenobu, T. Direct detection of radical cations of NADH analogues. *Journal of the American Chemical Society* **124**(49), 14538–14539 (2002).

37. Chmyrov, A., Sandén, T. & Widengren, J. Iodide as a Fluorescence Quencher and Promoter-Mechanisms and Possible Implications. *Journal of Physical Chemistry B* **114**(34), 11282–11291 (2010).

38. Anne, A., Hapiot, P., Moiroux, J., Neta, P. & Saveant, J. M. Dynamics of proton-transfer from cation radicals - kinetic and thermodynamic acidities of cation radicals of nadh analogs. *Journal of the American Chemical Society* **114**(12), 4694–4701 (1992).

39. Gebicki, J., Marcinek, A. & Zielonka, J. Transient species in the stepwise interconversion of NADH and NAD(+). *Accounts of Chemical Research* **37**(6), 379–386 (2004).

40. Zielonka, J., Marcinek, A., Adamus, J. & Gebicki, J. Direct observation of NADH radical cation generated in reactions with one-electron oxidants. *Journal of Physical Chemistry A* **107**(46), 9860–9864 (2003).

41. Czochralska, B., Kawczynski, W., Bartosz, G. & Shugar, D. Oxidation of excited-state NADH and NAD dimer in aqueous-medium involvement of O_{2-} as a mediator in the presence of oxygen. *Biochimica et Biophysica Acta* **801**(3), 403–409 (1984).

42. Akaike, H. A new look at the statistical model identification. *IEEE Transactions on automatic control* **19**(6), 716–723 (1974).

43. Schwarz, G. Estimating the dimension of a model. *The Annals of statistics* **6**(2), 461–464 (1978).

44. Wagenmakers, E. & Farrell, S. AIC model selection using Akaike weights. *Psychonomic Bulletin & Review* **11**(1), 192–196 (2004).

45. Patterson, G. H. & Piston, D. W. Photobleaching in two-photon excitation microscopy. *Biophysical Journal* **78**(4), 2159–2162 (2000).

46. Eggeling, C., Widengren, J., Rigler, R. & Seidel, C. A. M. Photobleaching of fluorescent dyes under conditions used for single-molecule detection: Evidence of two-step photolysis. *Analytical Chemistry* **70**(13), 2651–2659 (1998).

47. Widengren, J. & Rigler, R. Mechanisms of photbleaching investigated by fluorescence correlation spectroscopy. *Bioimaging* **4**, 149–157 (1996).

48. Xu, C., Zipfel, W., Shear, J. B., Williams, R. M. & Webb, W. W. Multiphoton fluorescence excitation: New spectral windows for biological nonlinear microscopy. *Proc. Natl. Acad. Sci. USA* **93**(20), 10763–10768 (1996).

49. Hopt, A. & Neher, E. Highly nonlinear photodamage in two-photon fluorescence microscopy. *Biophysical Journal* **80**(4), 2029–2036 (2001).

50. König, K., Becker, T. W., Fischer, P., Riemann, I. & Halbhuber, K. J. Pulse-length dependence of cellular response to intense near-infrared laser pulses in multiphoton microscopes. *Optics Letters* **24**(2), 113–115 (1999).

51. Loomis, W. F. & Lipmann, F. Reversible inhibition of the coupling between phosphorylation and oxidation. *Journal of biological chemistry* **173**, 807–808 (1948).

52. Blacker, T. S., Marsh, R. J., Duchen, M. R. & Bain, A. J. Activated barrier crossing dynamics in the non-radiative decay of NADH and NADPH. *Chemical Physics* **422**, 184–194 (2013).

53. König, K., So, P. T. C., Mantulin, W. W., Tromberg, B. J. & Gratton, E. Two-photon excited lifetime imaging of autofluorescence in cells during UVA and NIR photostress. *Journal of Microscopy* **183**, 197–204 (1996).

54. Blacker, T. S. *et al.* Separating NADH and NADPH fluorescence in live cells and tissues using FLIM. *Nature Communications* **5**, 3936 (2014).

55. Mücksch, J., Spielmann, T., Sisamakis, E. & Widengren, J. Transient state imaging of live cells using single plane illumination and arbitrary duty cycle excitation pulse trains. *Journal of Biophotonics* **8**(5), 392–400 (2015).

56. Spielmann, T., Xu, L., Gad, A. K. B., Johansson, S. & Widengren, J. Transient state microscopy probes patterns of altered oxygen consumption in cancer cells. *FEBS Journal* **281**(5), 1317–1332 (2014).

57. Bresnahan, W. T. & Elving, P. J. Spectrophotometric investigation of products formed following the initial one-electron electrochemical reduction of nicotinamide adenine-dinucleotide (NAD. *Biochimica et Biophysica Acta* **678**(2), 151–156 (1981).

Acknowledgements

Author contributions

J.T., E.S., M.R. established instruments. J.T. and E.S. performed experiments. J.T. analysed data. J.T. and J.W. wrote the paper. J.W. designed research and supervised work.

Competing interests

J.W. is the inventor and holder of a patent (WO2006130105-A1) related to parts of the methodology used.

Additional information

Supplementary information is available for this paper at https://doi.org/10.1038/s41598-019-51526-w.

Correspondence and requests for materials should be addressed to J.W.

Reprints and permissions information is available at www.nature.com/reprints.

Publisher's note Springer Nature remains neutral with regard to jurisdictional claims in published maps and institutional affiliations.

PAPER

YVO$_4$:Eu^{3+} nanopowders: multi-mode temperature sensing technique

IOP ebooks™

Bringing you innovative digital publishing with leading voices to create your essential collection of books in STEM research.

Start exploring the collection - download the first chapter of every title for free.

YVO$_4$:Eu^{3+} nanopowders: multi-mode temperature sensing technique

D Sevic[1,3] , **M S Rabasovic**[1] , **J Krizan**[2] , **S Savic-Sevic**[1] , **M G Nikolic**[1],
B P Marinkovic[1] **and M D Rabasovic**[1]

[1] Institute of Physics Belgrade, University of Belgrade, Serbia
[2] Ami DOO, Ptuj, Slovenia

E-mail: sevic@ipb.ac.rs

Abstract
In this paper we study several temperature sensing techniques using the same thermographic
phosphor: luminescence intensity ratio, lifetime, rise time. Moreover, we analyze some
recently presented techniques, based on host luminescence intensity ratio method and delayed
gate intensity ratio technique. We have selected YVO$_4$:Eu^{3+} nano powder as an appropriate
material for this study, because it has easily detectable luminescence rise time and host
luminescence. The material was prepared using simple solution combustion synthesis. The
time resolved analysis of emission spectra was achieved using the streak camera system. We
present a very detailed analysis of measured lifetimes and rise times of all emission lines
and their temperature dependence. We propose a multi-mode temperature sensing technique
based on the concept of luminescence detection part of the temperature sensor capable of
switching between several measurements modes to obtain the best sensitivity in desired range
of operation.

Keywords: temperature sensing, phosphors, optical properties, luminescence, time-resolved
optical spectroscopy

(Some figures may appear in colour only in the online journal)

1. Introduction

Thermographic phosphors offer many advantages for temperature measurement compared to other methods [1–10]. Optical thermometry is very accurate, contactless method of remote sensing. Moreover, it is conceptually simple. There are several ways to use phosphors for thermometry purposes. Spectroscopy techniques are usually employed to remotely measure effects of temperature on phosphors photoluminescence. The most common method is based on intensity ratio of two, appropriately selected, spectral peaks of thermophosphor. The method is called fluorescence intensity ratio (FIR). The second commonly used method is based on phosphor luminescence lifetime. This technique needs to measure only one spectral peak. Some phosphors have temperature dependent

luminescence rise time sufficiently long to be of practical use for thermometry. Many thermophosphors offer the possibilities for two promising modifications of the FIR method. First, using of host luminescence instead of one of the two dopant luminescence peaks for intensity ratio calculations could improve the sensitivity or overall characteristics of the FIR basic, in regard of simplicity and reliability [11–15]. Another possible improvement of the sensitivity could be achieved by proper selection of the time frame for calculating the intensity ratio [3, 15, 16].

Aim of this study is to compare the before mentioned thermometry techniques using the same nanophosphor. Our previous studies of europium, dysprozium or samarium doped hosts implied that, among the nanophosphors analyzed in [15–21], only Yttrium Vanadate (YVO$_4$) doped with europium ions (YVO$_4$:Eu^{3+}) offers the long enough luminescence rise time, in microsecond domain, to be of practical use for thermometry. Nano phosphors Y$_2$O$_3$ [8, 22–24], SrY$_2$O$_4$ [25] and

---

[3] Author to whom any correspondence should be addressed.

J. Phys. D: Appl. Phys. **53** (2020) 015106

D Sevic *et al*

BaY$_2$ZnO$_5$ [26] are also used for temperature measurements based on rise time.

It is well known fact that absorption and excitation times are typically in femtosecond domain, see [8]. The detected long rise time of some $^5D_0$ emission lines is related to the specific energy transfer mechanism of analyzed nanophosphor. A detailed time resolved luminescence analysis of optical emission presented in this paper will provide an insight into energy transfer mechanism of YVO$_4$:Eu^{3+}.

Studies of structural and luminescent characteristics of YVO$_4$:Eu^{3+} phosphors, including various methods of synthesis, are reported in [27–50] and references therein. Compared with other oxide luminescence compounds such as Y$_2$O$_3$, YVO$_4$ has lower formation energy and higher crystallinity, which makes it easier to form regular morphology and shows higher luminous efficiency [27].

Transitions from the $^5D_0$ state, from which most of europium luminescence comes, have a slow decay. Lifetimes of slow decay lines of europium doped YVO$_4$ are measured and reported in many publications. The luminescence intensity of $^5D_0$-$^7F_2$ transition is the most intensive, so it is usually used for europium luminescence lifetime measurements [42, 48, 51, 52]. However, there are not so many publications regarding any europium doped host, where measured lifetimes of europium fast decay transitions or rise times of slow decay transitions [23, 25, 26, 35, 51, 53] are provided. To the best of our knowledge, the results of measurements of the rise time of transitions from the $^5D_0$ state and lifetime of fast decay transitions from the $^5D_1$ state of YVO$_4$:Eu^{3+} phosphors are only presented in [19], measured only at the room temperature and [35] measured at and bellow room temperature. In this work we will focus on temperature dependency of YVO$_4$:Eu^{3+} luminescence, not analyzed in our previous papers.

2. Experimental procedures

Europium doped YVO$_4$ nanophosphor was efficiently prepared using a solution combustion synthesis (SCS) method [54]. The structure of synthesized Y$_{0.98}$VO$_4$: Eu$^{3+}_{0.02}$ material has been confirmed and characterized in our earlier publication [19], using x-ray powder diffraction (XRD), scanning electron microscope (SEM), Raman and photoluminescence (PL) techniques. The average grain size of about 51 nm was estimated by the Scherer equation.

As an excitation source for photoluminescence measurements we used the optical parametric oscillator (Vibrant OPO), continuously tunable over a spectral range from 320 nm to 475 nm. The emission spectra and luminescence lifetimes and rise time of synthesized nanopowders were analyzed using the streak camera system. The camera is equipped with the spectrograph. The details of our experimental setup can be found in [16, 19]. The part of experimental setup for luminescence measurement as a function of temperature is described in [55].

3. Results and discussion

3.1. Optical properties

The streak images of time resolved photoluminescence spectrum of YVO$_4$:Eu^{3+} material are presented in figure 1. It was shown that optical spectral properties reported for YVO$_4$:Eu^{3+} in the literature remain the same for GdVO$_4$:Eu^{3+} as well [56]. Excitation spectra of VO$_4$ groups are very similar for both phosphors. This fact is explained, proved in detail and generalized for rare earth doped vanadates in [57–60]. Moreover, it was shown in [57–61] that absorption of VO$_4^{3-}$ group shifts to longer wavelengths with increasing temperature, and that it could be used for improved temperature sensing characteristics [57–60].

In [38, 46, 49, 50, 56–60, 62] it was shown that the VO$_4$ excitation spectra consist of a strong absorption band between 250 and 350 nm, corresponding to the charge transfer from O$_2$- to the central vanadium ion V^{5+} of vanadate VO$_4^{3-}$ groups. So, it should be pointed out that the excitation of Eu^{3+} ion is basically caused by energy transfer from vanadate groups to Eu^{3+} ion. Due to the weak intensities of *f–f* transitions of Eu^{3+} ions compared with that of VO$_4^{3-}$ ion, these transition lines often have not been observed in measured excitation spectra, or simply neglected in many publications. In our work [16] we showed that it is possible to exploit the direct excitation of europium for temperature and pressure sensing purposes.

However, there is another interesting phenomenon regarding the direct excitation of europium. It is discovered and explained for the first time in [57]. As described there, excitation spectra with respect to the characteristic excitations of Eu^{3+} ions from $^7F_0$, $^7F_1$ and $^7F_2$ states to $^5D_2$ state are temperature dependent, so the phenomenon could be used for temperature measurements. Further, it is explained that beside temperature quenching, another factor that affects the emission intensity is the population of the initial state for the excitation. Namely, the populations between $^7F_0$, $^7F_1$ and $^7F_2$ states of Eu^{3+} ions follow Boltzmann distribution due to their appropriate energy gaps [57]. Thus, with increasing temperature, the population of the ground state $^7F_0$ as the initial state of 395 nm excitation decreases because of the thermally populating of high energy levels ($^7F_1$ and $^7F_2$), leading to the decreasing of response intensity for excitation at 395 nm [57]. Because of the relatively weak measured signal of optical response of europium excited at this wavelength in our present experimental setup, we declined of further analysis of this mode of operation for temperature sensing.

We have used the excitation at 330 nm, which is slightly on right-hand side from the excitation peak of YVO$_4$:Eu^{3+} on wavelength scale. As usual, the streak image is presented in pseudocolor. Note that, because of streak camera automatic lookup table (LUT) for generating pseudocolor which is nice to eye, the luminescence intensities on different streak images should not be compared visually. The Eu transitions
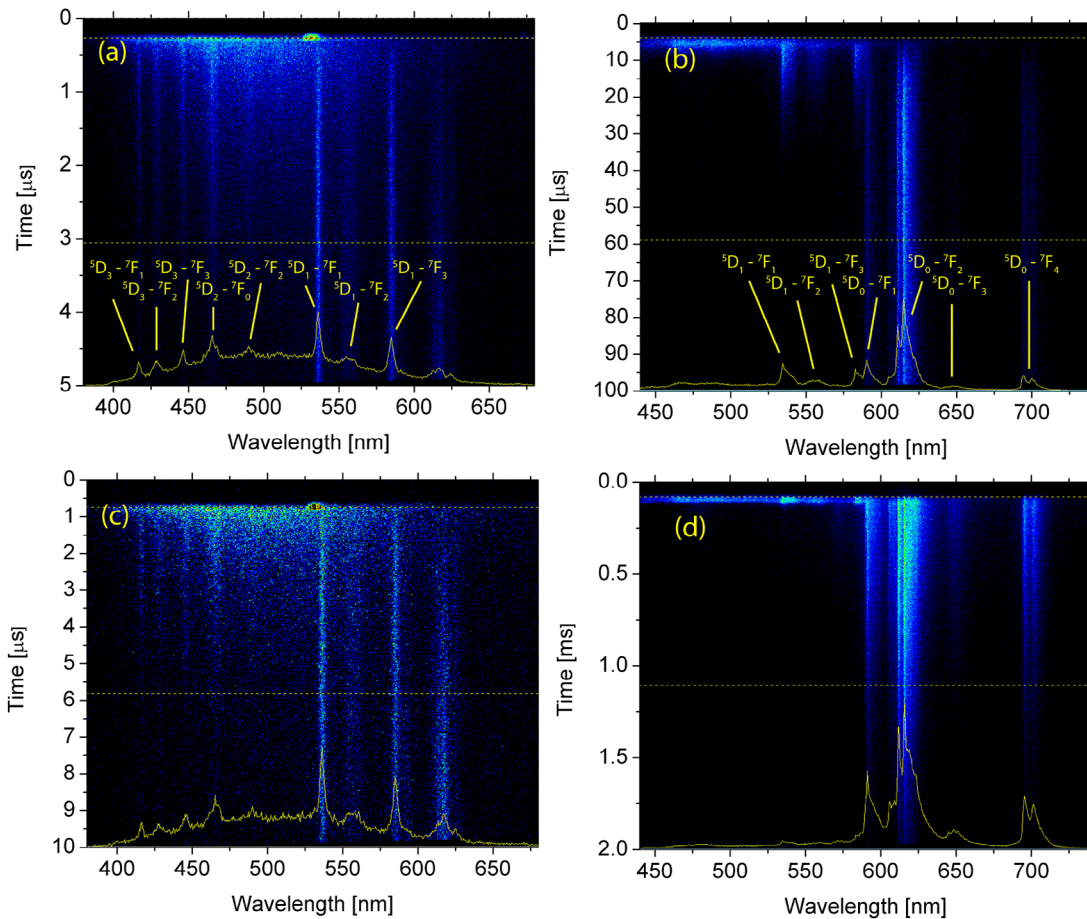
Figure 1. Streak images of photoluminescence spectrum of YVO_4:Eu^{3+} nano phosphor. Time ranges of acquired spectral streak images are (a) 5 μs, (b) 100 μs, (c) 10 μs and (d) 2 ms. Spectral line profiles (yellow curves) are integrated-in-time as marked by dashed yellow lines. OPO excitation is at 330 nm.

are denoted in figure 1 according to [51, 63]. Because we use OPO blocking filter, host optical emission is measured only above 400 nm, showing wide luminescence band up to about 550 nm. The host emission of similar spectral shape is presented and analyzed in [31, 35, 41]. It could be seen in figure 1 that the host emission, compared to europium transitions, has very fast decay. The observed host emission is also of very short duration in [35]. The slow decay transitions observable in figure 1, originating from $^5D_0$ level, are well explained in literature and their detailed description can be found in our previous work [19]. In this study, we have conducted the time resolved analysis for all transitions which are identified in figure 1.

Looking at streak image presented in figure 1(a) or (c) it could be estimated that the raising edges of optical emissions of YVO_4 host and of lines originating from transitions from $^5D_3$, $^5D_2$ and $^5D_1$ europium levels are almost instantaneous and that the lifetimes of host emission and transitions from $^5D_3$ and $^5D_2$ are very short. Figure 1(b) implies that the lifetime of transitions from $^5D_1$ level and rise time of transitions from $^5D_0$ level are in the microsecond domain. Figure 1(d)

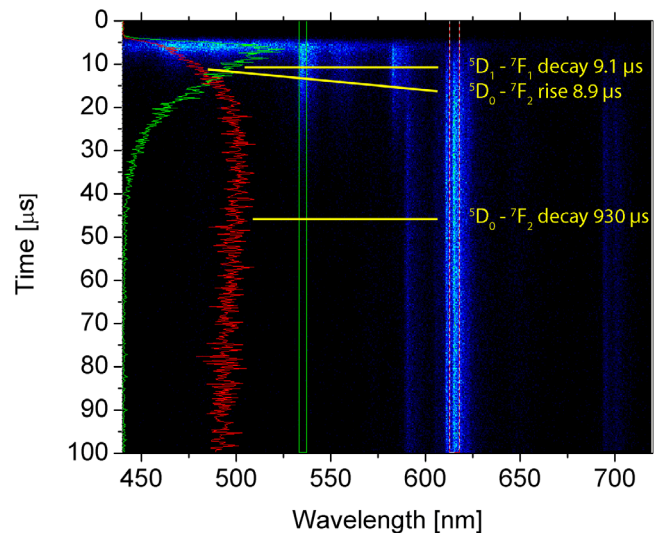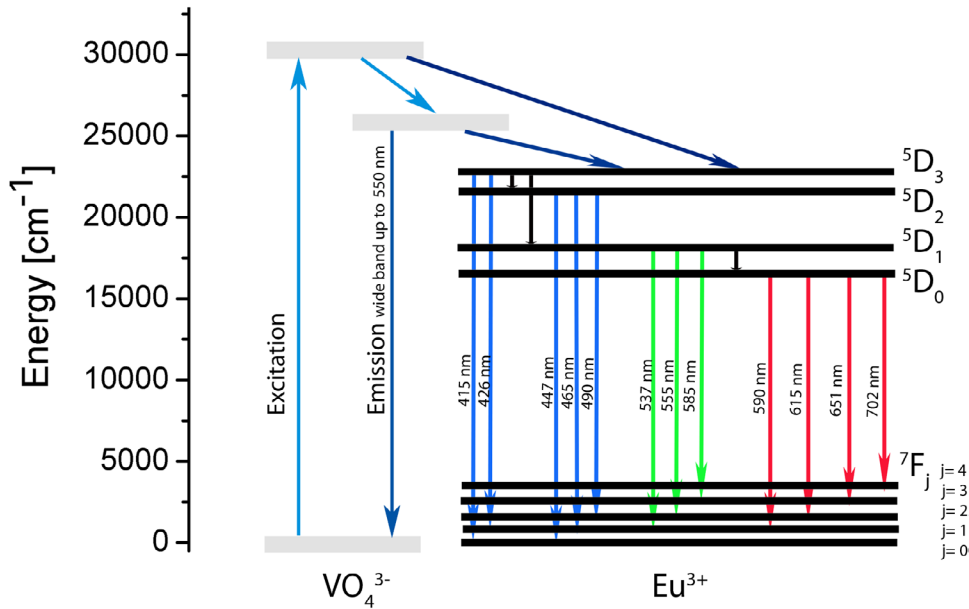**Figure 2.** Temporal responses of optical emission of two europium lines in YVO_4:Eu^{3+} nano phosphor, shown as projections on time axis, integrated in spectral range marked as green for $^5D_1$-$^7F_1$ transition (green curve) and dashed red for $^5D_0$-$^7F_2$ transition (red curve).

J. Phys. D: Appl. Phys. **53** (2020) 015106

D Sevic *et al*

Table 1. Values of lifetimes of detected $YVO_4:Eu^{3+}$ transitions measured at room temperature, excited at 330 nm. The rise time of $^5D_0$ transitions is 8.9 μs.

Transition	$^5D_3$-$^7F_1$	$^5D_3$-$^7F_2$	$^5D_3$-$^7F_3$	$^5D_2$-$^7F_0$	$^5D_2$-$^7F_2$	$^5D_1$-$^7F_1$	$^5D_1$-$^7F_2$	$^5D_1$-$^7F_3$	$^5D_0$-$^7F_1$	$^5D_0$-$^7F_2$	$^5D_0$-$^7F_3$	$^5D_0$-$^7F_4$	YVO$_4$ host
Wavelength (nm)	416	428	446	465	490	537	556	584	591	615 618	648	693 700	Up to 550 nm
Lifetime (μs)		2.2			2.7		9.1			930			2

Figure 3. Schematic view of $YVO_4:Eu^{3+}$ energy transfer processes.

shows that the lifetime of transitions from $^5D_0$ level is in millisecond domain.

General shapes of temporal response of optical emissions of fast decay $^5D_1$-$^7F_1$ transition and slow decay $^5D_0$-$^7F_2$ transition of $YVO_4:Eu^{3+}$ nano phosphor are illustrated in figure 2. The rise component of $^5D_0$-$^7F_2$ transition and the decay component of $^5D_1$-$^7F_1$ transition look almost mirrored, implying that there is an energy transfer mechanism between them. The phenomenon that the rise time of europium slow decay $^5D_2$ luminescence is similar to the lifetime of fast decay $^5D_1$ emission was observed long ago [53]; and analyzed in detail, including energy transfer, in [35]. The explanation of energy transfer between the host YVO_4 and Eu^{3+} ions is also provided in [32].

To check the presumption that the rise times of fast decay transitions can be considered as instantaneous, we have used the time scales of streak camera even shorter than 5 μs.

We have concluded that, at the present time, rise times of fast decay transitions of $YVO_4:Eu^{3+}$ are not of any practical use for temperature sensing. The only measurable rise time is of $^5D_0$ transitions; it is 8.9 μs. We have calculated the rise time according to Ranson equation [23, 24].

The values of lifetimes of $YVO_4:Eu^{3+}$ transitions detected in our study, measured at room temperature, excited at 330 nm, are presented in table 1. We also made preliminary estimations of temperature dependences of lifetimes of transitions from YVO_4 host and $^5D_3$ and $^5D_2$ levels. We concluded

that lifetime measurements of $^5D_3$ and $^5D_2$ transitions are not so appropriate for temperature sensing, because of small signal intensities compared to intensities of luminescence of $^5D_0$ and $^5D_1$ transitions. The host luminescence is more rapidly quenched by temperature than europium transitions, providing possibility of improved sensitivity in physiological temperature range. The integrated-in-time host luminescence signal strength is quite satisfactory for intensity ratio calculations. On the other hand, measuring the host luminescence lifetime with temperature raise, although possible, showed itself to us as unreliable at the present time. However, with some improvements in detection, the lifetime of host could be of interest for temperature sensing in physiological temperature range.

Based on our estimations of shape of temporal response and time durations of luminescence of host and of europium transitions shown in figures 1 and 2, we propose the schematic view of $YVO_4:Eu^{3+}$ energy transfer processes presented in figure 3.

3.2. Temperature sensing using luminescence intensity ratio with variable delayed gating

Luminecence intensity ratio technique is based on measuring the intensities of two emission lines in luminescence spectra of thermographic phosphors. The temperature is calculated by the emission intensity ratio of these two lines. Many problems
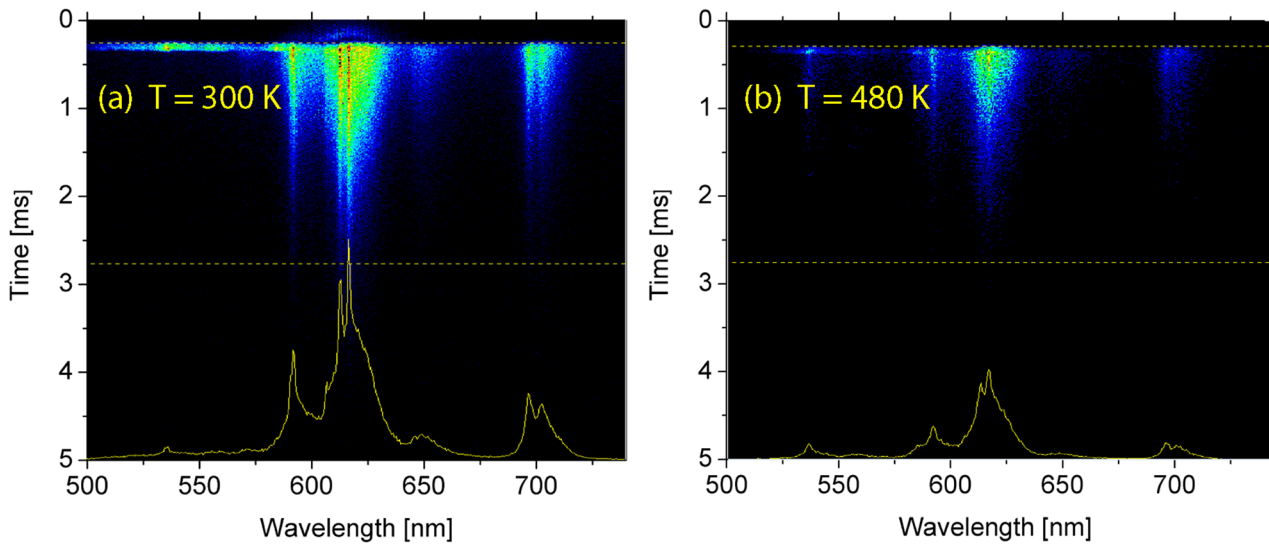
Figure 4. Streak images of photoluminescence spectra of YVO$_4$:Eu^{3+} and their integrated-in-time (time range marked by yellow dashed line) spectral line profiles (yellow curves): (a) $T = 300$ K, (b) $T = 480$ K, selected for illustration of FIR analysis.

regarding measuring errors, optical condition deviations and excitation power fluctuation are eliminated in this way. Two closely spaced energy levels of rare earth ion, which are thermally coupled, are usually selected for temperature sensing. Small energy gap between these two levels allows the upper level to be populated from the lower level by thermalization. The upper level becomes more populated as the temperature increases and hence the fluorescence from this level gradually increases. Relative population between two levels, $^5D_1$ level (I_1) and $^5D_0$ level (I_0), IR, follows Boltzmann type population distribution given by [1, 2]:

$$\text{IR} = \frac{I_1}{I_0} = C \cdot \exp\left(-\frac{\Delta E}{kT}\right) \qquad (1)$$

where k is the Boltzmann constant, $k = 0.69503476(63)$ cm^{-1} K^{-1}, C is a constant and ΔE is the energy gap between two excited levels, in case analyzed here, between $^5D_1$ and $^5D_0$ europium levels.

Instruments for measuring luminescence often detect small signals, even when there is no emission, because of detector dark currents, etc. Moreover, spectrograph stray light introduces error in measured intensity of a signal. Therefore, another constant, A, should be introduced to equation (1), to account for the finite value of IR at low temperatures [14]:

$$\text{IR} = A + C \cdot \exp\left(-\frac{\Delta E}{kT}\right). \qquad (2)$$

It should be noted that ΔE corresponds to energy gap between two excited states only in the case of measuring the intensity ratio in conventional way, i.e. without any gate delay in our study. However, when we introduce the delay for gating of measured signals, using ΔE from equation (2) for an estimation of energy gap of excited levels would be quite misleading, although it can be well exploited for fitting the temperature calibration curve. The same holds for calculating the intensity ratio between optical emissions of the host and the selected europium line.

The spectral line intensities from the $^5D_0$ and $^5D_1$ transitions depend on two physical processes. The first process is the thermalization of the $^5D_1$ level with rising temperature, where the energy difference to populate the $^5D_1$ level from the $^5D_0$ level is fully covered by phonons. The second process is nonradiative quenching of the $^5D_0$ and $^5D_1$ levels through the charge transfer state. Both processes can be recognized by the analysis of integrated-in-time profiles of luminescence spectra in figure 4. Namely, the intensity ratio between the lines at 537 nm and 618 nm increases with temperature. However, both lines are thermally quenched. Again, because of streak camera automatic LUT, comparison of luminescence intensities should be not done simply by looking at images.

In our study the intensity ratio method has been improved by introducing the temporal dependence in the intensity ratio measurements, as proposed in [3]. We have implemented this method in [15, 16] where we have shown that it is possible to increase the sensitivity of temperature calibration curve if appropriately selected part of luminescence temporal evolution is used in calculation.

To determine the temperature calibration curves, the luminescence spectra of YVO$_4$:Eu^{3+} nano phosphor were measured at various temperatures, using OPO excitation at 330 nm and the streak camera. For calculation of intensity ratio in a usual way the narrow bands (5 nm) of europium luminescence around 537 nm and around 618 nm were used integrated in time from their beginning. Then, to improve the temperature sensitivity of the FIR method, we have varied the gating times for beginning of 618 nm signal in-time-integration. In this way, because smaller portion of falling 618 nm luminescence signal was integrated, the intensity ratio was increased in favor of 537 nm signal, following the general increase of ratio of 537 nm and 618 nm signals with temperature.

Here, the thermalization and quenching through charge transfer both have significant influence on the fluorescence intensity ratio (FIR). This means that the measured results cannot be simply fitted to the Boltzmann distribution. To
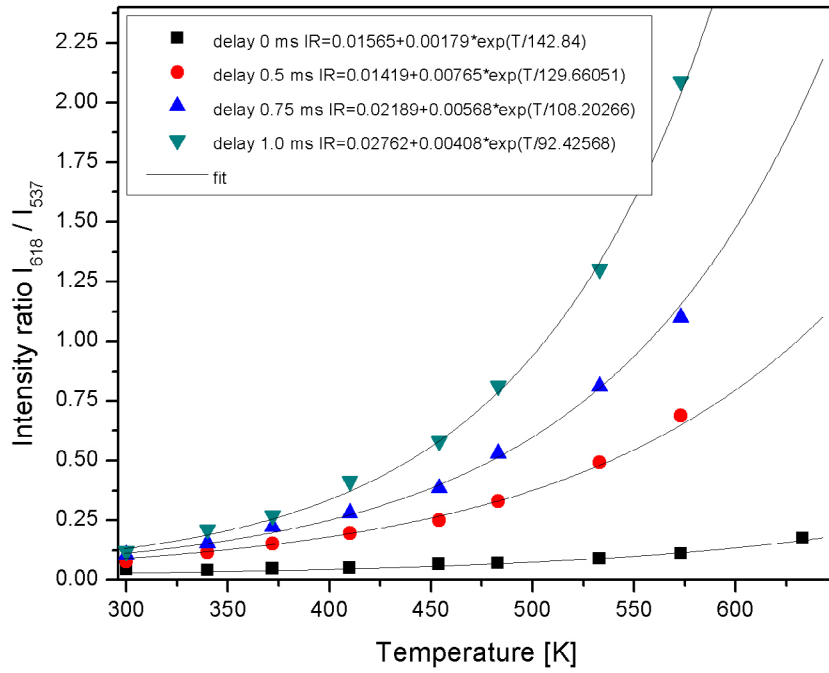
Figure 5. Temperature sensing calibration curve of YVO$_4$:Eu^{3+} nanopowder sample.
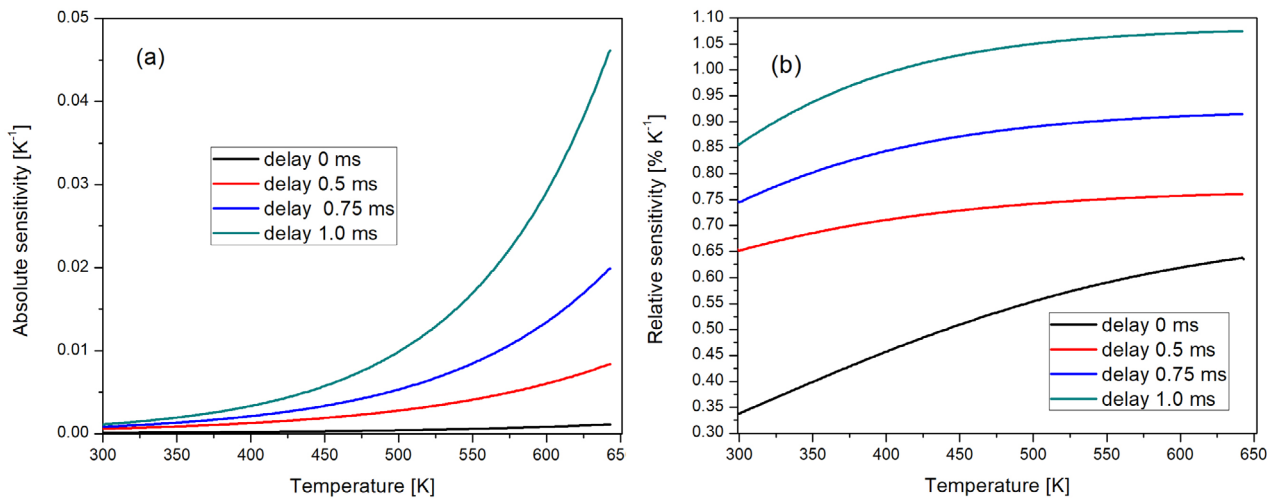

Figure 6. (a) Absolute and (b) relative sensitivities of YVO$_4$:Eu^{3+} nanopowder as the functions of temperature shown in figure 4.

implement the fluorescence intensity ratio method in thermometry it is necessary to fit a calibration function of analyzed thermophosphor. Based on considerations in [15, 16, 55, 64] we decided to use the simple empirical equation for fitting the calculated intensity ratios of experimental data: IR(T) = A + C · e$^{-T/\alpha}$, where T is temperature in K, and A, C and α are empirical constants obtained through fitting of measured data. In principle, for temperature sensing, it is enough to determine the temperature calibration sensing curve, no further knowledge regarding the underlying physics is necessary [65]. The results are shown in figure 5, where delay of 0 ms corresponds to the FIR, the usual way of calculating the intensity ratio.

It could be seen in figure 5 that intensity ratio increases with increasing the gate delay time of signal. However, increasing the gate delay time decreases the integrated signal intensity, so we refrained from using delays longer than 1 ms.

The absolute thermal sensitivity Sa of the intensity ratio method is defined as the rate at which IR changes with the temperature:

$$\mathrm{Sa} = \left| \frac{d\mathrm{IR}}{dT} \right|. \tag{3}$$

The relative thermal sensitivity of the intensity ratio method Sr is determined using formula:

$$\mathrm{Sr} = \left| \frac{1}{\mathrm{IR}} \frac{d\mathrm{IR}}{dT} \right|. \tag{4}$$

Absolute sensitivity is of a small or no use for comparison of different samples. We will provide its values here for comparison of the improvements of various FIR methods used with the same sample.

Absolute and relative temperature sensitivities of YVO$_4$:Eu^{3+} nanophosphor are shown in figure 6. Best
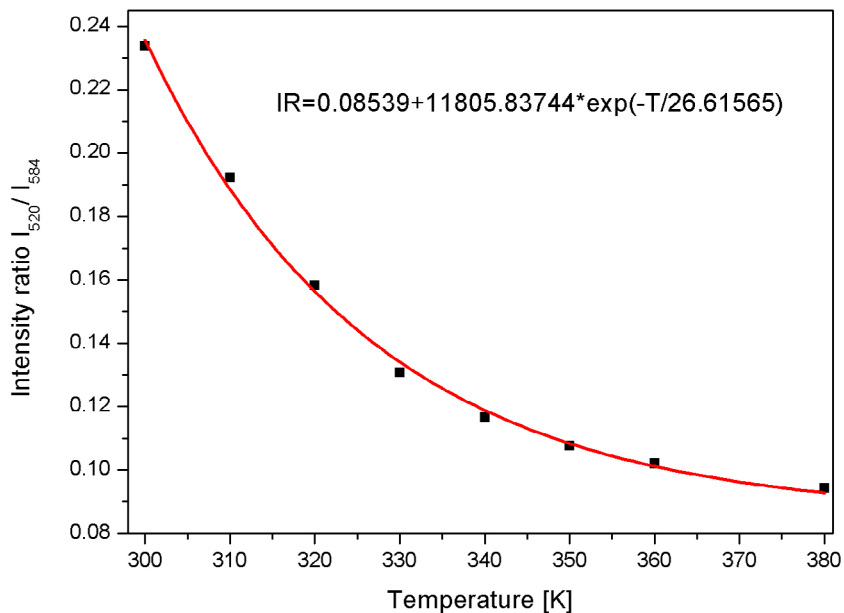
Figure 7. The temperature sensing calibration curve, calculated as intensity ratio of host luminescence and $^5D_2$-$^7F_3$ transition (584 nm).
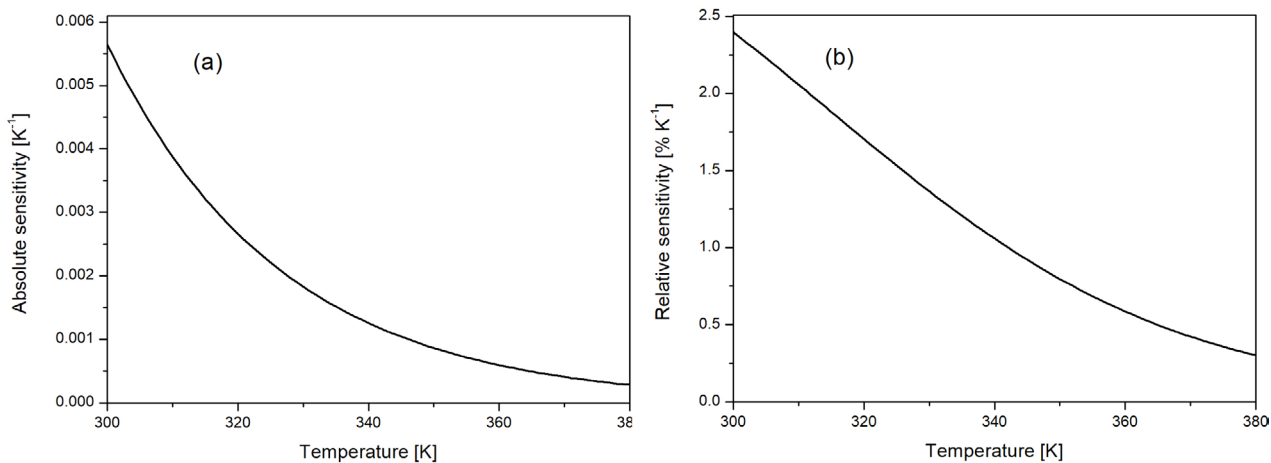

Figure 8. (a) Absolute and (b) relative sensitivities of YVO_4:Eu^{3+} nanopowder as the function of temperature shown in figure 7.
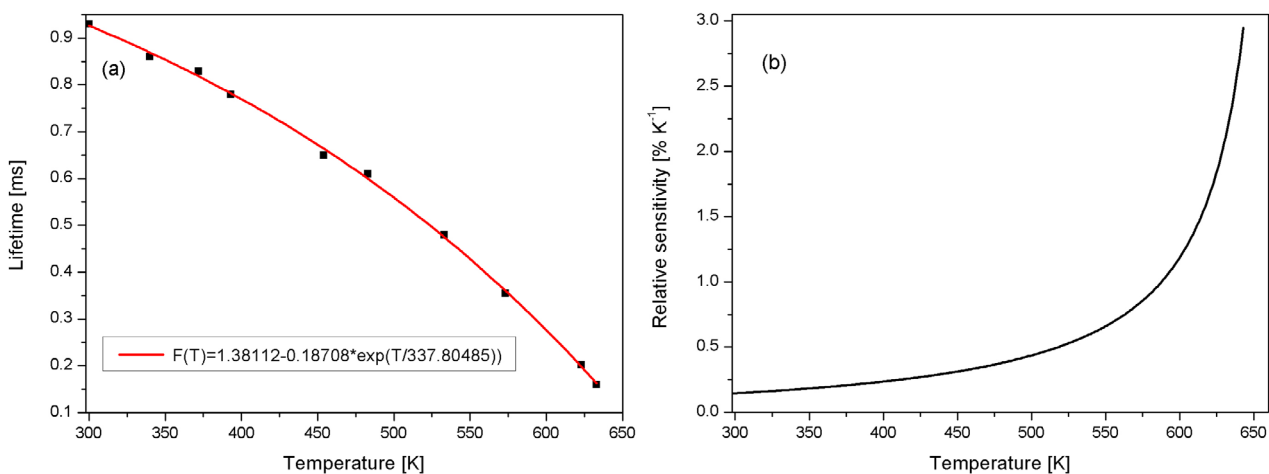

Figure 9. (a) Luminescence lifetime temperature dependence of YVO_4:Eu^{3+} nano phosphor and (b) its relative sensitivity.
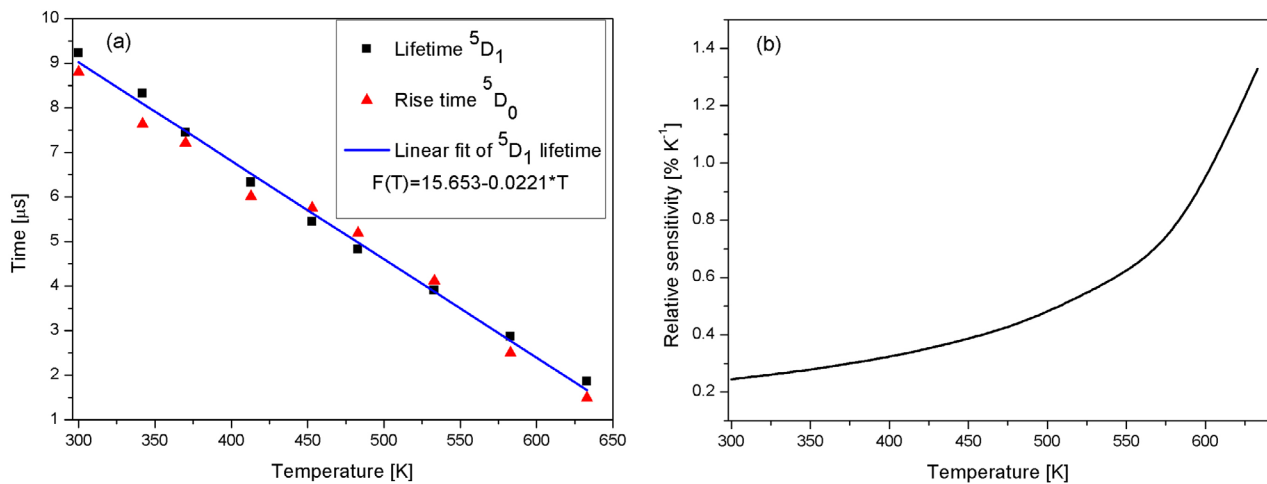
Figure 10. (a) Temperature calibration curve of luminescence lifetime of $^5D_1$ and rise time of $^5D_0$ transitions of YVO$_4$:Eu^{3+} nano phosphor and (b) the relative sensitivity of temperature calibration curve based on fit $^5D_1$ lifetime.

sensitivity is obtained by gate time of 1 ms. We estimate that this kind of temperature sensing is useful up to about 650 K, where intensities of both measured signals become too low for reliable calculating.

3.3. Temperature sensing using luminescence intensity ratio between YVO$_4$ host and europium $^5D_1$-$^7F_2$ transition

Our measurements show that the host luminescence, although much weaker than emission from $^5D_1$ and $^5D_0$ transitions, is easily detected. Its emission is in the wide band, so its integration could be done in a wider spectral range (we used a band of 10 nm). Host luminescence is rapidly quenched with temperature. We have determined the temperature sensing calibration curve, presented in figure 7, as intensity ratio of host luminescence and $^5D_2$-$^7F_3$ transition (584 nm). The line at 584 nm is prominent and it has no overlap with the host luminescence, see figure 1. We see that the sensitivity in physiological temperature range is greatly improved; however, the sensing range is reduced to about 380 K.

Absolute and relative sensitivities of YVO$_4$:Eu^{3+} nanopowder are shown in figure 8. Compared to sensitivities of other temperature sensing curves of this nano phosphor shown in figures 6, 9 and 10, we see that this method offers the best sensitivity in physiological range of temperatures.

3.4. Luminescence lifetime temperature dependency

All transitions from the same level have the same lifetime, so it is usual practice for estimation of decay time to use the line with highest intensity of luminescence. To determine the temperature sensing calibration curve we used the most prominent europium spectral line at 618 nm. Analysis presented in [11] confirms that it is possible to use the same form of empirical equation for fitting the lifetime experimental data as we have used for fitting the intensity ratio, namely: $F(T) = A + C \cdot \mathrm{e}^{-T/\alpha}$, [15, 16, 55, 64], where T is temperature in K, and A, C and α are empirical constants obtained through fitting of measured data. The temperature sensing calibration curve is shown in figure 9. For our sample of YVO$_4$:Eu^{3+} nano

Table 2. The sensing characteristics of various temperature sensing modes.

Sensing mode	Quality of sensing at temperature (K)		
	300–340	340–500	500–650
Intensity ratio	Poor	Between poor and good	Good
Intensity ratio with delayed gating	Good	Good	Good
Intensity ratio using host	Excellent	Good up to 380	No signal
Slow decay lifetime	Poor	Good	Excellent
Slow decay rise time/ fast decay lifetime	Poor	Good	Fairly excellent

phosphor the method is reliable up to 650 K. The sensitivity increases by temperature raising.

3.5. Luminescence rise time temperature dependency

Temperature dependence of luminescence lifetime of $^5D_1$ and rise time of $^5D_0$ transitions of YVO$_4$:Eu^{3+} nano phosphor and the relative sensitivity of temperature calibration curve based on fit $^5D_1$ lifetime are shown in figure 10.

In this range of temperatures, the rise time dependence is linear, similarly as observed in [22, 23, 25]. Moreover, it seems that it is the same if we use decay of 537 nm line, or rise time of 618 nm line. The choice would be dependent on which signal is overall stronger and easier to analyze for a given sample. It should be also mentioned that, instead of measuring the rise time, the measured time of achieving the signal maximum at 618 nm could be efficiently used for temperature measurements [22, 25, 66].

3.6. Multi-mode temperature sensing technique

Comparing temperature sensing characteristics of YVO$_4$:Eu^{3+}, shown in figures 5–10, we conclude that europium lines intensity ratio method, the luminescence lifetime method and rise time method offer the same sensing range. Lifetime and rise

Table 3. The sensing characteristics of various hosts doped with Eu^{3+}.

Host	Sensing range (K)	Relative sensitivity (% K^{-1})	Reference
YVO_4	300–650	0.2–2.9	This work
YVO_4	300–650	0.33–0.63	This work, FIR
YVO_4	300–650	2.4–2.9	This work, optimal sensing mode
$Gd_2Zr_2O_7$	300–650	0.4–0.92	[21]
Sr_2CeO_4	300–400	1.0–2.4	[16]
$YNbO_4$	300–720	0.3–2.6	[67, 68]
Gd_2O_3	300–800	0.25–3.25	[69]
$Lu2O_3$	300–800	0.3–0.33	[70]
$Gd2Ti_2O_7$	300–420	0.3–0.95	[14]
TiO_2	300–530	0.12–2.3	[11]
$GdAlO_3$	300–750	0.3–2.9	[71]
YBO_3	330–760	0.3–1.8	[72]

time methods have improved sensitivity on higher temperatures. Delayed gating of intensity ratio method provides improved sensitivity. The sensing characteristics of various temperature sensing modes are summarized in table 2. The luminescence detection part of the temperature sensor should be capable of switching between several measurements modes, so the best sensitivity could be obtained in desired range of operation.

Comparison of temperature sensing characteristics of various hosts doped with Eu^{3+} is presented in table 3. The values of relative sensitivity are usually used for comparison purposes between various materials because relative sensitivity is much better performance indicator than absolute sensitivity. We can see that only Gd_2O_3:Eu^{3+} has slightly better value of maximal relative sensitivity and higher sensing range. Some of hosts listed in table 3 have similar but slightly inferior performances compared to YVO_4:Eu^{3+}. Other hosts are obviously inferior. We conclude that performance of YVO_4:Eu^{3+} nano phosphor analyzed here is more than satisfactory. However, it seems that analysis of multi-mode technique applied to the Gd_2O_3:Eu^{3+} nano phosphor could be a worthy effort.

4. Conclusions

In this paper we have analyzed the several temperature sensing techniques using the YVO_4:Eu^{3+} nanopowder. The material was prepared by simple solution combustion synthesis method. We have showed that, for analyzed YVO_4:Eu^{3+} material, the temperature sensing techniques based on ratio of intensities of two lines, lifetime or rise time are useful up to 650 K. We have obtained sensitivity improvement of the intensity ratio method by simulating the delayed gating of integrating-in-time intensity of one of spectral lines. If the YVO_4 host luminescence is used in intensity ratio method, the sensitivity in physiological temperature range is greatly improved; however, the sensing range is reduced to about 380 K.

So, our analysis shows that remote temperature sensor based on of YVO_4:Eu^{3+} nano phosphor has good sensitivity not only in the physiological temperature range but also for the higher temperatures that are of interest when monitoring the thermal behavior of electronic devices and engines. The luminescence detection part of the temperature sensor should be capable of switching between several measurements modes in order to obtain the best sensitivity in desired range of operation. We have proved the proposed concept by using the streak camera. Real application should be based on less expensive equipment.

Beside luminescence kinetics of slow decay transitions we also estimated rise times and lifetimes of fast decay transitions and the host luminescence. The rise times of fast decay transitions and host luminescence is estimated as negligible for effects that are here of interest. At the present time, the lifetimes of luminescence of fast decay transitions, $^5D_3$ and $^5D_2$, and the host are also too small to be of interest. However, with some improvements in detection, the lifetime of host could be of interest for temperature sensing in physiological temperature range.

ORCID iDs

D Sevic ⓘ https://orcid.org/0000-0002-7206-6370
M S Rabasovic ⓘ https://orcid.org/0000-0002-4882-8080
J Krizan ⓘ https://orcid.org/0000-0003-4195-8322
S Savic-Sevic ⓘ https://orcid.org/0000-0002-6406-0745
B P Marinkovic ⓘ https://orcid.org/0000-0002-6904-6360
M D Rabasovic ⓘ https://orcid.org/0000-0002-9235-4388

References

[1] Jaque D and Vetrone F 2012 *Nanoscale* **4** 4301–26
[2] Brites C D S, Lima P P, Silva N J O, Millan A, Amaral V S, Palacio F and Carlos L D 2012 *Nanoscale* **4** 4799–829
[3] Aldén M, Omrane A, Richter M and Särner G 2011 *Prog. Energy Combust. Sci.* **37** 422–61
[4] Allison S W and Gillies G T 1997 *Rev. Sci. Instrum.* **68** 2615–50
[5] Goss L P, Smith A and Post M E 1989 *Rev. Sci. Instrum.* **60** 3702–6

J. Phys. D: Appl. Phys. **53** (2020) 015106

D Sevic *et al*

[6] Heyes A L 2009 *J. Lumin.* **129** 2004–9
[7] Gentleman M M and Clarke D R 2004 *Surf. Coat. Technol.* **188–9** 93–100
[8] Khalid A H and Kontis K 2008 *Sensors* **8** 5673–744
[9] Wade S A, Collins S F and Baxter G W 2003 *J. Appl. Phys.* **94** 4743–56
[10] Wade S A, Forsyth D I and Grattan K T V 2001 *Rev. Sci. Instrum.* **72** 3186–90
[11] Nikolic M G, Antic Z, Culubrk S, Nedeljkovic J M and Dramicanin M D 2014 *Sens. Actuators* B **201** 46–50
[12] Dramicanin M D, Antic Z, Culubrk S, Ahrenkiel S P and Nedeljkovic J M 2014 *Nanotechnology* **25** 485501
[13] Lojpur V, Nikolic M G, Jovanovic D, Medic M, Antic Z and Dramicanin M D 2013 *Appl. Phys. Lett.* **103** 141912
[14] Lojpur V, Culubrk S and Dramicanin M D 2016 *J. Lumin.* **169** 534–8
[15] Rabasovic M S, Krizan J, Savic-Sevic S, Mitric M, Rabasovic M D, Marinkovic B P and Sevic D 2018 *J. Spectrosc.* **2018** 3413864
[16] Vlasic A, Sevic D, Rabasovic M S, Krizan J, Savic-Sevic S, Rabasovic M D, Mitric M, Marinkovic B P and Nikolic M G 2018 *J. Lumin.* **199** 285–92
[17] Rabasovic M S, Sevic D, Krizan J, Terzic M, Mozina J, Marinkovic B P, Savic Sevic S, Mitric M, Rabasovic M D and Romcevic N 2015 *J. Alloys Compd.* **622** 292–5
[18] Rabasovic M S, Sevic D, Krizan J, Rabasovic M D, Savic-Sevic S, Mitric M, Petrovic M, Gilic M and Romcevic N 2015 *Opt. Mater.* **50** 250–5
[19] Sevic D, Rabasovic M S, Krizan J, Savic-Sevic S, Mitric M, Gilic M, Hadzic B and Romcevic N 2017 *Mater. Res. Bull.* **88** 121–6
[20] Rabasovic M S, Krizan J, Gregorcic P, Rabasovic M D, Romcevic N and Sevic D 2016 *Opt. Quantum Electron.* **48** 163
[21] Nikolic M G, Rabasovic M S, Krizan J, Savic-Sevic S, Rabasovic M D, Marinkovic B P, Vlasic A and Sevic D 2018 *Opt. Quantum Electron.* **50** 258
[22] Khalid A H and Kontis K 2009 *Meas. Sci. Technol.* **20** 025305
[23] Allison S W, Goedeke S M, Cates M R, Hollerman W A, Eldridge J I and Bencic T J 2005 *Oak Ridge National Laboratory Report* No. 123055
[24] Ranson R M, Evangelou E and Thomas C B 1998 *Appl. Phys. Lett.* **72** 2663–4
[25] Lojpur V, Antic Z and Dramicanin M D 2014 *Phys. Chem. Chem. Phys.* **16** 25636–41
[26] Li X, Wei X, Qin Y, Chen Y, Duan C and Yin M 2016 *J. Alloys Compd.* **657** 353–7
[27] Liu R, Liu L and Liang Y 2018 *Opt. Mater. Express* **8** 1686
[28] Riul A, Justino L G and Caiut J M A 2017 *Nanotechnology* **28** 235601
[29] Xie D, Peng H, Huang S, You F, Zhang X and Wang G 2015 *Mater. Lett.* **157** 307–10
[30] Huong T T, Phuong H T, Vinh L T, Khuyen H T, Anh T K and Minh L Q 2016 *J. Sci.* **1** 295–300
[31] Shirmane L, Feldmann C and Pankratov V 2017 *Physica* B **504** 80–5
[32] Ningthoujam R S, Singh L R, Sudarsan V and Singh S D 2009 *J. Alloys Compd.* **484** 782–9
[33] Huignard A, Gacoin T and Boilot J-P 2000 *Chem. Mater.* **12** 1090–4
[34] Huignard A, Buissette V, Laurent G, Gacoin T and Boilot J-P 2002 *Chem. Mater.* **14** 2264–9
[35] Riwotzki K and Haase M 2001 *J. Phys. Chem.* B **105** 12709–13
[36] Bhatkar V B 2013 *Int. J. Eng. Sci.* **2** 426–32
[37] Georgescu S, Cotoi E, Voiculescu A M and Toma O 2008 *Rom. Rep. Phys.* **60** 947–55
[38] Park W J, Jung M K, Masaki T, Im S J and Yoon D H 2008 *Mater. Sci. Eng.* **146** 95–8
[39] Sanson A, Giarola M, Rossi B, Mariotto G, Cazzanelli E and Speghini A 2012 *Phys. Rev.* B **86** 214305
[40] Thakur S and Gathania A K 2015 *J. Electron. Mater.* **44** 3444–9
[41] Grandhe B K, Bandi V R, Jang K, Ramaprabhu S, Yi S-S and Jeong J-H 2011 *Electron. Mater. Lett.* **7** 161–5
[42] Chang Y-S, Huang F-M, Tsai Y-Y and Teoh L-G 2009 *J. Lumin.* **129** 1181–5
[43] Han R, Hu R and Chen K 2009 *Opt. Mater.* **32** 329–33
[44] Yan-bo Q, Xiao-feng L, Qiang Z, Dan-ping C, Ye-wen W and Wen-bo M 2010 *Mater. Lett.* **64** 1306–8
[45] Yu M, Lin J, Wang Z, Fu J, Wang S, Zhang H J and Han Y C 2002 *Chem. Mater.* **14** 2224–31
[46] Matos M G, de Faria E H, Rocha L A, Calefi P S, Ciuffi K J, Nassar E J, Hugo V and Sarmento V 2014 *J. Lumin.* **147** 190–5
[47] Kumari P, Baitha P K and Manam J 2015 *Indian J. Phys.* **89** 1297–306
[48] Shanta Singh N, Ningthoujam R S, Niraj Luwang M, Dorendrajit Singh S and Vatsa R K 2009 *Chem. Phys. Lett.* **480** 237–42
[49] Saltarelli M, Matos M G, de Faria E H, Ciuffi K J, Rocha L A and Nassar E J 2015 *J. Sol-Gel Sci. Technol.* **73** 283–92
[50] Saltarelli M, Luz P P, Matos M G, de Faria E H, Ciuffi K J, Calefi P S, Rocha L A and Nassar E J 2012 *J. Fluoresc.* **22** 899–906
[51] Chambers M D, Rousseve P A and Clarke D R 2009 *J. Lumin.* **129** 263–9
[52] Chang Y-S, Lin H-J, Chai Y-L and Li Y-C 2008 *J. Alloys Compd.* **460** 421–5
[53] Darwent J R, Flint C D and O'Grady P J 1986 *Chem. Phys. Lett.* **127** 547–50
[54] Krizan J, Mazaj M, Kaucic V, Bajsic I and Mozina J 2014 *Acta Chim. Slov.* **61** 608–14
[55] Rabasovic M D, Muric B D, Celebonovic V, Mitric M, Jelenkovic B M and Nikolic M G 2016 *J. Phys. D: Appl. Phys.* **49** 485104
[56] Anitha M, Ramakrishnan P, Chatterjee A, Alexander G and Singh H 2002 *Appl. Phys.* A **74** 153–62
[57] Zhou S, Duan C, Yin M, Zhang S and Wang C 2019 *J. Alloys Compd.* **784** 970–4
[58] Zhou S, Duan C and Han S 2018 *Dalton Trans.* **47** 1599–603
[59] Zhou S, Duan C, Yin M, Liu X, Han S, Zhang S and Li X 2018 Optical thermometry based on cooperation of temperature-induced shift of charge transfer band edge and thermal coupling *Opt. Express* **26** 27339–45
[60] Zhou S, Duan C and Wang M 2017 *Opt. Lett.* **42** 4703–6
[61] Nikolic M G, Jovanovic D J and Dramicanin M D 2013 *Appl. Opt.* **52** 1716–24
[62] Shao B, Zhao Q, Guo N, Jia Y, Lv W, Jiao M, Lu W and You H 2013 *CrystEngComm* **15** 5776–83
[63] Binnemans K 2015 *Coord. Chem. Rev.* **295** 1–45
[64] Ananias D, Brites C D S, Carlos L D and Rocha J 2016 *Eur. J. Inorg. Chem.* **2016** 1967–71
[65] Culubrk S, Lojpur V, Ahrenkiel S P, Nedeljkovic J M and Dramicanin M D 2016 *J. Lumin.* **170** 395–400
[66] Dramicanin M D 2016 *Methods Appl. Fluoresc.* **4** 042001
[67] Đacanin L R, Dramicanin M D, Lukic-Petrovic S R, Petrovic D M and Nikolic M G 2013 *Radiat. Meas.* **56** 143–6
[68] Đacanin L R, Lukic-Petrovic S R, Petrovic D M, Nikolic M G and Dramicanin M D 2014 *J. Lumin.* **151** 82–7
[69] Nikolic M G, Al-Juboori A Z, Djordjevic V and Dramicanin M D 2013 *Phys. Scr.* **T157** 014056
[70] Lojpur V, Antic Z, Krsmanovic R, Medic M, Nikolic M G and Dramicanin M D 2012 *J. Serb. Chem. Soc.* **77** 1735–46
[71] Lojpur V, Culubrk S, Medic M and Dramicanin M D 2016 *J. Lumin.* **170** 467–71
[72] Lu Z, Zhongmin C, Xiantao W, Min Y and Yonghu C 2017 *J. Rare Earths* **35** 356–60

XUV-driven plasma switch for THz: new spatio-temporal overlap tool for XUV–THz pump–probe experiments at FELs[1]

E. Zapolnova,[a] R. Pan,[a] T. Golz,[a] M. Sindik,[a] M. Nikolic,[a] M. Temme,[a] M. Rabasovic,[b] D. Grujic,[b] Z. Chen,[c] S. Toleikis[a] and N. Stojanovic[a]*

[a]Deutsches Elektronen-Synchrotron (DESY), Notkestrasse 85, 22607 Hamburg, Germany, [b]Institute of Physics Belgrade, Pregrevica 118, 11080 Belgrade, Serbia, and [c]SLAC National Accelerator Laboratory, Menlo Park, CA 94025, USA. *Correspondence e-mail: nikola.stojanovic@desy.de

A simple and robust tool for spatio-temporal overlap of THz and XUV pulses in in-vacuum pump–probe experiments is presented. The technique exploits ultrafast changes of the optical properties in semiconductors (i.e. silicon) driven by ultrashort XUV pulses that are probed by THz pulses. This work demonstrates that this tool can be used for a large range of XUV fluences that are significantly lower than when probing by visible and near-infrared pulses. This tool is mainly targeted at emerging X-ray free-electron laser facilities, but can be utilized also at table-top high-harmonics sources.

1. Introduction

Intense THz pulses combined with synchronized X-ray pulses enable investigation of the dynamics of the light–matter interaction, non-linear response of materials and control of the properties of matter selectively on femtosecond time scales. Therefore, achieving the temporal overlap between pump and probe pulses in the femtosecond range is essential. Certain pump–probe schemes, e.g. THz streaking (Frühling et al., 2009; Schmid et al., 2019), are comparatively tolerant against the spatial overlap between XUV and THz pulses and the actual focal position of the THz beam. The observable, i.e. the kinetic energy of the photoelectrons, is furthermore of considerable magnitude and can be utilized for further optimization of the pump–probe signal. This is almost never the case in pump–probe experiments on solid-state samples, utilizing one of the XUV probing techniques [e.g. X-ray magnetic circular dichroism (XMCD) (Pfau et al., 2012; Willems et al., 2015) and resonant inelastic X-ray scattering (Dell'Angela et al., 2016)]. There, the spatio-temporal overlap between THz and XUV and in particular diffraction-limited focusing of the THz beam have to be achieved with the aid of versatile in-vacuum diagnostics.

The so-called plasma-switch, the transient change of optical constants in the visible (VIS) and near-infrared (NIR) spectral ranges by X-ray and XUV pulses, has been used for the temporal characterization of these pulses (Harmand et al., 2012; Gahl et al., 2008; Krupin et al., 2012; Riedel et al., 2013; Danailov et al., 2014). Transient changes of optical properties in the THz range, driven by femtosecond laser pulses, have been used for pickup of individual pulses from MHz trains at infrared free-electron lasers (FELs) (Schmidt et al., 2015) as well as for THz spectral shaping at table-top THz sources (Cartella et al., 2014; Mayer et al., 2014).
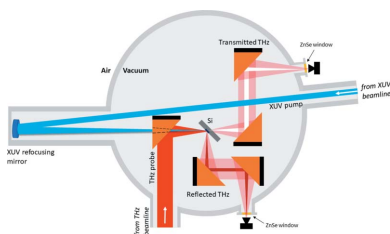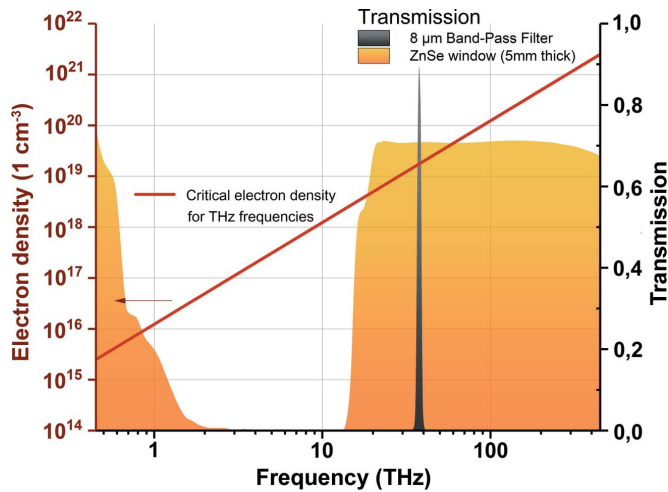
Figure 1
Calculation of the critical electron density for the THz range (red line). Transmission of the 5 mm-thick ZnSe vacuum window and the bandpass filter (at 8 μm wavelength) used in the experiment are presented as the shadowed areas.

As shown in Fig. 1, for lower probing frequencies the effect of the plasma switch is more efficient because lower electron density is required to change the material reflectivity. In this work we present a technique to establish the temporal overlap between XUV and THz pulses, based on the transient change of optical properties of a silicon target in the THz spectral range, induced by the intense femtosecond XUV pulse.

The presented method can be applied in facilities employing THz radiation for time-resolved XUV–THz pump–probe experiments where it is necessary to temporally overlap XUV and THz pulses on a sub-picosecond level.

2. XUV driven THz plasma switch: theoretical background

The process of electronic excitation of materials by an intense XUV pulse happens on an ultrafast time scale, within a few femtoseconds (Gahl *et al.*, 2008; Riedel *et al.*, 2013), and is governed by the photoionization of the electrons in the material: photoabsorption of the bound electrons within the valence band, secondary processes as elastic and inelastic scattering of free electrons, Auger decay, and electron pair creation. Other processes may contribute to the photo-ionization depending on the energy of the incoming photon and the material (Medvedev & Rethfeld, 2010). Previous theoretical studies have shown that the density of the created free electrons follows the photon flux of the XUV pulse linearly (Riedel *et al.*, 2013) in a wide intensity range, below fluences required for the sample melting, ablation and plasma formation.

Optical properties of the photo-excited material strongly depend on the density of free electrons and can be modelled [*e.g.* via the continuity equation (Mezentsev *et al.*, 2007)] and expressed in terms of relative permittivity. According to the Drude model, free electrons in a material can be treated as free-electron plasma with a corresponding plasma frequency

ω_p (Ashcroft & Mermin, 1976). We assume that the damping can be neglected in our case (refer to Appendix *A* for a short discussion on this topic) and the relative permittivity ε in this case can be presented as a function of the incoming frequency ω and the plasma frequency ω_p,

$$\varepsilon(\omega) = 1 - \frac{\omega_p^2}{\omega^2}.$$

This indicates that light with a higher frequency than the plasma frequency, $\omega > \omega_p$, can penetrate the plasma whereas light with lower frequency, $\omega < \omega_p$, will be reflected. Taking into account the oscillatory motion of the electron, the critical electron density, n_e, required to make the sample reflective to light with a certain frequency can be presented as

$$n_e = \frac{\varepsilon_0 m_e}{e^2} \omega_p^2,$$

where ε_0 is the vacuum permittivity, e is the charge and m_e is the mass of an electron.

In our experiment, the critical electron density for the probing pulse at a wavelength of 8 μm (37.5 THz) is $n_{e\,8\mu m} = 1.8 \times 10^{19}\ cm^{-3}$, and at wavelengths over 100 μm (<3 THz) it is less than $n_{e\,100\mu m} = 1.1 \times 10^{17}\ cm^{-3}$.

3. Description of the setup

The experiment was performed with the pump XUV wavelength at 13.5 nm (91.8 eV) and two different probing conditions: (i) a THz pulse with a central wavelength of 8 μm, and (ii) a broadband THz pulse with a wavelength >100 μm. The expected pulse duration for THz was ∼300 fs and ∼3 ps, respectively, and the XUV pulse duration was 160 fs, estimated by electron bunch length measurements by a transverse deflecting RF-structure (Düsterer *et al.*, 2014).

The THz beam is collimated using five toroidal mirrors in order to keep the beam size within the range of the beam transport and optics. This additional folding of the THz beam results in a ∼6.5 m longer optical path with respect to the XUV beam. In order to overlap the XUV and THz pulses in time, an additional delay for the XUV is introduced: pulses travel 3.25 m longer distance and then are refocused by a mirror with 3.5 m focal length back to the experiment (Pan *et al.*, 2019). The scheme of the experiment is presented in Fig. 2.

The THz and XUV pulses are collinearly focused and spatially overlapped in the experimental chamber on a 400 μm-thick Si sample at a 45° incident angle. The transmitted and reflected portions of the THz beam are picked up and collimated using parabolic mirrors. Then they are focused through ZnSe vacuum windows (5 mm thick) on two 2 mm × 2 mm pyro detectors (InfraTec LME-301) located outside of the experimental chamber in air ∼5 mm from the window. The detectors were custom-designed by collaboration of the DESY FLA group and InfraTec to reduce internal THz interferences (Wesch, 2012). The detectors are without optical windows, which makes them suitable for measurements along a broad spectral range and sensitive to XUV radiation. ZnSe
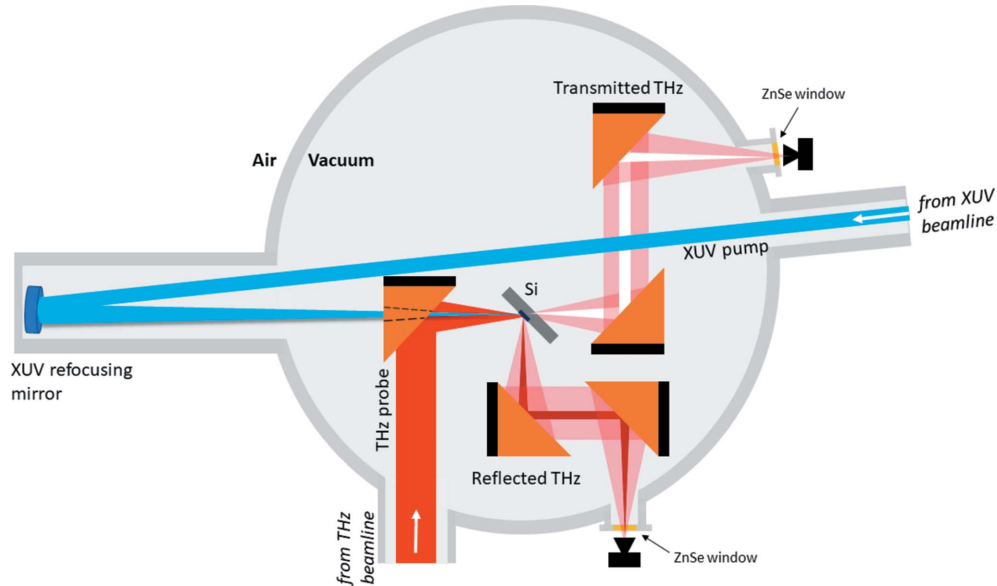
Figure 2
Scheme of the XUV-driven plasma switch experiment for the THz beam. The THz and XUV beams are collinearly focused and spatially overlapped on a 400 μm-thick Si sample at a 45° incidence angle. Transmitted and reflected THz beams are picked up by off-axis parabolic mirrors and further focused on the corresponding pyro detectors through 5 mm-thick ZnSe vacuum windows.

Table 1
Transmission of XUV at 13.5 nm.

XUV pulse energy via GMD	112 μJ ± 17 μJ
Beamline transmission	78%
Refocusing mirror	62%
Si_3N_4 500 nm filter transmission	1.3%
Total transmission	700 nJ ± 10 nJ

vacuum windows have good transmission in the VIS to IR range as well as in the long-THz wavelength range (see Fig. 1).

Pulse energies of the XUV, measured with the gas-monitor detector (GMD), were 110 μJ ± 20 μJ (r.m.s.) (Tiedtke *et al.*, 2009) and 0.5 μJ ± 0.1 μJ (r.m.s.) for the THz beam measured with a calibrated pulse energy meter (Zapolnova *et al.*, 2018; Pan *et al.*, 2019).

The estimated XUV pulse energy through the beamline (Tiedtke *et al.*, 2009) after the refocusing mirror and through attenuation filters was 700 nJ ± 10 nJ (refer to Table 1 for details), yielding a final intensity on the sample of 6.76 × 10^9 W cm^{-2} and 2.65 × 10^9 W cm^{-2}, for the two measured XUV beam sizes (see Section 4 for details). By measuring both transmitted and reflected intensities of the THz beam and assuming that absorption in the excited Si layer is negligible, we are able to correct the pulse-to-pulse energy fluctuations of the THz beam (3.6% RMS at 100 μm, 14% RMS at 8 μm).

4. THz and XUV 2D beam profile

The THz and XUV beams were characterized by 2D profile measurements in the focal position. A pyro detector with a 100 μm pinhole was mounted on an *xy* positioner, facing the incoming THz and XUV beams at normal incidence, and was moved through the focus of the beam with defined steps along the *z* axis. The pyro detector also showed a good response for XUV radiation, and therefore it was used for both the THz and XUV beam profile characterizations.

The results of 2D scans are presented in Fig. 3. The THz beam in focus has an ellipsoidal profile, elongated in the vertical direction, because of imperfect alignment of the off-axis parabolic mirror for the THz beam. The full width at half-maximum (FWHM) diameter of the THz beam with the THz undulator set at a 100 μm nominal wavelength was 400 ± 20 μm × 1470 ± 30 μm, and at 8 μm it was 180 ± 15 μm × 320 ± 15 μm. In an attempt to match the XUV and THz beam sizes we inserted a pinhole (3 mm diameter) in the XUV beam, 30 m upstream of the experiment, to optimize the ratio between beam sizes. The FWHM diameters of the XUV beam with and without a pinhole were 230 ± 30 μm and 140 ± 20 μm, respectively. The ratio between the areas of the THz and XUV beams was 1:9 for the THz beam at 100 μm and 2:3 at 8 μm.

5. Transient reflectivity and transmission

Results of time-dependent reflectivity measurements [presented as $(R - R_0)/R_0$, where R_0 is the equilibrium reflectivity] are presented in Fig. 4. Once the probing THz pulse arrives following the XUV pulse, a portion of the THz pulse, which spatially overlaps with the XUV pulse, is reflected more because of the plasma created by the XUV pulse. The observed duration of the transition (slope) $\Delta\tau_{\lambda_{THz}}$ is the convolution of the pulse durations of the THz $\Delta\tau_{THz}$ and XUV pulses $\Delta\tau_{XUV}$, the jitter $\Delta\tau_{jitter}$ between them, and the timescale of the free carrier excitation process $\Delta\tau_{excitation}$, and can be described as
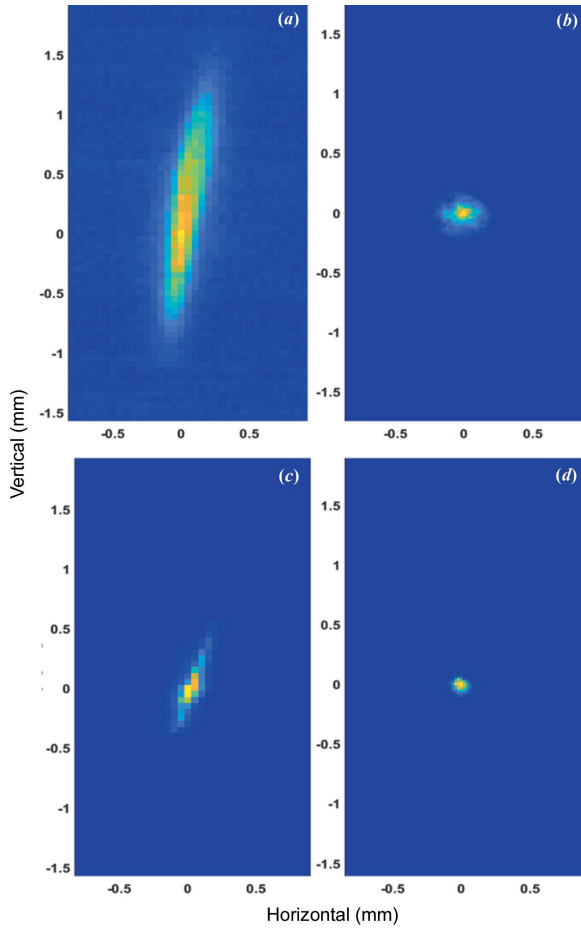
Figure 3
Measured 2D profiles of the THz and XUV beams. (*a*) THz beam profile at 100 μm with an FWHM of 400 ± 20 μm × 1470 ± 30 μm. (*b*) XUV beam at 13.5 nm wavelength through a 3 mm pinhole placed ~30 m upstream of the experiment with an FWHM of 230 ± 30 μm. (*c*) THz beam profile at 8 μm wavelength with an FWHM of 180 ± 15 μm × 320 ± 15 μm. (*d*) XUV beam at 13.5 nm wavelength with a 10 mm pinhole at the same position as in (*b*) with an FWHM of 140 ± 20 μm.

$$\Delta \tau_{\lambda_{THz}} = \left(\Delta \tau_{THz}^2 + \Delta \tau_{XUV}^2 + \Delta \tau_{jitter}^2 + \Delta \tau_{excitation}^2 \right)^{1/2}.$$

For a THz wavelength of ~100 μm, the observed slope width is $\Delta \tau_{100\mu m} = 2.2$ ps and for 8 μm wavelength it is $\Delta \tau_{8\mu m} = 1.2$ ps (calculated as the time between the points corresponding to the 10% and 90% levels of total amplitude of the signal). The XUV and THz pulses are naturally synchronized in this experiment, with jitter smaller than 5 fs (RMS) (Frühling *et al.*, 2009), and its contribution is negligible. We assume that the excitation of the free carriers is much faster than other time-scales in the experiment so we neglect it as well.

6. Dependence on the XUV fluence

Fig. 5 shows a comparison of the transient THz reflectivity change for different fluences of the pump XUV pulse. We used different combinations of the attenuation filters: Si_3N_4 350 nm (red line), Si_2N_4 350 nm + Nb 405 nm (orange line) and Si_3N_4 500 nm (green line). The effect of the plasma switch in
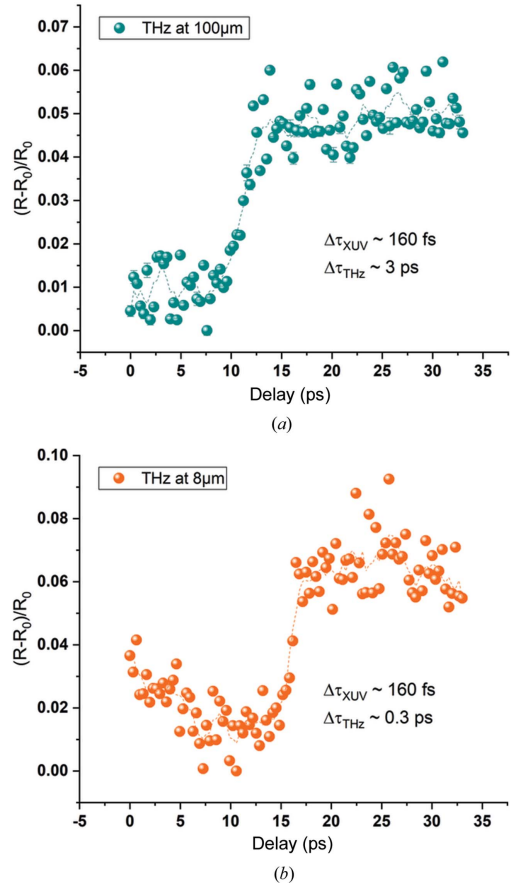

Figure 4
Transient optical reflectivity curves for the THz undulator set at 100 μm and 8 μm wavelengths for a 13.5 nm XUV pump wavelength.

the THz spectral range is very efficient and can be clearly observed even at XUV fluences as low as 45 μJ cm^{-2}.

7. Quantitative estimate of the effect

The amplitude of the reflectivity change for a broadband THz beam >100 μm is around 6.4% and for 8 μm is around 6.0%. Using the details of the actual THz and XUV beam sizes
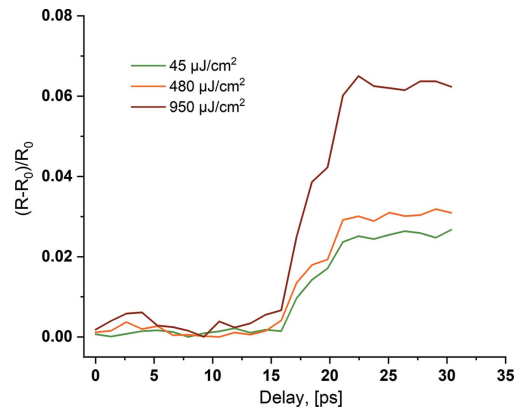

Figure 5
Transient THz reflectivity curves as a function of the THz/XUV pulse delay for three different fluences of the XUV pulse on the sample.

from the 2D profile measurements, we can estimate the actual switched fraction of the THz pulse. Comparing total areas of the beams and assuming that the electron density follows the intensity envelope of the XUV beam linearly, we can assume that, if the XUV beam size matches the size of the THz beams for a 100 μm wavelength (400 μm FWHM beam size) and for a 8 μm wavelength (180 μm FWHM beam size), the overall effect on the reflectivity change would be 9 times higher (∼57.6%) and 1.5 times higher (∼10%) than observed.

8. Summary

We have developed a tool for temporal and spatial overlap of XUV and THz pulses in pump–probe experiments, based on an XUV plasma switch for the THz range on an Si sample. During several pump–probe experiments at FLASH, it was demonstrated that the arrival time of XUV and THz pulses can be established down to at least the pulse duration of the THz pulse.

The experiment has been performed at different XUV fluences from 0.045 mJ cm^{-2} up to 0.95 mJ cm^{-2} for 8 μm wavelength and for the broadband >100 μm wavelength of the probe pulse. The observed change of the transient normalized reflectivity $(R - R_0)/R_0$ of THz beam due to the plasma switch is approximately 6% from the initial level.

Since this effect uses low XUV fluences, far below the damage threshold, and uses room-temperature broadband THz detectors, it is robust and simple. This technique can be further applied at facilities employing XUV–THz pump–probe experiments, and enables a straightforward and efficient method for temporal overlap of XUV and THz pulses on the picosecond time scale.

APPENDIX A
Comparison of the excited-layer thickness with the penetration depth of THz radiation

The frequency-dependent dielectric constant, according to the simple Drude model, where damping is independent of the free electron energy, can be expressed as (Van Exter & Grischkowsky, 1990)

$$\varepsilon(\omega) = \varepsilon(\infty) - \frac{\omega_p^2}{\omega(\omega + i\Gamma)},$$

where ω_p is the plasma frequency, $\Gamma = 1/\tau_c$ is the damping frequency and τ_c is the average free-electron collision time. From the literature, we estimate the average free-electron collision time to be between 1 fs and 100 fs (Ashcroft & Mermin, 1976; Temnov et al., 2006; Van Exter & Grischkowsky; 1990; Riedel et al., 2013). Finally, this gives us the estimated minimum penetration depth for probing THz frequencies (2–40 THz) in XUV-excited plasma in silicon to be ≥2 μm.

For an XUV wavelength of 13.5 nm impinging at a 45° angle of incidence, the thickness of the excited area in silicon is 400 nm, as determined by the penetration depth (Henke et al.,

1993). The XUV pulses from FLASH, used in this work (as presented in Fig. 5), result in free-electron densities in the range from 1.2×10^{17} cm^{-3} up to 2.8×10^{18} cm^{-3}.

This leads to the conclusion that only a small fraction of the probing THz radiation (<20%) is absorbed in the investigated sample excited by the XUV pulse.

References

Ashcroft, N. W. & Mermin, D. N. (1976). *Solid State Physics*. New York: Holt, Rinehart and Winston.

Cartella, A., Bonora, S., Först, M., Cerullo, G., Cavalleri, A. & Manzoni, C. (2014). *Opt. Lett.* **39**, 1485–1488.

Danailov, M. B., Bencivenga, F., Capotondi, F., Casolari, F., Cinquegrana, P., Demidovich, A., Giangrisostomi, E., Kiskinova, M. P., Kurdi, G., Manfredda, M., Masciovecchio, C., Mincigrucci, R., Nikolov, I. P., Pedersoli, E., Principi, E. & Sigalotti, P. (2014). *Opt. Express*, **22**, 12869–12879.

Dell'Angela, M., Hieke, F., Malvestuto, M., Sturari, L., Bajt, S., Kozhevnikov, I. V., Ratanapreechachai, J., Caretta, A., Casarin, B., Glerean, F., Kalashnikova, A. M., Pisarev, R., Chuang, Y. D., Manzoni, G., Cilento, F., Mincigrucci, R., Simoncig, A., Principi, E., Masciovecchio, C., Raimondi, L., Mahne, N., Svetina, C., Zangrando, M., Passuello, R., Gaio, G., Prica, M., Scarcia, M., Kourousias, G., Borghes, R., Giannessi, L., Wurth, W. & Parmigiani, F. (2016). *Sci. Rep.* **6**, 1–8.

Düsterer, S., Rehders, M., Al-Shemmary, A., Behrens, C., Brenner, G., Brovko, O., DellAngela, M., Drescher, M., Faatz, B., Feldhaus, J., Frühling, U., Gerasimova, N., Gerken, N., Gerth, C., Golz, T., Grebentsov, A., Hass, E., Honkavaara, K., Kocharian, V., Kurka, M., Limberg, Th., Mitzner, R., Moshammer, M., Plönjes, E., Richter, M., Rönsch-Schulenburg, J., Rudenko, A., Schlarb, H., Schmidt, B., Senftleben, A., Schneidmiller, E. A., Siemer, B., Sorgenfrei, F., Sorokin, A. A., Stojanovic, N., Tiedtke, K., Treusch, R., Vogt, M., Wieland, M., Wurth, W., Wesch, S., Yan, M., Yurkov, M. V., Zacharias, H. & Schreiber, S. (2014). *Phys. Rev. ST Accel. Beams*, **17**, 120702.

Exter, M. van & Grischkowsky, D. (1990). *Phys. Rev. B*, **41**, 12140–12149.

Frühling, U., Wieland, M., Gensch, M., Gebert, T., Schütte, B., Krikunova, M., Kalms, R., Budzyn, F., Grimm, O., Rossbach, J., Plönjes, E. & Drescher, M. (2009). *Nat. Photon.* **3**, 523–528.

Gahl, C., Azima, A., Beye, M., Deppe, M., Döbrich, K., Hasslinger, U., Hennies, F., Melnikov, A., Nagasono, M., Pietzsch, A., Wolf, M., Wurth, W. & Föhlisch, A. (2008). *Nat. Photon.* **2**, 165–169.

Harmand, M., Murphy, D., Brown, D., Cammarata, M., Döppner, T., Düsterer, S. & Toleikis, S. (2012). *J. Instrum.* **7**, P08007.

Henke, B. L., Gullikson, E. M. & Davis, J. C. (1993). *Atom Data Nucl. Data*, **54**, 181–342.

Krupin, O., Trigo, M., Schlotter, W. F., Beye, M., Sorgenfrei, F., Turner, J. J. & Wurth, W. (2012). *Opt. Express*, **20**, 11396–11406.

Mayer, B., Schmidt, Ch., Bühler, J., Seletskiy, D. V., Brida, D., Pashkin, A. & Leitenstorfer, A. (2014). *New J. Phys.* **16**, 063033.

Medvedev, N. & Rethfeld, B. (2010). *New J. Phys.* **12**, 73037.

Mezentsev, V., Petrovic, J. S., Dubov, M., Bennion, I., Dreher, J., Schmitz, H. & Grauer, R. (2007). *Proc. SPIE*, **6459**, 64590B.

Pan, R., Zapolnova, E., Golz, T., Krmpot, A. J., Rabasovic, M. D., Petrovic, J., Asgekar, V., Faatz, B., Tavella, F., Perucchi, A., Kovalev, S., Green, B., Geloni, G., Tanikawa, T., Yurkov, M., Schneidmiller, E., Gensch, M. & Stojanovic, N. (2019). *J. Synchrotron Rad.* **26**, 700–707.

Pfau, B., Schaffert, S., Müller, L., Gutt, C., Al-Shemmary, A., Büttner, F., Delaunay, R., Düsterer, S., Flewett, S., Frömter, R., Geilhufe, J., Guehrs, E., Günther, C. M., Hawaldar, R., Hille, M., Jaouen, N., Kobs, A., Li, K., Mohanty, J., Redlin, H., Schlotter, W. F., Stickler, D., Treusch, R., Vodungbo, B., Kläui, M., Oepen, H. P., Lüning, J., Grübel, G. & Eisebitt, S. (2012). *Nat. Commun.* **3**, 1100.

Riedel, R., Al-Shemmary, A., Gensch, M., Golz, T., Harmand, M., Medvedev, N., Prandolini, M. J., Sokolowski-Tinten, K., Toleikis, S., Wegner, U., Ziaja, B., Stojanovic, N. & Tavella, F. (2013). *Nat. Commun.* **4**, 1731–1737.

Schmid, G., Schnorr, K., Augustin, S., Meister, S., Lindenblatt, H., Trost, F., Liu, Y., Stojanovic, N., Al-Shemmary, A., Golz, T., Treusch, T., Gensch, M., Kübel, M., Foucar, L., Rudenko, A., Ullrich, J., Schröter, C. D., Pfeifer, T. & Moshammer, R. (2019). *Phys. Rev. Lett.* **122**, 073001.

Schmidt, J., Winnerl, S., Seidel, W., Bauer, C., Gensch, M., Schneider, H. & Helm, M. (2015). *Rev. Sci. Instrum.* **86**, 063103.

Temnov, V. V., Sokolowski-Tinten, K., Zhou, P., El-Khamhawy, A. & von der Linde, D. (2006). *Phys. Rev. Lett.* **97**, 237403.

Tiedtke, K., Azima, A., Von Bargen, N., Bittner, L., Bonfigt, S., Düsterer, S., Faatz, B., Frühling, U., Gensch, M., Gerth, Ch., Gerassimova, N., Hahn, U., Hesse, M., Honkavaara, K., Jastrow, U., Juranic, P., Kapitzki, S., Keitel, B., Kracht, T., Kuhlman, M., Li, W. B., Martins, M., Nuñez, T., Plönjes, E., Redlin, H., Saldin, E. L., Schneidmiller, E. A., Schneider, J. R., Schreiber, S., Stojanovic, N., Tavella, F., Toleikis, S., Treusch, R., Weigelt, H., Wellhöfer, M., Wabnitz, H., Yurkov, M. V. & Feldhaus, J. (2009). *New J. Phys.* **11**, 023029.

Wesch, S. (2012). Dissertation. DESY, Hamburg, Germany.

Willems, F., Smeenk, C. T. L., Zhavoronkov, N., Kornilov, O., Radu, I., Schmidbauer, M., Hanke, M., von Korff Schmising, C., Vrakking, M. J. J. & Eisebitt, S. (2015). *Phys. Rev. B*, **92**, 220405.

Zapolnova, E., Golz, T., Pan, R., Klose, K., Schreiber, S. & Stojanovic, N. (2018). *J. Synchrotron Rad.* **25**, 39–43.

OPEN

Altered organization of collagen fibers in the uninvolved human colon mucosa 10 cm and 20 cm away from the malignant tumor

Sanja Z. Despotović[1*], Đorđe N. Milićević[2], Aleksandar J. Krmpot[3], Aleksandra M. Pavlović[4], Vladimir D. Živanović[4], Zoran Krivokapić[5], Vladimir B. Pavlović[6], Steva Lević[6], Gorana Nikolić[7] & Mihailo D. Rabasović[3]

Remodelling of collagen fibers has been described during every phase of cancer genesis and progression. Changes in morphology and organization of collagen fibers contribute to the formation of microenvironment that favors cancer progression and development of metastasis. However, there are only few data about remodelling of collagen fibers in healthy looking mucosa distant from the cancer. Using SHG imaging, electron microscopy and specialized softwares (CT-FIRE, CurveAlign and FiberFit), we objectively visualized and quantified changes in morphology and organization of collagen fibers and investigated possible causes of collagen remodelling (change in syntheses, degradation and collagen cross-linking) in the colon mucosa 10 cm and 20 cm away from the cancer in comparison with healthy mucosa. We showed that in the lamina propria this far from the colon cancer, there were changes in collagen architecture (width, straightness, alignment of collagen fibers and collagen molecules inside fibers), increased representation of myofibroblasts and increase expression of collagen-remodelling enzymes (LOX and MMP2). Thus, the changes in organization of collagen fibers, which were already described in the cancer microenvironment, also exist in the mucosa far from the cancer, but smaller in magnitude.

Extracellular matrix (ECM) is no longer considered as an inert substrate, a three-dimensional network which only "fills the spaces" between cells and provide mechanical support[1,2]. Today, ECM is known to be a complex and dynamic structure, whose chemical and biophysical properties affect cell adhesion[3], proliferation[4] morphology[5], migration[6], regulate tissue morphogenesis[7,8] and fluid volume in tissues[9]. The most abundant component of ECM in the lamina propria of the colon mucosa is type I collagen.

Remodelling of collagen fibers has been described in almost every solid cancer, including colorectal cancer. During tumor formation and progression, collagen remodelling is constantly carried out: degradation, synthesis, cross-linking of fibers, change of fiber orientation, and interaction of cells of the innate and acquired immune system with collagen fibers[10,11]. Changes in morphology, representation, and organization of collagen fibers contribute to the formation of the microenvironment that favors tumor progression, primarily through its effect on cell migration and polarization[12]. Also, remodelling of collagen fibers on premetastatic sites is of great importance in determination of survival and growth of disseminated cancer cells, and thus, formation of metastasis[13,14].

Remodelling of collagen fibers may be a result of changes in synthesis, degradation or cross-linking. Main cells responsible for synthesis of collagen in colon mucosa are fibroblasts and myofibroblasts. The most important enzymes for degradation of collagen fibers are matrix metalloproteinases (MMPs). It has been shown that expression of MMP2 and MMP9 is increased in colorectal cancer and influences its progression and

[1]University of Belgrade, Faculty of Medicine, Institute of Histology and embryology, Belgrade, Serbia. [2]Saarland University, Department of Internal Medicine V- Pulmonology, Allergology, Intensive Care Medicine, Homburg/Saar, Germany. [3]University of Belgrade, Institute of Physics Belgrade, Belgrade, Serbia. [4]University Hospital Center "Dr Dragiša-Mišović-Dedinje", Belgrade, Serbia. [5]Clinic for Abdominal Surgery- First surgical clinic, Clinical Center of Serbia, Belgrade, Serbia. [6]University of Belgrade, Faculty of Agriculture, Belgrade, Serbia. [7]University of Belgrade, Faculty of Medicine, Institute of Pathology, Belgrade, Serbia. *email: sanjadesp@gmail.com

metastatic potential[15,16]. Covalent cross-linking of collagen fibrils is catalyzed by enzyme lysyl oxidase (LOX). LOX-dependent collagen crosslinking enhances proliferation of cancer cells and metastatic capacity[17,18].

The quantification of changes of collagen within the primary tumor and metastatic niches has been the subject of numerous studies and it is recognized to play an important role in both cancer development and progression[19–21]. However, much less is known about remodelling of collagen fibers in healthy looking colon mucosa distant from the cancer. In the previous study of uninvolved colon mucosa[22], we described changes in the representation and organization of collagen fibers as far as 10 cm and 20 cm away from the colon cancer. Because remodelling of collagen fibers is an important process, crucial for creating specific microenvironmental milieu, we felt that further studies were necessary to investigate the finer aspects of this phenomenon. Thus, the aim of our study was to quantify morphological parameters and organization of collagen fibers and to investigate possible causes of collagen remodelling (change in syntheses, degradation and collagen cross-linking) in the colon mucosa 10 cm and 20 cm away from the cancer in comparison with healthy mucosa. Indeed, we showed that this far from the colon cancer there are changes in collagen architecture, increased representation of myofibroblasts and increase expression of collagen-remodelling enzymes.

Results

Changes in morphology and organization of collagen fibers in the uninvolved colon lamina propria visualized using SHG imaging.
On SHG images, in the lamina propria of healthy patients, collagen fibers were wavy, orderly organized throughout lamina propria and around the crypts (Fig. 1a). At the distance 10 cm (Fig. 1b,c) and 20 cm (Fig. 1d) away from the cancer, proper arrangement of collagen fibers appeared partly disturbed. It was possible to observe regions with parallel collagen fibers (Fig. 1b), thick collagen fibers (Fig. 1c), regions with edema of lamina propria where collagen fibers were separated with large pores (Fig. 1d) and regions with fibers organized as in healthy subjects.

By analyzing whole SHG images using CT-FIRE software (Fig. 2a,b; 23–25), we have shown that there was a statistically significant increase in the width of collagen fibers in the lamina propria of the colon mucosa at a distance 10 cm (p = 0.032) and 20 cm from the tumor (p = 0.021), compared with healthy subjects (Fig. 2e). Collagen fibers in the lamina propria 10 cm and 20 cm away from the cancer were significantly more straight (p = 0.004 and p < 0.0001, Fig. 2f) compared with collagen fibers in lamina propria of healthy colon. Using CurveAlign software (Fig. 2c,d)[23–25], based on curvelet transform, it was shown that collagen fibers in colon lamina propria 10 cm and 20 cm away from the cancer were significantly more aligned compared with collagen fibers in healthy lamina propria (p = 0.022 and p = 0.041; Fig. 2g).

Because of the heterogeneity in morphology and organization of collagen fibers in the lamina propria of colon mucosa and according to the studies which showed that the remodelling of collagen fibers within the tumor primarily could be observed in the immediate vicinity of epithelial cells[25,26], we also performed computational analyses of collagen fibers within 3 regions of interest per each SHG image (Fig. 3a–d). The regions of interest included lamina propria of colon mucosa in the immediate vicinity of Liberkün's crypts. The observed differences in morphology and organization of collagen fibers, detected by analyzing whole images, were even more pronounced when analysis were conducted inside the regions of interest: At a distance of 10 cm and 20 cm from the tumor, there was a statistically significant increase in width and straightness of collagen fibers compared to lamina propria of colon mucosa of healthy subjects (p < 0.0001, Fig. 3e,f). Also, collagen fibers in colon lamina propria both 10 cm and 20 cm away from the cancer were significantly more aligned compared with collagen fibers in healthy lamina propria (p < 0.0001 and p = 0.035, Fig. 3g).

We also quantified alignment of collagen fibers using another approach. With FiberFit software, based on FFT, we obtained the dispersion parameter k[27]. The dispersion parameter k was significantly increased 10 cm and 20 cm away from cancer (indicated more aligned collagen fibers), compared with healthy lamina propria (p = 0.031 and p = 0.0013; Table 1).

Changes in SHG polarization anisotropy in the uninvolved colon lamina propria.
In the lamina propria of colon mucosa at distance 10 cm and 20 cm away from cancer, anisotropy coefficient β[28,29] was significantly higher (indicating more orderly organized collagen molecules inside fibrils), compared with lamina propria of healthy patients (p < 0.0001; Table 1).

Electron microscopy analysis of collagen fibers in the uninvolved colon lamina propria.
On SEM collagen fibers in healthy patients were thin, curvy, and the network they were forming was relatively dense, with small pores between bundles (Fig. 4a). At the distance 10 cm and 20 cm away from the tumor the thick collagen fibers were more frequently observed (4b). Also, regions with more aligned collagen fibers were alternating with regular, network-like distribution of collagen fibers (Fig. 4c).

Changes in synthesis, cross-linking and degradation of collagen fibers in the uninvolved colon lamina propria.
Next, we wanted to find out if the changes in morphology and organization of collagen fibers are due to changes in synthesis, cross-linking or degradation of collagen. The main cells involved in collagen synthesis are fibroblast and myofibroblast. We detected myofibroblasts in colon lamina propria, immunohistochemically, using αSMA-antibody. In the lamina propria of healthy patients, myofibroblasts formed continuous layer around crypts, with few αSMA-positive cells throughout lamina propria (elongated, spindle-shaped, most probably also myofibroblasts) and around blood vessels (smooth muscle cells) (Fig. 5a). At the distance 10 cm and 20 cm away from the cancer, pericryptal myofibroblast were readily identifiable, forming thicker-appearing layer. More αSMA positive cells were visible throughout lamina propria (Fig. 5a). Quantitative analysis, using Color Picker Threshold plugin, showed significantly higher representation of αSMA-positive cells 10 cm away from cancer,
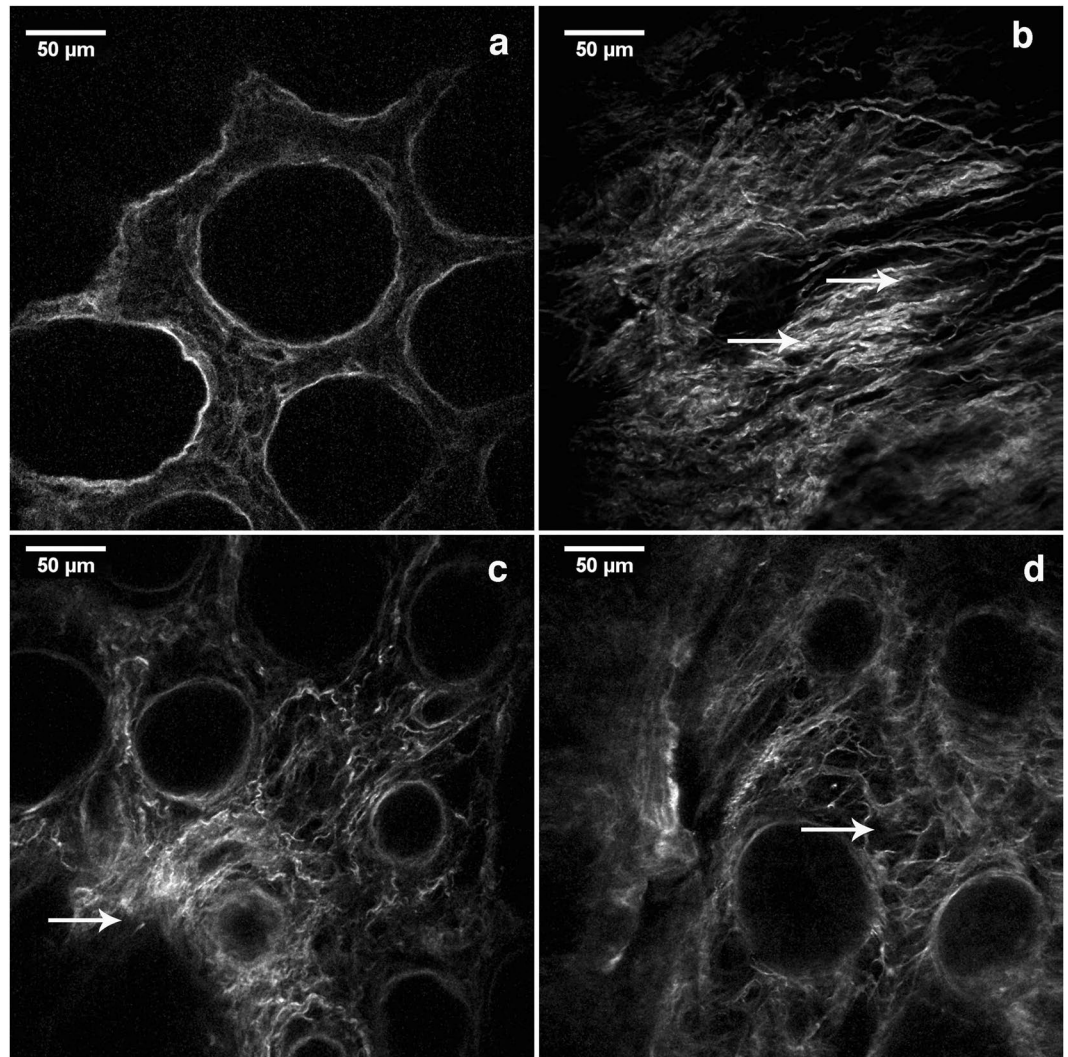
Figure 1. SHG images showing patterns of collagen fibers organization in the lamina propria of colon mucosa in the healthy patients and 10 cm and 20 cm away from the malignant tumor. Collagen fibers were wavy, orderly organized throughout lamina propria and around the crypts in the mucosa of healthy patients (**a**); In the lamina propria at the distance 10 cm (**b,c**) and 20 cm away from the cancer (**d**), proper arrangement of collagen fibers was partly lost: regions with parallel collagen fibers (**b**, arrows), thick and dense collagen fibers (**c**, arrow), regions with edema of lamina propria where collagen fibers were separated with large pores (**d**, arrow showing pore) were frequently observed.

compared with healthy lamina propria and lamina propria at the distance 20 cm away from the cancer ($p = 0.018$ and $p = 0.037$) (Fig. 5b).

Lysyl Oxidase (LOX) catalyzes crosslinking of collagen molecules during collagen fibrils assembly. We detected LOX expression in epithelial cells (both surface epithelium and epithelium of Lieberkühn glands) and in lamina propria of colon mucosa (Fig. 6a). In the colon epithelial cells, LOX mainly showed perinuclear expression pattern. LOX expression was significantly higher in epithelial cells of colon mucosa 10 cm and 20 cm away from the cancer, compared with healthy mucosa ($p < 0.0001$; Fig. 6b). In colon lamina propria, LOX was predominantly expressed by fibroblasts and myofibroblasts and subepithelial macrophages (Fig. 6a). LOX expression was significantly higher in lamina propria of colon mucosa 10 cm and 20 cm away from the cancer, compared with healthy controls ($p < 0.0001$ and $p = 0.013$; Fig. 6b).

Matrix metalloproteinases play an important role in degradation of ECM including collagen fibers. Their expression is changed in colon cancer[15]. We wanted to find out if MMPs were involved in remodelling of collagen fibers this far from the colon cancer. MMP2 in the colon epithelial cells showed supranuclear expression. Some intraepithelial lymphocytes were also MMP2-positive (Fig. 6a). MMP2 expression was significantly higher in epithelial cells of colon mucosa 10 cm and 20 cm away from the cancer, compared with healthy mucosa ($p = 0.037$ and $p = 0.034$; Fig. 6c). MMP2 was expressed by mononuclear cells in colon lamina propria (Fig. 6a). MMP2 expression was significantly higher in lamina propria of colon mucosa 10 cm away from the cancer, compared with healthy controls ($p < 0.0001$; Fig. 6c).
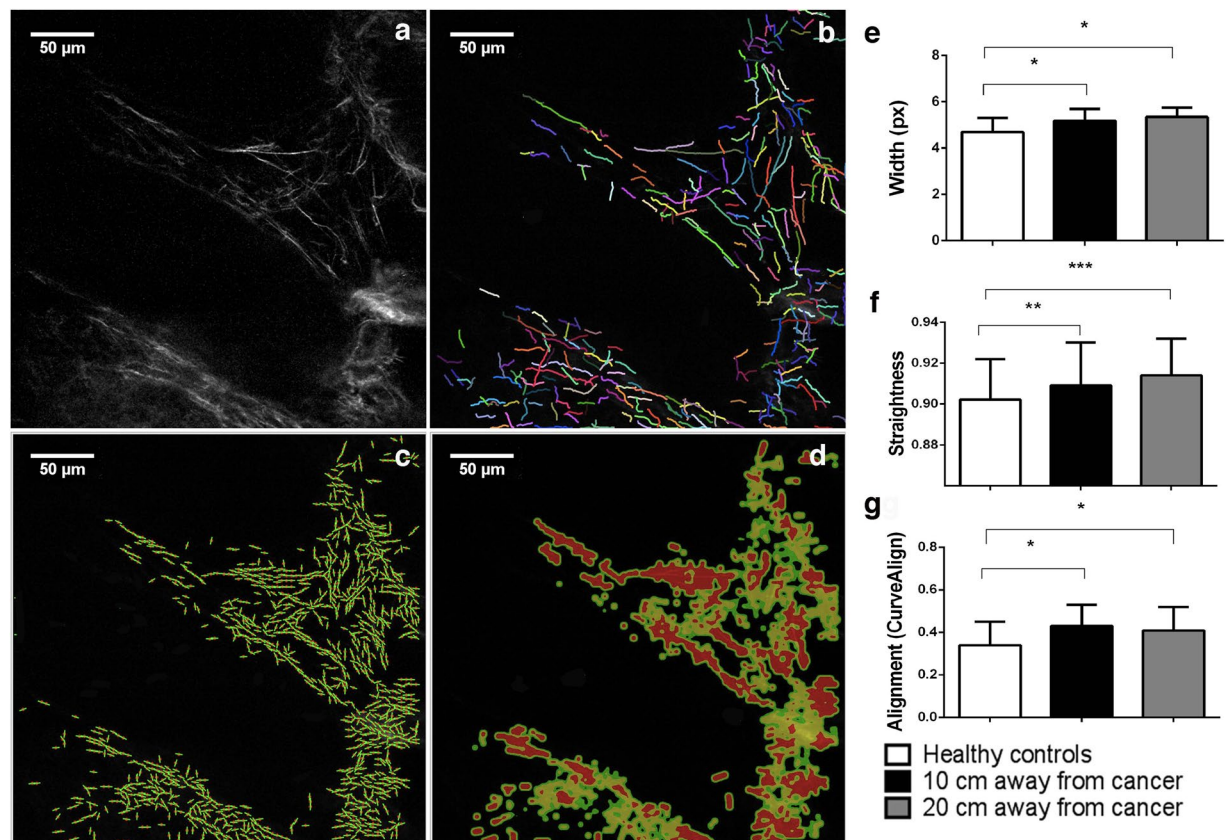
Figure 2. CT FIRE and CURVE Align in analyzing whole SHG images of collagen fiber in the lamina propria of colon mucosa in the healthy patients and 10 cm and 20 cm away from the malignant tumor. Original SHG image of lamina propria of healthy patient. (**a**) Graphical output from CT FIRE showing automatic extraction of collagen fibers, same patient. (**b**) Graphical outputs from CURVE Align for calculating alignment of collagen fibers. (**c,d**) Graphs are showing increased width (**e**), straightness (**f**) and alignment (**g**) of collagen fibers in the lamina propria 10 cm and 20 cm away from the cancer, calculated using CT FIRE and CURVE Align. *p < 0.05, **p < 0.001, ***p < 0.0001 (n = 32 healthy patients/96 images and n = 35 cancer patients/105 images; Values are express as mean ± sd; ANOVA).

MMP9 was barely detectable both in healthy colon mucosa and 10 cm and 20 cm away from the cancer: only few scattered cells through lamina propria, most likely macrophages, were MMP9 positive (Supplementary Fig S1).

Discussion

Our work demonstrated the changes in morphology and organization of collagen fibers in the colon mucosa 10 cm and 20 cm away from the cancer and provided a brief insight into the possible causes of the collagen remodelling.

Intriguingly, these changes were already described in the cancer microenvironment but larger in magnitude[15,23,25,30,31].

Change in deposition, alignment and cross-linking of collagen fibers, influence cell polarity and cell-cell interactions, increases growth factor signaling and stimulate migration of cancer cells[2,32]. Cells are able to sense and response to changes of both biochemical and biomechanical properties of the local microenvironment. Some of the main parameters determining biomechanical properties of collagen network are thickness of the fibers, alignment, stiffness and porosity. Increasement of collagen fibers thickness was shown to correlate with formation of invadopodia, change in cancer cells shape and increase migratory capacity[2,33]. Increased alignment of collagen fibers has significant impact on gene expression, differentiation, proliferation and especially migration of cancer cell, with align collagen fibers acting as "highways" for cancer cell migration[2]. Stiffness is strongly related to LOX-induced cross-linking of collagen fibers, which as a consequence favors cell adhesion and MMPs secretion[2,34,35].

More recently, the importance of tissue away from the cancer is being recognized, and the number of papers investigating changes in the uninvolved tissue, on genetic, epigenetic, biochemical and structural level, is increasing[36–38]. The most studied was the uninvolved mucosa immediately around the colon cancer, commonly up to 2 cm away from the cancer, so called transitional mucosa[39]. Recent studies showed that there are localized densification and increased alignment of collagen fibers in the transitional mucosa immediately around the cancer[40]. Rare groups of authors also analyzed healthy looking mucosa further from the cancer: Roy and
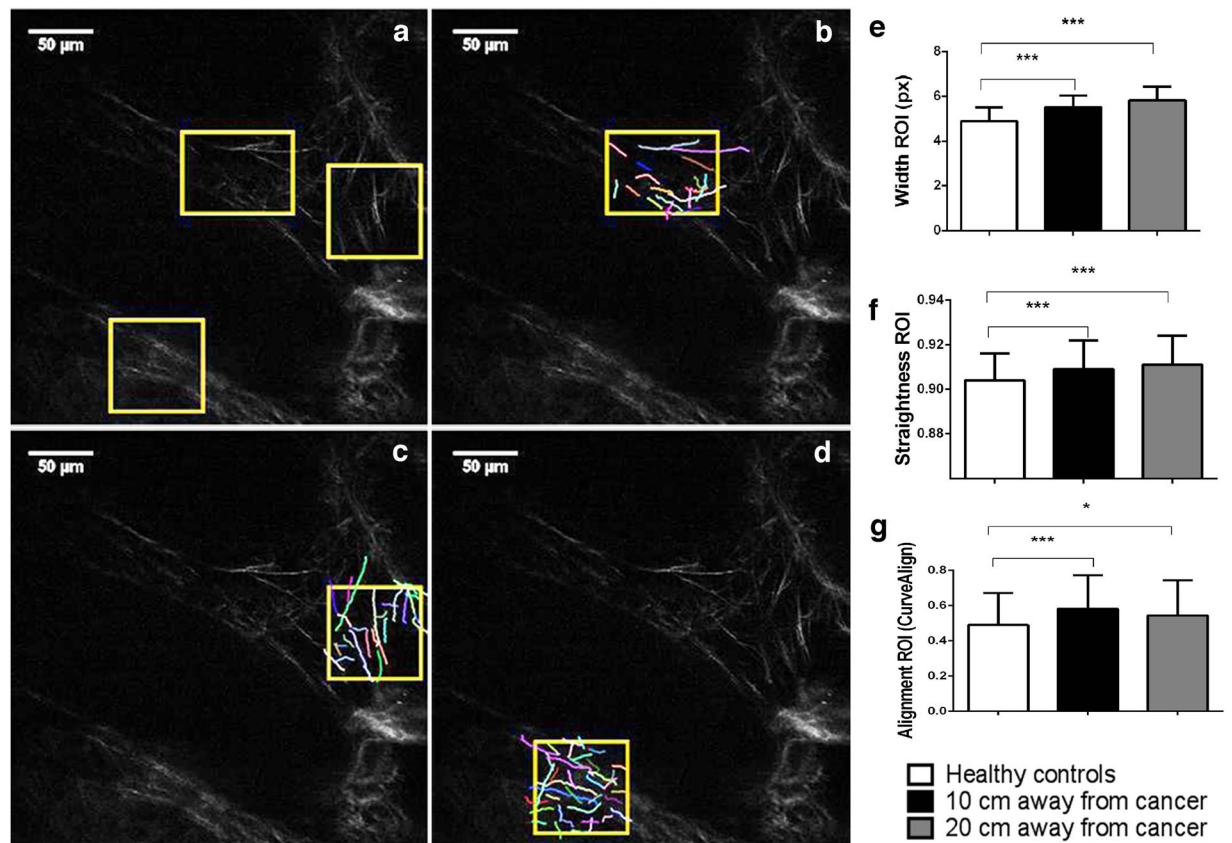
Figure 3. CT FIRE and CURVE Align in analyzing regions of interest (ROIs) on SHG images of collagen fiber in the lamina propria of colon mucosa in the healthy patients and 10 cm and 20 cm away from the malignant tumor. Original SHG image of lamina propria of healthy patient, with labeled rectangular ROIs which include collagen fibers near the Liberkün's crypts (**a**) and example of CT FIRE collagen fiber extraction within ROIs (**b–d**). Graphs are showing increased width (**e**), straightness (**f**) and alignment (**g**) of collagen fibers in the lamina propria 10 cm and 20 cm away from the cancer, calculated using CT FIRE and CURVE Align. *$p < 0.05$, **$p < 0.001$, ***$p < 0.0001$ (n = 32 healthy patients and n = 35 cancer patients; Values are express as mean ± sd, ANOVA).

	Healthy controls (n = 32)	10 cm away from cancer (n = 35)	20 cm away from cancer (n = 35)
k dispersion parameter	0.51 ± 0.22	0.91 ± 0.53*	1.11 ± 0.67**
β coefficient	0.26 ± 0.03	0.31 ± 0.04***	0.32 ± 0.05***

Table 1. Dispersion parameter k and anisotropy coefficient β in the lamina propria of colon mucosa in healthy patients and 10 cm and 20 cm away from the cancer. *$p < 0.05$, **$p < 0.01$, ***$p < 0.001$.

colleagues have described changes in the rectal mucosa of patients bearing advanced adenomas elsewhere in the colon: metabolic reprograming, including evidence of Warburg effect, early increase in microvascular blood supply and also, increased cross-linking and local alignment of collagen fibers[36,38]. They have also shown that increased cross-linking of collagen in the uninvolved colon mucosa fibers was due to increased expression of LOX enzyme[36]. Using microarray, qRT-PCR and immunohistochemistry Trujillo *et al.* have demonstrated changed gene expression signature in the tissue 1 cm and 5 cm away from the breast cancer: differentially expressed genes were involved in extracellular matrix remodelling, including genes for MMPs, wound healing, fibrosis and epithelial to mesenchymal transition[41]. Sanz-Pamplona et. al. revealed number of genes that were preferentially activated in adjacent mucosa from colorectal cancer, compared with mucosa of healthy patients: among other, these were genes involved in TGF-beta signaling pathway which is associated with fibrosis, genes for MMPs, cell adhesion molecules, cell-ECM integrin signaling pathways and BMP2 signaling pathways[37].

So, our results are consistent with and complement the works cited: Genes involved in ECM remodelling are differentially express in the mucosa around the cancer[41], and, by analyzing morphology, organization and cellular composition in the colon mucosa far from the cancer, we showed the consequences of these altered gene expression.
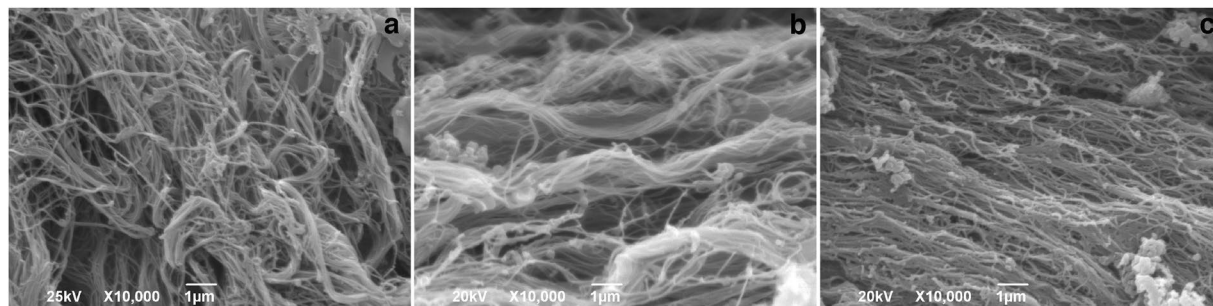
Figure 4. Representative SEM images of collagen fibers in the lamina propria of colon mucosa in the healthy patients (**a**) and 10 cm (**c**) and 20 (**b**) cm away from the malignant tumor. In the lamina propria of healthy patients (**a**) thin collagen fibers were forming relatively dense network. At the distance 10 cm and 20 cm away from the tumor, regions with thick (**b**, 20 cm away from tumor) and aligned collagen fibers (**c**, 10 cm away from tumor) were more frequently observed. Magnification x10 000.
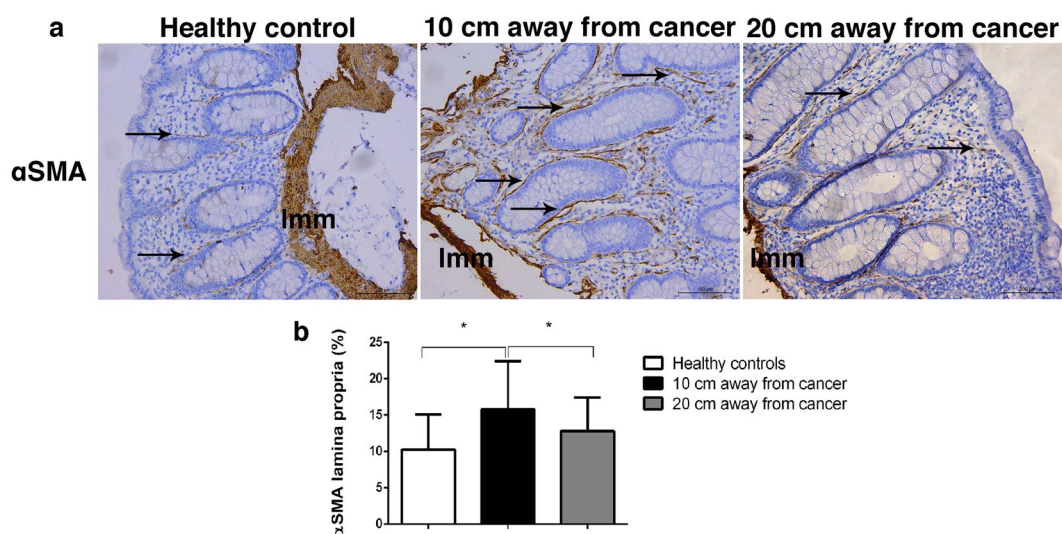
Figure 5. Representative images of αSMA-positive cells in the lamina propria of colon mucosa in healthy patients and at the distance 10 cm and 20 cm away from the tumor. Arrows are showing αSMA-positive myofibroblasts (**a**); Graph is showing increased representation (in %) of αSMA-positive cells in the lamina propria 10 cm and 20 cm away from the cancer, compared with healthy patients. *p < 0.05, **p < 0.001, ***p < 0.0001 (n = 27 healthy patients and n = 30 cancer patients; Values are express as mean ± sd; ANOVA).

We have analyzed uninvolved colon mucosa quite far from the colon cancer, 10 cm and 20 cm away, respectively. Most authors still consider tissue located more than 5 cm away from the colon cancer completely healthy and use it as a control in their research[42]. We had at least two reasons to believe that, although distant, this tissue could also bear changes: the systemic effects of tumors and, so-called, field carcinogenesis effect[36,43,44].

More recently, very interesting concept has emerged, according to which tumor initiation and progression are shaped by body's systemic response to tumor, which implied involvement of distant, uninvolved tissues and organs. Tumor produce a vast number of cytokines (for example, VEGF-A, TGF-β, TNF-α) and extrude different microvesicles, which act in a systemic fashion, modulating the behavior of host cells in distant tissues, most notably bone marrow, spleen and pre-metastatic niches. So, by secreting cytokines, tumor induce changes in distant tissues, which lead to the formation of local microenvironment that makes that particular tissue more permissive for seeding and survival of metastatic cancer cells[43]. Remodelling of extracellular matrix play particularly important role in creating microenvironment permissive for metastatic cancer cells: activation of fibroblasts/myofibroblasts, reorganization of collagen fibers, and change in expression of ECM-remodelling enzymes such as MMP2, MMP9 and LOX[43,45].

On the other hand, according to the field carcinogenesis concept, environmental carcinogens and genetic risk factors act on the entire organ (in our case, entire colon mucosa) leading to the emergence of an altered field, so called "field of injury". On this altered field, additional stochastic genetic and epigenetic events within the enabling microenvironment could give rise to focal cancers[36,44]. ECM, especially collagen and myofibroblasts, is recognized to play an important role in the field carcinogenesis concept by participating in the formation of enabling microenvironment. It is believed that altered epithelial cells induce change in the surrounding microenvironment
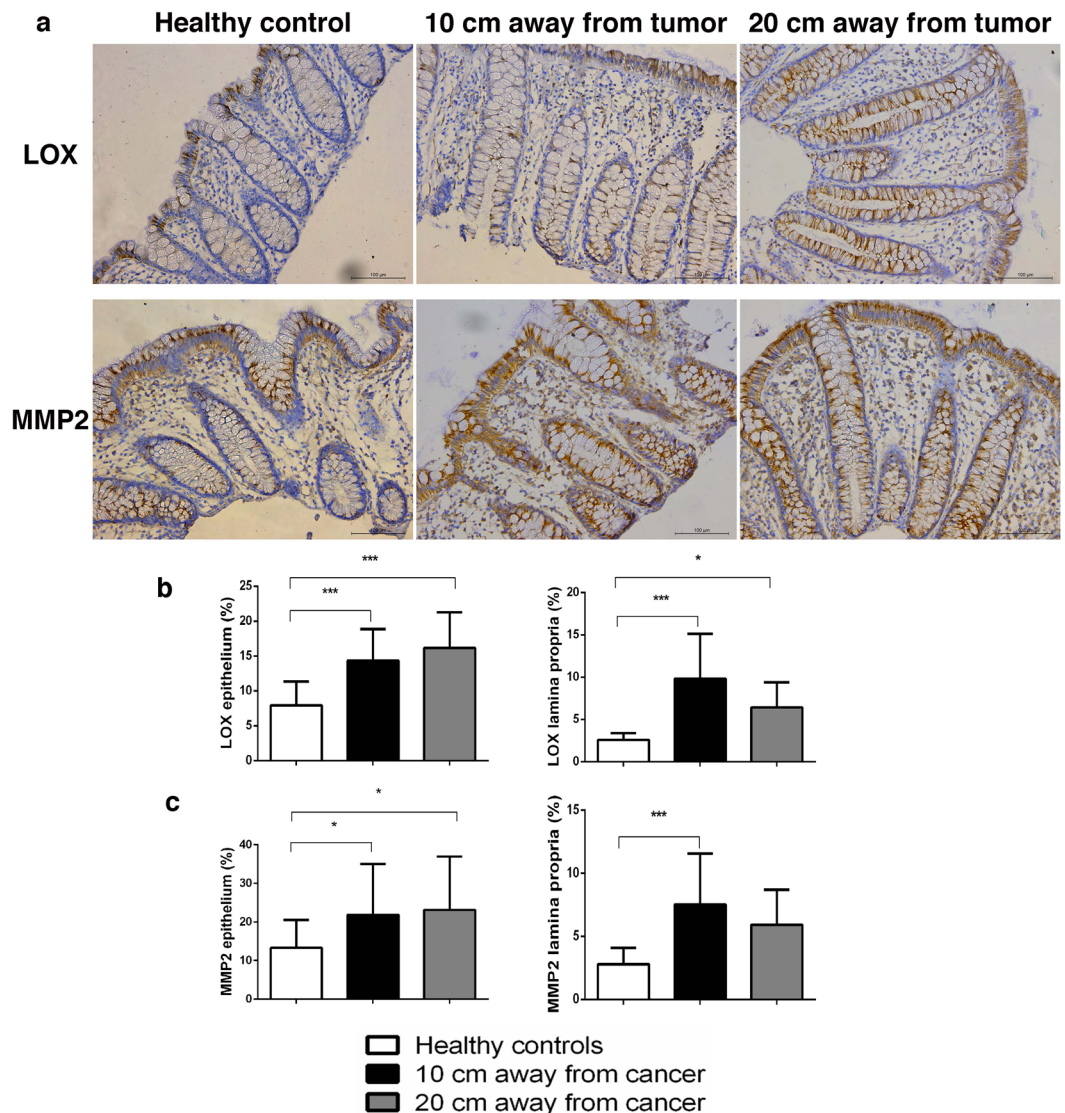
Figure 6. Representative images of LOX and MMP2 staining in the epithelium and lamina propria of colon mucosa in healthy patients and at the distance 10 cm and 20 cm away from the tumor (**a**); Graphs are showing increased representation (in%) of LOX (**b**) and MMP2-positive cells (**c**) in the lamina propria 10 cm and 20 cm away from the cancer, compared with healthy patients; *p < 0.05, **p < 0.001, ***p < 0.0001 (n = 27/28 healthy patients and n = 30 cancer patients; Values are express as mean ± sd; ANOVA).

that, in turn, promote or modify expansion of altered cells, or, there are even evidence indicating that ECM changes could play a primary role in both cancer initiation and progression[46].

Whether the changes in morphology and organization of collagen fibers 10 cm and 20 cm away from the cancer, represent a consequence of a growing tumor or a field effect, or a combination, we have no answer. Further analyses of mucosa more distant from the cancer are needed. Subsequently, detailed analyses of changes in the epithelium (genetic, epigenetic, biochemical and morphological) this far from the cancer and analysis of epithelial-stromal interactions on molecular level would be the next step in more thorough understanding of complex ways in which cancer interact with surroundings, distant parts of the same organ and systemically, with distant tissues and organs. Also, it would be important to conduct described analyses on the larger number of patient- to explore their potential in colon cancer screening or stratification of patients for colonoscopy.

Materials and methods

Tissue samples. Tissue samples were obtained during colonoscopy at the Department of gastrointestinal endoscopy, University Hospital Center "Dr Dragiša Mišovic-Dedinje", Belgrade, Serbia, from patients suspected to suffer from colon cancer based on clinical symptoms. When the experienced gastroenterologist noticed a suspected change during colonoscopy, they took samples of unaffected colon mucosa 10 cm and 20 cm away in caudal direction. The samples of unaffected colon mucosa were obtained from 41 patients older than 50 years (24 males and 17 females; Table 2). Only tissue samples for which pathologist confirmed that the suspected change

			Gender	
Patients	Number	Age (years)	Male	Female
Cancer	41	74.3	24	17
Healthy	39	71.9	20	19

Table 2. Demographic characteristics of patients included in the study.

was colorectal adenocarcinoma, were included in the study. For all patients, it was newly discovered cancer, so they haven't been on any kind of treatment for the malignant disease before.

As a control, the samples of colon mucosa were collected in the same institution, from 39 patients (20 males and 19 females; Table 2) who were indicated colonoscopy because of rectal bleeding, anemia or weight loss, and were without any pathological finding or diagnosed only with uncomplicated hemorrhoids (Haemorrhoides non specificatae sine complicationibus). Patients with inflammatory bowel disease, infectious colitis or diverticular disease of colon were excluded from the study. Our study was approved by the Ethics Committee of University Hospital Center "Dr Dragiša-Mišović-Dedinje", Belgrade, Serbia (18/10/2017). All methods were carried out in the accordance with relevant guidelines and regulations.

Second harmonic generation imaging of colon tissue samples. The images of collagen fibers in the label-free human colon tissue samples were obtained using an original lab frame nonlinear laser-scanning microscope[47,48]. For second harmonic generation (SHG) imaging of collagen fibers following experimental setup for nonlinear laser scanning microscope (NLM) was used[22]: The tunable mode-locked Ti:sapphire laser (Coherent, Mira 900) has been source of the infrared femtosecond pulses. The laser light was directed onto the sample by a short-pass dichroic mirror (cut-off at 700 nm) through the Zeiss EC Plan-Neofluar 40×/1.3 NA Oil objective. The laser wavelength was 840 nm. The SHG was detected in back-reflection arm. The narrow bandpass filter at 420 nm (Thorlabs FB420-10, FWHM 10 nm) blocks the scattered laser light and auto-fluorescence, and passes second harmonic at 420 nm. The average laser power on the sample was 30 mW. According to the pulse duration (160 fs) and repetition rate (76 MHz), we estimate the peak laser power to be 2.5 kW.

Quantitative analysis of collagen fibers in colon lamina propria. To analyze morphology and organization of collagen fibers in colon lamina propria, on SHG images, we used two complementary morphology based and one morphology-independent approach. For morphological assessment of collagen fibers we used methods based on curvelet transform and Fourier transform. As a morphology-independent approach, we measured SHG polarization anisotropy.

Computational collagen fiber quantification. CT-FIRE, an open-source software package, was used for calculation of width and straightness of collagen fibers. CT-FIRE was developed to automatically extract and analyze individual collagen fibers from SHG images[23–25]. Widths of collagen fibers are expressed in pixels. Straightness is represented on a scale 0–1, where 1 corresponds to perfectly straight fibers. CURVE Align software was used to calculate alignment of collagen fibers. Alignment was represented on a scale from 0–1, where 1 indicates all fibers orientated at the same angle[23–25]. CT-FIRE and CURVE Align measurements were applied both on whole images (from 32 healthy patients and 35 cancer patients, 3 SHG images per patient) and on 3 regions of interest (300×300 px^2) per image, located in the close vicinity to Liberkün glands.

An additional software, FiberFit, which is based on fast Fourier transforms (FFT) was use to quantify orientation of collagen fibers in colon tissue samples (from 32 healthy patients and 35 cancer patients, 3 SHG images per patient). Using FiberFit, we obtained the dispersion parameter k, used to quantify collagen fiber alignment (low k values indicates disordered networks, large k values indicates aligned networks[27].

SHG polarization anisotropy. The SHG anisotropy could be used to quantify alignment of collagen molecules inside fibers. The anisotropy parameter β was calculated by:

$$\beta = \left(I_{\text{par}} - I_{\text{orth}}\right)/\left(I_{\text{par}} + 2 \cdot I_{\text{orth}}\right)$$

where I_{par} and I_{orth} represented SHG intensity detected when the analyzing polarizer is oriented parallel (I_{par}) and orthogonal (I_{ort}) to the laser polarization[28,29]. Values of β range from 0 to 1, where 0 represents completely random and 1 completely aligned collagen molecules inside fibers.

We analyzed 32 samples from healthy patients and 35 from cancer patients. From each tissue sample 3 randomly chosen regions on magnification x400 were measured.

SEM analysis of collagen fibers in colon lamina propria. The surface morphology of collagen fibers (for 7 healthy patients and 6 cancer patients) has been examined using a JEOL JSM-6390LV SEM (JEOL, Japan) at an accelerating voltage of 10 kV. After fixation in 3% glutaraldehyde in cacodulte buffer, dehydration in graded alcohols (50%, 70%, 96%, 100%, 100%) the colon tissue samples were immediately dried using Critical Point Dryer K850 (Quorum Technologies, Laughton, UK). Prior to visualization, the dry samples were sputtered with gold using a Bal-Tec SCD 005 Cool putter Coater.

Immunohistochemistry. Immunohistochemical analysis was performed on formalin-fixed, paraffin-embedded sections using following antibodies and dilution ratios: anti-alphaSMA (Dako, M0851 1:500), anti-MMP9

	Number of analyzed healthy patients	Number of analyzed cancer patients (tissue away from the cancer)	
		10 cm away	20 cm away
αSMA (Dako, M0851)	27	30	30
LOX (Abcam, ab174316)	27	30	30
MMP2 (Abcam, ab37150)	28	30	30
MMP9 (Abcam, ab38898)	12	15	13

Table 3. The number of patients analyzed and the list of antibodies used for immunohistochemical analysis of myofibroblast, MMPs and LOX in the healthy lamina propria, 10 cm and 20 cm away from the cancer.

(Abcam, ab38898, 1:500), anti-MMP2 (Abcam, ab37150, 1:500), anti-LOX (Abcam, ab174316, 1:500) (Table 3). After heat-induced antigen retrieval using citrate buffer (pH = 6) and subsequent washing in PBS, primary antibodies were incubated for 60 minutes. The sections were treated with commercial Ultra Vision/3,3'-diaminobenzidine (DAB) staining kit (Thermo Scientific Lab Vision TL-060-HD, Rockford, IL, USA). The reactions were developed using DAB substrate.

For quantification of immunohistchemically stained sections, Color Picker Threshold plugin within open community platform for bioimage informatics Icy was used, as previously described[22]. On images stained with anti-alphaSMA antibody, the representation of myofibroblast in colon lamina propria was determined as a relative percentage of the area occupied by myofibroblast divided by the area of the lamina propria selected with an imaging processor. For slides stained with anti-MMP2 and anti-LOX antibody, the percentage of MMP2/LOX-positive area was determined separately in lamina propria and epithelial region. The number of analyzed patients for each antibody is in the Table 3. For one patient, one slide was stained with each antibody and a random selection of 10 fields per slide on magnification x200 was analyzed.

Statistical analysis.
Data were presented as means and standard deviations. The statistical package SPSS for Windows 12.0 (SPSS inc., Chicago, IL, USA) was used to indicate significant differences (two-way ANOVA followed by Tukey's multiple comparison test). Statistical significance was determined by $p < 0.05$.

Data availability
The dataset generated during and/or analyzed during the current study are available from the corresponding author on reasonable request.

References
1. Vannucci, L. Stroma as an active player in the development of the tumor microenvironment. *Cancer Microenviron* **8**, 159–66 (2015).
2. Fang, M., Yuan, J., Peng, C. & Li, Y. Collagen as a double-edged sword in tumor progression. *Tumor Biol.* **35**, 2871–2882 (2014).
3. Gopal, S., Malthaupt, H., Pocock, R. & Couchman, J. R. Cell-extracellular matrix and cell-cell adhesion are linked by syndecan-4. *Matrix Biol.* **60–61**, 57–69 (2017).
4. Schrader, J. *et al.* Matrix stiffness modulates proliferation, chemotherapeutic response and dormancy in hepatocellular carcinoma cells. *Hepatol. Baltim. Md* **53**, 1192–205 (2011).
5. Rozario, T. & DeSimone, D. W. The extracellular matrix in development and morphogenesis: A dynamic view. *Dev. Biol.* **341**, 126–140 (2010).
6. Zaman, M. H. *et al.* Migration of tumor cells in 3D matrices is governed by matrix stiffness along with cell-matrix adhesion and proteolysis. *Proct. Natl. Acad. Sci* **103**, 10889–94 (2006).
7. Handorf, A. M., Zhou, Y., Halanski, M. A. & Li, W. J. Tissue stiffness dictates development, homeostasis, and disease progression. *Organogenesis.* **11**, 1–15 (2015).
8. Taufalele, P. V., VanderBurgh, J. A., Muñoz, A., Zanotelli, M. R. & Reinhart-King, C. A. Fiber alignment drives changes in architectural and mechanical features in collagen matrices. *Plos one.* **14**, 20216537 (2019).
9. Voutouri, C., Polydorou, C., Papageorgis, P., Gkretsi, V. & Stylianopoulos, T. Hyaluronan-derived swelling of solid tumors, the contribution of collagen and cancer cells, and implications for cancer therapy. *Neoplasia* **18**, 732–741 (2016).
10. Giussani, M., Triulzi, T., Sozzi, G. & Tagliabue, E. Tumor extracellular matrix remodelling: New perspectives as a circulating tool in the diagnosis and prognosis of solid tumors. *Cells.* **8**, 81 (2019).
11. Crotti, S. *et al.* Extracellular Matrix and colorectal cancer: How surrounding microenvironment affects cancer cell behavior? *J. Cell. Physiol.* **232**, 967–975 (2017).
12. Fischer, T., Wilharm, N., Hayn, A. & Mierke, C. T. Matrix and cellular mechanical properrties are driving factors for facilitating human cancer cell motility into 3D engineered matrices. *Converg. Sci. Phys. Oncol* **3**, 044004 (2107).
13. Massague, J. New concepts in tissue-specific metastases. *Clin. Adv. Hematol. Oncol.* **1**, 576–7 (2003).
14. Doglioni, G., Parik, S. & Fendt, S. M. Interactions in the (pre)metastatic niche support metastasis formation. *Front. Oncol* **9**, 219 (2019).
15. Siad, A. H., Raufman, J. P. & Xie, G. The role of matrix metalloproteinases in colorectal cancer. *Cancer (Basel).* **6**, 366–375 (2014).
16. Brown, G. T. & Murray, G. I. Current mechanistic insights into the roles of matrix metalloproteinases in tumor invasion and metastasis. *J. Pathol.* **237**, 273–281 (2015).
17. Wei, B. *et al.* Human colorectal cancer progression correlates with LOX-induced ECM stiffening. *Int. J. Biol. Sci.* **13**, 1450–1457 (2017).
18. Murdocca, M. *et al.* Targeting LOX-1 inhibits colorectal cancer metastasis in an animal model. *Front. Oncol.* **9**, https://doi.org/10.3389/fonc.2019.00927 (2019).
19. Paidi, S. K. *et al.* Label-free Raman spectroscopy detects stromal adaptations in pre-metastatic lungs primed by breas cancer. *Cancer Res.* **77**, 247–256 (2017).

20. Whatcott, C. J. *et al*. Desmoplasia in primary tumors and metastatic lesions of pancreatic cancer. *Clin. Cancer Res.* **21**, 3561–3568 (2015).
21. Zhou, Z. H. *et al*. Reorganized collagen in the tumor micorenvironment of gastric cancer and its association with prognossis. *J. Cancer* **8**, 1466–1476 (2017).
22. Despotović, S.Z. *et al*. Remodelling of extracellular matrix of the lamina propria in the uninvolved human rectal mucosa 10 cm and 20 cm away from the malignant tumor. *Tumour Biol.* **39**, https://doi.org/10.1177/1010428317711654 (2017).
23. Bredfeldt, J. S. *et al*. Computational segmentation of collagen fibers from second-harmonic generation images of breast cancer. *J. Biomed. Opt.* **19**, 016007 (2014).
24. Capella, H. *et al*. Methods for quantifying fibrilar collagen alignment in Methods In *molecular biology* (ed. Rittié, L) 1627, 429–449 (Springer Science, 2017).
25. Drifka, C. R. *et al*. Periductal stromal collagen topology of pancreatic ductal adenocarcinoma differs from that of normal and chronic pancreatitis. *Mod. Pathol.* **28**, 1470–1480 (2015).
26. Mo, A. *et al*. Distinct transcriptional changes and epithelial-stromal interactions are altered in early stage colon cancer development. *Mol. Cancer Res.* **14**, 795–804 (2016).
27. Morrill, E. E. *et al*. A validated software application to measure fiber organization in soft tissue. *Biomech. Model. Mechanobiol.* **15**, 1467–1478 (2016).
28. Chen, X., Nadiarynkh, O., Plotnikov, S. & Campagnola, P. J. Second harmonic generation microscopy for quantitative analysis of collagen fibrillar structure. *Nat. Protoc.* **7**, 654–669 (2012).
29. Nadiarnykh, O., Lacomb, R. B., Brewer, M. A. & Campagnola, P. J. Alterations of the extracellular matrix in the ovarian cancer studied by Second Harmonic Generation imaging microscopy. *BMC Cancer.* **10**, 94 (2010).
30. Bissell, M. J. & LaBarge, M. A. Context, tissue plasticity, and cancer: Are tumor stem cells also regulated by the microenvironment? *Cancer Cell.* **7**, 17–23 (2005).
31. Wei, B. *et al*. Human colorectal cancer progression correlates with LOX-induced ECM stiffening. *Int. J. Biol. Sci.* **13**, 1450–1457 (2017).
32. Paszek, M. J. *et al*. Tensional homeostasis and the malignant phenotype. *Cancer Cell.* **8**, 241–54 (2005).
33. Artym, V. V. *et al*. Dense fibrilar collagen is a potent inducer of invadopodia via specific signaling network. *J. Cell Biol.* **208**, 331–350 (2015).
34. Yu, H., Mouw, J. K. & Weaver, V. M. Forcing form and function: Biomechanical regulation of tumor evolution. *Trends Cell Biol.* **21**, 47–56 (2011).
35. Sheieh, A. C. Biomechanical forces shape the tumor microenvironment. *Ann Biomed. Eng.* **39**, 1379–89 (2011).
36. Backman, V. & Roy, H. K. Advances in biophotonics detection of field carcinogenesis for colon cancer risk stratification. *J. Cancer* **4**, 251–261 (2013).
37. Sanz-Pamplona, R. *et al*. Aberratnt gene expression in mucosa adjacent to tumor reveals a molecular crosstalk in colon cancer. *Mol. Cancer.* **13**, 1–19 (2014).
38. Dela Cruz, M. *et al*. Metabolic reprogramming of the premalignant colonic mucosa is an early event in carcinogenesis. *Oncotarget* **8**, 20543–20557 (2017).
39. Boland, C. R. & Kim, Y. S. Transitional mucosa of the colon and tumor growth factors. *Med. Hypotheses.* **22**, 237–243 (1987).
40. Ferruzzi, J. *et al*. Compressive remodelling alters fluid transport properties of collagen networks- implications for tumor growth. *Sci Rep.* **9**, 17151 (2019).
41. Trujillo, K. A. *et al*. Markers of fibrosis and epithelial to mesenchymal transition demonstrate field cancerization in histologically normal tissue adjacent to breast tumors. *Int. J. Cancer.* **129**, 1310–1321 (2011).
42. Genovese, L. *et al*. Cellular localisation, invasion, and turnover are differently influenced by healthy and tumor-derived extracellular matrix. *Tissue Eng. Part A.* **20**, 2005–18 (2014).
43. McAllister, S. S. & Weinberg, R. A. The tumour-induced systemic environment as a critical regulator of cancer progression and metastasis. *Nat.Cell Biol.* **16**, 717–727 (2014).
44. Curtius, K., Wright, N. A. & Graham, T. A. An evolutionary perspective on field cancerization. *Cancer.* **28**, 19–32 (2018).
45. Hiratsuka, S. *et al*. MMP9 induction by vascular endothelial growth factor receptor-1 is involved in lung-specific metastasis. *Cancer Cell* **2**, 289–300 (2002).
46. Dotto, P. G. Multifocal epithelial tumors and field cancerization: stroma as a primary determinant. *J. Clin. Invest.* **124**, 1446–1453 (2014).
47. Rabasović, M. D. *et al*. Nonlinear microscopy of chitin and chitinous structures: a case study of two cave-dwelling insects. *J. Biomed. Opt.* **20**, 016010 (2015).
48. Bukara, K. *et al*. Mapping of hemoglibin in erythrocyte ghosts using two photon excitation fluorescence microscopy. *J. Biomed. Opt.* **22**, 26003 (2017).

Acknowledgements

Author contributions

S.D., Đ.M., V.Ž., M.R., A.K., A.P. designed the work, S.D., Đ.M., A.P., M.R. A.K., G.N., V.Ž., V.P., Z.K., S.L. conducted the experiment; S.D., Đ.M., M.R., A.P., Z.K. analyzed and interpreted the data.

Competing interests

The authors declare no competing interests.

Additional information

Supplementary information is available for this paper at https://doi.org/10.1038/s41598-020-63368-y.

Correspondence and requests for materials should be addressed to S.Z.D.

Reprints and permissions information is available at www.nature.com/reprints.

Publisher's note Springer Nature remains neutral with regard to jurisdictional claims in published maps and institutional affiliations.

FULL ARTICLE

Polarization-resolved SHG imaging as a fast screening method for collagen alterations during aging: Comparison with light and electron microscopy

Irena Miler[1] | Mihailo D. Rabasovic[2] | Marija Aleksic[3] |
Aleksandar J. Krmpot[2] | Andjelika Kalezic[4] | Aleksandra Jankovic[4] |
Bato Korac[3,4] | Aleksandra Korac[3*]

[1]Institute for Application of Nuclear Energy-INEP, University of Belgrade, Belgrade-Zemun, Serbia

[2]Institute of Physics, University of Belgrade, Belgrade, Serbia

[3]Faculty of Biology, Center for Electron Microscopy, University of Belgrade, Belgrade, Serbia

[4]Institute for Biological Research "Sinisa Stankovic", National Institute of Republic of Serbia, University of Belgrade, Belgrade, Serbia

*Correspondence
Dr. Aleksandra Korac, Full Professor, University of Belgrade-Faculty of Biology, Chair for Cell & Tissue Biology, Center for Electron Microscopy, Studentski trg 16, 11000 Belgrade, Serbia.
Email: aleksandra.korac@bio.bg.ac.rs
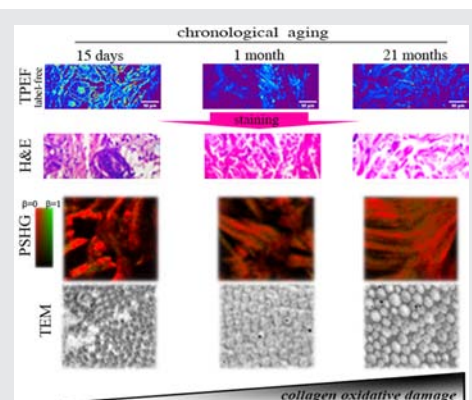
Funding information
Ministarstvo Prosvete, Nauke i Tehnološkog Razvoja

Abstract

Our previous study on rat skin showed that cumulative oxidative pressure induces profound structural and ultrastructural alterations in both rat skin epidermis and dermis during aging. Here, we aimed to investigate the biophotonic properties of collagen as a main dermal component in the function of chronological aging. We used second harmonic generation (SHG) and two-photon excited fluorescence (TPEF) on 5 μm thick skin paraffin sections from 15-day-, 1-month- and 21-month-old rats, respectively, to analyze collagen alterations, in comparison to conventional light and electron microscopy methods. Obtained results show that polarization-resolved SHG (PSHG) images can detect collagen fiber alterations in line with chronological aging and that this method is consistent with light and electron microscopy. Moreover, the β coefficient calculated from PSHG images points out that delicate alterations lead to a more ordered structure of collagen molecules due to oxidative damage. The results of this study also open the possibility of successfully applying this fast and label-free method to previously fixed samples.

KEYWORDS

chronological aging, collagen, electron microscopy, light microscopy, polarization-resolved SHG imaging, second-harmonic generation microscopy, two-photon excited fluorescence microscopy

1 | INTRODUCTION

Skin aging is a complex phenomenon that includes chronological and photoaging, which are both oxidative damage-related processes. Our previous study on rat skin showed that cumulative oxidative pressure during aging induces profound structural and ultrastructural alterations in rat skin epidermis and dermis.[1] Here, we focus

on underlying structural alterations of the dermis components during chronological aging.

The dermis has an essential role in determining the morphology and providing mechanical support of the skin. The main dermal component—collagen, is a chiral molecule that consists of three polypeptide α-chains organized in a highly crystalline triple-helix structure and is mainly produced by fibroblasts in the form of procollagen.[2] Detailed analysis of collagen morphology is critical for assessing structural modifications of the fibrillar matrix since they are often associated with various physiological and pathological processes, for example, wound healing,[3] cancer,[4] diabetes and aging.[5]

The commonly used methods for collagen visualization are conventional histological staining (hematoxylin-eosin staining), histochemistry (van Gieson staining, picrosirius red), immunohistochemistry and electron microscopy. These methods are often costly, time-consuming, and have the disadvantage of affecting the sample structure. Namely, chemical alterations to the native molecular structure can occur during the sample preparation procedures. The application of improved and advantageous methods based on nonlinear multiphoton microscopy is showing promising results in overcoming this problem.

Nonlinear laser scanning microscopy utilizing ultrashort laser pulses is an imaging technique with two modalities: two-photon excited fluorescence (TPEF) providing significantly reduced phototoxicity and photobleaching when compared with, for example, confocal or epifluorescent microscopy, whereas second harmonic generation (SHG) is absolutely photobleaching and phototoxicity free.[6–8] These characteristics come mostly because of the near-infrared light used in TPEF and SHG imaging and the interaction-free pathway of the laser beam through the sample, except in the tiny focal volume where the power is high enough. All of these aforementioned properties provide increased penetration depth for nonlinear imaging, which makes it superior for in vivo imaging nowadays.[9,10] Moreover, TPEF and SHG have been used in multimodal imaging studies simultaneously with the third harmonic generation (THG), as one more modality of label-free nonlinear imaging, revealing, even more, mutually complementary information of the specimen.[11–13]

Numerous studies showed that SHG microscopy is the best currently available choice for examining collagen fibers and their structural alterations in tissues. The molecular structure of collagen, a non-centro-symmetric structure, satisfies the criteria for generating the second harmonic signal.[3,14,15] Type I collagen produces the strongest SHG signal since it has the most ordered structure out of 28 types of collagens that have been identified so far in vertebrates.[3,16]

For all of these reasons, the number of studies using advantageous TPEF and SHG techniques, both ex vivo and in vivo, has increased significantly in recent years. However, these methods still have limited application due to the lack of protocol standardization, especially in terms of the number of examined samples and correlation of the results with conventional microscopy methods.

To resolve this, we used advantageous TPEF and SHG methods to analyze the biophotonic properties of rat dermis and collagen alterations during chronological aging, in comparison to the conventional light and electron microscopy methods. To avoid potential degradation during the sample preparation procedures, which is of particular concern with native tissues, and standardize the procedure concerning tissue thickness, we used 5 μm thick skin paraffin sections from 15-day-, 1-month- and 21-month-old rats, respectively.

2 | EXPERIMENTAL

2.1 | Sample preparation for light and transmission electron microscopy

Previously prepared paraffin and Araldite embedded skin samples from three animals per examined group were used for light and electron microscopy analyses.[1] Paraffin blocks were serially cut in 5 μm tick sections, mounted on glass slides, routinely deparaffinized, and used unstained for TPEF and SHG or conventional hematoxylin & eosin (H&E) staining. Namely, for correlative imaging, after TPEF and SHG examination sections along with their serial pairs were stained with H&E, dehydrated, and mounted for light microscopy (Leica DMLB microscope, Leica Microsystems). Thus, using two sets of serial pairs sections, both stained with H&E, we were able to compare and correlate overall tissue morphology and collagen structure and organization.

Araldite blocks of skin samples from the same region used for light microscopy were cut in 1 μm or 80 nm thick sections using a Leica UC6 ultramicrotome (Leica Microsystems, Wetzlar, Germany), mounted on glass slides or copper grids, and stained with basic fuchsine and methylene blue (BF&MB), or contrasted using Leica EM STAIN (Leica Microsystems), respectively. Sections were examined on an optical light microscope or a Philips CM12 transmission electron microscope (Philips/FEI, Eindhoven, Netherlands) equipped with a digital camera (SIS MegaView III, Olympus Soft Imaging Solutions, Münster, Germany). The diameter of collagen fibers was measured in triplicate; 70/230/218 per 15-day/1-month/21-month group were randomly selected. All measurements and analyses were performed using iTEM software (Olympus Soft Imaging Solutions).

2.2 | Experimental setup for TPEF and SHG microscopy

A homemade experimental setup for TPEF and SHG imaging was described in detail by Rabasović et al.[17] The brief description is as follows: The beam from mode-locked Ti:Sa laser (MIRA 900, Coherent Inc) was tuned to 730 nm for TPEF and 840 nm for SHG imaging. Neutral density filters attenuate the laser beam making it linearly polarized, which enables PSHG measurement only. Further, the laser beam is scanned by two galvo-scanning mirrors (Cambridge technology), passed through the beam expander, and reflected by the short pass dichroic mirror (700 nm cut off) toward the objective lens Zeiss EC Plan-Neofluar 40x NA = 1.3. The signal, either the TPEF or SHG, is collected by the same objective lens in back reflection. It passes through the dichroic mirror and is filtered out by broadband transmission filter (400-700 nm) for TPEF or narrow band (420 nm center, 10 nm bandwidth) for SHG imaging and detected by a photo-multiplier tube (PMT). All images throughout the study were taken using pulse energies in the range 40 to 60 pJ for TPEF and 80 to 100 pJ for SHG in the object plane. Corresponding power densities in the focus are estimated to 4 to 6 MW/cm^2 and 8 to 10 MW/cm^2, respectively, assuming diffraction-limited spot.

For PSHG measurements, an additional polarizer, that is, an analyzer in the rotation stage, was inserted into the detection arm. The laser beam's polarization state at the focal plane of the objective lens was determined by means of polarization optics. The ellipticity of the polarization was negligible. The slight rotation (cca. 4 °) was measured, and the analyzer in the transmission arm was set accordingly.

2.3 | Image acquisition and analysis

The first hyperpolarizability or β coefficient was calculated from PSHG images[11] defined as:

$$\beta = \frac{I_{\parallel} - I_{\perp}}{I_{\parallel} + 2I_{\perp}}$$

where $I_{\parallel}$ and $I_{\perp}$ represent SHG intensity in a pixel of an image detected through the analyzer oriented parallel and perpendicularly to the incident laser polarization, respectively. The incident laser polarization was kept constant throughout the measurements, and it was parallel to the horizontal axis of all images. The values for the β coefficient were calculated according to the given formula in each pixel from the values $I_{\parallel}$ and $I_{\perp}$ in the given pixel from the corresponding images. The

map of β values was displayed according to the following scheme:
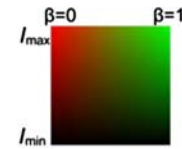
Here, β is the color-coded, and I is the SHG signal intensity in a given pixel according to an average value of two images taken through the analyzer oriented parallel and perpendicularly to the incident laser polarization. The results are corresponding to β values map.

According to Chen et al.,[18] the borderline case when $\beta = 1$ corresponds to the complete alignment of fibrilar collagen. In this case, the SHG intensities are the maximal in the image taken through the analyzer oriented parallel to the incident laser polarization, while SHG intensities are 0 for the image when the analyzer is perpendicular.

β coefficient was calculated at standard PC using our own script for Math Lab. The calculation time for 1024 × 1024 image is 5 to 10 seconds on average. The program was not optimized; thus, the calculating time could be even faster.

There are numerous methods for detailed collagen fibers analysis based on PSHG developed for both biological[19,20] and nonbiological samples[21] where predominant axes are easy to predict or even to control. The measurement of the angular dependence of SHG signal, from which the details on SHG emitters (e.g., collagen fibers) alignment are extracted, is common for all aforementioned methods. The signal analysis requires a sophisticated approach and expert experience.

Hence, the simple procedure described by Chen et al.[18] and applied here is easy to implement yet sufficient to obtain necessary information on a large number of samples (e.g., screening). This makes the procedure user-friendly even for non-experts or easy to be automated.

2.4 | Immunohistochemistry

Semi-fine (2 μm thick) skin sections from Araldite blocks were used for 4-hydroxynonenal (4-HNE) and 3-nitrotyrosine (N-Tyr) detection with primary antibodies anti-4-HNE (1:400, ab48506, Abcam, Cambridge, UK), and anti-N-Tyr (1:100, MAB5404, Chemicon, Houston) for routine immunohistochemistry previously described in detail by Janković et al.[1] All sections were counter-stained with hematoxylin, dehydrated and mounted for light microscopy analysis.

2.5 | Statistical analysis

Statistical analysis using GraphPad Prism software (GraphPad Prism, Version 5.03) was performed by the analysis of variance (ANOVA) considering P values $\leq$ .05 as the level of significance.

3 | RESULTS AND DISCUSSION

3.1 | Comparison of light, TPEF and SHG microscopy

To compare the commonly used histological method, H&E staining, for conventional light microscopy with advanced TPEF and SHG methods, we analyzed the same region of interest (ROI) in parallel on serial 5 μm thick paraffin sections.

Light microscopy analysis (Figure 1, H&E) of the skin from 15-day-old rats revealed the process of extracellular matrix organization in the dermis, numerous fibroblasts with the intensive synthesis of procollagen, and the small number of collagen fibers found in their vicinity. Although less numerous, collagen bundles already showed specific packaging and a tendency to organize in bundles, suggesting that this pattern is predetermined. The dermis of 1-month-old rats showed a well-structured extracellular matrix with a compact and well-organized collagen bundle orientation. Among collagen bundles, numerous fibroblasts were still observed. At this stage of aging, our results showed consistency in synthesis, packing and orientation of collagen bundles in rat dermis. In
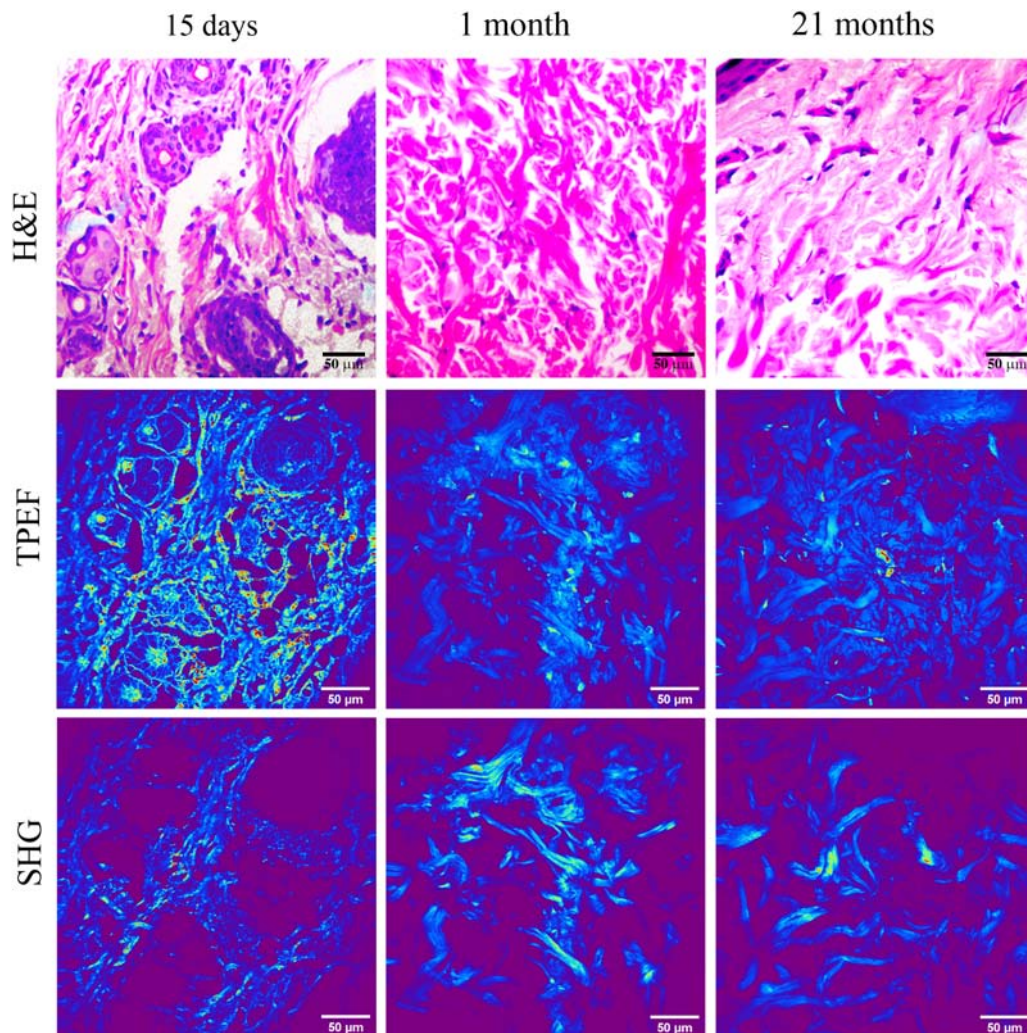
FIGURE 1 H&E staining in parallel with TPEF and SHG showing dermal collagen structure and organization in the skin of 15-day-, 1-month- and 21-month-old rats. Less numerous collagen bundles (15 days) become compact with well-organized orientation through skin maturation (1 month), suggesting a predetermined specific packaging pattern. In aged skin (21 months) vast quantity of tightly packed, large collagen bundles is present. TPEF and SHG-signal correspond to light microscopy without losing information about collagen fiber position, density and orientation. Five-micrometer thick sections; H&E staining; area analyzed with TPEF or SHG microscopy, Bars: 50 μm

aged skin (21-month-old), we found a vast quantity of tightly packed, large collagen bundles, while the number of fibroblasts was significantly reduced. Comparative analysis also showed that collagen from rat dermis in all examined groups produced strong TPEF and SHG signals corresponding to light microscopy without the loss of information about the position, density and orientation of collagen fibers.

Over the last years, among nonlinear imaging techniques, TPEF emerged as a powerful tool for skin imaging.[8,22] Like other tissue, the skin could be easily studied with multiphoton microscopy without the use of any fluorescent dyes or agents due to the presence of endogenous fluorophores. Autofluorescence properties of the skin originate either from cells (reduced pyridine and oxidized flavin nucleotides), or extracellular components (collagen and elastin).[23] Thanks to significant advantages—fast screening and label-free procedures, this technique has already been widely used for morphological characterization on ex vivo tissue samples.[24,25]

Another nonlinear imaging technique, SHG, has mainly been used to visualize unstained collagenous tissues.[15,26] Because of its non-centro-symmetrical structure, fibrillar collagen is the primary source of the SHG signals in the skin dermis.[3,18,27] Lately, besides skin (dermis), SHG has also been used for investigation of collagen fiber orientation and structural changes in scars and keloid,[3,28,29] tendon and ligaments,[30,31] cardiovascular system,[32,33] cornea[34] and tumor microenvironment.[35–37]

The combination of TPEF and SHG is also very useful for capturing both components of the dermis (collagen and elastin) and generating high-resolution three-dimensional images.[22] Second-harmonic to Autofluorescence Aging Index of Dermis (SAAID method), introduced by Lin et al.,[38] is a simple scoring method applied when TPEF and SHG are used simultaneously for the imaging of connective tissue. SAAID provides a measure of the relative abundance of collagen against elastic fibers within the skin dermis. In this particular case, we were not able to use this method since in rat skin, in contrast to human skin, collagen fibers are highly dominant over rare elastin fibers. Nonetheless, in general, the TPEF-SHG combination is a promising, reliable and powerful tool for studying skin physiology and pathology.

3.2 | β Coefficient calculation from PSHG images

To analyze structural alterations of collagen fibers and packing patterns caused by aging, which are unobservable by light microscopy, we calculated the β coefficient from PSHG images (Figure 2) obtained from

the same serial paraffin sections. Namely, the SHG images in Figure 1 are the raw SHG images that correspond to the same field of view as in β maps shown in Figure 2A. The two orthogonal components of the SHG signal recorded at the same field of view are used for the calculation of the β coefficient (Figure 2B).

We had three sections (one/animal) for each examined group (15-days-, 1-month and 21-month-old). Three different ROIs from each section were randomly selected for imaging. The β coefficient was calculated by the given formula for each pixel in the ROI. The average β coefficient was calculated for each ROI (the whole image in Figure 2A). Results were analyzed upon β coefficient calculation and arbitrarily categorized as either less, more, or highly ordered until ultrastructural examination.

The lowest β values were found in the skin of young, 15-day-old rats with an average value of 0.13. This is expected since young skin is in the phase of development characterized by intensive collagen synthesis. More ordered fibers were found in the skin of 1-month-old rats, going through maturation, with the average value of 0.20, while aged skin (21-month-old) showed the highest β coefficient, with the average value of 0.25, suggesting highly ordered organization of collagen fibers, great density and tight packing in collagen bundles. All of this data was consistent with TPEF, light and electron microscopy findings.

β Coefficient calculation from PSHG images has been frequently used in studies to establish differences between normal and malignant tissues.[39,40] In tumors, variations in diameter and cross-sectional profile of the collagen fibrils are evident. In some cases, this is a consequence of abnormal collagen fibril aggregation,[41] while in others, extracellular matrix remodeling occurs through the degradation of collagen fibers.[42] Moreover, this method enables the characterization and tracking of various experimental treatments in different tissues.[41] Thus, SHG and PSHG imaging of fibrillar collagen type I have been applied on various samples so far, but collagen samples of tendon and skin remain the most commonly analyzed.[3]

Ericson et al.[41] concluded that qualitative evaluation of angular dependence of the SHG signal varies in a manner related to the structural order of collagen fibrils and that data points generated from less ordered fibril structures could be useful in determining the distribution of the fiber segments orientation. They suggested that this finding could be valuable for the characterization of the fibril structure and possible structure alterations.

Bearing in mind that only ordered structures produce strong SHG signal and that immature fibrils can be distinguished from mature fibrils in the backward direction,[27] the β coefficient calculation seems to be the
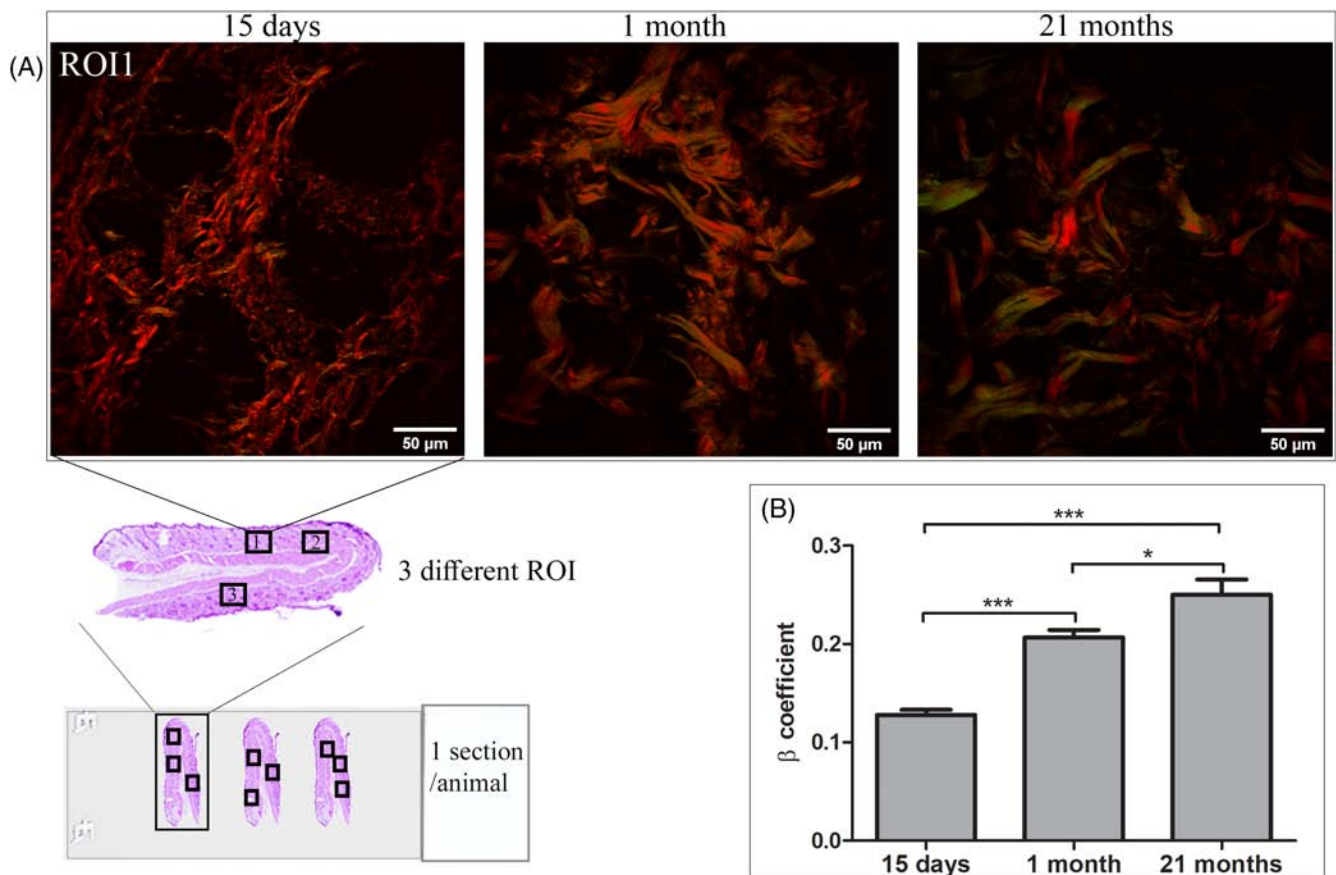
FIGURE 2 Representative ROI (A) for each tissue sample used for β coefficient calculation from PSHG images during chronological aging (15-days-, 1-month- and 21-months-old). B, Young skin (15 days) has the lowest β value (the average β value of 0.13) due to intensive collagen synthesis, while maturation and aging induced a significant increase in β value. Through maturation (1 month), skin shows more ordered collagen fiber structures with an average β value of 0.20. Aged skin (21 month) has the highest β coefficient with an average value of 0.25, suggesting highly ordered organization of collagen fibers, high density and tight packing in collagen bundles. The values represent the means of nine β values per group, 27 ROI in total (3 ROI randomly chosen from each of three different paraffin rat skin sections per slide $\pm$ SEM). $*P < .05$ and $***P < .001$. Bars: 50 µm

perfect tool for the study of extracellular matrix structure, as we did in our experiment.

Comparison of the β coefficient and collagen ultrastructure confirmed their correlation regarding tightness degree in the bundle as less, more, or highly ordered. The interaction of cells with the extracellular matrix is essential to cell positioning, growth and differentiation in order to form and maintain complex tissue structure and function. The mechanical properties (rigidity/stiffness) of the extracellular matrix could be evaluated through matrix density and organization. Since β values represent molecular order, the given type of anisotropy directly reflects dense packing and orientation of collagen in fibrils, for example, rigidity.

Although SHG is well known as a fixation- and label-free method, we performed it on fixed and paraffin-embedded, 5 µm tick samples to avoid differences, problems and doubts regarding the use of native, unfixed and unlabeled tissue samples. We prepared all samples in the same way, and the fixation procedure was strictly followed to preserve the tissue structure as near, to the natural state, as possible.

Our results provide significant proof that this method is convenient for use on previously fixed samples, opening the possibility for the re-examination of archived paraffin-embedded tissue samples. Thus, new insights into the dermal structure and comparison could lead to potentially entirely new findings regarding skin aging or conditions.

3.3 | Transmission electron microscopy (TEM) analysis

To confirm that the sample preparation procedure for light and electron microscopy does not affect overall tissue structure and ultrastructure, we compared the analyses of semi-fine sections stained with BF&MB with H&E and ultrastructure of the dermis (Figure 3).
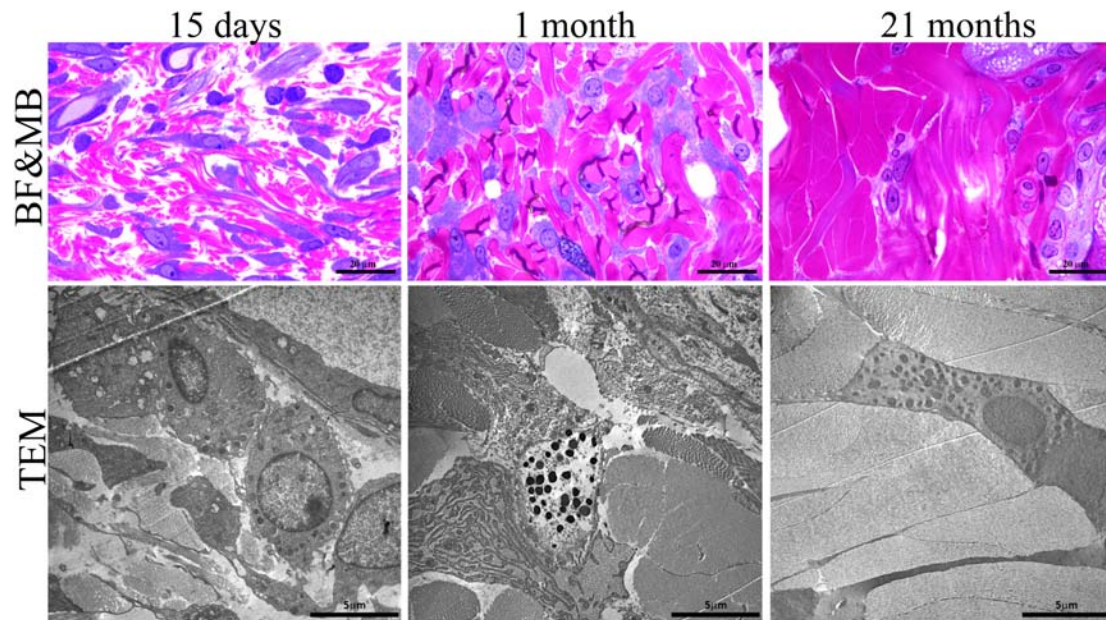
FIGURE 3 BF&MB staining shows the area analyzed with TEM. Semi-fine sections; Bars: BF&MB-20 μm, TEM-5 μm

Results confirmed the consistency in tissue and collagen structure, bundle density and quantity of ground substance, and were in line with our previous findings.[1] We further measured the diameter of collagen fibrils in randomly selected cross-sections and compared their distribution between all examined groups (Figure 4).

Obtained results showed a striking difference between young (15-day-old), maturating (1-month-old) and aged (21-month-old) rat skin. Namely, the majority of cross-sectioned collagen fibers in 15-day-old dermis had average diameters of 50 to 60 nm, along with a similar number of diameters ranging from 40 to 50 and 60 to 80 nm. This is in line with ongoing collagen synthesis in young skin[1] and ultrastructural findings of small quantities of loosely packed collagen fibers embedded in ground substances (Figure 3, TEM).

In contrast, maturating and aged dermis had an average value of cross-sectioned collagen fibers of 80 to 90 nm (1-month-old) and 90 to 100 nm (21-month-old). Besides the fact that the observed increase in the average collagen fiber diameter is a consequence of natural skin maturation, it is important to point out the absence of collagen with the diameter of 50 to 60 nm and the shift toward higher values (>120 nm). On the ultrastructural level, although collagen bundles in the aged dermis were large and tightly packed like in the mature skin, they presented as thicker, more turgid and electron-lucent, suggesting damage and swelling, all of which can lead to the tight packing of collagen molecules.

Knowing that collagen damage is a significant factor in age-related dermal alterations, at this level of observation,

we could not detect alterations on the molecular level. Thus, comparing these results with the β coefficient calculated from PSHG images, we observed consistency in the alignment of collagen fibers. Collagen microstructure and index of alignment were in line, however, was it a consequence of collagen degradation remained unclear. In a highly ordered collagen bundle, microfracture may induce an observed shift in diameter and rigidity, in contrast to the loose connective tissue. To clarify this, we used immunohistochemistry to analyze the expression of matrix metalloproteinases (MMP). We used two different antibodies but did not find the presence of either MMP2 or MMP9 in all examined samples (data not shown). These findings may not be surprising, bearing in mind strict and well-ordered synthesis and packing of collagen bundles in the rat dermis.

Since degradation is clearly not taking part in causing collagen alterations observed by TPEF and SHG/PSHG or differences in individual collagen fibers and collagen diameter observed by electron microscopy, we further analyzed the oxidative damage of collagen fibers on serial paraffin skin sections, in particular, per- and nitro-oxidative damage.

3.4 | Immunohistochemical detection of 4-hydroxynonenal (4-HNE) & 3-nitrotyrosine (N-Tyr)

A large body of evidence indicates that reactive oxygen species (ROS) accumulation and damage caused by ROS is one of the most important mechanisms involved in cellular aging.[1,43] However, such evidence for the extracellular
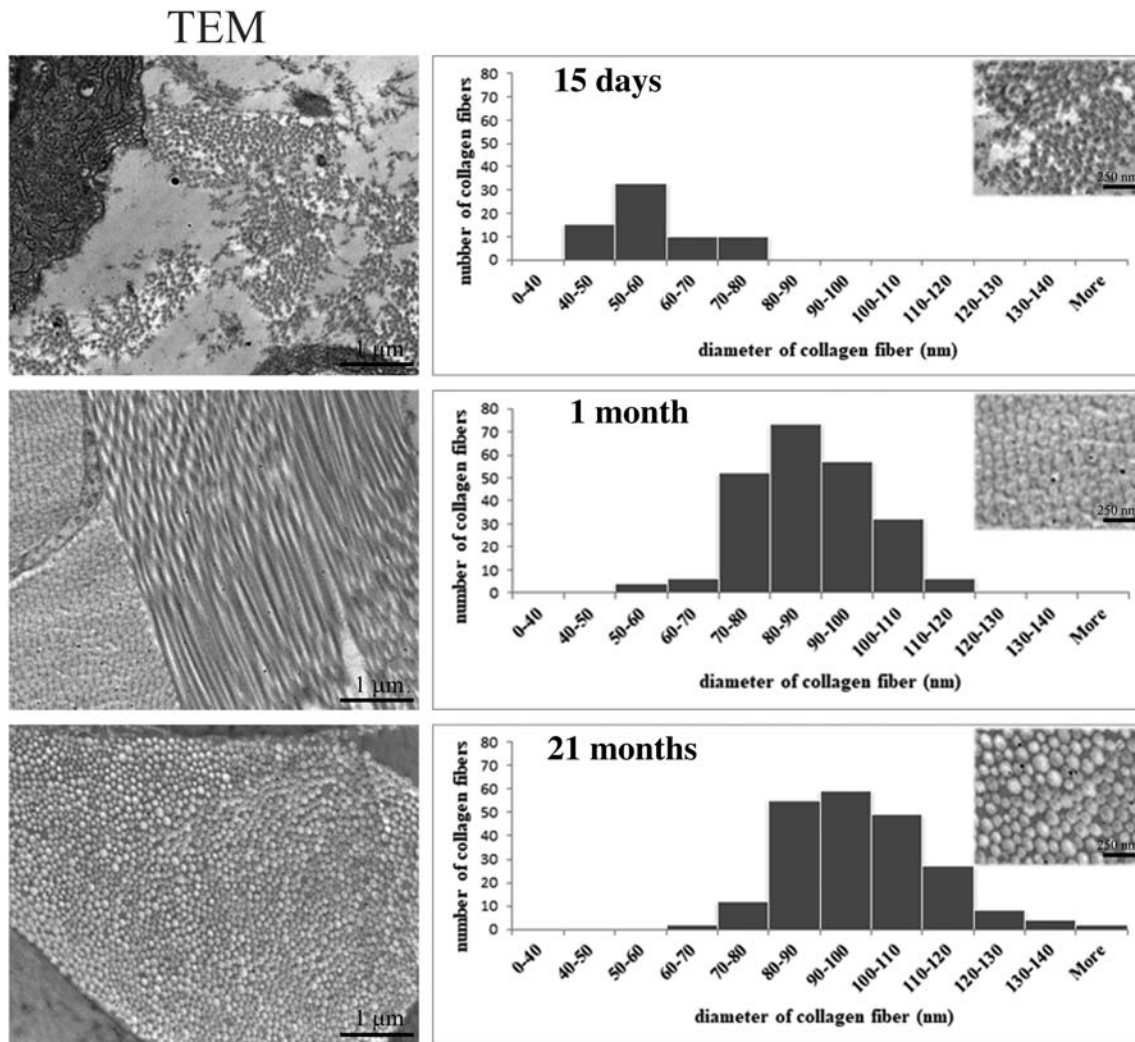
FIGURE 4 Structural alteration and collagen fiber diameter distribution in the dermis of 15-day-, 1-month- and 21-month-old rats. Aging induces a shift in collagen fiber diameter and tight packing of collagen molecules that leads to collagen organization in bundles and dermal rigidity. Bars: TEM-1 μm, insets-250 nm
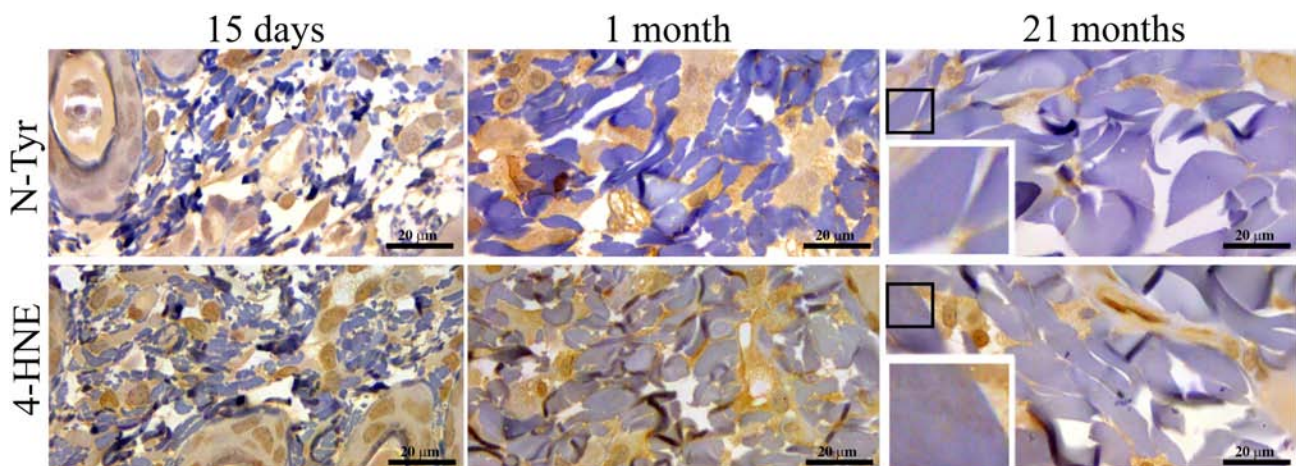

FIGURE 5 Immunohistochemical detection of 4-hydroxynonenal (4-HNE) & 3-nitrotyrosine (N-Tyr)—biomarkers of oxidative tissue damage. Insets represent the enlarged area (black square): Collagen (blue) showed immunopositivity for 4-HNE and N-Tyr only in the aged dermis (21-month-old rats). Bars: 20 μm

matrix is still sparse. It was recently shown that increased ROS might affect collagen density directly by damaging fibers and indirectly by interfering with collagen synthesis,[44] fibroblast proliferation and senescence.[45]

In general, biomarkers of oxidative stress have been considered as biomarkers of aging.[46] N-Tyr is a marker of oxidative damage caused by nitration of the free amino acid form of tyrosine or tyrosine residues in proteins, while 4-HNE is a reactive aldehyde, formed as a product of lipid peroxidation, which binds to macromolecules, proteins in particular. Thus, 4-HNE is also a propagator of lipid and protein oxidation (Figure 5).

Our results revealed the presence of 4-HNE and N-Tyr modifications on collagen fibers in 21-month-old rat dermis. Extracellular matrix molecules, such as collagens, are good targets for oxygen-free radicals. Collagen is susceptible to fragmentation by superoxide anion, as demonstrated by the liberation of small 4-hydroxyproline-containing-peptides,[47] but the absence of MMP2 and MMP9 in our study suggests that this damage leads to more significant aggregation rather than collagen degradation. Amino acids susceptible to oxidative damage[48] are highly present in collagen molecules, and as a result of amino acid residue oxidation, protein fragmentation, aggregation and proteolytic digestion can occur.

To the best of our knowledge, this is the first report of collagen positivity for 4-HNE and N-Tyr. This could be the underlying reason for the observed alterations in the biophotonic properties, rigidity (higher β coefficient) and ultrastructural damage of collagen during chronological aging that overwrites genetic and structural stability of collagen molecules in the rat skin.

4 | CONCLUSIONS

Our results clearly show that analysis of TPEF and SHG images of rat dermis is consistent with histological one; rat dermis is a good model not only due to collagen photonic features but bundles stability. The β coefficient calculated from PSHG is consistent with transmission electron microscopy analysis and should be used widely. Moreover, the β coefficient reflects fine collagen fiber alterations due to oxidative damage observable only by immunohistochemistry and on the ultrastructural level.

These advantageous methods work nicely on previously fixed samples and could be used along with or for further conventional analysis. In this way, degradation of samples would be avoided, and reproducibility and standardization of protocols would be fully achieved.

Hence, PSHG imaging is a fast and reliable screening method for studying collagen alteration during chronological aging linked to oxidative stress; it may be used in any

further analysis that concerns collagen structure alteration, for example, photoaging, drug delivery, cancer, and opens the opportunity for investigation of the archived samples. Our future research is directed toward it.

CONFLICT OF INTEREST
The authors declare no financial or commercial conflict of interest.

DATA AVAILABILITY
The data that support the findings of this study are available from the corresponding author upon request.

AUTHOR CONTRIBUTIONS
Conception and design: All authors. Acquisition of data: Irena Miler, Mihailo D. Rabasovic, Marija Aleksic, Aleksandar J. Krmpot. Analysis and interpretation of data: All authors. Drafting the manuscript: Irena Miler and Aleksandra Korac, with the contribution of all the authors. Critically revising the manuscript: All authors. Final approval of the manuscript: All authors.

AUTHOR BIOGRAPHIES
Please see Supporting Information online.

ORCID
Aleksandra Korac https://orcid.org/0000-0002-3044-9963

REFERENCES
[1] A. Jankovic, L. Saso, A. Korac, B. Korac, *Oxid. Med. Cell. Longev.* **2019**, *2019*, 2471312.
[2] M. D. Shoulders, R. T. Raines, *Annu. Rev. Biochem.* **2009**, *78*, 929.
[3] L. Mostaco-Guidolin, N. L. Rosin, T. L. Hackett, *Int. J. Mol. Sci.* **2017**, *18*, 1772.
[4] S. Xu, H. Xu, W. Wang, S. Li, H. Li, T. Li, W. Zhang, X. Yu, L. Liu, *J. Transl. Med.* **2019**, *17*, 309.
[5] J. G. Snedeker, A. Gautieri, *Muscles Ligaments Tendons J.* **2014**, *4*, 303.
[6] V. V. Dudenkova, M. V. Shirmanova, M. M. Lukina, F. I. Feldshtein, A. Virkin, E. V. Zagainova, *Biochemistry (Mosc.)* **2019**, *84*, S89.
[7] R. Cicchi, S. Sestini, V. De Giorgi, D. Massi, T. Lotti, F. S. Pavone, *J. Biophotonics* **2008**, *1*, 62.
[8] R. Cicchi, D. Kapsokalyvas, V. De Giorgi, V. Maio, A. Van Wiechen, D. Massi, T. Lotti, F. S. Pavone, *J. Biophotonics* **2010**, *3*, 34.
[9] B. R. Masters, P. T. So, E. Gratton, *Biophys. J.* **1997**, *72*, 2405.
[10] N. G. Horton, K. Wang, D. Kobat, C. G. Clark, F. W. Wise, C. B. Schaffer, C. Xu, *Nat. Photonics* **2013**, *7*, 205.

[11] E. Gavgiotaki, G. Filippidis, V. Tsafas, S. Bovasianos, G. Kenanakis, V. Georgoulias, M. Tzardi, S. Agelaki, I. Athanassakis, *Sci. Rep.* **2020**, *10*, 11055.

[12] S. You, H. Tu, E. J. Chaney, Y. Sun, Y. Zhao, A. J. Bower, Y. Z. Liu, M. Marjanovic, S. Sinha, Y. Pu, S. A. Boppart, *Nat. Commun.* **2018**, *9*, 2125.

[13] D. Tokarz, R. Cisek, M. N. Wein, R. Turcotte, C. Haase, S. C. A. Yeh, S. Bharadwaj, A. P. Raphael, H. Paudel, C. Alt, T. M. Liu, H. M. Kronenberg, C. P. Lin, *PLoS One* **2017**, *12*, e0186846.

[14] P. J. Campagnola, in *Second Harmonic Generation Imaging* (Eds: F. S. Pavone, P. J. Campagnola), Taylor & Francis, Boca Raton **2014** Series in Cellular and Clinical Imaging; Chap. III.

[15] R. Cicchi, N. Vogler, D. Kapsokalyvas, B. Dietzek, J. Popp, F. S. Pavone, *J. Biophotonics* **2013**, *6*, 129.

[16] C. A. Couture, S. Bancelin, J. Van der Kolk, K. Popov, M. Rivard, K. Legare, G. Martel, H. Richard, C. Brown, S. Laverty, L. Ramunno, F. Legare, *Biophys. J.* **2015**, *109*, 2501.

[17] M. D. Rabasovic, D. V. Pantelic, B. M. Jelenkovic, S. B. Curcic, M. S. Rabasovic, M. D. Vrbica, V. M. Lazovic, B. P. Curcic, A. J. Krmpot, *J. Biomed. Opt.* **2015**, *20*, 16010.

[18] X. Chen, O. Nadiarynkh, S. Plotnikov, P. J. Campagnola, *Nat. Protoc.* **2012**, *7*, 654.

[19] G. L. Gusachenko, M. C. Schanne-Klein, *Opt. Express* **2010**, *18*, 19339.

[20] G. Latour, I. Gusachenko, L. Kowalczuk, I. Lamarre, M. C. Schanne-Klein, *Biomed. Opt. Express* **2012**, *3*, 1.

[21] S. Psilodimitrakopoulos, L. Mouchliadis, I. Paradisanos, G. Kourmoulakis, A. Lemonis, G. Kioseoglou, E. Stratakis, *Sci. Rep.* **2019**, *9*, 14285.

[22] R. Cicchi, D. Kapsokalyvas, F. S. Pavone, *Biomed. Res. Int.* **2014**, *2014*, 903589.

[23] E. Yew, C. Rowlands, P. T. So, *J. Innov. Opt. Health Sci.* **2014**, *7*, 1330010.

[24] J. Paoli, M. Smedh, M. B. Ericson, *Semin. Cutan. Med. Surg.* **2009**, *28*, 190.

[25] E. Baria, G. Nesi, R. Santi, V. Maio, D. Massi, C. Pratesi, R. Cicchi, F. S. Pavone, *J. Biophotonics* **2018**, *11*, e201800106.

[26] R. Cicchi, F. S. Pavone, *Methods Mol. Biol.* **2017**, *1627*, 409.

[27] R. M. Williams, W. R. Zipfel, W. W. Webb, *Biophys. J.* **2005**, *88*, 1377.

[28] P. J. Su, W. L. Chen, J. B. Hong, T. H. Li, R. J. Wu, C. K. Chou, S. J. Chen, C. Hu, S. J. Lin, C. Y. Dong, *Opt. Express* **2009**, *17*, 11161.

[29] H. B. Yu, S. Chen, X. Q. Zhu, H. Q. Yang, J. X. Chen, *J. Phys. Conf. Ser.* **2011**, *277*, 012046.

[30] I. Gusachenko, V. Tran, Y. Goulam Houssen, J. M. Allain, M. C. Schanne-Klein, *Biophys. J.* **2012**, *102*, 2220.

[31] J. C. Mansfield, C. P. Winlove, J. Moger, S. J. Matcher, *J. Biomed. Opt.* **2008**, *13*, 044020.

[32] C. Doras, G. Taupier, A. Barsella, L. Mager, A. Boeglin, H. Bulou, P. Bousquet, K. D. Dorkenoo, *Opt. Express* **2011**, *19*, 15062.

[33] A. L. Lopez, I. V. Larina, *Biomed. Opt. Express* **2019**, *10*, 2898.

[34] P. Matteini, F. Ratto, F. Rossi, R. Cicchi, C. Stringari, D. Kapsokalyvas, F. S. Pavone, R. Pini, *Opt. Express* **2009**, *17*, 4868.

[35] A. Keikhosravi, J. S. Bredfeldt, A. K. Sagar, K. W. Eliceiri, *Methods Cell Biol.* **2014**, *123*, 531.

[36] K. Tilbury, P. J. Campagnola, *Perspect. Med. Chem.* **2015**, *7*, 21.

[37] R. A. Natal, J. Vassallo, G. R. Paiva, V. B. Pelegati, G. O. Barbosa, G. R. Mendonca, C. Bondarik, S. F. Derchain, H. F. Carvalho, C. S. Lima, C. L. Cesar, L. O. Sarian, *Tumour Biol.* **2018**, *40*, 1010428318770953.

[38] S. J. Lin, R. J. Wu, H. Y. Tan, W. Lo, W. C. Lin, T. H. Young, C. J. Hsu, J. S. Chen, S. H. Jee, C. Y. Dong, *Opt. Lett.* **2005**, *30*, 2275.

[39] R. Hristu, S. G. Stanciu, D. E. Tranca, G. A. Stanciu, *J. Biophotonics* **2017**, *10*, 1171.

[40] V. Tsafas, E. Gavgiotaki, M. Tzardi, E. Tsafa, C. Fotakis, I. Athanassakis, G. Filippidis, *J. Biophotonics* **2020**, *13*, e202000180.

[41] A. Erikson, J. Ortegren, T. Hompland, C. de Lange Davies, M. Lindgren, *J. Biomed. Opt.* **2007**, *12*, 044002.

[42] R. Mercatelli, T. Triulzi, F. S. Pavone, R. Orlandi, R. Cicchi, *J. Biophotonics* **2020**, *13*, e202000159.

[43] V. Lobo, A. Patil, A. Phatak, N. Chandra, *Pharmacogn. Rev.* **2010**, *4*, 118.

[44] J. P. Borel, J. C. Monboisse, G. Bellon, *Med. Sci. (Paris)* **1988**, *4*, 304.

[45] G. Gunin, N. K. Kornilova, V. V. Petrov, O. V. Vasilyeva, *Adv. Gerontol.* **2012**, *1*, 299.

[46] M. Rinnerthaler, J. Bischof, M. K. Streubel, A. Trost, K. Richter, *Biomolecules* **2015**, *5*, 545.

[47] C. L. Hawkins, M. J. Davies, *Biochim. Biophys. Acta* **1997**, *1360*, 84.

[48] S. Silva, B. Michniak-Kohn, G. R. Leonardi, *An. Bras. Dermatol.* **2017**, *92*, 367.

AUTHOR BIOGRAPHIES

Irena Miler received her MSc degree in biology from the Faculty of Biology, University of Belgrade, Serbia. Currently, she is a Ph.D. student in the Biophotonics group at the University of Belgrade, Serbia. Her research focuses on biophotonics; Light interactions with cells and tissues.

Dr. Mihailo D. Rabasovic received his MSc degree from the Physics department, University of Belgrade, Belgrade, Serbia in 2004. He received his Ph.D. in physics from the University of Belgrade, Belgrade, Serbia in 2007. His research focuses on photo-acoustics, microscopy and correlation spectroscopy. He has published over 60 articles.

Marija Aleksic received her MSc degree in molecular biology and physiology from the University of Belgrade, Belgrade, Serbia. Currently, she is a Ph.D. student in cell and tissue biology at the University of Belgrade, Serbia. Her research focuses on organelle biogenesis and remodeling in physiology and pathology.

Dr. Aleksandar J. Krmpot is an Associate Research Professor at the Institute of Physics Belgrade (IPB), University of Belgrade. He completed his master's and

Ph.D. in physics/quantum optics at the University of Belgrade, Serbia, and acquired the experience in microscopy at Institute for Electronic Structure and Lasers, Foundation for research and technology Hellas (IESL-FORTH), Heraklion, Greece. His research focuses on developing and applications of novel optical microscopic techniques, for example, nonlinear laser scanning microscopy (multiphoton, second and third harmonic generation) and fluorescent correlation spectroscopy for biomedical research and applications. He is the head of the Laboratory for biophysics at IPB and a visiting researcher at Karolinska Institute, Stockholm, Sweden. Aleksandar is a professor at Ph.D. studies in Biophotonics at the University of Belgrade.

Andjelika Kalezic received her MSc degree in molecular biology and physiology from the University of Belgrade, Belgrade, Serbia. Currently, she is a Ph.D. student in cell and tissue biology at the University of Belgrade, Serbia. Her research focuses on the tumor microenvironment.

Dr. Aleksandra Jankovic received her Ph.D. from the Faculty of Biology, University of Belgrade, Belgrade, Republic of Serbia in 2010. Her research focuses on redox regulation in physiological and pathophysiological states and processes including aging. She has published over 50 articles.

Prof. Bato Korac is a Professor of Physiology, Pathophysiology and Redox Biology at the University of Belgrade-Faculty of Biology. His research group focuses on developing new approaches in redox biology for biomedical research and applications. He has published over 70 articles and is a board member of several established journals. He is a president of the Serbian Society for Mitochondrial and Free Radical Physiology and a council member of Society for Free Radical Research—Europe.

Prof. Aleksandra Korac is a Professor of Cell and Tissue Biology at the University of Belgrade-Faculty of Biology. She is the head of Chair of Cell & Tissue Biology, head of Center for Electron Microscopy and a recognized authority in microscopy. Her research group focuses on cell and tissue ultrastructure, application and development of innovative methods for biomarker molecules visualization and bioimaging. She has published over 77 articles.

Remodeling of extracellular matrix of the lamina propria in the uninvolved human rectal mucosa 10 and 20 cm away from the malignant tumor

Sanja Z Despotović[1], Novica M Milićević[1], Dragoslav P Milošević[2,3], Nebojša Despotović[2,3], Predrag Erceg[2,3], Petar Svorcan[2,4], Udo Schumacher[5], Sebastian Ullrich[5], Gordana Mihajlović[3], Dragan Kalem[4], Srđan Marković[4], Ivana M Lalić[1], Aleksandar J Krmpot[6], Mihailo D Rabasović[6], Dejan V Pantelić[6], Svetlana Z Jovanić[6], Thomas Rösch[7] and Živana Milićević[1]

Abstract

In recent years, it has been demonstrated that malignancy arises and advances through the molecular interplay between tumor cells and non-malignant elements of the tumor stroma, that is, fibroblasts and extracellular matrix. However, in contrast to the mounting evidence about the role of tumor stroma in the genesis and progression of the malignant disease, there are very few data regarding the uninvolved stromal tissue in the remote surrounding of the tumor. Using the objective morphometric approach in patients with adenocarcinoma, we demonstrate the remodeling of extracellular matrix of the lamina propria in the uninvolved rectal mucosa 10 and 20 cm away from the neoplasm. We show that the representation of basic extracellular matrix constituents (reticular and collagen fibers and ground substance) is decreased. Also, the diameter of empty spaces that appear within the extracellular matrix of the lamina propria is increased. These spaces do not represent the blood or lymphatic vessel elements. Very likely, they reflect the development of tissue edema in the remote, uninvolved lamina propria of the mucosa in patients with the malignant tumor of the rectum. We hypothesize that the remodeling of extracellular matrix in lamina propria of the rectal mucosa may increase its stiffness, modulating the mechano-signal transduction, and thus promote the progression of the malignant disease.

[1]Institute of Histology and Embryology, Faculty of Medicine, University of Belgrade, Belgrade, Serbia
[2]Faculty of Medicine, University of Belgrade, Belgrade, Serbia
[3]Department of Geriatrics, Zvezdara University Clinical Center, Belgrade, Serbia
[4]Center for Gastroenterology and Hepatology, Zvezdara University Clinical Center, Belgrade, Serbia
[5]Institute of Anatomy and Experimental Morphology, University Cancer Center, University Medical Center Hamburg-Eppendorf, Hamburg, Germany

[6]Institute of Physics, University of Belgrade, Belgrade, Serbia
[7]Department of Interdisciplinary Endoscopy, University Hospital Hamburg-Eppendorf, Hamburg, Germany

Corresponding author:
Živana Milićević, Institute of Histology and Embryology, Faculty of Medicine, University of Belgrade, Višegradska 26 11000 Belgrade, Serbia.
Email: emilicen@etf.bg.ac.rs

Table 1. Demographic characteristics of patients included in the study.

Patients	Number	Age (years)	Gender	
			Male	Female
Cancer	32	72.12	18	14
Healthy	30	70.90	16	14

Introduction

The surrounding tissue of colorectal cancers has attracted considerable interest in recent years for two main reasons. The first reason is that carcinogens act on an entire tissue exposed to this carcinogen, and consequently, genetic alterations are expected to occur at sites distant from the tumor itself. Therefore, several malignant or pre-malignant lesions may occur in the vicinity of an actual tumor. This concept of field carcinogenesis has originally been proposed for the oral mucosa but has been expanded to practically all tissues of the human body.[1–3] While the field carcinogenesis primarily targets the epithelial cells of the colorectum, the connective stroma has attracted considerable interest too. The masters of colorectal carcinogenesis Vogelstein and Kinzler[4] stated recently that "Despite intensive efforts, no genetic alterations have been shown to be required to convert a malignant primary tumor into a metastatic lesion." With reference to distant metastasis formation, the decreased presence of lymphatic vessels and reduced immune cytotoxicity have recently been highlighted as hallmarks for the occurrence of metastasis,[5] thus putting the tumor stroma into the focus of metastasis research. Malignancies arise and advance through the interactions with the elements of the neighboring tissues, that is, the tumor microenvironment.[6,7] Special significance has been attributed to the molecular interplay between tumor cells and non-malignant elements of the tumor stroma, that is, fibroblasts and extracellular matrix (ECM).[8] Tumor progression and aggressiveness are promoted by the surrounding tissue through cell-to-cell contacts or secreted molecules.[9,10] In return, tumor cells uphold the recruitment of fibroblasts into a tumor mass and their transdifferentiation into myofibroblasts, which produce factors stimulating cancer progression.[11–14] In this way, the interplay between the cancer cells and stromal cells is established, a positive feedback loop is closed and the advancement of malignant disease is promoted.

However, despite the mounting evidence about the role of tumor stroma in the genesis and progression of the malignant disease, there are very few data regarding the uninvolved stromal tissue in the remote surrounding of the tumor. Only very recently, we performed a morphometric study of the mucosa of rectum and revealed the alterations of Lieberkühn crypts, as well as reduced cellularity, 10 and 20 cm away from the malignant tumor. Our study also provided indications that ECM of the lamina propria could be affected.[15]

Therefore, the aim of this study was to investigate the organization of ECM components of the lamina propria of the rectal mucosa in the remote surrounding of the malignant tumor and quantitate them using an objective morphometric approach.

Our work is the first to reveal a profound remodeling of ECM of the lamina propria of the uninvolved human rectal mucosa in the remote surrounding of the malignant tumor. Thus, we document the interactions between the cancer and distant mucosal tissue of the affected organ.

Materials and methods

Tissue samples

This study has been approved by the Ethics Committee of Zvezdara Clinical Center, Belgrade, Serbia (27 November 2013) and performed in accordance with ethical standards laid down in the 1964 Declaration of Helsinki. All individuals involved received detailed verbal information and gave their informed consent prior to their inclusion into the study.

Only patients with newly discovered tumor were included in the study. Thus, they had not received any previous treatment for the malignant disease. Tissues were endoscopically sampled at the Center for Gastroenterology and Hepatology, Zvezdara Clinical Center, Belgrade, Serbia, from patients suspected on clinical grounds to suffer from a rectal cancer, which all were subsequently diagnosed as adenocarcinoma according to World Health Organization (WHO) histological classification of tumors. Patients with diverticular disease of the colon, previous infectious colitis, or inflammatory bowel disease were excluded from the study. Patients were divided into groups according to their gender. All patients were on standard mixed meals regimen and not on any particular form of diet.

Samples of rectal mucosa were obtained from 32 patients older than 60 years (18 males and 14 females; Table 1). Cancers were located in the sigmoid colon 25−30 cm from the external anal verge and the biopsies were taken 10 and 20 cm away from the malignant tumor in the caudal direction. The samples of rectal mucosa collected at the same institution from 30 healthy persons of the corresponding age (16 males and 14 females; Table 1) during the active endoscopy screening of individuals with a family history of intestinal malignancy, possibly suffering from an as yet unidentified, asymptomatic cancer in which no disease involving the rectal mucosa was found, were used as control. Samples were collected from the upper third of rectum.

Tissue preparation, staining, and morphometric measurements

The biopsies of the rectal mucosa were fixed in 10% neutral buffered formalin, processed to Paraplast. Tissue sections (3–5 μm thick) were routinely stained with hematoxylin–eosin, while Gomori's silver impregnation

and Masson trichrome staining were used for demonstration of reticular and collagen fibers, respectively.[16]

Microphotographs were acquired with a digital camera Olympus C3030-Z (Olympus Deutschland GmbH, Hamburg, Germany) connected to a light microscope Opton Photomicroscope III (Carl Zeiss AG, Oberkochen, Germany) or digital camera Leica DFC295 (Leica, Heerbrugg, Switzerland) connected to a light microscope Leica DM4000 B LED (Leica, Wetzlar, Germany).

Gomori's silver impregnation technique was used to identify the reticular fibers which stained black. A random selection of three fields per slide from the subepithelial region, between the crypts, and above the lamina muscularis mucosae was assessed for further analysis.

The diameters of spaces between reticular fibers were measured at the magnification 630×. In order to avoid the inclusion of crypts in the measurement of the spaces between reticular fibers, a rectangle was drawn that always occupied the same area of the lamina propria ($3600\,\mu m^2$) excluding the crypts, and our measurements were performed within this rectangle. The plugin BoneJ within open-source software Fiji[17] was used to estimate the diameter of spaces between reticular fibers in the lamina propria of the rectal mucosa of healthy individuals (n=30), as well as 10 cm (n=27) and 20 cm (n=22) away from the malignant tumor. BoneJ determines the diameter (µm) of the largest sphere that can be inserted into the spaces between the reticular fibers and assigns different colors to these spaces according to their diameter.

The presence of reticular fibers in colonic lamina propria was determined in the following manner. A random selection of 15 fields per slide (5 fields in subepithelial region, 5 fields between the crypts of lamina propria, and 5 fields above lamina muscularis mucosae) was assessed at the magnification of 400× (n=as above). Reticular fibers were extracted using Color Picker Threshold Plugin within open community platform for bioimage informatics Icy.[18] For each slide, 10 positive and 10 negative colors were selected as recognition patterns of stained and unstained tissue elements. The resulting images were systematically compared with the corresponding originals, and in cases in which the detection of reticular fibers was not accurate, the threshold was fixed manually. The presence of reticular fibers in rectal lamina propria was expressed as the relative percentage of the area occupied by the reticular fibers divided by the area of the lamina propria selected with an imaging processor.

Masson's trichrome staining identified collagen fibers, which were green. The presence of collagen fibers of healthy individuals (n=30), as well as 10 cm (n=32) and 20 cm (n=32) away from the malignant tumor, was determined in the same manner as described above for reticular fibers.

Also, for the identification of collagen fibers, the unfixed and label-free colon tissue samples were imaged on an original labframe nonlinear laser scanning microscope (NLM). The microscope is described elsewhere.[19]

Experimental setup for NLM was used for second harmonic generation (SHG) imaging of 3D collagen distribution from the samples. The incoming infrared femtosecond pulses from the tunable mode-locked Ti:sapphire laser (Coherent, Mira 900) were directed onto the sample by a dichroic mirror through the Zeiss EC Plan-Neofluar 40×/1.3 NA Oil objective. The laser wavelength was 840 nm. The SHG was selected by narrow bandpass filter at 420 nm (Thorlabs FB420-10, FWHM 10 nm). The average laser power on the sample was 30 mW and the peak laser power was 2.5 kW.

Immunohistochemical analysis was performed on formalin-fixed, paraffin-embedded sections using following antibodies and dilution ratios: monoclonal mouse anti-human CD34 (M7165, dilution 1:100; Dako, Carpinteria, CA, USA), CD105 (clone SN6h, MA5-11854, dilution 1:100; Thermo Fisher Scientific, Rockford, IL, USA), podoplanin (clone D2-40, M3619, dilution 1:100; Dako), as well as hyaluronic acid binding protein (HABP, biotinylated, 385911-50 UG, dilution 1:75; Calbiochem, Spring Valley, CA, USA).

For anti-CD34, -CD105, and -podoplanin antibodies, the following procedure was used. Briefly, after dewaxing and rehydration, a heat-inducing antigen retrieval procedure using Tris-EDTA at pH 9.0 for 30 min was performed on all tissue sections, with subsequent washing in Tris-buffered saline (TBS) with Tween and incubation with primary antibodies for 60 min. The sections were treated by applying the commercial Ultra Vision/3,3′-diaminobenzidine (DAB) staining kit (Thermo Scientific Lab Vision TL-060-HD, Rockford, IL, USA). Immunoreactions were developed by DAB substrate.

For HABP antibody, Dako retrieval solution (S1699 at pH=6) was used. After washing in TBS, protein blocking was performed with 1% bovine serum albumin (BSA) in TBS. After incubation with primary biotinylated antibodies for 60 min and with VECTASTATIN ABC-AP kit (Vector Laboratories, Burlingame, CA, USA) for 30 min, staining with Permanent Red (Dako K0640, Carpinteria, CA, USA) was used for visualization. The sections were counter-stained with Mayer's hematoxylin. Negative controls were performed on colon sections using the same methodology, but with the omission of primary antibody. For CD105 antibody, sections of human colon cancers were used as a positive control and for HABP antibody, sections of human nasal mucosa.

The number of blood vessels demonstrated with CD34 or CD105 in rectal lamina propria (per $0.1\,mm^2$ of the tissue) was determined at 5 fields per slide at 200× magnification using the open-source software Fiji. A region of interest was drawn on each field, which excluded the crypts and included only the lamina propria. Counting of blood vessels was performed on healthy tissue (n=25), 10 and 20 cm away from tumor (n=10), using the Multi-point tool.

The diameter of spaces within ECM and the representation of hyaluronan, as demonstrated with HABP staining, in healthy tissues (n=4) 10 cm (n=10) and 20 cm (n=12) away from the malignant tumor, were determined as described for reticular fibers.

Statistical analysis

The statistical package SPSS for Windows 12.0 (SPSS Inc., Chicago, IL, USA) was used to calculate the means and standard deviations, as well as to indicate significant differences (Student's t-test and one-way analysis of variance (ANOVA) at $p < 0.05$).

Results

Morphological alterations of the uninvolved rectal mucosa in cancer patients

The mucosa of normal, healthy persons exhibited an orderly organization. The crypts were well developed, generally regular and round in shape, with luscious epithelium consisting mostly of goblet cells and fewer enterocytes (Figure 1(a)). The connective tissue of lamina propria also displayed a tidy appearance with very little free space within ECM (Figure 1(a)).

At the distance of 10 cm away from the tumor, the number of crypts appeared decreased, with diminished diameter, slightly irregular in shape, and with frail epithelium (Figure 1(b)). The connective tissue of lamina propria showed a disorderly organization, whereby the prominent spaces were notable within the ECM (Figure 1(b)). Similar alterations of lamina propria of the rectal mucosa, but less prominent in comparison with the normal tissue, were observed in cancer patients 20 cm away from the tumor (not shown).

Therefore, we wished to objectively investigate the extent of disorderly organization of the mucosal lamina propria 10 and 20 cm away from the adenocarcinoma of the rectum and quantify the basic components of ECM (namely, reticular and collagen fibers, as well as ground substance). To this end, we used the computer-aided image analysis of the affected tissue to estimate the diameter of spaces and the representation of the components of ECM in the lamina propria of the rectal mucosa 10 and 20 cm away from the malignant tumor.

Disorganization of reticular fibers in the lamina propria of the uninvolved rectal mucosa in cancer patients

In normal tissue, the reticular fibers were orderly organized and showed a tidy appearance. They were thick and intimately appositioned to the epithelium of the crypts. The basal lamina of the crypts was surrounded by three to four layers of reticular fibers. A dense meshwork of reticular fibers leaving little space for non-fibrous ground substance connected the crypts with each other (Figure 1(c)).

At the distance of 10 and 20 cm away from the tumor, the reticular fibers around the crypts consisted only of one thin layer, and those fibers spanning the ECM were also thin, thus leaving the prominent empty spaces between the reticular fibers (Figure 1(d)). We revealed that the diameter of spaces between the reticular fibers was significantly increased at the distance of 10 cm away from the tumor lesion ($5.66 \pm 2.21\,\mu m$), in comparison with both healthy controls ($3.32 \pm 0.81\,\mu m$; $p < 0.01$; Figures 1(e)–(h)) and tissue samples taken 20 cm away from the tumor ($3.72 \pm 1.27\,\mu m$; $p < 0.01$). There was no statistically significant difference between samples taken 20 cm away from the tumor and control (Table 2). These results clearly documented the disturbed organization of the lamina propria in the remote, uninvolved rectal mucosa 10 cm away from the malignant lesion.

Furthermore, we wished to explore whether the increased diameter of spaces was accompanied by a decreased representation of reticular fibers in the lamina propria of the remote rectal mucosa 10 and 20 cm away from the neoplasia. We revealed that the representation of reticular fibers was significantly decreased in the lamina propria of rectal mucosa 10 cm (27.99 ± 7.86; $p < 0.01$) but not 20 cm (38.76 ± 10.01) away from the tumor in comparison with the tissue of healthy individuals (42.72 ± 11.33; Table 2). The representation of reticular fibers was significantly lower ($p < 0.01$) in the lamina propria at the distance of 10 cm away from the tumor compared with the representation at the distance of 20 cm (Table 2).

Disorganization of collagen fibers in the lamina propria of the uninvolved rectal mucosa in cancer patients

In normal tissue, the collagen fibers showed a notably tidy appearance: the fibers were massive, intimately appositioned, and orderly organized (Figure 2(a)).

At the distance of 10 and 20 cm away from the tumor, the collagen fibers were frail and loosely arranged. Thus, the prominent spaces were notable between the collagen fibers (Figure 2(b)).

We further wished to exclude the possibility that the observed changes of the collagen fibers in the mucosal lamina propria were artificially produced (i.e. due to fixation or staining procedure). Therefore, NLM was used for SHG imaging of collagen distribution. In this method, the fresh, unfixed, and unstained tissue is used for demonstration of collagen fibers. SHG images wholly confirmed the above-described findings: in healthy individuals, the collagen fibers were massive, closely appositioned, and orderly organized around the crypts and throughout the lamina propria (Figure 2(c) and Online Resource 1). In the lamina
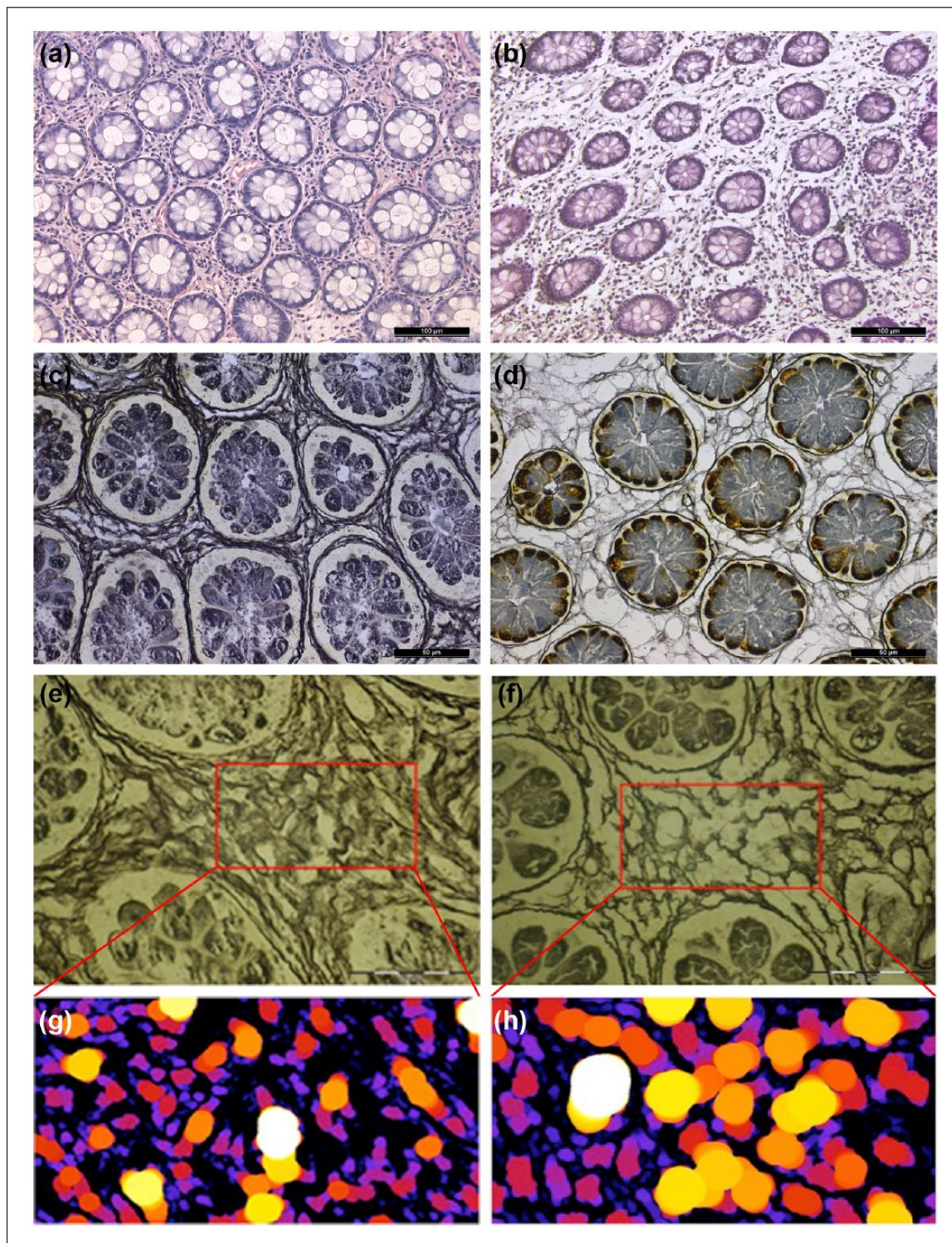
Figure 1. Representative photomicrographs of rectal mucosa in healthy persons (a, c, e, and g) and cancer patients 10 cm away from the tumor (b, d, f, and h). (a) On hematoxylin–eosin staining, the connective tissue of lamina propria of healthy person shows orderly organization with very little free space within extracellular matrix, (b) while at the distance of 10 cm away from the tumor, lamina propria is disorganized with prominent spaces notable within extracellular matrix. Gomori's silver impregnation technique identified reticular fibers which were (c) thick and closely appositioned in normal mucosa and (d) feeble and loosely arranged at the distance 10 cm away from the tumor. Measurement of the spaces between reticular fibers in (e) a healthy person and (f) 10 cm away from tumor was performed within the rectangle using plugin BoneJ (Fiji). BoneJ determines the diameter of the largest sphere that can be inserted into the spaces between reticular fibers and assigns different colors to these spaces according to their diameter. Brighter spheres have larger diameter. Graphical output from (g) BoneJ of healthy tissue and (h) 10 cm away from tumor.

Table 2. Morphometric measurements of the rectal mucosa in healthy subjects and cancer patients 10 and 20 cm away from tumor.

	Healthy controls	10 cm away from tumor	20 cm away from tumor
Diameter of spaces between reticular fibers (μm)	3.32 ± 0.81	5.66 ± 2.21*	3.72 ± 1.27[+]
Representation of reticular fibers (%)	42.72 ± 11.33	27.99 ± 7.86*	38.76 ± 10.01[+]
Representation of collagen fibers (%)	48.05 ± 8.92	26.43 ± 6.22*	35.15 ± 8.34**[+]
Diameter of spaces between HABP (μm)	2.00 ± 0.40	4.27 ± 1.58*	3.78 ± 1.45[§]
Representation of HABP (%)	60.41 ± 9.31	42.71 ± 11.81*	45.42 ± 13.35**

HABP: hyaluronic acid binding protein.
*10 cm away from tumor versus healthy controls ($p < 0.01$).
[+]10 cm away from tumor versus 20 cm away from tumor ($p < 0.01$).
**20 cm away from tumor versus healthy controls ($p < 0.01$).
[§]20 cm away from tumor versus healthy controls ($p < 0.05$).

propria 10 cm away from tumor, the collagen fibers were thinner, disordered, and loosely arranged with noticeable spaces between them (Figure 2(d) and Online Resource 2).

We also wished to explore whether the presence of free spaces between the collagen fibers was accompanied by a decreased representation of collagen in the lamina propria of the uninvolved rectal mucosa 10 and 20 cm away from the neoplasia. We revealed that the representation of collagen fibers in the lamina propria in the remote rectal mucosa 10 and 20 cm away from the cancer was significantly lower (26.43 ± 6.22 and 35.15 ± 8.34, respectively; $p < 0.01$) in comparison with the control, healthy individuals (48.05 ± 8.92; Table 2). Notably, the representation of collagen fibers was significantly lower ($p < 0.01$) in the lamina propria at the distance of 10 cm away from the tumor compared with that at the distance of 20 cm (Table 2).

Disorganization of ground substance in the lamina propria of the uninvolved rectal mucosa in cancer patients

The ECM ground substance was visualized by demonstration of HABP binding to hyaluronan in affinity histochemically stained tissue sections of healthy individuals and cancer patients and analyzed using computer-aided morphometric approach.

In normal tissue, the ECM ground substance was organized in confluent, uniform bands between the crypts with very few small spaces within it (Figure 2(e)).

At the distance of 10 and 20 cm away from the tumor, the ECM ground substance recapitulated the structural organization similar to that observed for reticular and collagen fibers: namely, the prominent spaces were notable within it (Figure 2(f)). The morphometric analysis revealed that the diameter of spaces within the ground substance was significantly increased at the distance of 10 and 20 cm away from the tumor lesion (4.27 ± 1.58 μm, $p < 0.01$ and 3.78 ± 1.45 μm, $p < 0.05$, respectively), in comparison with healthy controls (2.00 ± 0.40 μm; Table 2). Furthermore, we revealed that the representation of ECM ground substance in the lamina propria of the remote rectal mucosa 10 and 20 cm away from

the cancer was significantly lower (42.71 ± 11.81 and 45.42 ± 13.35, respectively; $p < 0.01$) in comparison with the control, healthy individuals (60.41 ± 9.31; Table 2).

Edema of the lamina propria of the uninvolved rectal mucosa in cancer patients

Finally, we wanted to elucidate whether the enlarged spaces within the ECM in the lamina propria of the remote, unaffected rectal mucosa 10 and 20 cm away from the tumor could represent the blood or lymphatic vessel elements.

On the routinely stained sections of the healthy tissue, the small blood vessels and capillaries were readily discernible, but infrequently seen. On the contrary, in lamina propria of the rectal mucosa 10 and 20 cm away from the tumor, the small blood vessels and capillaries were abundant and much more frequent than in the healthy tissue. To more specifically uphold our observation, we stained the tissue samples immunohistochemically with CD34 and CD105 antibodies for total and newly formed blood vessels, respectively. We counted the number of blood vessel profiles per unit area of tissue (0.1 mm^2 of the lamina propria).

The CD34-positive blood vessels were abundant in healthy tissue (Figure 3(a)), as well as 10 and 20 cm away from the malignant tumor (Figure 3(b)). However, their number per 0.1 mm^2 of the lamina propria 10 cm away (65.15 ± 18.94, $p < 0.01$) and 20 cm away from the tumor (45.77 ± 16.48; $p < 0.01$) was significantly higher compared with the lamina propria of healthy tissue (36.57 ± 7.59). The number of CD34-positive blood vessels 10 cm away from the tumor was significantly increased compared with lamina propria 20 cm away from the tumor ($p < 0.01$; Table 3).

The microvessels in rectal lamina propria from healthy controls were either minimally positive or totally CD105-negative. Rare CD105-positive blood vessels were preferentially located either superficially immediately below the basement membrane or at the cryptal base (Figure 3(c)). The number of CD105-positive blood vessels was significantly increased 10 and 20 cm away from the rectal adenocarcinoma (Figure 3(d), 14.93 ± 5.65 and 9.53 ± 4.97, respectively; $p < 0.01$) in comparison with the control,
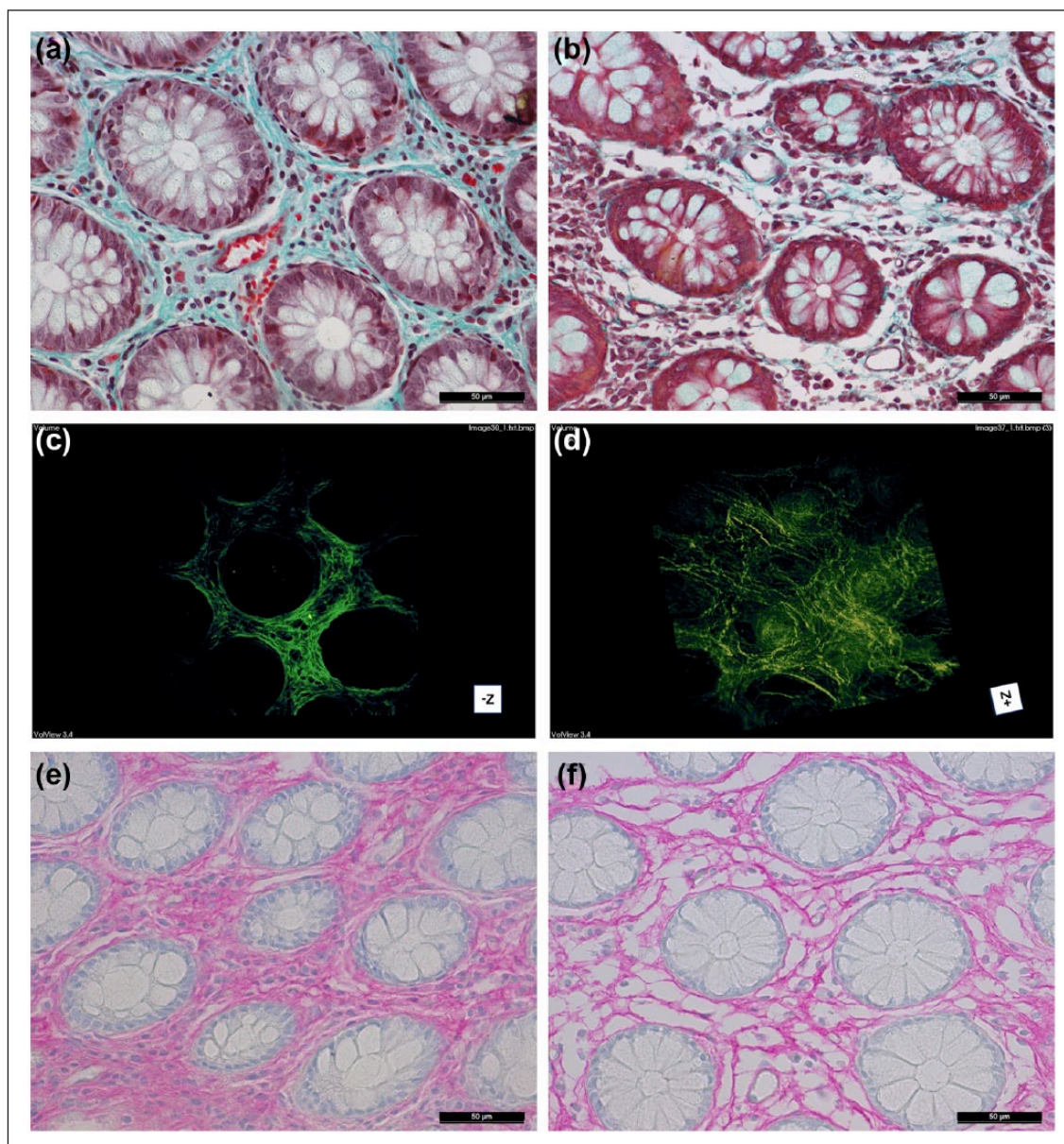
Figure 2. Representative photomicrographs of rectal mucosa in healthy persons (a, c, and e) and cancer patients 10 cm away from the tumor (b, d, and f). Masson's trichrome staining identified collagen fibers, which were massive, intimately appositioned, and orderly organized in (a) normal rectal tissue and (b) frail and loosely arranged 10 cm away from the tumor. NLM was used for SHG imaging of collagen fibers in (c) unfixed and unstained healthy tissue and (d) tissue 10 cm away from the tumor. SHG images confirmed the findings described above. (e) Immunohistochemical staining for hyaluronan using HABP in healthy person shows hyaluronan (red) organized in confluent bands between the crypts with small spaces within it. (f) At the distance 10 cm away from the tumor, hyaluronan formed thin bands with prominent spaces notable within it.

healthy tissue (5.8±2.52). Also, the number of CD105-positive blood vessels 10 cm away from the tumor was significantly increased compared with lamina propria 20 cm away from the tumor ($p < 0.01$; Table 3).

So, we demonstrate that both the number of total and newly formed blood vessels in the lamina propria 10 and 20 cm away from the tumor was increased in comparison with the lamina propria of healthy tissue. However, as the large spaces within the ECM of diseased rectal lamina propria remained CD34- and CD105-negative, we concluded

that they do not represent the blood vessel elements. Thus, the question of their nature remained unanswered.

Therefore, we decided to investigate whether these spaces could represent newly developed lymphatic vessels. To clarify this issue, we immunostained the tissue samples with anti-podoplanin that labels lymphatic endothelium, whereas it is unreactive with vascular endothelium. We did not reveal any lymphatic vessels in the lamina propria of healthy colon and they were present only at the level of lamina muscularis mucosae where an abundant array could
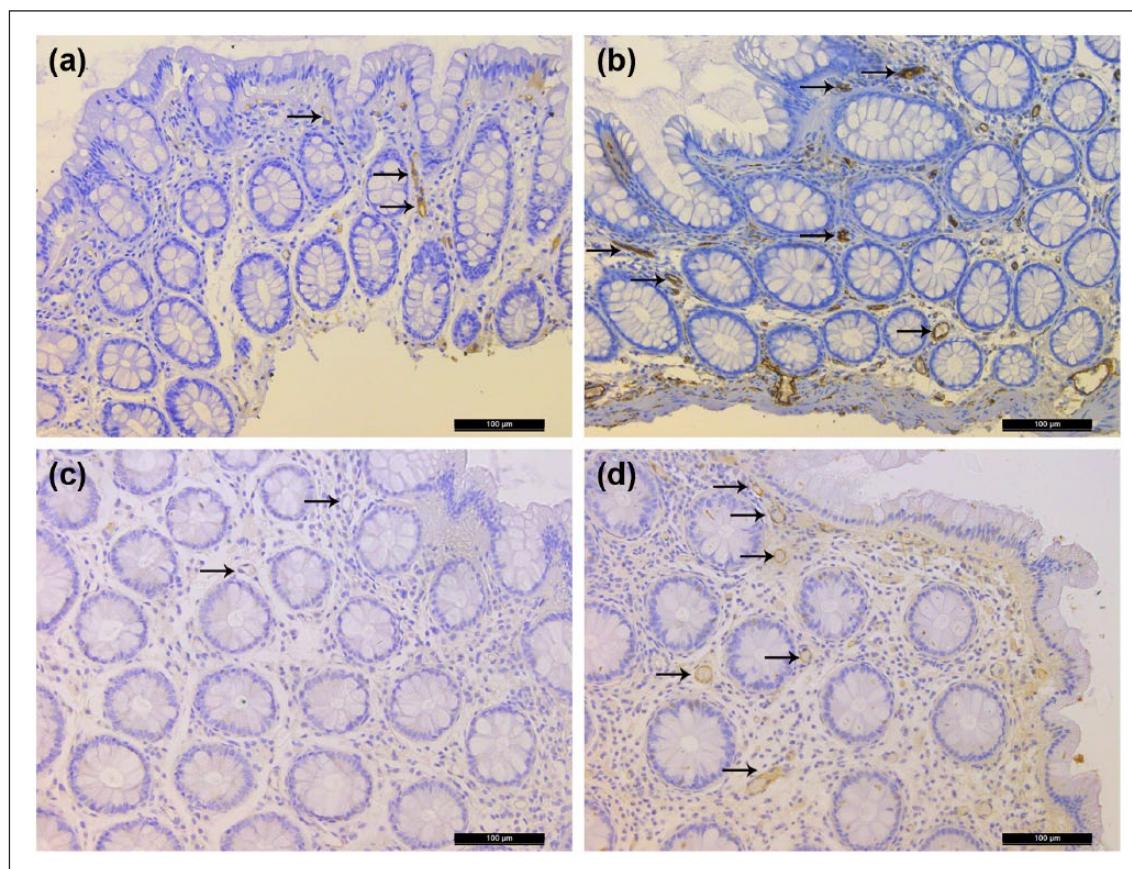
Figure 3. Immunohistochemical staining for CD34 and CD105 of rectal mucosa in healthy persons (a and c) and cancer patients 10 cm away from the tumor (b and d). (a) The CD34-positive blood vessels were abundant in healthy tissue. (b) Their number was significantly increased 10 cm away from the tumor. (c) The blood vessels in healthy lamina propria were either minimally positive or totally CD105-negative. (d) The number of CD105-positive blood vessels was significantly increased 10 cm away from the rectal adenocarcinoma (some blood vessels are indicated by arrows).

Table 3. Number of CD34- and CD105-positive blood vessels per 0.1 mm² of the rectal mucosa in healthy subjects and cancer patients 10 and 20 cm away from tumor.

	Healthy controls	10 cm away from tumor	20 cm away from tumor
Number of CD34-positive blood vessels (per 0.1 mm² of lamina propria)	36.57 ± 7.59	65.15 ± 18.94*	45.77 ± 16.48**+
Number of CD105-positive blood vessels (per 0.1 mm² of lamina propria)	5.8 ± 2.52	14.93 ± 5.65*	9.53 ± 4.97**+

*10 cm away from tumor versus healthy controls ($p < 0.01$).
**20 cm away from tumor versus healthy controls ($p < 0.01$).
+10 cm away from tumor versus 20 cm away from tumor ($p < 0.01$).

be seen (not shown). On the contrary, tiny profiles of lymphatic vessels were sometimes identifiable within the lamina propria 10 and 20 cm away from the tumor (not shown). These results neatly corresponded to those of Kenney and Jain.[20] However, the lymphatic vessels in such cases were very few and could not account for numerous spaces in the lamina propria, which were podoplanin-negative. Therefore, we concluded that these spaces do not represent the newly developed lymphatic vessels.

It should be notified that no differences in structure of the mucosal elements were observed between male and female healthy persons. Also, no gender difference for any structural element of the rectal mucosa was observed neither at 10 cm nor at 20 cm distance away from the tumor.

Taking our results together, we concluded that they reflect the development of a veritable tissue edema in the remote, uninvolved lamina propria of the mucosa in patients with the neoplastic tumor of the rectum.

Discussion

Our present work, to the best of our knowledge, is the first to document the remodeling of lamina propria in the uninvolved rectal mucosa remote from the malignant lesion

using an exact morphometric analysis. We demonstrate the decreased representation of basic ECM constituents (reticular and collagen fibers, and ground substance), as well as the increased diameter of free spaces within the ECM in the lamina propria of the distant, uninvolved rectal mucosa.

These findings are in line with the finding that collagen is reduced in tumor-associated lamina propria.[21,22] Recent studies show that modifications of collagen fibers (e.g. cross-linking), associated with changes of pore sizes, strongly affect the ECM stiffness.[7,23–25] The cells grown in fibrillar collagen gels, which are nowadays extensively used to study tumor–microenvironment interactions in vitro, adopted a motile phenotype in gels with larger pores and a less motile phenotype in gels with small pores.[26] The increased rigidity of the ECM modulates the mechano-signal transduction and promotes the aggressiveness of neoplastic cells.[27,28] One is tempted to speculate that the remodeling of the lamina propria in the remote rectal mucosa that we registered in vivo corresponds to these in vitro modifications of ECM, which sustain the aggressive behavior of tumor cells.

Two main questions arise from our study. First, what do the free spaces observed within the ECM represent? Second, does the remodeling of the remote rectal lamina propria reflect the influence of the malignant tissue, or conversely, denotes the intrinsic modifications of the stromal tissue which provide a suitable ground for tumor development?

Regarding the first question, and having in mind that enlarged spaces in the remote rectal lamina propria of cancer patients are CD34-, CD105-, and podoplanin-negative, we favor the possibility that these changes disclose a tissue edema at the greater distance from the tumor. This observation extends the finding that edema is observed in the immediate vicinity of tumors.[29]

Regarding the second question, the former hypothesis is strengthened by the fact that neoplastic tissues can affect the structure and function of very distant organs.[30,31] It is also supported by our finding that the changes of lamina propria are somewhat more prominent at the distance of 10 cm than at 20 cm away from the tumor. The latter notion is underpinned by our finding that the remodeling of the rectal lamina propria still remains evident at a greater distance (20 cm) away from the tumor. This is in line with the concept of "field carcinogenesis": it postulates that genetic and environmental risk factors induce large areas of tissue injury suitable for cancer development.[32,33] So, it remains possible that the remodeling of lamina propria that we observed in cancer patients reflects the overall alteration of larger fields of the colorectal mucosa and its connective tissue. At this moment, based on our data, it cannot be concluded with certainty which hypothesis holds true. However, studies currently in progress in our laboratories—in which the samples of mucosal lamina propria are taken from the part of the large bowel the most distant from the neoplastic lesion—are expected to greatly clarify the situation.

In very recent time, a view has emerged that the role of stroma is not secondary to that of epithelium in the phenomenon of "field carcinogenesis."[34,35] Our results strongly support this opinion and suggest that the concept of "field carcinogenesis" should incorporate not only the changes in epithelial component, but the stroma of the malignantly affected organ as well.[2]

Our findings are in fine agreement with the results of genetic studies which showed that the significant gene expression alterations exist in the unaffected colon mucosa from patients with colon tumor.[36–38] In addition to changes in ECM components, we also found an increased number of CD34- and CD105-positive capillaries and small blood vessels in the remote rectal mucosa. This was also detected in endoscopically normal rectal mucosa in patients with multiple adenomas anywhere in the colon and was completely absent in patients with benign colonic diseases.[33] Together, these data show that the use of remote uninvolved mucosa from patients with tumors of the gut as control tissue[39] should be regarded as unjustified. Despite its unremarkable endoscopic appearance, this tissue is not normal and only truly healthy tissue should be used as controls.

In conclusion, our study reveals profound remodeling of the ECM of lamina propria in the rectal mucosa 10 and 20 cm away from the malignant lesion. It documents the complex interplay between the tumor and stromal tissues not only of the neoplasm itself, but of the distant, uninvolved rectal lamina propria, as well. The search for these changes may be used as a diagnostic tool and a valuable indicator of occult tumors of the large bowel.

References

1. Hawthorn L, Lan L and Mojica W. Evidence for field effect cancerization in colorectal cancer. *Genomics* 2014; 103(2–3): 211–221.
2. Lochhead P, Chan AT, Nishihara R, et al. Etiologic field effect: reappraisal of the field effect concept in cancer predisposition and progression. *Mod Pathol* 2015; 28(1): 14–29.
3. Patel A, Tripathi G, Gopalakrishnan K, et al. Field cancerisation in colorectal cancer: a new frontier or pastures past? *World J Gastroenterol* 2015; 21(13): 3763–3772.

4. Vogelstein B and Kinzler KW. The path to cancer—three strikes and you're out. *N Engl J Med* 2015; 373(20): 1895–1898.

5. Mlecnik B, Bindea G, Kirilovsky A, et al. The tumor microenvironment and immunoscore are critical determinants of dissemination to distant metastasis. *Sci Transl Med* 2016; 8(327): 327ra26.

6. Goubran HA, Kotb RR, Stakiw J, et al. Regulation of tumor growth and metastasis: the role of tumor microenvironment. *Cancer Growth Metastasis* 2014; 7: 9–18.

7. Vannucci L. Stroma as an active player in the development of the tumor microenvironment. *Cancer Microenviron* 2015; 8(3): 159–166.

8. Hemmings C. Is carcinoma a mesenchymal disease? The role of the stromal microenvironment in carcinogenesis. *Pathology* 2013; 45(4): 371–381.

9. Hale MD, Hayden JD and Grabsch HI. Tumour-microenvironment interactions: role of tumour stroma and proteins produced by cancer-associated fibroblasts in chemotherapy response. *Cell Oncol* 2013; 36(2): 95–112.

10. Valcz G, Sipos F, Tulassay Z, et al. Importance of carcinoma-associated fibroblast-derived proteins in clinical oncology. *J Clin Pathol* 2014; 67(12): 1026–1031.

11. Fuyuhiro Y, Yashiro M, Noda S, et al. Upregulation of cancer-associated myofibroblasts by TGF-β from scirrhous gastric carcinoma cells. *Br J Cancer* 2011; 105: 996–1001.

12. Mazzocca A, Dituri F, Lupo L, et al. Tumor-secreted lysophostatidic acid accelerates hepatocellular carcinoma progression by promoting differentiation of peritumoral fibroblasts in myofibroblasts. *Hepatology* 2011; 54: 920–930.

13. Polanska UM and Orimo A. Carcinoma-associated fibroblasts: non-neoplastic tumour-promoting mesenchymal cells. *J Cell Physiol* 2013; 228(8): 1651–1657.

14. Martinez-Outschoorn UE, Curry JM, Ko YH, et al. Oncogenes and inflammation rewire host energy metabolism in the tumor microenvironment: RAS and NFκB target stromal MCT4. *Cell Cycle* 2013; 12(16): 2580–2597.

15. Despotović SZ, Milićević NM, Milosević DP, et al. Morphometric study of uninvolved rectal mucosa 10 cm and 20 cm away from the malignant tumor. *Histol Histopathol* 2014; 29(2): 229–234.

16. Bradbury P and Gordon KC. Connective tissues and stains. In: JD Bancroft and A Stevans (eds) *Theory and practice of histological techniques*. Edinburgh: Churchill Livingstone, 1982, pp. 121–144.

17. Doube M, Kłosowski MM, Arganda-Carreras I, et al. BoneJ: free and extensible bone image analysis in ImageJ. *Bone* 2010; 47: 1076–1079.

18. de Chaumont F, Dallonqeville S, Chenouard N, et al. Icy: an open bioimage informatics platform for extended reproducible research. *Nat Methods* 2012; 9(7): 690–696.

19. Rabasović MD, Pantelić DV, Jelenković BM, et al. Nonlinear microscopy of chitin and chitinous structures: a case study of two cave-dwelling insects. *J Biomed Opt* 2015; 20(1): 016010.

20. Kenney BC and Jain D. Identification of lymphatics within the colonic lamina propria in inflammation and neoplasia using the monoclonal antibody D2–40. *Yale J Biol Med* 2008; 81(3): 103–113.

21. Tarpey SG and White FH. Ultrastructural morphometry of collagen from lamina propria during experimental oral carcinogenesis and chronic inflammation. *J Cancer Res Clin Oncol* 1984; 107(3): 183–194.

22. Fu Z, Song P, Li D, et al. Cancer-associated fibroblasts from invasive breast cancer have an attenuated capacity to secrete collagens. *Int J Oncol* 2014; 45(4): 1479–1488.

23. Ng MR and Brugge JS. A stiff blow from the stroma: collagen crosslinking drives tumor progression. *Cancer Cell* 2009; 16(6): 455–457.

24. Yi J, Radosevich AJ, Stypula-Cyrus Y, et al. Spatially resolved optical and ultrastructural properties of colorectal and pancreatic field carcinogenesis observed by inverse spectroscopic optical coherence tomography. *J Biomed Opt* 2014; 19(3): 36013.

25. Sapudom J, Rubner S, Martin S, et al. The phenotype of cancer cell invasion controlled by fibril diameter and pore size of 3D collagen networks. *Biomaterials* 2015; 52: 367–375.

26. Carey SP, Kraning-Rush CM, Williams RM, et al. Biophysical control of invasive tumor cell behavior by extracellular matrix microarchitecture. *Biomaterials* 2012; 33(16): 4157–4165.

27. Parekh A and Weaver AM. Regulation of cancer invasiveness by the physical extracellular matrix environment. *Cell Adh Migr* 2009; 3(3): 288–292.

28. Seewaldt V. ECM stiffness paves the way for tumor cells. *Nat Med* 2014; 20(4): 332–333.

29. White LM, Wunder JS, Bell RS, et al. Histologic assessment of peritumoral edema in soft tissue sarcoma. *Int J Radiat Oncol Biol Phys* 2005; 61(5): 1439–1445.

30. Lopez DM, Charyulu V and Adkins B. Influence of breast cancer on thymic function in mice. *J Mammary Gland Biol Neoplasia* 2002; 7(2): 191–199.

31. Carrio R and Lopez DM. Insights into thymic involution in tumor-bearing mice. *Immunol Res* 2013; 57(1–3): 106–114.

32. Vannucci L, Fiserova A, Horvath O, et al. Cancer evolution and immunity in a rat colorectal carcinogenesis model. *Int J Oncol* 2004; 25(4): 973–981.

33. Backman V and Roy HK. Advances in biophotonic detection of field carcinogenesis for colon cancer risk stratification. *J Cancer* 2013; 4: 251–261.

34. Dotto GP. Multifocal epithelial tumors and field cancerization: stroma as a primary determinant. *J Clin Invest* 2014; 124(4): 1446–1453.

35. Ge L, Meng W, Zhou H, et al. Could stroma contribute to field cancerization? *Med Hypotheses* 2010; 75(1): 26–31.

36. Chen LC, Hao CY, Chiu YS, et al. Alteration of gene expression in normal-appearing colon mucosa of APC(min) mice and human cancer patients. *Cancer Res* 2004; 64(10): 3694–3700.

37. Belshaw NJ, Pal N, Tapp HS, et al. Patterns of DNA methylation in individual colonic crypts reveal aging and cancer-related field defects in the morphologically normal mucosa. *Carcinogenesis* 2010; 31(6): 1158–1163.

38. Lian J, Ma L, Yang J, et al. Aberrant gene expression profile of unaffected colon mucosa from patients with unifocal colon polyp. *Med Sci Monit* 2015; 21: 3935–3940.

39. Genovese L, Zawada L, Tosoni A, et al. Cellular localization, invasion, and turnover are differently influenced by healthy and tumor-derived extracellular matrix. *Tissue Eng Part A* 2014; 20(13–14): 2005–2018.

CrossMark

Luminescence thermometry using $Gd_2Zr_2O_7$:Eu^{3+}

M. G. Nikolic[1] · M. S. Rabasovic[1] · J. Krizan[2] · S. Savic-Sevic[1] · M. D. Rabasovic[1] ·
B. P. Marinkovic[1] · A. Vlasic[1] · D. Sevic[1]

Abstract In this paper we study the possibility of using the synthesized nanopowder samples of $Gd_2Zr_2O_7$:Eu^{3+} for temperature measurements by analyzing the temperature effects on its photoluminescence. The nanopowder was prepared by solution combustion synthesis method. The photoluminescence spectra used for analysis of $Gd_2Zr_2O_7$:Eu^{3+} nano phosphor optical emission temperature dependence were acquired using continuous laser diode excitation at 405 nm. The temperature dependencies of line emission intensities of transitions from $^5D_0$ and $^5D_1$ energy levels to the ground state were analyzed. Based on this analysis we use the two lines intensity ratio method for temperature sensing. Our results show that the synthesized material can be efficiently used as thermographic phosphor up to 650 K.

1 Introduction

Phosphor thermometry is a non-contact technique that uses photoluminscence to remotely measure the temperature. Being a non-contact technique it has many advantages compared to conventional contact ones. Thermographic phosphors are materials that are synthesized in such a way that their structural stability regarding various parameters including the

---

✉ D. Sevic
  sevic@ipb.ac.rs

1 Institute of Physics Belgrade, University of Belgrade, Belgrade, Serbia

2 AMI d.o.o, Ptuj, Slovenia

temperature, pressure, magnetic field, electromagnetic radiation could be obtained. They typically consist of a ceramic host and rare-earth dopant. These materials are widely used in many applications. The temperature dependencies of their various luminescence characteristics are used for temperature sensing (Goss et al. 1989; Feist et al. 1999; Heyes 2009; Gentleman and Clarke 2004; Cates et al. 2002; Eldridge et al. 2012). The comprehensive reviews of the topic could be found in (Allison and Gillies 1997; Alden et al. 2011; Brites et al. 2012; Jaque and Vetrone 2012; Khalid and Kontis 2008). Study of luminescence sensing of temperature in pyrochlore zirconate materials could be found in (Gentleman and Clarke 2005).

This paper is extension of previous work regarding $Gd_2Zr_2O_7{:}Eu^{3+}$ nanopowder, presented in (Rabasovic et al. 2015). Recently, we have begun research of the potentials of using rare earth doped nano powders as temperature and high pressure sensors (Vlasic et al. 2018; Rabasovic et al. 2018). Europium doped nano powders are now investigated intensively for remote temperature sensing, using various hosts: TiO_2 (Nikolic et al. 2014), Gd_2O_3 (Nikolic et al. 2013), $YNbO_4$, (Đačanin et al. 2013, 2014), Lu_2O_3 (Lojpur et al. 2012), $Gd_2Ti_2O_7$ (Lojpur et al. 2016), $Sr_2CeO_4{:}Eu^{3+}$ (Vlasic et al. 2018), including references therein. Here, we study the possibility of using the synthesized nanopowder samples of $Gd_2Zr_2O_7{:}Eu^{3+}$ for temperature measurements. The analysis is based on two lines intensity ratio method for temperature sensing. To the best of our knowledge, this kind of a study of the thermographic potentials of $Gd_2Zr_2O_7{:}Eu^{3+}$ nanomaterial, prepared by simple and cost effective process, is firstly presented in this paper.

The studied nanopowder material was prepared by solution combustion synthesis (SCS) method and its structural characteristics were confirmed by SEM images and XRD analysis (Rabasovic et al. 2015). The $Gd_2Zr_2O_7{:}Eu^{3+}$ material received the renewed interest recently, regarding the infrared (Mitric et al. 2018) and Raman (Krizan et al. 2017) spectroscopy studies.

2 Experimental procedures

In our experiments luminescence of samples were measured both using pulsed and continuous excitation (Rabasovic et al. 2015). Pulsed excitation was necessary for lifetime measurements (Rabasovic et al. 2015). For temperature measurements using two lines intensity ratio we decided to use continuous excitation due to larger acquisition count rates compared to pulsed excitation.

The photoluminescence spectra used for analysis of $Gd_2Zr_2O_7{:}Eu^{3+}$ nano phosphor optical emission temperature dependence were acquired using continuous laser diode excitation at 405 nm and Ocean Optics spectrometer USB2000. The detailed explanation of the setup is provided in (Rabasovic et al. 2016). The structure of nanopowders was observed by high resolution scanning electron microscope (SEM) equipped with a high brightness Schottky Field Emission gun (FEGSEM, TESCAN) operating at 4 kV.

3 Results and discussion

The representative SEM image of our sample of $Gd_2Zr_2O_7{:}Eu^{3+}$ material is presented in Fig. 1. The detailed structural study, including the XRD, of the material from which our sample was taken is provided in (Rabasovic et al. 2015). The detailed time resolved

Fig. 1 SEM image of Gd$_2$Zr$_2$O$_7$:Eu^{3+} nano phosphor prepared by SCS method
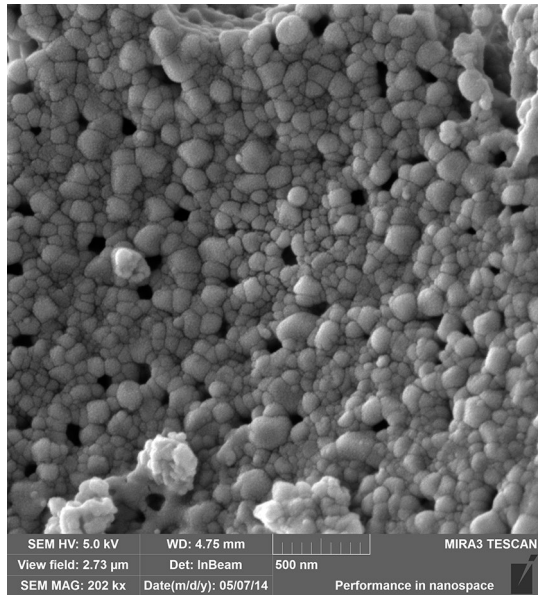
analysis of emission spectra under pulsed excitation is also provided in (Rabasovic et al. 2015). The obtained lifetimes from $^5D_0$ level are about 1.5 ms. XRD analysis confirmed that sample was crystallized in fluorite (F) type structure (space group Fm3m). The image of the synthesized material, see Fig. 1, shows the irregular crystallite size distribution. Particles with dimensions from 50 nm to over 100 nm are easily discernible. The agglomerated grains could be also noticed.

Photoluminescence spectra of Eu^{3+} doped Gd$_2$Zr$_2$O$_7$ were recorded over the temperature range 300–700 K, with a step of 20 K. In order to make the image clear, only spectra with the temperature distance of 100 K are displayed in Fig. 2. The emission band at 537 nm corresponds to $^5D_1 \rightarrow {}^7F_1$, the emission band at 553 nm corresponds to $^5D_1 \rightarrow {}^7F_2$, and the emission bands at 580, 592, 614 and 631 nm, 654 and 713 nm correspond to the

Fig. 2 Luminescence spectra of Eu^{3+} doped Gd$_2$Zr$_2$O$_7$ at several temperatures (continuous laser diode excitation at 405 nm)
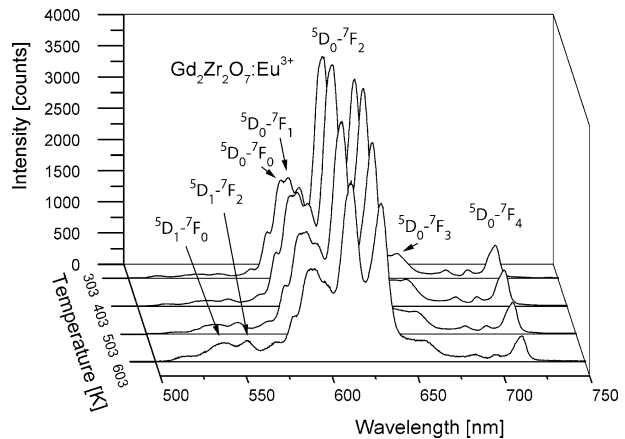
$^5D_0 \rightarrow {}^7F_1$, $^5D_0 \rightarrow {}^7F_2$, $^5D_0 \rightarrow {}^7F_3$, $^5D_0 \rightarrow {}^7F_4$ transitions of Eu3+ions, respectively. To minimize the effects of host luminescence we used excitation at 405 nm, where europium optical response to direct excitation is still good.

Fluorescence intensity ratio technique is based on monitoring the two emission lines in luminescence spectra of thermographic phosphors. The temperature is calculated by the emission intensity ratio of these two lines. Many problems regarding measuring errors, optical condition deviations and excitation power fluctuation are eliminated in this way. Two closely spaced energy levels of rare earth ion, which are thermally coupled, are usually selected for temperature sensing. Small energy gap between these two levels allows the upper level to be populated from the lower level by thermalization. The upper level becomes more populated as the temperature increases and hence the fluorescence from this level gradually increases. Relative population between two levels, *IR*, follows Boltzmann-type population distribution given by (Brites et al. 2012; Jaque and Vetrone 2012; Đačanin et al. 2014):

$$IR = \frac{I_{31}}{I_{21}} = C \exp\left(-\frac{E_{32}}{kT}\right) \tag{1}$$

where k is the Boltzmann constant, $k = 0.695\,034\,76(63)$ cm^{-1} K^{-1} and E_{32} is the energy gap between two excited levels.

However, in fluorescence measurements, instruments frequently detect small signals, even when there is no emission, because of detector dark currents, etc. Moreover, spectrograph stray light introduces error in measured intensity of a signal. Therefore, another constant, *A*, should be introduced to Eq. (1), to account for the finite value of *IR* at low temperatures (Lojpur et al. 2016):

$$IR = \frac{I_{31}}{I_{21}} = A + C \exp\left(-\frac{E_{32}}{kT}\right) \tag{2}$$

We have analyzed the temperature sensing calibration curves based on various combinations of ratios of measured intensities of two europium optical emission lines. The lines should be from different energy levels, of strong intensity and close proximity of their upper levels on energy diagram, so the thermalization effect will be effective. After preliminary analysis of all obtained spectra, the $^5D_1 \rightarrow {}^7F_2$ (553 nm) and $^5D_0 \rightarrow {}^7F_2$ (614 nm) transitions were selected to be used to obtain values in the intensity ratio method.

The dependences of $^5D_1 \rightarrow {}^7F_2$ and $^5D_0 \rightarrow {}^7F_2$ emission line intensities of Eu^{3+} doped Gd$_2$Zr$_2$O$_7$ as a function of temperature are shown in Fig. 3. We have used the band of about 2 nm to integrate areas of peaks, thus alleviating the various measurements problems. The intensity of the europium $^5D_1 \rightarrow {}^7F_2$ emission line slightly increases from 300 to 600 K and then decreases. The intensity of the $^5D_0 \rightarrow {}^7F_2$ emission line was reduced almost three times in the same temperature interval. Line intensity measurements are sensitive, regarding errors, to variations of laser excitation power and light detection efficiency. Our repeated measurements (not presented for clarity purposes in Fig. 3) prove the good repeatability and very low hysteresis which is a good characteristic of this material for applicability in temperature measurement.

Temperature dependence of the intensity ratio of two Eu emission lines, at 553 and 614 nm, is shown in Fig. 4. Temperature sensing calibration curve was fitted using Eq. (2). Because of small signal intensity we discarded the measured points above 650 K. Calculated value for the energy gap, $E_{32} = 1787.9987$ cm^{-1}, is in good agreement with the europium energy level positions $E_{553} - E_{614} = 1746$ cm^{-1} (Dieke 1968; Binnemans 2015).

Fig. 3 Measured intensity-temperature dependencies of two Eu emission lines, at 553 and 614 nm, for Eu^{3+} doped Gd$_2$Zr$_2$O$_7$
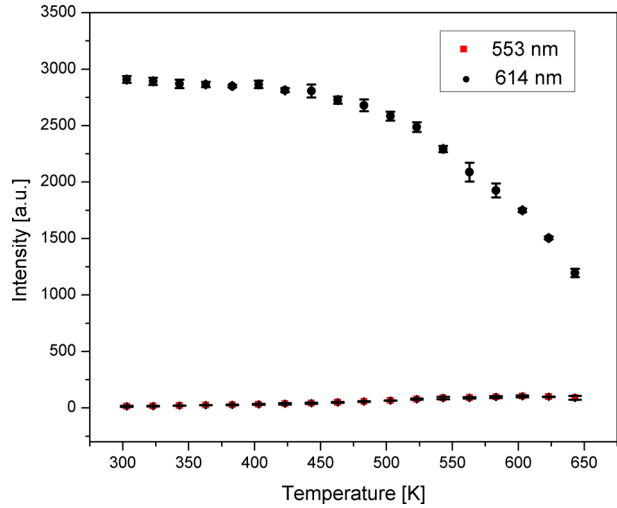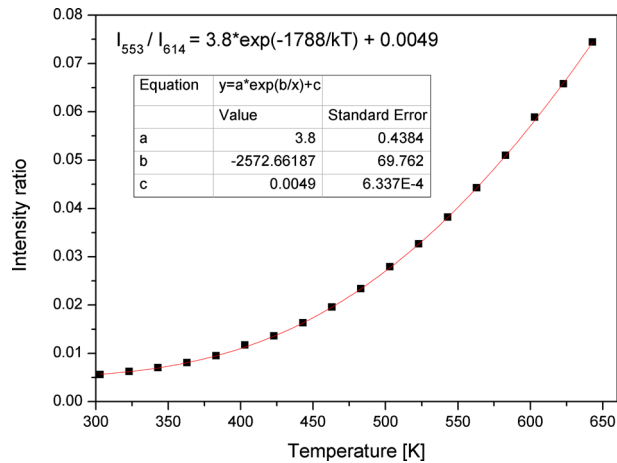

Fig. 4 Temperature dependence of the intensity ratio of two Eu emission lines, at 553 and 614 nm, for Eu^{3+} doped Gd$_2$Zr$_2$O$_7$. Experimental points are denoted by black squares and fitted temperature calibration curve is denoted by red line

The absolute thermal sensitivity, *S*, is defined as the rate at which *IR* changes with the temperature:

$$S = \left| \frac{dIR}{dT} \right| \tag{3}$$

The relative thermal sensitivity, *Sr*, is given by:

$$Sr = \left| \frac{1}{IR} \frac{dIR}{dT} \right| \tag{4}$$

Absolute sensitivity [calculated according to Eq. (3)] and relative sensitivity [calculated according to Eq. (4)] curves as the function of temperature are presented in Fig. 5. Relative sensitivity is highest around 425 K and its value is 0.92% K^{-1}, and is lowest value is about
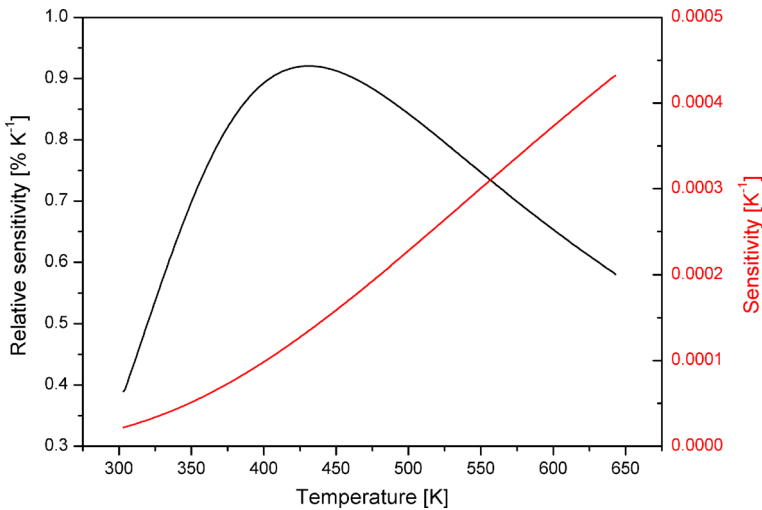
Fig. 5 Absolute and relative sensitivity curves as the function of temperature for Eu^{3+} doped $Gd_2Zr_2O_7$

0.4% K^{-1} at 303 K, proving that this material could be used as a good temperature sensor within the studied temperature range.

Table 1 shows comparison of temperature sensing characteristics of various hosts doped with Eu^{3+}. The relative sensitivity is much better indicator than absolute sensitivity for comparison purposes between various materials. Comparing temperature sensing characteristics of various hosts doped with europium, presented in Table 1, it is easy to notice that there is usual trade-off between the sensitivity and sensing range, so the optimal host could be selected based on desired sensing range.

Methods for temperature sensing based on fluorescence intensity ratio are not sensitive, regarding errors, to variations of laser excitation power and light detection efficiency (Alden et al. 2011). So, using the same line of reasoning as in (Vlasic et al. 2018) we conclude that measurement errors mostly originate from the fitting procedures and least-square errors in extracting the temperatures from the calibration curve (Alden et al. 2011). For presented measurements the relative errors are smaller than 5% in the whole measuring

Table 1 Comparison of temperature sensing characteristics of various hosts doped with Eu^{3+}

Host	Sensing range (K)	Rel. sensitivity (% K^{-1})		References
		Min	Max	
$Gd_2Zr_2O_7$	300–650	0.4	0.92	This work
Sr_2CeO_4	300–400	1	2.4	Vlasic et al. (2018)
$YNbO_4$	300–720	0.3	2.6	Đačanin et al. (2013), Đačanin et al. (2014)
Gd_2O_3	300–800	0.25	3.25	Nikolic et al. (2013)
Lu_2O_3	300–800	0.3	0.33	Lojpur et al. (2012)
$Gd_2Ti_2O_7$	300–420	0.3	0.95	Lojpur et al. (2016)
TiO_2	300–530	0.12	2.3	Nikolic et al. (2014)

range and bellow 2% for temperatures above 350 K. For used Ocean Optics spectrometer with 12 bit resolution, the estimated resolution of temperature measurements is about 7 K. However, aim of our work is to prove the concept of using the Gd$_2$Zr$_2$O$_7$:Eu^{3+} nanoposphor for thermometry. So, the estimated resolution of our measurements is, before all, the characteristics of our equipment, not of the analyzed phosphor.

4 Conclusion

In this paper we have analyzed the temperature effects on photoluminescence of nanopowder samples of Gd$_2$Zr$_2$O$_7$:Eu^{3+}. The nanopowder was prepared by solution combustion synthesis (SCS) method. After plotting and analyzing the temperature sensing calibration curves based on various combinations of two europium optical emission lines, we selected the spectral lines at 553 and 614 nm to be used for temperature measurements. Our results show that the synthesized material can be efficiently used as thermographic phosphor up to 650 K. Relative sensitivity is highest around 425 K and its value is 0.92% K^{-1}, its lowest value is about 0.4% K^{-1} at 303 K, and it is 0.76% K^{-1} at 643 K. Comparing these results with characteristics of other state-of-the-art materials, we prove that this material could be used as a good temperature sensor within the studied temperature range.

References

Alden, M., Omrane, A., Richter, M., Särner, G.: Thermographic phosphors for thermometry: a survey of combustion applications. Prog. Energy Combust. Sci. **37**, 422–461 (2011)

Allison, S.W., Gillies, G.T.: Remote thermometry with thermographic phosphors: instrumentation and applications. Rev. Sci. Instrum. **68**, 2615–2650 (1997)

Binnemans, K.: Interpretation of europium(III) spectra. Coord. Chem. Rev. **295**, 1–45 (2015)

Brites, C.D.S., Lima, P.P., Silva, N.J.O., Millan, A., Amaral, V.S., Palacio, F., Carlos, L.D.: Thermometry at the nanoscale. Nanoscale **4**, 4799–4829 (2012)

Cates, M.R., Allison, S.W., Jaiswal, S.L., Beshears, D.L.: YAG:Dy and YAG:Tm Fluorescence Above 1400 C. Oak Ridge National Laboratory, Report ORNL/TM-2002/71 (2002)

Dieke, G.H.: Spectra and Energy Levels of Rare Earth Ions in Crystals. Interscience Publishers, New York (1968)

Đačanin, L.R., Lukić-Petrović, S.R., Petrović, D.M., Nikolić, M.G., Dramićanin, M.D.: Temperature quenching of luminescence emission in Eu^{3+}- and Sm^{3+}-doped YNbO$_4$ powders. J. Lumin. **151**, 82–87 (2014)

Đačanin, L.R., Dramićanin, M.D., Lukić-Petrović, S.R., Petrović, D.M., Nikolić, M.G.: Eu^{3+} doped YNbO$_4$ phosphor properties for fluorescence thermometry. Radiat. Meas. **56**, 143–146 (2013)

Eldridge, J.I., Jenkins, T.P., Allison, S.W., Wolfe, D.E., Jordan, E.H.: Development of YAG:Dy thermographic phosphor coatings for turbine engine applications. In: 58th International Instrumentation Symposium San Diego, CA, June 5–8 (2012)

Feist, J.P., Heyes, A.L., Choy, K.L., Su, B.: Phosphor thermometry for high temperature gas turbine applications. In: Proceedings of IEEE; 6.1 (1999)

Gentleman, M.M., Clarke, D.R.: Concepts for luminescence sensing of thermal barrier coatings. Surf. Coat. Technol. **188–189**, 93–100 (2004)

Gentleman, M.M., Clarke, D.R.: Luminescence sensing of temperature in pyrochlore zirconate materials for thermal barrier coatings. Surf. Coat. Technol. **200**, 1264–1269 (2005)

Goss, L.P., Smith, A.A., Post, M.E.: Surface thermometry by laser-induced fluorescence. Rev. Sci. Instrum. **60**, 3702–3706 (1989)

Heyes, A.L.: On the design of phosphors for high-temperature thermometry. J. Lumin. **129**, 2004–2009 (2009)

Jaque, D., Vetrone, F.: Luminescence nanothermometry. Nanoscale **4**, 4301–4326 (2012)

Khalid, A.H., Kontis, K.: Thermographic phosphors for high temperature measurements: principles, current state of the art and recent applications. Sensors **8**, 5673–5774 (2008)

Krizan, G., Gilic, M., Ristic-Djurovic, J.L., Trajic, J., Romcevic, M., Krizan, J., Hadzic, B., Vasic, B., Romcevic, N.: Raman spectroscopy and electron-phonon coupling in Eu^{3+} doped $Gd_2Zr_2O_7$ nanopowders. Opt. Mater. **73**, 541–544 (2017)

Lojpur, V., Ćulubrk, S., Dramićanin, M.D.: Ratiometric luminescence thermometry with different combinations of emissions from Eu^{3+} doped $Gd_2Ti_2O_7$ nanoparticles. J. Lumin. **169**, 534–538 (2016)

Lojpur, V., Antic, Z., Krsmanovic, R., Medic, M., Nikolic, M.G., Dramićanin, M.D.: Thermographic properties of Eu^{3+} and Sm^{3+} doped Lu_2O_3 nanophosphor. J. Serb. Chem. Soc. **77**, 1735–1746 (2012)

Mitric, J., Krizan, J., Trajic, J., Krizan, G., Romcevic, M., Paunovic, N., Vasic, B., Romcevic, N.: Structural properties of Eu^{3+} doped $Gd_2Zr_2O_7$ nanopowders: far-infrared spectroscopy. Opt. Mater. **75**, 662–665 (2018)

Nikolic, M.G., Antic, Z., Culubrk, S., Nedeljkovic, J.M., Dramicanin, M.D.: Temperature sensing with Eu^{3+} doped TiO_2 nanoparticles Sens. Actuators B **201**, 46–50 (2014)

Nikolic, M.G., Al-Juboori, A.Z., Djordjevic, V., Dramicanin, M.D.: Temperature luminescence properties of Eu^{3+}-doped Gd_2O_3 phosphors. Phys. Scr. (2013). https://doi.org/10.1088/0031-8949/2013/T157/014056

Rabasovic, M.S., Krizan, J., Savic-Sevic, S., Mitric, M., Rabasovic, M.D, Marinkovic, B.P., Sevic, D.: Orange-reddish light emitting phosphor $GdVO_4:Sm^{3+}$ prepared by solution combustion synthesis (SCS). J. Spectrosc. (2018). https://doi.org/10.1155/2018/3413864

Rabasovic, M.D., Muric, B.D., Celebonovic, V., Mitric, M., Jelenkovic, B.M., Nikolic, M.G.: Luminescence thermometry via the two-dopant intensity ratio of $Y_2O_3:Er^{3+}$, Eu^{3+}. J. Phys. D Appl. Phys. (2016). https://doi.org/10.1088/0022-3727/49/48/485104

Rabasovic, M.S., Sevic, D., Krizan, J., Terzic, M., Mozina, J., Marinkovic, B.P., Savic-Sevic, S., Mitric, M., Rabasovic, M.D., Romcevic, N.: Characterization and luminescent properties of Eu^{3+} doped $Gd_2Zr_2O_7$ nanopowders. J. Alloys Compd **622**, 292–295 (2015)

Vlasic, A., Sevic, D., Rabasovic, M.S., Krizan, J., Savic-Sevic, S., Rabasovic, M.D., Mitric, M., Marinkovic, B.P., Nikolic, M.G.: Effects of temperature and pressure on luminescent properties of $Sr_2CeO_4:Eu^{3+}$ nanophosphor. J. Lumin. **199**, 285–292 (2018)

Check for updates

One-step synthesis of amino-functionalized up-converting NaYF$_4$:Yb,Er nanoparticles for *in vitro* cell imaging†

Lidija Mancic, [ID] *[a] Aleksandra Djukic-Vukovic, [ID] [b] Ivana Dinic,[c] Marko G. Nikolic,[d] Mihailo D. Rabasovic,[d] Aleksandar J. Krmpot,[d] Antonio M. L. M. Costa,[e] Bojan A. Marinkovic, [ID] [e] Ljiljana Mojovic[b] and Olivera Milosevic[a]

The emerging up-conversion nanoparticles (UCNPs) offer a wide range of biotechnology applications, from biomarkers and deep tissue imaging, to single molecule tracking and drug delivery. Their successful conjugation to biocompatible agents is crucial for specific molecules recognition and usually requires multiple steps which may lead to low reproducibility. Here, we report a simple and rapid one-step procedure for *in situ* synthesis of biocompatible amino-functionalized NaYF$_4$:Yb,Er UCNPs that could be used for NIR-driven fluorescence cell labeling. X-ray diffraction showed that UCNPs synthesized through chitosan-assisted solvothermal processing are monophasic and crystallize in a cubic α phase. Scanning and transmission electron microscopy revealed that the obtained crystals are spherical in shape with a mean diameter of 120 nm. Photoluminescence spectra indicated weaker green ($^2H_{11/2}$, $^4S_{3/2} \rightarrow {}^4I_{15/2}$) and stronger red emission ($^4F_{9/2} \rightarrow {}^4I_{15/2}$), as a result of enhanced non-radiative $^4I_{11/2} \rightarrow {}^4I_{13/2}$ Er^{3+} relaxation. The presence of chitosan groups at the surface of UCNPs was confirmed by Fourier transform infrared spectroscopy, thermogravimetry and X-ray photoelectron spectroscopy. This provides their enhanced internalization in cells, at low concentration of 10 μg ml^{-1}, without suppression of cell viability after 24 h of exposure. Furthermore, upon 980 nm laser irradiation, the amino-functionalized NaYF$_4$:Yb,Er UCNPs were successfully used *in vitro* for labeling of two human cell types, normal gingival and oral squamous cell carcinoma.

Introduction

Nanotechnology research in the last few decades has been driven by both technological and fundamental interests, in an effort to develop advanced multifunctional biomaterials for a broad range of applications. It has been shown already that functionalized inorganic nanoparticles could be used as theranostic nanoplatforms when grafting of drugs/antigens is successfully completed at their surface.[1,2] Particularly, tailored coupling of optically active lanthanide doped inorganic fluorides and oxides, that have the ability to convert long-

wavelength near infrared (NIR) excitation into shorter-wavelength emission of visible light (up-conversion, UC), with a variety of biomolecules, generates hybrid nanoparticles which possess superior bioimaging and therapeutic characteristics.[3,4] Compared with traditional fluorescent dyes, up-converting nanoparticles (UCNPs) offer several advantages, including excellent chemical and thermal stability, narrow-band emission, a large anti-Stokes shift and a long lifetime. The absence of photobleaching and blinking are other advantages that meet the requirements of background free detection in deeper tissues, as well as time-resolved imaging of morphological details from cells. Intrinsic optical properties of UCNPs originate from abundant energy states of lanthanide ions doped in a host matrix. The electron transitions between partially filled 4f orbitals which are effectively shielded by 5s and 5p are Laporte forbidden, so gaining of their intensity occurs through the mixing in higher electronic states of opposite parity, either by "vibronic coupling" or through the effect of a ligand field.[5] To enhance probability of radiative transitions, at least two lanthanide ions (sensitizer and activator) are usually doped in host material with a strong crystal field and low phonon energy (like oxides and fluorides). The UC goes on through following mechanisms: excited state absorption (ESA), energy transfer

[a] Institute of Technical Sciences of the Serbian Academy of Sciences and Arts, Belgrade, Serbia. E-mail: lidija.mancic@itn.sanu.ac.rs

[b] Department of Biochemical Engineering and Biotechnology, Faculty of Technology and Metallurgy, University of Belgrade, Serbia

[c] Innovation Center of the Faculty of Chemistry, University of Belgrade, Serbia

[d] Photonic Center, Institute of Physics Belgrade, University of Belgrade, Zemun, Belgrade, Serbia

[e] Department of Chemical and Materials Engineering, Pontifical Catholic University of Rio de Janeiro, Rio de Janeiro, Brazil

† Electronic supplementary information (ESI) available: Photostability, HRTEM/FFT and XPS analyses of the amino-functionalized UCNP. See DOI: 10.1039/c8ra04178d

(ET), photon avalanche (PA), cooperative energy transfer (CET) and energy migration-mediated up-conversion (EMU). For ET to occur, the excited energy levels of both ions must be resonant, and ions should be in close spatial proximity.[6] For instance, $^2F_{5/2}$ level of ytterbium resonates well with energy levels of erbium, thulium and holmium, so it is used as a very efficient sensitizer for achieving efficient UC in NaYF$_4$ host. In Yb^{3+}/Er^{3+} co-doped NaYF$_4$ nanoparticles, green (520 nm and 540 nm) and red (660 nm) emissions are most commonly observed under 980 nm excitation, while violet emission at 415 nm is usually weakened. The emission is dependent on dopants concentration and crystal arrangement of the NaYF$_4$ phase. In the structure of cubic α phase lanthanide and sodium ions occupy eight-coordinated cation site randomly, whilst in hexagonal β phase cation sites are of three types: a one-fold site occupied solely by lanthanides; a one-fold site occupied randomly by 1/2 lanthanides and 1/2 sodium; and a two-fold site occupied by sodium and vacancies stochastically.[7] As a result, green and red emissions are both prominent in the spectra of cubic phase, whereas green dominates in spectra of hexagonal one.

The rapid progress in development of different protocols which give rise to the synthesis of monodisperse lanthanide doped NaYF$_4$ UCNPs through decomposition of organometallic precursors, proposed initially by Mai et al.,[8] is replaced nowadays with studies devoted to in situ obtaining of biocompatible UCNPs.[9,10] This is due to the fact that synthesis from toxic organometallic, performed in an oxygen-free environment, must be followed by SiO$_2$ encapsulation, ligands exchange/oxidation or by coating with a biocompatible polymer towards achieving a demanded chemical functionality for conjugation of the targeting molecular moiety. Although well established, the reproducibility of multiple steps involved in such synthesis is not trivial, since toxicity of UCNPs produced throughout is not easily predictable.[11] In order to obtain physiologically stable NaYF$_4$:Yb^{3+}/Er^{3+} nanoparticles in situ, some biopolymers are already being used as surfactants during hydro/solvothermal synthesis. Wang et al.[12] were the first who reported a simple one-step approach for the synthesis of hydrophilic UCNPs which comprises polyethylenimine (PEI), polyacrylic acid (PAA), polyvinylpyrrolidone (PVP) and polyethylene glycol (PEG) usage during hydrothermal treatment. Many years later it was shown that such functionalized particles could be easily conjugated to folic acid, a commonly used cancer targeting agent, and then loaded with doxorubicin hydrochloride to achieve pH-responsive release at target cells.[13] Furthermore, PEGylated nanoparticles of α-NaYF$_4$:Yb,Er, prepared under the cooperative influence of two ligands, demonstrated low cytotoxicity and excellent distribution in small animals.[14] Under the guidance of the same concept we have shown that PEG, PVP and EDTA capped NaYF$_4$:Yb,Er nano- and micro-particles could be easily obtained in a controlled manner through tuning of hydro/solvothermal processing conditions.[15,16]

In this study, amino-functionalized NaYF$_4$:Yb,Er nanoparticles with a high degree of size uniformity and efficient up-conversion were prepared through solvothermal treating of rare earth nitrates in the presence of chitosan (CS). Chitosan is a linear polysaccharide composed of randomly distributed β-linked D-glucosamine and N-acetyl-D-glucosamine. Inter-dispersed acetamido groups, as well as an abundance of external –NH$_2$ and –OH functional groups offer excellent biocompatibility and bio-reactivity, making it to be one of the most valuable polymer for medical and pharmaceutical applications. It is widely used today in encapsulation and controlled delivery of drugs, wound dressing, construction of contact lenses and artificial skin substitutes.[17,18] An immense array of depicted benefits was recently complemented with its prominent antitumor activity.[19] Lately, several reports related to chitosan coupling to inorganic UCNPs were also reported. Thus, an effective coating of DMSA-modified NaYF$_4$:Yb/Er UC with folic acid–chitosan conjugates was achieved through a robust approach which comprised covalent bonding of amine groups with carboxyl groups located at particle surface.[20] Besides, amphiphilic N-succinyl-N'-octyl chitosan modified UCNPs coupled with Zn(II)-phthalocyanine photosensitizer, in form of novel drug delivery system, ZnPc-loaded SOC-UCNPs, demonstrated promising potential for NIR triggered photodynamic therapy of human breast adenocarcinoma.[21] More recent studies shown that quaternized chitosan hydrogels incorporated with NaYF$_4$:Er/Yb/Mn@photosensitizer-doped silica could be used for effective killing of both Gram-positive and Gram-negative bacteria,[22] whilst spherical chitosan–NaYF$_4$:Yb^{3+}/Tm^{3+} composite beads have excellent drug loading capacity and release performance upon near-infrared (NIR) laser irradiation.[23] Although presented results provide evidence of the significant therapeutic effects, all of aforementioned hybrid UCNPs were actually obtained through multiple steps. It is worth noting that there is only one report, as far as the authors are aware of, on the usages of O-carboxymethyl chitosan during solvothermal preparation of NaYF$_4$:Yb^{3+}/Tm^{3+}/Er^{3+} nanoparticles (UCNPs@OCMC), but successful staining of the HeLa cancer cells was achieved only after additional bio-conjugation of synthesized UCNPs@OCMC with folic acid.[24]

Hence, the main goal of the present study is in situ synthesis of chitosan functionalized NaYF$_4$:Yb,Er nanoparticles capable of transforming continual NIR radiation into visible light and their successful utilization in visualization of the oral squamous cell carcinoma (OSCC). OSCC is the most common malignant tumor of the head and neck. Its incidence has increased in the recent years, thus development of a new contrast-enhanced agent useful for its detection at an early stage is essential. The potential cytotoxicity of the as-obtained UCNPs synthesized in this study was additionally tested against human gingival cells (HGC) isolated from healthy gingival tissue.

Materials and methods

Reagents and materials

Chitosan (low molecular weight, 50 000–190 000 Da), sodium fluoride (NaF, 99.99%), yttrium(III) nitrate hexahydrate (Y(NO$_3$)$_3$x6H$_2$O, 99.9%), ytterbium(III) nitrate pentahydrate (Yb(NO$_3$)$_3$x5H$_2$O, 99.9%), erbium(III) nitrate pentahydrate (Er(NO$_3$)$_3$x5H$_2$O,99.9%), anhydrous ethylene glycol (C$_2$H$_6$O$_2$, 99.8%), phosphate-buffered saline (PBS), fetal bovine serum (FBS), dimethyl sulfoxide (DMSO), Dulbecco's Modified Eagle

Medium (DMEM), penicillin–streptomycin (100 U ml^{-1}), 3-(4,5-dimethylthiazol-2-yl)-2,5 diphenyltetrazolium bromide (MTT, 0.5 mg ml^{-1}), paraformaldehyde (PFA) and Mowiol were all purchased from Sigma-Aldrich, St. Louis, USA. TrypLE Express enzyme, Gibco™ Dulbecco's modified Eagle's F12 medium (D-MEM/F12) and antibiotic/antimycotic solution (ABAM, 1%) were bought from Thermo Fisher Scientific. Deionized water was used throughout the experiments.

Synthesis of amino modified NaYF$_4$:Yb,Er

Monodispersed NaY$_{0.8}$Yb$_{0.17}$Er$_{0.03}$F$_4$ nanoparticles were synthesized using facile one-pot solvothermal synthesis. Stoichiometrically defined amounts of rare earth nitrates (5 mmol in total) were dissolved initially in 10 ml of water and then added to a chitosan solution (0.1 g CS in 15 ml of water). Obtained clear solution was then gradually dropped into NaF solution (1.75-fold excess, 10 ml) and mixed further with 35 ml of ethylene glycol (EG). Stirring of the mixture is performed until homogeneous transparent solution was obtained at pH = 4, then transferred into a 100 ml Teflon-lined stainless steel autoclave and sealed. Solvothermal treating was carried out at temperature of 200 °C (2 h) with a slow continual stirring (~100 rpm). Afterwards, the autoclave was cooled to room temperature, the precipitate were centrifuged at 8000 rpm and then washed with ethanol three times. The as-obtained white powder was dried at 60 °C for 2 h.

Characterization of amino-functionalized NaYF$_4$:Yb,Er

Structural and morphological characteristics of amino-functionalized NaYF$_4$:Yb,Er powder were obtained through the X-ray powder diffraction (XRPD), scanning and transmission electron microscopy (JEOL JSM-6701F SEM and JEOL JEM 2010 TEM), Fourier transform infrared spectroscopy (FTIR, Thermo Scientific Nicolet 6700 with a Smart iTR Diamond Attenuated Total Reflectance accessory) and thermogravimetric analysis (Perkin-Elmer Simultaneous Thermal Analyzer, STA 6000). The XRPD pattern was recorded using Bruker D8 Discovery equipped with a Cu-Kα source ($\lambda = 1.5406$ Å) with a step scan of 0.02° and accounting time of 5 s per step. Structure refinement was done in Topas 4.2 software[25] using a fundamental parameter approach. The background was refined using a fifth-order Chebyshev polynomial. Refinement of the cubic phase was carried out in Fm-3m (no. 225) space group, starting from ICSD 60257 data. Isotropic size-strain analysis was performed using a predefined double-Voigt approach (volume weighted mean column height, FWHM based LVol). Due to the observed preferential orientation, the spherical harmonic formulation, also referred as "orientation distribution function", is included in fitting of diffraction lines intensities. The size, shape and chemical purity of the nanoparticles were determined by SEM coupled with energy dispersive spectroscopy (EDS). The Sem-Afore 5.21 JEOL software was used to construct histogram of particle size from backscatter SEM images presenting more than 300 particles. Dynamic light scattering measurements of hydrodynamic radius (R_H) were performed on a Malvern Zetasizer Nano ZS in the de-ionized water and medium used for

testing of the cell viability and imaging. For that purpose UCNPs were dispersed at the concentration of 1 mg ml^{-1} and passed through a 0.45 μm cellulose syringe filter before DLS measurements. For TEM analysis nanoparticles were sonicated 20 min in isopropyl alcohol and dropped directly on lacey carbon film supported on a Cu grid. Confirmation of the crystal structure was carried out using selected area electron diffraction (SAED) and Fourier processing in Digital Micrograph 3.7.4 (Gatan Inc.) software. Presence of the chitosan ligands on the nanoparticles surface was investigated by FTIR, TG and XPS analyses. FTIR spectrum was recorded using typically 128 scans at the resolution of 4 cm^{-1}. TGA was conducted in nitrogen flux (100 ml min^{-1}) in the temperature range between 30 and 730 °C, applying a heating rate of 5 °C min^{-1}. XPS was carried out using an Alpha 100 hemispherical analyser from VG thermo and the K_α line from Mg (1486.6 eV) radiation. Photoluminescence spectrum was recorded at room temperature using Spex Fluorolog with C31034 cooled photomultiplier under diode laser excitation at 980 nm, and based on it CIE chromaticity coordinates were calculated.

OSCC and HGC cultures

Healthy gingival and tumor tissues were obtained from the patients at the Clinic of Maxillofacial Surgery of School of Dental Medicine, University of Belgrade immediately after surgical procedure. Signed informed consent approval from each patient was assured prior to participation in this study. Experiments were authorized by the Ethical Committee of the School of Dental Medicine, University of Belgrade (resolution 36/31).

Tumor cell lines were derived from tumor tissue taken from localized squamous cell carcinoma of the oral tongue. Preparation of the cell culture was performed using slightly modified procedure of Pozzi et al.[26] Briefly, DMEM supplemented with 20% fetal bovine serum (FBS) and 100 U ml^{-1} penicillin–streptomycin was used for tissue transport. The cells isolated from minced tissue were seeded onto T25 cell culture flasks and grown in DMEM supplemented with 10% FBS and 100 U ml^{-1} penicillin–streptomycin. Incubation was performed at 37 °C in a humidified atmosphere of 5% CO$_2$. The medium was changed thrice weekly and cells were passaged prior to reaching 80% confluence. To avoid fibroblast contamination, brief exposure to TrypLE Express (Thermo Fisher Scientific, Waltham, USA) was performed. OSCC used in this study were obtained after the third passage.

Human gingival tissues were obtained from three different, healthy patients, aged 19–25 years, during extraction of the impacted third molar. The gingival tissue was transported in Gibco™ D-MEM/F12 supplemented with 20% FBS and 1% ABAM solution. The gingival tissue was rinsed in PBS and subjected to outgrowth isolation method. Tissue was minced into approximately 1 mm^2 fragments, and placed in 25 cm^2 culture flasks with DMEM/F12 supplemented with 10% FBS and 1% ABAM. Incubation was performed at 37 °C in a humidified atmosphere of 5% CO$_2$. The cells were allowed to reach 80% confluence prior to passage. The medium was changed every 2–3 days. HGC used in this study were obtained after the second passage.

Cytotoxicity assay

MTT assays were carried out to evaluate the potential cytotoxicity of amino-functionalized NaYF$_4$:Yb,Er in both, HGC and OSCC. Cells were seeded into a 96-well cell culture plate at 10^4 per well and incubated at 37 °C in humidified 5% CO$_2$ atmosphere. Then, aseptically weighted UCNPs in concentrations of 10, 25 and 50 μg ml^{-1} were dispersed in sterile water by sonication (3 min). After 24 h hours of cells incubation 100 μl of UCNPs were added in each plate. Incubation of UCNPs with the cell cultures was stopped after 24 h by discarding of spent media, and medium containing MTT (0.5 mg ml^{-1}) was added to each well. After additional incubation for 4 h, supernatant was discarded and the precipitated formazan crystals were dissolved by DMSO (100 μl) under shaking at 37 °C for 20 min. Optical density was measured at 540 nm using ELISA microplate reader (enzyme-linked immunosorbent assay) RT-2100c, Rayto, China. Three wells without UCNPs were used as a control group. All experiments were performed in triplicate and repeated three times in the independent experiments. Cell viability, expressed by the ratio of absorbance of the cells incubated with UCNPs to that of the cells incubated with culture medium only, was given in diagram as the mean ± standard deviation (SD).

Cell imaging by laser scanning microscopy

For the visualization of UCNPs uptake by cells 10 μg ml^{-1} of sterile UCNPs suspension was filtered through 0.45 μm syringe filter to separate agglomerates that could provoke saturation during imaging. Sterilized 22 × 22 mm glass coverslips were placed in 6-well plates and 10^4 of cells were seeded per coverslip. Incubation was performed at 37 °C in humidified 5% CO$_2$ atmosphere. The next day cells were exposed to UCNPs and incubated for another 24 h. Coverslips with adherent cells were gently rinsed with fresh PBS twice and fixed with 4% PFA for 20 min. PFA residue was then washed by PBS (3 × 3 min), coverslips were dried, 10 μl of Mowiol was placed on fixed cells, and coverslips were placed on microscopic slides with cells positioned in between. Samples were stored in a dark until they were observed under laser scanning microscopy.

The homemade nonlinear laser scanning microscope used in this study was described in detail elsewhere.[27] The Ti:Sapphire laser (Coherent, Mira 900-F) was used as a laser light source operating either in femto-second (FS) pulse mode or continuous wave (CW) mode. FS mode at 730 nm was used for unlabeled cell imaging since it enables two photon excitation of cells auto-fluorescence. Please note that two-photon excitation is considered here as excitation of the molecule with no intermediate levels between ground and excited state and it is not related to UC process. From the other hand, 730 nm light do not interact with UCNPs. The CW radiation at 980 nm was used for the excitation of UCNPs in cells. Analogously to the previous case, CW 980 nm light cannot excite any other molecule except UCNPs. Due to the long UCNPs lifetime, the acquisition time at a single point has to be reduced during scanning in order to extend pixel dwell time. Hence, the pixel dwell time was several times longer than fluorescence lifetime. The laser focusing and

collection of the fluorescence during cell imaging were done using 40 × 1.3 oil immersion objective (Carl Zeiss, EC Plan-NEOFLUAR). A visible interference filter (415–685 nm) positioned in front of detector was used to remove scattered laser light. Thus, the whole visible range has been detected either for auto-fluorescence from cells or for up-conversion from amino-functionalized NaYF$_4$:Yb,Er UCNPs in cells.

Results and discussion

The morphology and size of amino-functionalized NaYF$_4$:Yb,Er UCNPs was evaluated by scanning electron microscopy (Fig. 1a). The SEM image showed that the as-obtained nanoparticles were spherical in shape, monodispersed and without obvious aggregation. Particle size varied between 50 and 200 nm and the bulk of the particles (>65%) are with diameter of 120 nm. The purity and expected chemical composition of the as-obtained NaYF$_4$:Yb,Er phase were confirmed by an energy dispersive spectrometer coupled to TEM, Fig. 1b. Based on the elemental analysis (inset at Fig. 1b), it is evident the presence of all constituting elements: sodium (Kα at 1.041), yttrium (Lα at 1.92 keV), ytterbium (Lα at 7.414 and Mα at 1.521 keV), erbium (Lα at 6.947 and Mα at 1.404 keV) and fluorine (Kα at 0.677). TEM/SAED analyses, Fig. 1c, showed a mixture of distinct spots and rings in the SAED pattern which correspond to d values of 3.119, 2.705, 1.923 and 1.104 Å and match fine with (111), (200), (220) and (423) crystal planes of the cubic α NaYF$_4$ phase (JCPDS 77-2042). Coexistence of much smaller crystallites of α phase at the UCNPs surface is evident from Fig. 1c and HRTEM/FFT images, Fig. S1.†

The XRPD pattern of the as-obtained sample was indexed to cubic α structure of NaYF$_4$:Yb,Er phase (JCPDS no. 77-2042, a = 5.47 Å, V = 163.67 Å), Fig. 1d. However, structural refinement confirmed the coexistence of two different particle populations (two NaYF$_4$:Yb,Er phases were used to adjust experimental pattern), both adopting the same Fm-$3m$ space group with a similar unit cell parameters (Å): a_1 = 5.51830(9) and a_2 = 5.53074(1), and a quite different crystallite size (nm): 84(4) and 12(1), respectively. Calculated crystallites sizes were in agreement with the size observed during TEM analysis. Small change of the refined unit cell volume (168.04 Å) might be due to the Yb^{3+} and Er^{3+} incorporation at Y^{3+} site. Occupation of 0.41(1) for Y^{3+} site, correlates well with the nominal NaY$_{0.8}$Yb$_{0.17}$Er$_{0.3}$F$_4$ composition (the value of 0.5 corresponds to the full occupation of the general site occupied by rare earths in the cubic NaYF$_4$ phase), whilst R_{Bragg} value of 5.7 confirmed good agreement between observed and computed patterns. The relevant information about Y^{3+} sites occupancy with rare earth ions in the phase with the smaller crystallite size were not acquired, due to the fact that better refinement was achieved when fixed values of occupation factor were used.

Hydrodynamic radius (R_H), polydispersity index (PDI) and stability of amino-functionalized NaYF$_4$:Yb,Er UCNPs colloids over time were estimated from dynamic light scattering measurements, Fig. 2. As one could see, the coexistence of different particle populations (one sized up to 30 nm and another bigger than 100 nm), indicated by TEM an XRPD
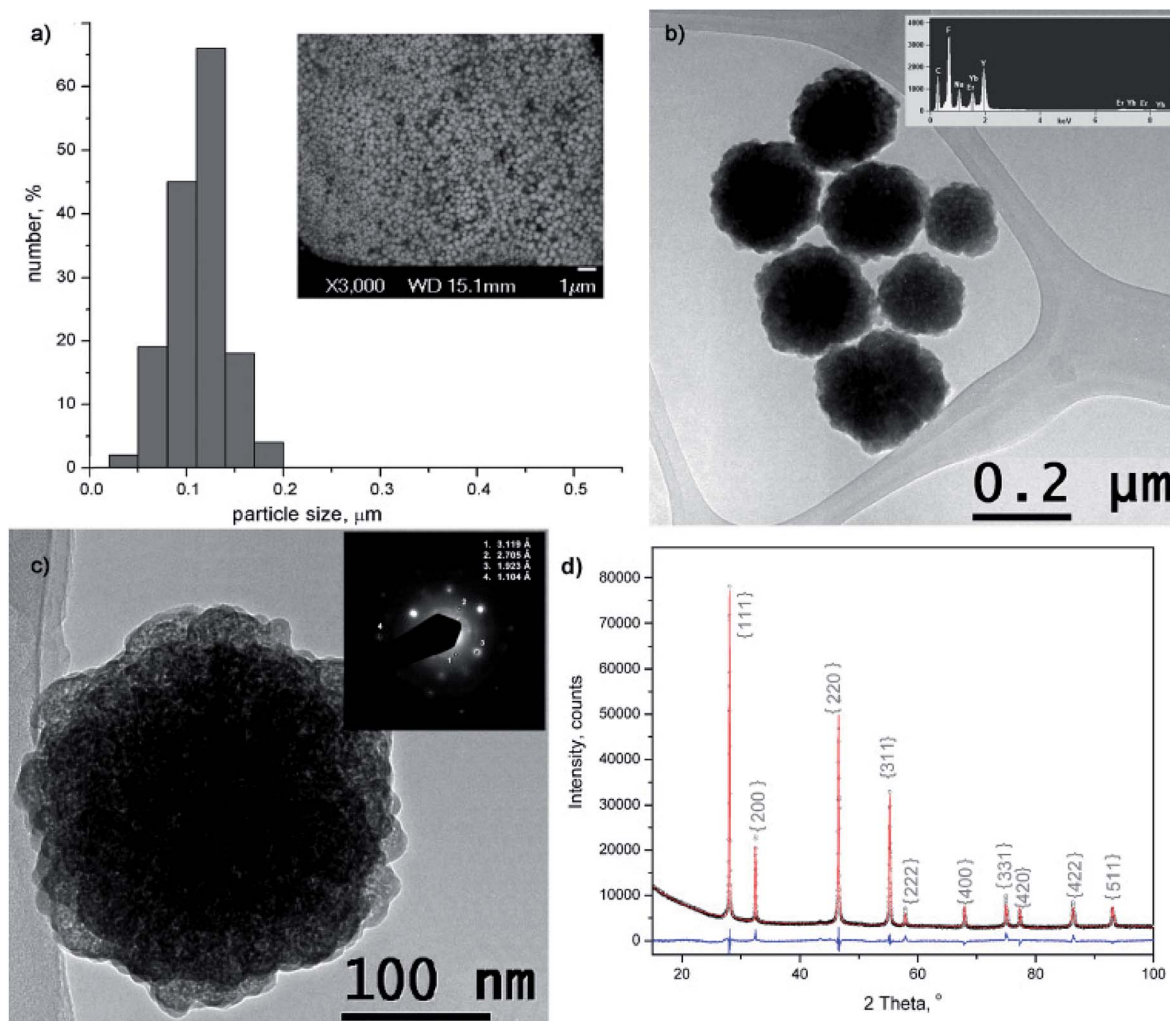
Fig. 1 Particle size distribution histogram (a) and TEM images (b and c) of amino-functionalized NaYF$_4$:Yb,Er UCNPs. Corresponding SEM, EDS, SAED and FFT were given as insets in (a), (b) and (c), respectively; XRPD pattern of amino-functionalized NaYF$_4$:Yb,Er (black), refined structure (red) and difference curve (blue) is presented in (d). Miller indices are indicated in {} by gray marks.

analysis is well preserved in medium solution over time confirming the long-term stability of this colloid (Fig. 2a). Since DLS measures actual particle size plus thickness of the strongly bounded solvent shell around particles, obtained average values are different (60 nm with PDI 1 in medium, and 311 nm with PDI 0.34 de-ionized water, respectively) than determined ones
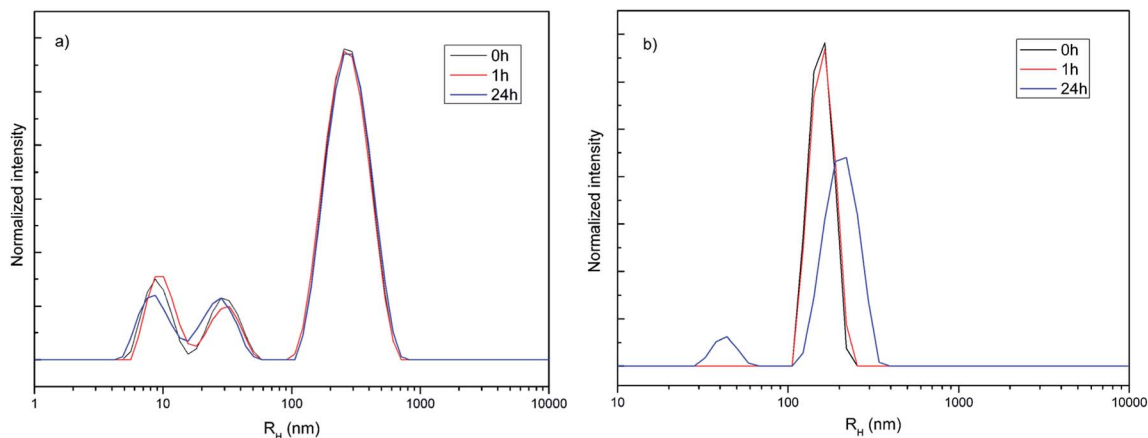
Fig. 2 Hydrodynamic radius distribution over time of amino-functionalized NaYF$_4$:Yb,Er UCNPs (1 mg ml^{-1}) in medium used for testing of cell viability and imaging (a) and deionized water (b).

from TEM images (120 nm). While average R_H and PDI of amino-functionalized NaYF$_4$:Yb,Er UCNPs in medium stay unchanged with time, slight increase of both parameters were detected after one hour (380 nm and PDI 0.4) in water (Fig. 2b). Decrease of R_H to 211 nm (PDI 0.34) after 24 h is observed and is due to appearance of a significant fraction of clusters (~50 nm) composed from nanoparticles sized up to 20 nm.

The successful *in situ* modification of the UCNPs surface with chitosan ligands was confirmed by FTIR spectroscopy (Fig. 3a). In accordance to the literature[28–30] observed bands in spectrum of pure chitosan were classified as follows: broad band in the range from 3500 to 3000 cm^{-1} is due to stretching vibration of OH groups, which partially overlaps stretching vibration of amine N–H; band at 2870.1 cm^{-1} is due stretching of C–H bond in –CH$_3$; band at 1651.7 cm^{-1} corresponds to vibrations of carbonyl bonds of the amide group CONHR (C=O stretching, secondary amide); band at 1587.1 cm^{-1} is due to protonated amine stretching; bands at 1417.9 cm^{-1} and 1374.1 cm^{-1} are due CH$_3$ and CH$_2$ bending vibrations; band at 1318.6 cm^{-1} is associated to the amide III (C–N stretching) and CH$_2$ wagging; band at 1149.8 cm^{-1} reflects asymmetric vibration of C–O group, whilst band at 1060.156 cm^{-1} is assigned to CO bending vibration of pyranose ring. The small band at 890 cm^{-1} corresponds to wagging of the saccharide structure of chitosan. The FTIR spectrum of the as-synthesized UCNPs showed a decrease in adsorption and slight shifting of chitosan related bands at: 3399.9 cm^{-1} (O–H and amine N^{3+}–H group stretching), 1651.7 cm^{-1} (C=O stretching), 1557 cm^{-1} (protonated amine stretching), 1373.5 cm^{-1} (CH$_2$ bending) and 1080.4 cm^{-1} (CO bending) implying their existence on the UCNPs surface. This confirmed that chitosan-assisted solvothermal synthesis of NaYF$_4$:Yb,Er was an effective way for *in situ* obtaining of biocompatible UCNPs.

The TGA also show chitosan presence at the UCNPs surface, Fig. 3b. TGA curve shows total weight loss of 9.5% in the temperature region from 30–730 °C. The initial weight loss of 2% (<200 °C) is ascribed to the dehydration of adsorbed moisture and possible ethanol impurity, whilst the more intense loss of 7.5% at higher temperatures is, predominantly, due to the

vaporization of the chitosan groups present on the UCNPs surface. In accordance to literature, the thermal degradation of chitosan in nitrogen is an one-step reaction which starts at 326.8 °C.[31] Meanwhile, a total mass loss of *ca.* 2–4% has been reported for bare NaYF$_4$:Yb,R (R: Pr, Nd, Sm, Eu, Tb, Dy or Er) UCNPs owning to the removal of water, ethanol and slow evaporation of NaF in the same temperature range.[32,33]

XPS analysis was also used to verify surface chemical composition of the amino-functionalized NaYF$_4$:Yb,Er UCNPs. All of the lanthanide elements, as well as, Na, F, C, N and O are detected in XPS spectrum, Fig.S2.† The peak at 1073.5 eV is assigned to the binding energy of Na 1s; peaks at 160.96, 174.29 and 185.72 eV were assigned to the binding energies of Y 3d, Er 4d and Yb 4d respectively; and peak at 685.71 eV is related to F 1s.[34,35] Peaks of C 1s, O 1s and N 1s were further decomposed in the fine-scan mode to confirm the bonding of chitosan at the NaYF$_4$:Yb,Er UCNPs surface. The C 1s peak showed three components: at 284.8 eV, typical of carbon bonding to carbon and hydrogen [C–(C,N)]; at 282.92 eV due carbon bonding to oxygen or nitrogen [C–(O,N)]; and at 286.59 eV typical for acetal or amide group [O–C–O, N–C=O]. The O 1s contributions at 532.70 and 531.4 eV were due to oxygen of the polysaccharide backbone and amide respectively.[36] The first two N 1s contributions at 399.71 and 397.9 eV confirm coexistence of the non-protonated and protonated amine groups, implying that approximately half of chitosan terminal amine groups are covalently bounded at UCNPs surface.

The up-conversion luminescence spectra of the amino-functionalized NaYF$_4$:Yb,Er UCNPs is given at Fig. 4a. It can be split into two emission segments, a green region of 520–550 nm and a red region of 630–690 nm, attributed to $^4S_{3/2} \rightarrow$ $^4I_{15/2}$ and $^4F_{9/2} \rightarrow$ $^4I_{15/2}$ transitions of Er^{3+} ions, respectively. According to energy transfer and relaxation pathways depicted at the energy level diagram of the Er^{3+}–Yb^{3+} couple (Fig. 4b), both were determined by the non-radiative decay from $^4F_{7/2}$ excited state.

Upon the 980 nm excitation, Yb^{3+} absorbs energy and promotes $^2F_{7/2} \rightarrow$ $^2F_{5/2}$ transitions. Afterward, it resonantly transfers the energy to the $^4I_{11/2}$ state of the neighbouring Er^{3+} ion. The $^4I_{11/2}$
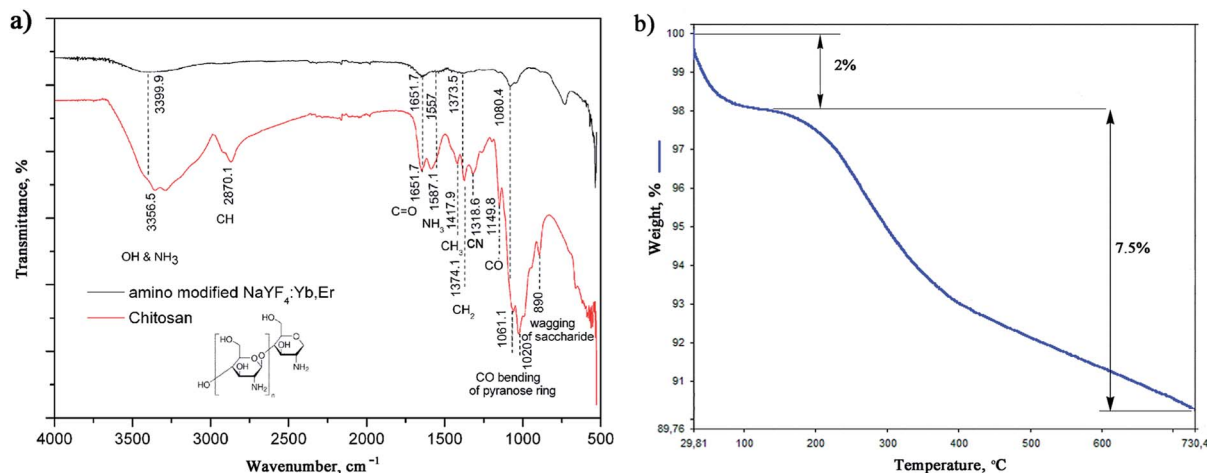

Fig. 3 FTIR of chitosan and amino-functionalized NaYF$_4$:Yb,Er (a) TGA of amino-functionalized NaYF$_4$:Yb,Er UCNPs (b).
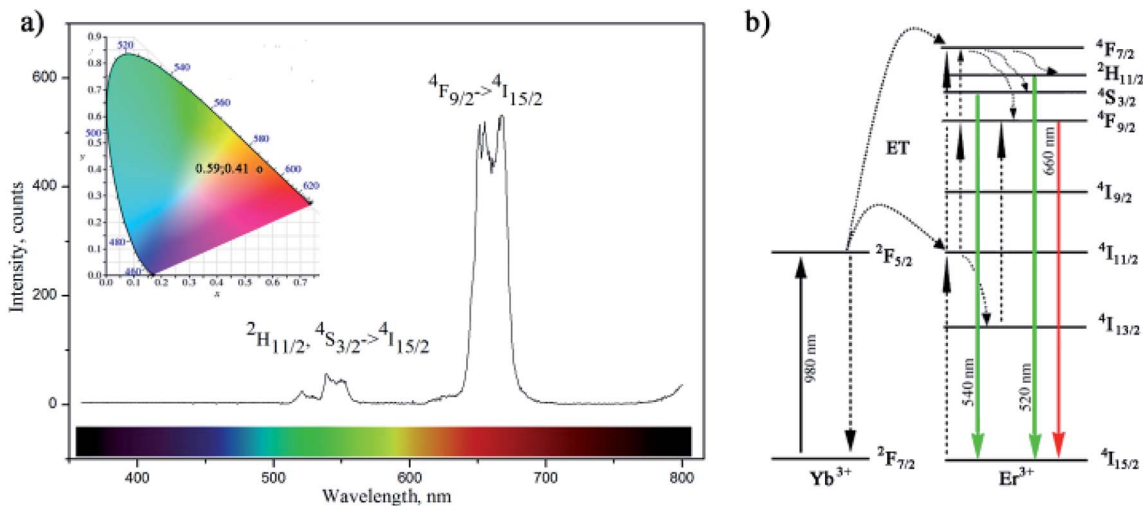
Fig. 4 Up-conversion luminescence of amino-functionalized NaYF$_4$:Yb,Er UCNPs upon excitation at 980 nm with corresponding CIE diagram given as inset (a) and energy level diagram of the Er^{3+}–Yb^{3+} couple (b).

level of Er^{3+} ion can be also populated by direct excitation of Er^{3+} ion from its $^4I_{15/2}$ ground state. Thus, the higher excited states of Er^{3+}, $^4F_{7/2}$ and $^4F_{9/2}$, will be further populated either through energy transfer from another excited Er^{3+} ion which is in close proximity, or through a two-step energy transfer from Yb^{3+} to the neighbouring Er^{3+} ions. The populated $^4F_{7/2}$ level of Er^{3+} then relaxes non-radiatively to the $^2H_{11/2}$ and $^4S_{3/2}$ levels, and further radiatively to the ground $^4I_{15/2}$ state generating green emissions at 520 nm ($^2H_{11/2} \rightarrow ^4I_{15/2}$) and 540 nm ($^4S_{3/2} \rightarrow ^4I_{15/2}$). Meanwhile, red emission appears due to the $^4F_{9/2} \rightarrow ^4I_{15/2}$ de-excitation, which could be additionally intensified by the non-radiative $^4F_{7/2} \rightarrow ^4F_{9/2}$ relaxation. Therefore, green and red emissions were obtained simultaneously through two-photon UC processes. Furthermore, due to the enhanced non-radiative relaxation of $^4I_{11/2} \rightarrow ^4I_{13/2}$ in nanocrystals[16,31] which proceeds to the direct population of $^4F_{9/2}$ level emission of red/orange light (defined by CIE 0.59, 0.41) was observed by bare eyes at room temperature. Photostability of amino-functionalized up-converting NaYF$_4$:Yb,Er nanoparticles emission was also traced during 1 h, Fig. S3.† As one could see at Fig. S3,† exceptionally stable UC luminescence signal was recorded.

The viability of OSCC and HGC following 24 h incubation with the amino-functionalized NaYF$_4$:Yb,Er UCNPs, expressed in terms of percentages evaluated through comparison to the number of surviving cells in the control group, was determined by MTT assay (Fig. 5). One could see that viability of HGC was highly preserved after 24 h exposure, being above 90% for all examined concentrations of UCNPs. However, viability of OSCC was found variable with the increase of UCNPs concentrations. Only in the case of the lowest concentration non-significant cytotoxicity (i.e. viability of 98%) was detected, whilst at higher UCNPs concentrations noteworthy cytotoxicity was observed, as reflected in a concentration dependent decrease in the percentage of viable cells up to the value of 66% for 50 μg ml^{-1}. Previous study reported low cytotoxicity of the ZnPc-loaded SOC-UCNPs toward the adenocarcinoma cells for concentrations up to 200 μg ml^{-1}.[21] Also, insignificant

difference in HeLa carcinoma cell viability (∼85%) has been observed when the concentrations of UCNPs@OCMC went up to 200 μg ml^{-1}.[24] When compared with latter two, the results obtained in this study are unanticipated and indicate certain theranostic effect of amino-functionalized NaYF$_4$:Yb,Er UCNPs toward OSCC at much lower doses.

To monitor the intracellular uptake and non-specific cell labelling in vitro, 10 μg ml^{-1} of amino-functionalized NaYF$_4$:Yb,Er UCNPs were incubated with OSCC and HGC and after 24 h laser scanning microscopy was performed. Images of the OSCC are shown at Fig. 6, top row. Fig. 6a shows bright field image of the cell, a pseudo color image of the cell auto-fluorescence upon femto-second excitation at 730 nm is shown at Fig. 6b, whilst the pseudo color image of the amino-functionalized NaYF$_4$:Yb,Er UCNPs upon CW excitation at 980 nm is given in Fig. 6c.

Overlapping the last two images (Fig. 6d), revealed that the UCNPs (green fluorescence spots) are positioned inside the cell, mainly in the cytoplasmic area adjacent to the plasma membrane. Images of the HGCs are shown in bottom row of
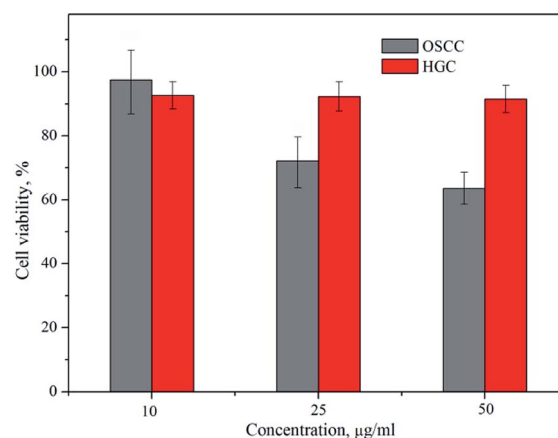

Fig. 5 Cytotoxicity assays of the amino-functionalized NaYF$_4$:Yb,Er UCNP in OSCC and HGC after 24 h exposure.
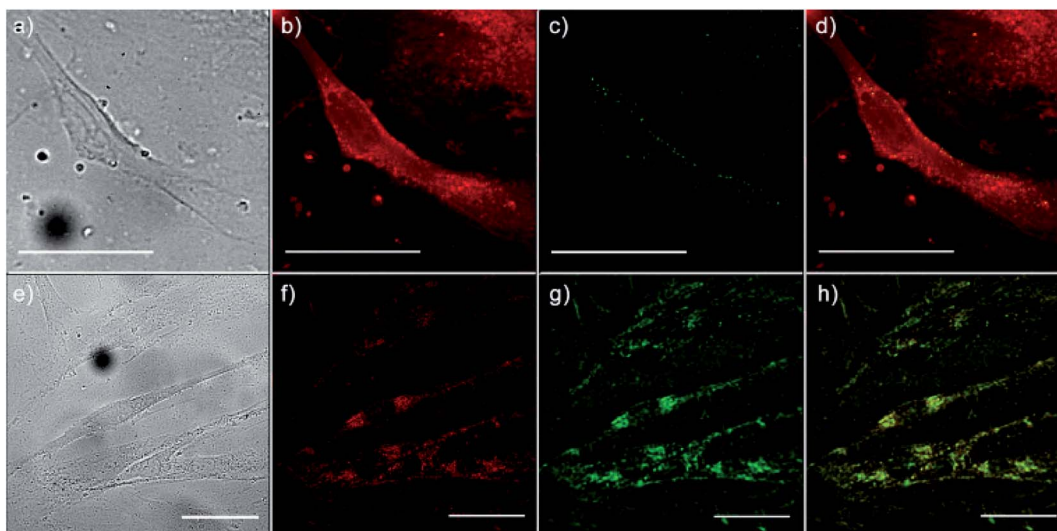
Fig. 6 Laser scanning microscopy images of OSCC (top row) and HGC (bottom row) following 24 h incubation with 10 μg ml^{-1} of amino-functionalized NaYF$_4$:Yb,Er UCNPs; bright field image of cells (a and e), cells auto-fluorescence upon femto-second excitation at 730 nm (b and f), image of the amino-functionalized NaYF$_4$:Yb,Er UCNPs upon CW excitation at 980 nm (c and g), and their positioning in cells, revealed through co-localization of the cell auto-fluorescence and the UCNPs emission (d and h); the scale bars correspond to 50 μm.

Fig. 6 following the same scanning procedure. As in a previous case, successful internalization of UCNPs in the cytoplasmic region of cells was achieved without disturbing cell nuclei. Since no auto-fluorescence was observed from cells upon NIR excitation (Figs. 6c and g), successful cells visualization with UCNPs demonstrated the possibility of utilizing the amino-functionalized NaYF$_4$:Yb,Er nanoparticles for nonspecific cell labelling. Furthermore, abundance of the chitosan ligands present at their surface (particularly amino groups), make them accessible for further conjugation with anti-cancer drugs, monoclonal antibodies or photosensitizes towards developing of specific theranostic agents.[37] As it is pointed out before, in prior studies which involved UCNPs surface modification with chitosan, multistep procedures were used to achieve the benefits of both, biocompatibility and near-infrared triggered up-conversion in cells. We believe that facile approach presented in this study may be extended to the synthesis of UCNPs with other biocompatible ligands too, raising at that way their potential use in biomedicine.

Conclusions

Monodisperse, hydrophilic and biocompatible NaYF$_4$:Yb,Er UCNPs were synthesized *in situ* using chitosan-assisted solvothermal synthesis. Spherical particles sized around 120 nm contain a single crystal structure of a cubic α phase (*Fm-3m*) and emit intense orange light (CIE 0.59, 0.41) upon 980 nm laser excitation. Due to the presence of amino functional groups at their surface, NaYF$_4$:Yb,Er UCNPs presented suitable properties for application in non-specific *in vitro* cell labelling. The superior biocompatibility detected toward normal human gingival cells with regard to oral squamous cell carcinoma, under similar cellular internalization, indicates their great potential in diagnostic and cancer therapy, particularly in a deeper tissue up to the penetration depth of NIR light.

Conflicts of interest

There are no conflicts of interest to declare.

Acknowledgements

References

1 Z. Yaari, D. da Silva, A. Zinger, E. Goldman, A. Kajal, R. Tshuva, E. Barak, N. Dahan, D. Hershkovitz, M. Goldfeder, J. Shainsky Roitman and A. Schroeder, *Nat. Commun.*, 2016, **7**, 13325.

2 Y. Chen, H. Zhang, X. Cai, J. Ji, S. He and G. Zhai, *RSC Adv.*, 2016, **6**, 92073–92091.

3 F. Zhang, *Photon Upconversion Nanomaterials*, Springer-Verlag Berlin Heidelberg, 2015.

4 D. Li, W.-Y. Lai, Q. Shao and W. Huang, *RSC Adv.*, 2017, **7**, 11491–11495.

5 S. Cotton, *Lanthanide and Actinide Chemistry*, John Wiley & Sons, Inc., 2006.

6 D. J. Naczynski, M. C. Tan, R. E. Riman and P. V. Moghe, *J. Mater. Chem. B*, 2014, **2**, 2958–2973.

7 H. Dong, L.-D. Sun and C.-H. Yan, *Chem. Soc. Rev.*, 2015, **44**, 1608–1634.

8 H.-X. Mai, Y.-W. Zhang, R. Si, Z.-G. Yan, L.-d. Sun, L.-P. You and C.-H. Yan, *J. Am. Chem. Soc.*, 2006, **128**, 6426–6436.

9 L. Grana-Suarez, W. Verboom, S. Sarkar, V. Mahalingam and J. Huskens, *ChemistrySelect*, 2016, **1**, 4068–4074.

10 Z. Zhang, X. Ma, Z. Geng, K. Wang and Z. Wang, *RSC Adv.*, 2015, **5**, 33999–34007.

11 A. Gautam and F. C. J. M. van Veggel, *J. Mater. Chem. B*, 2013, **1**, 5186–5200.

12 M. Wang, C.-C. Mi, J.-L. Liu, X.-L. Wu, Y.-X. Zhang, W. Hou, F. Li and S.-K. Xu, *J. Alloys Compd.*, 2009, **485**, L24–L27.

13 X. Liang, J. Fan, Y. Wang, Y. Zhao, R. Jin, T. Sun, M. Cheng and X. Wang, *J. Rare Earths*, 2017, **35**, 419–429.

14 T. Cao, Y. Yang, Y. Sun, Y. Wu, Y. Gao, W. Feng and F. Li, *Biomaterials*, 2013, **34**, 7127–7134.

15 I. Dinic, M. E. Rabanal, K. Yamamoto, Z. Tan, S. Ohara, L. T. Mancic and O. B. Milosevic, *Adv. Powder Technol.*, 2016, **27**, 845–853.

16 I. Dinic, S. Ohara, T. Koji, M. E. Rabanal, A. M. Costa, B. A. Marinkovic, L. Mancic and O. Milosevic, *Adv. Powder Technol.*, 2017, **28**, 73–82.

17 M. N. V. R. Kumar, *React. Funct. Polym.*, 2000, **46**, 1–27.

18 F. Croisier and C. Jérôme, *Eur. Polym. J.*, 2013, **49**, 780–792.

19 L. Gibot, S. Chabaud, S. Bouhout, S. Bolduc, F. A. Auger and V. J. Moulin, *Int. J. Biol. Macromol.*, 2015, **72**, 370–379.

20 Q. Chen, X. Wang, F. Chen, Q. Zhang, B. Dong, H. Yang, G. Liu and Y. Zhu, *J. Mater. Chem.*, 2011, **21**, 7661–7667.

21 S. Cui, H. Chen, H. Zhu, J. Tian, X. Chi, Z. Qian, S. Achilefu and Y. Gu, *J. Mater. Chem.*, 2012, **22**, 4861–4873.

22 M. Yin, Z. Li, L. Zhou, K. Dong, J. Ren and X. Qu, *Nanotechnology*, 2016, **27**, 125601.

23 H. Yan, X. Chen, J. Shi, Z. Shi, W. Sun, Q. Lin, X. Wang and Z. Dai, *Mater. Sci. Eng., C*, 2017, **71**, 51–59.

24 L. Hao and L. Y. Wang, *Chin. Sci. Bull.*, 2013, **58**, 4051–4056.

25 TOPAS, *General Profile and Structure Analysis Software for Powder Diffraction Data, V4.2*, Bruker AXS GmbH, Karlsruhe, Germany.

26 V. Pozzi, D. Sartini, R. Rocchetti, A. Santarelli, C. Rubini, S. Morganti, R. Giuliante, S. Calabrese, G. Di Ruscio, F. Orlando, M. Provinciali, F. Saccucci, L. Lo Muzio and M. Emanuelli, *Cell. Physiol. Biochem.*, 2015, **36**, 784–798.

27 K. Bukara, S. Jovanic, I. T. Drvenica, A. Stancic, V. Ilic, M. D. Rabasovic, D. Pantelic, B. Jelenkovic, B. Bugarski and A. J. Krmpot, *J. Biomed. Opt.*, 2017, **22**, 026003.

28 I. A. Latif, H. M. Abdullah and M. Hameed Saleem, *Am. J. Polym. Sci.*, 2016, **6**, 50–57.

29 S. M. L. Silva, C. R. C. Braga, M. V. L. Fook, C. M. O. Raposo, L. H. Carvalho and E. L. Canedo, in *Infrared spectroscopy – Material Science, Engineering and Technology*, ed. T. Theophile, InTechOpen, 2012, pp. 44–61.

30 Y. Yang, J. Cui, M. Zheng, C. Hu, S. Tan, Y. Xiao, Q. Yang and Y. Liu, *Chem. Commun.*, 2012, **48**, 380–382.

31 P.-Z. Hong, S.-D. Li, C.-Y. Ou, C.-P. Li, L. Yang and C.-H. Zhang, *Appl. Polym. Sci.*, 2007, **105**, 547–551.

32 T. Laihinen, M. Lastusaari, L. Pihlgren, L. C. V. Rodrigues and J. Hölsä, *J. Therm. Anal. Calorim.*, 2015, **121**, 37–43.

33 J. Hölsä, T. Laamanen, T. Laihinen, M. Lastusaari, L. Pihlgren and C. V. Rodrigues, *Opt. Mater.*, 2014, **6**, 1627–1630.

34 H. Guo, Z. Li, H. Qian, Y. Hu and I. N. Muhammad, *Nanotechnology*, 2010, **21**, 125602.

35 M. Ding, D. Chen, S. Yin, Z. Ji, J. Zhong, Y. Ni, C. Lu and Z. Xu, *Sci. Rep.*, 2015, **5**, 12745.

36 H. Maachou, M. J. Genet, D. Aliouche, C. C. Dupont-Gillain and P. G. Rouxhet, *Surf. Interface Anal.*, 2013, **45**, 1088–1097.

37 A. Zhou, Y. Wei, B. Wu, Q. Chena and D. Xing, *Mol. Pharmaceutics*, 2012, **9**, 1580–1589.

Characterization of Neodymium Doped Calcium Tungstate Single Crystal by Raman, IR and Luminescence Spectroscopy

Rouaida Mohamed Abozaid[1], Zorica Ž. Lazarević[2*)], Vesna Radojević[1], Maja S. Rabasović[2], Dragutin Šević[2], Mihailo D. Rabasović[2], Nebojša Ž. Romčević[2]

[1]Faculty of Technology and Metallurgy, University of Belgrade, Belgrade, Serbia
[2]Institute of Physics, University of Belgrade, Pregrevica 118, Zemun, Belgrade, Serbia

Abstract:

The aim of the current work was to assess obtain a single crystal of calcium tungstate doped with neodymium - ($CaWO_4{:}Nd^{3+}$), and after that, the crystal was characterized with various spectroscopic methods. The single crystal was grown from the melt using the Czochralski method in air. By optimizing growth conditions, <001>-oriented $CaWO_4{:}Nd^{3+}$ crystalc up to 10 mm in diameter were grown. Number of dislocations in obtained crystal was 10^2 per cm^2. Micro hardness was measured with the Vickers pyramid. Anisotropy in <001> direction was not observed. Selected $CaWO_4{:}Nd^{3+}$ single crystal was cut into several tiles with the diamond saw. The plates were polished with a diamond paste. The crystal structure is confirmed by X-ray diffraction. The obtained crystal was studied by Raman and infrared spectroscopy. Seven Raman and six IR optical active modes predicted by group theory are observed. FTIR confirmed the occurrence of all the functional groups and bonds in this material. From the FTIR spectrum, a strong peak of 862 cm^{-1} has been obtained due to the stretching vibration of WO_4^{2-} in scheelite structure, and a weak but sharp band at 433 cm^{-1} has been noticed due to the metal-oxygen (Ca-O) band. Estimated luminescence lifetime of $^4F_{5/2}$ - the $^4I_{9/2}$ transition is about 120 µs; estimated luminescence lifetime of $^4F_{3/2}$ - the $^4I_{9/2}$ transition is about 140 µs. All performed investigations show that the obtained $CaWO_4{:}Nd^{3+}$ single crystal has good optical quality, which was the goal of this work.

Keywords: $CaWO_4{:}Nd^{3+}$*; Raman spectroscopy; IR spectroscopy; Luminescence.*

1. Introduction

In recent years, molybdates and tungstates belonging to the scheelite-type tetragonal structure [1-4] have been extensively investigated by the scientific community for technological applications in acousto-optic filters [5], solid state lasers [6, 7], light-emitting diodes [8], photocatalysts [9, 10], phosphors [11-13], scintillators [14-16], microwave dielectrics [17, 18], and cryogenic scintillation detectors [19, 20]. Among these materials, the pure or rare earth-doped calcium tungstate ($CaWO_4$) has been studied because of its photoluminescence (PL) emissions in the visible wavelength regions of the electromagnetic spectrum [21-25].

Tungsten and its alloys because of their unique characteristic have wide application in many sectors of the industrial production [26]. Calcium tungstates are natural minerals.

_____

)*Corresponding author:** lzorica@yahoo.com

Furthermore, they can be made synthetically. The mineral name associated with these materials is $CaWO_4$. The name used to describe the common crystal structure of these materials is scheelite [27]. The scheelite-ABO_4 (A=Ca and B=W) crystal structure (Figure 1) is characterized by the tetragonal space group $I4_1/a$ (n° 88). The B atoms are surrounded by four O atoms in an approximately tetrahedral symmetry configuration, and the A atoms are surrounded by eight O atoms in an approximately octahedral symmetry. Many material properties can be associated to the existence of these [BO_4] (Fig. 1b) and [AO_8] (Fig. 1a) approximate polyhedrons into crystalline structure. The B cation tetrahedra (with W) behave as rigid structural elements with no observed cation oxygen compression [28]. On the other hand, compression of the eight-coordinated A=Ca polyhedron, is more favorable parallel to *c* than perpendicular to *c* [26].
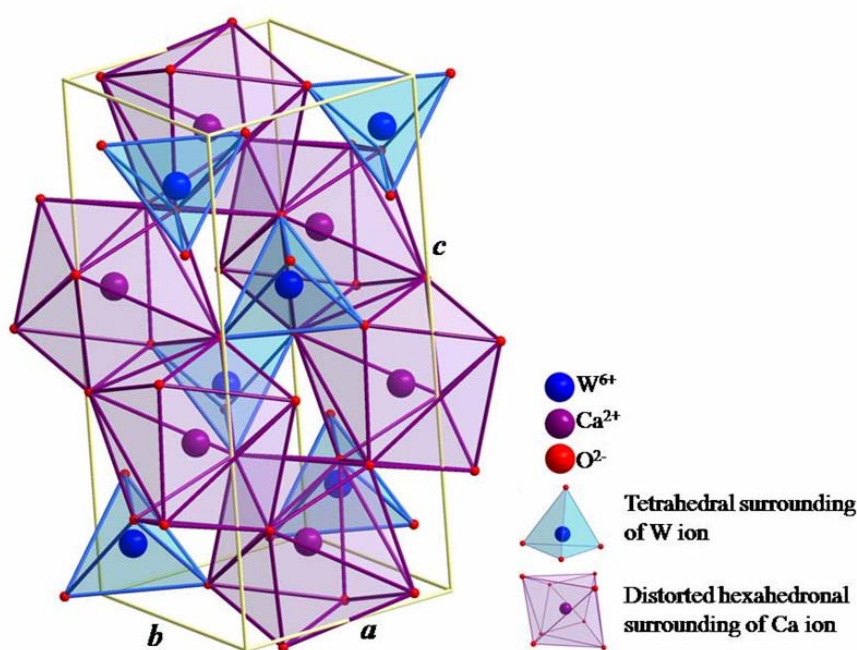
Fig. 1. Unit cell of $CaWO_4$:Nd^{3+} single crystal.

Various techniques such as the Czochralski technique, flux method, and solid-state reactions have been used to synthesize single crystals, whiskers, and powder of $CaWO_4$:Nd^{3+} [29]. Some attempts were made on the preparation of single crystal films, but these experiments had limited success because of the high vaporization pressure of WO_3 and obtained films did not have a uniform structure. The growth of single crystals from melt by the Czochralski method has a number of advantages, such as the absence of contact between the crystal and the crucible walls, that essentially reduces stresses in the crystals; the possibility to control the crystal growth visually and the processes which occur at crystal-melt interface, relative simplicity of its technical realization. Moreover, the method allows to grow large-size and sufciently perfect high-melting oxide crystals, to control the character of the melt convection and as consequence to choose the most optimal conditions for the growth of optically homogeneous crystals. Possibilities of the method are able to provide the obtaining of crystals of different shape.

The aim of our work was to produce neodymium doped calcium tungstate single crystal ($CaWO_4$:Nd^{3+}) good optical quality. The Nd^{3+} content was 0.8 at. %, as is usual for laser materials. The structural and optical properties obtained crystal was characterized using Raman, IR and luminescence spectroscopy.

2. Materials and Experimental Procedures

Czochralski method was used to obtain single crystals of $CaWO_4:Nd^{3+}$. The observations relating to the dislocation were recorded by observing an etched surface of $CaWO_4:Nd^{3+}$ crystal, using a Metaval of Carl Zeiss Java metallographic microscope with magnification of 270x. A selected $CaWO_4:Nd^{3+}$ single crystal was cut into several tiles with the diamond saw. The plates were polished with a diamond paste, which were later used for the characterization of Raman, IR and luminescence spectroscopy. The crystal plane of cleavage of $CaWO_4:Nd^{3+}$ crystal is <001>. Thin panels for testing dislocations we obtained by splitting of individual pieces of crystal. A solution for etching the crystals consisted of one part of 40 % HF and the two parts of a saturated solution of CrO_3. The sample was etched for 15 min.

Hardness of samples was obtained by Vickers microhardness tester "Leitz, Kleinharteprufer DURIMET I", using the load of 4.9 N. Three indentations were made at each load, yielding six indentation diagonals measurements, from which the average hardness could be calculated. The indentation was done at room temperature.

The structural characteristics were obtained by the XRD powder technique using Philips PW 1050 diffractometer equipped with a PW 1050 generator, 40kV x 20mA, using Ni filtered Co Kα radiation of λ = 1.54178 Å at room temperature. Measurements were carried out in the range of 10-90° with a scanning step of 0.05^o and scanning time 4 s per step. Unit cell parameters were determined by Le Bail's full profile refinement using *FullProf* computing program. The crystallite size and microstrain were determined by using X-Fit software packages which is based on Fundamental Parameter convolution approach [30].

Raman spectra measurements were performed on a system of Princeton TriVista 557 triple monochromator and CCD detector (charged-coupled-device). As an excitation laser line is used the wavelength of 532 nm. Monochromator used the configuration 900/900/1800 point per millimeter, and a resolution of 1.5 inverse centimeters. The laser power at the sample amounted to 0.25 mW, a laser beam is focused on the sample by means of microscopic lenses with a magnification 50x. Spectra were recorded in the range from 100 to 1200 cm^{-1}.

The infrared reflectivity measurements were performed at room temperature with a BOMEM DA-8 Fourier-transform infrared spectrometer [31]. A hyper beamsplitter and deuterated triglycine sulfate (DTGS) pyroelectric detector were used to cover the wavenumber region from 80 to 650 cm^{-1}. Spectra were collected with 2 cm^{-1} resolution and with 500 interferometer scans added for each spectrum.

FTIR spectra of the samples in KBr discs were obtained by transmission spectroscopy (Hartmann & Braun, MB-series). The FTIR spectra were recorded between 4000 and 400 cm^{-1} wavenumber region at a resolution of 4 cm^{-1}.

The photoluminescence (PL) response is not simple [32]. Photoluminescence emission spectra can be used for investigation of the possible outcomes of photoinduced electrons and holes in a materials, since photoluminescence emission results from the recombination of free charge carriers [33]. The time resolved optical characteristics of samples were analyzed using streak camera and Nd:YAG laser as excitation source (Fig. 2). The setup is described in more detail in our earlier publication [34]. Shorty, the basic setup of time resolved laser induced fluorescence measurement system consists of Vibrant OPO laser system and Hamamatsu streak camera. The output of the OPO can be continuously tuned over a spectral range from 320 nm to 475 nm. The samples can be also excited by the second harmonic (532 nm) of the Nd-YAG OPO pump laser. After analysis of preliminary results, we decided to use excitation at 532 nm for time resolved analysis of $CaWO_4:Nd^{3+}$ near infrared luminescence. This pulsed laser excitation has duration of about 5 ns and repetition rate 10 of Hz. The emission spectra were recorded using a streak scope (Hamamatsu model C4334-01) with integrated video streak camera.
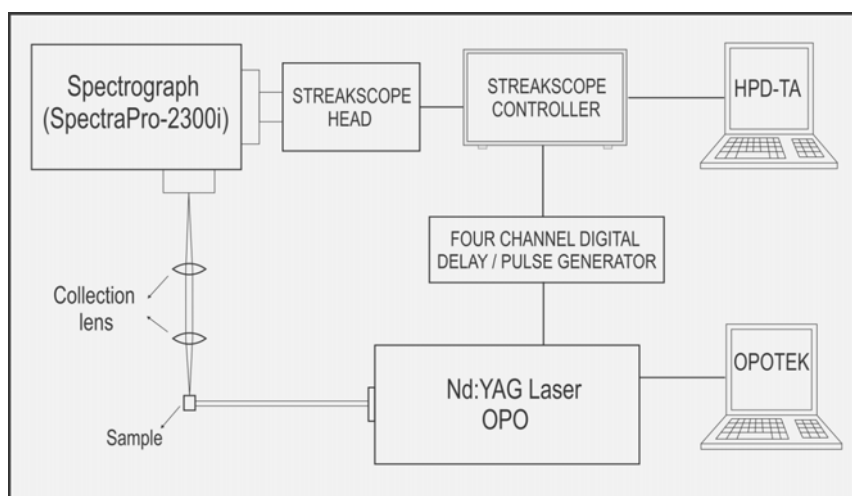
Fig. 2. Schematic illustration of experimental setup for time-resolved laser fluorescence (TR-LIF).

3. Results and Discussion

CaWO$_4$:Nd^{3+} single crystals were grown by the Czochralski technique in air. The best results were obtained with a crystal growth rate of 6.7 mm h^{-1}. The critical rotation rate was 30 rpm. The obtained single crystal was about 70 mm in length and 10 mm in diameter (Fig. 3).

Fig. 3. Photographs of CaWO$_4$:Nd^{3+} single crystal.

From the Fig. 4a), the dislocations of can be observed. Number of dislocations in CaWO$_4$:Nd^{3+} crystal was 638 per cm^2. Before individual dislocations can be observed little corner of the border. One of them is shown in Fig. 4b).
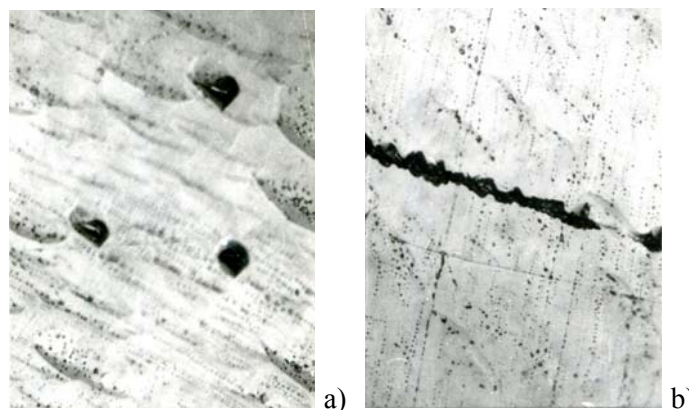
Fig. 4. The microscopic image of the surface CaWO$_4$:Nd^{3+} crystal plate in the direction <001> after etching 15 min: a) appearance of individual dislocations and b) look of low-angle boundaries on the surface. Magnification of 270x.

Hardness of the samples was HV = 1.5 GPa.

Structure of synthesized CaWO$_4$:Nd^{3+} powdered sample was identified by XRD pattern as shown in Fig. 5. The diffractogram confirms that sample is monophased, and that it crystallized in scheelite type of structure in 88. space group, $I4_1/a$. All of the observed diffraction peaks are indexed according to this space group. In this structural type, Ca ions occupy 4*b* Wyckoff positions [[0, 1/4, 5/8]] with local symmetry $\bar{4}$, while W ions occupy 4*a* Wyckoff positions [[0, 1/4, 1/8]] with the same local symmetry. W ions are in tetrahedral surrounding of O ions (coordination number 4), while Ca ions are in distorted hexahedral surrounding of O ions (coordination number 8) as shown in Fig. 1. W tetrahedrons share common vertices with Ca polyhedrons, while Ca polyhedrons between each other share common edges (Fig. 1). Unit CaWO$_4$ cell is tetragonal with cell parameters $a = b = 5.24318$ Å and $c = 11.37104$ Å according to Inorganic Crystal Structure Database (ICSD) card N° 15586. X-Fit [30] was used to extract the unit cell parameters through peak fitting analysis, which determines the unit cell parameter from least squares analysis of the positions of the peaks. The value crystallite size was 177 nm. In principle, this is expected, because the test sample obtained by milling of the single crystals. The crystallites were significantly larger and out of range of accurate measurement using XRD methods. On the other hand, the size of microstrain (0.276 %) is high, which is also characteristic of the samples obtained by milling of the single crystal.
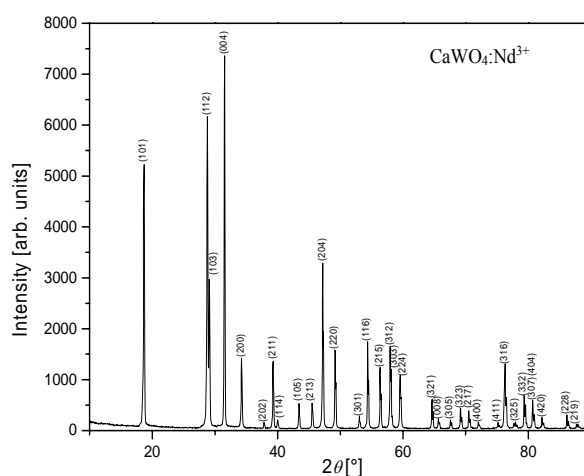
Fig. 5. XRD pattern of CaWO$_4$:Nd^{3+}. All peaks are indexed according to 88. space group, $I4_1/a$.

Factor group analysis in the C space group gives the following set of irreducible representations that characterize all the vibration modes (Raman and infrared) for a tetragonal scheelite primitive cell (*k*=0) [35, 36]:

$$\Gamma_{(Raman + Infrared)} = 3A_g + 5B_g + 5E_g + 5A_u + 3B_u + 5E_u \tag{1}$$

were the A_g, B_g and E_g are Raman-active modes. The A and B modes are nondegenerate, while the E modes are doubly degenerate. The subscripts ``g and u`` indicate the parity under inversion in centrosymmetric $CaWO_4$ crystals. The A_u and E_u modes correspond to the zero frequency of acoustic modes, while the others are optic modes. In addition, the A_g, B_g and E_g modes arise from the same motion in a $CaWO_4$ phase. Thus, 13 zone-center Raman-active modes for the $CaWO_4$ crystals are expected, as described in Eqn. (2) [37, 38]:

$$\Gamma_{(Raman)} = 3A_g + 5B_g + 5E_g \tag{2}$$

According to the literature [39, 40], the vibrational modes detected in the Raman spectra of tungstates can be classified into two groups, external and internal modes [41]. In vibrational infrared spectra, $1A_u$ and $1E_u$ acoustic are infrared-inactive mode and $3B_u$ forbidden infrared modes. Therefore, only 8 infrared-active vibration modes remain, as presented by Eqn. (3) [42]:

$$\Gamma_{(Infrared)} = 4A_u + 4E_u \tag{3}$$

Fig. 6 shows a Raman spectrum of the $CaWO_4$:Nd^{3+} excited 532 nm line of an Ar-ion laser kept at a power of 0.25 mW on sample. The internal vibrations are related to the $[WO_4]^{2-}$ molecular group with a stationary mass center. The external vibrations or lattice phonons are associated to the motion of the Ca^{2+} cation and rigid molecular units. In the free space, $[WO_4]^{2-}$ tetrahedrons show T_d-symmetry. In this case, the vibrations of the $[WO_4]^{2-}$ ions are constituted by four internal modes ($v_1(A_1)$, $v_2(E)$, $v_3(F_2)$ and $v_4(F_2)$), one free rotation mode ($v_{fr}(F_1)$) and one transition mode (F_2), When $[WO_4]^{2-}$ ions are present in a scheelite-type structure, its point symmetry reduces to S_4. The $3B_u$ vibration is a silent mode. The Raman modes in Fig. 6 were detected as $v_1(A_g)$, $v_3(B_g)$, $v_3(E_g)$, $v_4(B_g)$, $v_2(B_g)$, rotation (E_g) and rotation (A_g) vibrations at 912, 835, 798, 395, 329, 281 and 216 cm^{-1}, respectively, which provide evidence of a Scheelite structure. The well-resolved sharp peaks for the $CaWO_4$ indicate that the synthesized particles are highly crystallized.
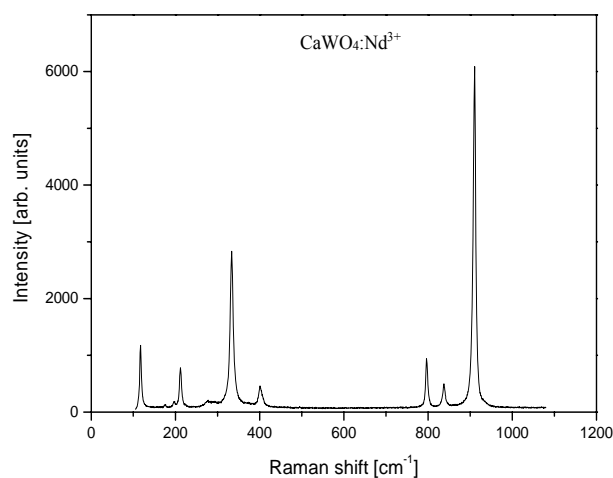
Fig. 6. Raman spectrum of $CaWO_4$:Nd^{3+} single crystal, recorded at room temperature.

Fig. 7 illustrate the IR spectrum and corresponding positions of IR-active modes of crystal. The tungstates with scheelite-type structure have eight stretching and/or bending IR-active vibrational modes [43, 44]. In our case, no more than six modes [$2A_u$, $1(A_u + E_u)$ and $3E_u$] were identified in the spectra (Fig. 7).
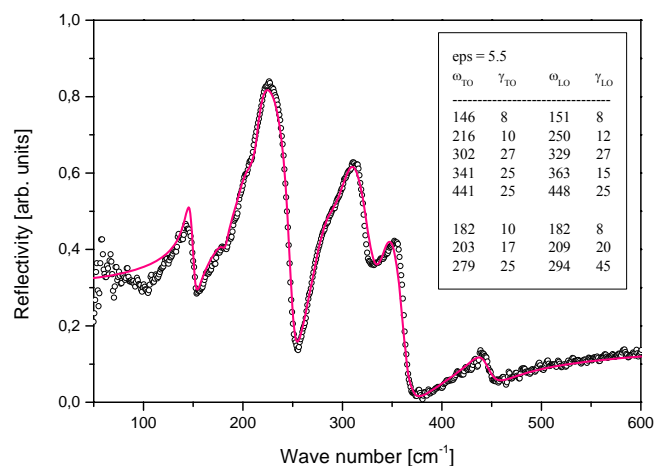

Fig. 7. IR spectrum of $CaWO_4:Nd^{3+}$ single crystal, recorded at room temperature.

Fig. 8 shows FTIR spectrum of the obtained $CaWO_4:Nd^{3+}$ at the wavenumber range of 4000-400 cm⁻¹. The band at around 2916 cm⁻¹ correspond to the stretching vibration of the hydroxyl ion [45]. The band at 2323 cm⁻¹ shows the existence of CO_2. The bands below 1000 cm⁻¹ are characteristic of the W-O bond. The absorption band at around 742 cm⁻¹ and strong band at 862 cm⁻¹ are attributed to the O-W-O stretches of the $[WO_4]^{2-}$ tetrahedron, because the AWO_4-type scheelite oxides S_4 site symmetry for the WO_4 groups [45, 46]. The weak vibration band detected at 436 cm⁻¹ could be ascribed to the W-O bending vibration [47]. The band at 1560 cm⁻¹ corresponds to the O-H stretching and the H-O-H bending vibrations, due to small quantity of surface-absorbed water [47, 48]. From the FTIR spectrum (Fig. 7), a strong peak at 862 cm⁻¹ has been obtained due to the stretching vibration of $[WO_4]^{2-}$ in scheelite structure, and a weak but sharp band at 433 cm⁻¹ has also been noticed due to the metal, oxygen (Ca-O) band.
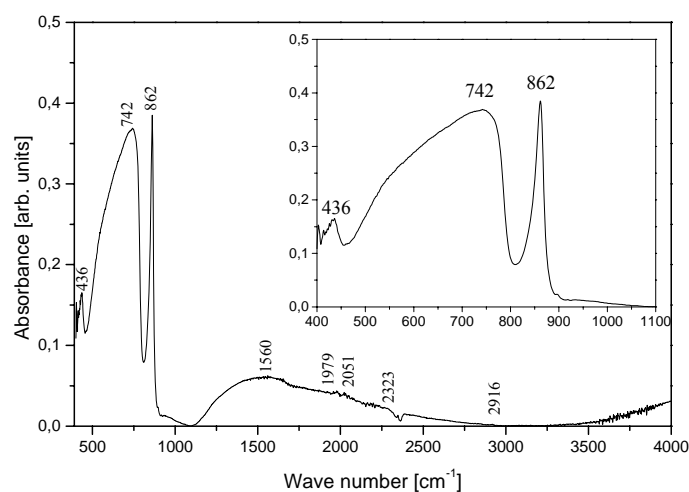
Fig. 8. FTIR spectrum of $CaWO_4:Nd^{3+}$ single crystal.

Near infrared luminescence of Nd^{3+} doped phosphors have received the renewed interest recently [49-51]. The time resolved optical characteristics of samples were analyzed using streak camera and Nd:YAG laser as excitation source. The setup is described in more detail in our earlier publication [34]. Here, we use pulsed laser excitation at 532 nm for time resolved analysis of $CaWO_4$:Nd^{3+} near infrared luminescence. We have analyzed the part of the spectrum corresponding to $^4F_{5/2}$ - $^4I_{9/2}$ and $^4F_{3/2}$ - $^4I_{9/2}$ transitions. These transitions are of interest for remote temperature sensing, as described in [49-51]. Fluorescence intensity ratio of these two transitions is used to determine temperature sensing calibration curves. The analyzed samples of $SrF2$:Nd^{3+} [49], and La_2O_2S:Nd^{3+} [50] phosphors were excited by CW laser at 532 nm. The extensive study of using Nd^{3+}-based luminescent nanothermometers is provided in [51]. Streak images of near infrared luminescence of Nd^{3+} doped crystal is shown in Fig. 9.
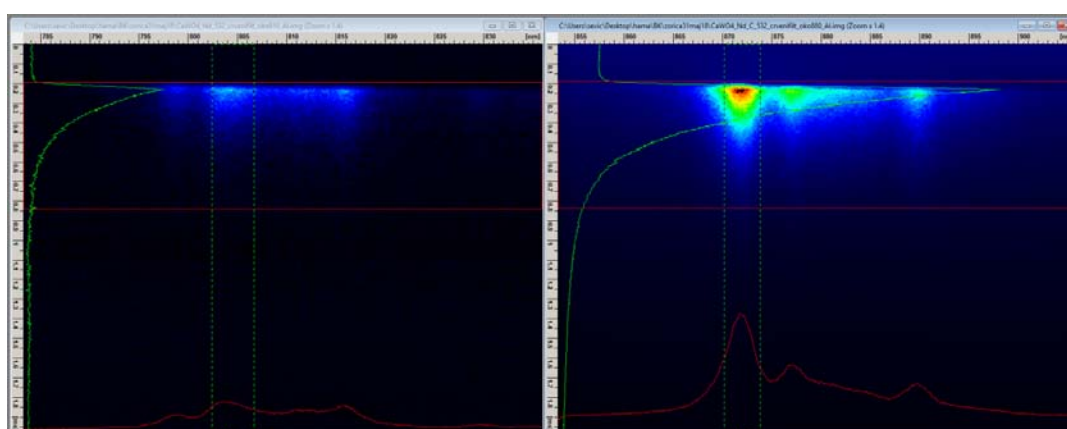
Fig. 9. Streak images of $CaWO_4$:Nd^{3+} luminescence emission, excited at 532 nm. Bands around 810 nm ($^4F_{5/2}$ - $^4I_{9/2}$ transition) and around 880 nm ($^4F_{3/2}$ - $^4I_{9/2}$ transition) were recorded separately, using diffraction grating of 300 g mm^{-1} for better wavelength resolution.
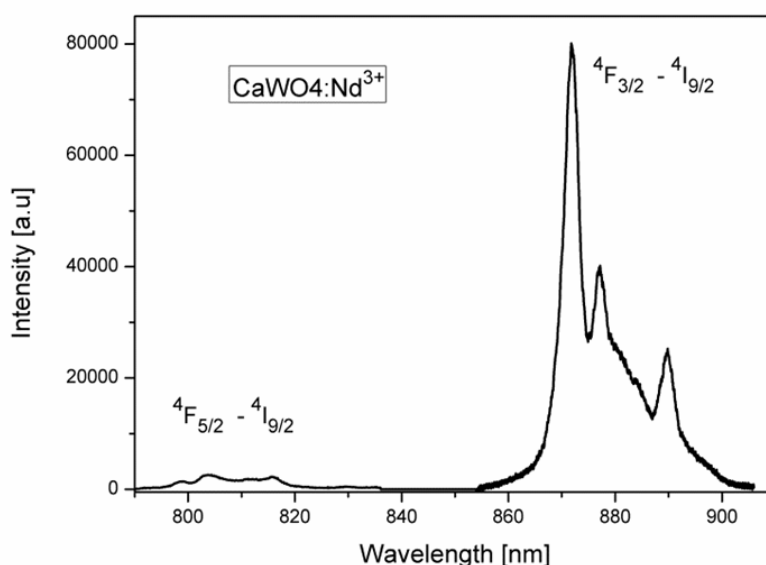
Fig. 10. Near infrared spectrum of $CaWO_4$:Nd^{3+} luminescence excited at 532 nm.

We have used HPD-TA software, provided by Hamamatsu, to calculate the lifetime of $CaWO_4$:Nd^{3+} luminescence. Estimated luminescence lifetime of $^4F_{5/2}$ - $^4I_{9/2}$ transition is

about 120 µs; estimated luminescence lifetime of $^4F_{3/2}$ - $^4I_{9/2}$ transition is about 140 µs. This result (regarding the $^4F_{3/2}$ - $^4I_{9/2}$ transition) is almost the same as provided in [51], ($Gd_2O_3:Nd^{3+}$), where corresponding lifetime at room temperature is about 142 µs. Our results are not far from the value of 220 µs provided in table 4 of [52], where Nd^{3+} doped BGO crystal was analyzed. Comparing our results with a few results provided in other references, we see that the lifetimes could be strongly dependent on host [53]. Measured lifetimes for the same transitions in [49], ($SrF_2: Nd^{3+}$) are about 5 µs for $^4F_{5/2}$ - $^4I_{9/2}$ transition and about 1230 µs for $^4F_{3/2}$ - $^4I_{9/2}$ transition. Fig. 10 shows near infrared spectrum of $CaWO_4:Nd^{3+}$ luminescence excited at 532 nm, obtained by background and sensitivity correction of streak images presented in Fig. 9.

The properties of the crystal, such as density of dislocations, cystallinity, and impurities concentrations, determine the optical quality.

4. Conclusion

Nd^{3+} doped calcium tungstate single crystals were grown from melt using the Czochralski method in air. The value of the crystal growth rate was experimentally found to be 6.7 mm h^{-1}. The critical diameter of obtained crystal was about 10 mm. The obtained transparent light blue single crystal and powdered sample were characterized by X-ray diffraction, Raman and IR spectroscopy. The XRD confirms that sample is monophasd, and that it crystallized in scheelite type of structure in 88. space group, $I4_1/a$. A good correlation was found between the experimental and theoretical Raman and infrared active modes. FTIR confirmed the occurrence of all the functional groups and bonds in this material. From the FTIR spectrum, a strong peak of 862 cm^{-1} has been obtained due to the stretching vibration of WO_4^{2-} in scheelite structure, and a weak but sharp band at 433 cm^{-1} has been noticed due to the metal, oxygen (Ca-O) band. Micro hardness was measured with the Vickers pyramid. Anisotropy in [001] direction was not observed. The crystal showed a micro hardness of 1.5 GPa. Based on our work and observations during the experiment, it could be concluded that the obtained $CaWO_4:Nd^{3+}$ single crystal is of good optical quality, which was the goal of our work.

Acknowledgments

5. References

1. G. Jia, C. Wang, S. Xu, J. Phys. Chem. C, 114 (2010) 17905.
2. X. Yan-Ling, Z. Hong, W. Rui, Z. Chun-Yu, Chin. Phys. Lett., 6 (2011) 064210.
3. H. Lei, S. Zhang, XZ. Zhu, Y. Sun, Y. Fu, Mater.Lett., 64 (2010) 344.
4. D. Errandonea, R. S. Kumar, X. Ma, C. Tu, J. Solid State Chem., 181 (2008) 355.
5. V. I. Balakshy, K. Asratyan, V. Y. Molchanov, J. Opt. A: Pure Appl. Opt., 3 (2001) S87.
6. L. Fan, Y. X./ Fan, Y. H. Duan, Q. Wang, H. T. Wang, G. H. Jia, C. Y. Tu, Appl. Phys. B: Lasers Opt., 94 (2009) 553.
7. J. Sulc, H. Jelinkova, T. T. Basiev, M. E. Doroschenko, L. I. Ivleva, V. V. Osiko, P. G. Yverev, Opt. Mater., 30 (2007) 195.

8. P. G. Yang, J. Liu, H. Yang, X. Yu, Y. Guo, Y. Zhou, J. Liu, J. Mater. Chem., 19 (2009) 3771.
9. J. Bi, L. Wu, Y. Zhang, Z. Li, j. Li, X. Fu, Appl. Catal. B, 91 (2009) 135.
10. J. Yu, L. Qi, B. Cheng, X. Zhao, j. Hazard. Mater., 160 (2008) 621.
11. J. Liu, H. Lian, C. shi, Opt. Mater., 29 (2007) 1591.
12. J. Liao, B. Qiu, H. Wen, J. Chen, W. You, Mater. Res. Bull., 44 (2009) 1863.
13. J. Liao, B. Qiu, H. Wen, J. Chen, W. You, L. Liu, j. Alloys Compd., 487 (2009) 758.
14. A. V. Vereswnikova, B. K. Lubsandorzhiev, I. R. Barabanov, P. Grabmayr, D. Greiner, J. Jochum, M. Knapp, C. Ostwald, R. V. Poleshuk, F. Ritter, B. A. M. Shaibonov, Y. E. Vyatchin, G. Meierhofer, Nucl. Instrum. Methods Phys. Res. Sect. A, 603 (2009) 529.
15. V. B. Mikhailika, S. Henrya, H. Krausa, I. Solskii, Nucl. Instrum. Methods Phys. Res. Sect. A, 583 (2007) 350.
16. I. Annenkov, O. A. Buzanov, F. A. Danevich, A. Sh. Georgadze, S. K. Kim, H. J. Kim, Y. D. Kim, V. V. Kobychev, V. N. Kornoukhov, M. Korzhik, J. I. Lee, O. Missevitch, V. M. Mokina, S. S. Nagorny, A. S. Nikolaiko, D. V. Poda, R. B. Podviyanuk, D. J. Sedlak, O. G. Shkulkova, J. H. So, I. M. Solsky, V. I. Tretyak, S. S. Yurchenko, Nucl. Instrum. Methods Phys. Res. Sect. A, 584 (2008) 334.
17. G. K. Choi, J. R. Kim, S. H. Yoon, K. S. Hong, J. Eur. Ceram. Soc., 27 (2007) 3063.
18. G. K. Choi, S. Y. Cho, J. S. An, K. S. Hong, J. Eur. Ceram. Soc., 26 (2006) 2011.
19. H. Kraus, V. B. Mikhailik, Nucl. Instrum. Methods Phys. Res. Sect. A, 621 (2010) 395.
20. J. Ninkovic, G. Angloher, C. Bucci, C. Cozzini, T. Frank, D. Hauff, H. Kraus, B. Majorovits, V. Mikhailik, F. Petricca, F. Probat, Y. Ramachers, W. Rau, W. Seidel, S. Uchaikin, Nucl. Instrum. Methods Phys. Res. Sect. A, 537 (2005) 339.
21. I. Trabelsi, M. Dammak, R. Maalej, M. Kamoun, Phys. B, 406 (2011) 315.
22. W. Wang, P. Yang, S. Gai, N. Niu, F. He, J. Lin, J. Nanopart. Res., 12 (2010) 2295.
23. Q. Xiao, Q. Zhou, M. Li, J. Lumin., 130 (2010) 1092.
24. A. B. Campos, A. Z. Simões, E. Longo, J. A. Varela, V. M. Longo, A. T. de Figueiredo, F. S. de Vicente, A. C. Hernandes, Appl. Phys. Lett., 91 (2007) 051923.
25. L. S. Cavalcante, V. M. Longo, J. C. Sczancoski, M. A. P. Almeida, A. A. Batista, J. Varela, M. O. Orlandi, E. Longo, M. Siu Li, Cryst. Eng. Comm., 14 (2012) 853.
26. I. V. Andreiev, V. p. Bondarenko, L. G. Tarasenko, Sci. Sinter., 48 (2016) 191.
27. C. Tablero, Chem. Phys. Lett., 635 (2015) 190.
28. R. M. Hazen, L. W. Finger, J. W. E. Mariathasan, J. Phy. Chem. Solids, 46 (1985) 253.
29. A. Golubovic, R. Gajic, Z. Dohcevic, S. Nikolic, Sci. Sinter., 38 (2006) 265.
30. R. W. Cheary, A. Coelho, J. Appl. Crystallography, 25 (1992) 109.
31. H. I. Elswie, Z. Ž. Lazarević, V. Radojević, M. Gilić, M. Rabasović, D. Šević, N. Ž. Romčević, Sci. Sinter., 48 (2016) 333.
32. M. A. Almessiere, Sci. Sinter., 50 (2018) 63.
33. M. Petrović, M. Gilić, J. Ćirković, M. Romčević, N. Romčević, J. Trajić, I. Yahia, Sci. Sinter., 49 (2017) 167.
34. M. S. Rabasovic, D. Sevic, M. Terzic, B. P. Marinkovic, Nucl. Inst. Meth., B 279 (2012) 16.
35. M. Crane, R. L. Frost, P. A. Williams, J. T. Kloprogge, J. Raman Spectrosc., 33 (2002) 62.
36. R. L. Rousseau, R. P. Bauman, S. P. Porto, J. Raman Spectrosc., 10 (1981) 253.
37. D. Christofilos, G. A. Kourouklis, S. Ves, J. Phys. Chem. Solids, 56 (1995) 1125.
38. S. P. S. Porto, J. F. Scott, Phys. Rev, 157 (1967) 716.
39. M. Nicol, J. F. Durana, J. Chem. Phys., 54 (1971) 1436.
40. T. T. Basiev, A. A. Sobol, Y. K. Voronko, P. G. Zverev, Opt. Mater., 15 (2000) 205.

41. A. Phuruangrat, T. Thongtem, S. Thongtem, J. Exp. Nanosci., 5 (2010) 263.
42. T. T. Basiev, A. A. Sobol, P. G. Zverev, l. I. Ivleva, V. V. Osiko, R. C. Powell, Opt. Mater., 11 (1999) 307.
43. A. S. Barker Jr., Phys. Rev., 135 (1964) A742.
44. Z. C. Ling, H. R. Xia, D. G. Ran, F. Q. Liu, S. Q. Sun, J. D. Fan, H. J. Zhang, J. Y. Wang, L. L. Yu, Chem. Phys. Lett., 426 (2006) 85.
45. P. Suneetha, Ch. Rajesh, M. V. Ramana, Mater. Res. Express, 4 (2017) 085020.
46. Q. Li, Y. Shen, T. Li, J. Chem., 2013 (2013) 952954.
47. N. A. Sabu, X. Francis, J. Anjaly, S. Sankararaman, T. Varghese, Eur. Phys. J. Plus, 32 (2017) 290.
48. X. Lai, Y. Wei, D. Qin, Y. Zhao, Y. Wu, D. Gao, J. Bi, D. Lin, G. Xu, Integr. Ferroelec., 142 (2013) 7.
49. N. Rakov, G. S. Maciel, J. Appl. Phys., 121 (2017) 113103.
50. G. Jiang, X. Wei, S. Zhou, Y. Chen, C. Duan, M. Yin, J. Lumin., 152 (2014) 156.
51. S. Balabhadra, M. L. Debasu, C. D. S. Brites, L. A. O. Nunes, O. L. Malta, J. Rocha, M. Bettinellie, L. D. Carlos, Nanoscale, DOI: 10.1039/c5nr05631d.
52. F. Chen, M. Ju, G. L. Gutsev, X. Kuang, C. Lu, Y. Yeung, J. Mater. Chem. C, 5 (2017) 3079.
53. X. Fu, Z. Jia, Y. Li, D. Yuan, C. Dong, X. Tao, Opti. Mat. Express, 2 (2012) 1242.

Садржај: *Циљ овог рада је био да се добије монокристал калцијум волфрамата допиран са неодимијумом - (CaWO$_4$:Nd^{3+}), а након тога добијени кристал карактерише са различитим спектроскопским методама. Монокристал је добијен методом раста кристала по Чокралском на ваздуху. Оптимизацијом услова раста, добијени су CaWO$_4$:Nd^{3+} кристали <001>-оријентације пречника до 10 милиметара. Број дислокација у добијеном кристалу је 102 по центиметру квадратном. Микро тврдоћа је мерена са Викерс пирамидом. Анизотропија у <001> правцу није примећена. Одабрани CaWO$_4$:Nd^{3+} кристал је сечен на неколико плочица дијамантском тестером. Плочице су полиране дијамантском пастом. Кристална структура је потврђена рендгенском дифракционом анализом. Добијени кристал је испитиван методам Раман и инфрацрвеном спектроскопијом. У складу са теоријом група примећено је седам Раман и шест инфрацрвених оптичких модова. Фуријеовом трансформационом инфрацрвеном спектроскопијом је потврђена појава свих карактеристичних функционалних група и веза у овом материјалу. Из ФТИР спектра, добијен је изражен пик на 862 cm^{-1} услед вибрације истежања WO$_4^{2-}$ у шелитној структури, а слаб али оштар пик на 433 cm^{-1} је примећен због везе метал-кисеоник (Са-О). Процењено време живота луминисценције $^4F_{5/2}$ - $^4I_{9/2}$ је око 120 µs; процењено време живота луминисценције $^4F_{3/2}$ - $^4I_{9/2}$ је око 140 µs. Сва обављена истраживања показују да добијени монокристал CaWO$_4$:Nd^{3+} има добар оптички квалитет, што је и био циљ овог рада.*
Кључне речи: *CaWO$_4$:Nd^{3+}, Раман спектроскопија, инфрацрвена спектроскопија, луминисценција.*

Effects of temperature on luminescent properties of Gd$_2$O$_3$:Er, Yb nanophosphor

D. Šević[1] · **M. S. Rabasović**[1] · **J. Križan**[2] · **S. Savić-Šević**[1] · **M. D. Rabasović**[1] · **B. P. Marinkovic**[1] · **M. G. Nikolic**[1]

Abstract

In this study we analyze nano powder Gd$_2$O$_3$ doped with Er^{3+} and Yb^{3+}. Material was synthesized by simple and efficient solution combustion method. The nano phosphor was optically excited at 980 nm by using pulsed laser diode. We have obtained time resolved upconversion luminescence spectra of nano powder samples of Gd$_2$O$_3$:Er,Yb using a streak camera and analyzed temperature dependence of erbium optical line emission intensities. The possibilities of using Gd$_2$O$_3$:Er,Yb for temperature sensing were analyzed by means of luminescence intensity ratio method. We show that synthesized Gd$_2$O$_3$:Er,Yb material is useful for temperature measurements up to 550 K.

1 Introduction

There is a growing interest in recent years for luminescence upconverting (UC) materials (Zhao et al. 2019; Gavrilovic et al. 2016; Ang et al. 2011). Using of upconversion nanoparticles provides many advantages compared to using of conventional phosphors. The effects of autofluorescence and of stray excitation light are inherently removed. Moreover, signal-to-noise ratio is notably improved.

The optical thermometry is widely used to remotely measure the temperature. There are several techniques of temperature sensing by using the thermographic phosphors, analyzed by us in (Sevic et al. 2020); they are based on intensity ratio, lifetime or rise time of luminescence. However, the luminescence intensity ratio (LIR) based temperature sensing is

---

This article is part of the Topical Collection on Advanced Photonics Meets Machine Learning.

Guest edited by Goran Gligoric, Jelena Radovanovic and Aleksandra Maluckov.

✉ D. Šević
   sevic@ipb.ac.rs

1   Institute of Physics Belgrade, University of Belgrade, Belgrade, Serbia

2   AMI D.O.O, Ptuj, Slovenia

 Springer

most commonly used and will be analyzed here. The technique is based on calculating the optical emission intensity variations of thermally coupled transitions, measured at different temperatures. Literature survey shows that the Er^{3+} ion is a prevalently used for the LIR based temperature sensing with UC phosphors (Li X. et al. 2016; Li L. et al. 2016; Avram et al. 2018; Du et al. 2017; Du et al. 2018; Dong et al. 2007; Xu et al. 2012; Liu et al. 2016; Santos et al. 1999; Wang et al. 2015; Manzani et al. 2017; Singh et al. 2009; Krizan et al. 2014).

The luminescence temperature dependence of downconverting materials is exhaustively analyzed in literature (Goss et al. 1989; Feist et al. 1999; Heyes 2009; Cates et al. 2002; Eldridge et al. 2012). The detailed analyses of thermographic phosphors are provided in review papers (Allison et al. 1997; Alden et al. 2011; Brites et al. 2012; Jaque and Vetrone 2012; Khalid and Kontis 2008). Studies of sensing of temperature using UC materials doped with Er,Yb could be found in (Li X. et al. 2016; Li L. et al. 2016; Avram et al. 2018; Du et al. 2017; Du et al. 2018; Dong et al. 2007; Xu et al. 2012; Liu et al. 2016; Santos et al. 1999; Wang et al. 2015; Manzani et al. 2017; Singh et al. 2009; Krizan et al. 2014).

The aim of this study is analysis of potentials of using the Gd_2O_3:Er^{3+},Yb^{3+} for temperature measurements. Gd_2O_3 host doped with Er and Yb was prepared by simple and cost effective process. There are various improvements of nano phosphor materials in regard the luminescent efficiency (Li et al. 2017; May et al. 2018; Ou et al. 2018; Su et al. 2019; Xing et al 2017; Zhang et al. 2019). However, due to appropriately positioned erbium transition lines, Gd_2O_3:Er^{3+},Yb^{3+} is a very good candidate for luminescence intensity ratio based remote temperature sensing.

This is not our first study about Gd_2O_3 host. Analysis of temperature effects on Gd_2O_3:Er^{3+},Yb^{3+}, using continuous excitation, was presented in (Krizan et al. 2014). The pulsed laser excitation, used in this study, has some advantages compared to continuous excitation in regard of local heating of material. The luminescence temperature dependence of the Gd_2O_3 host doped with Eu was also analyzed before (Nikolic et al. 2013).

2 Experimental procedures

The Solution Combustion Synthesis (SCS) method, explained in detail in (Krizan et al. 2014), was used to prepare the studied nano phosphor.

Stoichiometric quantities of starting chemicals $Gd(NO_3)_3*6H_2O$, $Er(NO_3)_3*5H_2O$ and $Yb(NO_3)_3*5H_2O$ with the high purity were chosen to obtain the Er concentration of 2.0 at.% and Yb concentration of 0.5 at.% in Gd_2O_3:Er,Yb ($Gd_{1.95}Er_{0.04}Yb_{0.01}O_3$).

For solution combustion synthesis we have used the dry mixture of 14.67 g (32.5 mmol = 195/6 mmol) of $Gd(NO_3)_3*6H_2O$, 0.296 g (0.667 mmol = 4/6 mmol) of $Er(NO_3)_3*5H_2O$ and 0.075 g (0.167 mmol = 1/6 mmol) of $Yb(NO_3)_3*5H_2O$, combined with the mixture of 1 g of β-alanine and 5 g of urea which were used as organic fuels.

Pulsed laser diode excitation at 980 nm was used to acquire the photoluminescence emission spectra of Gd_2O_3:Er^{3+},Yb^{3+} nano phosphor. The optical emission of analyzed samples was detected by using the streak camera system, used and explained in (Sevic et al. 2020; Vlasic et al. 2018). The detailed explanation of the setup for temperature measurements is provided in (Rabasovic et al. 2016).

A high resolution scanning electron microscope (SEM) equipped with a high brightness Schottky Field Emission gun (FEGSEM, TESCAN) operating at 4 kV was used to check the structure of studied nano phosphor.
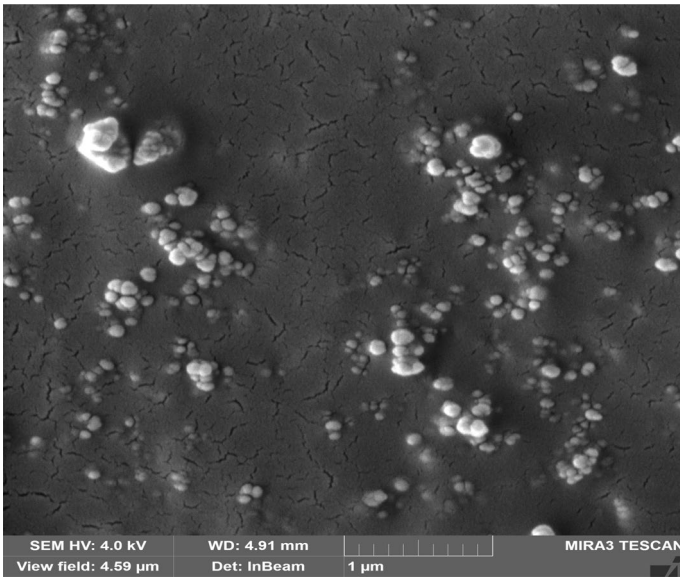
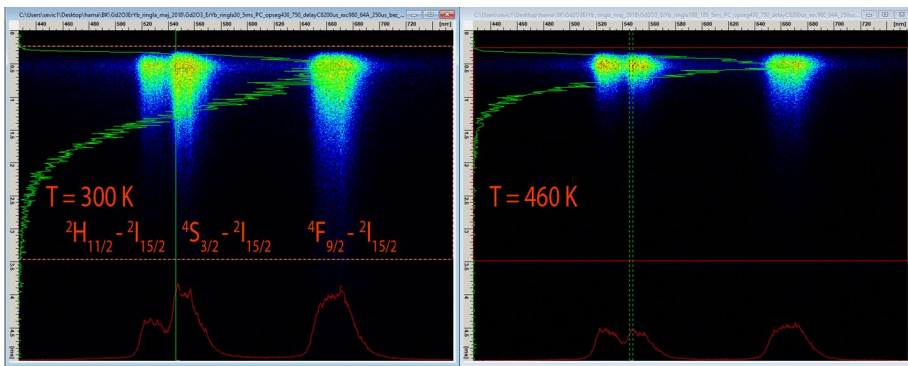**Fig. 1** SEM image of Gd_2O_3:Er^{3+},Yb^{3+} nano phosphor prepared by SCS method

Fig. 2 Time-resolved luminescence spectra of Gd_2O_3:Er^{3+},Yb^{3+} at two temperatures. Pulsed laser diode excitation is at 980 nm

3 Results and discussion

The representative SEM image of the synthesized Gd_2O_3:Er^{3+},Yb^{3+} nano material, see Fig. 1, shows the agglomerated grains and particles with dimensions from 50 nm to over 100 nm.

The photoluminescence emission of Gd_2O_3:Er^{3+},Yb^{3+} was measured over the temperature range 300–660 K. To get the general impression of luminescence temperature dependence, time-resolved luminescence spectra of Gd_2O_3:Er^{3+},Yb^{3+} at two temperatures are displayed in Fig. 2. The emission band centered at 528 nm originates from $^2H_{11/2} \rightarrow {}^2I_{15/2}$ transition, the emission band at 553 nm originates from to $^4S_{3/2} \rightarrow {}^2I_{15/2}$

transition, and the emission bands at 670 nm originates from $^4F_{9/2} \rightarrow {}^2I_{15/2}$ transition of Er^{3+} ion.

Luminescence quenching, i.e. decreasing of luminescence quantum yield at increasing concentrations of dopants in phosphors is a well known phenomenon. Literature survey (Lojpur et al. 2013; Li X. et al. 2016; Li L. et al. 2016; Avram et al. 2018; Du et al. 2017; Du et al. 2018; Dong et al. 2007; Xu et al. 2012; Liu et al. 2016; Santos et al. 1999; Wang et al. 2015; Manzani et al. 2017; Singh et al. 2009) shows that concentrations of dopants in our work are too small in regard the concentration quenching phenomenon, so it was neglected.

Concentration effects on luminescence intensities of Er transitions were analyzed in (Lojpur et al. 2013). It was shown that by varying the concentration of Yb, it is possible to vary the intensity and lifetime ratio of green and red component of luminescence (color tuning). By decreasing the Yb concentration the ratio between the green and red component increases in favor of the green component, emitted at two Er transitions, namely $^2H_{11/2} \rightarrow {}^2I_{15/2}$ and $^4S_{3/2} \rightarrow {}^2I_{15/2}$ transitions.

At the room temperature, the sample of Gd_2O_3:Er,Yb analyzed in this work has similar intensities and lifetimes (in order of about 0.7 ms, measured from data obtained by streak image shown in Fig. 2) of green and red component of luminescence. So, in regard of using of this material for remote temperature sensing, the dopant concentrations could be considered as optimal.

Integrated–in-time luminescence spectra of Gd_2O_3:Er^{3+},Yb^{3+} at several temperatures are shown in Fig. 3. We see that for temperatures above 550 K the measured signal gets weak and impractical for reliable analysis.

Based on our estimations of shape of spectral response and time durations of luminescence of erbium transitions shown in Fig. 2, we propose the schematic view of Gd_2O_3:Er^{3+},Yb^{3+} energy transfer processes presented in Fig. 4.
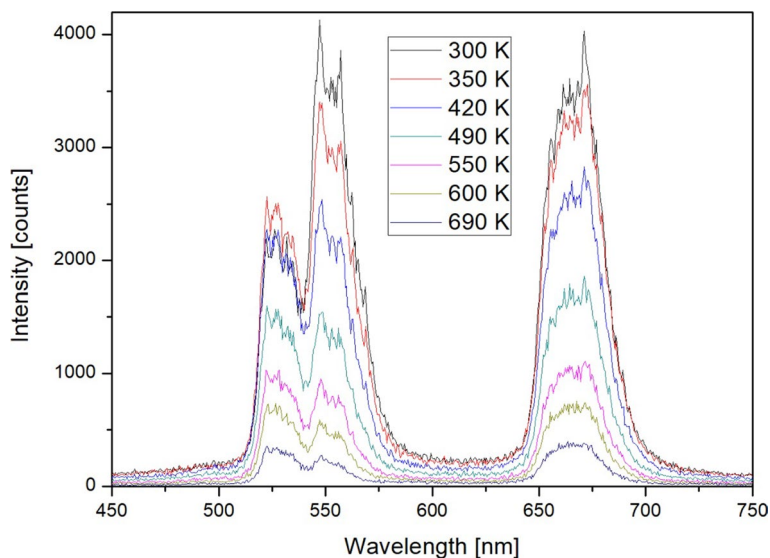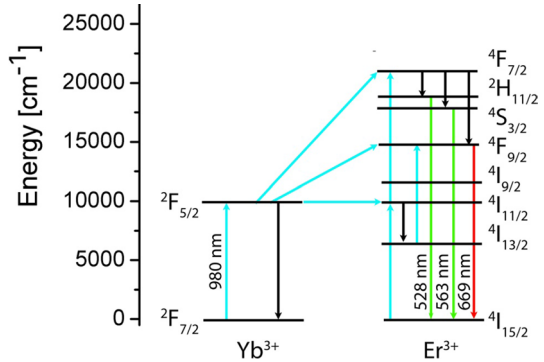

Fig. 3 Luminescence spectra of Gd_2O_3:Er^{3+},Yb^{3+} at several temperatures. Pulsed laser diode excitation is at 980 nm

Fig. 4 Schematic view of Gd₂O₃:Er³⁺,Yb³⁺ energy transfer processes

Looking at Figs. 2 and 3 it is easily noticed that luminescence intensity ratio between lines at 528 nm and 553 nm is temperature dependent. It is well known that the luminescence intensity ratio is independent on small variations of laser excitation energy or optical gain of acquisition system (Brites et al. 2012; Jaque and Vetrone 2012). Two emission lines, with a small energy gap between them, are mostly chosen to implement the temperature sensing. The higher energy level becomes more populated with increasing of temperature by thermalization effects from the lower energy level. In this way, relative intensity of higher level, in regard the lower level, gradually increases by temperature increase.

Ratio of intensities of two levels, *IR*, is determined by Boltzmann-type population distribution given by (Brites et al. 2012; Jaque and Vetrone 2012; Đačanin et al. 2014; Nikolic et al. 2018):

$$IR = \frac{I_{31}}{I_{21}} = C \exp\left(-\frac{\Delta E}{kT}\right) \tag{1}$$

where k is the Boltzmann constant, $k = 0.695\,034\,76(63)$ cm⁻¹ K⁻¹ and ΔE is the energy gap between two excited levels.

However, as explained in (Lojpur et al. 2016; Sevic et al. 2020) another constant, *A*, should be introduced to Eq. (1), to account for the finite value of *IR* at low temperatures:

$$IR = \frac{I_{31}}{I_{21}} = A + C \exp\left(-\frac{\Delta E}{kT}\right) \tag{2}$$

Figure 5 shows temperature sensing calibration curve based on luminescence intensity ratio of two Er emission lines, at 528 nm and 553 nm. Being of strong intensity and closely located, these two lines satisfy all criteria for choosing them for LIR method. Estimated value of the energy gap is $\Delta E = 728$ cm⁻¹. It is obtained by fitting the sensing calibration curve by Eq. (2). Our estimation of the energy gap is similar to results presented in (Li X. et al. 2016; Li et al. 2016; Avram et al. 2018; Du et al. 2017; Du et al. 2018; Dong et al. 2007; Xu et al. 2012; Liu et al. 2016; Santos et al. 1999; Wang et al. 2015; Manzani et al. 2017; Singh et al. 2009). We have discarded the measured points above 550 K to avoid large fitting errors.

The rate at which *IR* changes with the temperature defines the absolute thermal sensitivity, *S*:
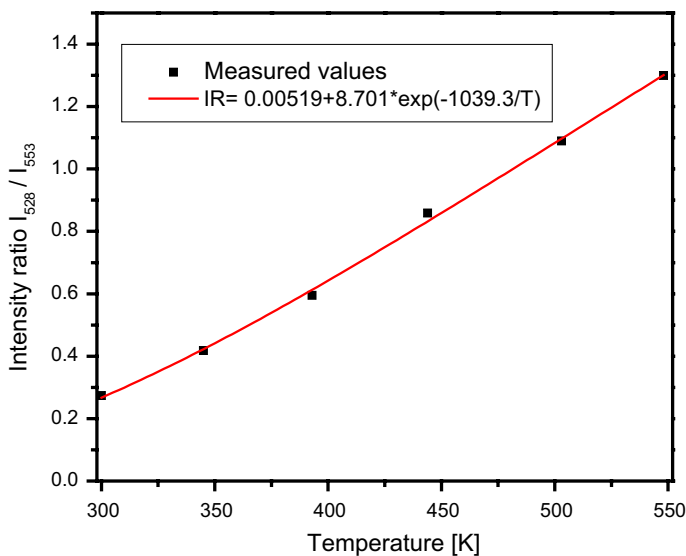
Fig. 5 Temperature sensing calibration curve of Gd_2O_3:Er,Yb, using intensity ratio of two Er emission lines, at 553 nm and 529 nm. Experimental points are denoted by black squares and fitted temperature calibration curve is denoted by red line

$$S = \left| \frac{dIR}{dT} \right| \tag{3}$$

The absolute thermal sensitivity is of a small practical use for comparison purposes, so, we use the relative thermal sensitivity, Sr, defined by Eq. (3):

$$Sr = \left| \frac{1}{IR} \frac{dIR}{dT} \right| \tag{4}$$

Figure 6 shows the relative sensitivity curve, calculated by Eq. (4). Looking at the Fig. 6 we see that the relative sensitivity is highest at room temperature, its value is 1.18% K^{-1}, and its lowest value is about 0.35% K^{-1} at 550 K.

Comparing the results presented here and in (Krizan et al. 2014), we see that the temperature sensing calibration curves look very similar, only slightly in favor of pulsed excitation because of somewhat better intensity ratio. However, the pulsed excitation offers possibility for using the luminescence lifetime for temperature sensing, providing grounds for multi-mode temperature sensing described in (Sevic et al. 2020).

4 Conclusion

We have studied the possibilities of using Gd_2O_3:Er^{3+},Yb^{3+} for remote temperature sensing. Analyzed samples were fabricated by simple and low-cost Solution Combustion Synthesis (SCS) method. We have used the pulsed laser excitation because it has some advantages compared to continuous excitation in regard of local heating of material. Erbium spectral lines at 528 nm ($^2H_{11/2} \rightarrow \, ^2I_{15/2}$ transition) and 553 nm ($^4S_{3/2} \rightarrow \, ^2I_{15/2}$ transition)

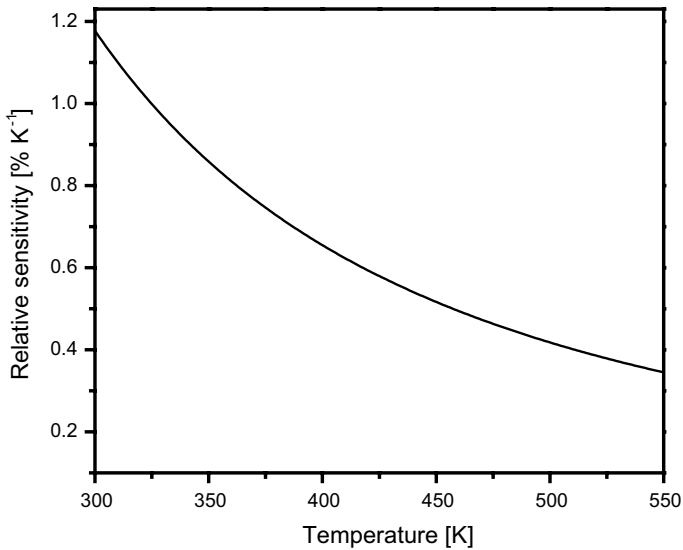**Fig. 6** Relative sensitivity curve as the function of temperature for Gd_2O_3:Er,Yb

were selected for implementation of luminescence intensity ratio method for temperature measurements. Our analysis shows that synthesized Gd_2O_3:Er,Yb material is useful for temperature measurements up to 550 K, with relative sensitivity of 1.18% K^{-1} at room temperature. With increasing the temperature the relative sensitivity decreases up to 0.35% K^{-1} at 550 K. In our future work we will analyze prospects of using the erbium optical emission lifetime for temperature sensing.

References

Alden, M., Omrane, A., Richter, M., Särner, G.: Thermographic phosphors for thermometry: A survey of combustion applications. Prog. Energy Combust. Sci. **37**, 422–461 (2011)

Ang, L.Y., Lim, M.E., Ong, L.C., Zhang, Y.: Applications of upconversion nanoparticles in imaging, detection and therapy. Nanomedicine **6**, 1273–1288 (2011)

Allison, S.W., Gillies, G.T.: Remote thermometry with thermographic phosphors: Instrumentation and applications. Rev. Sci. Instrum **68**, 2615–2650 (1997)

Avram, D., Tiseanu, C.: Thermometry properties of Er, Yb–Gd_2O_2S microparticles: dependence on the excitation mode (cw versus pulsed excitation) and excitation wavelength (980 nm versus 1500 nm). Methods Appl. Fluoresc. **6**, 025004 (2018)

Brites, C.D.S., Lima, P.P., Silva, N.J.O., Millan, A., Amaral, V.S., Palacio, F., Carlos, L.D.: Thermometry at the nanoscale. Nanoscale **4**, 4799–4829 (2012)

Cates, M.R., Allison, S.W., Jaiswal, S.L., Beshears, D.L.: YAG:Dy and YAG:Tm Fluorescence above 1400. Oak Ridge National Laboratory, Report ORNL/TM-2002/71 (2002)

Dong, B., Liu, D.P., Wang, X.J., Yang, T., Miao, S.M., Li, C.R.: Optical thermometry through infrared excited green upconversion emissions in Er^{3+}–Yb^{3+} codoped Al_2O_3. Appl. Phys. Lett. **90**, 181117 (2007)

dos Santos, P.V., de Araujo, M.T., Gouveia-Neto, A.S., MedeirosNeto, J.A., Sombra, A.S.B.: Optical Thermometry Through Infrared Excited Upconversion Fluorescence Emission in Er -and Er –Yb -doped Chalcogenide Glasses. IEEE J. Quantum Electron. **35**, 395–399 (1999)

Du, P., Deng, A.M., Luo, L., JaeYu, J.S.: Simultaneous phase and size manipulation in $NaYF_4$:Er^{3+}/Yb^{3+} upconverting nanoparticles for a non-invasion optical thermometer. New J. Chem. **41**, 13855–13861 (2017)

Du P., Yu J.S.: Synthesis of Er(III)/Yb(III)-doped BiF_3 upconversion nanoparticles for use in optical thermometry. Microchimica Acta **185,** 237–1–8 (2018)

Đačanin, LjR, Lukić-Petrović, S.R., Petrović, D.M., Nikolić, M.G., Dramićanin, M.D.: Temperature quenching of luminescence emission in Eu^{3+}- and Sm^{3+}-doped $YNbO_4$ powders. J. Lumin. **151**, 82–87 (2014)

Eldridge, J.I., Jenkins, T.P., Allison, S.W., Wolfe, D.E., Jordan, E.H.: Development of YAG:Dy Thermographic Phosphor Coatings for Turbine Engine Applications, 58h International Instrumentation Symposium San Diego, CA, 5–8, (2012)

Feist, J.P., Heyes, A.L., Choy, K.L., Su, B.: Phosphor Thermometry for High Temperature Gas Turbine Applications. Proceedings of IEEE; **6.1** (1999)

Gavrilovic, T.V., Jovanovic, D.J., Smits, K., Dramicanin, M.D.: Multicolor upconversion luminescence of $GdVO_4$:Ln^{3+}/Yb^{3+}(Ln^{3+} = Ho^{3+}, Er^{3+}, Tm^{3+}, Ho^{3+}/Er^{3+}/Tm^{3+}) nanorods. Dyes Pigm. **126**, 1–7 (2016)

Goss, L.P., Smith, A.A., Post, M.E.: Surface thermometry by laser-induced fluorescence. Rev Sci. Instrum **60**, 3702–3706 (1989)

Heyes, A.L.: On the design of phosphors for high-temperature thermometry. J. Lumin. **129**, 2004–2009 (2009)

Jaque, D., Vetrone, F.: Luminescence nanothermometry. Nanoscale **4**, 4301–4326 (2012)

Khalid, A.H., Kontis, K.: Thermographic phosphors for high temperature measurements: principles, current state of the art and recent applications. Sensors **8**, 5673–5774 (2008)

Krizan, J., Mazaj, M., Kaucic, V., Bajsic, I., Mozina, J.: Synthesis of Er- and Yb-doped Gadolinium Oxide Polymorphs and Influence of Their Structureson Upconversion Properties. Acta Chim. Slov. **61**, 608–614 (2014)

Li, X., Song, Y., Yang, Y., Mi, C., Liu, Y., Yu, F., Liu, L., Zhang, J., Li, Z.: Structure and Optical Thermometry Characterization of Er^{3+}/Yb^{3+} Co-Doped $BaGd_2CuO_5$. J. Nanosci. Nanotechnol. **16**, 3542–3546 (2016)

Li, D., Qin, W., Zhang, P., Wang, L., Lan, M., Shi, P.: Efficient luminescence enhancement of Gd_2O_3:Ln^{3+} (Ln = Yb/Er, Eu) NCs by codoping Zn^{2+} and Li^+ inert ions. Optical Materials Express **7**, 329 (2017)

Li, L., Zheng, L., Xu, W., Liang, Z., Zhou, Y., Zhang, Z.: Cao W (2016) Optical thermometry based on the red upconversion fluorescence of Er3+ in CaWO4:Yb3+/Er3+ polycrystalline powder. Opt. Lett. **41**, 1458–1461 (2016)

Liu, L., Qin, F., Lv, T., Zhang, Z., Cao, W.: Accurate thermometry based on the red and green fluorescence intensity ratio in $NaYF_4$: Yb. Er nanocrystals for bioapplication. Optics Letters **41**, 4664–4667 (2016)

Lojpur, V., Ćulubrk, S., Dramićanin, M.D.: Ratiometric luminescence thermometry with different combinations of emissions from Eu^{3+} doped $Gd_2Ti_2O_7$ nanoparticles. J. Lumin. **169**, 534–538 (2016)

Lojpur, V., Ahrenkiel, P., Dramićanin, M.D.: Color-tunable up-conversion emission in Y_2O_3:Yb^{3+}, Er^{3+} nanoparticles prepared by polymer complex solution method. Nanoscale Res. Lett. **8**, 131 (2013)

Manzani D., Petruci J. F. da S., Nigoghossian K., Cardoso A.A., Ribeiro S.J.L.: A portable luminescent thermometer based on green upconversion emission of Er^{3+}/Yb^{3+} co-doped tellurite glass. Scientific Reports 7:41596 (2017) DOI: 10.1038/srep41596

May, P.S., Baride, A., Hossan, M.Y., Berry, M.: Measuring the Internal Quantum Yield of Upconversion Luminescence for Ytterbium-Sensitized Upconversion Phosphors Using the Ytterbium(III) Emission as an Internal Standard. Nanoscale **10**, 17212–17226 (2018)

Nikolic, M.G., Al-Juboori, A.Z., Djordjevic, V., Dramicanin, M.D.: Temperature luminescence properties of Eu^{3+}-doped Gd_2O_3 phosphors. Phys. Scr. **T157**, 014056–1–14065 (2013)

Nikolic, M.G., Rabasovic, M.S., Krizan, J., Savic-Sevic, S., Rabasovic, M.D., Marinkovic, B.P., Vlasic, A., Sevic, D.: Luminescence thermometry using $Gd_2Zr_2O_7$:Eu^{3+}. Opt Quant Electron. **50**, 1–8 (2018)

Ou, Q., Zhang, Y., Wang, Z., Yuwono, J.A., Wang, R., Dai, Z., Li, W., Zheng, C., Xu, Z.-Q., Qi, X., Duhm, S., Medhekar, N.V., Zhang, H., Bao, Q.: Strong Depletion in Hybrid Perovskite p–n Junctions Induced by Local Electronic Doping. Adv. Mater. **30**, 1705792 (2018)

Rabasovic, M.D., Muric, B.D., Celebonovic, V., Mitric, M., Jelenkovic, B.M., Nikolic, M.G.: Luminescence thermometry via the two-dopant intensity ratio of Y_2O_3:Er^{3+}, Eu^{3+}. J. Phys. D: Appl. Phys. **49**(485104), 1–6 (2016)

Sevic D, Rabasovic M.S., Krizan J., Savic-Sevic S., Nikolic M.G., Marinkovic B.P., Rabasovic M.D., "YVO_4:Eu^{3+} nanopowders: multi-mode temperature sensing technique", J. Phys. D: Appl. Phys. **53**, 015106–1–10 (2020)

Singh, S.K., Kumar, K., Rai, S.B.: Er^{3+}/Yb^{3+} codoped Gd_2O_3 nano-phosphor for optical thermometry. Sensors and Actuators A **149**, 16–20 (2009)

Su L., Fan X., Yin T., Wang H., Li Y., Liu F., Li J., Zhang H., and Heping Xie.: Inorganic 2D Luminescent Materials: Structure, Luminescence Modulation, and Applications. Adv. Optical Mater. 1900978 (2019)

Vlasic, A., Sevic, D., Rabasovic, M.S., Krizan, J., Savic-Sevic, S., Rabasovic, M.D., Mitric, M., Marinkovic, B.P., Nikolic, M.G.: Effects of temperature and pressure on luminescent properties of Sr_2CeO_4:Eu^{3+} nanophosphor. J. Lumin. **199**, 285–292 (2018)

Wang, X., Liu, Q., Bu, Y., Liu, C.-S., Liua, T., Yan, X.: Optical temperature sensing of rare-earth ion doped phosphors. RSC Adv. **5**, 86219–86236 (2015)

Xing C., Xie Z., Liang Z., Liang W., Fan T., Ponraj J.C, Dhanabalan S.C., Fan D., Zhang H.: 2D Nonlayered Selenium Nanosheets: Facile Synthesis, Photoluminescence, and Ultrafast Photonics. Adv. Optical Mater. 1700884 (2017)

Xu, W., Gao, X., Zheng, L., Wang, P., Zhang, Z., Cao, W.: Optical Thermometry through Green Upconversion Emissions in Er^{3+}/Yb^{3+}-Codoped $CaWO_4$ Phosphor. Appl. Phys. Express **5**, 072201 (2012)

Zhang, Y., Chang-Keun Lim, C.-K., Dai, Z., Yu, G., Haus, J.W., Zhang, H., Prasad, P.N.: Photonics and optoelectronics using nano-structured hybrid perovskite media and their optical cavities. Phys. Rep. **795**, 1 (2019)

Zhao, Y., Wang, X., Zhang, Y., Li, Y., Yao, X.: Optical temperature sensing of up-conversion luminescent materials: Fundamentals and progress. J. Alloy. Compd. (2019). https://doi.org/10.1016/j.jallcom.2019.152691

Laser Fluence Recognition Using Computationally Intelligent Pulsed Photoacoustics Within the Trace Gases Analysis

M. Lukić[1] · **Ž. Ćojbašić[2]** · **M. D. Rabasović[3]** ·
D. D. Markushev[3] · **D. M. Todorović[4]**

Abstract In this paper, the possibilities of computational intelligence applications for trace gas monitoring are discussed. For this, pulsed infrared photoacoustics is used to investigate SF_6–Ar mixtures in a multiphoton regime, assisted by artificial neural networks. Feedforward multilayer perceptron networks are applied in order to recognize both the spatial characteristics of the laser beam and the values of laser fluence Φ from the given photoacoustic signal and prevent changes. Neural networks are trained in an offline batch training regime to simultaneously estimate four parameters from theoretical or experimental photoacoustic signals: the laser beam spatial profile $R(r)$, vibrational-to-translational relaxation time τ_{V-T}, distance from the laser beam to the absorption molecules in the photoacoustic cell $r*$ and laser fluence Φ. The results presented in this paper show that neural networks can estimate an unknown laser beam spatial profile and the parameters of photoacoustic signals in real time and with high precision. Real-time operation, high accuracy and the possibility of application for higher intensities of radiation for a wide range of laser fluencies are factors that classify the computational intelligence approach as efficient and powerful for the in situ measurement of atmospheric pollutants.

✉ M. Lukić
mladenalukic@gmail.com

1   Faculty of Occupational Safety, University of Niš, Čarnojevića 10a, Niš 18000, Serbia

2   Mechanical Engineering Faculty, University of Niš, Aleksandra Medvedeva 14, Niš 18000, Serbia

3   Institute of Physics, University of Belgrade, Pregrevica 118, Belgrade-Zemun 11080, Serbia

4   Institute for Multidisciplinary Research, University of Belgrade, P.O. Box 33, Belgrade 11030, Serbia

 Springer

1 Introduction

The development of numerous spectroscopic methods and techniques is a result of the requirement for the fast, accurate and selective monitoring of atmospheric pollutants. Photoacoustic spectroscopy (PAS) is a very successful detection technique for air pollutants due to its universality, high sensitivity, high selectivity, wide dynamic range, simple handling and fast data processing. PAS is a powerful technique for the infrared linear and nonlinear absorption and relaxation processes of molecules in different gas mixtures [1–3]. For the temporal shape analysis of the pulsed infrared photoacoustics signal, we employed artificial neural networks to investigate SF_6–Ar mixtures in a multiphoton (MP) regime. Knowledge of the infrared absorption and nonradiative relaxation of molecules in the atmosphere is important for different models of energy transfer responsible for global warming and climate change. The SF_6 molecule is a typical greenhouse gas with high infrared absorption and energy transfer potential [4,5] which can have a significant impact on the climate in the future.

Many studies have been published on the multiphoton excitation (MPE) of polyatomic molecules [4,5]. Multiphoton absorption (MPA) in various polyatomic molecules in the gas phase can be characterized by the dependency of the average energy absorbed by one molecule on radiation energy fluence Φ. The functional dependence of the MPA signal amplitude (intensity and shape) and other physical parameters (spatial and temporal laser beam characteristics, excited molecules relaxation time) on laser fluence Φ is the most commonly measured characteristic in experiments in MPA. Small variations in Φ could change well-known dependencies and mask the real ratio between the absorption efficiency of the SF_6 and other trace gases within the same experimental conditions [6–9]. In our investigation, Ar was used as the buffer gas due to its simplest case collisional behavior and the absence of vibrational-to-vibrational energy transfer between the absorbing molecule and buffer [4,7]. Using pulse photoacoustic spectroscopy (PAS), the absorption and relaxation processes in the gas mixture were analyzed based on features of the generated acoustic waves, which are determined by the propagation medium and sound source temporal and spatial characteristics.

Computational intelligence has proven itself as a practical and powerful collection of techniques with successful applications in numerous fields. Artificial neural networks (ANNs) are a powerful tool which is complementary to conventional approaches for classification, pattern recognition and prediction. Several important features including high processing speeds and the ability to learn the solution to a problem from a set of examples make ANNs suitable for application in photoacoustics. One feature of ANNs is that they are capable of recognizing the shape of the PA signal and simultaneously in real time developing a spatial profile of the laser beam, in order to determine the relaxation time of the excited molecule and the distance from the microphone to the laser beam. Further development of the already successful implementation of ANNs in photoacoustics [10] is proposed here through the application of determining

the laser fluence Φ. As mentioned above, in MPA experiments the laser fluence Φ can fluctuate between two consequent pulses, changing intensity I significantly. In order to control and overcome such changes, artificial neural networks can be applied to recognize the values of Φ in real time, with improved accuracy. Since this method of simultaneously determining the spatial characteristics of laser radiation, laser fluence and relaxation time works in real time, it can be considered as a substitute for the instruments used to measure spatial profiles for higher laser beam intensities.

In previous articles, we have shown that the three experimental parameters (relaxation time τ_{V-T}, distance between the laser beam and microphone $r*$, and laser beam spatial profile R(r)) can be calculated in real time simultaneously with the help of intelligent photoacoustics methods. Now we show that the simultaneous calculation of four independent parameters (τ_{V-T}, $r*$, R(r) and laser fluence Φ) can be carried out in real time using a more complex neural network, thereby combining our previous results [10,11] and the results developed here. The agreement between the experiment and simulation results is about as good as can be expected. The opportunity for expanding the number of parameters that can be simultaneously calculated exists through knowing the relationship between the laser fluence and the intensity of the photoacoustics signal (the concentration of the absorbing molecules and an instrumental "one point" calibration factor as defined in [11]). We believe that this work appears promising as a basis for developing a versatile and comprehensive instrument that can carry out the real-time measurements of trace gas analysis, at the same time controlling some instrumental parameters as well.

2 Theoretical Background

The intensity of the PA signal is directly proportional to the energy absorbed and the concentration of the absorber. The shape of the PA signal is determined by the relaxation characteristics of the gas mixture, and it also depends on the excitation energy density (or spatial distribution of the absorbing molecules). Therefore, the spatial profile of the laser beam should be investigated in more detail. The shape of an acoustic wave generated by a given energy source can be calculated by solving the nonhomogeneous linearized wave equation [12,13]:

$$\frac{\partial^2 \delta p(\mathbf{r}, t)}{\partial t^2} - c^2 \Delta \delta p(\mathbf{r}, t) = S(\mathbf{r}, t) \tag{1}$$

where $\delta p(\mathbf{r}, t)$ is the pressure discrepancy from its equilibrium state value, c is the speed of sound and $S(\mathbf{r}, t)$ is the source function. The source function $S(\mathbf{r}, t)$ is determined by means of its spatial and temporal characteristics. If the distribution of the excited molecules at location r and time t is given by energy function $E(\mathbf{r}, t) = R(r)T(t)$, then the source function is defined as [13]:

$$S(\mathbf{r}, t) = -\frac{\partial^2 E(\mathbf{r}, t)}{\partial t^2} H(t) - \frac{\partial E(\mathbf{r}, t)}{\partial t} \delta(t) \tag{2}$$

where $H(t)$ is the Heaviside step function and $\delta(t)$ is the Dirac delta function. The spatial part $R(\mathbf{r})$ of the energy density $E(\mathbf{r},t)$ is determined by the geometrical characteristics of the laser radiation and absorption properties of the medium. The temporal part $T(t)$ describes the evolution of the excitation energy, i.e., relaxation characteristics of the excited molecules. It can be presented as:

$$T(t) = \exp(-t/\tau_{V\_T}) \tag{3}$$

Two of the methods used to solve the wave equations for a known source function and defined initial and boundary conditions are: (a) Fourier transform and (b) Green's functions method. Green's functions method allows us to calculate the photoacoustic signal for an arbitrary laser beam profile and excitation energy decay. The general solution of linearized wave equation (1) using Green's functions method can be written in the form:

$$\delta P(\mathbf{r}, t) = \int d^3\mathbf{r}' \int dt' g(\mathbf{r}, t | \mathbf{r}', t') S(\mathbf{r}', t'), \tag{4}$$

where $g(\mathbf{r}, t|\mathbf{r}', t')$ is Green's function for a 2D wave equation. Green's function can be numerically averaged over the spatial part (e.g., the laser profile) in cylindrical geometry. For the averaged Green's function $G(r, t - t')$ in cylindrical geometry, an acoustic wave takes the form:

$$\delta P(\mathbf{r}, t) = -\frac{\partial T(0)}{\partial t} G(r, t) - \int_0^t \frac{\partial^2 T}{\partial t^2} G(r, t - t') dt' \tag{5}$$

The acoustic wave obtained consists of two components: a positive-going condensation peak of amplitude P^+, followed by a negative-going rarefaction peak of amplitude P^-. The amplitude ratio P^-/P^+ depends on the quantity ε, defined as:

$$\varepsilon = \frac{\tau_p}{\tau_{V-T}} = \frac{r_L}{c\tau_{V-T}}, \tag{6}$$

where r_L is the distance from the microphone to the center of the laser beam and c is the speed of sound inside the experimental chamber for the given gas mixture.

Dimensionless parameter ε is suitable for calculations and used instead of the relaxation time τ_{V-T}. Another useful dimensionless quantity reduced time t^* can be written as $t* = t/\tau_p$, where t is the time and τ_p is the sonic transit time ($\tau_p = r_L/c$). Based on Eq. 6, it can be concluded that for constant temperature (constant c) and geometrical conditions (constant r_L), it is only changes in a relaxation parameter that change the value of parameter ε. The shape and intensity of the photoacoustic signal are changed too. The method for laser fluence recognition proposed in this paper includes a constant value of parameter ε and shape of the PA signal. The intensity of the PA signals P^+ is directly proportional to the absorbed energy E_a, and their ratio is constant for the constant concentration of the absorbing molecules [11]. The PA signal intensity varies with changes in the absorbed energy (the shape of the PA signal remains

the same). Also, the intensity of the PA signal depends on the geometric parameters of the system such as the radius of the laser beam r_L and the distance r between the beam and the microphone. These experimental parameters define dimensionless quantities r^* ($r^* = r/r_L$). Although changes in parameter r^* (different positions of the photoacoustic cell, blend, etc.) can substantially change the PA signal intensity, it is not the case in our study.

We recently developed a method based on analysis of the photoacoustic signal temporal shape which employs computational intelligence to simultaneously calculate the symmetric laser beam spatial profile, vibrational-to-translational relaxation time (τ_{V-T}) and distance from the laser beam to the absorption molecules (SF_6) within the photoacoustic cell (r^*) [10,14–16]. Previously, a mathematical algorithm developed for photoacoustic tomography (PAT) was used for simultaneous determination of the laser beam spatial profile and relaxation time [17], but practical usage of this method is limited due to the long computational time. The main aim in our previous research was to improve the existing experimental apparatus in order to avoid additional optical instruments for measuring the spatial profile of the laser beam. Random variation of the spatial profile of the laser beam increases the error in determining the important parameters of MPA. Computational intelligence applied to the simultaneous calculation of the laser beam spatial profile and τ_{V-T} values provides results for times ranging around a few microseconds. The real-time operation provides exact knowledge of the laser beam profile during two consecutive pulses and allows its correction [15–17].

3 Neural Network Laser Fluence Recognition

Artificial neural networks are highly parallel connectionist systems modeled on biological neurons [18]. Neural networks represent a computational paradigm in which the solution to a problem is learned from a set of examples. Computational power in an ANN is derived from the density and complexity of the interconnections. Here, feed-forward multilayer perception networks were used, which were trained in an offline batch training regime to recognize the values of laser fluence Φ, and above-mentioned quantities $R(r)$, τ_{V-T}, and r^* from the intensity and shape of the given PA signal. A simple ANN is composed of several layers: the input layer, a number of hidden layers and the output layer. Between the layers are connections containing weights. Determination of the weights is called learning or training. Neural networks used for laser fluence recognition are trained by a supervised learning process in which the network is supplied with input vectors (PA signals) together with corresponding target vectors (characteristic parameters of the laser beam, i.e., Φ values). The weights are chosen during the training process so as to minimize the error. Once the weights have been fixed, new data can be processed by the network very rapidly, which is an obvious advantage of ANNs. A suitable error function is defined with respect to a set of data points, and is usually defined as the squares of the individual errors summed for all output units and for all patterns. For a multilayer perceptron, there is a computationally efficient procedure for updating the connection weights based on the technique of error backpropagation. Another important issue, generalization, shows the ability of the network to perform with newly presented data which did not form part of the train-

ing set. To achieve successful generalization, we consider three data sets: the training, test and validation sets.

The ANN developed for the simultaneous determination of $R(\mathbf{r})$, τ_{V-T}, and r^*, had theoretical PA signals as training, validation and testing inputs. The PA signals were calculated using the Fourier transform method and Green's functions method [10] for a specific laser beam profile and exponential excitation energy decay, in accordance with the experimental conditions. With the aim to improve and compare the experimental results in real time, an additional parameter had to be taken into account: the photoacoustic signal intensity I and corresponding values of the laser fluence Φ (Fig. 1). The ANNs used in this study, presented in Fig. 1, had an input layer, one or two hidden layers and an output layer. Structures with up to two hidden layers were selected on the basis of numerous experiments and performance trials. The architecture of the ANNs consisted of four neurons in the output layer (three output neurons to be included by merging with our previously published results). The outputs of the neural network were: value of ε, value of r^*, profile shape class and laser fluence Φ. The Levenberg–Marquardt algorithm was used to train the feedforward multilayer perception network. The mean squared error was used as a performance measure during training. Three outputs of the neural networks were estimated values of ε and r^* (previously defined), and the profile shape class, which distinguished: Gauss, top hat, Lorentz and Lorentz with the hole laser beam profiles [10]. Additional output of the network estimated the value of Φ.

In contrast to our previous results in which we introduced neural networks capable of determining three parameters from a PA signal (τ_{V-T}, r, R), the networks developed here demonstrate that a fourth parameter, laser fluence Φ, can be determined with the same success. We therefore kept the sampling of the PA signal in 21 or 28 points, maintaining compatibility with our previous results. This approach makes it possible for the three previous parameters and the fourth parameter introduced here to be estimated by two separate networks in a parallel fashion, or be combined into a single network's solution to estimate all four parameters, as illustrated in Fig. 1. A combined solution is more elegant, but it demands a more complex network structure, while a parallel solution is less elegant but clearly separates the additional results presented here from our previously published results.

4 Experimental Results

A typical experimental photoacoustic device to investigate samples in the gaseous phase and measure the relaxation time consists of a laser, photoacoustic cell and a microphone. The TEA CO_2 laser with a 45-ns FWHM pulse was used as a nonfocused beam source. The beam spatial profile was defined by the iris. The iris defines a characteristic spatial profile consisting of concentric rings. The number of rings depends on the iris size, wavelength and so on. Usually, we have had only one ring; thus, this profile can be described by the Lorentz profile with the hole. The profile was not quantified by other methods, but it was visualized by thermal tape or a graphite plate. The stainless-steel photoacoustic cell was 18.5 cm long and had a diameter of 9.3 cm. We examined the gas mixture SF_6–Ar. Measurements were carried out on the
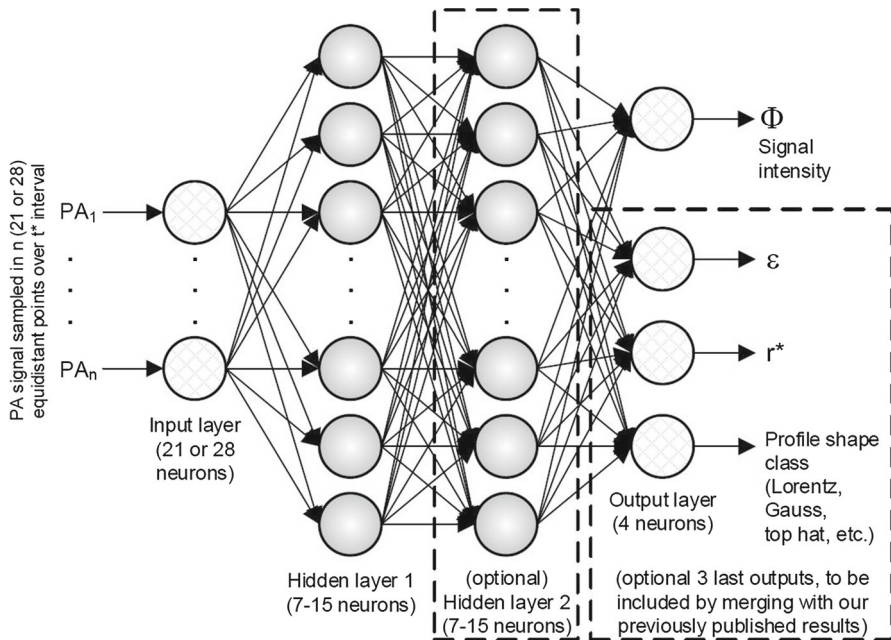
Fig. 1 ANN trained to recognize laser fluence Φ from PA signal intensity, with possibility of extension for simultaneous determination of the profile shape class, vibrational-to-translational relaxation time (τ_{V-T}) and distance from the laser beam to the absorption molecules (SF_6) within the photoacoustic cell (r^*)

mixture under a pressure of 100 mbar with a fluence range of 0.2 J·cm^{-2}–1.5 J·cm^{-2}. The absorber pressure (SF_6) was kept constant at 0.47 mbar. With such experimental conditions, we can assume that all of the irradiated molecules took part in the excitation processes, allowing for the average number of absorbed photons and those corresponding to the real excitation level of molecules to be calculated [4]. Also, our experimental results confirmed that, for a fixed total SF_6–Ar pressure, the variations of ε (τ_{V-T}) as a function of the real excitation level are much smaller than those due to noise deviations, especially at lower fluences [4,8]. The photoacoustic wave generated was detected by an appropriate microphone (Knowles Electronics Co., Model 2832), which was placed in the chamber. The experimental settings contained optical (beam splitter, lenses) and additional instruments (joulemeter, photon-drag detector, oscilloscopes), a vacuum system and a system for introducing gases.

Experimental PA signals were obtained for five different values of Φ (0.2, 0.4, 0.6, 0.8, 1.0 and 1.4) J·cm^{-2}. These values fulfill the conditions for the study of MP processes in a gas mixture. The experimental PA signals obtained from the SF_6–Ar gas mixture for five different Φ values are shown in Fig. 2. The theoretical PA signals were calculated using Green's function method for parameter $\varepsilon = 3.6$ for the Lorentz with the hole profile shape, which corresponds to the experimental setup. A comparison between the five experimental PA signals and a single theoretical PA signal is presented in Fig. 2, revealing mainly satisfactory agreement. Still, there are certain disagreements between theoretical and experimental PA signals. Discrepancies
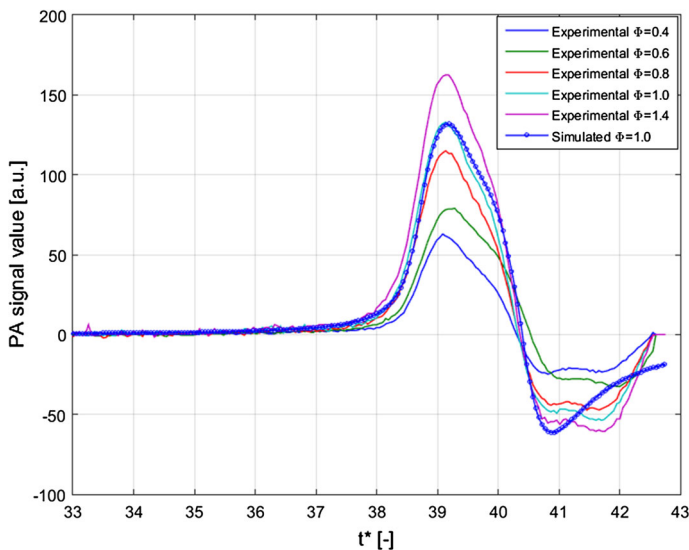
Fig. 2 Comparison of five experimental signals (obtained from SF_6–Ar mixture for absorber pressures of $p_{SF6} = 0.47$ mbar and $p_{total} = 100$ mbar) for laser fluences $\Phi = (0.4, 0.6, 0.8, 1.0, 1.4)$ J·cm^{-2} and single simulation signal for $\Phi = 1.0$ J·cm^{-2}. The theoretical signal was calculated for the Lorentz with the hole laser beam profile and for the parameter $\varepsilon = 3.6$. Signal intensity is shown in arbitrary units (a.u.), and the x-axis values represent reduced time (t^*). Discrepancies between experimental and theoretical signals are caused by well-known phenomena

Table 1 Results—training by simulation, guess of experimental data

Real Φ	1.4	1.0	0.8	0.6	0.4	MaxError	AvgError
ANN estimate	1.4552	1.2650	0.9941	0.4967	0.3240		
ANN error	3.94 %	26.50 %	24.26 %	17.22 %	19.00 %	26.50 %	18.18 %

between the signals are the result of variations in the laser beam profile (nonideal profile in experiments). The difference between the theoretical spatial laser beam profile and the real laser beam (experimental) profile leads to the difference between the theoretical and experimental signal. In some cases, small deviations may occur due to different deexcitation dynamics, particularly in the case of MP processes. The SF_6–Ar mixtures investigated under our experimental conditions for their pressure and fluence ranges satisfy the exponential decay approximation. The influence of the laser beam spatial profile and excitation energy decay on measuring the relaxation time and calibration of the photoacoustic system has already been explained in detail [19].

In PAS experiments, the signal measured corresponds to the pressure change detected by the microphone. Some deformations of a real signal may arise due to pressure changes. We should note that the existing disagreements between the theoretical and experimental signal are caused by numerous factors, and this has some influence on the accuracy of the computational intelligence method proposed in this paper (Table 1).
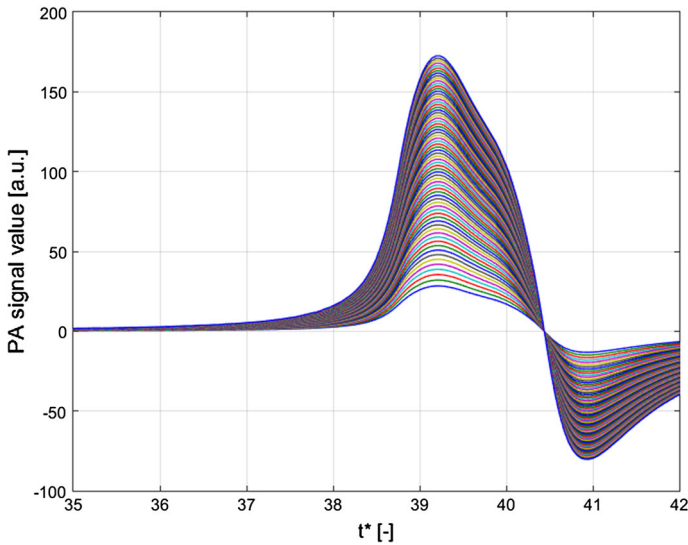
Fig. 3 ANN training dataset of 71 simulation PA signals for laser fluence Φ ranging from (0.2 to 1.5) $J \cdot cm^{-2}$. Dataset of 71 PA signals was calculated using Green's function method for Lorentz with the hole spatial laser beam profile and parameter $\varepsilon = 3.6$, which provide the best match with the experimental PA signal

The average number of absorbed photons per molecule <n> is a function of fluence Φ. It was found that the average number of photons absorbed per molecule <n> is proportional to $\Phi^{2/3}$ [20]. Also, the intensity of the PA signal is a function of fluence Φ through the number of absorbed photons <n>. We define the PA signal intensity I as the maximum value of the first peak P^+ [11]. We measured the absorbed energy based on the transmitted energy for a cell filled by the gas mixture and the transmitted energy for the evacuated cell. Due to low absorption, the number of measurements must be large enough for precise determination of the absorbed energy. The intensity ratio for two PA signals (I_1/I_2) as well as the ratio of absorbed energy (E_{01}/E_{02}) must follow the fluence ratio (Φ_1/Φ_2)$^{2/3}$. This dependency was proven on a set of theoretical and experimental PA signals. The validity of these relations has enabled us to form an input set of theoretical PA signals for network training which contains the necessary information about laser fluence, in order to achieve good generalization in the network. Using this known relation between the signal intensity I and laser fluence Φ, and based on comparison between the experimental and theoretical (for the Lorentz with the hole profile shape) signal intensities, we defined a sufficient number of PA signals for the network training.

Datasets for the network training, validation and testing were randomly selected from the same dataset of 71 PA signals calculated using Green's function method for parameter $\varepsilon = 3.6$ and spatial laser beam profile Lorentz with the hole. The Lorentz with the hole profile provides the best match with the experimental PA signal [10]. A complete dataset of 71 theoretical (PA) signals for network learning is shown in Fig. 3. In order to form a statistical model for network generalization, the dataset is divided
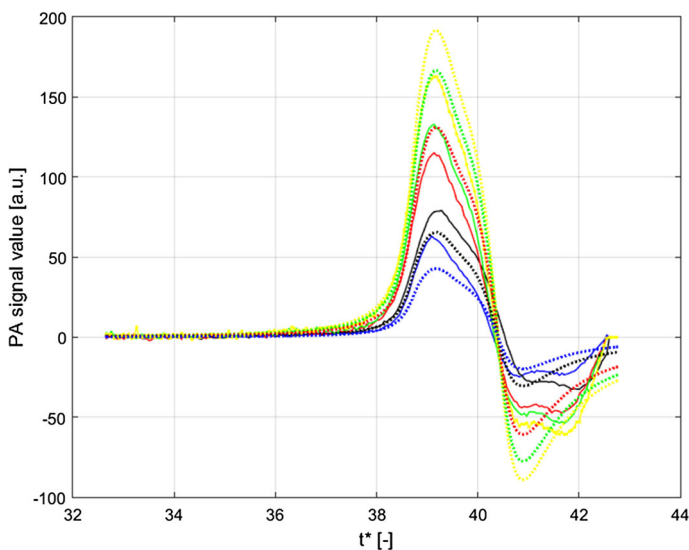
Fig. 4 ANN fit for five different laser fluence values, $\Phi = (0.4, 0.6, 0.8, 1.0, 1.4)$ J·cm^{-2}. Solid line and dotted line of the same color are experimental and ANN fit, respectively (signal intensity in arbitrary units is a function of reduced time t^*)

into: the training, test and validation sets. The training set, that contained 49 PA signals with a corresponding pairs of input–output data, was presented to the network during training. The ANN adjusted the weights during training in order to obtain a minimal error. The validation sample (11 PA signals) was used to measure the network generalization during training. Error in the validation sample was monitored during training, and the training was stopped when the ability to generalize stopped improving. The testing sample of 11 PA signals had no effect on training and provided an independent measure of network performance during and after training. To evaluate the error, a test set was used. When the training of the network was completed, it was able to process new experimental PA signals (with unknown parameters) in the application phase and produce reasonable output instantaneously with sufficient accuracy. The optimum number of neurons required in the hidden layer depends on the complexity of the input and output data. The network inputs were 21 or 28 equidistant points, which proved to be sufficient for efficient network operation. All the PA signals were sampled at 21 or 28 equidistant points on the t^* axis.

The method was tested by five experimental PA signals with different Φ values. The estimated values of the parameter Φ and errors in the percentages are shown at Table 1. The error bars are lower for higher fluences because the signal-to-noise ratio is the best at the highest fluence. The ANN fit for five different Φ values is illustrated in Fig. 4, which shows that the difference presented in Fig. 2 between the experimental and simulation signals used for the ANN training is similar to the ANN results. We can conclude that for the given task the ANN performed efficiently, but some differences between the real and estimated Φ values occurred for reasons which have already been discussed.

5 Conclusion

ANNs as a technique is currently having a vast practical impact in measurement technology and many other fields. Feedforward neural networks are very suitable for modeling nonlinear relationships and are particularly useful in solving problems for which there are no suitable conventional mathematical models. Neural network training can in some cases be computationally intensive and slow, but in the implementation phase feedforward networks have high speed parallel data processing as an inherent feature. In this paper, we have focused our attention on artificial neural networks applied to the problem of determining the values of Φ, based on the intensity of theoretical and experimental PA signals. One of the easily varied parameters in an MPE experiment is laser fluence Φ. Variations in fluence Φ produce profound changes in the absorption cross section and the dissociation probability. This could mask the real ratio between the absorption efficiency of the SF_6 and other trace gases within the same experimental conditions. To prevent such changes, neural networks can be applied to recognize the values of Φ in real time from the intensity of the PA signal.

The proposed method for the application of computational intelligence to photoacoustic measurements was successfully tested by theoretical and experimental PA signals. Trained networks were capable of recognizing four parameters simultaneously: the laser beam spatial profile, excited molecule relaxation time, distance between the laser and the microphone and laser fluence. The networks were trained using the calculated (theoretical) PA signals adjusted for our experimental setup. This methodology can be used to efficiently find the parameters of unknown (experimental) PA signals with acceptable precision. In the application phase, ANNs determine the laser fluence and the aforementioned parameters practically instantaneously, providing real-time operation. These advantages of the computational intelligence method allow for its more efficient usage in trace gas monitoring with the possibility of its application for higher intensities of laser radiation. Although the solution to the problem of finding Φ values from theoretical PA signals networks is satisfactorily precise, it is necessary to improve the accuracy on a set of experimental PA signals. As explained, there are several reasons which cause the differences between theoretical and experimental signals, and consequently differences in the real and estimated values of Φ. Further directions of our research could be to improve precision in determining the parameter Φ on a set of experimental PA signals with the application of fuzzy systems or by applying more complex hybrid neuro-fuzzy-genetic solutions. Also, as an important research direction, along with the analysis of atmospheric pollutants considered here, is to consider more practical applications and case studies for our methodology in order to further prove its usability.

As we have mentioned before, we believe that this intelligent photoacoustic approach could thoroughly establish the ground work to fulfill the goal of developing a versatile instrument capable of tracing and monitoring gas species with a self-correction capability. Such an instrument could be a completely application-oriented system, one that does not need any change in the experimental setup, and all are just matter of modified software.

References

1. V. Zeninari, R. Vallon, C. Risser, B. Parvitte, J. Thermophys. **37**, 7 (2016)
2. X. Mao, X. Zhou, Z. Gong, Q. Yu, Sens. Actuators B Chem. **232**, 251 (2016)
3. V. Spagnolo, P. Patimisco, A. Sampaolo, M. Giglio, L. Dong, G. Scamarcio, F. K. Tittel, in *Proceedings of SPIE 9899, Optical Sensing and Detection IV, 98990S*, 29 Apr 2016. doi:10.1117/12.2228701
4. D.D. Markushev, J. Jovanović-Kurepa, M. Terzić, J. Quant. Spectrosc. Radiat. Transf. **76**, 85 (2003)
5. J. Gajević, M. Stević, J. Nikolić, M. Rabasović, D. Markushev, Facta Universitatis **4**, 57 (2006)
6. M. Terzić, D.D. Markushev, J. Jovanović-Kurepa, Rev. Sci. Instrum. **74**, 322 (2003)
7. J.D. Nikolić, M.D. Rabasović, D.D. Markushev, J. Jovanović-Kurepa, Opt. Mater. **30**, 1193 (2008)
8. D.D. Markusev, J. Jovanovic-Kurepa, J. Slivka, M. Terzic, J. Quant. Spectrosc. Radiat. Transf. **61**, 825 (1999)
9. M. Terzic, J. Jovanović-Kurepa, D.D. Markušev, J. Phys. B At. Mol. Opt. Phys. **32**, 1193 (1999)
10. M. Lukić, Ž. Ćojbašić, M. Rabasović, D. Markushev, Meas. Sci. Technol. **25**, 125203 (2014)
11. M.D. Rabasović, D.D. Markushev, J. Jovanović-Kurepa, Meas. Sci. Technol. **17**, 1826 (2006)
12. K.M. Beck, R.J. Gordon, J. Chem. Phys. **87**, 5681 (1987)
13. K.M. Beck, R.J. Gordon, J. Chem. Phys. **89**, 5560 (1988)
14. M. Lukić, Ž. Ćojbašić, M. Rabasović, D. Markushev, D. Todorović, Int. J. Thermophys. **34**, 1466 (2013)
15. M. Lukić, Ž. Ćojbašić, M. Rabasović, D. Markushev, D. Todorović, Int. J. Thermophys. **34**, 1795 (2013)
16. M. Lukić, Ž. Ćojbašić, M. Rabasović, D. Markushev, D. Todorović, Facta Universitatis Ser. Phys. Chem. Technol. **10**, 1 (2012)
17. M.D. Rabasović, J. Nikolić, D.D. Markushev, Appl. Phys. B **88**, 309 (2007)
18. L. Liu, J. Rong, L. Huang, K. Lu, X. Zhong, in *5th IEEE International Symposium on Computational Intelligence and Design (ISCID)*, 28–29 Oct 2012, Hangzhou, China, pp. 2515–2518 (2012)
19. M.D. Rabasović, J.D. Nikolić, D.D. Markushev, Meas. Sci. Technol. **17**, 2938 (2006)
20. J. Jovanovic-Kurepa, D.D. Markusev, M. Terzic, Chem. Phys. **211**, 347 (1996)

CrossMark

ICPPP 18

Thermal Diffusivity of High-Density Polyethylene Samples of Different Crystallinity Evaluated by Indirect Transmission Photoacoustics

M. Nesic[1,2] · **M. Popovic**[2] · **M. Rabasovic**[3] ·
D. Milicevic[2] · **E. Suljovrujic**[2] · **D. Markushev**[3] ·
Z. Stojanovic[2]

Abstract In this work, thermal diffusivity of crystalline high-density polyethylene samples of various thickness, and prepared using different procedures, was evaluated by transmission gas-microphone frequency photoacoustics. The samples' composition analysis and their degree of crystallinity were determined from the wide-angle X-ray diffraction, which confirmed that high-density polyethylene samples, obtained by slow and fast cooling, were equivalent in composition but with different degrees of crystallinity. Structural analysis, performed by differential scanning calorimetry, demonstrated that all of the used samples had different levels of crystallinity, depending not only on the preparing procedure, but also on sample thickness. Therefore, in order to evaluate the samples' thermal diffusivity, it was necessary to modify standard photoacoustic fitting procedures (based on the normalization of photoacoustic amplitude and phase characteristics on two thickness levels) for the interpretation of photoacoustic measurements. The calculated values of thermal diffusivity were in the range of the expected literature values. Besides that, the obtained results indicate the unexpected correlation between the values of thermal diffusivity and thermal conductivity with the degree of crystallinity of the investigated geometrically thin samples. The results indicate the necessity of additional investigation of energy transport in

---

✉ M. Nesic
mioljub@gmail.com; mioljub.nesic@vin.bg.ac.rs

1 School of Electrical Engineering, University of Belgrade, Bul. kralja Aleksandra 73, Belgrade 11120, Serbia

2 Vinca Institute of Nuclear Sciences, University of Belgrade, PO Box 522, Belgrade 11001, Serbia

3 Institute of Physics, University of Belgrade, Pregrevica 118, Belgrade-Zemun 11080, Serbia

🖄 Springer

macromolecular systems, as well as the possible employment of the photoacoustic techniques in order to clarify its mechanism.

1 Introduction

Polyethylene (PE) is well known and one of the most frequently used polymers. Its universal value is proven throughout its whole lifespan—from its straightforward and easily adoptable industrial production process to the myriad of application fields, depending on the type, i.e., on its physical and chemical properties [1–3]. The material of interest in this work is high-density polyethylene (HDPE), the type of PE characterized by low degree of branching (which results in linear molecule packing with stronger intra-molecular bonds) and relatively high density and level of crystallinity compared to other PEs [4–9]. Due to excellent impact resistance, high tensile strength, low moisture absorption and chemical resistance, HDPE is used in a variety of applications such as product packaging, piping production, electrical insulation, as well as in many other plastic product industries [1,10,11].

In all of these applications, it is of great importance to be familiar with experimentally evaluated thermal properties of HDPE as well as with their relation to the structure of macromolecular materials and dynamic processes in them, in order to achieve the engineering of these properties for the specific applications [1]. These experimental investigations are also significant from the point of view of fundamental research of energy transport mechanism through macromolecular systems [12,13]. In recent decades, dynamic thermal properties have been investigated by photothermal (PT) and photoacoustic (PA) methods, and the results have shown good agreement with literature values, obtained by other methods [12,14–19]. This fact represents an encouragement for further application of PT/PA methods in thermal characterization of polymer materials, but also the stimulus for their further development, including inverse procedures, in order to provide a better explanation between structural changes, thermal properties and energy transport mechanisms of these materials.

In this paper, thermal diffusivity of crystalline HDPE films, of various thickness and prepared using different procedures, is examined using transmission gas-microphone PA frequency method. In the first part of the work, the preparation procedure of the samples is presented in brief, along with the results and the discussion of the examination performed by wide-angle X-ray diffraction (WAXD) and differential scanning calorimetry (DSC) techniques. After that, the measured PA responses, both amplitude and phase, are displayed. The analysis of WAXD and DSC results indicates that the processing of PA measurements, based on the normalization of amplitude and phase characteristics to two thickness levels, must be modified. In the second part, the developed inverse procedure for the evaluation of thermal properties from the PA measurements is explained, and the obtained results are presented in table form. Finally, the most important conclusions are drawn.
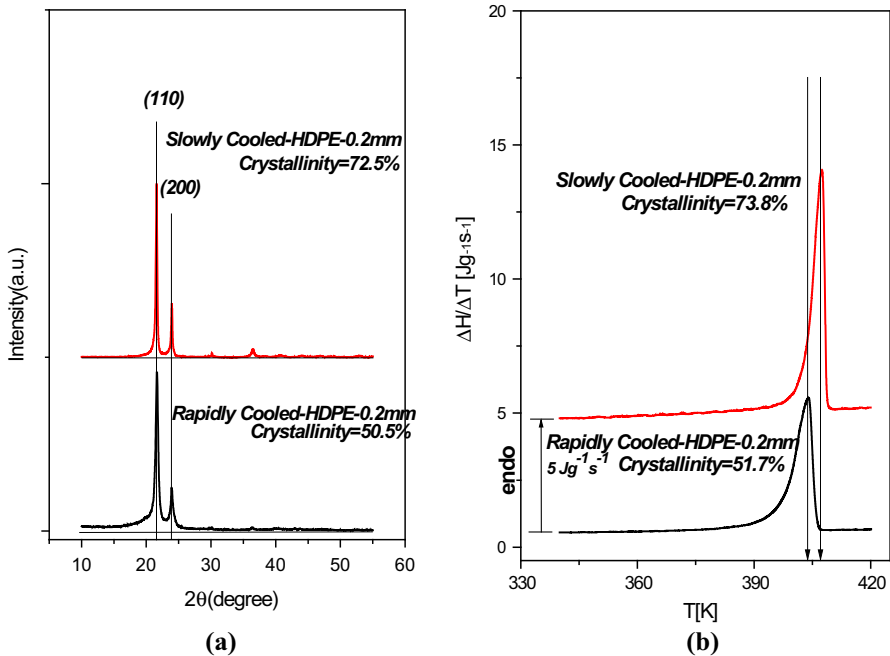
Fig. 1 The results of (a)WAXD and (b) DSC measurements

2 Experiment

2.1 Preparation of Samples and Results of WAXD and DSC Measurements

The polymer used in the present study was HDPE Hiplex HHM 5502 (ρ = 0.955 g cm^{-3}, M$_w$ = 300 000). Square-shaped isotropic sheets of different thickness (200 μm, 400 μm and 600 μm) were obtained by 20 min compression molding in a Carver laboratory press at 160 °C and with gradual pressure increment, up to 3.28 MPa. One set of the molded sheets was rapidly cooled by swift sinking in the mixture of ice and water ($\sim$ 0 °C), in order to obtain samples with low level of crystallinity. The other set was prepared by slow cooling from melting temperature to room temperature ($\sim$ 20 °C), keeping the samples between the press platens without pressure for the period of 6 h, thus attaining samples of high crystalline content. The composition of PE samples obtained by these two different preparing procedures was determined from WAXD measurements, using a Bruker D8 Advance Diffractometer (in normal mode, with Cu Kα emission). Parallel beam optics was adjusted by a parabolic Göbel mirror (push plug Ni/C) with horizontal grazing incidence soller slit of 0.12° and a LiF monochromator. Diffractometer scans were taken within the angular range of 2θ = 10°–45°, at steps of 0.02°, with the 10 s exposure step (see Fig. 1a for the thinnest samples). Stationary thermal properties of all samples were obtained by DSC, using a PerkinElmer DSC-7 differential scanning calorimeter with nitrogen as the purge gas. Samples weighing 7–8 mg were analyzed by heating from 320 K to 450 K at the

Table 1 Crystallinity as a function of preparation conditions and thickness of the sample

χ (%)	200 μm		400 μm	600 μm
	DSC	WAXD	DSC	DSC
Fast cooled	51.7	50.5	57.4	59.3
Slowly cooled	73.8	72.5	71.5	70.8

rate of 10 K min^{-1}, and their heats of fusion (ΔH_f) were derived (see Fig. 1b for the thinnest samples). From the DSC measurements, the degree of crystallinity (DoC) was calculated as $\chi = \Delta H_f/\Delta H_{f0}$, where $\Delta H_{f0}$is the heat of fusion of a perfectly crystalline PE sample ($\Delta H_{f0} = 289\,J\,g^{-1}$) [1,20]; from the WAXD measurements, the DoC was evaluated from the diffraction patterns by resolving multiple peak data into individual crystalline peaks and an amorphous halo [21,22]. Quantitative analysis was performed using a standard software package for fitting the experimental spectra.

The results of the analysis of DSC and WAXD measurements are summarized in Table 1.

It can be observed, from Table 1, that in slowly cooled samples crystallinity is higher (around 70 %, compared to the rapidly cooled ones, where it is around 50 %) and is slightly growing as the sample thickness decreases (around 3 %, overall). In rapidly cooled samples, the opposite trend is present: the crystallinity falls with the decrease in sample thickness (around 7.5 %, overall). Higher degree of crystallinity in slowly cooled samples is related to the longer period of cooling, during which the parts of the macromolecule chain have sufficient time to line up more regularly. The difference in the influence of sample thickness on the crystallinity between slowly and rapidly cooled samples can be related to the greater influence of surface effects in slowly cooled ones. Namely, the production of crystalline materials from the melting via rapid cooling introduces defect centers at surface. The influence of defect centers on thermal properties is more pronounced in thinner samples, in particular, because the defect centers decrease the mean free path of thermal energy carriers.

2.2 PA Experiment and Evaluation of Thermal Diffusivity

The samples, both slowly and rapidly cooled ones, at three levels of thickness—$l_s = 200\,\mu$m, 400 μm, 600 μm—were made disk-shaped (r = 5 mm), and a thin absorption layer ($\sim$10 μm) was deposited using the air-brush technique. They were put into a minimum volume PA cell [23], which is part of a larger instrument used for PA frequency response measurements.

The instrument setup consists of a detection unit and a signal processing/power supply unit (a box containing batteries and home-made electronics, Fig. 2a). The setup also contains a PC, with the appropriate acquisition software and a stereo input sound card, acting as a lock-in amplifier. The modulation signal, representing the input to the driver, which controls the operation of the laser/LED, comes from the sound card line-out connector (standard 3.5 mm stereo connector, Fig. 2b). The reference signal from the photodiode, carrying the information about the input source power and phase as well, is amplified ten times, while the microphone signal is amplified 10
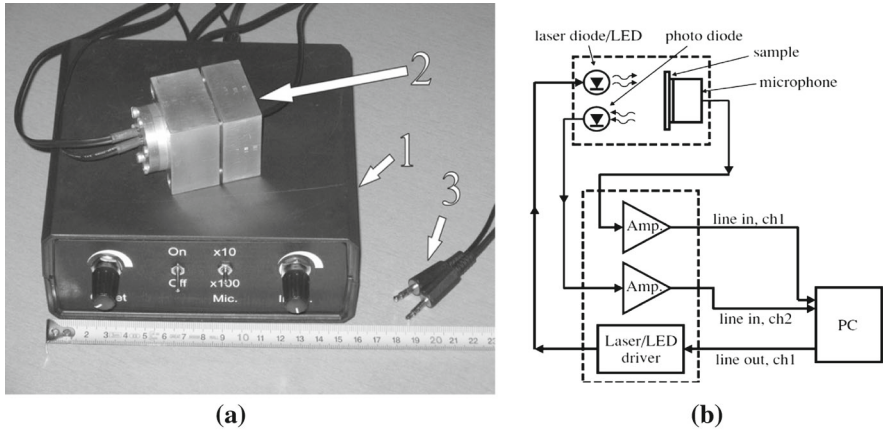
(a)   **(b)**

Fig. 2 Experimental setup: (a) Photograph of the apparatus: 1—The box which contains the electronics and the batteries, 2—PA cell, 3—standard 3.5 mm stereo connectors; (b) Schematic diagram—the PA cell marked with the dotted line.

(or 100) times—all achieved by the use of a set of low-noise, high-speed operational amplifiers OP37. This type of amplifier has demonstrated a flat amplitude response in the 10 Hz–20 kHz frequency range, showing no phase change. Both signals are processed by the two line-in stereo connector channels of the sound card [24].

The PA cell is made from duralumin, with the electret microphone (ECM60, 9.8 mm in diameter, 2.5 mV Pa^{-1} of sensitivity), laser diode/LED and photodiode (all replaceable) embedded in it. It is a *minimum volume* type cell, with the interior of the microphone (confined with its orifice on one and its diaphragm on the other end) acting as the PA cell chamber—the configuration that guarantees high sensitivity and low level of losses [23,24]. The absorption layer, which plays a significant role as the absorber of electromagnetic (EM) energy and the light radiation protector for the microphone, is illuminated ("PA transmission configuration") and is considered a surface heat source for the sample, whose influence on heat transfer and consequently to the PA response can be neglected [14–19].

Experimentally obtained values of amplitude and phase PA response of both rapidly cooled and slowly cooled HDPE, at all three thickness levels, are presented in Fig. 3.

In order to make a connection between the thermoelastic (TE) properties of a single-layered sample and its PA response, the composite piston theoretical model is deployed where the sample is modeled as a simply supported plate [25–27]. This model predicts that the resulting pressure, in theory, is the sum of two components, namely p_{th}—the component that originates from the periodic expansion of a thin gas layer closest to the sample—and p_{ac}—the component which sums up all the TE movements inside the sample and on its surface (Eq. 1):

$$\tilde{p} = \tilde{p}_{th} + \tilde{p}_{ac} \quad \rightarrow \quad
\begin{aligned}
\tilde{p}_{th} &= \frac{\gamma P_0}{l_a T_0} \int\limits_{l_s}^{l_s+2\pi\mu_a} \tilde{\vartheta}_s(l_s) e^{-\tilde{\sigma}_a(x-l_s)} dx, \\
\tilde{p}_{ac} &= \frac{3\gamma P_0}{l_a} \alpha_S \frac{R^2}{l_s^3} \int\limits_{0}^{l_s} (x - \tfrac{l_s}{2}) \tilde{\vartheta}_s(x) dx.
\end{aligned}
\tag{1}$$

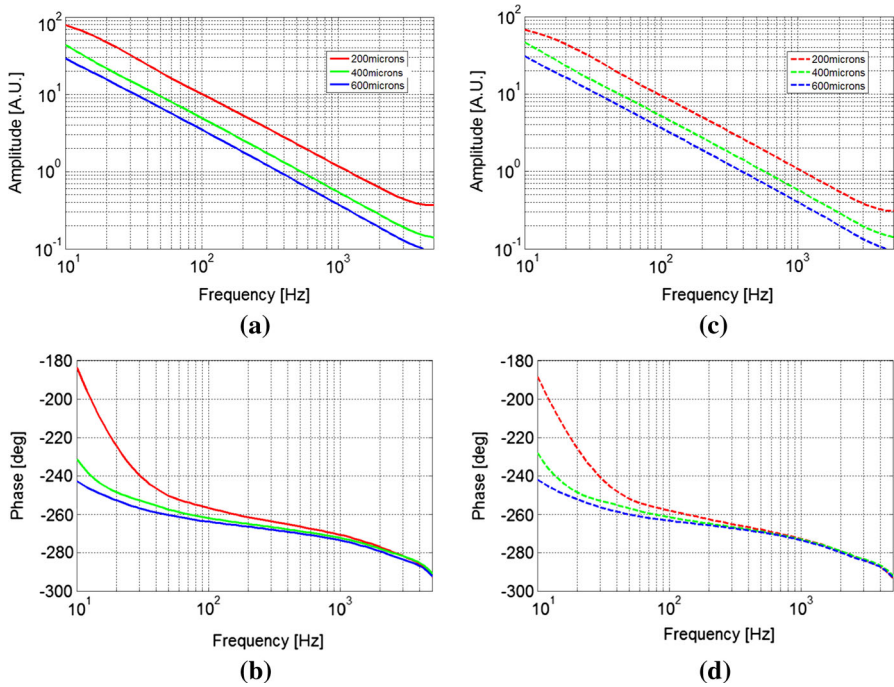**Fig. 3** Experimental results: rapidly cooled samples (low crystalline) on the left, amplitude and phase (*a* and *b*, respectively), and slowly cooled ones () on the right, amplitude and phase (*c* and *d*, respectively)

Here, γ annotates the adiabatic coefficient, P_0 is the atmospheric pressure, l_a is the length of the gas column inside the PA chamber, while T_0 stands for the room temperature. Furthermore, α_S is the linear coefficient of thermal expansion of the sample, R is its radius, while l_s annotates its thickness. The symbols $\tilde{\vartheta}_s$ and μ_a represent the distribution of temperature variations across the sample and the thermal diffusion length in the air (gas). These equations, when solved (and having accounted for the influence of thermal memory effect on the distribution of temperature variations in the sample and its environment) take their final form [28,29]:

$$\tilde{p}_{th} = \frac{\gamma P_0 S_0}{T_0} \frac{\tilde{Z}_{cs}}{\tilde{\sigma}_a l_a} \frac{1}{\sinh(\tilde{\sigma}_s l_s)},$$
$$\tilde{p}_{ac} = 6\gamma P_0 S_0 \alpha_s \frac{R^4}{R_c^2 l_a l_s} \tilde{Z}_{cs} \frac{\cosh(\tilde{\sigma}_s l_s) - \frac{\tilde{\sigma}_s l_s}{2}\sinh(\tilde{\sigma}_s l_s) - 1}{(\tilde{\sigma}_s l_s)^2 \sinh(\tilde{\sigma}_s l_s)}. \tag{2}$$

In the above expressions, S_0 stands for the surface heat source, which equals half of the excitation energy intensity, R_c represents the radius of the circle where the sample is *simply supported*, $\tilde{\sigma}_i$ and $\tilde{Z}_{ci}$, $i = a, s$ are the heat wave vector and the thermal impedance of the environment (air or sample), given by:

$$\tilde{\sigma}_i = \frac{1}{\sqrt{D_{Ti}}}\sqrt{j\omega(1 + j\omega\tau_i)},$$
$$\tilde{Z}_{ci} = \frac{\sqrt{D_{Ti}}}{k_i}\sqrt{\frac{(1 + j\omega\tau_i)}{j\omega}}, \tag{3}$$

where k_i, and D_{Ti} $i = a, s$, stand for the thermal conductivity. The radial modulation frequency is $\omega = 2\pi f$, and τ_i, $i = a, s$, is the parameter which describes the influence of thermal memory of the medium, referred to as *thermal relaxation time* [28–31].

The appearance of the parameter τ_i in this work is the consequence of the use of the *generalized model of photothermal wave propagation* [30]. However, the comparisons of the experimental measurement in Fig. 3 to earlier theoretical investigations which include thermal memory effects [28–31], and also to previously obtained experimental measurements on certain plastics in the frequency range up to 1 kHz [14–19], lead us to the conclusion that τ_i is small enough and that its influence can be neglected in the measured frequency range.

3 Self-Consistent Inverse PA Procedure: Results and Discussion

The results of DSC and WAXD analysis (Table 1) implied that, in both rapidly and slowly cooled set of samples, not a single pair of samples with the same crystallinity could be identified! Therefore, we had to presume that not two samples, structurally the same but of the different thickness, could be found. Consequently, the standard procedure of normalizing the results to two thickness levels, although widely adopted in solving inverse PA problems [14,32,33], could not be deployed for the samples obtained by the described process. That is why our own system of evaluating thermal parameters from the measured PA response had to be developed.

In HDPE and macromolecular materials, the contribution of the p_{th} component is significant at very low frequencies (under 50 Hz), and in this region microphone transfer characteristic is no longer flat [34]. However, in the measurement range 100 Hz–1 kHz, where the influence of the measurement chain on the shape of the signal is considered negligible, the dominance of the TE component of the PA response is crucial [14]. So, basing our concept on the experimental data shown in Fig. 3, and on the detailed analysis of the model [35] given by Eq. 2 which can be found in the literature [34], the model is simplified as:

$$\tilde{p}_{TE}^{(HF)} = P_0 I_0 \frac{\gamma}{l_a} \cdot \frac{3\alpha_s R^4}{4k_s R_c^2} \cdot \frac{1}{x} \left(1 - \frac{1}{\sqrt{x}}\right) \cdot \exp\left(-i\left[\frac{3}{2}\pi - \frac{1}{\sqrt{x}}\right]\right),$$
$$x = \frac{\pi f}{D_{Ts}} l_s^2$$

where

$$\left|\tilde{p}_{TE}^{(HF)}\right| = P_0 I_0 \frac{\gamma}{l_a} \cdot \frac{3\alpha_s R^4}{4k_s R_c^2} \cdot \frac{1}{x} \left(1 - \frac{1}{\sqrt{x}}\right),$$
$$\arg(\tilde{p}_{TE}^{(HF)}) = \frac{3}{2}\pi - \frac{1}{\sqrt{x}}, \tag{4}$$

although the four unknown properties of the sample still influence the PA response in the measurement range: (1) thermal conductivity ($k_s[\text{W} \cdot \text{m}^{-1} \cdot \text{K}^{-1}]$), (2) thermal

Table 2 Literature and fitted values of HDPE's thermodynamic parameters

	Intervals
HDPE—high-density polyethylene	
k_s thermal conductivity $\left[\frac{W}{m \cdot K}\right]$	0.33–0.53
D_{Ts} thermal diffusivity $D_{Ts} = \frac{k_s}{C_p} = \frac{k_s}{c \cdot \rho}, \left[\times 10^{-6} \frac{m^2}{h} boxs\right]$	(0.265–0.313)

diffusivity ($D_{Ts}[m^2 \cdot s^{-1}]$), (3) linear expansion coefficient ($\alpha_s[K^{-1}]$) and (4) sample thickness ($l_s[m]$). Fortunately, the phase characteristic depends only on thermal diffusivity and sample thickness. Having this in mind, a rough fitting of the phase characteristic was done and a range of values for D_{Ts} of the used samples was obtained, which is presented in Table 2, along with the range of literature values of k_s. The value of $\alpha_s = 225 \cdot 10^{-6} K^{-1}$ was found in the literature, too [36,37].

Intervals of k_s and D_{Ts} are presented by five equidistant points, which are put into the computing program, written in Matlab, and twenty-five theoretical PA response vectors are derived (over the experimental frequency range), each corresponding to the exact set of parameters (k_s, D_{Ts}). Then, the standard deviation (StD) from the experimental data is computed on the defined region of interest (RoI) for each vector; the minimum value of the calculated StD determines the theoretical vector, based on the set of parameters ($k_s D_{Ts}$) which are closest to the set corresponding to the actual, experimentally measured data. The calculated StD values are mapped on the $k_s - D_{Ts}$ plane as 3D mesh-figures (Figs. 4, 5), and this procedure is repeated for each sample thickness level (200 μm, 400 μm, 600 μm), for both rapidly and slowly cooled samples. The evaluated sets of (k_s, D_{Ts}) parameters, corresponding to each of the minima, are presented in Table 3.

The comparison of literature and roughly fitted thermal parameter values (Table 2) with ($k_s D_{Ts}$) obtained parameter set (Table 3) indicates the high level of compliance [14,18,36,37].

As can be clearly observed in Fig. 4, the two thick sets of samples (at 400 μm and 600 μm) show no observable differences, when it comes to the evaluation of (k_s,D_{Ts}) parameters (Table 2). On the other hand, in thinnest samples (at 200 μm), these characteristics emerge in Fig. 5, where the minima of the *StD*-planes are clearly not the same, and, consequently, the (k_s, D_{Ts}) parameter sets are different, too (Table 3, data given in bold). In thinnest samples, both slowly and rapidly cooled ones, the increase in thermal conductivity is observed in comparison with thicker samples. This result is not expected if thermal energy carriers are considered to be phonons. The observed rise is larger in slowly cooled (more crystalline) samples than in rapidly cooled (less crystalline) ones, which is expected. On the other hand, in slowly cooled samples, thermal diffusivity remains intact, regardless of the thickness and is the same as in two thick, slowly cooled ones. The thinnest rapidly cooled sample exerts the decrease of thermal diffusivity, which is in accordance with expectations.
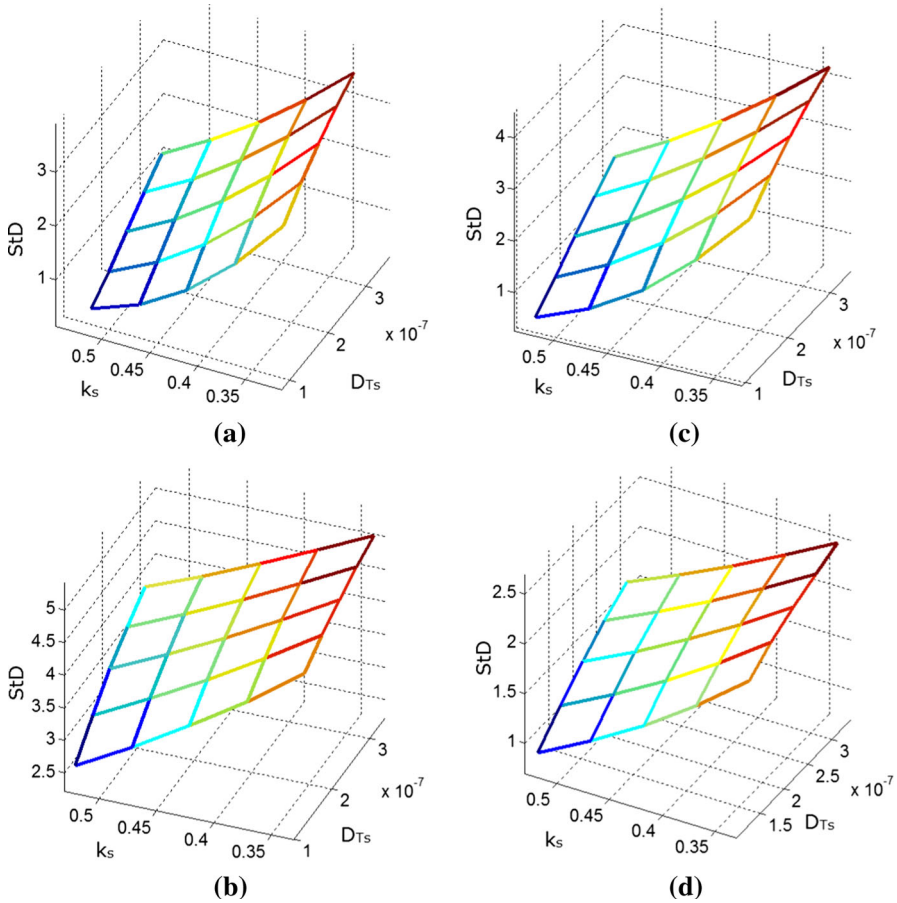
Fig. 4 Comparison of the computed StD over RoI as the function of (k_s, D_{Ts}) sets, for the samples 400 µm and 600 µm thick: rapidly cooled samples on the left (low crystalline, *a* and *b*, respectively), slowly cooled on the right (highly crystalline, *c* and *d*, respectively)

From Table 3, it can be remarked that thermal parameters obtained by amplitude and phase fitting do not correlate with the degree of crystallinity (DoC) of thicker samples (400 µm and 600 µm), notwithstanding the way of their preparation. However, this correlation exists in both thin samples, meaning that PA transmission method could be employed for the DoC determination of the samples thinner or equal to 200 µm only.

In rapidly cooled samples, the fall of crystallinity is correlated with the rise of thermal conductivity (Tables 1, 3), which contradicts the conclusions of [14,18]. In slowly cooled samples, the rise of the DoC is correlated with the rise of thermal conductivity (Tables 1, 3), which is in accordance with results from [18]. However, our results indicate the correlation of crystallinity falls in rapidly cooled samples with thermal diffusivity decrease, meaning that less crystalline samples have higher volumetric thermal capacity, which is also contradictory to the results of [18]. The

(a)

(b)
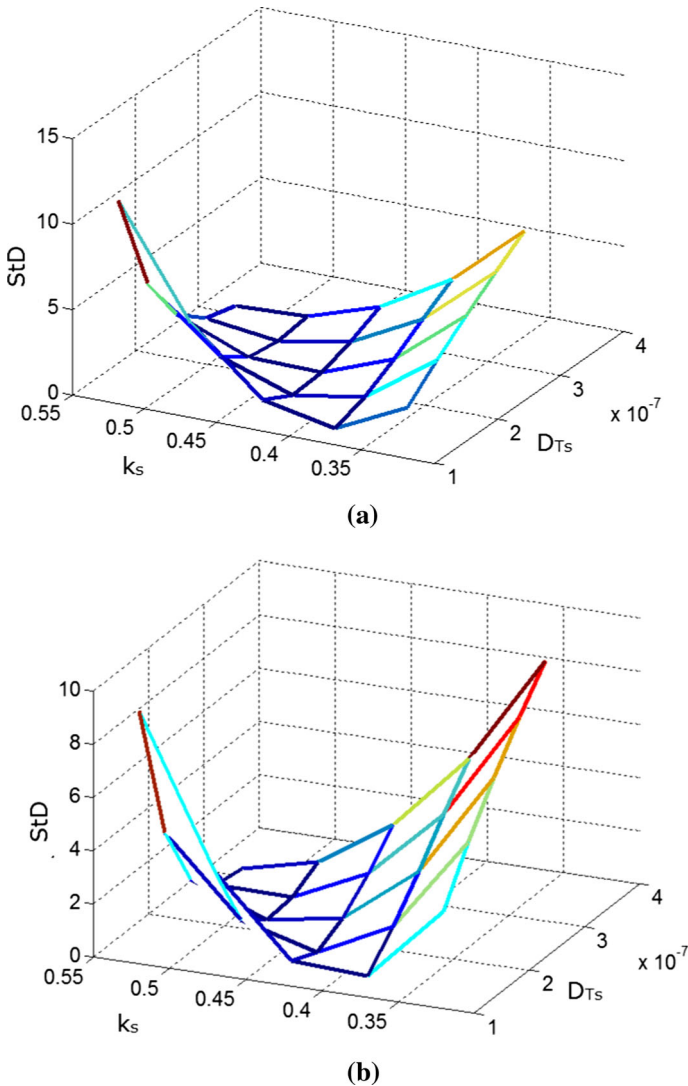
Fig. 5 Comparison of the computed StD over RoI as the function of (k_s, D_{Ts}) sets, for the samples 200 μm thick—highly and low crystalline (*a* and *b*, respectively)

assumption of an alternative approach to heat transfer is supported in some papers dealing with polaron-assisted heat transfer mechanism in macromolecular chains [38].

Throughout the literature, however, in PA measurements, thin aluminum foil was used as optical absorption layer, while in our measurements it was the dye. Besides the heat transfer mechanism, the observed phenomena could be attributed to the influence of the absorption layer on the TE component of the PA response.

Both of these possibilities represent the subject of our current research.

Table 3 Evaluated values of HDPE's thermodynamic parameters, with uncertainty estimated as the half-distance between the points

Thickness [μm]		HDPE—high-density polyethylene		
		Fast cooled	Slowly cooled	Uncertainty
400, 600	$k_s \left[\frac{W}{m \cdot K} \right]$	0.33	0.33	(± 0.02)
	$D_{Ts} \left[\times 10^{-6} \frac{m^2}{s} \right]$	0.313	0.313	(± 0.019)
200	$k_s \left[\frac{W}{m \cdot K} \right]$	**0.48**	**0.53**	(± 0.02)
	$D_{Ts} \left[\times 10^{-6} \frac{m^2}{s} \right]$	**0.265**	**0.313**	(± 0.019)

Finally, it should be stressed out that all the values of thermal conductivity and thermal diffusivity obtained by the developed self-consistent inverse procedure fall within the range of literature values presented in Table 2.

4 Conclusions

The first conclusion of this paper is that, in the process of the estimation of thermal parameters in macromolecular materials, the inverse procedure, based on the normalization of the recorded amplitude and phase characteristics, should be modified. Moreover, the modification is suggested which consists of the PA response model approximation and the fitting of both amplitude and phase characteristics, in order to augment the accuracy of the parameter estimation.

Second, the employment of the suggested inverse procedure results in obtaining the values of thermal conductivity and thermal diffusivity which highly correlate with the literature values.

Third, by investigating two groups of HDPE samples (with low and high level of DoC) it is shown that the correlation between thermal parameters and crystallinity can be established in samples of 200 μm and thinner only, stressing out the possibility of employing the photoacoustics in the determination of the DoC of thin polymer films.

Finally, different tendencies in correlating thermal parameters with crystallinity are noticed in rapidly cooled (low crystalline) and slowly cooled (highly crystalline) thin samples, demanding more scrutiny in further explorations, both theoretical and experimental, which is the subject of our future work in this area.

References

1. B. Wunderlich, *Thermal Analysis of Polymeric Materials* (Springer, Berlin, 2005)
2. T.C.M. Chung, Macromolecules **46**, 6671–6698 (2013)
3. A.A. Basfar, J. Mosnáček, T.M. Shukri, M.A. Bahattab, P. Noireaux, A. Courdreuse, J. Appl. Polym. Sci. **107**, 642–649 (2008)

4. S. Galovic, B. Secerov, S. Trifunovic, D. Milicevic, E. Suljovrujic, Radiat. Phys. Chem. **81**, 1374–1377 (2012)
5. D. Milicevic, M. Micic, G. Stamboliev, A. Leskovac, M. Mitric, E. Suljovrujic, Fibers Polym. **13**, 466–470 (2012)
6. D. Milicevic, S. Trifunovic, M. Popovic, T. Vukasinovic Milic, E. Suljovrujic, Nucl. Instrum. Methods B **260**, 603–612 (2007)
7. D. Milicevic, M. Micic, E. Suljovrujic, Polym. Bull. **71**, 2317–2334 (2014)
8. Q. Yuan, Y. Yang, J. Chen, V. Ramuni, R.D.K. Misra, K.J. Bertrand, Mater. Sci. Eng. A Struct **527**, 6699–6713 (2010)
9. E. Suljovrujic, M. Micic, D. Milicevic, J. Eng. Fibers Fabr. **8**, 131–143 (2013)
10. S. Kumar, A.K. Panda, R.K. Singh, Resour. Conserv. Recycl. **55**, 893–910 (2011)
11. M. Faizal, A. Bouazza, R.M. Singh, Renew. Sustain. Energy Rev. **57**, 16–33 (2016)
12. X. Zaoli, X. Shen, X. Tang, X. Wang, AIP Adv. **4**, 017131 (2014)
13. P.B. Allen, Phys. Rev. B **88**, 144302 (2013)
14. A.M. Mansanares, H. Vargas, F. Galembeck, J. Buijs, D. Bicanic, J. Appl. Phys. **70**, 7046–7050 (1991)
15. R. Sanchez, J. Rieumont, S. Cardoso, M. Silva, M. Sthel, M. Massunaga, C.N. Gatts, H. Vargas, J. Braz. Chem. Soc. **10**, 97–103 (1999)
16. A.C. Bento, D.T. Dias, L. Olenka, A.N. Medina, M.L. Baesso, Braz. J. Phys. **32**, 483–494 (2002)
17. L.H. Poley, A.P.L. Siqueira, M.G. da Silva, H. Vargas, Polímeros **14**, 8–12 (2004)
18. B. Bonno, J.L. Laporte, R. Tascon, R.T. D'Leon, Instrum. Sci. Technol. **33**, 151–160 (2005)
19. L.H. Poley, H. Vargas, M.G. da Silva, A.P.L. Siqueira, R. Sanchez, Polímeros **14**, 8–12 (2004)
20. B. Wunderlich, C.M. Cormier, J. Polym. Sci. A **2**, 987–988 (1967)
21. C.G. Vonk, J. Appl. Crystallogr. **6**, 148–152 (1973)
22. V. Jokanovic, Instrumental Methods: Key to Understanding Nanotechnologies and Nanomedicine, (Engineering Academy of Serbia: VINCA Institute for Nuclear Sciences, Belgrade, 2014—in Serbian) (title of the original: Instrumentalne metode ključ za razumevanje nanotehnologija i nanomedicine). ISBN 978-86-7306-123-8
23. L.F. Perondi, L.C.M. Miranda, J. Appl. Phys. **62**, 2955–2959 (1987)
24. M.D. Rabasovic, M.G. Nikolic, M.D. Dramicanin, M. Franko, D.D. Markushev, Meas. Sci. Technol. **20**, 095902 (2009)
25. G. Rousset, F. Lepoutre, L. Bertrand, J. Appl. Phys. **54**, 2383 (1983)
26. D.M. Todorovic, P.M. Nikolic, *Progress in Photothermal and Photoacoustic Science and Technology*, vol. 4, ed. by A. Mandelis (SPIE Press Book, 2000), p. 272. ISBN: 9780819435064
27. D.M. Todorovic, B. Cretin, Y.Q. Song, P. Vairac, J. App. Phys. **107**, 023516 (2010)
28. D. Markushev, M.D. Rabasovic, M. Nesic, M. Popovic, S. Galovic, Int. J. Thermophys. **33**, 2210–2216 (2012)
29. M. Nesic, P. Gusavac, M. Popovic, Z. Soskic, S. Galovic, Phys. Scr. **T149**, 014018 (2012)
30. S. Galovic, D. Kostoski, J. Appl. Phys. **93**, 3063–3070 (2003)
31. S. Galovic, Z. Soskic, M. Popovic, D. Cevizovic, Z. Stojanovic, J. Appl. Phys. **116**, 024901 (2014)
32. J.A. Balderas-Lopez, A. Mandelis, Rev. Sci. Instrum. **74**, 5219 (2003)
33. J.A. Balderas-Lopez, Rev. Sci. Instrum. **77**, 064902 (2006)
34. Z. Soskic, S. Ciric-Kostic, S. Galovic, Int. J. Therm. Sci. **109**, 217–230 (2016)
35. P.C. Hansen, Numer. Algorithms **6**, 1–35 (1994)
36. http://www.engineeringtoolbox.com/pipes-temperature-expansion-coefficients-d_48.html.   Accessed 09 Nov 2017
37. http://www.maropolymeronline.com/Properties/HDPE%20Prop.asp. Acccessed 09 Nov 2017
38. D. Cevizovic, S. Galovic, A. Reshetnyak, Z. Ivic, Chin. Phys. B **22**, 060501 (2013)

Research Article

Orange-Reddish Light Emitting Phosphor GdVO$_4$:Sm^{3+} Prepared by Solution Combustion Synthesis

M. S. Rabasovic [iD],[1] **J. Krizan** [iD],[2] **S. Savic-Sevic** [iD],[1] **M. Mitric** [iD],[3] **M. D. Rabasovic** [iD],[1] **B. P. Marinkovic** [iD],[1] and **D. Sevic** [iD][1]

[1]*Institute of Physics, University of Belgrade, P.O. Box 68, Pregrevica 118, 11080 Belgrade, Serbia*
[2]*AMI d.o.o, Ptuj, Slovenia*
[3]*Vinca Institute of Nuclear Science, University of Belgrade, P.O. Box 522, 11001 Belgrade, Serbia*

Correspondence should be addressed to D. Sevic; sevic@ipb.ac.rs

The gadolinium vanadate doped with samarium (GdVO$_4$:Sm^{3+}) nanopowder was prepared by the solution combustion synthesis (SCS) method. After synthesis, in order to achieve the full crystallinity, the material was annealed in air atmosphere at 900°C. Phase identification in the postannealed powder samples was performed by X-ray diffraction, and morphology was investigated by high-resolution scanning electron microscopy (SEM). Photoluminescence characterization of the emission spectrum and time-resolved analysis have been performed using the tunable laser optical parametric oscillator excitation and the streak camera. Several strong emission bands in the Sm^{3+} emission spectrum were observed, located at 567 nm ($^4G_{5/2}$–$^6H_{5/2}$), 604 nm ($^4G_{5/2}$–$^6H_{7/2}$), and 646 (654) nm ($^4G_{5/2}$–$^6H_{9/2}$), respectively. The weak emission bands at 533 nm ($^4F_{3/2}$–$^6H_{5/2}$) and 706 nm ($^4G_{5/2}$–$^6H_{11/2}$) and a weak broad luminescence emission band of VO$_4^{3-}$ were also observed by the detection system. We analyzed the possibility of using the host luminescence for two-color temperature sensing. The proposed method is improved by introducing the temporal dependence in the line intensity ratio measurements.

1. Introduction

Many investigations have been devoted to rare earth orthovanadates RVO$_4$ (R = Sc, Y, La, Gd, or Lu) (see [1–4] and references therein). Gadolinium vanadate (GdVO$_4$) is a very important host for the luminescence of rare earth activators which find applications in the high-power solid state lasers, X-ray medical radiography, energy-saving fluorescent lamps, artificial production of light, other display devices [5–11], and temperature sensing [4]. Phosphors based on gadolinium compounds play an important role because the Gd^{3+} ion (4f^7) has its lowest excited level at relatively high energy, which is due to the stability of the half-filled shell ground state [6]. The GdVO$_4$:Sm nanopowder is an efficient orange-reddish light emitting material due to a strong absorption of ultraviolet light by GdVO$_4$ and

efficient energy transfer from vanadate groups (VO$_4^{3-}$) to dopants (Sm^{3+}).

In this paper, we present the results of experimental investigation of Sm^{3+}-doped GdVO$_4$ nanopowders, prepared by the solution combustion synthesis (SCS) method [12, 13].

Simplicity and low cost are the main characteristics of this process. Phase identification in the postannealed powder samples was performed by X-ray diffraction, and morphology was investigated by high-resolution scanning electron microscopy (SEM). The main aim of this study is time-resolved analysis of luminescence properties of GdVO$_4$: Sm^{3+} nanopowders. The possibility for GdVO$_4$:Sm^{3+} usage in phosphor thermometry was analyzed in [4], where temperature determination of sensing calibration curves was based on intensity ratios of luminescence of samarium lines. Here, we have taken a different approach. First, we use intensity

ratio of the host and samarium line luminescence emissions (two-color thermometry). This new approach to the ratiometric luminescence thermometry was proposed recently, using TiO_2 nanopowders doped with Eu^{3+} [14] and Sm^{3+} [15], Zn_2SiO_4 doped with Mn^{2+} [16], and Eu^{3+} $Gd_2Ti_2O_7$ doped with Eu^{3+} [17]. So, this concept, used in our study, provides high relative sensitivities by itself. However, the method presented here is further improved by introducing the temporal dependence in the luminescence intensity ratio measurements, as proposed in [18], providing even more increased sensitivity.

2. Experimental

2.1. Synthesis. $GdVO_4$ nanopowder doped with samarium ions was prepared by the solution combustion method, as described in [12, 13]. Stoichiometric quantities of starting chemicals $Sm(NO_3)_3$, $Gd(NO_3)_3 * 6H_2O$, and NH_4VO_3 with the purity of 99.99% were chosen to obtain the Sm^{3+} concentration in $GdVO_4$ of 1 at.% ($Gd_{1-0.01}Sm_{0.01}VO_4$). The used chemicals and ammonium nitrate (NH_4NO_3) were purchased from ABCR, and urea ($(NH_2)_2CO$) from Sigma-Aldrich. The dry mixture of 0.134 g (0.4 mmol) of $Sm(NO_3)_3$, 18.05 g (40 mmol) of $Gd(NO_3)_3*6H_2O$, and 4.676 g (40 mmol) of NH_4VO_3 was combined with the mixture of 4.8 g (60 mmol) of ammonium nitrate and 3.003 g (50 mmol) of urea which were used as organic fuels. The prepared starting reagents were combusted with the flame burner at approximately 500°C, yielding a voluminous foamy powder in an intensive exothermic reaction. After the solution combustion synthesis, the nanopowder was annealed for 2 hours, in air atmosphere, at 900°C. Annealing has an effect on increasing the grain size of the nanopowders, and it is widely used to achieve the higher emission intensity.

2.2. Instruments and Measurements. The structure of the nanopowder was verified by X-ray diffraction analysis, using a Philips PW 1050 instrument, with Ni filtered $Cu \cdot K_{\alpha1,2}$ radiation ($\lambda = 0.15405$ nm). X-ray diffraction measurements were done at room temperature over the 2θ range of 10–90° with a scanning step width of 0.05° and a counting time of 8 s per step. The morphology of nanopowders and the size of crystallites were determined by high-resolution scanning electron microscopy (SEM) equipped with a high-brightness Schottky field emission gun (FEGSEM, TESCAN) operating at 4 kV. Photoluminescence (PL) studies reported in this work were performed using an optical parametric oscillator (Vibrant OPO), as described in [12, 13]. The output of the OPO can be continuously tuned over a spectral range from 320 nm to 475 nm. Time-resolved streak images of the emission spectrum excited by the OPO system were collected by using a spectrograph (SpectraPro 2300i) and recorded with a Hamamatsu streak camera (model C4334). All streak camera operations were controlled by the HPD-TA (High Performance Digital Temporal Analyzer) software. We used a homemade temperature control system for luminescence measurements presented here.
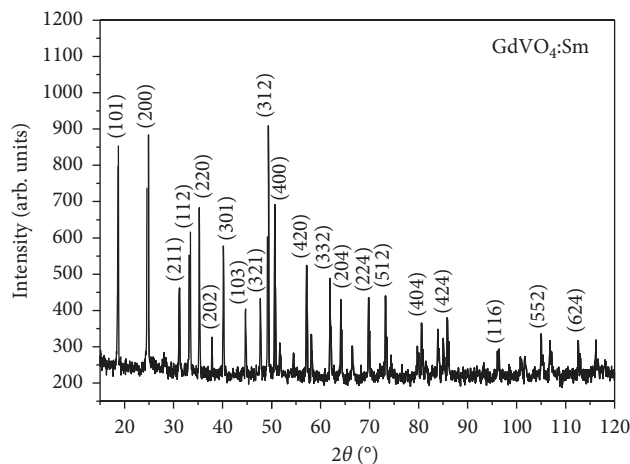

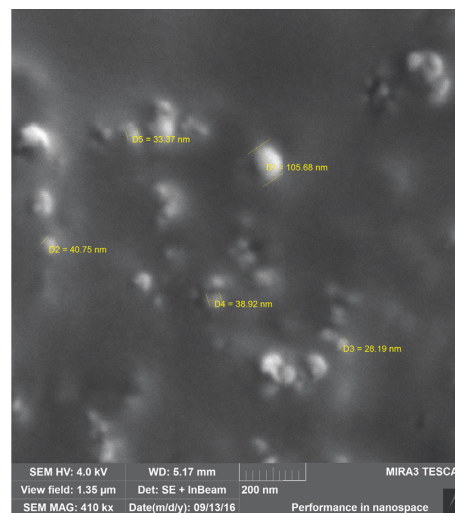Figure 1: The XRD patterns of the $GdVO_4$:Sm nanopowder with respective Miller indices.

Figure 2: The SEM image of the $GdVO_4$:Sm nanopowder annealed at 900°C.

3. Results

3.1. XRD and SEM Study. In order to know the structural properties and differences in the phase purities of the prepared $GdVO_4$:Sm nanopowder, XRD analysis was recorded and is presented in Figure 1. XRD confirmed the successful formation of the pure-phase $GdVO_4$ powder with the $I4_1/amd$ space group (JCPDS Card no. 86-0996). Ionic radius of the Sm^{3+} ion (0.964 Å) is a slightly larger than that of Gd^{3+} ion (0.938 Å), which indicates that Sm^{3+} could be successfully incorporated into the $GdVO_4$ host lattice by substituting Gd^{3+} without changing the tetragonal zircon type structure of $GdVO_4$ [9]. The particle size and morphology of the $GdVO_4$:Sm nanopowder annealed at 900°C were characterized by SEM (Figure 2). Some particles are agglomerated as clusters; however, individual spherical-shaped particles are also visible and labeled in Figure 2. The average grain size, D, was estimated by the Scherer equation, $D = K\lambda/\beta \cos\theta$, where K is a constant related to
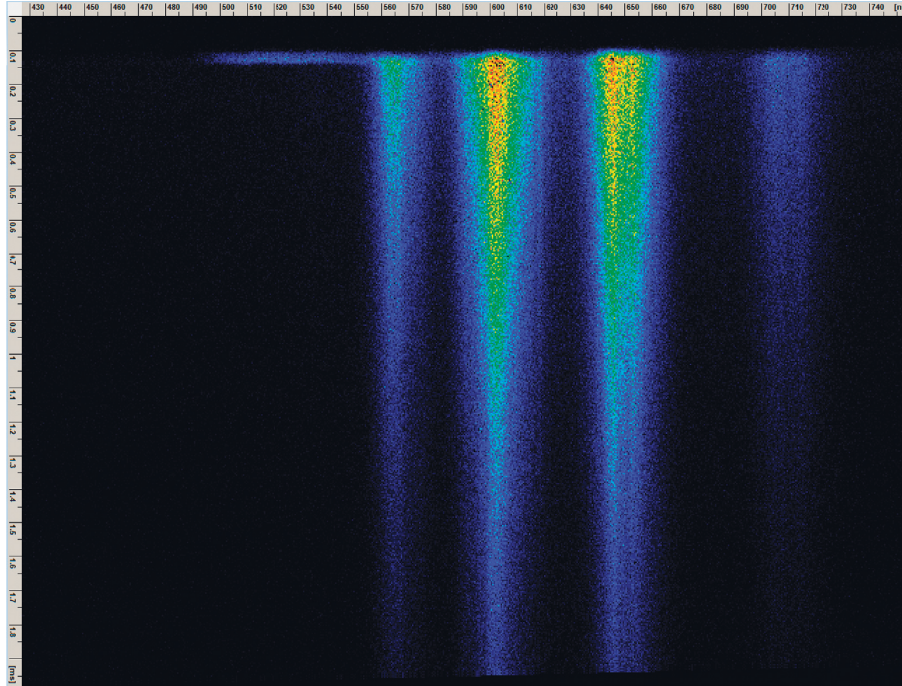
FIGURE 3: The streak image of the photoluminescence spectrum of GdVO$_4$:Sm^{3+} nanophosphor (OPO excitation at 330 nm).

the shape of the crystallite and is approximately equal to unity, we used $K = 0.89$ as in [19], λ is the X-ray wavelength (0.15405 nm), and θ and β are the diffraction angle and full width at half maximum (FWHM, in radians) of the corresponding peak, respectively. The strongest peaks (2θ) from XRD were used to calculate the average crystallite size (D) in the GdVO$_4$:Sm nanopowder. The estimated particle size is about 43 nm. The SEM image (Figure 2) reveals that sizes of individual particles of nanopowders are between 30 nm and 105 nm, which is in agreement with the calculated averaged result from XRD.

3.2. Photoluminescence and Lifetime Analysis.

The streak image of the time-resolved photoluminescence spectrum of the GdVO$_4$:Sm^{3+} nanopowder using the 330 nm excitation is presented in Figure 3. Horizontal scale of the streak image corresponds to wavelength, and the vertical scale shows development of spectra in time. Images are presented in pseudocolor, where different colors mean different optical intensities.

Spectral characteristics of luminescence emission intensities of the synthesized GdVO$_4$:Sm^{3+} (1 at.%) nanopowder sample are shown in Figure 4. The spectrum was obtained by integrating in time the spectral image acquired by the streak camera in the photon counting mode, with the time scale of 5 ms, at the excitation of 330 nm.

It could be seen in Figure 4 that the GdVO$_4$:Sm nanopowder sample have comparable luminescence emission intensities in green, orange, and red regions. All those emission bands correspond to the transitions from excited energy level $^4G_{5/2}$ of Sm^{3+} ion to $^6H_{5/2}$ (~567 nm), $^6H_{7/2}$ (602 nm), $^6H_{9/2}$ (646 and 654 nm), and $^6H_{11/2}$ (~706 nm) level, respectively. The strong emission of Sm^{3+} is due to efficient energy transfer from the VO$_4^{3-}$ group to Sm^{3+} ion
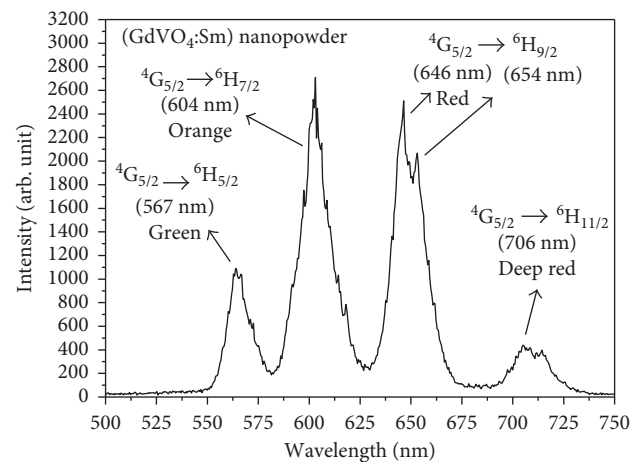

FIGURE 4: The photoluminescence (PL) emission spectrum of our GdVO$_4$:Sm nanopowder sample (OPO excitation at 330 nm).

in the GdVO$_4$:Sm^{3+} sample. However, the deep red emission of these samples is almost on the end of the region of human eye color sensitivity, so the small influence of this emission on the color chromaticity coordinates of GdVO$_4$:Sm^{3+} is expected. The transitions at 604 and 646 nm have relatively higher emission intensities over the other transitions causing an orange-reddish emission from the Sm^{3+}.

Fluorescence lifetime analysis for the GdVO$_4$:Sm^{3+} nanopowder has also been performed, and the obtained result is presented in Figure 5. We present the fluorescence lifetime analysis for the most intense emission peak ($^4G_{5/2}$–$^6H_{7/2}$) in Sm^{3+} ion. Luminescence decay curve is well fitted using a double-exponential function. The average luminescence lifetime can be determined by the following formula [20–24]:
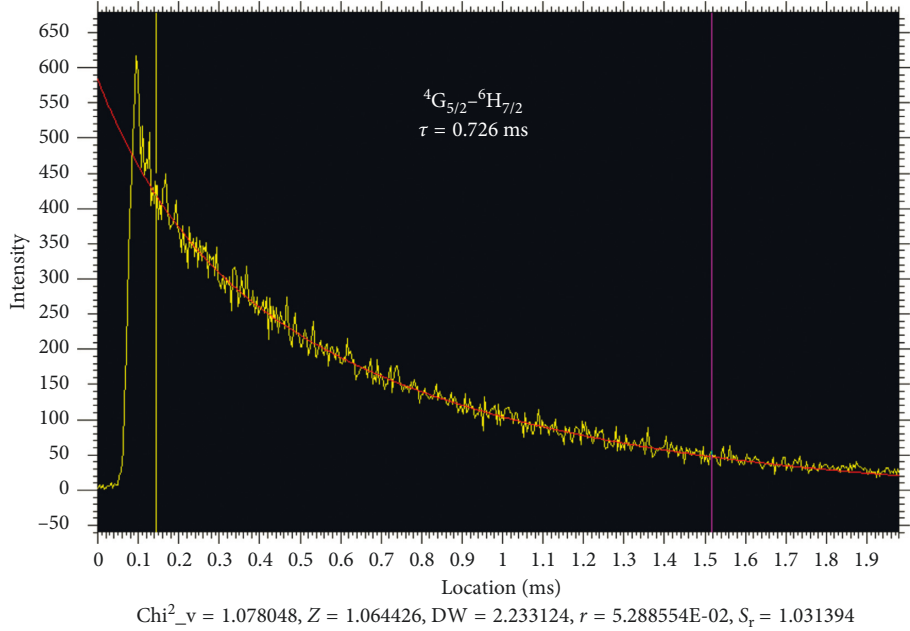
FIGURE 5: The luminescence decay curve for the $^4G_{5/2}$–$^6H_{7/2}$ transition in Sm^{3+} ion fitted by a double-exponential decay.

$$\tau = \frac{(A_1\tau_1^2 + A_2\tau_2^2)}{(A_1\tau_1 + A_2\tau_2)}, \qquad (1)$$

where A_1 and A_2 denote the amplitudes of respective decay components and τ_1 and τ_2 are fluorescence lifetime components contributing to the average lifetime. The obtained result for average lifetime for Sm^{3+} ion is 0.726 ms. It is found that our result for lifetime of Sm^{3+} ion in the $GdVO_4$ nanopowder is longer in comparison with 0.66 ms [20], 0.55 ms [25], and 0.42 ms [6]. It is well known that the luminescent lifetime of rare earth ion is influenced by the structure of the host, the rare earth located sites (on the surface or bulk) of the host, defects, and impurity [26]. The defect and impurity may act as quenching centers and reduce luminescent lifetime.

The double-exponential decay behavior of the activator is frequently observed when the excitation energy is transferred from the donor [6]. The energy transfer is not the main cause of the deviation from the single-exponential behavior of the decay curve since the energy transfer from the VO_4^{3-} groups to Sm^{3+} ions mainly influences the rise time of the decay curve [27]. The streak image of $GdVO_4$: Sm^{3+} nanopowder luminescence with a time scale of $100\,\mu s$ is shown in Figure 6. In this time scale, the host luminescence and weak samarium line at 533 nm ($^4F_{3/2}$–$^6H_{5/2}$), barely discernible and not denoted in Figures 3 and 4, are easily identified. In our measurements, all luminescence bellow 500 nm is cut off by the optical filter used for blocking the OPO excitation. The spectral shape of host luminescence, detected by us only above 500 nm, is similar to spectra presented in [1, 9, 28]. The $GdVO_4$ luminescence is ascribed to the VO_4^{3-} group. Calculated lifetime of host luminescence of $2.82\,\mu s$ agrees well with the time-resolved analysis provided in [28]. Moreover, as we have shown in the next subsection, this luminescence is gradually quenched by

raising the temperature, which means that it is not measuring error caused by stray light of laser excitation.

The estimated rise time of samarium luminescence shown in Figure 6 is negligible for effects of interest. For used time scale, it is determined mainly by the instrumental response. So, the multiexponential behavior should be ascribed to the absorbed impurities, which lead to the defects and the quenching centers [27, 29]. Decay kinetics behavior depends also on the number of different luminescent centers [20, 27]. If rare earth ions occupy several different sites in host lattices, they can generate several different luminescent centers which lead to a multiexponential behavior [29]. Tian et al. [30] explained that, in Dy^{3+}-doped bulk $GdVO_4$:Dy phosphors, the energy transfers mainly happen between Dy^{3+} ions [31, 32]. In the case of nanoparticles, the energy transfer starting from the luminescent level can be more complicated, since the defects, which can act as quenching centers, in nanoparticles are more plenteous than those in bulk phosphors [29, 31, 33]. Due to the defects produced during the preparation process and trace impurities contained in the raw materials, the samples necessarily have quenching centers (traps) with very low concentrations. When the excited luminescent center is in the vicinity of the trap, the excited energy could be transferred easily to the trap from which it is lost nonradiatively [33]. As a result, decay time should become short. In our case, longer lifetime of 0.726 ms may be due to the better crystallization and less defects, which reduces the nonradiative probability and results in the longer lifetimes.

3.3. Temperature Sensing Using $GdVO_4$:Sm Nanophosphor.
Recently, the new concept of using the host luminescence for the fluorescence intensity ratio method was introduced (see [14–17] and references therein). In our study, the method is
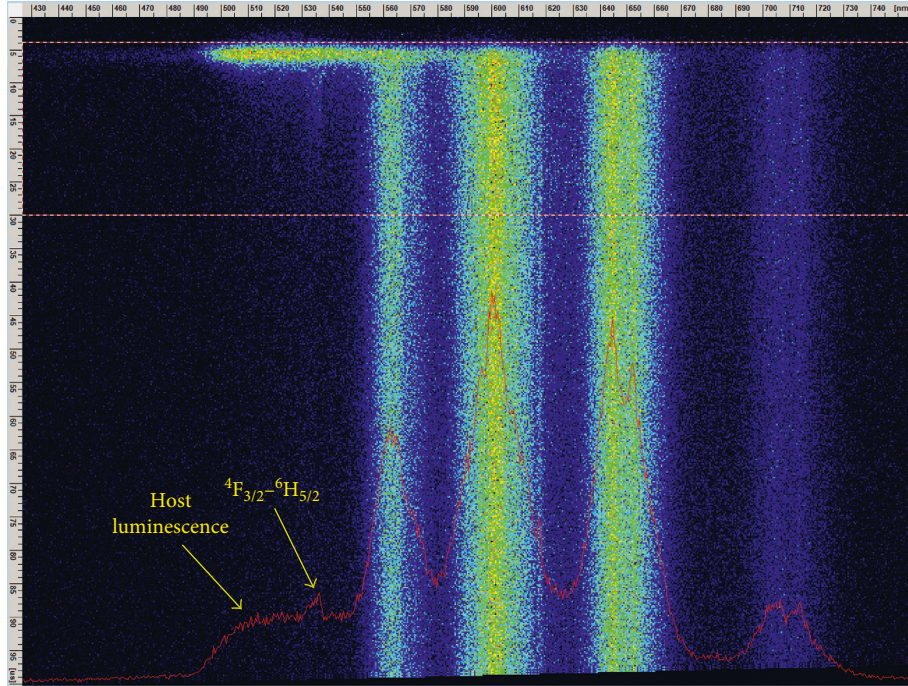
FIGURE 6: The streak image of the GdVO$_4$:Sm nanopowder. The time scale of 100 μs was adjusted for analysis of rise time of samarium lines and detection of fast host luminescence emission (OPO excitation at 330 nm).

improved by introducing the temporal dependence in the intensity ratio measurements, as proposed in [18]. Namely, it is possible to increase the sensitivity of the curve of intensity ratio between the host and samarium luminescence if an appropriately selected part of temporal evolution is used in calculation. We used the streak camera to prove the concept. The real application of this method will be based on using the gated CCD cameras and appropriate bandwidth filters for selecting the emission region of interest.

The luminescence spectra of the GdVO$_4$:Sm nanopowder were measured at various temperatures, using the OPO excitation at 330 nm and the streak camera. For calculation of intensity ratio, the narrow bands (5 nm) of host luminescence around 520 nm and the samarium line at 602 nm were used and integrated in time from their beginning. However, we varied gating times for end of signal integration. In order to apply the intensity ratio method in thermometry, it is required to fit a calibration function of analyzed thermophosphor. Based on considerations in [34, 35], we decided to use the simple empirical equation for fitting the calculated intensity ratios of experimental data: IR$(T) = A + C \cdot e^{-T/\alpha}$ [34, 35], where T is the temperature in K and empirical A, C, and α are the constants obtained through fitting of measured data. The results are shown in Figure 7.

It could be seen in Figure 7 that the intensity ratio between the host luminescence band centered at 520 nm and the line at 602 nm increases with decreasing the gate time of the signal. However, decreasing the gate time decreases the integrated signal intensity, so we did not use delays smaller than 30 μs.
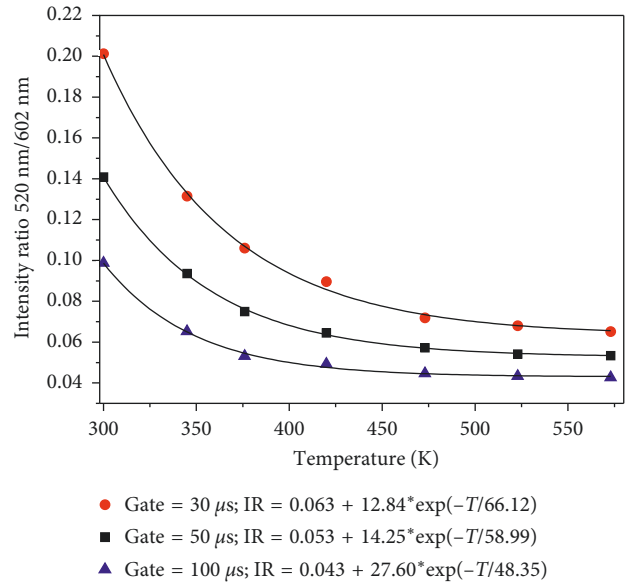

- Gate = 30 μs; IR = 0.063 + 12.84*exp($-T$/66.12)
- Gate = 50 μs; IR = 0.053 + 14.25*exp($-T$/58.99)
- Gate = 100 μs; IR = 0.043 + 27.60*exp($-T$/48.35)

FIGURE 7: The temperature sensing calibration curve of the GdVO$_4$: Sm^{3+} nanopowder sample.

The absolute thermal sensitivity, S_a, of the intensity ratio method is defined as the rate at which IR changes with the temperature:

$$S_a = \left| \frac{d\text{IR}}{dT} \right|. \tag{2}$$

The relative thermal sensitivity, S_r, of the intensity ratio method Sr is determined using the following formula:

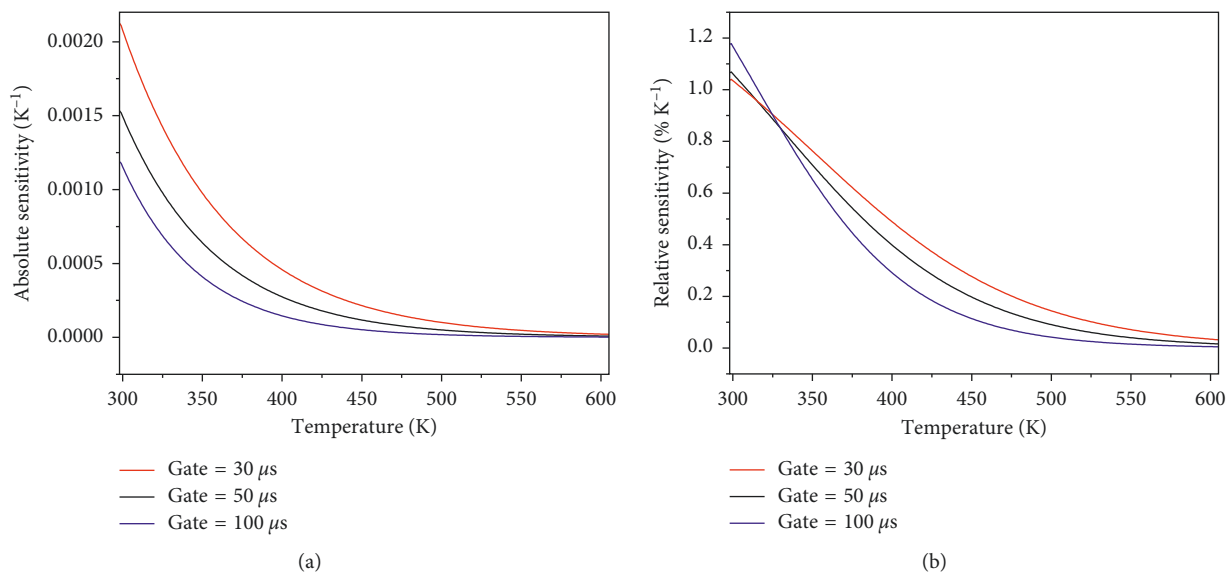FIGURE 8: (a) Absolute sensitivity and (b) relative sensitivity of GdVO$_4$:Sm^{3+} nanophosphor as a function of temperature.

$$S_r = \left| \frac{1}{\mathrm{IR}} \frac{d\mathrm{IR}}{dT} \right|. \tag{3}$$

Absolute and relative temperature sensitivities of GdVO$_4$:Sm^{3+} nanophosphor are shown in Figure 8. The best sensitivity is obtained by the gate time of 30 μs. We estimate that this kind of temperature sensing is useful up to 500 K, where the calculated intensity ratio values stop increasing and the curve flattens, resulting in small sensitivity, even for the optimal gate time of 30 μs (see Figures 7 and 8). The proposed method provides better sensitivity than that reported in [4] for the same nanophosphor.

The CIE (Commission Internationale de I'Eclairage, 1931) chromaticity coordinates of GdVO$_4$:Sm^{3+} are presented in Figure 9. It could be seen that the GdVO$_4$:Sm^{3+} sample shows the orange-reddish luminescence color, and the chromaticity coordinates at room temperature are $x = 0.5963$ and $y = 0.3989$. Denoted points correspond to the temperature range from 300 K up to 673 K. The CIE diagram shows that the luminescence intensities corresponding to the last two points, 623 K and 673 K (350°C and 400°C), are obviously measured with high uncertainty, and they were not included in fitting the temperature sensing calibration curves of GdVO$_4$:Sm^{3+}.

4. Conclusion

The time-resolved analysis of GdVO$_4$:Sm^{3+} nanophosphor luminescence was conducted. The estimated lifetime of the most prominent optical emission of samarium from the ^{4}G$_{5/2}$ level is 0.726 ms. The host luminescence was also identified. Lifetime of host luminescence is 2.82 μs. The rise time of samarium luminescence is estimated as negligible for effects that are here of interest.

We have shown that, for the analyzed GdVO$_4$:Sm^{3+} material, the temperature sensing based on ratio of intensities of the host luminescence and the samarium line
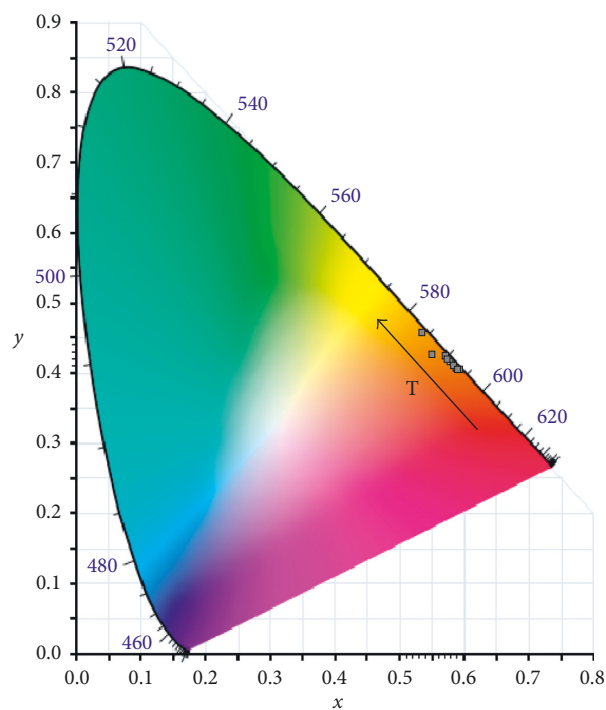

FIGURE 9: The CIE chromaticity diagram of emission spectra of 1 mol% GdVO$_4$:Sm^{3+}. Denoted points correspond to the temperature range from 300 K up to 673 K.

is useful up to 500 K. The used method was improved by introducing the temporal dependence in the ratio measurements. Our analysis shows that the gating time of 30 μs is optimal for acquiring the integrated luminescence intensity.

By using the CIE chromaticity diagram of emission spectra, it has been shown that this GdVO4:Sm^{3+} nanophosphor material (chromaticity coordinates $x = 0.596$, $y = 0.398$) can be used for development of orange-reddish light emitting

optical devices. We also plotted the temperature dependency of CIE chromaticity coordinates for this nanophosphor.

In summary, results of all our analyses prove that the Sm^{3+}-doped $GdVO_4$ nanopowder prepared by a simple and low-cost solution combustion synthesis method is an appropriate material for light-emitting optoelectronic devices and remote temperature sensing.

Conflicts of Interest
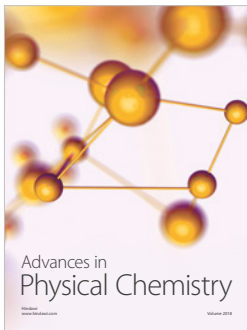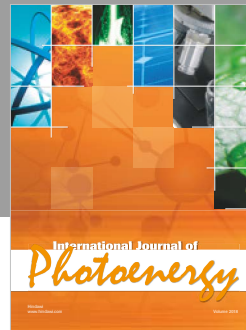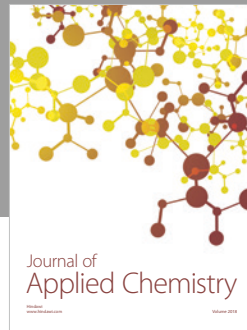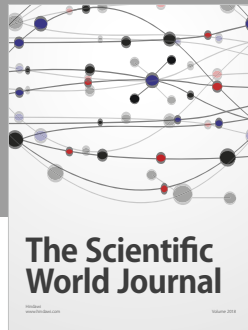
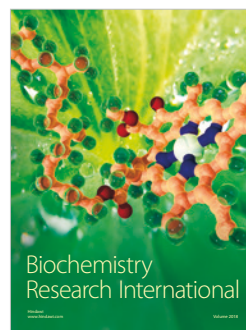The authors declare that they have no conflicts of interest.

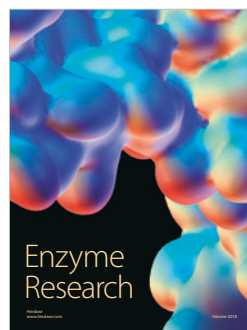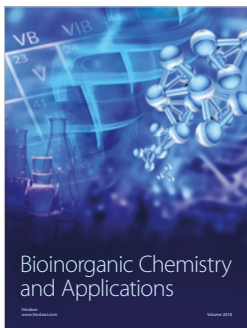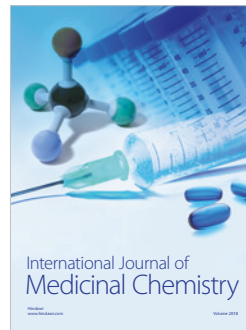## Acknowledgments

References

[1] M. Anitha, P. Ramakrishnan, A. Chatterjee, G. Alexander, and H. Singh, "Spectral properties and emission efficiencies of $GdVO_4$ phosphors," *Applied Physics A: Materials Science & Processing*, vol. 74, no. 2, pp. 153–162, 2012.

[2] Z. Hou, P. Yang, C. Li et al., "Preparation and Luminescence Properties of YVO_4:Ln and Y(V, P)O_4:Ln (Ln = Eu^{3+}, Sm^{3+}, Dy^{3+}) nanofibers and microbelts by sol-gel/electrospinning process," *Chemistry of Materials*, vol. 20, no. 21, pp. 6686–6696, 2008.

[3] D. J. Jovanovic, Z. Antic, R. M. Krsmanovic et al., "Annealing effects on the microstructure and photoluminescence of Eu^{3+}-doped $GdVO_4$ powders," *Optical Materials*, vol. 35, no. 10, pp. 1797–1804, 2013.

[4] M. G. Nikolic, D. J. Jovanovic, V. Đorđevic, Z. Antic, R. M. Krsmanovic, and M. D. Dramicanin, "Thermographic properties of Sm^{3+}-doped $GdVO_4$ phosphor," *Physica Scripta*, vol. T149, p. 014063, 2012.

[5] S. Kaowphong, N. Chumha, P. Nimmanpipug, and S. Kittiwachana, "Nanosized $GdVO_4$ powders synthesized by sol–gel method using different carboxylic acids," *Rare Metals*, 2016.

[6] X. Li, M. Yu, Z. Hou et al., "One-dimensional $GdVO_4$:Ln^{3+} (Ln = Eu, Dy, Sm) nanofibers: electrospinning preparation and luminescence properties," *Journal of Solid State Chemistry*, vol. 184, no. 1, pp. 141–148, 2011.

[7] H. Xin, L. X. Lin, J. H. Wu, and B. Yan, "Hydrothermal synthesis and multi-color photoluminescence of $GdVO_4$: Ln^{3+} (Ln = Sm, Dy, Er) sub-micrometer phosphors," *Journal of Materials Science: Materials in Electronics*, vol. 22, no. 9, pp. 1330–1134, 2011.

[8] F. Zheng, W. Wang, and P. Yang, "$GdVO_4$: Ln^{3+} (Ln = Sm, Dy, and Er) microstructures: solvothermal and luminescent properties," *Optoelectronics and Advanced Materials: Rapid Communications*, vol. 5, no. 6, pp. 596–599, 2011.

[9] Y. Liu, G. Liu, J. Wang, X. Dong, and W. Yu, "Reddish-orange-emitting and paramagnetic properties of $GdVO_4$: Sm^{3+}/Eu^{3+} multifunctional nanomaterials," *New Journal of Chemistry*, vol. 39, no. 11, pp. 8282–8290, 2015.

[10] Y. K. Voron'ko, A. A. Sobol', V. E. Shukshin, A. I. Zagumennyĭ, Y. D. Zavartsev, and S. A. Kutovoĭ, "Raman spectroscopic study of structural disordering in YVO_4, $GdVO_4$, and $CaWO_4$ crystals," *Physics of the Solid State*, vol. 51, no. 9, pp. 1886–1893, 2009.

[11] A. A. Kaminskii, O. Lux, H. Ghee et al., "Low-temperature stimulated Raman scattering spectroscopy of tetragonal $GdVO_4$ single crystals," *Physica Status Solidi B*, vol. 251, no. 5, pp. 1045–1062, 2014.

[12] M. S. Rabasovic, D. Sevic, J. Krizan et al., "Structural properties and luminescence kinetics of white nanophosphor YAG: Dy," *Optical Materials*, vol. 50, pp. 250–255, 2015.

[13] M. S. Rabasović, D. Sević, J. Krizan, M. D. Rabasović, and N. Romcević, "Annealing effects on luminescent properties of Eu^{3+} doped $Gd_2Zr_2O_7$ nanopowders," *Science of Sintering*, vol. 47, no. 3, pp. 269–272, 2015.

[14] M. G. Nikolic, Z. Antic, S. Culubrk, J. M. Nedeljkovic, and M. D. Dramicanin, "Temperature sensing with Eu^{3+} doped TiO_2 nanoparticles," *Sensors and Actuators B: Chemical*, vol. 201, pp. 46–50, 2014.

[15] M. D. Dramicanin, Z. Antic, S. Culubrk, S. P. Ahrenkiel, and J. M. Nedeljkovic, "Self-referenced luminescence thermometry with Sm^{3+} doped TiO_2 nanoparticles," *Nanotechnology*, vol. 25, no. 48, p. 485501, 2014.

[16] V. Lojpur, M. G. Nikolic, D. Jovanovic, M. Medic, Z. Antic, and M. D. Dramicanin, "Luminescence thermometry with Zn_2SiO_4:Mn^{2+} powder," *Applied Physics Letters*, vol. 103, no. 14, p. 141912, 2013.

[17] V. Lojpur, S. Ćulubrk, and M. D. Dramićanin, "Ratiometric luminescence thermometry with different combinations of emissions from Eu^{3+} doped $Gd_2Ti_2O_7$ nanoparticles," *Journal of Luminescence*, vol. 169, pp. 534–538, 2016.

[18] M. Alden, A. Omrane, M. Richter, and G. Särner, "Thermographic phosphors for thermometry: a survey of combustion applications," *Progress in Energy and Combustion Science*, vol. 37, no. 4, pp. 422–461, 2011.

[19] B. K. Grandhe, V. R. Bandi, K. Jang, S. Ramaprabhu, S.-S. Yi, and J.-H. Jeong, "Enhanced red emission from YVO_4:Eu^{3+} nano phosphors prepared by simple co-precipitation method," *Electronic Materials Letters*, vol. 7, no. 2, pp. 161–165, 2011.

[20] S. Tang, M. Huang, J. Wang, F. Yu, G. Shang, and J. Wu, "Hydrothermal synthesis and luminescence properties of $GdVO_4$:Ln^{3+} (Ln = Eu, Sm, Dy) phosphors," *Journal of Alloys and Compounds*, vol. 513, pp. 474–480, 2012.

[21] N. Shanta Singh, R. S. Ningthoujam, M. Niraj Luwang, S. Dorendrajit Singh, and R. K. Vatsa, "Luminescence, lifetime and quantum yield studies of YVO_4:Ln^{3+} (Ln^{3+} = Dy^{3+}, Eu^{3+}) nanoparticles: concentration and annealing effects," *Chemical Physics Letters*, vol. 480, no. 4–6, pp. 237–242, 2009.

[22] G. Z. Li, Z. L. Wang, M. Yu, Z. W. Quan, and J. Lin, "Fabrication and optical properties of core–shell structured spherical SiO_2@$GdVO_4$:Eu^{3+} phosphors via sol–gel process," *Journal of Solid State Chemistry*, vol. 179, no. 8, pp. 2698–2706, 2006.

[23] H. Wang, M. Yu, C. K. Lin, and J. Lin, "Core–shell structured SiO_2@YVO_4:Dy^{3+}/Sm^{3+} phosphor particles: Sol–gel preparation and characterization," *Journal of Colloid and Interface Science*, vol. 300, no. 1, pp. 176–182, 2006.

[24] M. Yu, J. Lin, and J. Fang, "Silica spheres coated with YVO_4: Eu^{3+} layers via sol–gel process: a simple method to obtain spherical core–shell phosphors," *Chemistry of Materials*, vol. 17, no. 7, pp. 1783–1791, 2005.

[25] X. He, L. Zhang, G. Chen, and Y. Hang, "Crystal growth and spectral properties of Sm:$GdVO_4$," *Journal of Alloys and Compounds*, vol. 467, no. 1-2, pp. 366–369, 2009.

[26] V. Sudarsan, F. C. J. M. van Veggel, R. A. Herring, and M. Raudsepp, "Surface Eu^{3+} ions are different than "bulk" Eu^{3+}

ions in crystalline doped LaF_3 nanoparticles," *Journal of Materials Chemistry*, vol. 15, no. 13, pp. 1332–1342, 2005.

[27] G. Jia, Y. Song, M. Yang, Y. Huang, L. Zhang, and H. You, "Uniform $YVO_4:Ln^{3+}$ (Ln = Eu, Dy, and Sm) nanocrystals: solvothermal synthesis and luminescence properties," *Optical Materials*, vol. 31, no. 6, pp. 1032–1037, 2009.

[28] J. Leppert, S. Peudenier, E. Bayer, B. C. Grabmaier, and G. Blasse, "Time resolved emission spectroscopy of gadolinium vanadate ceramics ($GdVO_4:Bi^{3+}$)," *Applied Physics A Solids and Surfaces*, vol. 59, no. 1, pp. 69–72, 1994.

[29] F. He, P. P. Yang, N. Niu et al., "Hydrothermal synthesis and luminescent properties of $YVO_4:Ln^{3+}$ (Ln = Eu, Dy, and Sm) microspheres," *Journal of Colloid and Interface Science*, vol. 343, no. 1, pp. 71–78, 2010.

[30] Y. Tian, B. Chen, B. Tian et al., "Size-dependent energy transfer and spontaneous radiative transition properties of Dy^{3+} ions in the $GdVO_4$ phosphors," *Journal of Nanoparticle Research*, vol. 15, no. 6, pp. 1757–1767, 2013.

[31] B. N. Tian, B. J. Chen, Y. Tian et al., "Concentration and temperature quenching mechanisms of Dy^{3+} luminescence in $BaGd_2ZnO_5$ phosphors," *Journal of Physics and Chemistry of Solids*, vol. 73, no. 11, pp. 1314–1319, 2012.

[32] H. Zhong, X. P. Li, R. S. Shen et al., "Spectral and thermal properties of Dy^{3+}-doped $NaGdTiO_4$ phosphors," *Journal of Alloys and Compounds*, vol. 517, pp. 170–175, 2012.

[33] W. P. Zhang, P. B. Xie, C. K. Duan et al., "Preparation and size effect on concentration quenching of nanocrystalline Y_2SiO_5: Eu," *Chemical Physics Letters*, vol. 292, no. 1-2, pp. 133–136, 1998.

[34] M. D. Rabasovic, B. D. Muric, V. Celebonovic, M. Mitric, B. M. Jelenkovic, and M. G. Nikolic, "Luminescence thermometry via the two-dopant intensity ratio of $Y_2O_3:Er^{3+}$, Eu^{3+}," *Journal of Physics D: Applied Physics*, vol. 49, no. 48, p. 485104, 2016.

[35] D. Ananias, C. D. S. Brites, L. D. Carlos, and J. Rocha, "Cryogenic nanothermometer based on the MIL-103 (Tb, Eu) metal–organic framework," *European Journal of Inorganic Chemistry*, vol. 2016, no. 13-14, pp. 1967–1971, 2016.
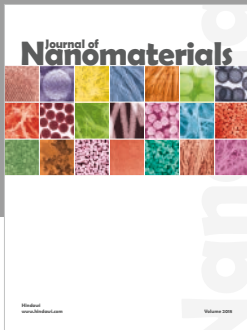
**THE EUROPEAN
PHYSICAL JOURNAL D**

Check for
updates

Regular Article - Molecular Physics and Chemical Physics

Time-resolved luminescence spectra of greater celandine plant extract (Chelidonium majus L.)

M. S. Rabasovic[a] , B. P. Marinkovic , M. D. Rabasovic , M. G. Nikolic, and D. Sevic

Institute of Physics, Belgrade, Serbia

Abstract.
In this work, we analyze optical characteristics of greater celandine (*Chelidonium majus* L.) ethanol solution extracts and fresh leaf samples. Optical emission of samples was measured using a pulsed laser excitation of tunable wavelengths (320–470 nm) and time-resolved detection system. Results of our analysis reveal two distinct alkaloid optical emission bands with different excitation characteristics. Chlorophyll fluorescence emission band was also detected. Time-resolved analysis of luminescent spectra shows that lifetimes of both alkaloid fluorescence bands and chlorophyll band are in nanosecond domain

1 Introduction

Alkaloid-enriched species *greater celandine* (*Chelidonium majus* L.) is a medicinal plant of the poppy family that grows mainly in Europe and Asia. It has segmented laticifers filled with yellowish—brown content that is rich in biologically active substances (alkaloids, flavonoids and phenolic acids) used for the treatment of various diseases and viruses The alkaloid content in Chelidonium majus plant can change sufficiently in depending on the development phases of the flowering period (from spring to the fruit—bearing time in autumn) [1,2]. Flavonoids (plant pigments) are responsible for the yellow color of the greater celandine flower. The concentration of flavonoids is the greatest just before flowering and before fruiting [3] The antioxidant activity was also correlated with the concentration of total phenolics (including flavonoids), and it is the highest in the spring months [3]. It has been demonstrated that both alkaloid extracts and purified alkaloids from that plant exhibit distinct anti-inflammatory, spasmolytic, anti-microbial (antibacterial, antiviral, antifungal) and anti-tumor activities [2–11]. The most important alkaloid components of this plant are protopine, chelidonine, coptisine, sanguinarine, allocryptopine, chelerythrine and stylopine. Identification and quantitative analysis of these individual alkaloids are important in developing and utilizing resources of greater celandine. Moreover, this analysis provides better insight into the mechanism of the biological action of specific alkaloids It was found by the authors in reference [2] that the concentration of the main alkaloid coptisine is maximal during the

flowering time. The fluorescent properties of greater celandine were also studied in detail in [12,13]. The important alkaloid responsible for fluorescence of Chelidonium majus extracts is sanguinarine. Its fundamental fluorescence properties were in detail described a decade ago [14] as well as its interaction with proteins [15], with DNA [16], and its biological activity [17]. Greater celandine leaves and flowers were analyzed by microspectrofluorimeter in [18] and later in 2020 by laser-scanning confocal microscopy [19]. The book [18] summarizes information on autofluorescence of plant secretory cells as a phenomenon and the possibilities of the practical use of light emission by cell biologists, biophysists, biochemists and botanists. Another book [19] describes how fluorescence in plant secretory cells, leaves and flowers can be used to localize ingredients in plants important for pharmacy and medicine. The optical properties of aforementioned alkaloids, isolated from the plant families Berberidaceae, Papaveraceae, Fumariaceae and Rutaceae are analyzed in detail in [20–22]. The chlorophyll luminescence analyses of some other plants, presented in [23–25], were also of interest to us, for comparative purposes

The aim of this study is analysis of optical characteristics of *C. majus* solution extracts and fresh leaf samples, using the time—resolved technique based on streak camera. To the best of our knowledge, the high-resolution time-resolved analysis of some of greater celandine components is presented only in [20], where fluorescence properties of protopine and allocryptopine, isolated from other plant families, were analyzed. The slow decay of chlorophyll photoluminescence of water plant, *Vallisneria spiralis* L, was analyzed in [23]. Interestingly enough, the luminescence decay, denoted in [23] as "degradation," was measured in minutes. The
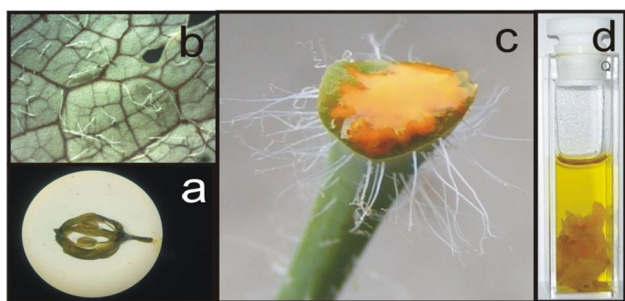
---

[a] e-mail: majap@ipb.ac.rs (corresponding author)

Fig. 1 a Bud and **b** leaf of the plant *C. majus* imaged under a microscope using a magnifying glass, **c** juice (latex) from cross-sections of the stem, **d** ethanol solution extracts of dry buds

luminescence kinetics of chlorophyll in *Chlorelia vulgaris* were studied in the time range from 200 ns to 20 μs [24] In [25]; the luminescence kinetics of chlorophyll was measured in seconds. Here, we analyze the optical characteristics of the ingredients of this medicinal plant *C. majus*, in order to gain a more detailed insight into the complex alkaloid composition.

2 Experimental procedure

The samples of *Chelidonium majus* L. were collected during the flowering period (spring) near the Danube in the courtyard of our Institute of Physics, Belgrade. That plant grows on the south side of the river (at a distance of about 100 m from the water). The stem laticifer extract of celandine dissolved in ethanol was used as the sample (Fig. 1) Laticifer is the tissue inside the stem or leaf in *C. majus* that contains yellow milky fluid named latex. The optical emission of leaf samples was measured immediately after they were collected (Fig. 1b).

The time-resolved optical characteristics of samples were analyzed using TR-LIF (Time-Resolved Laser-Induced Fluorescence) spectroscopy experimental setup presented in Fig. 2. The details about its operation could be found in [26–28]. In this study, the experiment setup was modified for analysis of samples of biological interest (solution samples and directly plant parts). To acquire streak images presented here, as an excitation source, we have used the output of the Optical Parametric Oscillator (Vibrant OPO), tunable over a spectral range from 320 to 475 nm.

As shown in Fig 2, we have used the beamsplitter, so the excitation and detection optical axes are collinear. Optical emission from the sample was detected in the reflection mode of the operation.

We recorded fluorescence optical emission using a streak scope (Hamamatsu model C4334-01) with integrated analog video camera. A triple grating imaging spectrograph (SpectraPro-2300i) was used as a dispersion system. The spectrograph grating of 50 lines/mm was used covering a spectral range of 330 nm (horizontal axis). The striking feature of the streak scope

is its two dimensional nature (wavelength and time). This is very advantageous for recording optical emission and lifetime measurements in biological samples. Streak images shown in this article are obtained by counting photons (1000–4000 exposures) and photon counts values are presented in pseudocolor. The streak images were acquired and analyzed using the HPD-TA (High Performance Digital Temporal Analyzer) streak camera control software. Fluorescence lifetime fitting analysis was carried out using the TA-Fit program.

3 Results and discussion

Absorption spectrum of *C. majus* extract displayed in Fig. 3 shows that the best excitation would be at 230 nm and 270 nm. It was found previously that all seven alkaloid components of greater celandine, excited at 280 nm, emit fluorescence in the range of 341–600 nm [2,13]. OPO system for excitation of samples used by us is tunable from 320 up to 475 nm, so the 320 nm was the lowest excitation wavelength that could be used. The excitation band around 354 nm was applied in our measurements for obtaining the corresponding emission spectra.

Absorbance spectrum for the bud from Fig. 1a and leaf from Fig. 1b is presented in Fig. 4. We can observe a small peak located at 675 nm at both of these spectra shown in Fig. 4. It is the site of the absorption maximum for chlorophyll **a** pigment. Chlorophylls absorb light in the blue (430–490 nm) and red (630–760 nm) part of the spectrum. Chlorophyll **a** pigment has an absorption maximum in the region of 665–670 nm [29].

In time-resolved images of fluorescence emission of *C. majus* solution extracts sample, we can notice two emission ranges with different intensities (Fig. 5). That measurements on laticifer tissue of *C. majus* (without the separation of the components) provided information about the complexity of the latex and various ratios of the alkaloids in the tissues. We tried to make a comparison with the published results of the alkaloids standards. The paper [2] is explained that, excited at 280 nm, chelidonine, protopine, allocryptopine and stylopine exhibit bands around 360 nm (first band), while sanguinarine, chelerythrine and coptisine exhibit bands around 570 nm (second band). In Fig. 5, the first emission band at 400–450 nm is pronounced for excitation of 320 nm, and its intensity decreases as excitation wavelength increases. It is also red shifted compared to [2], because we use higher excitation wavelengths than in [2]. As excitation wavelength increases, up to 367 nm, the second emission band around 570 nm band becomes more pronounced. Chelerythrine and sanguinarine are the most important alkaloids that always coexist in plants such as *C. majus*. In the paper [14], it was shown that fluorescence spectra of different forms of sanguinarine strictly depend on the pH of the solution. Upon excitation at 327 nm, they observed two peaks in the emission spectrum at 418 nm and 590 nm. In regards the position of peaks, these results are very similar to
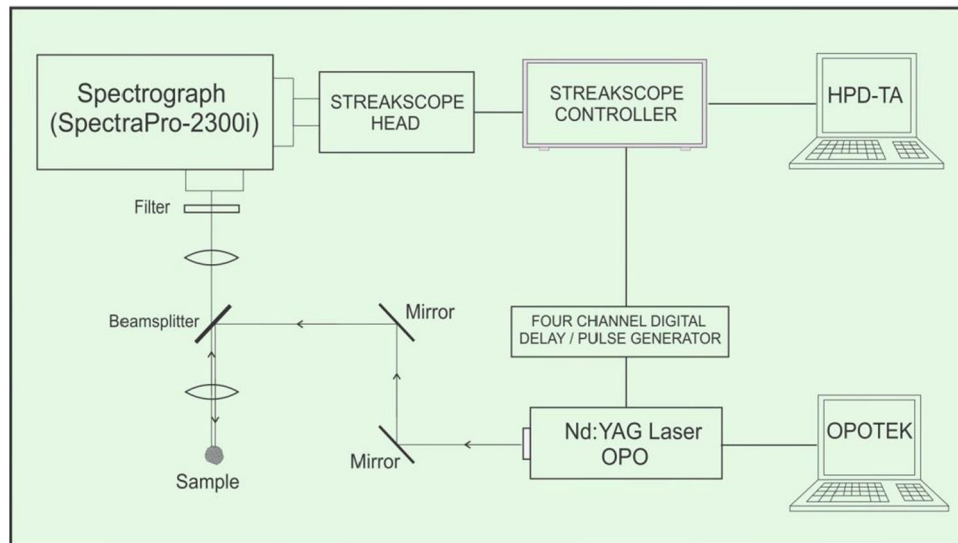
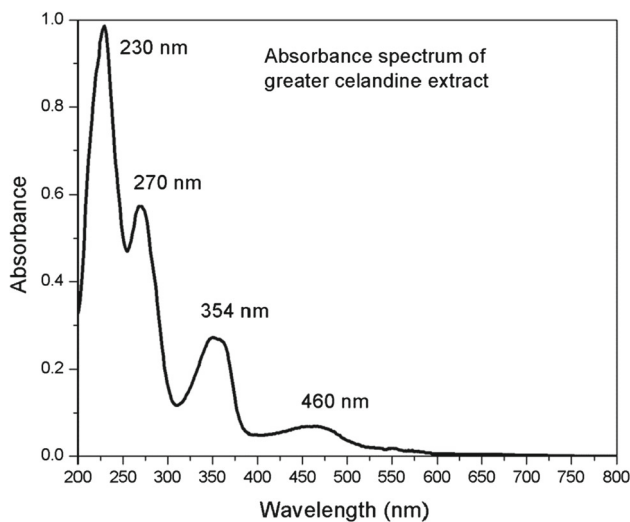**Fig. 2** Time-resolved laser induced fluorescence measurement system

Fig. 3 Absorbance spectrum of *C. majus* solution extracts sample
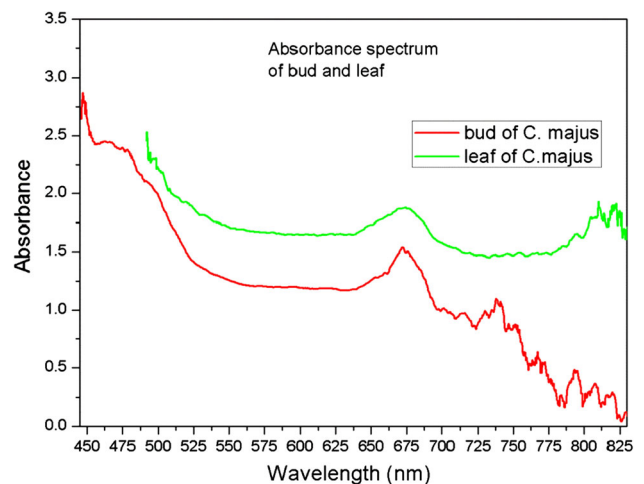

Fig. 4 Absorbance spectrum bud and leaf of *C. majus* samples

our results shown in Fig. 5 for excitation at 320 nm. In the paper [22], it was presented that the fluorescence emission peaks were 570 nm and 589 nm for chelerythrine and sanguinarine, respectively, for the excitation wavelength of 340 nm. Definitely the emission area depends on excitation. From our results (Fig. 5), we concluded that the excitation at 345 nm is the boundary region between two emission areas.

With further increasing in wavelength excitation up to 397 nm, we can see a nice difference in the fluorescence emission of stem laticifer and fresh leaf extract of *C. majus* sample (Fig. 6). The emission spectrum of the leaf sample in Fig. 6b shows that chlorophyll is the most pronounced, while the stem is dominated by alkaloids in Fig. 6a. Emission band corresponding to chlorophyll fluorescence has the main component at 680 nm in our

results of fresh leaf of *C. majus*; the other component at 740 nm is less visible in Fig. 6a. According to the literature [23], chlorophyll in *Vallisneria spiralis L* has two bands with emission peaks at 740 nm and 685 nm. In our measurements, these two bands are blue shifted to 675 nm and 730 nm. In the paper [12], the authors obtained the peak at 680 nm related to chlorophyll for the excitation at 405 nm. If the excitation increases up to 488 nm, the emission maximum shifted to longer wavelength [12]. Photon counts in Figs. 5 and 6 are presented in pseudocolor defined by scale color bar on right side of figures. Spectral band width of one pixel is 0.5156 nm (330 nm/640 px) and time width of one pixel is 0.10417 ns (50 ns/480 px).

The fluorescence lifetime of greater celandine components was determined using the HPD-TA software. Estimated fluorescence lifetimes of both alkaloid bands are about 2.6 ns, obtained as the results of the single—
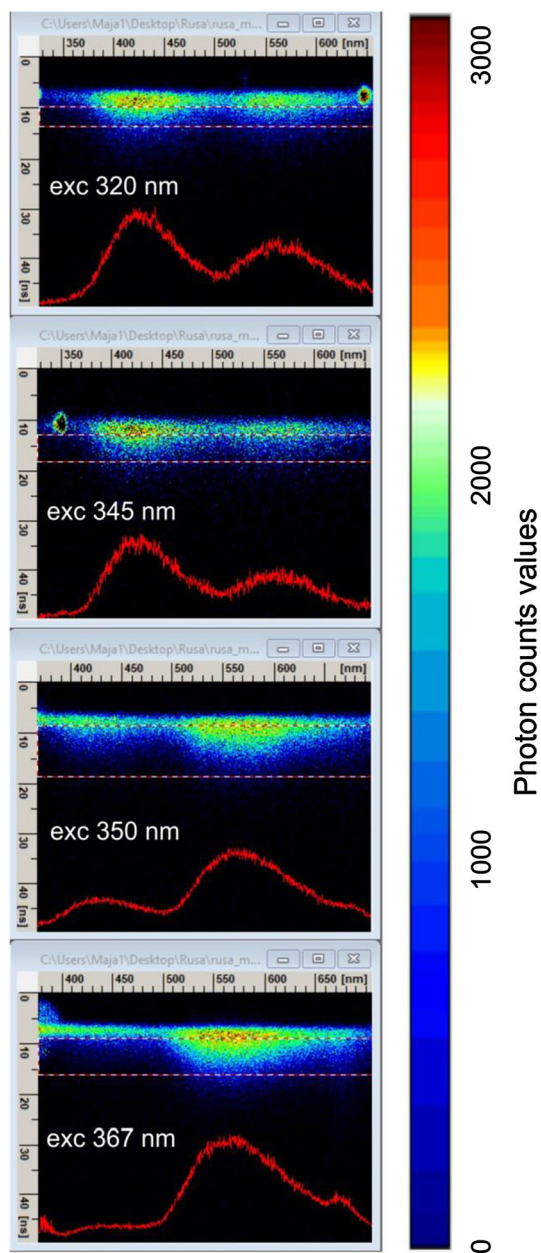
Fig. 5 Streak images of fluorescence emission of *C. majus* solution extracts sample. Excitation wavelengths were: **a** 320 nm, **b** 345 nm, **c** 350 nm, **d** 367 nm

Fig. 6 Streak images of fluorescence emission of *C. majus* solution extracts and fresh leaf sample. Excitation wavelength was 397 nm

cence lifetime strongly depends on plant species These lifetime measurements are used to monitor the photosynthesis process in healthy and damaged leaves (due to viruses or other diseases) [31]. Typically, the chlorophyll bound to the photosystem proteins exhibits fluorescence lifetime in ps range, free chlorophyll in extract has a lifetime in ns range, and there is also extensive literature describing delayed fluorescence and phosphorescence with substantially longer lifetimes. Comparison of optical characteristics (excitation and emission peaks) and lifetime results of different fluorescent components of *C. majus* collected from the literatures is presented in Table 1.

4 Conclusion

In this study, we have carried out the time-resolved analysis of optical characteristics of *C. majus* solution extracts and fresh leaf samples. Two distinct alkaloid optical emission bands with different excitation characteristics are revealed in our analysis. Chlorophyll fluorescence emission band was also detected. Time-resolved analysis of luminescent spectra shows that lifetimes of both alkaloid fluorescence bands are in nanosecond domain. Fluorescence lifetime of chlorophyll band is distinctly longer; however, it is still in

exponential fit, slightly longer than reported in [20]. Fluorescence lifetime of chlorophyll band from Fig. 6b is distinctly longer and it is estimated to be about 6.7 ns. Analysis of chlorophyll **a** kinetics was performed in [30]. Their study showed that there are two lifetime components; fast of 262 ps is dominant and slow of 728 ps. In [23], it is reported that photoluminescence lifetime of chlorophyll band is in order of minutes, however, in different plant, *Vallisneria spiralis* L, and with quite different excitation. The measured luminescence lifetime of chlorophyll in *Chlorelia vulgaris* was in order of micro seconds in reference [24]. Chlorophyll lumines-
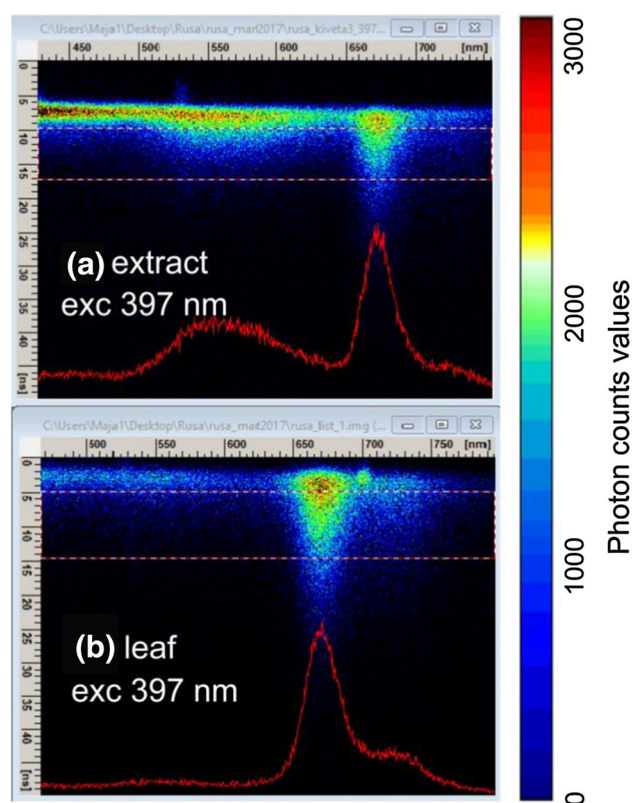
Table 1 Optical characteristics of fluorescent components of *greater celandine (C. majus)*

	Fluorescence excitation peak (nm)	Fluorescence emission peak (nm)	Luminescence lifetime	References
Sanguinarine	270, 320 in ctDNA	575		[16]
Coptisine	240, 350	450, 525 solvent dependent		[14]
Chelerythrine	270, 320, 340 in ctDNA	57		[16]
Stylopine	290	326		[13]
Chelidonine	291	330		[13]
Protopine	290	317–328	2 ns	[14]
Allocryptopine	285	316–327	2.4 ns	[14]
Chlorophyll in different plants	488	685	Minutes microseconds seconds	[17–19]

nanosecond domain. A more detailed insight into the composition of latex in the plant *C. majus* and comparison with alkaloid standards will be the topic of our future work. The study of this plant is important due to its practical application in medical sciences and antiviral activity, which is especially important nowadays.

Data Availability Statement This manuscript has no associated data, or the data will not be deposited. [Authors' comment: All relevant data are in the paper.]

References

1. K. Seidler-Lozykowska, B. Kedzia, J. Bocianowski, A. Gryszczynska, Z. Lowicki, B. Opala, A. Pietrowiak, Acta Sci. Pol. Hortorum Cultus **15**(4), 161–172 (2016)
2. M. Kulp, O. Bragina, P. Kogerman, M. Kaljurand, J. Chromatogr. A **1218**, 5298–5304 (2011)
3. D. Jakovljevic, M. Stankovic, M. Topuzovic, EXCLI J. **12**, 260–268 (2013)
4. M. Kulp, O. Bragina, Anal. Bioanal. Chem. **405**, 3391–3397 (2013)
5. G.-Y. Zuo, F.-Y. Meng, X.-Y. Hao, Y.-L. Zhang, G.-C. Wang, G.-L. Xu, J. Pharm. Pharm. Sci. **11**, 90–94 (2008)
6. V. Kaminskyy, M.D. Lootsik, R. Stoika, Centr. Eur. J. Biol. **1**, 2–15 (2006)
7. S. Zielinska, M. Wójciak-Kosior, M. Dziagwa-Becker, M. Glensk, I. Sowa, K. Fijalkowski, D. Ruranska-Smutnicka, A. Matkowski, A. Junka, Toxins **11**, 406 (2019)
8. Mala Gilca, Laura Gaman, Elena Panait, Irina Stoian, Valeriu Atanasiu, Forsch Komplementmed **17**, 241–248 (2010)
9. M. Parvu, L. Vlase, L. Fodorpataki, O. Parvu, O. Rosca-Casian, C. Bartha, L. Barbu-Tudoran, A.E. Parvu, Not. Bot. Horti Agrobo. **41**, 414–426 (2013)
10. A. Sarkosi, Novel data contributing to our knowledge of the greater celandine, Ph.D. Thesis, The Semmelweis University (2007)
11. A.K. Maji, P. Banerji, Int. J. Herb. Med. **3**(1), 10–27 (2015)
12. V.V. Roshchina, A.V. Kuchin, V.A. Yashin, Int. J. Pharm. and Chem. **2**, 31–38 (2016)
13. J. Kovar, K. Simek, E. Kozouskova, H. Klukanova, J. Slavik, Coll. Czech. Chem. Commun. **501**, 1312–1328 (1985)
14. M. Janovská, M. Kubala, V. Šimánek, J. Ulrichová, Anal. Bioanal. Chem. **395**, 235–240 (2009)
15. M. Janovská, M. Kubala, V. Šimánek, J. Ulrichová, Phys. Chem. Chem. Phys. **12**, 11335–11341 (2010)
16. J. Vacek, E. Vrublova, M. Kubala, M. Janovská, M. Fojta, E. Šimkova, J. Stýskala, J. Skopalová, J. Hrbác, J. Ulrichová, Electroanalysis **23**(7), 1671–1680 (2011)
17. M. Janovská, M. Kubala, V. Šimánek, J. Ulrichová, Toxicol. Lett. **196**, 56–59 (2010)
18. V.V. Roshchina, *Fluorescing World of Plant Secreting Cells*, 1st edn. (CRC Press, 2008)
19. V.V. Roshchina, *Fluorescence of Living Plant Cells for Phytomedicine Preparations*, 1st edn. (CRC Press, 2020). https://doi.org/10.1201/9780429319464
20. M. Kubala, J. Vacek, I. Popa, M. Janovská, P. Kosina, J. Ulrichová, Z. Travnicek, V. Šimanek, J. Lumin. **131**, 1340–1345 (2011)
21. R. Mi, X.-T. Bai, B. Tu, Y.-J. Hu, RSC Adv. **5**, 47367–47376 (2015)
22. J. Li, B. Li, Y. Wu, S. Shuang, C. Dong, M.M.F. Choi, Spectrochim. Acta A Mol. Biomol. Spectrosc. **95**, 80–85 (2012)
23. O.V. Vakulenko, O.O. Grygorieva, O.I. Dacenko, Ukr. J. Phys. **57**, 256–259 (2012)
24. J.A. van Best, L.N.M. Duysens, Biochim. Biophys. Acta **459**, 187–206 (1977)
25. W. Bilger, U. Schreiber, Photosynth. Res. **25**, 161–171 (1990)
26. B.P. Marinkovic, A. Delneri, M.S. Rabasovic, M. Terzic, M. Franko, D. Sevic, J. Serb. Chem. Soc. **79**, 185–198 (2014)
27. M.S. Rabasovic, D. Sevic, M. Terzic, B.P. Marinkovic, Phys. Scr. **T149**, 014076 (2012)

28. M.S. Rabasovic, D. Sevic, M. Terzic, B.P. Marinkovic, Nucl. Inst. Methods B **279**, 16–19 (2012)
29. P. Akhtar, C. Zhang, T.N. Do, G. Garab, P.H. Lambrev, H.-S. Tan, J. Phys. Chem. Lett. **8**, 257–263 (2017)
30. A.S. Kristoffersen, B. Hamre, Ø. Frette, S.R. Erga, Eur. Biophys. J. **45**, 259–268 (2016)
31. R. Lei, H. Jiang, F. Hu, J. Yan, S. Zhu, Plant Cell Rep. **36**, 327–341 (2017)

arrangement which could accommodate higher concentration of dopants at shorter distance. Stabilization of this phase in nanoparticles is usually achieved through thermal decomposition of organic precursors in the presence of solvents with a high boiling point. Here, for the same purpose, we used gadolinium co-doping during chitosan assisted solvothermal processing of inorganic precursor salts. Precursor concentration, solvent type, and synthesis time were varied in order to determine their influence on the β-NaY$_{0.65}$Gd$_{0.15}$F$_4$:Yb$_{0.18}$Er$_{0.02}$ phase crystallization. The XRPD analysis showed that lower surplus of fluoride ions during synthesis leads to formation of Y$_{0.65}$Gd$_{0.15}$F$_4$:Yb$_{0.18}$Er$_{0.02}$ orthorhombic phase, while the increase of fluoride content or prolongation of the processing time enhances formation α-NaY$_{0.65}$Gd$_{0.15}$F$_4$:Yb$_{0.18}$Er$_{0.18}$ phase. Along with it, the changes of UCNPs morphology from spindle to spherical shape is detected. All samples emit intense green emission due to the $(^2H_{11/2}, ^4S_{3/2}) \rightarrow ^4I_{15/2}$ electronic transitions, after been excited with infrared light (λ=978 nm).

INV

Nonlinear laser scanning microscopy for imaging of the cells labeled by up-converting NaYF$_4$:Yb,Er nanoparticles

Mihailo D. Rabasovic[1], Ivana Dinic[2], Aleksandra Djukic-Vukovic[3], Milos Lazarevic[4], Marko G. Nikolic[1], Aleksandar J. Krmpot[1], Lidija Mancic[2]

[1]Photonic Center, Institute of Physics Belgrade, University of Belgrade, Zemun, Belgrade, Serbia
[2]Institute of Technical Sciences of the Serbian Academy of Sciences and Arts, Belgrade, Serbia
[3]Department of Biochemical Engineering and Biotechnology, Faculty of Technology and Metallurgy, University of Belgrade, Serbia
[4]Institute of Human Genetics, School of Dental Medicine, University of Belgrade, Serbia

The Nonlinear Laser Scanning Microscopy (NLSM) contributes to the cell labeling through addressing two main issues: photobleaching and phototoxicity. Moreover, an increase of the penetration depth and a reduction of background autofluorescence are achieved. We have used a multidisciplinary approach combining expertise in material science, nanoparticles synthesis and characterization, cancer cell and tissue labeling, and high resolution imaging, in order to accomplish *in vitro* imaging of the cancer cells. We have imaged the oral squamous carcinoma cells and human gingival cells. We have demonstrated that we are able to take high contrast images. We have shown position of the nanoparticles in cells, through co-localization of the cell auto-fluorescence and the nanoparticles up-conversion. We plan to improve our abilities through further optimization of the up-converting nanoparticles (smaller and brighter particles) and microscopy technique.

SPATIAL MEASUREMENTS OF LASER-INDUCED BREAKDOWN IN AIR

M. S. Rabasovic, M. D. Rabasovic, B. P. Marinkovic and D. Sevic

Institute of Physics, University of Belgrade, Serbia

Abstract. We present time resolved measurements of the plasma expansion produced by laser induced breakdown in atmospheric air. A Q-switched Nd:YAG laser is employed as the excitation source. The detection part of the acquisition system is based on a streak camera equipped with the spectrograph. A simple modification of the spectrograph enables the easy switching between the spectral and spatial measurement modes.

1. INTRODUCTION

The formation of laser induced breakdown (LIB) refers to a plasma production by focusing an intense laser beam in a gas, liquid or solid target. Parameters of laser induced plasma depend on irradiation conditions, such as laser intensity, pulse duration, laser wavelength or ambient gas. To understand the process of laser induced breakdown it is required to obtain the detailed knowledge of the initial stages of various processes involving laser duration and irradiation, plasma formation and its expansion. The nanosecond laser pulse generates plasma through thermal and non-thermal mechanisms. Studying the plasma formation with a high temporal, spectral and spatial resolution is of a great interest and formation of laser induced breakdown plasma in air has been studied by many researchers [1-6], including references therein.

After the initial breakdown, plasma plume propagates towards the focusing lens [1,3]. The bright plasma core of the LIB plasma in open air is surrounded by a layer of cold, moderately ionized gas called the sheath [1]. Glow of plasma sheath, although fainter than the core, is also visible to the naked eye. An explosive plasma expansion induces optodynamic phenomena, i.e., the propagation of a shock, acoustical and ultrasonic waves.

In this paper we present an experimental system that is capable of both spatial and spectral measurements of laser-induced plasma with picosecond temporal resolution. We performed a simple modification of our spectrograph that enables easy switching between the spectral and spatial measurement modes. Later, we became aware that this modification was already proposed and successfully used in the study of Siegel et al. [7], where imaging device was ICCD camera.

2. EXPERIMENTAL SET-UP

Time resolved LIB system implemented in our laboratory is shown in Figure 1. In this study we use the fundamental output at of OPO pumping laser (1064 nm, pulse energy up to 270 mJ, pulse duration of about 5 ns) to create an optical breakdown in ambient air. Timing considerations regarding the laser pulse and streak camera synchronization are very important in our measurements, so we added a photodiode and digital oscilloscope to our experimental setup, Figure 1.
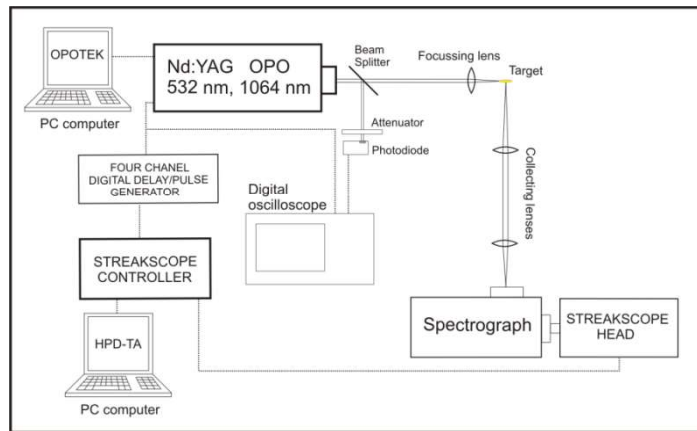

Figure 1. Setup for time-resolved laser induced breakdown measurements.

The optical emission from the plasma is collected by using a spectrograph and recorded with a streak camera. The streak images are time resolved thus enabling monitoring of temporal evolution of the ionic and atomic emission lines or spatial development of the plasma.

Our research of optical emission of plasma was limited so far to analysis of time resolved optical emission spectra acquired by the streak camera [8-10]. To make our study more comprehensive we saw the need for measuring the spatial distribution of plasma optical emission. So we improved the set up and accomplished requirement for easy switching between the spectral and spatial measurement modes of our streak camera system.

We performed a simple modification of our spectrograph that enables easy switching between the spectral and spatial measurement modes, see Figure 2. The spectrograph contains the triple grating turret. In the place of the 150 g/mm grating we mounted the plain mirror. Now, if position of turret corresponding to grating of 150 g/mm is selected, streak camera takes the image of the spatial distribution of the optical emission of the laser induced breakdown. The spectrograph entrance slit should be fully open to utilize as much as possible of the CCD camera active area. The calibration procedure showed that 1 mm on the target position corresponds to 72 pixels of the CCD camera.
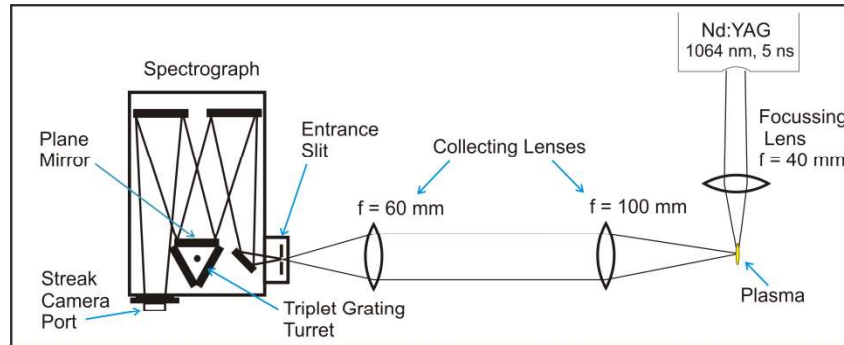
Figure 2. A simple modification of our spectrograph that enables easy switching between the spectral and spatial measurement modes.

3. RESULTS AND DISCUSSION

The streak image of the laser induced plasma (excitation at 1064 nm, energy of 51 mJ, peak intensity of $1.3 \cdot 10^{11}$ W/cm^2) is shown in Figure 3. The time axis is vertical, with zero on top of the image. The spatial axis is horizontal. The development of the plasma is seen on the streak image as vertical development (corresponding to a passing of time) of a narrow horizontal section of plasma optical emission, seen through the camera slit, along the direction of propagation of the laser beam. In other words, two dimensional (2-D) streak image corresponds to only 1-D spatial image, represented by rows of image matrix, the other dimension being the time. White points indicate the edges and peak values of plasma brightness, detected by our image processing algorithm.

Our analysis of data provided by streak image presented in Figure 3 shows that instantaneous-velocity of plasma is about 150 km/s at the beginning, and decrease towards about 25 km/s after 16 ns. At about 20 ns plume stops expanding.

4. CONCLUSION

We have the presented the possibilities of spatial measurements of the laser induced plasma development in air by using the streak camera equipped with spectrograph, after simple modification of spectrograph turret. The presented method is suitable for plasma sheath velocity measurements from the very beginning of the laser induced breakdown by using a picosecond time resolution of our streak camera.
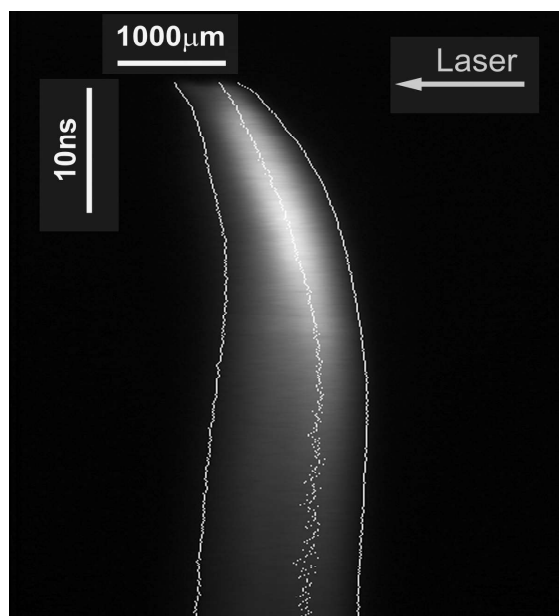
Acknowledgements

Figure 3. Streak image of the laser induced plasma (excitation at 1064 nm, energy of 51 mJ). The detected edges and peak values of brightness of the plasma plume are indicated by white points.

REFERENCES

[1] A. Robledo-Martinez, H. Sobral, M. Villagrán-Muniz, and F. Bredice, Physics of Plasmas **15**, 093510 (2008).

[2] M. Villagrán-Muniz, H. Sobral, and E. Camps, IEEE Trans. on Plasma Science **29**, 613 (2001).

[3] P. Gregorčič, J. Možina, Opt. Lett. **36**, 2782 (2011).

[4] Camacho, L. Díaz, M. Santos, L. J. Juan, J. M. L Poyato, Journal of Applied Physics **107**, 083306 (2010).

[5] N. Kawahara, J. L. Beduneau, T. Nakayama, E. Tomita, Y. Ikeda, Appl. Phys. B **86**, 605 (2007).

[6] T. Hori and F. Akamatsu, Jpn. J. of Appl. Phys. **47**, 4759 (2008).

[7] J. Siegel, G. Epurescu, A. Perea, F.J. Gordillo-Vazquez, J. Gonzalo, C.N. Afonso, Spectrochim. Acta Part B, 60, 915 (2005).

[8] D. Sevic, M. S. Rabasovic, B. P. Marinkovic, IEEE Trans. on plasma science **39**, 2782 (2011).

[9] M. S. Rabasović, D. Sevic, V. Pejčev, B. P. Marinković, Nucl. Instrum. Meth. B **279**, 61 (2012).

[10] M. S. Rabasovic, B. P. Marinkovic, D. Sevic, IEEE Transactions on Plasma Science **42**, 2388 (2014).

THE DAMPENING OF LIPID DROPLET OSCILLATORY MOVEMENT IN NITROGEN STARVED FILAMENTOUS FUNGI BY A LOW DOSE OF MITOCHONDRIAL RESPIRATION INHIBITOR

Tanja Pajic[1], Miroslav Zivic[1], Mihailo D. Rabasovic[2], Aleksandar Krmpot[2], <u>Natasa Todorovic</u>[3]

[1] Faculty of Biology, University of Belgrade, Studentski trg 16, 11158 Belgrade, Serbia
e-mail: tpajic@bio.bg.ac.rs
[2] Institute of Physics Belgrade, University of Belgrade, Pregrevica 118,11000 Belgrade, Serbia
[3] Institute for Biological Research "Sinisa Stankovic", University of Belgrade, Institute of National Importance for the Republic of Serbia, Bulevar Despota Stefana 142, 11000 Belgrade, Serbia
e-mail: mzivic@bio.bg.ac.rs, rabasovic@ipb.ac.rs , krmpot@ipb.ac.rs, nara@ibiss.bg.ac.rs

Abstract:

Lipid droplets (LDs) are small mobile organelles conserved in all eukaryotic cells. We wanted to test if the LD movement can be muffled by an incomplete inhibition of mitochondrial respiration, induced by treating hyphae of filamentous fungus *Phycomyces blakesleeanus* with 0.5 mM sodium azide. Nitrogen starved hyphae were used, in order to obtain LDs in larger sizes and numbers. The data obtained unequivocally showed: 1. Sodium azide treatment dramatically reduces the LD velocity and the distances LDs travel; 2. LDs in both controls and in azide-treated hyphae oscillate in a small confined space instead of travelling through the cell; 3. Azide-treated LDs oscillate less frequently and in smaller confinement than controls.

Key words: Sodium azide, *Phycomyces blakesleeanus*, *In vivo* microscopy, Nile Red

1. Introduction

Lipid droplets (LDs) are ubiquitous, highly phylogenetically conserved and seemingly simple organelles that are increasingly getting recognized as central coordinators of lipid metabolism between various cellular organelles [1]. LDs are often small and fairly mobile, found to form functional interactions with other cellular compartments [2]. During our filamentous fungi live microscopy investigations of LDs, the need has arisen to define a set of experimental conditions that will result in slowing down the LD movement just enough, to be able to perform colocalization studies *in vivo*. We present the results obtained by using a low concentration of sodium azide, the inhibitor of mitochondrial respiration. The azide effect and dose response on the model system fungi used in this study were previously measured in our lab [3].

2. Materials and Methods

Model organism was wild-type strain of the unicellular oleaginous filamentous fungus *Phycomyces blakesleeanus* (Burgeff) (NRRL 1555(−)), grown in lighted stationary plates from the spore stock as previously described [3]. In order to get larger LDs and possibly easer observe the movement of LDs, fungi were grown in nitrogen starvation conditions with the amino acids omitted from the standard medium. Live hyphae were stained with Nile Red. A drop of fungi culture was placed in custom built closed cover glass holder to be fitted on the microscope stage. The hyphae in the azide treated (0.5 mM) group were imaged by Two Photon Excitation (TPEF) microscopy with the time interval of 60 s. The

TPEF of Nile Red dye was excited by 1040 nm, 200 fs pulses from Yb KGW laser and the signal was collected through 400-700 nm band pass filter with the use of 40x1.3 objective. The details of the Nonlinear Laser Scanning Microscopy set-up can be found in [4]. The control group was imaged from independent hypha batch, cultured in the same conditions as the azide-treated group. Images for controls were taken on Zeiss Axiovert fluorescent microscope equipped with camera (Xenon lamp illuminated, DsRed filter, 20 X 0.8 NA objective), with image acquisition time interval: 1 s. LD movement was measured by the mTrack plugin of ImageJ freeware [5] from time lapse Nile Red image sequences. All parameters quantified were readily available from mTrack analysis, except mean frequency which was derived in the following way: for each LD tracked, the total path length was divided by the mean displacement from the starting point. The results are reported as mean ± SE at 95% confidence level. One way ANOVA or nonparametric rank sum (Mann Whitney) test was used for statistical testing.

2. Results and Discussion

Nile Red -stained LDs were imaged from nitrogen-starved hyphae with and without 0.5 mM azide (azide-treated and control group, respectively). The representative starting images of the time sequences are shown in Figure 1.A. It can be seen that images obtained by TPEF are much clearer, and probably represent true optical section of hypha, while in fluorescent microscope image, the various fainter structures around LDs are present, degrading the contrast of the image as expected. Since we were able to reliably identify LDs from both types of images, the LD movement analysis was not undermined with those differences in the image quality. The second methodological issue that could decrease the accuracy of the measurement is the possible occurrence of substantial bleaching of the dye, caused by the repeated illumination during the acquisition of image sequences.
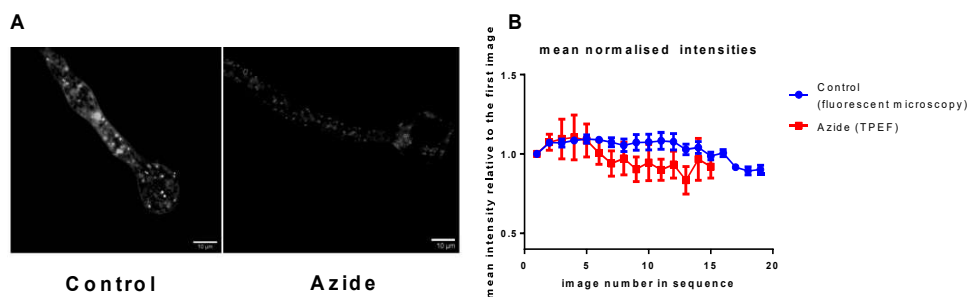

Fig. 1. Images of Nile Red -stained hyphae. A. Fluorescent microscopy image of hypha from the control group (left panel) and TPEF microscopy image of hypha from the azide-treatment group (right panel). The brightest small round features, visible on both images, represent the lipid droplets. B. Stability of Nile Red signal in images acquired in time sequence, quantified as mean normalized (to the intensity in first image of the sequence), intensity of randomly selected bright features in control and azide-treated group (n = 3 and n = 7 respectively).

As demonstrated in a graph shown in Figure 1B, the Nile Red signal intensity was stable during the time needed for sequence acquisition. At the end of the image sequence, the intensity was at $90 \pm 2\%$ from the starting values in the control group sequences, and at $92 \pm 7\%$ in the azide group, under the conditions used.
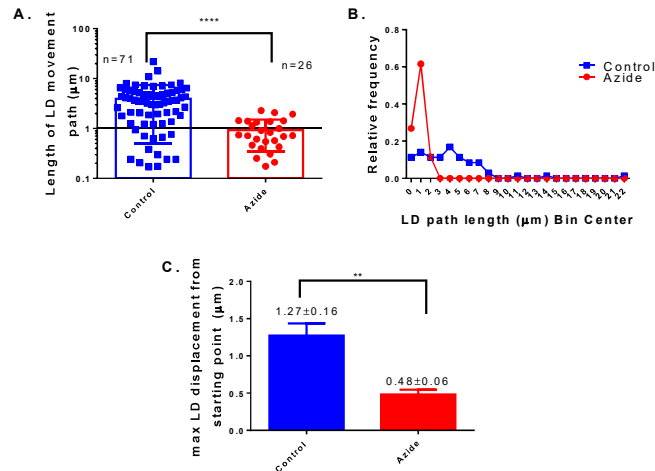
Fig. 2. The movement parameters obtained from LD tracking image analysis. A. The length of LD paths (µm). All obtained values from control and azide-treated hyphae are displayed; B. Distribution of LD path lengths, presented as a relative frequency histogram. C. Maximal displacement of LDs from the starting point, showing that most of LDs stayed close to the starting point throughout the imaging time.

All obtained LD path length values from control hyphae (mean: 4 ± 3 µm), from 12 s image sequences and azide-treated (mean: 0.9 ± 0.6 µm) from 11 min, are displayed in Figure 2A. Even measured on such different time frames, the control total path length values (movement in 12 s) were significantly larger than from azide-treated (movement in 11 min); Mann-Whitney test, $p< 0.0001$. Literally all of the visible LDs (in both groups) displayed oscillatory movement and were not transported further from the location occupied at the beginning of the image series. Maximal displacement from the starting point for each LD was pulled and mean value calculated for each experimental group: $maxD2S_{control}= 1.3 \pm 0.2$; $maxD2S_{azid} = 0.5 \pm 0.1$ (in µm); $p = 0.004$.
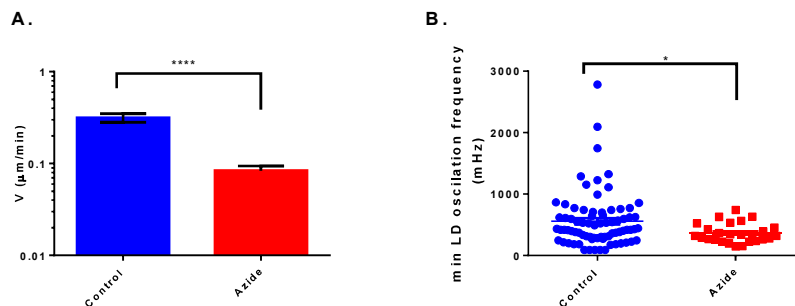

Fig. 3. The speed and frequency of LD movement were significantly lowered by azide treatment compared to control A. The mean speed of LD movement (µm / min) ($p< 0.0001$). B. The frequencies of LD oscillatory movement (mHz) ($p = 0.0333$).

Therefore, it can be concluded that LDs, under the conditions used, travelled just a few microns or less during acquisition. The average speed of LD movement (in µm / min) was dramatically reduced by azide-treatment: $V_{control} = 0.3155 \pm 0.034$; $V_{azide} = 0.084 \pm 0.01$. $p< 0.0001$ (Figure 3A).

Since the vast majority of the imaged LDs displayed oscillatory movement during the observation time, we expressed the LD movement as minimal oscillation frequency, in order to acknowledge the possibility of the presence of higher frequencies, outside of the frequency range of our observations. The minimal frequency of LD oscillatory movement (Figure 3B) was significantly lowered by azide treatment: $f_{control} = 558 \pm 52$ mHz compared to $f_{azid} = 363 \pm 31$ mHz ($p = 0.0333$).

It is possible that, due to the repeated illumination, LD transport was slowed down due to phototoxicity. Since the transport to more remote locations could not be observed even in the starting portions of image sequences, before the eventual photoxicity could take place, we concluded that

phototoxicity does not seem to be of importance for the phenomena observed.

Recent imaging study with extended spatial and temporal resolution of LDs in mammalian cells under control conditions also have shown that during the experiment LDs displayed mainly oscillatory movements, with short intermittent contacts with mitochondria [6]. There are two main types of LD movement described in the literature: oscillatory in confined space [7] and directional in short or long trajectories [8]. In addition, it would be expected that during autophagy processes, the periods of contact between LDs and mitochondria would be more frequent and/or of longer duration [9], possibly causing somewhat stationary LD behavior that we have observed.

4. Conclusions

LD movement in sodium azide-treated hyphae is significantly slowed down. The *in vivo* colocalization studies are feasible, if conditions used are replicated. The purely oscillatory movement and relative immobilization of LDs in controls should be investigated further.

References

[1] A. Meyers, T.M. Weiskittel, P. Dalhaimer, *Lipid Droplets: Formation to Breakdown*, Lipids, 52 (2017) 465-475.

[2] M.S. Murphy, R.G. Parton, *Lipid droplet-organelle interactions; sharing the fats*, Biochim Biophys Acta, 1791 (2009) 441-7.

[3] M. Stanić, J. Zakrzewska, M. Hadžibrahimović, M. Zižić, Z. Marković, Z. Vučinić, M. Zivić, *Oxygen regulation of alternative respiration in fungus Phycomyces blakesleeanus: connection with phosphate metabolism*. Research in Microbiology, 164 (2013) 770-8.

[4] I. Miler, M.D. Rabasovic, M. Aleksic, A.J. Krmpot, A. Kalezic, A. Jankovic, B. Korac, A. Korac. *Polarization-resolved SHG imaging as a fast screening method for collagen alterations during aging: Comparison with light and electron microscopy*. Journal of Biophotonics, 14 (2021) e202000362.

[5] E. Meijering, O. Dzyubachyk, I. Smal. *Methods for Cell and Particle Tracking*, Methods in Enzymology, 504 (2012) 183-200.

[6] M. Pribasnig, B. Kien, L. Pusch, G. Haemmerle, R. Zimmermann, H. Wolinski, *Extended-resolution imaging of the interaction of lipid droplets and mitochondria*, Biochim Biophys Acta Molecular Cellular Biology of the Lipids, 1863 (2018) 1285-1296.

[7] P. Targett-Adams, D. Chambers, S. Gledhill, R.G. Hope, J.F. Coy, A. Girod, J. McLauchlan, *Live Cell Analysis and Targeting of the Lipid Droplet-binding Adipocyte Differentiation-related Protein*. Journal of Biological Chemistry, 278 (2003) 15998–16007.

[8] Y. Jin, Z. Ren, Y. Tan, P. Zhao, J. Wu, *Motility Plays an Important Role in the Lifetime of Mammalian Lipid Droplets,* International journal of molecular sciences, 22 (2021) 3802.

[9] T.B. Nguyen, J.A. Olzmann, *Lipid droplets and lipotoxicity during autophagy*, Autophagy, 13 (2017) 2002-2003.

THE EFFECTS OF SELENITE ON FILAMENTOUS FUNGI LIPID DROPLETS MONITORED *IN VIVO* LABEL FREE USING ADVANCED NONLINEAR MICROSCOPY TECHNIQUE

Tanja Pajic[1], Natasa Todorovic[2], Dunja Stefanovic[1], Mihailo D. Rabasovic[3], Aleksandar Krmpot[3], <u>Miroslav Zivic</u>[1]

[1] Faculty of Biology, University of Belgrade, Studentski trg 16, 11158 Belgrade, Serbia
e-mail: tpajic@bio.bg.ac.rs
[2] Institute for Biological Research "Sinisa Stankovic", University of Belgrade, Institute of National Importance for the Republic of Serbia, Bulevar Despota Stefana 142, 11000 Belgrade, Serbia
[3] Institute of Physics Belgrade, University of Belgrade, Pregrevica 118, 11000 Belgrade, Serbia
e-mail: nara@ibiss.bg.ac.rs, rabasovic@ipb.ac.rs , krmpot@ipb.ac.rs, mzivic@bio.bg.ac.rs

Abstract:

Third Harmonic Generation (THG) microscopy was employed as a method of choice for lipid droplet (LD) measurements and quantification of the effect of selenite on LDs.

Nonlinear laser scanning microscopy (NLSM) employs ultra-short laser pulses for imaging. THG microscopy is the modality of NLSM. Strong THG signals can only be observed from regions with non-uniformities with respect to their refractive index. Such regions in biological samples are lipid-water interfaces, and by far the brightest features in cells are LDs. For that reason, THG microscopy is the appropriate method for imaging of LDs from live unfixed cells, without the need for additional labeling.

The biological effects of spore- to- end- of- exponential- phase duration (27 - 30 h) of exposure to 1 mM selenite were monitored *in vivo* on the cells of filamentous fungi in liquid culture. We measured the lipid droplet density and size distribution in a model fungi *Phycomyces blakesleeanus*. The in-house built microscope frame complemented with Yb KGW laser (1040 nm, 200 fs pulses) was used, while detection was enabled in the transmission arm by PMT through the Hoya glass UV filter (peak at 340 nm).

From THG images of control and Se^{+4}–treated hyphae, LD size and number were measured, showing that LD density was increased by more than 60% in Se^{+4}–treated hyphae, compared to control. The average LD size distribution seemed slightly changed by Se^{+4}-treatment. The obtained results suggest that 1 mM selenite treatment probably induces cellular stress response in filamentous fungi.

Keywords: Lipid droplets, Selenite, Third Harmonic Generation Microscopy, *Phycomyces blakesleeanus*

1. Introduction

Selenium is an essential trace element for humans and animals, while it is not necessary for plants and fungi. The availability and biological activity of selenium depend on its dose and chemical form [1]. In trace amounts, selenium enhances antioxidant capacity in a number of selenoproteins while at higher concentrations, selenium is toxic due to its prooxidative effects like oxidation of protein thiols and reactive oxygen species generation [2]. Since the oxidative stress is among the main intracellular signals sustaining autophagy [3], and lipid droplet (LD) biogenesis seems to be a general cellular response to high autophagic flux according to recent studies [4], we hypothesized that increased LD formation could be an immediate cellular response to a high selenium exposure.

In order to reliably monitor LDs *in vivo* by imaging, and measure the effects of selenite-induced oxidative stress- mediated cellular changes, it would be necessary to employ the imaging method that causes minimal additional phototoxicity. Otherwise, the oxidative stress induced by, for example, confocal imaging of labeled LDs, could potentially interfere with the processes underlying the measurements. For those reasons, Third Harmonic Generation (THG) microscopy was employed as a method of choice for LD measurements and quantification of the effect of selenite on LD number and sizes. THG microscopy is one of the modalities of nonlinear laser scanning microscopy (NLSM). In NLSM, the high laser intensity, and low average power due to employing ultra-short laser pulses, allow for the generation of nonlinear imaging signals. Although THG microscopy is not chemically specific, strong THG signals can only be observed from regions with non-uniformities with respect to their refractive index. Such regions in biological samples are lipid-water interfaces, and by far the brightest features in live cells are LDs [5]. For that reason, THG microscopy is especially appropriate method for LD imaging from live unfixed cells, without the need for additional labeling.

The biological effects (on the lipid droplet density and size distribution) of exposure to 1mM selenite were monitored *in vivo* on the cells of filamentous fungi in liquid culture. Filamentous fungi are one of the main pathways for selenium entrance into ecosystems and able to concentrate selenium in the mycelia [6]. Additionally, fungi are simple to manipulate, unicellular model system, that is naturally without selenoproteins encoded in genome [7]. Therefore, in fungi the prooxidative effects of selenium can be observed unhindered with simultaneous beneficial selenium-mediated effects.

2. Materials and Methods

Model organism was unicellular wild-type strain of the oleaginous filamentous fungus *Phycomyces blakesleeanus* (Burgeff 1925) (NRRL 1555(−)), grown in lighted stationary plates from the spore stock as previously described [8]. To observe the effect of treatment with 1mM sodium selenite, the prepared fungi activated spore culture volume was divided to control culture and treatment culture (same as control, with addition of sodium selenite in final concentration 1mM). The experiments were performed in triplicate.

As a method of choice for label free *in vivo* LD measurements, the application of THG microscopy was employed: 1040 nm, 200 fs pulses from Yb KGW laser were used; THG signal was detected by PMT in the transmission arm after passing through the Hoya glass UV filter with the peak at 340 nm. The obtained images were analyzed in ImageJ to quantify LDs number and size. The results are reported as mean ± Standard error (SE) and statistically tested by student t-test with 95% confidence level.

3. Results and Discussion

In THG images obtained from control and selenite (Se^{+4})-treated hyphae, LDs can be readily observed (Figure 1a).
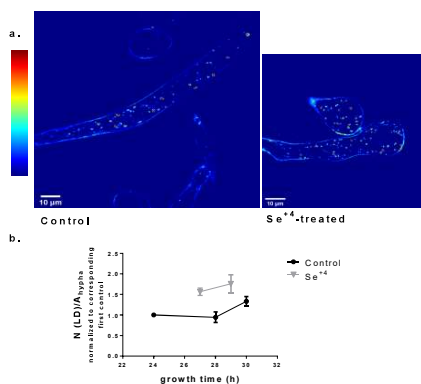

Figure 1. a.) THG images of: Control (28h), in the left panel; Se^{+4}–treated hypha (26h) in the right panel. Calibration bar is shown on the left (bottom: minimal; top: maximal intensity). Brightest spots represent LDs, and the faint cell wall THG signal can be seen as well. The increased LD density in treated group is visible. b.) LD density (LD number per unitary hypha area) was normalized for each independent experiment (n=3) to the LD

density value of the first control (24h) and plotted as a function of growth time. Control: black circles; Se^{+4}–treated: gray triangles.

From THG images of control and Se^{+4}–treated hyphae, LD number (Figure 1b) and size were measured (Figure 2). Fig. 1b. graph shows that average LD density increased by more than 60% in Se^{+4}-treated hyphae, compared to control. LD density was calculated as: (LD number in the hypha) / (Area of that hypha (μm^2)). Trend for slight increase of LD density in oldest controls is also evident, although it is less pronounced than in treated group ($33 \pm 16\%$ increase in aged controls vs. $88 \pm 26\%$ in aged Se^{+4}-treated). Average LD size was unchanged (Fig.2b.), not supporting the expectation that the stress induces generation of new LDs. Distribution of LD sizes on the other hand, shows that Se^{+4}–treated LDs are more frequently small (around 1 μm) compared to LDs in controls. In addition, LD distribution in controls, but not in treated group, always had a "right side shoulder"-telltale sign that the separate population of LDs with diameters larger than group average is present. Same finding is more clearly seen in Fig 2c. graph, where the obtained parameters of Gauss function fits to the distribution of LD diameters are shown.
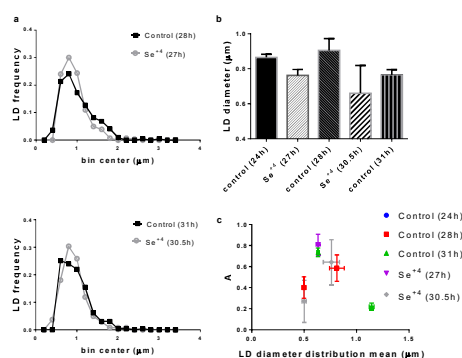

Figure 2. Size of LDs in the control and the Se^{+4}-treated group. a.) Distributions of LD size for the Se^{+4}-treated and for the age closest control. Top: 27 h treatment / 28 h control. Bottom: 30.5 h treatment / 31 h control. b.) Mean $\pm$ SD diameters of LDs in all groups (n = 200 - 400 LDs for each group). c.) Obtained parameters of the Gauss fit to LD size distribution. A - frequency of the component fitted. Some group distributions could be fitted with one normal distribution, but most often, two components were present.

LDs in the model fungus *Phycomyces blakesleeanus* are very small (mean diameters in all groups are less than 1 μm), while the resolution limit of the images presented is at around 0.4 μm. Smaller than average LDs were barely above the limit. Therefore, the close proximity to resolution limit is probably the cause for our inability to reliably detect the Se^{+4}–induced generation of the smallest LDs and subsequent lowering of the mean diameter.

3. Conclusions

We were able to measure shift of the distribution of sizes, and the increase of the number of LDs induced by 1 mM selenite treatment. THG modality of NLSM enabled *in vivo* and label free physiological study that provided data in support of the hypothesis presented. Based on our data, it can be concluded that selenite induces cellular stress leading to autophagy and subsequent LD formation.

References

[1] C.M. Weekley, H.H. Harris, *Which form is that? The importance of selenium speciation and metabolism in the prevention and treatment of disease*. Chemical Society Reviews, 42 (2013) 8870 – 8894.

[2] J.E. Spallholz, V.P. Palace, T.W. Reid, *Methioninase and selenomethionine but not Se-methylselenocysteine generate methylselenol and superoxide in an in vitro chemiluminescent assay:*

implications for the nutritional carcinostatic activity of selenoamino acids, Biochemical pharmacology, 67 (2004) 547-54.

[3] G. Filomeni, D. De Zio, F. Cecconi, *Oxidative stress and autophagy: the clash between damage and metabolic needs.* Cell death and differentiation, 22 (2015) 377-88.

[4] T.B. Nguyen, J.A. Olzmann, *Lipid droplets and lipotoxicity during autophagy*. Autophagy, 13 (2017) 2002-2003.

[5] T. Watanabe, A. Thayil, A. Jesacher, K. Grieve, D. Debarre, T. Wilson, M. Booth, S. Srinivas, *Characterisation of the dynamic behaviour of lipid droplets in the early mouse embryo using adaptive harmonic generation microscopy*, BMC Cell Biology, 11 (2010) 38.

[6] J. Falandysz, *Selenium in edible mushrooms*, Journal of Environmental Science and Health. Part C, Environmental Carcinogenesis & Ecotoxicology Reviews, 26 (2008) 256-99.

[7] M. Mariotti, G. Salinas, T. Gabaldón, V.N. Gladyshev, *Utilization of selenocysteine in early-branching fungal phyla*, Nature Microbiology, 4 (2019) 759-765.

[8] M. Stanić, J. Zakrzewska, M. Hadžibrahimović, M. Zižić, Z. Marković, Z. Vučinić, M. Zivić, *Oxygen regulation of alternative respiration in fungus Phycomyces blakesleeanus: connection with phosphate metabolism*. Research in Microbiology, 164 (2013) 770-8.

THE INFLUENCE OF SELENITE ON FILLAMENTOUS FUNGI HYPHA MORPHOMETRY PARAMETERS

Tanja Pajic[1], Natasa Todorovic[2], Dunja Stefanovic[1], Mihailo D. Rabasovic[3], Aleksandar Krmpot[3], Miroslav Zivic[1,*]

[1] Faculty of Biology, University of Belgrade, Studentski trg 16, 11158 Belgrade, Serbia
e-mail: tpajic@bio.bg.ac.rs
[2] Institute for Biological Research "Sinisa Stankovic", University of Belgrade, Institute of National Importance for the Republic of Serbia, Bulevar Despota Stefana 142, 11000 Belgrade, Serbia
[3] Institute of Physics Belgrade, University of Belgrade, Pregrevica 118,11000 Belgrade, Serbia
e-mail: nara@ibiss.bg.ac.rs, rabasovic@ipb.ac.rs , krmpot@ipb.ac.rs, mzivic@bio.bg.ac.rs

Abstract

Selenium salts have been known for long time to have a potential for both beneficial and harmful effects on living organisms. It is present in the environment, where it can be readily assimilated by plants and fungi, thus entering the food chain. We investigated the cell growth dynamics in the presence of selenite which is considered to have more toxic potential than selenate. The effects of selenite (1 mM) on the growth of fungi from the activated spores to the end of the exponential growth were measured on several hypha morphological parameters by microscopy *in vivo*. *Phycomyces blaekesleneeanus* was used as model filamentous fungus. The most striking effect of Se^{+4} treatment was inhibition of hypha growth, resulting in more than four times shorter hypha in Se^{+4} –treatment group than in the control (200 ± 50 μm, n = 50 vs 900 ± 100 μm, n = 40 respectively) at the end of exponential growth period under controlled conditions. The Se^{+4} effect was an inhibition and not a simple delay in growth, as hypha length did not change significantly from 27th to 30th hour of culture in Se^{+4}-treatment group. Since the microscopy was performed on live cultured cells, undisturbed cytoplasmic streaming was observed, confirming that hyphae were alive at all time points measured. 30h old spore diameters were also significantly reduced by Se^{+4} treatment (p = 0.0365), while hypha diameters were not significantly altered.

Keywords: growth inhibition, *Phycomyces blakesleeanus*, live microscopy

1. Introduction

Selenium salts have been known for long time to have a potential for both beneficial and harmful effects on living organisms. Selenium is essential to many organisms, including some archaea, bacteria, protozoans, green algae and animals. It is present in the environment, where it can be readily assimilated by plants and fungi, thus entering the food chain. The narrow gap between necessary and toxic doses of Se [1], warrants the need for better understanding of the effects of Se salts on living organisms. Fungi are one of the main pathways for Se entrance into ecosystems, due to their intensive exchange with the extracellular milieu and very large surface to volume ratio. Se can be concentrated in their mycelia [2] or fungi can mediate Se concentration from the soil by stimulating its absorption by plant roots as mycorrhizal symbionts [3]. Moreover, fungi are, with rare exceptions, the only kingdom of life entirely devoid of genome encoded selenoproteins which are the basis of selenium beneficial effects in the organisms that do possess the machinery to synthesize them [4]. Therefore, filamentous fungi could be a very useful model system for research on harmful selenium effects.

We investigated the filamentous fungi cell growth dynamics in the presence of selenite. The effects

of selenite (1 mM) on the growth of fungi from the activated spores to the end of the exponential growth phase were measured on several hypha morphological parameters by microscopy *in vivo*. *Phycomyces blakesleeanus* was used as well-defined model for filamentous fungus with rapid growth, since it finishes the exponential growth stage by the 30th hour of culture in control conditions.

2. Material and Methods

The model organism was unicellular wild-type strain of the filamentous fungus *Phycomyces blakesleeanus* (Burgeff) (NRRL 1555(−)), grown in lighted stationary plates from the spore stock as previously described [5]. To observe the effect of treatment with 1 mM sodium selenite, the prepared fungi activated spore culture volume was divided into control culture and a treatment culture (same as control, with addition of sodium selenite in final concentration 1 mM). Live fungi were imaged unstained on the conventional bright field upright microscope, in six randomly chosen fields of view. The morphometric traits were quantified from obtained images using ImageJ software. The data are presented as mean ± SE, and the differences were tested by student t-test at a 95% confidence level. Correlation matrix Principal component analysis (PCA) was done in XLSTAT.

3. Results and Discussion

Morphometric analysis was based on the data extracted from the images like the one in Figure 1. There are numerous small bright and dark structures which were continuously in motion. This feature which was observed in all groups at all growth times imaged. Vigorous movement of cytoplasm and organelles, cytoplasmic streaming, is characteristic for all large cells and is a marker of viability, since in the conditions of ATP depletion the streaming stops.
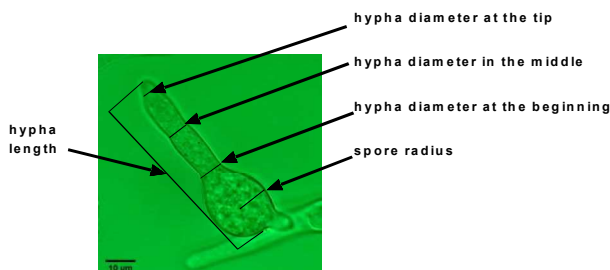

Figure 1. Representative brightfield image used for extraction of morphometric data. Hypha on the picture is from Se^{+4} treated culture (27 h old). The main features measured are marked with hair lines. The inherent variability of the fungi cultures that might obscure some differences between groups was controlled by growing all cultures to be compared from the same initial batch culture, by randomization of the samples and by a large number of hyphae analyzed (n_{total} = 255).

The most striking effect of Se^{+4} treatment was inhibition of hypha growth, with more than four times shorter hyphae in the Se^{+4} –treatment group than in the control (200 ± 50 µm, n = 50 *vs.* 900 ± 100 µm, n = 40 respectively) after 30 h of the beginning of the growth, which corresponded to the end of exponential growth in control conditions (Figure 2A., left panel).
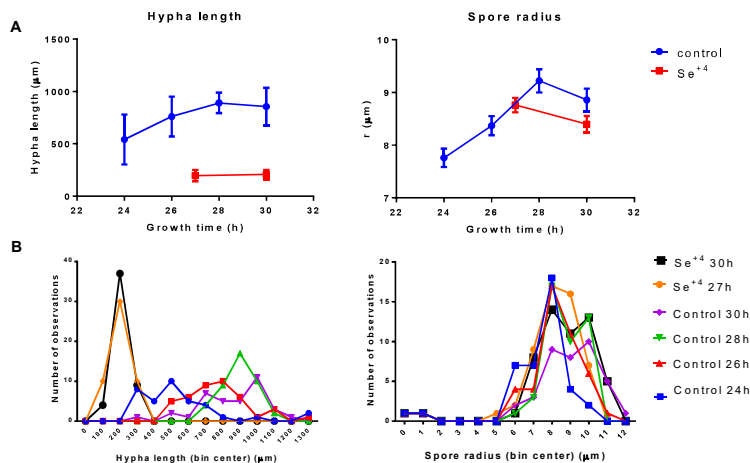
Figure 2. The effect of Se^{+4} on the most prominent hypha morphometric traits, hypha length and the size of the remaining spore "head" of the hypha. A. The hypha length (left panel) and spore radius (right panel) obtained for control and Se^{+4}–treatment group vs. time of growth. The data for Se^{+4}–treated fungi earlier than 27 h is lacking, because at that times the growing hyphae were very scarce. B. Histograms showing the distribution of all values obtained for hypha length (left panel) and spore radius (left panel).

Because hypha length did not increase significantly between 27 and 30 hour of culture in the Se^{+4}– treatment group (Figure 2A left), it seems that the Se^{+4} -mediated effect is an inhibition, and not a simple delay in growth followed by the unchanged speed of growth at later times. Undisturbed cytoplasmic streaming confirmed that hyphae were alive at all time points measured.

From distribution of lengths (Figure 2B left), it can be seen that in control group, "the spread" of the lengths distribution is very wide. In contrast, the Se^{+4} -treated hyphae are less diverse, and seem to be synchronized in growth. Spore size was slightly decreased by the Se^{+4} -treatment but values had similar distributions to controls (Figure 2B right panel). The statistical significance of spore radius decrease was reached with the 30 h old spores (p = 0.0365) (Figure 2A, right panel).

The diameters of the specific hypha regions, were not significantly changed by Se^{+4} -treatment (Figure 3A). The spore circumference was measured independently from radius, in case any deviations in shape are found. This parameter was deemed not useful, since it was not sensitive to any perturbation tested (data not shown).

In correlation matrix principal component analysis we used just three non-correlated variables: the hypha diameter at the middle, the hypha diameter at the tip and the spore circumference out of 6 measured. Scree plot showed that first three axes described entire variability and therefore they are retained for presentation. The 3-axis plot shows that the Se^{+4}-treated groups lump together on the opposite side of middle hypha diameter, meaning that it is negatively correlated with the Se^{+4}-treatment. Based on the result of PCA, new variable is defined, the ratio of middle to tip width (Figure 3C). New variable showed that changes in hypha width ratio are significant after Se^{+4} treatment (at 30 h, p< 0.0001), and that during growth in control conditions, the hypha width ratio gradually declines in the period of intensive elongation (until 28 h, as can be seen at Figure 2A). At the 30 h point, an abrupt increase in the ratio is evident.
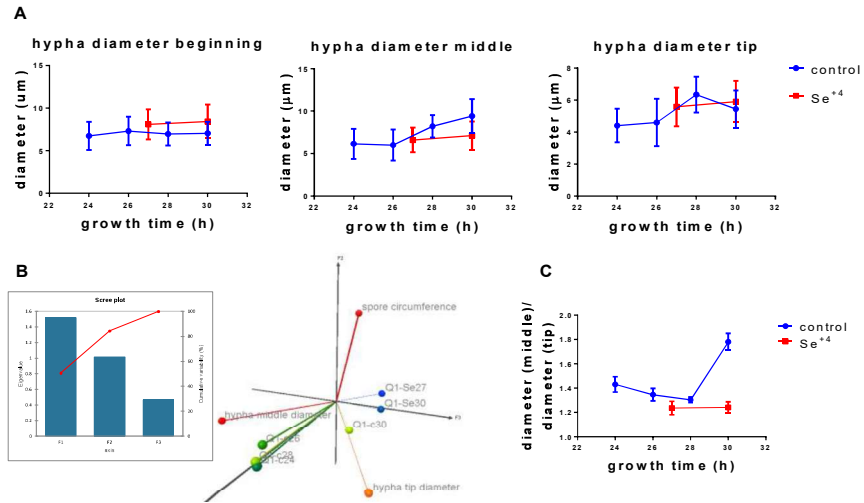
Figure 3. A. Diameters of hyphae measured (beginning, middle, tip) were seemingly unchanged by Se^{+4}.
B. Principal Component Analysis (PCA) biplot. Se^{+4}-treated groups: blue symbols; Control groups: green symbols. On the left side, the Scree plot shows variability % explained by F1, F2 and F3. C. Newly generated compound parameter, the ratio of hypha diameter at the middle to hypha diameter at the tip, calculated for each measured hypha individually, plotted against growth time.

3. Conclusions

Hypha morphology can provide a range of useful information if randomly sampled from sister cultures (treatment and matched control), despite the notorious intragroup variability of hypha cultures. Selenite in concentration of 1 mM acted as an inhibitor of hypha elongation. Although diameters of hypha measured (beginning, middle, tip) were seemingly unchanged by Se^{+4}, PCA showed that that is not the case with hypha middle parameter which was negatively correlated with the Se^{+4}-treated groups. Based on the result of PCA, new variable is defined, the ratio of middle to tip width, that seems to be more informative about hypha physiology.

References

[1] S.A.Z. Ibrahim, A. Kerkadi, A. Agouni., *Selenium and Health: An Update on the Situation in the Middle East and North Africa*, Nutrients, 11 (2019) 1457.
[2] J. Falandysz., *Selenium in edible mushrooms*, Journal of Environmental Science and Health. Part C, Environmental Carcinogenesis & Ecotoxicology Reviews, 26 (2008) 256-99.
[3] Y. Yu, S. Zhang, B. Wen, H. Huang, L. Luo., *Accumulation and speciation of selenium in plants as affected by arbuscular mycorrhizal fungus Glomus mosseae*, Biological Trace Element Research, 143 (2011) 1789-98.
[4] M. Mariotti, G. Salinas, T. Gabaldón, V.N. Gladyshev., *Utilization of selenocysteine in early-branching fungal phyla*. Nature Microbiology, 4 (2019) 759-765.
[5] M. Stanić, J. Zakrzewska, M. Hadžibrahimović, M. Zižić, Z. Marković, Z. Vučinić, M. Zivić., *Oxygen regulation of alternative respiration in fungus Phycomyces blakesleeanus: connection with phosphate metabolism*. Research in Microbiology, 164 (2013) 770-8.

One-step synthesis of NIR-responsive NaYF$_4$:Yb,Er@Chitosane nanoparticles for biomedical application

I. Dinic[1], A. Djukic-Vukovic[2], L. Mojovic[2], M.G. Nikolic[3], M.D. Rabasovic[3],
A.J. Krmpot[3], O. Milosevic[1] and L. Mancic[1]

[1]Institute of Technical Sciences of SASA, Belgrade, Serbia
[2]Department of Biochemical Engineering and Biotechnology
Faculty of Technology and Metallurgy, University of Belgrade, Serbia
[3]Photonic Center, Institute of Physics Belgrade, University of Belgrade, Zemun, Belgrade, Serbia
e-mail: lidija.mancic@itn.sanu.ac..rs

There is a great technological interest in synthesis of lanthanide doped upconverting nanoparticles with specific morphological characteristics and efficient luminescence response suitable for biomedical use [1]. A conventional approach for generation of such particles comprises decomposition of organometallic compoundsin an oxygen-free environment and additional ligand exchange [2,3]. The biocompatible and water soluble NaYF$_4$:Yb,Er@Chitosane particles used in this study were synthesized through facile one-pot hydrothermal synthesis and were characterized using X-ray powder diffraction (XRPD), Fourier-transform infrared (FTIR) spectroscopy, field emission scanning and transmission electron microscopy (FESEM and TEM) and photoluminesce measurement (PL). Due to the presence of the amino groups at their surface these particles exhibit excellent hydrophilic properties and low cytotoxicity against human gingival fibroblasts (HGF), which was proven by MTT assay. Furthermore, upon 980 nm laser irradiation the as-prepared particles were successfully used for *in-vitro* visualization of the primary cell cultures of head and neck squamous carcinoma cells (HNSCC). In a NaYF4:Yb,Er phase upconversion is enabled by the sequential absorption of two or more near-infrared photons by Yb^{3+} and subsequent energy transfer to the long-lived metastable electron states of Er^{3+} which produces luminescence emission at visible spectra after relaxation.

REFERENCES
[1] C. Chen, C. Li, Z. Shi, Adv.Sci.1600029 (2016).
[2] H.X. Mai, Y.W. Zhang, R. Si, Z.G. Yan, L.S. Sun, L.P. You, C.H. Yan, J. Am. Chem. Soc., 128, 6426 (2006).
[3] Y. Wei, F.Q. Lu, X.R. Zhang, D.P. Chen, Chem. Mater., 18, 5733 (2006).

Luminescence thermometry using $Gd_2Zr_2O_7$:Eu^{3+}

M.G. Nikolic[1], M.S. Rabasovic[1], J. Krizan[2], S. Savic-Sevic[1], M.D. Rabasovic[1], B.P. Marinkovic[1], A. Vlasic[1]
and D. Sevic[1]

[1] *Institute of Physics,Belgrade, Serbia*
[2] *AMI d.o.o., Ptuj, Slovenia*
e-mail:sevic@ipb.ac.rs

Thermographic phosphors are materials that are synthesized in such a way that their structural stability regarding various parameters including the temperature, pressure, magnetic field, electromagnetic radiation could be obtained. They typically consist of a ceramic host and rare-earth dopant. These materials are widely used in many applications [1-9]. The temperature dependency of their luminescence is used for temperature sensing.

In this study we investigate temperature dependence of luminescence spectra of nanopowder samples of $Gd_2Zr_2O_7$:Eu^{3+}. Europium doped $Gd_2Zr_2O_7$ nanopowders were prepared by Solution Combustion Synthesis (SCS) method [10]. The structural characteristics of obtained material were confirmed by SEM images and XRD analysis [10]. The identification and time resolved analysis of fast decayed (from $^5D_1$ state) and slow decayed (from $^5D_0$ state) europium lines in this host were performed using TR-LIF (Time resolved Laser induced Fluorescence) spectroscopy experimental setup. The setup consist of tunable OPO (Optical Parametric Oscillator) laser and streak camera, explained in more detail in [11].

The photoluminescence spectra used for analysis of $Gd_2Zr_2O_7$:Eu^{3+} nano phosphor optical emission temperature dependence were acquired using continuous laser diode excitation at 405 nm and Ocean Optics spectrometer USB2000. We plotted the temperature sensing calibration curves based on various combinations of ratio of intensities of two europium optical emission lines. It seems that any combination of one slow decayed and one fast decayed line could be an optimal choice for temperature measurements. Finally, we concluded that the intensity ratio of spectral lines at 613 nm and 539 nm seems to be a good choice for temperature measurements. Our results show that the synthesized material can be efficiently used as thermographic phosphor up to 700 K.

REFERENCES
[1] M. Aldén, A. Omrane, M. Richter, G. Särner, 37, **422** (2011).
[2] S. W. Allison., G. T. Gillies, Rev. Sci. Instrum, 68, 2615 (1997).
[3] L.P. Goss, A.A. Smith, M.E. Post, Rev Sci. Instrum, 60, 370 (1989).
[4] J.P. Feist, A.L. Heyes, K.L. Choy, B. Su, Proceedings of IEEE; 6.1 (1999).
[5] A.L. Heyes, Journal of Luminescence, 129, 2004 (2009).
[6]M.M. Gentleman, D.R. Clarke, Surface & Coatings Technology, 93, 188 (2004).
[7] A. H. Khalid, K. Kontis, Sensors, 8, 5673 (2008).
[8] M R. Cates, S. W. Allison, S. L. Jaiswal, D. L. Beshears, Oak Ridge National Laboratory, Report ORNL/TM-2002/71
[9] J.I. Eldridge, T.P. Jenkins, S.W. Allison, D. E. Wolfe, E. H. Jordan, Development of YAG:Dy Thermographic Phosphor Coatings for Turbine Engine Applications, 58h International Instrumentation Symposium San Diego, CA, June 5-8, (2012).
[10] M.S. Rabasovic, D. Sevic, J. Krizan, M. Terzic, J. Mozina, B.P. Marinkovic, S. Savic-Sevic,
M. Mitric, M.D. Rabasovic, N. Romcevic, Journal of Alloys and Compounds, 622, 292 (2015).
[11] M.S. Rabasovic, D. Sevic, M. Terzic, and B.P. Marinkovic, Nucl. Inst. Meth. B.279, 16(2012).

Study on relationship between amyloid-β peptides and metal ions *via* two-photon excitation fluorescence microscopy

S. Jovanic[1], N. Loncarevic[2], M. Rabasovic[1], A. Krmpot[1], M. Jovic[2], S. Kanazir[2], and B. Jelenkovic[1]

[1]*Photonic centre, Institute of Physics,*
Belgrade, Serbia
[2]*Institute for Biological Research "SinišaStanković",*
University of Belgrade, Serbia
e-mail:sjovanic@ipb.ac.rs

We developed home-builtnonlinear laser scanning microscopy [1] which was used for the investigation of amyloid β(Aβ) peptide aggregation process in the presence of metal ions. Aβcascade aggregation process is one of the most studied hypothesis about causes of Alzheimer's disease (AD). AD is a progressive brain disorder that is the most prevalent cause of dementia in the elderly population and the third leading cause of death in developed countries. Factors that are believed to affect Aβ fibrillization*in vivo* include metal ions such as Cu(II) and Zn(II)[2].

Main technique in this research is most well known variation of nonlinear microscopy, two-photon excitation fluorescence microscopy (TPEF). Samples are originated from blood serums 4th to 12th months old AD mouse model system. Autofluorescence signal was obtained for the determination of Aβ level byTPEFmicroscopy. Absolute concentration of Cu(II) and Zn(II) ionswas measured by mass spectrometry. From this data we will be able to determine correlation level between Aβ level and metal ions concentration. Another approach to study relationship between Aβ development into mature fibrils and metal ionsconcentration was on *ex vivo* AD mousebrain slices. During defined time stages of Aβdevelopment each brain slicewastreated whit Cu(II) and Zn(II) ions and imaged *via* TPEF microscopy.

Accurate results on blood serums have potential to include this AD biomarker in standard diagnostic procedures. In general, our findings can be of the importance for novel treatments whit metal ions in AD.

REFERENCE
[1] M. D. Rabasovic ́ et al., J. Biomed. Opt. 20(1), 016010 (2015).
[2] D. J Selkoe and J. Hardy, EMBO Mol. Med. 8(6), 595-608 (2016).

Two-photon excited hemoglobin fluorescence for *ex vivo* microscopy analysis of erythrocytes at single cell level

I. T. Drvenica[1], A. Stančić[1], S. Jovanić[2], V. Lj. Ilić[1], M. D. Rabasović[2], D. V. Pantelić[2], B. M. Jelenković[2], B.M. Bugarski[3], A. J. Krmpot[2]

[1]*Institute for Medical Research, University of Belgrade, Dr Subotića 4, 11 129 Belgrade, Serbia*
[2]*Institute of Physics Belgrade, University of Belgrade, Pregrevica 118, 11 080 Belgrade, Serbia*
[3]*Department of Chemical Engineering, Faculty of Technology and Metallurgy, University of Belgrade, Karnegijeva 4, 11 000 Belgrade, Serbia*
e-mail:ivana.drvenica@imi.bg.ac.rs

Fluorescence of hemoglobin, the main intracellular component of erythrocytes, upon excitation by ultra-short pulses in red and near infrared region [1-3], allows two-photon excited fluorescence (TPEF) microscopy to be used as a tool for label-free imaging of these cells, even *in vivo* [4]. Despite wide applicability of erythrocytes in diagnostic tests, and distribution of hemoglobin as a marker of their functional status under physiological or pathological conditions [5], data on spatial distribution of hemoglobin at the single cell level are scarce.

Based on findings reported by Zheng and co-workers [1], we have utilized TPEF microscopy to map the spatial distribution of hemoglobin in porcine erythrocytes *ex vivo*. Porcine erythrocytes were used as extremely susceptible cells to stress and thus represent a good model system to study influence of different factors (heat, humidity, malnutrition, infections…) on erythrocyte morphology and hemoglobin distribution. The custom made experimental set up for NLSM utilized the train of the femtosecond pulses from Ti:Sapphire laser (Coherent, Mira 900-F) at 730 nm. The repetition rate was 76MHz, and pulse duration was 160fs.

The results demonstrate that the resolution of the TPEF microscopy is good enough for the analysis of erythrocytes at single cell level. Two different morphological types of porcine erythrocytes, normocytes and echinocytes, collected during mild autumn and extremely hot summer, respectively, were clearly differed by TPEF microscopy. Besides, erythrocytes having intermediate morphology i.e. having some characteristics of both abovementioned morphological extremes were also found. The distribution of hemoglobin in erythrocytes noticeably followed the cells' shape, where erythrocytes with altered morphology demonstrated significant accumulation of hemoglobin in cells' protrusions. During TPEF microscopy experiments fluorescence emission from the exposed cells increased, but longer exposure led to irreversible change of erythrocytes, as already shown in literature [3]. Since functional status of erythrocytes *in vivo* (both in physiological or pathological states) and *ex vivo* (e.g. transfusion bag) [3] is accompanied with change of morphology and consequently altered distribution and functionality of hemoglobin, result of this study even though obtained on animal cell model, confirmed strong potential of TPEF microscopy for such application in biomedical research. However, *in vivo* tests by TPEF microscopy merit further experimental optimization.

REFERENCES
[1] W. Zheng, D. Li, Y. Zeng, Y. Luo, J. Y. Qu, Biomed. Opt. Express. 2, 71 (2010).
[2] G. O. Clay, C. B. Chaffer, D. Kleinfeld, J. ChemPhys. 126, 025102 (2007).
[3] I. Saytashev, R. Glenn, G.M. Murashova, S.Osseiran, D. Spence, C. L. Evans, M. Dantus, Biomed. Opt. Express. 7, 3449 (2016).
[4] D. Li, W. Zheng, W. Zhang, S. K. Teh, Y. Zeng, Y. Luo, J. Y. Qu, Opt. Lett. 36, 2638 (2011).
[5] V. V. Revin, et al. BioMed. Res. Int. 973973 (2015).

Phycomyces blakesleeanus hypha cell wall surgery by Ti:Sapphire laser

T.Pajic[1], K.Stevanovic[2], N. Todorovic[3], A. Krmpot[4], M. Rabasovic[4], V. Lazovic [4], D. Pantelic[4], B. Jelenkovic[4] and M. Zivic[2]

[1] *University of Belgrade, Serbia*
[2] *University of Belgrade - Faculty of Biology, Serbia*
[3] *Institute for Biological Research, University of Belgrade, Serbia*
[4] *Institute of Physics,University of Belgrade, Serbia*
e-mail: tanjapajic4@gmail.com

The ion channels on the membrane of filamentous fungi remain uninvestigated to this day due to their inaccessibility to patch-clamp pipette, brought about by sturdy cell wall. Small number of described channels is from very specific types of cells (wall less mutants or sporangiophore aerial cell membrane). The enzymatic approaches of cell wall removal, albeit successful on plant cells, failed when applied to fungi. In order to obtain clean "patchable" membrane from any type of filamentous fungal cell we undertook a task of finding the conditions for cut of the small part of the hyphal wall by laser surgery on the model filamentous fungus organism, *Phycomyces blakesleeanus*. The successful wall surgery should result in exposure of large enough portion of cell membrane with a minimal damage to the protoplast. Therefore, we performed series of experiments with cell plasmolisys in hypoosmotic media and subsequent deplasmolisys, to determine the conditions for reliable retraction of cytoplasm that could be reversed. Next, hyphae, grown on glass coverslips coated with collagen, were plasmolysed and mounted on the stage of the homemade nonlinear laser scanning microscope for imaging and cell surgery [1]. The Ti:Sapphire laser (Coherent, Mira 900-F) has been used as a light source in the microscope. It has operated at 730nm. This wavelength enables two photon excitation of auto-fluorescence in cytoplasm, as well as dye (Calcofluor white), visualizing fungi wall. We have used Carl Zeiss, EC Plan-NEOFLUAR, 40×1.3 oil immersion objective for focusing of the laser beam and collection of fluorescence. A visible interference filter (415nm - 685 nm) in front of detector has been used to remove scattered laser light. The successful cutting of cell wall could be achieved within the range of laser intensities and cutting speeds (dwell times). Throughout the experiment, fungi were kept in azide or Brefeldin A in order to block the process of depositing the new wall material. Afterwards, hyphae were slowly deplasmolysed to induce exit of a portion of the protoplast through the laser-cut hole in the cell wall. However, in some instances, the part of the protoplast bulged through the hole immediately after cell surgery, while the cell was still in hypertonic solution. In other instances, the cytoplasm remained away from the cut hyphal apex even through series of slow incrementing hypotonic solutions. Finally, when laser cutting was applied on the side of the cell only, as to cut a small hole, the successful exit of a portion of protoplast through the hole during deplasmolisys could be reliably achieved.

REFERENCES

[1] Mihailo D. Rabasović, et al, J *Biomed Opt* 20 016010 (2015).

Nonlinear microscopy as a novel method for studying insect morphology

D. Pavlović[1], D. Pantelić[1], A. Krmpot[1], M. Rabasović[1], V. Lazović[1], M. Vrbica[2], S. Ćurčić[2]
[1]Institute of Physics, University of Belgrade, Serbia
[2]Institute of Zoology, University of Belgrade – Faculty of Biology, Serbia
e-mail: danica.pavlovic@ipb.ac.rs

Insects are the most numerous group of animals on the Earth, with more than a million described species and the total number of species estimated to be six to ten millions [1]. Insect taxonomists face difficult tasks of describing, classifying and identifying vast numbers of entirely new or little-known species. Most common classification of insects is based on morphological characteristics of adults. The mouthparts, wing venation, surface cuticular structure or even internal organs, such as different glands and reproductive organs could have each a high taxonomic value. These structures can be seen in most cases only under high-resolution microscope.

Fluorescence of chitin, as the most abundant component of insect integument, makes nonlinear microscopy (NLM) useful imaging technique in entomology. This is a novel technique [2, 3], with several advantages compared to classical or confocal microscopy. Namely, there is no need for staining or tissue clearing, penetration depth is large and photo-damage reduced [3]. Here we present a part of our morphological study of several insect species, inhabiting Serbia. Detailed images of the mouthparts, head, abdominal segments and genitalia were recorded by NLM using two-photon excited fluorescence (TPEF). All important taxonomic characters, such as number and position of certain setae, sub-micron structure of cuticle, shape of copulatory organs can be analyzed, performed measurements calculated quantitatively and further used in morphometrics, thus helping in taxa identification and taxonomy.

REFERENCES
[1] P. W. Price et al., Cambridge University Press. (2011).
[2] C. H. Chien et al., Journal of Biomedical Optics, 16(1), (2011).
[3] M. Rabasović et al., Journal of Biomedical Optics, 20(1), (2015).

Analysis of human healthy dentin microstructure by using two photon excitation fluorescence microscopy and second harmonic generation

Tijana Lainović[1], Mihailo Rabasović[2], Larisa Blažić[1,3], Dejan Pantelić[2],
Aleksandar Krmpot[2], Vladimir Lazović[2], Branislav Jelenković[2]
[1]*Faculty of Medicine, School of Dentistry, University of Novi Sad,Novi Sad, Serbia*
[2]*Institute of Physics,University of Belgrade,Belgrade, Serbia*
[3]*Clinic of Dentistry of Vojvodina,Novi Sad, Serbia*
e-mail:tijana.lainovic@gmail.com

Human dentin is an organized hard, mineralized tissue of a tooth, composed of 70 wt% calcified tissue (hydroxyapatite), 20 wt% the organic phase (mostly composed of collagen type 1 and the other fibrils, glycosaminoglycans and proteoglycans), and 10 wt% water [1]. Dentin has a specific tubular structure containing tubules, peritubular and intertubular parts, biologically arranged to meet the specificmechanical, nutritional, sensory and reparative needs of a tooth [2].

The aim of this study was to analyze the microstructure of human dentin with the advanced microscopy tools, in order to get better insight into the architecture of healthy dentin.

The healthy premolar teeth were extracted for the orthodontic reasons, and collected in accordance with the ethical requirements for ex-vivo investigations, which was approved by the Ethical Committee of the Clinic of Dentistry of Vojvodina. The teeth were cleaned, and kept in 0.5 % Chloramine solution until the examination. The slices of teeth were prepared using a hard tissues microtome. The images of dentinal microstructures were obtained by the homemade nonlinear microscopy setup [3]. Ti-sapphire laser, adjusted at 730 nm wavelength, was used as an excitation source for two-photon excitation fluorescence (TPEF), while 840 nm excitation was used for the second harmonic generation (SHG).

The dentinal tubular, peritubular and intertubular structures were clearly presented. Natural human dentin enables the label-free and fixation-free visualization of its architectural content by the TPEF microscopy, owing to its intrinsic autofluorescence. The SHG can be detected due to the presence of collagen type I in dentin, which is a triple helical molecule, assembled in organized, non-centrosymmetric directional fibrils [4].

Images of healthy dentin could serve as a reference point for comparison and investigation of internal structural changes in dentin, affected by caries or non-caries lesions, or changed after the use of various restorative materials and procedures.

REFERENCES
[1] M. Goldberg, A.B. Kulkarni, M. Young, A. Boskey, Front. Biosci. (Elite Ed). 3, 711 (2011).
[2] S.R. Stock, A.C. Deymier-Black, A. Veis, A. Telser, E. Lux, Z. Cai, Acta Biomater. 10, 3969 (2014).
[3] K. Bukara, S. Jovanić, I.T. Drvenica, A. Stančić, V. Ilić, M.D. Rabasović, D. Pantelić, B. Jelenković, B. Bugarski, A.J. Krmpot, J Biomed Opt 22, 026003 (2017).
[4] R. Elbaum, E. Tal, A.I. Perets, D. Oron, D. Ziskind, Y. Silberberg, H.D. Wagner, J. Dent. 35, 150 (2007).

Second harmonic generation imaging of collagen fibers in the uninvolved human rectal mucosa 10 cm and 20 cm away from the malignant tumor

Sanja Despotović[1], Ivana Lalić[1], Novica Milićević[1], Živana Milićević[1],Mihailo Rabasović[2], Dejan Pantelić[2], Svetlana Jovanić[2] and Aleksandar Krmpot[2]

[1]*Institute of Histology and embryology, Medical faculty, Unicersity of Belgrade, Serbia*
[2]*Institute of Physics Belgrade, University of Belgrade, Serbia*
e-mail:sanjadesp@med.bg.ac.rs

The aim of our study was to investigate the organization of collagen fibers utilizing second harmonic generation (SHG) microscopy in the lamina propria of the rectal mucosa in the remote surrounding of the malignant tumor. We demonstrated the structural alterations (reduced cellularity, alterations of Liberkühn crypts and tissue edema) of the lamina propria of the mucosa 10 cm and 20 cm away from the rectal adenocarcinoma. Our study also provided indications that the collagen fibers in the rectal lamina propria could be affected [1].

Tissue samples were endoscopically collected from 30 patients with adenocarcionoma located in the sigmoid colon. The biopsies were taken 10 cm and 20 cm away from the malignant tumor in the caudal direction. The samples of rectal mucosa collected at the same institution from 30 healthy persons with a family history of intestinal malignancy, were used as control.

Masson trichrome staining on formalin-fixed, paraffin-ebbedded tissue was used to visualize collagen fibers. Also, to exclude the possibility that the observed changes could be due to methodology used (fixation or staining), an original labframe nonlinear laser scanning microscope (NLM) [2] was used for SHG imaging of collagen distribution on fixation- and label-free colon tissue samples. The incoming infrared femtosecond pulses from the tunable mode-locked Ti:Sapphire laser (Coherent, Mira 900) were directed onto the sample by a dichroic mirror through the Zeiss EC Plan- Neofluar40x/1.3 NA oil imersion objective. The laser wavelenght was 840nm, and the SHG was selected by narrow bandpass filter at 420 nm (Thorlabs FB420-10, FWHM 10nm). The average laser power on the sample was 30 mW with pulse duration of 160fs and repetition rate of 76MHz which produced 2.5 kW of peak power.

On Masson trichrome stained tissue, the collagen fibers in the lamina propria of healthy persons were massive, intimately appositioned and orderly organized. At the distance 10 cm away from the tumor the collagen fibers were feeble and loosely arranged. The enlarged spaces were notable between the collagen fibers, indicating the presence of tissue edema. Similar alterations of collagen fibers, but less prominent, were observed 20 cm away from the tumor.

SHG images on fresh, label-free tissue completely confirmed the aforementioned findings. The profound remodeling of collagen fibers is even more clearly noticeable on 3D reconstruction model obtained from SHG images. In the lamina propria 10 cm away from the tumor collagen fibers became fragile, increasingly disordered and the crypts architecture appeared disturbed.

We documented the profound alterations of collagen fibers in the rectal lamina propria 10 cm and 20 cm away from the malignant tumor.

REFERENCES
[1] Despotović SZ, Milićević NM at al. Histol Histopathol **29,** 229-234(2014).
[2] Rabasovic MD, Pantelić DV et al. J Biomed Opt **20,** 016010(2015).

Time resolved luminescence spectra of greater celandine (*Chelidonium majus* L.)

M. S. Rabasovic, D. Sevic, M. D. Rabasovic, M. G. Nikolic and B. P. Marinkovic
Institute of Physics, Belgrade, Serbia
e-mail:majap@ipb.ac.rs

The greater celandine (*Chelidonium majus* L.) is a medicinal plant of the poppy family. It grows mainly in Europe and Asia. This herb is a rich source of biologically active substances used for the treatment of various diseases. It has been demonstrated that both alkaloid extracts and purified alkaloids from that plant exhibit distinct anti-inflammatory, spasmolytic, anti-microbial, and anti-tumour activities [1–4]. The most important alkaloid components of this plant are protopine, chelidonine, coptisine, sanguinarine, allocryptopine, chelerythrine. Identification and quantitative analysis of these individual alkaloids is important in developing and utilizing resources of greater celandine. Moreover, this analysis provides better insight into the mechanism of the biological action of specific alkaloids.

In this study we analyze optical characteristics of greater celandine solution extracts. The samples of *Chelidonium majus* L. were collected from courtyard of our institute. Solutions were extracted with ethanol from plant samples and their time resolved optical characteristics were analyzed using our TR-LIF (Time resolved Laser induced Fluorescence) spectroscopy experimental setup. The setup consist of tunable OPO (Optical Parametric Oscillator) laser and streak camera. It was used previously for analysis of solution samples of biological interest and it is described in more detail in our earlier publications [5-7].

Results of our analysis reveal two distinct optical emission bands with different excitation characteristics. Time resolved analysis of luminescent spectra show that lifetimes of both bands are in nanosecond domain.

REFERENCES
 [1] M. Kulp, O. Bragina, P. Kogerman, M. Kaljurand, Journal of Chromatography A, 5298, 1218 (2011).
[2] G.-Y. Zuo, F.-Y. Meng, X.-Y. Hao, Y.-L. Zhang, G.-C. Wang, G.-L. Xu, J. Pharm.
Pharm. Sci. 11, 90 (2008).
[3] V. Kaminskyy, M.D. Lootsik, R. Stoika, Centr. Eur. J. Biol. 1, 2 (2006).
[4] K.-M. Cho, I.-D. Yoo, W.-G. Kim, Biol. Pharm. Bull. 29, 2317 (2006).
[5] B. P. Marinkovic, A. Delneri, M. S. Rabasovic, M. Terzic, M. Franko, and D. Sevic,
J. Serb. Chem. Soc. 79, 185 (2014).
[6] M. S. Rabasovic, D. Sevic, M. Terzic, and B. P. Marinkovic, Phys. Scr.T149, 014076 (2012).
[7] M. S. Rabasovic, D. Sevic, M. Terzic, and B. P. Marinkovic, Nucl. Inst. Meth. B.279, 16 (2012).

Europium and Samarium dopant ions as luminescent sensors of Y_2O_3 phase transitions under high pressure

Ana Vlašić[1], Mihailo Rabasović[1], Branka Murić[1], Vladan Čelebonović[1] and Marko G. Nikolić[1]

[1]Institute of Physics,
Belgrade, Serbia
e-mail:vlasic.ana88@gmail.com

Rare earth ions (RE^{3+}) are highly sensitive to local symmetry. Any change in the symmetry is observable in their luminescence spectra [1]. In this work we investigated the photoluminescence properties of cubic and monoclinic Y_2O_3 matrix, doped with either Eu^{3+} or Sm^{3+} ions, under high pressure. Photoluminescence emission measurements for cubic Y_2O_3 were recorded in the pressure range from 0 to 20 GPa for Y_2O_3:Sm^{3+}, and from 0 to 15 GPa for Y_2O_3:Eu^{3+}. Measurements for the monoclinic matrix were recorded from 0 to 8 GPa for Y_2O_3:Eu^{3+}.

With varying pressure the intensity ratio of $^4G_{5/2} \rightarrow {}^6H_{7/2}$ and $^4F_{3/2} \rightarrow {}^6H_{7/2}$ Sm^{3+} emission lines has three distinct regions. In the pressure range from 9.2 GPa to 13.1 GPa it has a steep pressure dependence and could be used for detecting a pressure induced phase transition in the Y_2O_3 matrix from cubic to monoclinic crystal structure. Furthermore, the intensity ratio of $^5D_0 \rightarrow {}^7F_1$ and $^5D_0 \rightarrow {}^7F_2$ Eu^{3+} emission lines in the cubic matrix has a similar pressure dependence to the intensity ratio of these Sm^{3+} emission lines. It matches the behavior of the pressure sensitive Sm^{3+} dependence in the range from 9.1 GPa to 11.6 GPa, and is proven to contain a phase transition around 11 GPa [2].

The monoclinic Y_2O_3:Eu^{3+} also has a pressure-sensitive intensity ratio of $^5D_0 \rightarrow {}^7F_1$ and $^5D_0 \rightarrow {}^7F_2$ emission lines. The dependence is unambiguous, without phase transitions in the measured region. The definitive nature and high sensitivity suggests that this dependence can be used as an efficient high pressure sensor.

REFERENCES
[1] G. Blasse, B. C. Grabmaier, Luminescent Materials, Berlin, Springer Verlag (1994).
[2] J. Zhang, H. Cui, P. Zhu, C. Ma, X. Wu, H. Zhu, Y. Ma, Q. Cui, J. Appl. Phys. 115, 023502 (2014).

Second order optical autocorrelator for measuring ultra short laser pulses duration

Andreja Vladković[1], Mihailo Rabasović[1], Torsten Golz[2], Nikola Stojanović[2], Dejan Pantelić[1], Branislav Jelenković[1], Aleksandar Krmpot[1]

[1]*Insitute of physics Belgrade, University of Belgrade,*
Pregrevica 118,
11080 Belgrade, Serbia
[2]*Deutsches Elektronensynchrotron (DESY),*
Notkestrasse 85,
22607 Hamburg , Germany
e-mail: andrejav@ipb.ac.rs

Second order, i.e. intensity, optical autocorrelation is well established and commonly used technique for ultrashort laser pulse duration measurements [1]. More advanced technique that combines autocorrealtion and spectral mesurements provides even exact temporal shape of the pulse [2]. We report on development of an intesity autocorrelator for measuring femtosecond pulses duration using a nonlinear crystal. Autocorrelator setup is based on Michelson interferometer with BBO (β Barium Borate) crystal in the detection arm for second harmonic generation. Corner cube prism on a motorised stage provides variable delay line. Photodiode with spectral filter was used for signal detection. Data acqusition, the stage driving and the autocorrelation traces display is performed by comuputer, acqusition card and specialy developed software. The software performs simple data processing: filtering and calculation of the pulse duration as Full Width at Half Maximum (FWHM) of autocorrelation curve. Autocorrelator was used to measure duration of ultrashort pulses from a modelocked lasers. We have tested the set-up and the software for various pulse duration and wave lengths from two ultrafast lasers: Coherent Mira 900 (160fs, 700-1000nm) and Timebandwidth products, Yb GLX (200fs, 1040nm). For the longer pulse duration (150fs-5ps) regenrative amplifier Coherent RegA with external pulse compressor/strecher was used.

REFERENCES
[1] W. Demtroeder, Laser Specroscopy, Springer (1996).
[2] Rick Trebino, Frequency-Resolved Optical Gating: The Measurement of Ultrashort Laser Pulses, Springer (2002).

En route: single-shot THz characterization technique
for THz beamline at FLASH1

<u>R. Pan</u>[1], E. Zapolnova[1], T. Golz[1], M. Rabasovic[2], A. Krmpot[2], A. Vladkovic[2], J. Petrovic[3], N. Stojanovic[1]

[1] *Deutsches Elektronen-Synchrotron (DESY),*
Hamburg, Germany
[2]*Institute of Physics,*
Belgrade, Serbia
[3]*Vinca Institute of Nuclear Sciences,*
Belgrade, Serbia
e-mail:rui.pan@desy.de

High-field THz radiation is a fascinating tool to study the interaction of electromagnetic waves with matter, such as demagnetization dynamics [1], tracking the ultrafast motion of a signal molecule [2], resonant control of states of matter [3] and et al. THz beamline at FLASH1 provides both tunable narrow bandwidth (1-30THz) and broad bandwidth intense THz pulses for user's experiment.

Recently we have developed a THz characterization tool, optimized for FLASH's THz spectral range. It is based on THz electro-optic (EO) sampling, in combination of EO spectral decoding for THz pulse arrival timing jitter correction. It enables characterization of THz pulse, as a statistical average used in the experiment, with high temporal and spectral resolution.

Because of the highly fluctuating nature of the THz generation process at FLASH, for certain class of experiments, knowledge of the individual THz pulse properties is essential. Thus a fast diagnostic of THz parameters is required and single-shot method offers clear advantages. The EO spectral decoding subsystem in the THz pulse characterization tool can be used as independent setup at performing single-shot measurements. However, due to the frequency interference in a long chirped laser pulse, the measured THz temporal profile is almost always distorted [4], particularly when characterizing ultra-broadband THz pulses with realistic probing laser.

In order to study this single-shot technique, the broad bandwidth THz dump radiation is measured by EO spectral decoding setup. The distortion is analyzed in details and the measured profiles show agreement with our calculations.

The measurements can help us to study possible retrieval strategies of the original THz electric field from the distorted measured one. This as a final goal has a single shot characterization of THz pulses for FLASH user experiments.

REFERENCES
[1] B. Pfau, et al., Nature communications 3: 1100, (2012).
[2] Cocker L.Tyler, et al., Nature 539.7628: 263-267 (2016).
[3] Kampfrath Tobias, et al., Nature Photonics 7.9: 680-690(2013).
[4] S. P. Jamison, et al., In proceedings of EPAC08.

Tunable High- field THz source at FLASH:

Spectral and spatial characterization.

E. Zapolnova[1], T. Golz[1], R. Pan[1], A. Vladkovic[2].

M. Rabasovic[2]. A. Krmpot[2], J. Petrovic[3] and N. Stojanovic[1]

[1]Deutsches Elektronen-Synchrotron DESY,
Hamburg, Germany
[2]Institute of Physics,
Belgrade, Serbia
[3]Vinca Institute of Nuclear Sciences,
Belgrade, Serbia
Email: ekaterina.zapolnova@desy.de

[4]th generation X-ray light sources have attracted enormous attention of scientists from various fields, allowing conducting pump-probe experiments, which can reveal the mechanisms of chemical reactions and processes, occurring on the molecular and atomic level and on the time-scale of few femtoseconds.

FLASH (Free Electron Laser in Hamburg) has a world-wide unique ability to generate tunable, broadband, high-field THz pulses, which are synchronized with XUV pulses on the order of few femtoseconds [1, 2]. It opens the door to new exiting THz pump X-ray probe experiments, such as THz driven magnetization and ion dynamics, coherent spin control, etc. For such experiments it's extremely important to know the properties of the radiation, which is delivered to the experiment; therefore suitable tools for characterization are required.

We are presenting a custom made ultra-broadband FTIR Spectrometer (Fourier Transform Infrared), optimised for THz source at FLASH and a 2D beam-profiler, both optimized to detect high-field, broadband THz radiation (0.6 µm to 600 um) and which are used as a part of the THz characterization tool, developed at THz beamline at FLASH. THz characterization tool also includes the Electro-optic Sampling (EOS) set up and Spectral Decoding (EOSD) set up, developed together in collaboration with the Institute of Physics and Vinca Institute of Nuclear Sciences in Belgrade, Serbia. We will also present the experiments, which have been conducted in THz beamline during last couple of years to give an overview on the exiting opportunities for light-matter interaction experiments with such an intense and broadband THz source.

REFERENCES
[1] M. Gensch et. al., Infrared Phys. Technol. 51, 423(2008).
[2] F. Tavella, N. Stojanovic, G. Geloni, M. Gensch, Nat. Photon. 5, 162(2011).

OR-NOP2
In-vitro visualization of primary tumor cells using up-conversion nanophosphors

Lidija Mancic[1], Aleksandra Djukic-Vukovic[2], Ljiljana Mojovic[2], Mihailo Rabasovic[3], Aleksandar J. Krmpot[3], Ivana Dinic[4], Antonio MLM. Costa[5], Olivera Milosevic[1]

[1]Institute of Technical Sciences of SASA, Belgrade, Serbia
[2]Department of Biochemical Engineering and Biotechnology, Faculty of Technology and Metallurgy, University of Belgrade, Serbia
[3]Photonic Center, Institute of Physics Belgrade, University of Belgrade, Zemun, Belgrade, Serbia
[4]Innovation Center of the Faculty of Chemistry, University of Belgrade, Serbia
[5]Department of Chemical and Materials Engineering, Pontifical Catholic University of Rio de Janeiro, Rio de Janeiro, Brazil

Due to their unique luminescent features, lanthanide doped up-converting nanoparticles (Ln-UCNPs) have an important role in biomedical use, particularly in the area of NIR-excited fluorescent cell imaging. For such purpose, Ln-UCNPs should have specific morphological characteristics and efficient luminescence response. In this work, a biocompatible and water dispersible $NaYF_4$:Yb,Er@PLGA nanoparticles synthesized using a one-step hydrothermal synthesis were tested as fluorescent bio-labels of primary cell cultures obtained after passage of head and neck squamous carcinoma cells (HNSCC). Structural, morphological and optical properties of particles were obtained using X-ray powder diffraction (XRPD), field emission scanning and transmission electron microscopy (FESEM/TEM), energy dispersive X-ray (EDX), Fourier transform infrared (FTIR) and photoluminescence (PL) spectroscopy. The results revealed coexistence of the cubic (*Fm-3m*) and hexagonal (*P6₃/m*) phase in spherical and irregularly shaped nanoparticles, respectively. Moreover, preservation of the PLGA ligands at the particles surface facilitates their interactions with the cell membrane and provides permeation into cells. To asses a biological safety of their use, viability of human gingival fibroblasts (HFG) was additionally evaluated by a colorimetric MTT assay.

OR-EM1
Effect of annealing temperature on structural and surface morphology of ceramic electrolyte for IT-SOFC applications

Shabana P. S. Shaikh, Kiran P. Adhi

Center for Advanced Studies in Materials Science & Condensed Matter Physics
Department of Physics, Savitribai Phule Pune University, Pune 411007.India

In the present work the powder of $Gd_{0.1}Ce_{0.9}O_{1.95}$ Gadolinium-doped ceria (10GDC) is procured from Sigma Aldrich with 99.9% purity. Using powder 10GDC the electrolyte material in pellets form were sintered at different temperature of 800, 900, 1100 and 1200 ^{o}C for 4 hr in microwave high temperature furnace to investigate the effect of sintering temperature on density, structural and morphological properties of 10GDC. Density was measured using the Archimedes's method.

Ex vivo investigation of hemoglobin distribution in erythrocytes using two photon excitation microscopy: insight from an animal erythrocyte

Ana Z. Stančić (1), Ivana T. Drvenica (1), Svetlana Jovanić (2), Katarina Bukara (3), Vesna Lj. Ilić (4), Mihajlo D. Rabasović (5), Dejan V. Pantelić (1), Brana M. Jelenković (3), Branko M. Bugarski (3), Aleksandar J. Krmpot (3)

1) Institute for Medical Research, University of Belgrade, Dr Subotića 4, 11 129 Belgrade, Serbia

2) Department of Chemical Engineering, Faculty of Technology and Metallurgy, University of Belgrade, Karnegijeva 4, 11 000 Belgrade, Serbia

3) Institute of Physics Belgrade, University of Belgrade, Pregrevica 118, 11 080 Belgrade, Serbia

4) Department of Chemical Engineering, Faculty of Technology and Metallurgy, University of Belgrade, Karnegijeva 4, 11 000 Belgrade, Serbia

5) Department Pharmaceutics, University of Antwerp, Universiteitsplein 1, 2610 Antwerp, Belgium

Keywords: erythrocytes, two photon excitation microscopy

Introduction: Nonlinear laser scanning microscopy (NLSM) with its three modalities, two-photon excited fluorescence (TPEF), second and third harmonic generation (SHG/THG) is advanced optical technique mostly used in biomedicine for label free imaging (1). Hemoglobin, the main intracellular component of erythrocytes, emits strong Soret fluorescence with the peak at 438 nm upon two-photon excitation by femtosecond pulses in red and near infrared region (600-750 nm) (2, 3). Such optical properties of hemoglobin opened the possibility to use TPEF microscopy as a tool for label-free imaging of erythrocytes, even *in vivo* (4). Objective: Despite wide applicability of erythrocytes in diagnostic tests, and distribution of hemoglobin within erythrocytes as a marker of their functional status under physiological or pathological conditions [5], data on spatial distribution of hemoglobin at the single cell level are scarce. Materials & methods: Based on findings reported by Zheng and co-workers (2) we have utilized TPEF microscopy to map the spatial distribution of hemoglobin in porcine erythrocytes *ex vivo*.

Porcine erythrocytes were used as extremely susceptible cells to stress and thus represent a good model system to study influence of stress factors (heat, humidity, malnutrition, infections…) on erythrocyte morphology and hemoglobin distribution. The custom made experimental set up for NLSM utilized the train of the femtosecond pulses from Ti:Sapphire laser (Coherent, Mira 900-F) at 730nm. The repetition rate was 76MHz, and pulse duration was 160fs. Results: Two different morphological types of porcine erythrocytes, normocytes and echinocytes, are collected during mild autumn or extremely hot summer respectively (*Figure* 1a and 1c). Besides, erythrocytes having intermediate morphology i.e. having some characteristics of both abovementioned morphological extremes were also found (*Figure* 1b). Pseudo coloring in figures corresponds to the TPEF signal intensity and no further processing of image was performed. The results demonstrate that the resolution of the TPEF microscopy is good enough for the analysis of erythrocytes at single cell level. The distribution of hemoglobin in erythrocytes followed the cells' shape, where erythrocytes with altered morphology (*Figure* 1b and 1c) demonstrated significant accumulation of hemoglobin in cells' protrusions. Conclusion: Changes in erythrocytes morphology and hemoglobin distribution may influence erythrocytes' oxygen transport function. Erythrocytes monitoring might be of significance in analysis of their functional status in physiological condition, as well in numerous hematological and non-hematological disorders accompanied with erythrocyte morphology changes. Result of this studyeven though obtainedon animal cell model only, confirmed strong potential of TPEF for such application in human and veterinary medicine and basic biomedical research.

References:

1. Masters, B. R .& So, P. T. C. (2008) "Handbook of Biomedical Nonlinear Optical Microscopy", Oxford University Press.

2. W. Zheng, et al., "Two-photon excited hemoglobin fluorescence," Biomed Opt Express 2: 71-79. (2010) [doi:10.1364/BOE.2.000071].

3. G. O. Clay, C. B. Chaffer, and D. Kleinfeld, "Large two-photon absorptivity of hemoglobin in the infrared range of 780-880 nm," J ChemPhys. 126:025102. (2007) [doi:http://dx.doi.org/10.1063/1.2404678].

4. D. Li, et al., "Time-resolved detection enables standard two-photon fluorescence microscopy for
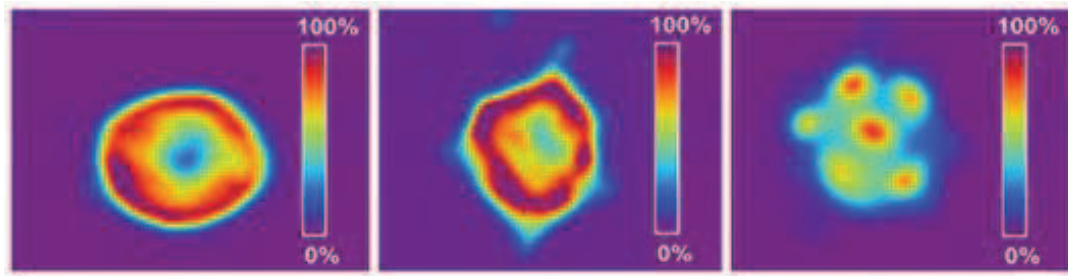
Figure 1. Representative raw TPEF image of (a) porcine erythrocytes with "normal" biconcave, (b) intermediate and (c) echinocytic morphology.TPEF signal is presented in pseudocolor.

Polyacrilic Acid and Chitosan Assisted Solvothermal Synthesis of Up-converting NaYF$_4$: Yb,Er Particles

Marina Vuković[1], Ivana Dinić[1], Lidija Mančić[2], Marko Nikolić[3], Mihailo Rabasović[3] and Olivera Milošević[2]

[1] *Innovation Center of the Faculty of Chemistry, University of Belgrade, Serbia*
[2] *Institute of Technical Sciences of SASA, Belgrade, Serbia*
[3] *Photonic Center, Institute of Physics Belgrade, University of Belgrade, Belgrade, Serbia*

There is a growing interest for development of a facile and reproducible approach for the synthesis of biocompatible lanthanide doped up-converting nanoparticles (UCNPs) for deep tissue imaging and targeted drug delivery [1]. Synthesis of such particles is usually performed through the decomposition of organometallic compounds, followed either with a ligands exchange or with a biocompatible layer coating [2,3]. In this work, biocompatible NaYF$_4$:Yb,Er (17 mol% Yb; 3 mol% Er) nanoparticles were synthesized by one-pot hydrothermal processing with an assistance of chitosan (Ch) or *polyacrylic acid* (PAA). Obtained powders were analyzed by X-ray powder diffraction (XRPD, Bruker D8 Discovery), field emission scanning electron microscopy (FE-SEM, *Zeiss*, DSM 960), transmission electron microscopy (TEM, JEOL JEM 2010), Fourier transform infrared (FTIR, Thermo Scientific Nicolet 6700) and photoluminescence (PL, Spex Fluorolog with C31034 cooled photomultiplier) spectroscopy.

The results showed that although both powders crystallize in the same crystal arrangement (cubic, *Fm-3m*), particles size, shape and optical properties are dependent on the polymer used. Powder which synthesis was performed in the presence of Ch is composed from spherical, monodispersed particles which size is of about 120 nm, Fig.1a. TEM observation revealed coexistence of much smaller crystallites on the surface of these particles, Fig. 1b. On the other hand, PAA functionalized UCNPs were consisted of very thin foils (~6 nm) sized around 10 μm in both in-plane directions, Fig.1c. Degree of the UCNPs functionalization was investigated using FTIR analysis. The obtained results confirm the presence of corresponding

196

PAA or Ch functional groups on the UCNPs surface, indicating that these could be used in biomedical field. The up-conversion luminescent spectra of the synthesized particles demonstrated both, green emissions in the range of 520–550 nm (assigned to the $^2H_{11/2} \rightarrow ^4I_{15/2}$ and $^4S_{3/2} \rightarrow ^4I_{15/2}$ electronic transitions) and red emission (assigned to $^4F_{9/2} \rightarrow ^4I_{15/2}$ electronic transitions) of Er^{3+} ion, Fig.2. Since more intense emission was observed for $NaYF_4$:Yb,Er monodispersed spherical particles obtained through Ch assisted synthesis than those obtained in the presence of PAA, former are additionally tested to check their citotoxicity and internalization capacity in human gingival fibroblasts (HGF) cells. MTT assay shows that viability of HGF cells was highly preserved after 24 h exposure to Ch functionalized UCNPs, being above 90% over the whole investigated concentration range (10–50 μg/mL). The homemade nonlinear laser scanning microscope used in this study comprises Ti:Sapphire laser (Coherent, Mira 900-F) capable to operate in femto-second (FS) pulse mode and continuous wave (CW) mode. FS mode at 730 nm was used for visualization of the unlabeled cells while CW radiation at 980 nm was used for the excitation of Ch functionalized UCNPs in cells. The results presented in Fig.3 confirm that observed fluorescence spots are related to the non-specific uptake of UCPNs through cell membrane, indicating that these could be used as new cell labeling agents in the future [4].

References:

[1] A Sedlmeier and H Gorris, Chem. Soc. Rev. **44** (2015), 1526.

[2] X Chen, D Peng, Q Ju and F Wang, Chem. Soc. Rev. **44** (2015), 1318.

[3] Z Gu *et al*, Adv. Mater. **25** (2013), 3758.

[4] This work was financially supported by the Ministry of Education, Science and Technological Development of Serbia project OI 172035.

252

Assessment of Three Microscopic Techniques in Observing Morphology of Pygidial Glands of Ground Beetles

Marija Nenadić[1], Aleksandar Krmpot[2], Nikola Vesović[1], Mihailo Rabasović[2], Srećko Ćurčić[1], Danica Pavlović[2], Vesna Lacković[3], Svetlana Savić-Šević[2] and Dejan Pantelić[2]

[1] *Institute of Zoology, University of Belgrade - Faculty of Biology, Belgrade, Serbia*
[2] *Institute of Physics, University of Belgrade, Belgrade, Serbia*
[3] *Institute of Histology and Embryology "Aleksandar Đ. Kostić", University of Belgrade - Faculty of Medicine, Belgrade, Serbia*

Pygidial glands represent an exocrine glandular system situated in abdomen of ground beetles and other representatives of the suborder Adephaga within the order Coleoptera [1]. This system plays a major role in the defense against predators [2] by discharging its products (secretions) outwards. It includes two sets of secretory lobes, collecting canals, collecting reservoirs and efferent ducts [1,3]. From a biological point of view, observing pygidial glands of ground beetles is important in taxonomy and promising due to potential medical significance of the secretions [4,5]. In order to better understand glandular functional mechanisms, it is necessary to examine the morphological aspects in detail.

Morphology of pygidial gland structures of certain ground beetle species (Insecta: Coleoptera: Carabidae) has been observed via three different microscopic techniques. Scanning electron microscopy (SEM), two-photon excitation fluorescence (TPEF) microscopy and conventional light microscopy (LM) were applied in order to identify complementarity of different methods of investigating the above-mentioned morphological structures. It is indisputable fact that the highest information content (level of details) on external morphology of biological structures is obtained by SEM. Examination of soft, fragile structures by SEM includes preparation of samples in a *series of alcohol/acetone* solutions of *increasing* concentrations up to 100% followed by a critical point drying (CPD), which is a well-established method for dehydrating biological tissues. In the case of pygidial glands of ground beetles, it has been noticed that tissue drying was excessive, resulting in the irreversible damage.

Samples somewhat changed their shape and their volume shrunk, precluding detailed analysis (Fig. 1a). This is not the case when CPD is omitted, and dehydration is applied only through a *series of ethanol* solutions of *increasing* concentrations (30, 50, 70, 90 and 100%) (Fig. 1b).

Concerning simplicity of different techniques, undeniable advantage must be given to LM (Fig. 2a), although the flaw of this technique is its insufficient informativity regarding a detailed insight into micro- and nanostructures of pygidial gland system (e.g., arrangement of reservoir myofibrils; diameter of collecting and efferent ducts; diameter, thickness and a more detailed structure of radial canals of secretory lobes). Additional three-dimensional information is obtained by TPEF (Fig. 2b). On the basis of all advantages/disadvantages of the three microscopy techniques compared, it can be concluded that the combination of SEM and TPEF enables the most detailed morphological and anatomical surveys of analyzed biological structures [6].

References:

[1] A Giglio *et al*, ZooKeys 100 (2011), 193-201.
[2] K Dettner, Annual Review of Entomology **32** (1987), 17-48.
[3] DJ Forsyth, Transactions of the Zoological Society of London **32** (1972), 249-309.
[4] M Nenadić *et al*, Bulletin of Entomological Research **106** (2016), 474-480.
[5] M Nenadić *et al*, The Science of Nature **103** (2016), 34.
[6] This study is financially supported by the Serbian Ministry of Education, Science and Technological Development (Grants Nos. ON173038, ON171038 and III45016).

INV-OGE 3

Detection of high pressure phase transitions in RE^{3+} doped Y_2O_3 and Y_2MoO_6 through luminescence measurements

Marko G. Nikolić[1], Ana Vlašić[1], Mihailo Rabasović[1], Branka Murić[1], Vladan Čelebonović[1], Nadežda Stanković[2], Branko Matović[2] and Branislav Jelenković[1]

[1] Institute of Physics, Belgrade University, Belgrade, Serbia
[2] Institute of Nuclear Sciences "Vinča", Belgrade University, Belgrade, Serbia

Rare earth ions (RE^{3+}) are highly sensitive to local symmetry so changing the symmetry is reflected in their luminescence spectra. In this work we investigated the high pressure photoluminescence properties of cubic and monoclinic Y_2O_3, as well as, monoclinic Y_2MoO_6, doped either with Eu^{3+} or Sm^{3+} ions.

Photoluminescence emission of cubic Y_2O_3:Sm^{3+} and Y_2O_3:Eu^{3+} phases were recorded up to the pressure of 20 GPa and 15 GPa, respectively. With varying pressure, the intensity ratio of $^4G_{5/2} \rightarrow {}^6H_{7/2}$ and $^4F_{3/2} \rightarrow {}^6H_{7/2}$ Sm^{3+} emission shows three distinct regions. Furthermore, the intensity ratio of $^5D_0 \rightarrow {}^7F_1$ and $^5D_0 \rightarrow {}^7F_2$ Eu^{3+} emission of the cubic matrix has similar pressure dependence as Sm^{3+} doped phase. A steep pressure dependence evident in the range of 9.2-13.1 GPa could be used for detecting a pressure induced cubic to monoclinic phase transition of Y_2O_3 matrix. It matches well the behavior of the pressure sensitive Sm^{3+} spectra in the range of 9.1-11.6 GPa, which is proven to appear due to a phase transition at ~ 11 GPa.

The monoclinic Y_2O_3:Eu^{3+} also has a pressure-sensitive intensity ratio of $^5D_0 \rightarrow {}^7F_1$ and $^5D_0 \rightarrow {}^7F_2$ emission lines. Measurements for the monoclinic Y_2O_3:Eu^{3+} matrix were recorded up to 8 GPa. The dependence is unambiguous, without any phase transitions in the measured region. The nature and high sensitivity suggests that this dependence can be used as an efficient high pressure sensor.

Photoluminescence emission measurements of Y_2MoO_6:Sm^{3+} and Y_2MoO_6:Eu^{3+} phases were recorded up to 12 and 11.5 GPa, respectivelly. Intensity ratio variation of $^4G_{5/2} \rightarrow {}^6H_{5/2}$ and $^4G_{5/2} \rightarrow {}^6H_{7/2}$ Sm^{3+} emission lines, as well as of $^5D_0 \rightarrow {}^7F_1$ and $^5D_0 \rightarrow {}^7F_2$ Eu^{3+} emission lines as a function of pressure can be also used for detection of the Y_2MoO_6 phase transition. The accomplished results demonstrate the properties of Y_2MoO_6:Sm^{3+} and Y_2MoO_6:Eu^{3+} inorganic phosphors, with emmision linear dependance of the intensity ratio on the pressure up to 8 GPa, could be used as an efficient high pressure sensor.

INV-OGE 4

Optical and stryctural properties of nanostructured semiconductors

Martina Gilić and Milica Ćurčić

Institute of Physics Belgrade, University of Belgrade, 11080 Belgrade, Serbia

Science and technologyof nanostructures is a broad and interdisciplinary area of research and development activity that has been growing explosively worldwide in the past decade. Ongoing studies cover not only basic research but also the broad applications range.

# X-ray induced synthesis of novel optical materials at extreme conditions

M. Pravica[1], M. D. Rabasovic[2], A. J. Krmpot[2], M. Nikolic[2],
E. Evlyukhin[1], B. Harris[1] and P. Cifligu[1]

[1]*Department of Physics and Astronomy, University of Nevada, Las Vegas, USA*
[2]*Institute of Physics, Belgrade, Serbia*
e-mail: pravica@physics.unlv.edu

We have demonstrated that highly ionizing, highly penetrating, and highly focused synchrotron hard x-rays (>7keV) can synthesize novel materials [1-2] and novel structures of materials [3] via *useful hard x-ray photochemistry*. We have also observed that some of these novel materials may have optical and electrical utility as wide bandgap material [4]. This material is a variant of polymeric CO which we call "doped poly-CO" that was produced by irradiating a relatively stable material (strontium oxalate powder) with synchrotron-produced hard x-rays (>7 keV) at ambient and high pressures generated by a diamond anvil cell (DAC) and a Paris Edinburgh Cell (PEC). We suspect that the sequence of x-ray photochemical reactions that produced the novel material is as follows:

$$SrC_2O_4 \xrightarrow{h\nu} SrCO_3 + CO$$
$$n(CO) \xrightarrow{h\nu} poly\text{-}CO$$
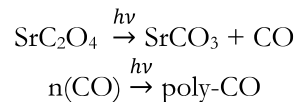
Here, we consider $SrCO_3$ as the dopant. This novel material appears to be very stable and does not decompose over periods of at least two years. It also traps CO_2 inside it for extremely long periods of time (> 2 years) - even when heated to 500K. We have produced doped poly-CO using different cations (Mg, Ca, etc) and using varying pressures. The synthesized products vary with pressure and irradiation flux and energy used and are all recoverable to ambient conditions.

We recently undertook a nonlinear optical study of doped poly-CO to examine its ability to withstand extreme conditions of photon flux in the desire to ascertain its viability as a sensor using 840 nm light as the excitation source. The smaller samples that were produced inside a pressurized DAC (~ 3 nl in volume) and recovered to ambient conditions deteriorated rapidly when irradiated by the high flux laser beam (in seconds). However, we observed that a larger sample (~3 µl in volume) that was synthesized by irradiation of SrC_2O_4 pressurized to 3 GPa in a PEC was not affected by the laser beam and exhibited Second Harmonic Generation (SHG) which was detected at 420 nm. This result suggests that our novel material may have practical relevance as a rugged easy-to-synthesize nonlinear optical generator or as sensor for extreme and ambient conditions.

REFERENCES
[1] M. Pravica et al., Chem. Phys. Lett. 686, 183 (2017).
[2] M. Pravica et al., Pap. Phys. 11, 110001 (2019).
[3] E. Evlyukhin et al., Phys. Chem. Chem. Phys. 20, 18949 (2018).
[4] E. Evlyukhin et al., J. Mater. Chem. C 6, 12473 (2018).

Strain of MoS2 mapped with second harmonic generation microscopy

M. Spasenović[1], A. J. Krmpot[2], M. D. Rabasović[2], N. Vujičić[3],
V. Jadriško[3], D. Čapeta[3] and M. Kralj[3]

[1]*Center for Microelectronic Technologies, Institute of Chemistry, Technology and Metallurgy, Belgrade, Serbia*
[2]*Institute of Physics, Belgrade, Serbia*
[3]*Center of Excellence for Advanced Materials and Sensing Devices, Institute of Physics, Zagreb, Croatia*
e-mail: spasenovic@nanosys.ihtm.bg.ac.rs

2D materials are an extremely intense and current field of research. After the experimental realization of graphene and the immense body of results that highlighted its spectacular properties, attention has started to shift to other 2D materials, namely those that might be of interest for various applications in flexible electronics, optoelectronics, sensing, and in other industrial branches. 2D semiconductors in particular are now drawing the interest of researchers, due to the existence of a bandgap.

Although the potential for applications is enormous, production processes for these materials are still being studied and refined. Chemical vapor deposition (CVD) is widely regarded as a good candidate growth process for wide-scale applications. Nevertheless, it is well known that CVD yields materials that consist of grains with varying orientation and size. Due to the ultrathin nature of these materials, studying the crystallographic orientation and grain size is not trivial.

Optical methods provide a useful tool to study the properties of 2D materials with high resolution. In particular, second harmonic generation (SHG) has been used to map crystal orientation of CVD-grown 2D semiconductors on standard growth and use substrates [1]. Further studies have shown high-resolution strain mapping using the same principles of nonlinear optics [2].

Here we show SHG microscopy studies of crystal orientation and the presence of strain of MoS2 grown on quartz. We show that the growth substrate as well as the speed of cooling during growth can have an influence on strain, and we propose to engineer strain by selecting or patterning the substrate, or tuning the growth process. Strain control on the nanoscale is an enabling tool for the emerging technology of straintronics.

REFERENCES
[1] S. Psilodimitrakopoulos et al., Light Sci. Appl. 7, 18005 (2018).
[2] L. Mennel et al., Nat. Commun. 9, 516 (2018).

Effects of temperature on luminescent properties of CaGdAlO$_4$:Er,Yb nanophosphor

<u>D. Sevic</u>[1], M. S. Rabasovic[1], J. Krizan[2], S. Savic-Sevic[1], M. D. Rabasovic[1],
B. P. Marinkovic[1] and M. G. Nikolic[1]
[1]*Institute of Physics, Belgrade, Serbia*
[2]*AMI d.o.o., Ptuj, Slovenia*
e-mail: sevic@ipb.ac.rs

CaGdAlO$_4$ crystal doped with Er, Yb or other rare earth is commonly used as infrared lasing material [1-4]. In this study we analyze effects of temperature on luminescent properties of nanocrystalline CaGdAlO$_4$ doped with Er^{3+} and Yb^{3+} cations. Material was synthesized by combustion method, as described in [5].

Our experimental setup is presented in detail in [6]; and its use for analysis of thermometric phosphors in [7-9]. However, in this study, because CaGdAlO$_4$:Er,Yb is upconverting material, we have used pulsed laser diode excitation at 980 nm. The structure of material was observed by high resolution scanning electron microscope (SEM). The experimental setup for luminescence measurement as a function of temperature is described in [10].

By using the results of our measurements of CaGdAlO$_4$:Er,Yb nanophosphor in temperature range from 300 K up to 680 K we have determined temperature sensing calibration curve and absolute and relative sensitivity of this material. The relative sensitivity is about 0.7 % K^{-1} on room temperature and decreases with temperature increase. Comparing this results with characteristics of other thermographic phosphors we conclude that synthesized CaGdAlO$_4$:Er,Yb nanophosphor is appropriate material for remote temperature sensing.

REFERENCES
[1] K. Hasse et al., Opt. Lett. 40, 3552 (2015).
[2] J Q. Di et al., Laser Phys. 26, 045803 (2016).
[3] P. Loiko, Opt. Mater. Express 4, 2241 (2014).
[4] Z. Zhu et al., Opt. Lett. 37, 4838 (2012).
[5] J. Krizan et al., Acta Chim. Slov. 61, 608 (2014).
[6] M. S. Rabasovic et al., Nucl. Inst. Meth. B 279, 16 (2012).
[7] A. Vlasic et al., J. Lumin. 199, 285 (2018).
[8] M. S. Rabasovic et al., J. Spectrosc. 2018, 3413864 (2018).
[9] M. G. Nikolic et al., Opt. Quant. Electron. 50, 258 (2018).
[10] M. D. Rabasovic, J. Phys. D: Appl. Phys. 49, 485104 (2016).

Nonlinear microscopy and time resolved fluorescence spectroscopy of *Chelidonium majus* L.

M. S. Rabasovic, D. Sevic, B. P. Marinkovic, A. J. Krmpot and M. D. Rabasovic
[1]*Institute of Physics, Belgrade, Serbia*
e-mail: majap@ipb.ac.rs

Greater celandine (*Chelidonium majus* L.) is a well-known healing plant. It has segmented laticifers filled with yellowish - brown content that is rich in biologically active substances (alkaloids, flavonoids and phenolic acids) [1, 2]. The concentration of these components can change significantly, depending on the time of year, from flowering period in spring to the fruit - bearing time in autumn [3]. Flavonoids (plant pigments) are responsible for the yellow color of the greater celandine flower [4]. The antioxidant activity was also correlated with the concentration of total phenolics (including flavonoids), which is the highest in the spring months [4].

This study presents the analysis of the physical phenomena diagnosed in Chelidonium majus components. Time resolved optical characteristics were analyzed by using TRLS (Time Resolved Laser Spectroscopy) experimental setup. Nonlinear optical properties of the plant have been studied using two-photon excited autofluorescence (TPEF), second - harmonic generation (SHG) and upconversion luminescence (UCL) simultaneously. The benefits of using UCL for biological applications are in reducing the photobleaching and providing photostability. Upconversion emission is also more efficient than the TPEF and SHG. Moreover, UCL could be achieved with a low power continuous wave (CW) laser.

REFERENCES
[1] K. Seidler-Łożykowska et al., Acta Sci. Pol. Hortorum Cultus 15, 161 (2016).
[2] V. N. Deulenko et al., Biochem Anal Biochem 7, 1000370 (2018).
[3] Z. D. Jakovljevic, M. S. Stankovic, M. D. Topuzovic, EXCLI J. 12, 260 (2013).
[4] P. C. H. Hollman, Pharm. Biol. 42, 74 (2004).

In vivo Third Harmonic Generation Imaging of *Phycomyces blakesleeanus*

T. Pajic[1], K. Stevanovic[1], N. Todorovic[2], A. Krmpot[3],
M. Rabasovic[3], B. Jelenkovic[3] and M. Zivic[1]
[1]Faculty of Biology, University of Belgrade, Serbia
[2]Institute for Biological Research, University of Belgrade, Serbia
[3]Institute of Physics, University of Belgrade, Serbia
e-mail: tpajic@bio.bg.ac.rs

Third Harmonic Generation is a nonlinear optical effect in which the incident laser beam interacts with a medium producing the light of exactly three times shorter wavelength than the incidental one. THG is generated in medium that have third order nonlinearity, but it is particularly pronounced at the interfaces where the steep change of refractive index takes a place [1]. THG phenomenon is employed in laser scanning microscopy that utilizes ultrashort laser pulses for imaging. The THG microscopy is a label free techniques that provides important information on the sample such as membrane imaging and lipid droplets distribution [2]. It is mostly used for *in vivo* imaging of small model organisms like zebrafish [3] and C. Elegance [4].

We present THG imaging of filamentous fungus organism *Phycomyces blakesleeanus*, combined with Two Photon Excitation fluorescence (TPEF). The hyphae were grown in various conditions on glass coverslips coated with collagen and concanavalin A. For THG imaging of label-free, 16-24 hour old hyphae, we used 1040 nm, 200 fs pulses from Yb KGW laser, while for TPEF, Ti:Sa pulses at 730 nm, 160 fs duration, were used. Both laser beams were focused with the same objective lens, Zeiss Plan Neofluar 40x1.3. Detection of THG was performed by PMT through Hoya glass UV filter with peak transmission at 340nm, while for TPEF 400-700 nm band pass filter was used. THG images revealed the chitinous cell wall and the membrane that are clearly separated. The appearance of the cell wall was confirmed by colocalization with TPEF images. Most prominent observation on the THG images is presence of numerous, seemingly randomly dispersed, round shiny features throughout the cytoplasm, for which we suspect that could be lipid droplets as indicated in Débarre et al., 2006.

REFERENCES
[1] R. W. Boyd, *Nonlinear Optics*, Academic Press, (2008).
[2] D. Débarre et al., Nat. Methods 3, 47 (2006).
[3] N. Olivier et al., Science 329, 967 (2010).
[4] G. J. Tserevelakis et al., Micron 41, 444 (2010).

Femtosecond laser for dentinal hard tissue ablation

T. Lainovic[1], A. J. Krmpot[2], M. D. Rabasovic[2], D. Pavlovic[2],
E. Novta[1], L. Blazic[1,3] and D. Pantelic[2]

[1]*University of Novi Sad, Faculty of Medicine, School of Dentistry, Serbia*
[2]*University of Belgrade, Institute of Physics, Serbia*
[3]*Dentistry Clinic of Vojvodina, Novi Sad, Serbia*
e-mail: tijana.lainovic@gmail.com

In this study we present testing and optimization of the use of femtosecond laser (FS) in diagnosis and treatment of caries in hard dentinal tissue [1]. We use non-invasive optical methods based on Nonlinear Laser Scanning Microscopy - NLSM, to visualize dentinal tissue "in vitro", noninvasively without damaging the sample.

In our home-made experimental set up for NLSM, we used two modalities for imaging: Two Photon Excitation fluorescence (TPEF) and Second Harmonic Generation (SHG) in reflection arm. A mode locked Ti:Sa laser emitting 160fs pulses in the range 700-900nm is used as the light source for these two modalities. For SHG imaging the laser is tuned to 840nm and 420nm narrowband (10nm) filter is used, while for TPEF the laser was set to 730nm and broad band (400-700nm) filter was used. SHG imaging is used for the label free visualization of caries related collagen degradation [2]. At the same time, fs laser does not cause tissue damage and can be controlled to work only on a chosen surface, avoiding collateral thermal and mechanical damaging of underlying healthy tissues.

We use results obtained by these microscopic techniques as the input diagnostic parameters for microscopically precise ablation of carious lesions. Fs pulses of higher power are used for minimally invasive, highly precise and selective removal of NLSM-diagnosed caries dental tissue, by the ablation process [3]. The procedure needs to be optimized in order to be able to be transferred potentially to clinical practice.

REFERENCES
[1] H. Chen et al., Sci. Rep. 6, 20950 (2016).
[2] R. W. Boyd, *Nonlinear Optics*, Academic Press (2008).
[3] T. Petrov et al., Mater. Sci. Eng. C 90, 433 (2018).

Ultrafast High-Field THz beamline at X-ray FEL

R. Pan[1], E. Zapolnova[1], T. Golz[1], M. Rabasovic[2], A. Krmpot[2],
J. Petrovic[1,3], M. Gensch[4], and <u>N. Stojanovic</u>[1]

[1]*DESY, Hamburg, Germany*
[2]*Institute of Physics Belgrade, Belgrade, Serbia*
[3]*Vinca Institute of Nuclear Sciences, Belgrade, Serbia*
[3]*Institute of Physics, Belgrade, Serbia*
[4]*Technical University of Berlin, Berlin, Germany*
e-mail: nikola.stojanovic@desy.de

THz sources at FLASH utilize spent electron beam from a soft X-ray FEL to generate very intense (up to 150µJ), tunable frequency (1-300THz) and ultrafast narrowband (~10%) THz pulses, which are naturally synchronized to soft X-ray pulses [1]. This unique combination allows for wide range of element specific pump-probe experiments in physics, material science and biology.

Here we discuss the unique features of the FLASH THz pulses and the accelerator source that bring along a set of challenges in the diagnostics of their key parameters: pulse energy, spectral, temporal and spatial profiles.

REFERENCES
[1] R. Pan et al., J. Synchrotron Rad. 26, (2019).

Combined two photon excitation fluorescence and third harmonic generation imaging of redox ratio for monitoring metabolic state of live cells of fungus *Phycomyces blakesleeanus*

TANJA PAJIĆ[1], KATARINA STEVANOVIĆ[1], NATAŠA TODOROVIĆ[2], ALEKSANDAR KRMPOT[3], MIHAILO RABASOVIĆ[3], BRANISLAV JELENKOVIĆ[3] AND MIROSLAV ŽIVIĆ[1]

[1] Faculty of Biology, University of Belgrade, Serbia; [2] Institute for Biological Research, University of Belgrade, Serbia; [3] Institute of Physics, University of Belgrade, Serbia

Label-free two photon nonlinear microscopy is well established as a powerful tool for monitoring metabolic state of the various cell types due to its non-perturbative nature and fairly low phototoxicity, while application of third harmonic generation (THG) for three-dimensional (3D) cell and tissue microscopy was enabled more recently. THG occurs at structural interfaces, such as local transitions of the refractive index, most generally speaking at interfaces that are formed between aqueous interstitial fluids and lipid-rich structures. Here we present preliminary data obtained by capturing both THG and optical redox ratio signal from the same regions of the hyphae of *Phycomyces blakesleeanus*.

Label- free metabolic intravital microscopy through application of both THG and NAD(P)H$^+$/FAD$^+$ autofluorescence ratio was used in alternating sequence on the same field of view on a fungal cells of a model filamentous fungus *Phycomyces blakesleeanus*. The glass coverslip with collagen coating bearing unstained hyphae was mounted on custom built microscope. Laser beams for both imaging modalities were focused with the same objective lens, Zeiss Plan Neofluar 40x1.3. The autofluorescence of NAD(P)H was excited by Ti:Sa laser pulses at 730 nm, 160 fs duration and signal was collected through 479/40 filter, while for autofluorescence of FAD we used excitation by the same laser pulses at 860 nm, 160 fs duration and 530/43 filter.

For THG, we used 1040 nm, 200 fs pulses from Yb KGW laser, and detection was performed by PMT through Hoya glass UV filter with peak transmission at 340nm. As a control for perturbation of optical redox ratio, rothenone (complex I inhibitor) was applied in some experiments. Nile red staining was used to confirm that the brightest structures of round shape in THG images consist of lipids and probably represent lipid droplets that serve as energy deposits in hyphea.

Quantifying organization of collagen fibers in the uninvolved human colon mucosa 10 cm and 20 cm away from the malignant tumor

SANJA DESPOTOVIĆ[1], NOVICA MILIĆEVIĆ[1], ŽIVANA MILIĆEVIĆ[1], ALEKSANDAR KRMPOT[2], MIHAILO RABASOVIĆ[2], ALEKSANDRA PAVLOVIĆ[3], VLADIMIR ŽIVANOVIĆ[3]

[1] Institute of Histology and embryology "Aleksandar Đ. Kostić", Faculty of Medicine, University of Belgrade;
[2] Institute of Physics, Belgrade; [3] University Hospital Center "Dr Dragiša Mišović-Dedinje", Belgrade, Serbia

1. Introduction

Changes in morphology and organization of collagen fibers contribute to the formation of a microenvironment which facilitate tumor progression through the impact on migration and polarization of the cells [1]. Changes in morphology and organization of collagen fibers in cancer, itself, are the subject of numerous studies, while it is far less known about the changes in collagen fibers in the uninvolved mucosa away from cancer.

The main histochemical staining for detection of collagen fibers under light micrsocpy is Masson trichrome staining. Recently, second harmonic generation (SHG) imaging of collagen fibers using nonlinear laser scanning micrscopy emerged as a poweful tool enabeling imaging of collagen fibers in unstained and unfixed tissue [2].

Due to growing interest in role of collagen fibers in cancer progression, the number of methods for quantification of different parameters of collagen fibers is increasing. Currently available methods are based on the intensity derivates, intensity variation, Fourier transform, Hough transform, directional filters and fiber tracking algorithm [3].

The aim of our study was to analyse changes in morphology and organization of collagen fibers in the uninvolved colonic mucosa 10 cm and 20 cm away from the cancer, in comparison with healthy subjects, using Masson trichrome staining, SHG imaging and multiple complementary methods for quantification.

2. Matherials and Methods

Tissue samples
Tissue samples were obtained during colonoscopy at the Department of gastrointestinal endoscopy, University Hospital Center "Dr Dragiša Mišovic-Dedinje", Belgrade, Serbia, from patients suspected to suffer from colon cancer based on clinical symptoms. The samples of colon mucosa were taken 10 cm and 20 cm away in caudal direction from the suspected lesion. The samples of unaffected colon mucosa were obtained from 15 patients older than 60 years. Only tissue samples for which pathologist confirmed that the suspected lesion was colorectal adenocarcinoma, were included in the study. As a control, 20 samples of colon mucosa were collected in the same institution, from patients of corresponding age, who were indicated colonoscopy and were without any pathological finding or diagnosed only with uncomplicated haemorrhoids (*Haemorrhoides non specificatae sine complicationibus*). Patients with inflammatory bowel disease, infectious colitis or diverticular disease of colon were excluded from the study. Our study was approved by ethical committee.
Histochemical staining
The biopsies of the colon mucosa were fixed in 10% neutral buffered formalin, processed to paraplast and stained with Masson's trichrome staining for demonstration of collagen fibers.
Second harmonic generation imaging of colon tissue samples
An original lab frame nonlinear laser-scanning microscope (NLM) was used for identification of collagen fibers in label-free colon tissue samples [4]. For second harmonic generation (SHG) imaging of collagen fibers following experimental setup for NLM was used: The incoming infrared femtosecond pulses from the tunable mode-locked Ti:sapphire laser (Coherent, Mira 900) were

directed onto the sample by a dichroic mirror through the Zeiss EC Plan-Neofluar 40×/1.3 NA Oil objective. The laser wavelength was 840 nm. The SHG was selected by narrow bandpass filter at 420 nm (Thorlabs FB420-10, FWHM 10 nm). The average laser power on the sample was 30mW and the peak laser power was 2.5 kW.

Quantitative analysis of collagen fibers in colon lamina propria

To quantify representation and alignment of collagen fibers in colon lamina propria different approaches were used: Colour Picker Threshold Plugin within Icy software on Masson's trichrome staining images, computational method based on curvalet transform (CT-FIRE and CurveAlign software) on SHG images and method based on SHG polarization anisotropy [3].

Quantifying representation of collagen fibers

Masson's trichrome staining identified collagen fibers, which were green. A random selection of 15 fields per slide was assessed with Colour Picker Threshold Plugin Icy. For each slide, 10 positive and 10 negative colours were selected as recognition patterns of stained and unstained tissue elements. The presence of collagen fibers in colon lamina propria was expressed as the relative percentage of the area occupied by the collagen fibers divided by the area of the lamina propra selected with and imaging processor [5].

Computational Collagen Fiber Segmentation and Quantification

Using CT-FIRE, an open-source software package, we assessed individual collagen fibers and calculated important parameters as length, straightness, and width. CT-FIRE is developed to automatically extract and quantify individual collagen fibers from second harmonic generation images. CT-FIRE could calculate overall alignment of collagen fibers as well as individual length, straightness, and width. Fiber length and width are calculated as pixel values. Alignment represents the overall directionality of fibers within the image on a scale from 0–1, where 1 indicates all fibers are orientated at the same angle. Straightness is calculated by dividing the distance between each fiber end point by the distance along the path of the fiber and is also on a scale from 0–1, where 1 indicates a perfectly straight fiber. Besides analysing individual collagen fibers on whole SHG images, we choose 3 regions of interest per image, in the close vicinity to crypths, where the fiber remodeling happens first, and conduct analyses within them [3].

SHG polarization anisotropy

The anisotropy of SHG images can be used to quantify allignment of collagen molecules inside fibers. The anisotropy parameter was calculated by:

$$\beta = (Ipar-Iorth)/(Ipar+2Iorth)$$

where Ipar and Iorth represented SHG intensity detected when the analyzing polarizer is oriented parallel and perpendicular/orthogonal to the laser polarization. Values of β range from 0 to 1, where 0 represents completely random and 1 completely aligned collagene molecules organization. From each tissue sample 3 randomly chosen regions were measured [3].

Statistical analysis

The means and standard deviations were calcualted and the Student's t-test or ANOVA were used to indicate significant differences.

3. Results

On Masson trichrome staining and SHG images, collagen fibers in healthy colon lamina propria were orderly organized: the wavy bundles of collagen fibers extended around the crypts and in all directions throughout the lamina propra. At the distance of 10 cm and 20 cm away from the tumor, their proper arrangment is partially lost. Different patterns of collagen fibers are noticable: regions with parallel collagen fibers, thick collagen fibers, regions with edema of lamina propra where the prominent spaces between fibers could be seen and regions with collagen fibers organization resembling one in healthy subjects (Figure 1). Thus, the morphology and organization of collagen fibers are very heterogeneous, both between differenet groups and within each group between individual subjects.

We revealed that the representation of collagen fibers (%) in the lamina propria in the remote colon mucosa 10 and 20 cm away from the cancer was significantly lower (26.43±6.22 and 35.15±8.34, respectively) in comparison with the control, healthy individuals (48.05±8.92). Notably, the representation of collagen fibers was significantly lower in the lamina propria at the distance of 10 cm away from the tumor compared with that at the distance of 20 cm.

Using CT-FIRE and CurveAlign softwares, on whole SHG images, we showed that the width and lenght of collagen fibers are statistically higher 10 cm and 20 cm away from cancer (5±0.7, 5.32±0.58 and 55.12±2.73, 56.28±5.12), compared with healthy subjects (4.49±0.43 and 52.12±2.98). When we analyzed 3 regions of interest, in close proximity to crypts, per each photo, detected changes were even more obvious. Also, the collagen fibers 10 cm and 20 cm away from the cancer were significantly more orderly allign (0.47±0.19 and 0.59±0.19), compared with healthy lamina propra (0.36±0.20).

Anisotropy parameter β is significantly lower 10 cm and 20 cm away from the cancer (0.26±0.05, 0.34±0.09), compared with healthy lamina propria (0.39±0.09), indicating changes in organisation of collagen moleculer within fibers.

4. Conclusion

Using different, complementary approaches we detected changes in representation, morphology and organization of collagen fibers 10 cm and 20 cm away from colon cancer, compared with healthy subjects.
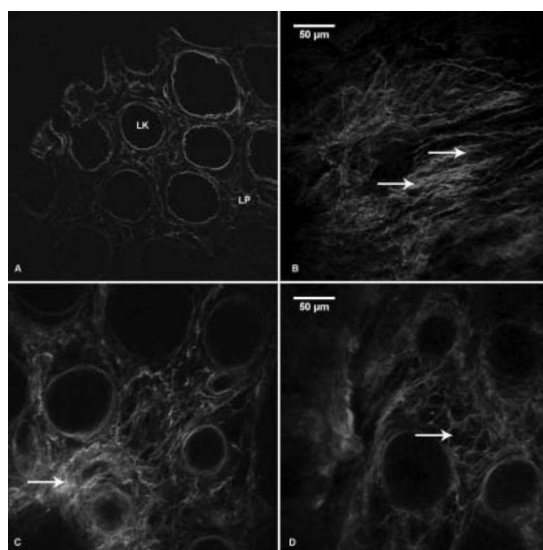
Figure 1. SHG images of collagen fibers in the colon lamina propria. A. Lamina propria of healthy subject; B.Lamina propria 20 cm away from cancer; arrows are showing regions with highly alligned collagen fibers; C. Lamina propria 10 cm away from cancer; arrow is showing region with dense collagen fibers; D. Lamina propria 10 cm away from cancer; arrow is showing enlarged spaces between collagen fibers;

References
[1] Vannucci L. Cancer Microenv 8 (2015) 159-166
[2] Rpuede D, Schaub E, Bellanger J. Sci Rep 7 (2017) 12197
[3] Rittie L. Methods in Mol Biol 1627 (2017) 429-450
[4] Rabasović MD, Pantelić DV, Jelenković BM. J Biomed Opt 20 (2015) 016010
[5] Despotović SZ, Milićević NM; Milošević DP. Tumour Biol 39 (2017)

"Fretted with golden fire": structural colouration based on micron and sub-micron structures in selected insects

Dejan Pantelić[1], Srećko Ćurčić[2], Aleksandar Krmpot[1], Dejan Stojanović[3], Dragana Cvetković[2], Mihailo Rabasović[1], Svetlana Savić-Šević[1], Danica Pavlović[1], Vladimir Lazović[1]

[1]Institute of Physics, University of Belgrade, Belgrade, Serbia. [2]Faculty of Biology, University of Belgrade, Belgrade, Serbia. [3]Institute of Lowland Forestry and Environment, University of Novi Sad, Novi Sad, Serbia

Abstract

Colouration and colour perception in insects have evolved in context of enormous diversity of visual tasks and light environments. Apart from pigment colouration, structural colouration in numerous insect taxa attracts much research interest, particularly with respect to its role in camouflage or sexual signaling, and calls for integration of different approaches. Here, researchers in both the physics and biology fields cooperated to study features of morphological structures underlying structural colouration in insects, particularly butterflies, moths and beetles. Optical structures of the insect cuticle were analysed using a wide array of methods - scanning electron microscopy (SEM), nonlinear microscopy, optical microscopy, spectroscopy, etc. We present the variety of morphological and optical solutions found in selected species of Lepidoptera and Coleoptera from the Balkan region and discuss the obtained results in eco-evolutionary context, with respect to putative selective pressures and adaptations.

XUV-driven plasma switch for THz: new spatio-temporal overlap tool for XUV–THz pump–probe experiments at FELs

E. Zapolnova[1,4], R. Pan[1], T. Golz[1], M. Sindik[1], M. Nikolic[1], M. Temme[1], M. Rabasovic[2], D. Grujic[2], Z. Chen[3], S. Toleikis[1] and N. Stojanovic[1]

[1]*Deutsches Elektronen-Synchrotron (DESY), Notkestrasse 85, 22607 Hamburg, Germany,*
[2]*Institute of Physics Belgrade, Pregrevica 118, 11080 Belgrade, Serbia, and*
[3]*SLAC National Accelerator Laboratory, Menlo Park, CA 94025, USA*
[4]*Class 5 Photonics GmbH, Notkestrasse 85, 22607 Hamburg, Germany*
e-mail: ekaterina.zapolnova@@@class5photonics.com

Intense THz pulses combined with synchronized X-ray pulses enable investigation of the dynamics of the light–matter interaction, non-linear response of materials and control of the properties of matter selectively on femtosecond time scales. Therefore, achieving the temporal overlap between pump and probe pulses in the femtosecond range is essential for both at table top high harmonic sources and Free Electron Lasers (FELs) [1].

A simple and robust tool for spatio-temporal overlap of THz and XUV pulses in in-vacuum pump–probe experiments is presented. The technique exploits ultrafast changes of the optical properties in semiconductors (i.e. silicon) driven by ultrashort XUV pulses that are probed by THz pulses. It enables the measurements of the arrival time between XUV and THz pulses with temporal resolution on the scale of the duration of the THz pulse. It enables the single shot measurement of the optical constants of the excited materials with the variable XUV wavelength [2].
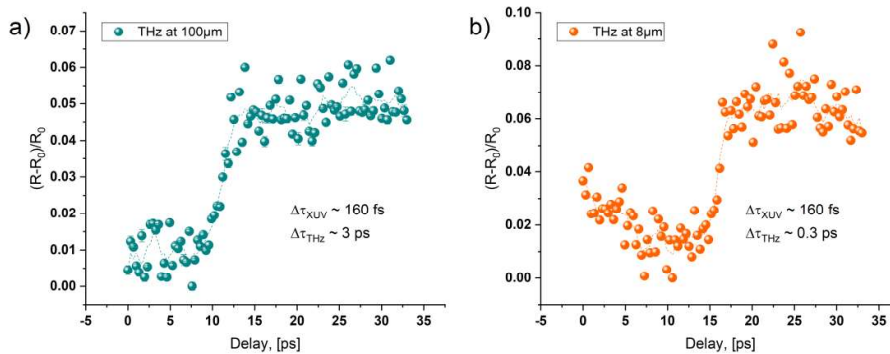
Figure 1. Transient THz reflectivity change of Si, excited by 13.5 nm XUV pulse probed with THz wavelengths of 100 µm and 8 µm.

REFERENCES
[1] E. Zapolnova, R. Pan, T. Golz, M. Sindik, M. Nikolic, M. Temme, M. Rabasovic, D. Grujic, Z. Chen, S. Toleikis and N. Stojanovic, Journal of Synchrotron Radiation, Vol. 27, p.1 (11-16) 2020
[2] Z. Chen, et. al., Nature Communications, 12 (1638), 2021

Laser Microsurgery of Filamentous Fungi: The Latest Protocol Enabling Patch-Clamp Amenable Protoplasts

K. Stevanović[1], T. Pajić[1], N. Todorović[2], A. Krmpot[3], M. Živić[1], M. Rabasović[3]
[1]University of Belgrade - Faculty of Biology, Serbia
[2]Institute for Biological Research, University of Belgrade, Serbia
[3]Institute of Physics, University of Belgrade, Serbia
e-mail: katarina.stevanovic@bio.bg.ac.rs

We have developed an advanced protocol for laser cell surgery to obtain protoplasts of filamentous fungi, suitable for investigation of ion channels, relying on few attempts already made in the past [1], [2]. Among obtained protoplasts, 32% were shown to be "patchable", meaning that formation of the gigaseal by the micropipette was possible. Protoplasts were produced by first making an incision on the cell wall of plasmolysed hyphae by a tightly focused femtosecond laser beam (Figure 1). Cell surgery is followed by a reduction of solution osmolarity to promote extrusion of protoplast (or more often, a part of it) through the cut. The two key points- cell surgery parameters and the proper sequence of the solutions used − were subjected to variations to gain insight into parameters that contribute to protoplast production and stability. The proper selection of the pipette size and shape with respect to the protoplast size was also of great importance.

Cell surgery and hyphae imaging was performed by a nonlinear laser scanning microscope. Ti:Sa laser was operating at 730nm, with 76MHz repetition rate and 160fs pulse duration. Water dipping objective lens (40 x 1.0, Zeiss W Plan-Apochromat) on the upright non-linear microscope system made possible to perform laser surgery and patch clamp on two separate systems, while working in the same microscopic chamber. Prior to microsurgery, two-photon excitation fluorescence was used to scan the hyphae cell wall stained with Calcofluor white dye, using the same wavelength as for the surgery.

Figure 1. Hyphae cell surgery a) before laser cutting b) extrusion of the protoplast through the incision after laser cutting c) the pipette on the enlarged protoplast

Two-step plasmolysis, with increased concentration of calcium in the more hyperosmotic solution was both efficient for microsurgery to be performed and had a stabilizing effect on protoplasts. Subtle deplasmolysis prior to the patch clamping effective enough to stimulate protoplasts to exit, without making the membrane overstretched to interact with the pipette was employed. Optimized concentration and type of chemical agens for inhibition of the cell wall production was continuously present in all solutions, as an indispensable factor for success.

REFERENCES:
[1] Roberts, S. K., Dixon, G. K., Dunbar, S. J., & Sanders, D. (1997), New Phytologist, Vol. 137, 579−585
[2] Véry, A. A., & Davies, J. M. (1998). Applied and Environmental Microbiology, 64(4), 1569−1572

Mapping of fluorescent compounds in lyophilized blackcurrant (*Ribes nigrum L.*) fruits using spectroscopy and nonlinear microscopy

M. S. Rabasovic[1], D. Sevic[1], B. P. Marinkovic[1], A. J. Krmpot[1], G. Zdunic[2], K. Savikin[2], M. D. Rabasovic[1]

[1]*Institute of Physics, Belgrade, Serbia*
[2] *Institute for Medicinal Plants Research "Dr Josif Pančić", Tadeuša Košćuška 1, 11 000, Belgrade, Serbia*
e-mail: majap@ipb.ac.rs

Blackcurrant (Ribes nigrum L.) belongs to the important medicinal plants that act preventively and therapeutically on the organism [1, 2]. Bioactive components in fruits and leaves of blackcurrant could have beneficial effects on the skin fibroblasts that produce collagen [3]. The influence of parts and extracts of this plant on erythrocyte membranes has been the subject of research in recent years [4]. Blackcurrants (Ribes nigrum L.) contain high levels of polyphenol anthocyanins in fruits and flavonoids in leaves that have beneficial effects on health, owing to antioxidant and anticarcinogenic properties. These compounds are responsible for the coloring of many plants, flowers and fruits. Cyanidin-3-O-glucoside (C3G) is one of the principal types of anthocyanidins and is the most common and abundant one in fruits blackcurrant [5]. Anthocyanidins/anthocyanins can be employed as probes for oxidation processes in biomedical experiments. Their advantages include biocompatibility and the lack of toxicity [6].

The present study aimed to present the analysis and mapping of the Blackcurrants (Ribes nigrum L.) components using spectroscopy and imaging measurements [1, 7]. Time resolved optical characteristics were analyzed by using TRLS (Time Resolved Laser Spectroscopy) experimental setup [1]. Nonlinear optical properties of the plant have been studied using two-photon excited autofluorescence (TPEF), and upconversion luminescence (UCL) simultaneously [7]. The benefits of using UCL for biological applications are in reducing the photobleaching and providing photostability. Upconversion emission is also more efficient than the TPEF and SHG. Moreover, UCL could be achieved with a low power continuous wave (CW) laser.

REFERENCES
[1] M. S. Rabasovic, B. P. Marinkovic, M. D. Rabasovic, M. G. Nikolic, D. Sevic, Eur. Phys. J. D 75, 180 (2021).
[2] G. Kendir, I. Süntar, A. O. Çeribaşı, A. Köroğlu, J. Ethnopharmacol. 237,141-148 (2019).
[3] N. Nanashima, K. Horie, H. Maeda, T. Tomisawa, M. Kitajima T. Nakamura, Nutrients 10, 495 (2018).
[4] D. Bonarska-Kujawa, S. Cyboran, R. Żyłka, J. Oszmiański, H. Kleszczyńska, BioMed Research International, 2014, 783059 (2014).
[5] L. Tang, D. Zhang, S. Xu, H. Zuo, C. Zuo, Y. Li, 29, 168-175 (2014).
[6] G. Bartosz, M. G-Pietrasiewicz, I. S-Bartosz, J. Agric. Food Chem. 68 (43) 12019 (2020).
[7] M. D. Rabasovic, D.V.Pantelic, B. M. Jelenkovic, S. B. Ćurčić, M. S. Rabasovic, M. D. Vrbica, V. M. Lazovic, B. P.M. Ćurčić, A. J. Krmpot, J. Biomed.Optics 20(1) 016010 (2015).

Interaction of ultrashort laser pulses with hemoglobin as a tool for selective erythrocytes photo-labeling

M. Radmilovic[1], I. Drvenica[2], M. D. Rabasovic[1], V. Ilic[2], D. Pavlovic[1], S.Nikolic[1], M. Matic[3] and A. Krmpot[1]

[1]*Institute of Physics Belgrade, Serbia*
[2]*Institute for Medical Research, University of Belgrade, Serbia*
[3]*Institute of Oncology and Radiology of Serbia*
e-mail:mihajlo.radmilovic@ipb.ac.rs

Interaction of hemoglobin (Hb) with ultrashort laser pulses is followed by fluorescence detection [1, 2]. The photophysical nature of fluorescence from Hb-containing specimens is not completely understood so far. There is some evidence of photoproduct formation in the process of Hb interaction with ultrashort laser pulses [3].

We measured Uv-Vis and Two-photon emission spectra of formed photoproduct in the way that Hb thin film was previously treated with a femtosecond Ti: Sapphire laser operating on 730nm. A relative relation and position of Uv-Vis Hb characteristic peaks such as Soret peak (410 nm), α and β peaks (577 nm and 541 nm respectively) served as a marker of structural changes in the laser treated Hb films[4].

Results suggest that the interaction of Hb with ultrashort laser pulses probably leads to the photodegradation of Hb, due to changes in α, β peaks relative relation and red shift of Soret peak in photoproduct Fig. 1 a).

Moreover, we emphasize that the photoproduct formed on thin Hb films has long durability, since we were able to detect its fluorescence after several months. This opens a possibility to apply the formed photoproduct as optical data storage and security tag.

We have also induced photoproduct formation in the human healthy erythrocytes Fig. 1 b) in order to selectively "label" and make them fluorescent in a whole blood. Two-photon selective labeling of erythrocytes can be used as a tool for studying red blood cells with different fluorescence detection methods, due to photoproduct fluorescence. This can be potentially applied in studying hemoglobin and erythrocytes in various physiological and pathophysiological states.
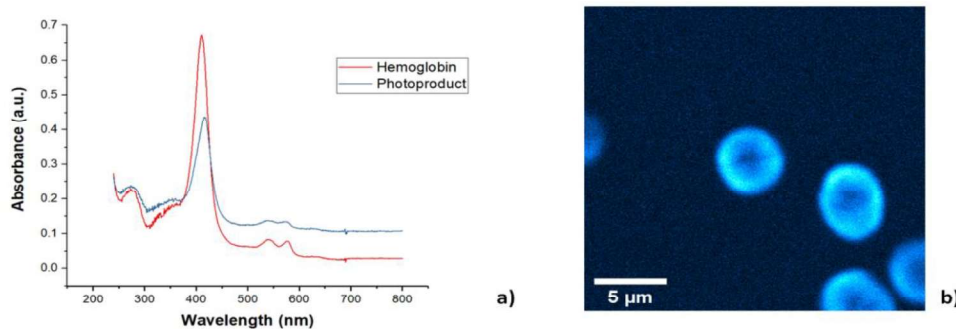
Figure 1. a) Uv-Vis absorption spectra of hemoglobin (red) and formed photoproduct (blue), b) Two-photon fluorescence image of selectively chosen erythrocytes with induced photoproduct formation.

REFERENCES
[1] D. Li, W. Zheng, Y. Zeng, Optics Lett. 36, 834 (2011).
[2] K. Bukara, S. Jovanic, I. Drvenica, J. Biomed. Opt. 22.2, 026003 (2017).
[3] E.A.Shirshin, B.P.Yakimov, S.A.Rodionov, Laser Phys. Lett. 15, 075604 (2018).
[4] E.H.Hanson, J.Ballantyne, PLoS One 5, e12830 (2010).

Discovering abnormal erythrocyte membranes - optical approaches

M. Matić[1], D. Pavlović[2], M. Radmilovic[2], M. D. Rabasovic[2],V. Ilić[3], A. Krmpot[2], I.Drvenica[3]
[1] Institute of Oncology and Radiology of Serbia, [2] Institute of Physics, Belgrade, Serbia
[3]Institute for Medical Research, University of Belgrade
e-mail: milica.matic1210@gmail.com

Due to their complex physiological role, erythrocytes have naturally very elastic membranes, however, extremely susceptible to various endogenous and exogenous factors. Therefore, it has been speculated that abnormalities in erythrocyte membrane deformability and shape can be seen as an early sign of some acute and chronic pathological states/diseases [1,2]. In the project HEMMAGINERO [3], we are exploring whether optical methods, ektactometry, and Two-Photon Excitation Fluorescence (TPEF) microscopy, can be used as potential diagnostics tools in identifying any changes in the shape/deformability of erythrocytes.Using ektacytometry (RheoScan D-300, RheoMeditech Inc., South Korea) we calculate the cell deformability from the intensity pattern of the laser light which is scattered by a suspension of red blood cells exposed to shear stress [4].Our previous researchalready demonstrated that in-house TPEF microscopy set-up is an effective tool for label- and fixation -free imaging of erythrocytes and their membranes [5], based on a peculiar feature of hemoglobin to produce a fluorescent molecule upon interaction with ultrashort laser pulses [6,7].

In the first phase of the project, we have used blood from healthy volunteer donors and *in vitro* made environments that simulate different conditions to which erythrocytes can be exposed in pathological processes (hyper- and hypo-osmolarity; acidosis, alkalosis). The obtained data on erythrocyte morphology by TPEF and erythrocytes deformability by ektacytometry are correlated with the results of routinely used biochemical tests for oxidative stress assessment,and mechanical and osmotic fragility indices.

Our results show that both ektacytometry and TPEF microscopy are sensitive and reliable in determining that membranes of erythrocytes have suffered under non-ideal (meaning non-physiological) conditions of the *in vitro*environment.Further investigation is needed to conclude theprecision of these optics methods in discovering abnormal erythrocyte membranes in actual patients' blood.

REFERENCES:
[1] H. Chen, W. Yunpeng, C. Shaoxi, et al.Clin. Hemorheol. Microcirc. 16,2 (1996).
[2] S. Shin, Y. H. Ku, J.X.Ho, et al. Clin. Hemorheol. Microcirc. 36, 3(2007).
[3] http://www.hemmaginero.rs/hemmaginero.html
[4] A.E.O.Finkelstein. Design and evaluation of a new diagnostic instrument for osmotic gradient ektacytometrie. PhD Thesis, Université Paris-Est (2017).
[5] K.S. Bukara, S.Z. Jovanić, I.T. Drvenica, et al. Mapping of hemoglobin in erythrocytes and erythrocyte ghosts using two photon excitation fluorescence microscopy J. Biomed. Optics 22(2), 026003 (2017).
[6] W. Zheng, D. Li, Y. Zeng, et al. Two-photon excited hemoglobin fluorescence, Biomed. Opt. Express 2, 71-79 (2011).
[7] E.A. Shirshin,B.P Yakimov,S.A.Rodionovet al. Formation of hemoglobin photoproduct is responsible for two-photon and single photon-excited fluorescence of red blood cells. Laser Phys. Lett. 15, 075604 (2018).

First glance at a multitude of ion currents on filamentous fungus *P. blakesleeanus* protoplasts obtained by femtosecond laser microsurgery

M. Zivic[1], K. Stevanovic[1], T. Pajic[1], M. D. Rabasovic[2], A. Krmpot[2], N. Todorovic[3]
[1]*University of Belgrade - Faculty of Biology, Serbia*
[2]*Institute of Physics, Belgrade, Serbia*
[3]*Institute for Biological Research "Sinisa Stankovic, University of Belgrade, Serbia*
e-mail:mzivic@bio.bg.ac.rs

Electrophysiology of cell membrane ion channels in filamentous fungi, unlike that in yeast, plant and animal cells is still in its infancy. The only two reports on single channel patch clamp recordings from native cell membrane of filamentous fungi were made on protoplasts obtained after cell wall microsurgery with UV pulsed laser more than 20 years ago [1, 2]. Both pioneering papers reported fairly high success rates of obtaining gigaohm contacts, but neither was followed by more studies. Advanced imaging techniques that enable more controllable surgery process and utilizing the femtosecond pulses, after optimizing the protocol, could result in minimally damaging cell wall microsurgery. The end result would be reproducibly high quality membrane of "de-walled" protoplasts. The membrane quality, property that is of utmost importance for application of patch clamp method, is a term describing not only mechanical integrity and cleanliness of the membrane, but the physiological fitness of the cell as well, as cells about to enter apoptosis or necrosis, or that were subjected to oxidative stress do not have it.

We are presenting here, to the best of our knowledge, the first electrophysiological snapshot obtained on filamentous fungi protoplast after cell wall removal by a femtosecond laser microsurgery. Utilization of the Ti:Sa femtosecond laser with optimizations of the cell wall microsurgery protocol explained in [3], this conference, resulted in protoplasts that were prone to form contacts of high electrical resistance (GΩ) with a patch pipette. Ti:Sa laser operating at 730 nm (76 MHz, 160 fs pulse duration) combined with homemade nonlinear laser scanning microscope, physiological 40x 1.0 NA objective was employed for microsurgery and imaging. Standard patch-clamp set up was used for electrophysiology. In single channel recordings from more than 30 patches, 11 different channel types were distinguished, based on the reversal potential in asymmetric ionic conditions and on the conductance. By far, the most frequent types of conductance were anionic. We have found four groups of ion channel currents, based on ion selectivity:

1. Unselective anion currents (not discriminating between chloride and glutamate) 44% of all recorded currents.

2. Anionic currents selective for chloride (carried exclusively or mostly by chloride) 35%.

3. Organic acid permeable anionic currents (discriminating for glutamate over chloride) 17%; 4. Calcium cationic current was recorded once.

The range of conductance size (g) was variable, with unselective anionic currents encompassing the smallest (5 pS) and largest (160 pS) recorded conductances. Calcium conductance was small (6 pS), while organic acid conductances and Cl⁻-selective conductances had similar ranges (10-60 pS). Most of the conductances displayed linear current-voltage relationships.

REFERENCES
[1] SK. Roberts, GK. Dixon, SJ. Dunbar and D. Sanders. New Phytol. 137, 579 (1997).
[2] AA. Véry, JM. Davies. Appl Environ Microbiol. 64,1569 (1998).
[3] K. Stevanovic, et al. http://www.photonica.ac.rs/ (2021)

Altered organization of collagen fibers in the uninvoled human colon mucosa 10 cm and 20 cm away from the colorectal cancer

S.Despotović[1], Đ. Milićević[2], A. Krmpot[3], A. Pavlović[4], V. Živanović[4], Z. Krivokapić[5], V. Pavlović[6], S. Lević[6], G. Nikolić[7], M. D. Rabasović[3]

1 University of Belgrade, Faculty of Medicine, Institute of Histology and embryology, Belgrade, Serbia
2 Saarland University, Department of Internal Medicine V- Pulmonology, Allergology, Intensive Care Medicine, Homburg/Saar, Germany
3 University of Belgrade, Institute of Physics Belgrade, Belgrade, Serbia
4 University Hospital Center "Dr Dragiša Mišović Dedinje", Belgrade, Serbia
5 Clinic for Abdominal Surgery- First surgical clinic, Clinical Center of Serbia, Belgrade, Serbia
6 University of Belgrade, Faculty of Agriculture, Belgrade, Serbia
7 University of Belgrade, Faculty of Medicine, Institute of Pathology, Belgrade, Serbia
e.mail: sanjadesp@gmail.com

Remodelling of collagen fibers has been described during every phase of cancer genesis and progression. Changes in morphology and organization of collagen fibers contribute to the formation of microenvironment that favors cancer progression and development of metastasis. However, there are only few data about remodelling of collagen fibers in healthy looking mucosa distant from the cancer. Using SHG imaging, scanning electron microscopy (SEM) and specialized softwares (CT-FIRE, CurveAlign and FiberFit), we objectively visualized and quantified changes in morphology and organization of collagen fibers. SHG polarization anysotropy was used to quantify alignment of collagen molecules inside fibers. Using immunohistochemistry (staining with anti-alphaSMA, anti-LOX, anti-MMP2 and anti-MMP9) we investigated possible causes of collagen remodelling (change in syntheses, degradation and collagen cross-linking) in the colon mucosa 10 cm and 20 cm away from the cancer in comparison with healthy mucosa. We showed that in the lamina propria this far from the colon cancer, there were changes in collagen architecture (width, straightness, alignment of collagen fibers and collagen molecules inside fibers), increased representation of myofibroblasts and increase expression of collagen-remodelling enzymes (LOX and MMP2). Thus, the changes in organization of collagen fibers, which were already described in the cancer microenvironment, also exist in the mucosa far from the cancer, but smaller in magnitude.

REFERENCES:
[1] S. Despotović, Đ. Milićević, A. Krmpot et al. Sci Rep 10, 6359 (2020).
[2] M. Rabasović et al. J Biomed Opt 20, 016010 (2015).

Label-free Third Harmonic Generation Imaging of Lipid Droplets in Live Filamentous Fungi

T. Pajić[1], N. Todorović[2], M. Zivić[1], M. D. Rabasović[3], A.H.A. Clayton[4], and A. Krmpot[3]

[1]*University of Belgrade – Faculty of Biology, Belgrade, Serbia*
[2]*Institute for Biological Research "Siniša Stanković", University of Belgrade, Serbia*
[3]*Institute of Physics, Belgrade, Serbia*
[4]*Optical Sciences Centre, Swinburne University of Technology, Victoria, Australia*
e-mail:tpajic@bio.bg.ac.rs

Oleaginous fungi can accumulate significant amounts of lipids in their mycelium (up to 80% of their biomass), primarily in the form of lipid droplets (LDs). LDs have optical properties that differ from the surrounding aquatic environment, which causes sudden changes in the refractive index. Here, we present *in vivo* and label-free imaging of individual hyphae of the oleaginous filamentous fungus *Phycomyces blakesleeanus* by Third Harmonic Generation (THG) microscopy method [1], where LDs are the main source of contrast [2] (Figure 1). The LDs quantification from THG images was performed by two image analysis techniques: Image Correlation Spectroscopy (ICS) and software particle counting – Particle Size Analysis (PSA). ICS measures the spatial variation of fluorescence intensity fluctuations in the images, which can then be related to particle density and aggregation state. In order to test and compare the two methods, we used hyphae that undergo nitrogen starvation, which is known to cause alterations in lipid metabolism and the increase in LDs number.

For *in vivo* THG imaging of label-free, > 24-hour old hyphae, we used 1040 nm, 200 fs pulses from Yb KGW laser. Detection was performed in the transmission arm by PMT through Hoya glass UV filter with peak transmission at 340nm. The laser beam was focused with the Zeiss Plan Neofluar 40x1.3 objective lens. For the imaging, the fungi were placed between two cover glasses of 0.17 μm thickness to match the objective lens requirements and for better transmission of the THG signal.
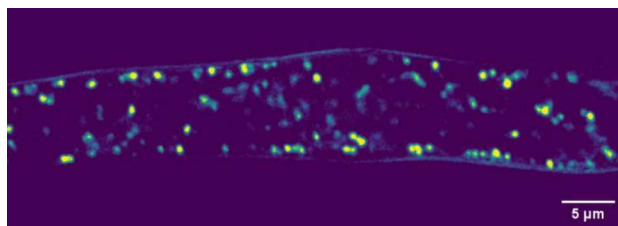
Figure 1. THG image of lipid droplets in hyphae of the fungus *Phycomyces blakesleeanus*. The bright objects are lipid droplets.

An increased number of LDs under nitrogen starvation was observed in THG images and their number and size were analyzed using two quantification methods. The comparison of LDs number and size obtained by ICS and PSA shows that the number of LDs is approximately the same on average, but that ICS consistently detects slightly larger LD number in older group. The mean ICS measured diameter was slightly lower. Using the THG method *in vivo* and label-free, we can accurately and reliably, over time, detect changes in the localization, total number, and size of LDs in hyphae of the oleaginous filamentous fungus *Phycomyces blakesleeanus.*

REFERENCES
[1] R. W. Boyd, Academic Press (2008).
[2] D. Débarre, W. Supatto, A. M. Pena, A. Fabre, T. Tordjmann, L. Combettes, E. Beaurepaire, *Nature Methods*, *3*(1), 47–53. (2006).

Nonlinear Imaging of Dentin-Adhesive Interface Treated by Cold Atmospheric Plasma

T. Lainović[1], A. Krmpot[2], M. D. Rabasović[2], N. Selaković[1], I. Pleštić[1], L. Blažić[1,3], N. Škoro[2], N. Puač[2]

[1]Faculty of Medicine, School of Dental Medicine, University of Novi Sad, Novi Sad, Serbia
[2]Institute of Physics, University of Belgrade, Belgrade, Serbia
[3]Dental Clinic of Vojvodina, Novi Sad, Serbia
e-mail: tijana.lainovic@mf.uns.ac.rs

The Nonlinear Laser Scanning Microscopy (NLSM) could be considered as a useful tool for the analysis of hard dental tissues, and tissue-material interfaces in dental medicine. Two-photon excitation fluorescence microscopy (TPEF) is able to detect the two-photon excited autofluorescence of dental tissues, and the second harmonic generation (SHG) can detect second-order nonlinear susceptibility of collagen type I, the most abundant dentinal organic substance [1,2].

The objective of this study was to microscopically test the effect of Cold Atmospheric Plasma (CAP) [3,4] on the morphology of the dentin-adhesive interface, using NLSM.

Human molar teeth were cut in half for the CAP-treated and control samples. The influence of CAP on standard etch-and-rinse (ER) or self-etch (SE) procedures was investigated. The following CAP configurations were used: feeding gas He, gas flow 1 slm, deposited power in the plasma power input 1 W or 2 W, and tip-to-surface distance 2 mm or 4 mm. The CAP-treated ER group was firstly etched and treated by CAP, before adhesive application. The SE group was treated by CAP before the adhesive placement. The control groups underwent the same process omitting the CAP phase. NLSM was used to image the morphology of hybrid layers.

The results demonstrated that the CAP causes the removal of the smear layer and opens the tubules. The tubules are not only more open but changed by CAP regarding their surface properties so that the permeation of the adhesive is highly favored. Compared to the control groups of around 20-30 μm hybrid layers, the length of resin tags in the CAP treated ER group was measured to even up to 600 μm, and in the CAP-treated SE group they were extended up to 100 μm.

CAP treatment of dentin drastically changes the morphology of the hybrid layer and the extension of resin tags. There is a need for additional analysis in the field to examine the influence of these changes on the quality of the dentin-adhesive interface.

REFERENCES
[1] T. Lainović, J. Margueritat, Q. Martinet, X. Dagany, L. Blažić, D. Pantelić, M.D. Rabasović, A.J. Krmpot and T. Dehoux, Acta Biomater 105, 214-222 (2020).
[2] T. Cloitre, I.V. Panayotov, H. Tassery, C. Gergely, B. Levallois and F.J.G. Cuisinier, J Biophotonics 6, 330-337 (2013)
[3] J.N. Stašić, N. Selaković, N. Puač, M. Miletić, G. Malović, Z.Lj. Petrović, D.N. Veljović and V. Miletić, Clin Oral Invest 23, 1383–1396 (2019).
[4] A. Stancampiano, D. Forgione, E. Simoncelli, R. Laurita, R. Tonini, M. Gherardi and V. Colombo, J Adhes Dent 21, 229-237 (2019).

Effects of laser heating on luminescent properties of Gd$_2$O$_3$:Er,Yb nanophosphor

D. Sevic[1], M.S. Rabasovic[1], J. Krizan[2], S. Savic-Sevic[1], M.D. Rabasovic[1], B.P. Marinkovic[1]
and M.G. Nikolic[1]

[1]*Institute of Physics, Belgrade, Serbia*
[2]*AMI d.o.o., Ptuj, Slovenia*
e-mail:sevic@ipb.ac.rs

In this study we analyze effects of laser heating on luminescent properties of nanocrystalline Gd$_2$O$_3$ doped with Er^{3+} and Yb^{3+} cations. Material was synthesized by combustion method, as described in [1]. Our experimental setup is presented in detail in [2,3,4]. In this study we have used pulsed laser diode excitation at 980 nm. Variable laser pulse energy was obtained by varying the laser pulse duration. Used laser diode has both continual and pulse mode. In continual mode its power is 1 W; in pulse mode it is possible to tune pulse duration and repetition, thus obtaining different average excitation powers. Here, we have used repetition rate of 200 Hz, with varying pulse duration between 20 µs and 200 µs, so average excitation power is between 8 mW and 80 mW.

Generally, laser power heating effects are unwanted and should be avoided in luminescence thermometry experiments; external heater and thermometer are used to calibrate the temperature sensing curve. Interestingly enough, the thermometry system, based on laser heating of sample, applicable for biomedical purposes, is described in [5].

Luminescence spectra of Gd$_2$O$_3$:Er^{3+},Yb^{3+} excited at room temperature with different laser excitation powers are shown in Figure 1. It should be noted that excitation power is intentionally much higher than used in [3]. Based on temperature sensing calibration curve presented in [3] for the same sample it could be estimated that the material is locally heated to about 375 K for pulse time of 200 µs.
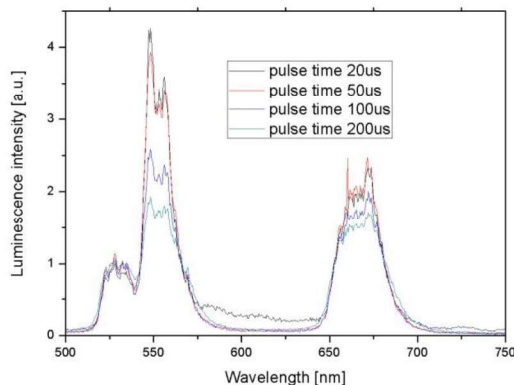
Figure 1. Luminescence spectra of Gd$_2$O$_3$:Er^{3+},Yb^{3+} excited at room temperature with different laser powers.

REFERENCES
[1] J. Krizan, M. Mazaj, V. Kaucic, I. Bajsic, J. Mozina, Acta Chim. Slov. 61, 608 (2014).
[2] A. Vlasic, D. Sevic, M.S. Rabasovic, J. Krizan, S. Savic-Sevic, M.D. Rabasovic, M. Mitric,
B.P. Marinkovic, M.G. Nikolic, Journal of Luminescence, 199, 285 (2018).
[3] D. Sevic, M.S. Rabasovic, J. Krizan, S. Savic-Sevic, M.D. Rabasovic, B.P. Marinkovic,
M.G. Nikolic, Optical and Quantum Electronics 52, 232 (2020).
[4] D. Sevic, M.S. Rabasovic, J. Krizan, S. Savic-Sevic, M.G. Nikolic, B.P. Marinkovic, M.D. Rabasovic, J. Phys. D: Appl. Phys. 53, 015106 (2020).
[5] M.F. Ferreira, K.Z.R. de Sousa, W.L. Massarotto, E.G. Ricci, E.H. de Faria, K.J. Ciuffi,
D. Sevic, L.A. Rocha, E.J. Nassar, J. Braz. Chem. Soc., 32(2) 376 (2021).

Using SOLO software package for classification of temperature dependent luminescence spectra

D. Sevic[1], M.S. Rabasovic[1], J. Krizan[2], S. Savic-Sevic[1], M.D. Rabasovic[1], M.G. Nikolic[1]
and B.P. Marinkovic[1]

[1]*Institute of Physics, Belgrade, Serbia*
[2]*AMI d.o.o., Ptuj, Slovenia*
e-mail:sevic@ipb.ac.rs

In this study we use SOLO software package (Version 8.8, Eigenvector Research Inc, USA) for classification of temperature dependent luminescence spectra of nanocrystalline Gd_2O_3 doped with Er and Yb. Material was synthesized by combustion method, as described in [1]. Our experimental setup is presented in detail in [2,3]. In [4,5] we have used Principal Component Analysis of luminescence spectra of thermophosphors; here, we use classification tools based on more sophisticated K-Nearest Neighbor and K-Means Nearest Group algorithms.

Classification results (shown as dendrograms) of luminescence spectra of $Gd_2O_3:Er^{3+},Yb^{3+}$ at different temperatures using K-Nearest Neighbor and K-Means Nearest Group algorithms are shown in Figure 1. Although dendrograms are different, the groups determined by both methods are the same; moreover, the test luminescence spectra are also classified in temperature groups where they belong. So, the machine could be trained to differentiate spectral data obtained on different temperatures.
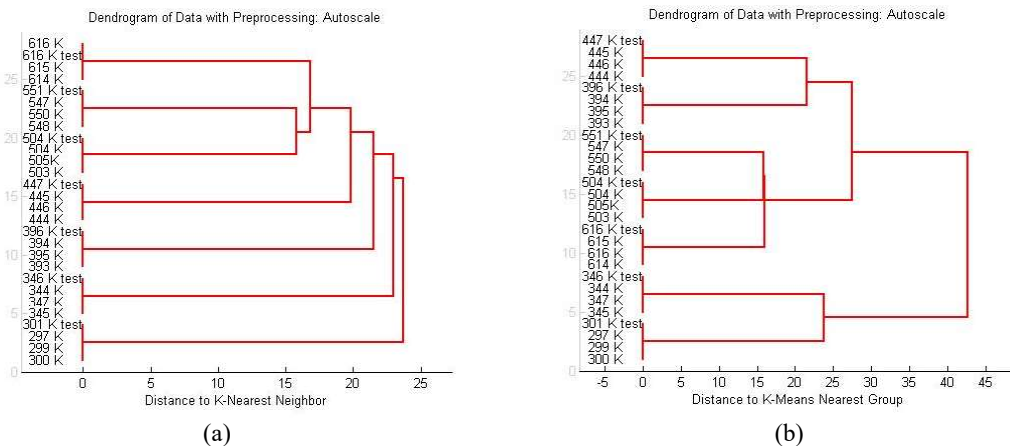
Figure 1. Classification results (shown as dendrograms) of luminescence spectra of $Gd_2O_3:Er^{3+},Yb^{3+}$ at different temperatures using (a) K-Nearest Neighbor and (b) K-Means Nearest Group algorithms.

REFERENCES

[1] J. Krizan, M. Mazaj, V. Kaucic, I. Bajsic, J. Mozina, Acta Chim. Slov. 61, 608 (2014).

[2] D. Sevic, M.S. Rabasovic, J. Krizan, S. Savic-Sevic, M.D. Rabasovic, B.P. Marinkovic, M.G. Nikolic, Optical and Quantum Electronics 52, 232 (2020).

[3] D. Sevic, M.S. Rabasovic, J. Krizan, S. Savic-Sevic, M.G. Nikolic, B.P. Marinkovic, M.D. Rabasovic, J. Phys. D: Appl. Phys. 53, 015106 (2020).

[4] D. Sevic, A. Vlasic, M.S. Rabasović, S. Savic-Sevic, M.D. Rabasović, M.G. Nikolić, B. D. Muric, B. P. Marinković, J. Križan, Tehnika 75(3), 279 (2020).

[5] D. Sevic, J. Krizan, M. S. Rabasovic, B.P. Marinkovic, Eur. Phys. J. D 75, 56 (2021).

Book of abstracts
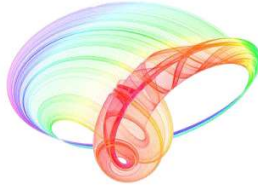
PHOTONICA2021

VIII International School and Conference on Photonics

& HEMMAGINERO workshop

23 - 27 August 2021,

Belgrade, Serbia

Editors

Mihailo Rabasović, Marina Lekić and Aleksandar Krmpot

Institute of Physics Belgrade, Serbia

Belgrade, 2021

Temperature Effects on Luminescent Properties of Sr₂CeO₄:Eu³⁺ Nanophosphor: a Machine Learning Approach

DRAGUTIN ŠEVIĆ, University of Belgrade,
Institute of Physics Belgrade, Belgrade
ANA VLAŠIĆ, University of Belgrade,
Institute of Physics Belgrade, Belgrade
MAJA S. RABASOVIĆ, University of Belgrade,
Institute of Physics Belgrade, Belgrade
SVETLANA SAVIĆ-ŠEVIĆ, University of Belgrade,
Institute of Physics Belgrade, Belgrade
MIHAILO D. RABASOVIĆ, University of Belgrade,
Institute of Physics Belgrade, Belgrade
MARKO G. NIKOLIĆ, University of Belgrade,
Institute of Physics Belgrade, Belgrade
BRANKA D. MURIĆ, University of Belgrade,
Institute of Physics Belgrade, Belgrade
BRATISLAV P. MARINKOVIĆ, University of Belgrade,
Institute of Physics Belgrade, Belgrade
JANEZ KRIŽAN, AMI, d. o. o, Ptuj, R. Slovenia

In this paper we analyze possibilities of application of Sr₂CeO₄:Eu³⁺ nanopowder for temperature sensing using machine learning. The material was prepared by simple solution combustion synthesis. Photoluminescence technique has been used to measure the optical emission temperature dependence of the prepared material. Principal Component Analysis, the basic machine learning algorithm, provided insight into temperature dependent spectral data from another point of view than usual approach.

Key words*: Photoluminescence, New materials, Thermographic phosphors*

1. INTRODUCTION

Nowadays, nano materials have more and more advantages over bulk materials. Nano science inevitably entered our world [1]. Thermographic nano phosphors are widely used in many applications [2-7]. They typically consist of a ceramic host and rare-earth dopant. The temperature dependency of their luminescence is used for remote temperature sensing. For obvious reasons, non contact measurements have many advantages. Thermographic remote monitoring of laser

cleansing is described in [8].

Strontium cerium oxide (Sr₂CeO₄) nano phosphors doped with europium ions (Eu³⁺), Sr₂CeO₄:Eu³⁺ are described in many scientific papers. As shown in [9], emission color change in a wide range of temperatures proves a great potential of Sr₂CeO₄:Eu³⁺ nanocrystals for industrial applications, particularly in nanothermometric technology. Moreover, additional application possibilities for this material are provided by the fact that the samples with different grain sizes are characterized by various luminescence colors [9]. The possibility of application of this nanophosphor in single-color and two-color fluorescence thermometry techniques in temperature range of 303–523 K has been proposed in [10]. In [11] it was shown that the Eu³⁺ doped Sr₂CeO₄ phosphors emitting white light (by combining blue, green and red emissions) has potential

applications not only in the fields of lamps and display devices under 280 nm excitation, but also in the field of LEDs under near UV (350 nm) excitation. $Sr_2CeO_4:Eu^{3+}$ considered as a source of anti-stokes white light generated under near infrared excitation was analyzed in [12]. Various methods of synthesis and studies of structural and luminescent characteristics of nanophosphors based on $Sr_2CeO_4:Eu^{3+}$ or nondoped Sr_2CeO_4 are reported in [9-13], and references therein.

In this study, we analyze $Sr_2CeO_4:Eu^{3+}$ nanopowders, efficiently prepared using a solution combustion synthesis (SCS) method [14,15]. The main characteristics of this process are simplicity and low cost. The structure of prepared materials has been confirmed and characterized using X-ray powder diffraction (XRD), scanning electron microscope (SEM) and photoluminescence (PL) techniques [15]. The most of europium luminescence comes from transitions from the $^5D_0$ and $^5D_1$ state; and they are usually used for fluorescence intensity ratio technique for remote temperature sensing.

In our recent publication [16] we have shown that $Sr_2CeO_4:Eu^{3+}$ made by solution combustion synthesis could be used as a red phosphor. In [15] we have studied the possibility of using the synthesized $Sr_2CeO_4:Eu^{3+}$ for temperature measurements, using usual approach of calculating the calibration curves.

However, availability of more and more fast computers, capable of machine learning, gave us an idea of different approach. Here, we analyze the possibilities of training the computer to recognize optical emission spectra of $Sr_2CeO_4:Eu^{3+}$ at different temperatures. So, this paper describes extension of our work presented in [15].

2. EXPERIMENTAL PROCEDURE

The preparation of samples

Europium doped Sr_2CeO_4 nanopowders were prepared by solution combustion method, similarly as described in [14,15]. Stoichiometric quantities of starting chemicals $Sr(NO_3)_2$, CH_4N_2O, $Ce(NO_3)_3 \times 6H_2O$, and $Eu(NO_3)_3 \times 6H_2O$ with the purity of 99.99% were chosen to obtain the Eu^{3+} concentration in Sr_2CeO_4 of 2.5 at.% ($Sr_{2-0.05}Eu_{0.05}CeO_4$). The used chemicals were purchased from ABCR, and urea, $(NH_2)_2CO$, from Sigma-Aldrich.

The dry mixture of 10.32 g (48.75 mmol) of $Sr(NO_3)_2$, 15.015 g (250 mmol) of CH_4N_2O, 10.86 g (25 mmol) of $Ce(NO_3)_3 \times 6H_2O$ and 0.558 g (1.25 mmol) of $Eu(NO_3)_3 \times 6H_2O$ was combined with the mixture of 4.8 g (60 mmol) of ammonium nitrate and 3.003 g (50 mmol) of urea which were used as organic fuels.

The prepared starting reagents were combusted with the flame burner at approximately 500 ºC, yielding a voluminous foamy pink powder in an intensive exotermic reaction. After the solution combustion synthesis, the nanopowder was annealed for 2 hours, in air atmosphere, at 900 °C. The annealing of the material is needed to achieve optimal optical characteristics of synthesized material.

Experimental details

As an excitation source for photoluminescence measurements we used the output of the optical parametric oscillator (Vibrant OPO), continuously tunable over a spectral range from 320 nm to 475 nm. Laser pulse duration is about 5 ns, at a repetition rate of 10 Hz. Time-resolved streak images of the luminescence response of $Sr_2CeO_4:Eu^{3+}$ nanopowder excited by the OPO system were acquired by Hamamatsu streak camera equipped with a spectrograph.

Emission spectra of $Sr_2CeO_4:Eu^{3+}$ were also acquired using Ocean Optics USB2000 and AVANTES AvaSpec 2048TEC USB2 spectrometers and continuous laser diode excitation at 405 nm. The experimental setup for luminescence measurement as a function of temperature is described in [17].

For machine learning simulation experiments we have used Solo software package (Version 8.8, Eigenvector Research Inc, USA).

3. RESULTS AND DISCUSSION

The structure of material was confirmed by XRD patterns and SEM images, see [15].

The streak image of the time resolved photoluminescence spectrum of the $Sr_2CeO_4:Eu^{3+}$ using the 330 nm excitation is presented in Figure 1. Horizontal scale of streak image corresponds to wavelength, vertical scale shows development of spectra in time. Images are presented in pseudocolor, where different colors mean different optical intensities.

The $^5D_1$-$^7F_3$ transition (583 nm), located closely between the $^5D_0$-$^7F_0$ (582 nm) and the $^5D_0$-$^7F_1$ (587 nm) transitions is easy to identify on the time resolved image. Its time integrated peak has a comparable intensity to the intensities of peaks originating from nearby $^5D_0$ levels (see the line profile denoted by a red curve in Fig. 4).

The luminescence spectra presented in publications usually do not have the time resolution, so it is hard to guess which transitions are short lived. Streak image presented in Figure 1 shows clearly that the $^5D_1$-$^7F_3$ transition (583 nm) has a much higher intensity and a much shorter lifetime than nearby transitions from $^5D_0$ state.
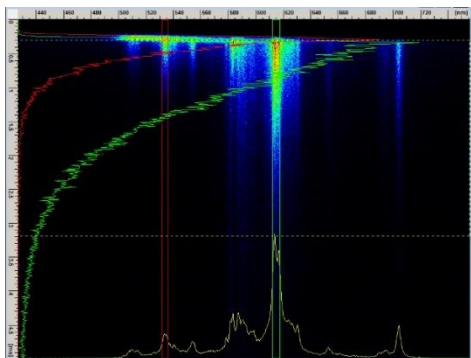
Figure 1 - Streak image of the photoluminescence spectrum of $Sr_2CeO_4:Eu^{3+}$ nanophosphor. (OPO excitation at 330 nm).

The temperature dependency of intensity ratio of spectral lines

The luminescence of samples was measured both using pulsed (OPO) and continuous excitation. The measured luminescence spectra of Eu^{3+} doped Sr_2CeO_4 at various temperatures are presented in Figure 2. The spectra were obtained by using continuous laser diode excitation at 405 nm.
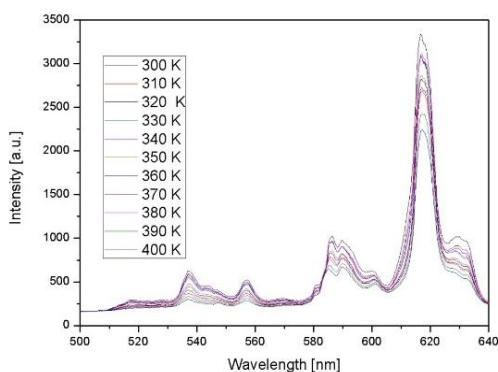

Figure 2 - Luminescence spectra of Eu^{3+} doped Sr_2CeO_4 at various temperatures. (Continuous laser diode excitation at 405 nm).

The fluorescence intensity ratio (FIR) of spectral line intensities from the $^5D_0$ and $^5D_1$ transitions depend on two physical processes: the thermalization of the $^5D_1$ level with rising temperature, where the energy difference to populate the $^5D_1$ level from the $^5D_0$ level is fully covered by phonons; and the nonradiative quenching of the $^5D_0$ and $^5D_1$ levels through the charge transfer state. Looking at Figure 2 we can see that intensity ratio between lines at 614 nm and 537 nm is temperature dependent.

The Principal Component Analysis of temperature dependent $Sr_2CeO_4:Eu^{3+}$ spectra

Principal component analysis (PCA) finds combinations of variables, or *factors*, that describe major trends in the data [18].

If X is a data matrix with *m* rows and *n* columns, each variable being a column and each sample a row,

PCA decomposes X as the sum of rt_i and p_i, where *r* is the rank of the matrix X:

$$X = t_1p^T{}_1 + t_2p^T{}_2 + ... + t_kp^Tk + ... + t_rp^Tr$$

where $r \leq \min\{m,n\}$

The t_i, p_i pairs are ordered by the amount of variance captured. The t_i vectors are known as scores and contain information on how the samples relate to each other. The p_i vectors are known as loadings and contain information on how the variables relate to each other.

For analysis presented here, we use luminescence spectra of Eu^{3+} doped Sr_2CeO_4 at temperatures between 300 and 400 K, measured with the step of 5 K. About a half of the spectral data (measured at 300, 310, 320 ... K) are used to train the PCA algorithm. Another half of the spectral data (measured at 305, 315, 325 .... K) are used to test the obtained PCA model.

Scores on first two principal components of measurement data of temperature dependence of luminescence of $Sr_2CeO_4:Eu^{3+}$ nanophosphor are shown in Figure 3. It could be seen that scores on PC 1 gradually move along the x axis, while scores on PC 2 oscillate along the y axis.
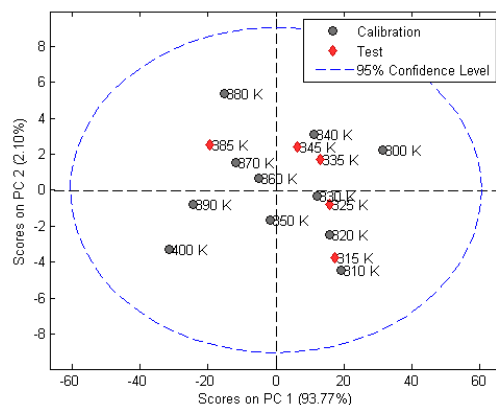

Figure 3 - Scores on first two principal components of measurement data of temperature dependence of luminescence of $Sr_2CeO_4:Eu^{3+}$ nanophosphor.

We see that the predictions for future measurements are well within the 95% confidence level. However, it should be noted that this approach is different, and not necessarily better, than usual method based on fitting the temperature sensing calibration curve. Namely, the machine is trained on restricted size of training data set. The remote temperature estimation is based on classification of newly obtained data in regard the calibrated data. The classification is implemented by comparing the scores distances between the calibrated data and the newly measured ones. So, the larger the training set, the better is resolution of the remote temperature sensing.

4. CONCLUSION

In this paper we have applied the Principal Component Analysis, the basic machine learning algorithm, on temperature dependent $Sr_2CeO_4:Eu^{3+}$ spectral data. We have shown that the machine could be trained to differentiate spectral data obtained on different temperatures. However, the resolution of this remote temperature sensing technique depends on the size of spectral data training set. For relatively small training set, the predicted data are well within the confidence level of 95 %.

5. ACKNOWLEDGEMENT

REFERENCES

[1] Uskokovic V, Nanoscience: Whence it entered our World, *Tehnika*, Vol. 22, pp 795-803, 2013.

[2] Jaque D, Vetrone F, Luminescence nanothermometry, *Nanoscale*, Vol. 4, pp 4301-4326, 2012.

[3] Brites C. D. S, Lima P. P, Silva N. J. O, Millan A, Amaral V. S, Palacio F, Carlos L. D, Thermometry at the nanoscale, *Nanoscale*, Vol. 4, pp. 4799-4829, 2012.

[4] Aldén M, Omrane A, Richter M, Särner G, Thermographic phosphors for thermometry: A survey of combustion applications, *Progress in Energy and Combustion Science*, Vol. 37, pp. 422-461, 2011.

[5] Allison S. W, Gillies G. T, Remote thermometry with thermographic phosphors: Instrumentation and applications, *Rev. Sci. Instrum*, Vol. 68, pp 2615-2650, 1997.

[6] Goss L. P, Smith A. A, Post M. E, Surface thermometry by laser-induced fluorescence, *Rev Sci. Instrum*, Vol. 60, pp 3702-3706, 1989.

[7] Heyes A. L, On the design of phosphors for high-temperature thermometry, *Journal of Luminescence*, Vol. 129, pp 2004-2009, 2009.

[8] Ristic S, Polic S, Knjezevic D, Radojkovic B, Linic S, Jegdic B, Termografija u kontroli efikasnosti i bezbednosti laserskog čišćenja, *Tehnika*, Vol. 28, pp 623-629, 2019.

[9] Stefanski M, Marciniak L, Hreniak D, Strek W, Size and temperature dependence of optical properties of $Eu^{3+}:Sr_2CeO_4$ nanocrystals for their application in luminescence thermometry, *Mat. Res. Bull.,* Vol. 76, pp 133–139, 2016.

[10] Shi L, Zhang H, Li C, Su Q., Eu^{3+} doped Sr_2CeO_4 phosphors for thermometry: single-color or two-color fluorescence based temperature characterization, *RSC Advances*, Vol. 1, pp. 298–304, 2011.

[11] Suresh K, Poornachandra Rao N. V, Murthy K. V. R, Photoluminescent properties of $Sr_2CeO_4:Eu^{3+}$ and $Sr_2CeO_4: Eu^{2+}$phosphors suitable for near ultraviolet excitation, *Bull. Mater. Sci.*, Vol. 37, pp 1191–1195, 2014.

[12] Stefanski M, Lukaszewicz M, Hreniak D, Strek W, Laser induced white emission generated by infrared excitation from $Eu^{3+}: Sr_2CeO_4$ nanocrystals, *Jour. Chem. Phys.*, Vol. 146, pp 104705-1-7, 2017.

[13] Stefanski M, Marciniak L, Hreniak D, Strek W, Influence of grain size on optical properties of Sr_2CeO_4 nanocrystals, *Jour. Chem. Phys.,* Vol. 142, pp 184701-1-7, 2015.

[14] Rabasovic M. S, Sevic D, Krizan J, Terzic M, Mozina J, Marinkovic B. P, Savic Sevic S, Mitric M, Rabasovic M. D, Romcevic N, Characterization and luminescent properties of Eu^{3+} doped $Gd_2Zr_2O_7$ nanopowders*, J. Alloys and Compounds* Vol. 622, pp 292-295, 2015.

[15] Vlasic A, Sevic D, Rabasovic M. S, Krizan J, Savic-Sevic S, Rabasovic M. D, Mitric M, Marinkovic B. P, Nikolic M. G, Effects of temperature and pressure on luminescent properties of $Sr_2CeO_4: Eu^{3+}$ nanophosphor, *Journal of Luminescence*, Vol. 199 pp 285–292, 2018.

[16] Rabasovic M. S, Krizan J, Gregorcic P, Rabasovic M. D, Romcevic N, Sevic D, Time-resolved luminescence spectra of Eu^{3+} doped YVO_4, Sr_2CeO_4 and $Gd_2Zr_2O_7$ nanopowders, *Optical and Quantum Electronics*, Vol. 48, pp163-1-4, 2016.

[17] Rabasovic M. D, Muric B. D, Celebonovic V, Mitric M, Jelenkovic B. M, Nikolic M. G, Luminescence thermometry via the two-dopant intensity ratio of $Y_2O_3:Er^{3+}$, Eu^{3+}, J. *Phys. D: Appl. Phys.*, Vol. 49, pp 485104-1-6, 2016.

[1] Hoteling H, Analysis of a Complex of Statistical Variables into Principal Components. *Journal of Educational Psychology*, Vol. 24, 417-441, 1933.

REZIME

TEMPERATURNA ZAVISNOST LUMINESCENTNIH OSOBINA SR_2CEO_4:EU^{3+}
NANOFOSFORA: PRISTUP MAŠINSKIM UČENJEM

U ovom radu analizirali smo mogućnosti primene Sr_2CeO_4:Eu^{3+} nanopraha za merenje temperaruture primenom mašinskog učenja. Materijal je pripremljen jednostavnom metodom sinteze sagorevanja rastvora. Fotoluminescentna tehnika je korišćena za merenje temperaturne zavisnosti optičke emisije pripremljenog materijala. Analiza ključnih faktora omogućila nam je uvid u temperaturnu zavisnost spektralnih podataka sa drugačije tačke gledišta nego što je uobičajeni pristup.

Ključne reči: *fotoluminescencija, novi materijali, termografski fosfori*

Effects of temperature on luminescent properties of YVO$_4$:Eu^{3+} nanophosphor

D. Šević[1], M.S. Rabasović[1], J. Križan[2], S. Savić-Šević[1], M. G. Nikolic[1], B. P. Marinkovic[1],

and M.D. Rabasović[1]

(1) *Institute of Physics, University of Belgrade, Belgrade, Serbia*

(2) *AMI d.o.o., Ptuj, Slovenia*

Contact: Dragutin Sevic (sevic@ipb.ac.rs)

Abstract. In this study we investigate time resolved luminescence spectra of nano powder samples of YVO$_4$:Eu^{3+}. Intensity ratios of spectral lines were used for determining the calibration curves for remote temperature sensing. Possibilities of using the luminescence lifetime and risetime for temperature sensing are also investigated. Our experimental setup and some results regarding this phosphor are presented in detail in [1,2]. We used OPO (Optical Parametric Oscillator) for excitation. The output of the OPO can be continuously tuned from 320 nm to 475 nm. For measurements presented here the output energy of OPO was about 5 mJ. The structure of material was observed by high resolution scanning electron microscope (SEM). The experimental setup for luminescence measurement as a function of temperature is described in [3]. Effects of temperature on luminescent properties of YVO$_4$:Eu^{3+} nanophosphor, for two temperatures, are shown in Fig. 1.
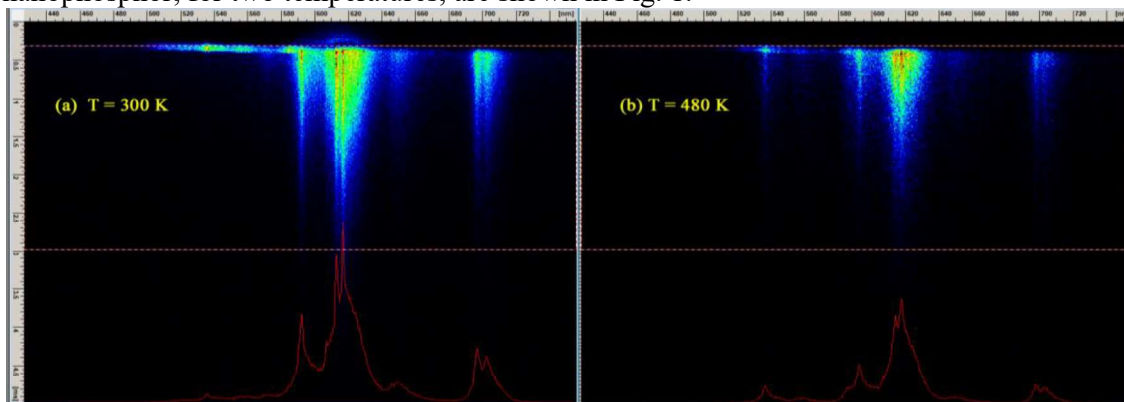
Figure 1. Streak images of Eu doped YVO$_4$ nanopowder, at (a) T = 300 K , (b) T = 480 K. Laser excitation is at 330 nm.

The luminescence lifetime and risetime of this phosphor were determined by streak camera (HPD-TA) software. We obtained that the lifetime of the level $^5D_1$ is about 8.7 μs and the level $^5D_0$ lifetime is about 0.93 ms [1]. We calculated the rise time according to Ranson equation [4]. We obtained that the rise time of luminescence of our sample of YVO4:Eu^{3+} for the $^5D_0 - ^7F_2$ line is about 8.1 μs. Our results show that Eu doped YVO$_4$ nanopowder could be used for remote temperature sensing.

REFERENCES
[1] D. Sevic, M.S. Rabasovic, et al, *Materials Research Bulletin* **88** (2017) 121−126.
[2] M. S. Rabasovic J. Krizan, et al, *Opt. Quant. Electron.* **48** (2016) 163.
[3] M. D. Rabasovic, B. D. Muric, M. G. Nikolic, et al, *J. Phys. D: Appl. Phys.* **49** (2016) 485104-1-6.
[4] R. M. Ranson, E. Evangelou, and C. B. Thomas, *Applied Physics Letters* **72** (1998) 2663-2664.

Development of method for obtaining free fungal protoplast in *Phycomyces blakesleeanus* by cell wall microsurgery using Ti:Sa laser

Tanja Pajić[1], Katarina Stevanović[1], Aleksandar Krmpot[2], Mihajlo Rabasovic[2], Vladimir. Lazović [2], Dejan Pantelić[2], Branislav Jelenković[2], Miroslav Zivić[1] and <u>Nataša Todorović</u>[3]

(1) *Faculty of Biology, University of Belgrade, Studenstski trg 3, 11000 Belgrade, Serbia*

(2) *Institute of Physics, University of Belgrade, Pregrevica 118, 11000 Belgrade, Serbia*

(3) *Institute for Biological Research «Siniša Stanković», University of Belgrade, Bulevar Despota Stefana 142, 11000 Belgrade Serbia*

Contact: N. Todorović (<u>nara@ibiss.bg.ac.rs</u>)

Abstract. Ion channels in filamentous fungi are poorly characterized, with only five ion channels described so far. This lack of data is due to significant technical difficulties caused by presence of sturdy and highly regenerative cell wall on the surface of hyphal plasma membrane. Knowledge about membrane physiology of fungi has much broader potential impact than the obvious need to fight pathogens (in humans and in crops), pertaining to evolutionary and structure-function aspects of membrane ion channel physiology and specifically, to important questions on micorhizal communication with plants.We want to remove the cell wall from hypha of model fungal organism, *Phycomyces blakesleeanu*s in a manner that leaves cell membrane intact, clean and functional. The goal is to develop a reliable method for electrophysiological (by patch-clamp technique) exploration of any fungal cell. The approach that we are pursuing is cell wall microsurgery by tightly focused femtosecond pulsed laser beam. *Phycomyces blakesleeanus* hypha are first imaged using homemade nonlinear laser scanning microscope by detecting two photon excitation fluorescence signal. The light source is focused Ti:Sa laser (operating at 730nm, with 76MHz repetition rate and 160fs pulse duration). Subsequently, the cell wall removal is acomplished by cell microsurgery by the same Ti:Sa laser. Calcofluor White, fluorescent dye that binds to chitinous fungal cell wall, is used to increase signal to noise ratio and Carl Zeiss, EC Plan-NEOFLUAR, 40×1.3 oil immersion objective is used for the collection of the fluorescence signal. A visible interference filter (415nm - 685nm) was placed in front of detector to remove scattered laser light. Current status of development of the procedure is that we can ablate the cell wall from hypha (plasmolysed, in order to keep the plasma membrane reasonably away from the surgery area), and obtain exposed bulbs of protoplast after deplasmolysis. Approximately 30% of protoplast spheres obtained by cell surgery remain attached to the hypha and are sufficiently large for patch pipette contact. No successful gigaohmic contacts have been achieved by now, indicating that protoplast membrane obtained under our current experimental conditions is probably insufficiently clean from cell wall material or, alternatively, somehow functionally changed by proximity of surgery.
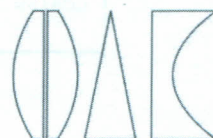
IP8
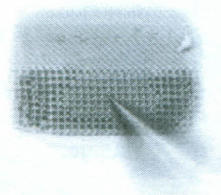
Зборник апстраката

Дванаеста радионица фотонике (2019)

(Конференција)

Book of Abstracts

12th Photonics Workshop

(Conference)

PHOTONICS CENTER

Програмски одбор:

др Бранислав Јеленковић

др Љупчо Хаџиевски,

др Павле Анђус

др Александер Ковачевић

др Зоран Грујић

др Марина Лекић

Scientific Committee:

Dr. Branislav Jelenković

Dr. Ljupčo Hadžievski,

Dr. Pavle Anđus

Dr. Aleksander Kovačević,

Dr. Zoran Grujić,

Dr. Marina Lekić

Организациони одбор:

др Зоран Грујић

др Марина Лекић

др Александер Ковачевић

др Дарко Васиљевић

др Драган Лукић

др Бранислав Јеленковић

Марија Ћурчић

Organizing Committee:

Dr. Zoran Grujić,

Dr. Marina Lekić,

Dr. Aleksander Kovačević,

Dr. Darko Vasiljević,

Dr. Dragan Lukic,

Dr. Branislav Jelenković,

Marija Curcic

Effects of temperature on luminescent properties of Gd_2O_3:Er,Yb nanophosphor

D. Šević[1], M.S. Rabasović[1], J. Križan[2], S. Savić-Šević[1], M.D. Rabasović[1], B. P. Marinkovic[1],

and M. G. Nikolic[1]

(1) *Institute of Physics, University of Belgrade, Belgrade, Serbia*

(2) *AMI d.o.o., Ptuj, Slovenia*

Contact: Dragutin Sevic (sevic@ipb.ac.rs)

Abstract. Recently, we have started investigations of upconverting nanophosphors and effects of temperature on their luminescent properties. In this study we analyze nanocrystalline Gd_2O_3 doped with Er^{3+} and Yb^{3+} cations. Material was synthesized by combustion method, as described in [1]. Fluorescence intensity ratios (FIR) were determined in a range from 50 $^{\circ}$C up to 300 $^{\circ}$C in [1]. Here, we have obtained time resolved luminescence spectra of nano powder samples of Gd_2O_3:Er,Yb. Streak image of Gd_2O_3:Er,Yb phosphor emission is shown in Fig. 1 (a). Our experimental setup is presented in detail in [2,3]. However, in this study we have used pulsed laser diode excitation at 980 nm. The structure of material was observed by high resolution scanning electron microscope (SEM). The experimental setup for luminescence measurement as a function of temperature is described in [4]. Effects of temperature on luminescent properties of Gd_2O_3:Er,Yb phosphor are shown in Fig. 1 (b), where varying FIR between different transitions could be observed.
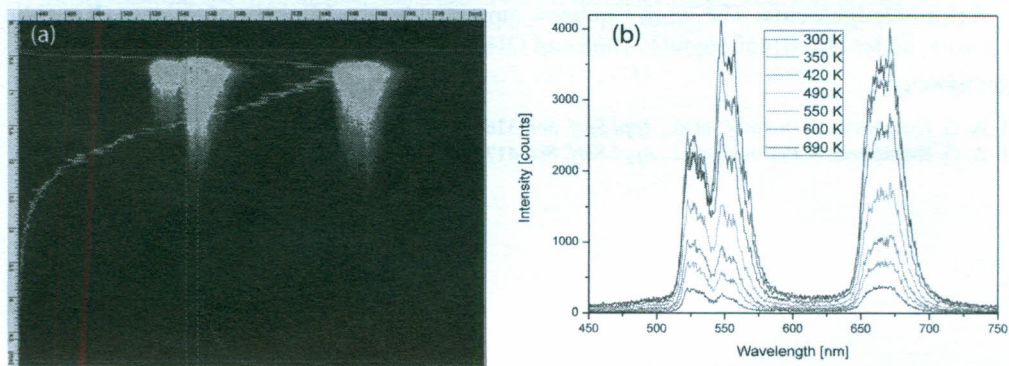
Figure 1. (a) Streak image of Er and Yb doped Gd_2O_3 nanopowder. (b) Emission spectra of Gd_2O_3:Er,Yb at different temperatures. Laser excitation is at 980 nm.

The luminescence lifetime of this phosphor was determined by streak camera (HPD-TA) software. Our preliminary results show that the lifetime of transition from the level $^4S_{3/2}$ is about 0.77 ms at room temperature, decreasing to about 0.07 ms at 623 K. Our analysis proves that synthesized Gd_2O_3:Er,Yb phosphor is appropriate for remote temperature sensing.

REFERENCES

[1] J. Krizan, M. Mazaj, et al, *Acta Chim. Slov.* **61** (2014), 608–614.
[2] D. Sevic, M.S. Rabasovic, et al, *Materials Research Bulletin* **88** (2017), 121–126.
[3] A. Vlasić, D. Šević, M.S. Rabasovic, et al, *Journal of Luminescence*, **199** (2018), 285-292.
[4] M. D. Rabasovic, B. D. Muric, M. G. Nikolic, et al, *J. Phys. D: Appl. Phys.* **49** (2016), 485104-1-6.

Photophysics and photochemistry of hemoglobin interaction with ultrashort laser pulses

Mihajlo D. Radmilović[1], Ivana Drvenica[2], Aleksandar Krmpot[1],Mihailo Rabasović[1]

(1)*Institute of Physics Belgrade, Pregrevica 118, 11080 Belgrade, Serbia*

(2) *Institute for Medical Research, University of Belgrade, Dr.Subotića 4, 11000 Belgrade, Serbia*

Contact:M. Radmilović (mihajlo.radmilovic@ipb.ac.rs)

Detection of fluorescence emission during the interaction of hemoglobin (Hb) with ultrashort laser pulses was observed in both *in vivo* and *in vitro* experiments[1,2], however, (Hb) is a non-fluorescent molecule at single-photon excitation. The mechanism of the two-photon fluorescence emission of specimens that contain (Hb) is unclear and still speculative. The latest results suggest that the interaction of ultrashort laser pulses with (Hb) is associated with the formation of (Hb) photoproduct [3]. Thus, two-photon fluorescence emission is probably related to the formed photoproduct, which chemical and photophysical properties are not completely understood so far. Here we present some revealed photophysical and photochemical properties of (Hb) photoproduct formation upon two-photon excitation. After irradiation at 730nm, using Ti: Sapphire laser (Coherent, Mira 900-F) with a pulse duration of 160fs, a fluorescent (Hb) photoproduct was formed. Square shape pattern of fluorescent (Hb) photoproduct (Figure 1.), created by raster-scanning using galvoscanning mirrors has been shown high stability and durability (for two-weeks). Moreover, it was possible to analyze formed (Hb) photoproducts by single-photon excitation microscopy, Uv-Vis, and Two-photon emission spectroscopy.
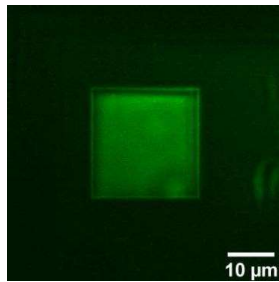

Figure 1. Scanning region of treated (Hb) thin layer with ultrashort laser pulses

There is a potential application of formed (Hb) photoproduct in studying Hemoglobin-related physiology and patophysiology [4, 5], as well as application out of biomedical field scope e.g., security and optical data storage.

REFERENCES

(1) Clay et al.,*The Journal of chemical physics* 126.2 (2007), 01B609.
(2) D. Li et al., *Optics letters*, **36**(6)(2011), 834-836.
(3) E. A. Shirshin et al., *Laser Physics Letters*, **15**(7)(2018), 075604.
(4) K. Bukara et al.,*Journal of biomedical optics*, **22**(2) (2017), 026003.
(5) G. D. Vigil & S. S. Howard,*Biomedical optics express*, **6**(10) (2015), 4098-4104.